WINTER 2024

GEMS & GEMOLOGY

90th ANNIVERSARY

VOLUME LX

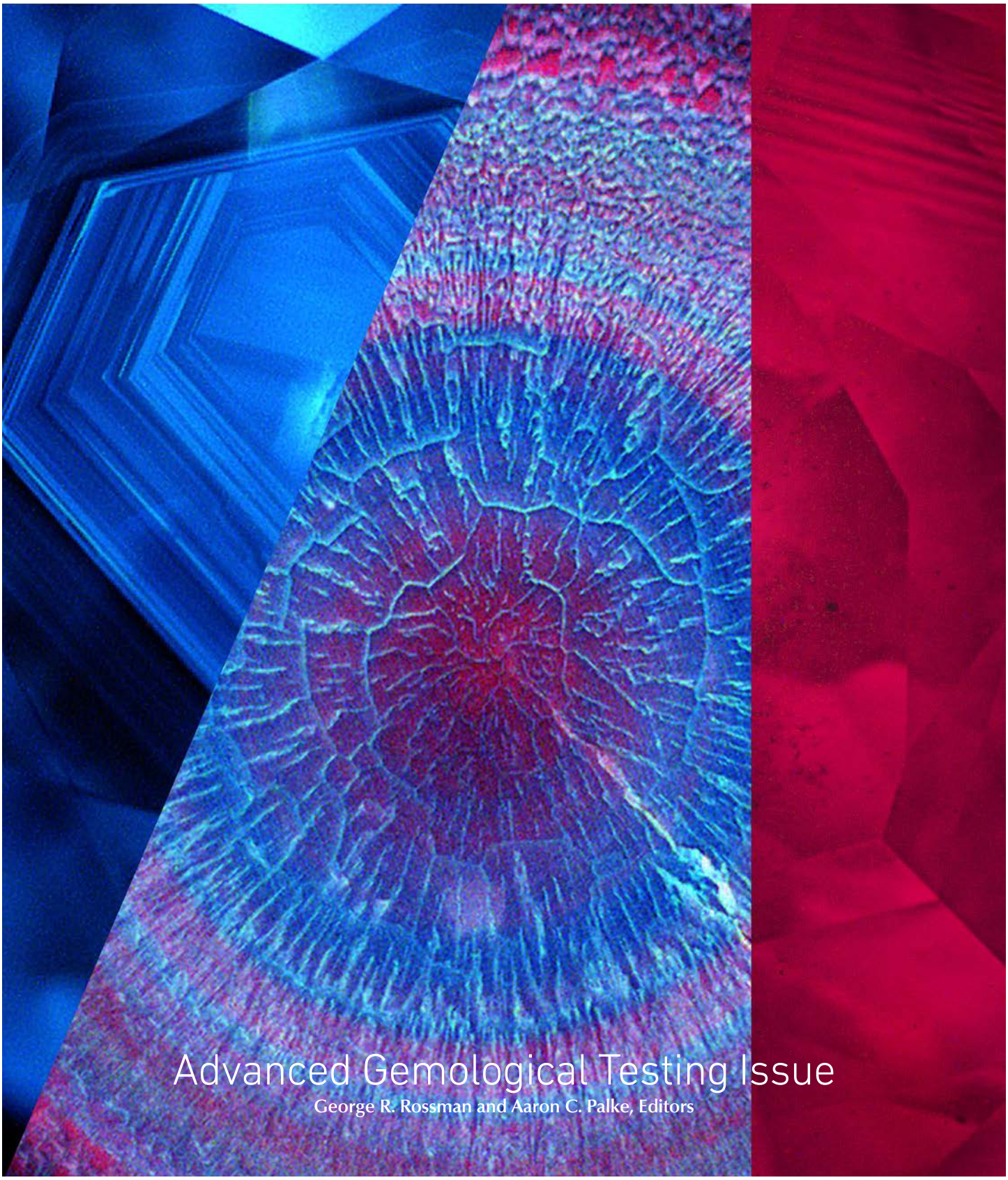

Advanced Gemological Testing Issue

George R. Rossman and Aaron C. Palke, Editors

THE QUARTERLY JOURNAL OF THE GEMOLOGICAL INSTITUTE OF AMERICA

GEMS & GEMOLOGY®
Winter 2024
VOLUME 60, No. 4

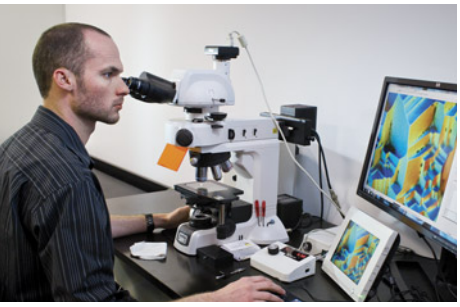
p. 446

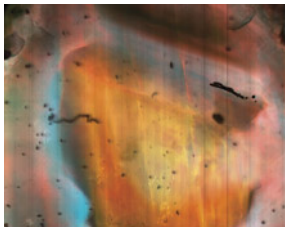
p. 507

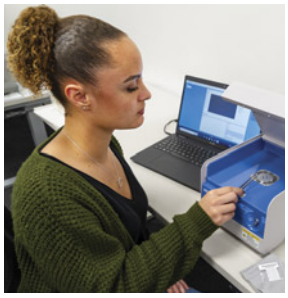
p. 538


p. 592


p. 601

p. 614

Introduction

Feature Articles

Afterword

In Memoriam

GEMS & GEMOLOGY®

gia.edu/gems-gemology

Customer Service
(760) 603-4200
gandg@gia.edu

Subscriptions
Copies of the current issue may be purchased for $29.95 plus shipping. Subscriptions are $79.99 for one year (4 issues) in the U.S. and $99.99 elsewhere. Canadian subscribers should add GST. Discounts are available for renewals, group subscriptions, GIA alumni, and current GIA students. To purchase print subscriptions, visit store.gia.edu or contact Customer Service. For institutional rates, contact Customer Service.

Database Coverage
Gems & Gemology's impact factor is 1.6, according to the 2023 Journal Citation Reports by Clarivate Analytics (issued June 2024). *G&G* is abstracted in Thomson Reuters products (Current Contents: Physical, Chemical & Earth Sciences and Science Citation Index—Expanded, including the Web of Knowledge) and other databases. For a complete list of sources abstracting *G&G*, go to gia.edu/gems-gemology, and click on "Publication Information."

Manuscript Submissions
Gems & Gemology, a peer-reviewed journal, welcomes the submission of articles on all aspects of the field. Please see the Author Guidelines at gia.edu/gems-gemology or contact the Managing Editor. Letters on articles published in *G&G* are also welcome. Please note that Field Reports, Lab Notes, Gem News International, Micro-World, Colored Stones Unearthed, Diamond Reflections, Charts, and In the Spotlight are not peer-reviewed sections but do undergo technical and editorial review.

Gems & Gemology is published quarterly by the Gemological Institute of America, a nonprofit educational organization for the gem and jewelry industry.

Postmaster: Return undeliverable copies of *Gems & Gemology* to GIA, The Robert Mouawad Campus, 5345 Armada Drive, Carlsbad, CA 92008.

Our Canadian goods and service registration number is 126142892RT.

About the Cover

This issue examines analytical tools used in modern gemology. One is DiamondView fluorescence imaging, which reveals structural features of the three gems on the cover (left to right): an I-color round brilliant diamond, a non-nacreous natural pearl cross section, and a blue sapphire. Images by Jemini Sawant, Ravenya Atchalak, and Aaron Palke.

Printing is by L+L Printers, Carlsbad, CA.

GIA World Headquarters The Robert Mouawad Campus 5345 Armada Drive Carlsbad, CA 92008 USA

ISSN 0016-626X

FSC www.fsc.org MIX Paper from responsible sources FSC® C006300

Analytical Techniques in Gemology: A Historical Overview

James E. Shigley

Gemology has become an increasingly technical field, driven by the need for more advanced analytical methods and instruments to test gem materials (figure 1). This shift reflects the evolving challenges of gem identification, a trend that has been well documented in major gemological journals. This special issue of *Gems & Gemology* will survey the testing instrumentation currently employed by GIA's laboratories, reviewing their applications, limitations, and the vital information each technology provides. Important aspects of their use for gem testing will be discussed. Note that equipment developed specifically for the GIA diamond quality grading system or other laboratory activities will not be included. This article opens the Winter 2024 edition by briefly examining the introduction and role of scientific instrumentation in gemology to address identification challenges in the marketplace.

HISTORICAL BACKGROUND

The use of scientific instruments for testing gems at GIA began a few years after its founding in 1931 (figure 2), as reported in early editions of this journal. Prior to that, there were few gem testing instruments designed specifically for jewelers. In the early 1900s, G.F. Herbert Smith at the British Museum in London championed the optical refractometer for gem testing (Herbert Smith, 1907). He and his contemporaries discussed additional practical tests such as dichroism, absorption spectra, density, and hardness. GIA founder Robert M. Shipley sought to expand the de-

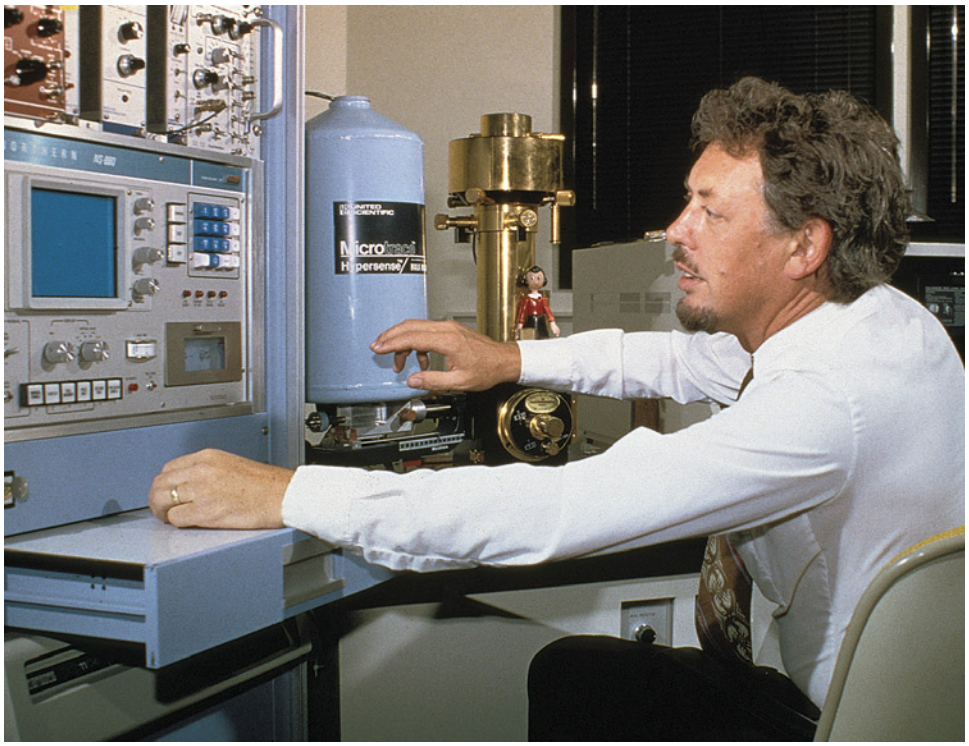

Figure 1. Dr. Vince Manson using GIA's first scanning electron microscope, acquired in 1976.

Figure 2. Robert Shipley Jr. working with gem testing equipment at GIA's early headquarters in Los Angeles. This 1937 photo is from a three-minute color film by Paramount Pictures for its "Popular Science" series, produced between 1935 and 1949 and shown in movie theaters nationwide.

velopment of testing instruments tailored to meet the needs of jewelers and gemologists, while educating them on these tools (figure 3).

In the late 1930s, GIA began evaluating and teaching the proper use of devices such as the loupe, microscope, hand spectroscope, refractometer, and

Figure 3. Standard testing equipment produced or distributed by GIA during the 1980s and 1990s.

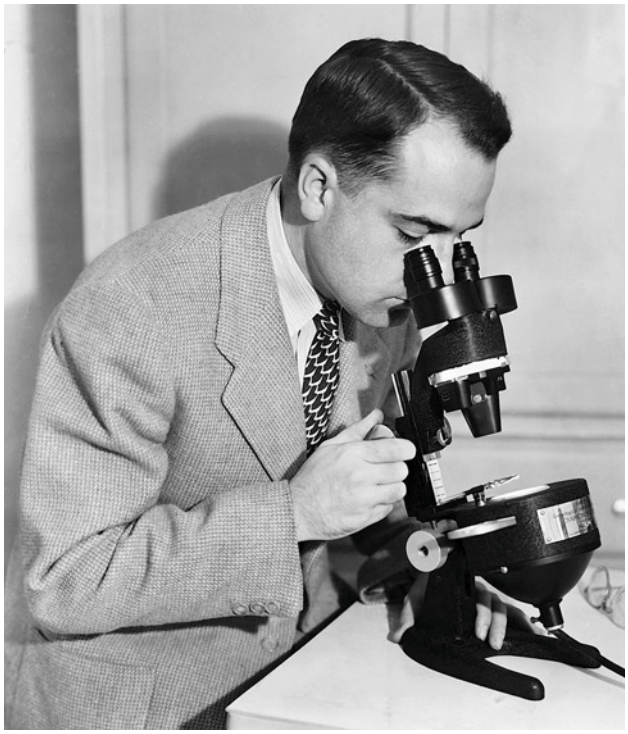

Figure 4. Richard Liddicoat using a stereomicroscope (the GIA Diamondscope) with darkfield illumination. Introduced in 1938, it provided improved viewing of inclusions and clarity features in gemstones.

dichroscope. These were produced by various manufacturers, including GIA. Some commercially available scientific instruments were useful for gem studies, but the special needs for holding, manipulating, and illuminating gems often required modifications (such as light source additions to the microscope). Some methods were adopted from the field of mineralogy. By the end of the decade, GIA was the exclusive U.S. distributor for several gemological instruments made abroad and had begun manufacturing its own specialized equipment, including a commercially available stereomicroscope fitted with darkfield illumination, introduced in 1938 (figure 4).

With the establishment of the GIA Gem Trade Laboratory in New York in the fall of 1949, gem testing for trade clients and the use of gemological instruments became more routine at GIA. This use increased with the introduction of the first GIA diamond grading reports in 1955. GIA Gem Instruments was established in 1966 to develop new equipment and refine existing tools. The acquisition of more advanced scientific instrumentation accelerated following the creation of GIA's research department in 1976. Investment in research staff and analytical instrumentation has continued to the present day, as evidenced by the articles in this special issue.

SCIENTIFIC INSTRUMENTS FOR GEM TESTING

Instrument development for gem testing often resulted from the need to address new identification challenges in the marketplace when existing instruments and methods were no longer sufficient. The introduction of a new piece of scientific equipment often inspired gem researchers to adapt it for their own needs. In recent decades, the increasing sophistication of gem synthesis and treatment techniques has accelerated the need for more advanced scientific instrumentation.

Several aspects of advanced instrumentation are worth mentioning. The testing procedure for gems submitted by laboratory clients must not result in visible damage or destruction to the samples, because these samples tend to be rare and highly valued by their owners. For testing, they must fit into and be held within the sample compartment of the instrument. Modification of the sample compartment may therefore be necessary. When recording spectra or conducting a chemical analysis, the testing location on the gem sample must be positioned so that it is accessible. For example, it may be more effective to bring the light signal directly to the gem using some type of flexible optical cable to capture a visible spectrum. In a high-volume production environment, both the analysis time and the ease of positioning and removing gem samples from an instrument are important factors.

The value of any data gathered from gems using scientific instruments becomes much more significant and useful when the results are stored in a searchable database and when they are collected on samples of known natural, synthetic, or treated origin. Many gems submitted to a laboratory for testing are of less certain origin, so the analytical data obtained from them can be problematic.

MICROSCOPY AND PHOTOMICROGRAPHY

Although glass lenses have been employed for magnification for many centuries, the use of what today would be called a microscope began in the mid-1600s. Scientists at the time were able to study materials at magnifications of up to about 300×. Over the following centuries, their application became extensive in many scientific fields (Kile, 2003). Microscopes using polarized light specifically designed for petrographic studies in geology became available in the 1870s. According to Gunter (2004), over the past

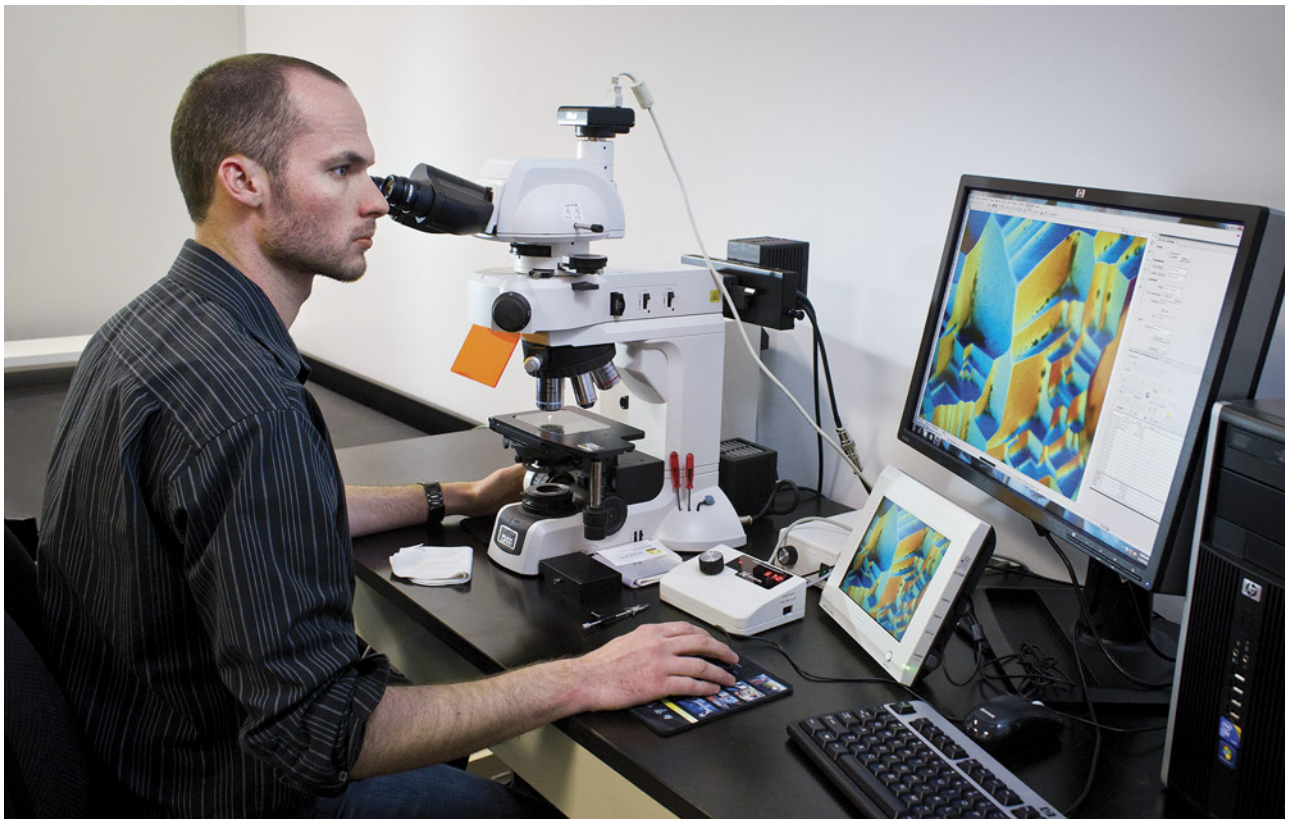

Figure 5. Nathan Renfro using the Nikon photomicroscope for observation and photography of inclusions and other micro-features at magnifications up to 1000×. Photo by Kevin Schumacher.

century these microscopes have "since contributed more to our knowledge of minerals and rocks than any other single instrument."

One of the first to describe gemstone inclusions observed with a microscope was the naturalist Isaac Lea, who published sketches of some of these micro-features (Lea, 1866, 1869, 1876, 1877). The geologist Henry Sorby pioneered the study of rocks and minerals using the microscope and also published works on mineral inclusions in gems (Sorby, 1869; Sorby and Butler, 1869).

The diagnostic value of inclusions in gem identification was first elucidated in the 1940s by the legendary gemologist Edward J. Gübelin (1945a,b,c, 1948; see also Kane et al., 2005). These micro-features could provide information on a gem's identity, quality grade, geologic and geographic origin, method of synthesis, and evidence of treatment. The three-volume *Photoatlas of Inclusions in Gemstones* (Gübelin and Koivula, 1986, 2005, 2008) remains the most significant reference work on mineral and fluid inclusions encountered in the major commercial

Figure 6. Photomicrography of inclusions: pyrochlore in a Cambodian sapphire (A), multiphase in a Colombian emerald (B), and sulfides in a Mozambique ruby (C). Photomicrographs by Nathan Renfro and Jonathan Muyal (C).

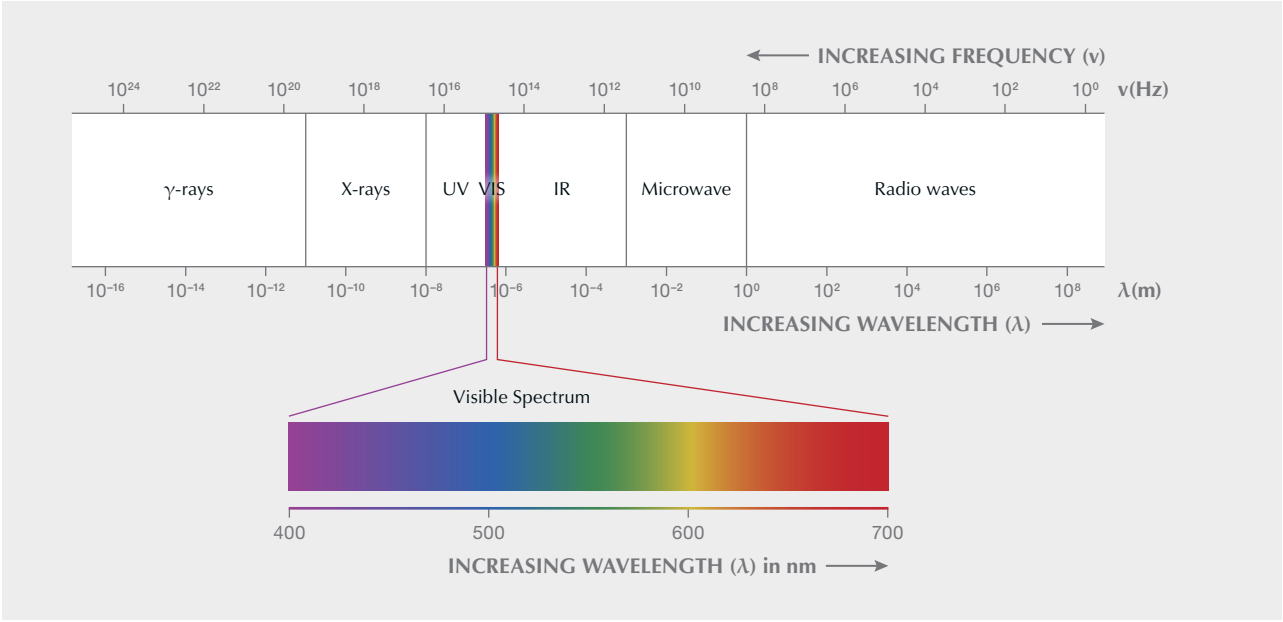

Figure 7. The electromagnetic spectrum encompasses the range of all possible frequencies of electromagnetic radiation. This form of energy travels through space in waves, which can be characterized by their wavelength and frequency. Note that as frequency increases (and wavelength decreases), energy also increases. Spectroscopic techniques are used to study gems in the ultraviolet, visible, and infrared regions of the spectrum.

gemstones. The past several decades have witnessed the introduction of polarizing and color filters, various kinds of illumination (brightfield, darkfield, reflected, diffused, indirect, and fiber-focused), and more recently digital photography and computer processing techniques to enhance photographic images (Koivula, 2003; Renfro, 2015a,b) (figures 5 and 6).

SPECTROSCOPY

Spectroscopy is the scientific study of how light interacts with materials (whether reflected, absorbed, or emitted). A spectrum is a graphical representation of that interaction as a function of light wavelength or frequency. The electromagnetic spectrum is the range of energy vibrations that correspond to wavelengths extending from many kilometers down to a fraction of the size of an atomic nucleus (figure 7). This wide range of frequency is divided into separate regions of interest.

Visible light is the limited portion of the electromagnetic spectrum that can be detected by the human eye. Each color of visible light corresponds to a particular range of wavelength and vibration frequency. When white light passes from the air into a triangular glass prism and then back into the air, the component colors propagate at different speeds. This causes the colored light rays to refract at different angles, dispersing into the familiar rainbow pattern.

Among the earliest uses of the spectroscope were observations of the sun's light emission spectrum and of the distinctive spectrum patterns produced when chemical elements were heated to incandescence by a flame. These breakthroughs demonstrated that visible spectra could be used to analyze the chemical composition of either nearby objects or very distant celestial bodies. When matter is heated to incandescence at high temperatures, it can emit a nearly continuous light spectrum. As this emitted light passes through a lower-temperature material, a pattern of narrow absorption and transmission bands appears. This pattern is based on the object's composition.

A visible transmission/absorption spectrum of a gemstone, as seen using a spectroscope (figure 8), reveals information on the causes of coloration. The hand spectroscope, championed by Anderson (1944a,b) and Crowningshield (1957; see also Moses et al., 2003), gives a visual representation of the wavelength regions of both selective light transmission and absorption by a gem. Each gem has its own characteristic pattern of narrow to wide, lighter to darker absorption bands, so viewing the spectrum pattern with a spectroscope can provide a quick means of identification for the gemologist (figure 9).

A spectrophotometer captures that same visible spectrum information but produces a graphical rep-

Figure 8. Robert Shipley Jr. using a spectroscope to examine the absorption spectrum of a gemstone at GIA for a 1937 Paramount Pictures film for its "Popular Science" series.

resentation with wavelength values along the plot's horizontal axis and the relative amount of light transmission or absorption along the vertical axis. The spectrophotometer offers several advantages over the spectroscope: a wider wavelength range of spectral features, the detection of very weak features not visible with the spectroscope, and the accurate wavelength locations of these features. Spectral features at wavelengths beyond the red end of the spectrum (the infrared) and those beyond the violet (the ultraviolet) are also of importance for gem characterization, and these can be captured with similar types of equipment. Although first developed several decades earlier, visible light spectrophotometers began to appear in gem testing laboratories in the mid- to late 1980s. This was followed by infrared and then other spectroscopy techniques (Nassau, 1981; Lind and Schmetzer, 1983; McMillan 1985, 1989; Fritsch and Stockton, 1987; McMillan and Hofmeister, 1988).

Figure 9. Left: Reproductions of Robert Crowningshield's hand-drawn spectrum patterns for colored diamonds, first published in the fifth edition of Richard Liddicoat's Handbook of Gem Identification *in 1957. Right: Artistic color renderings of the spectra for emerald (top) and zircon (bottom) currently used in GIA educational material.*

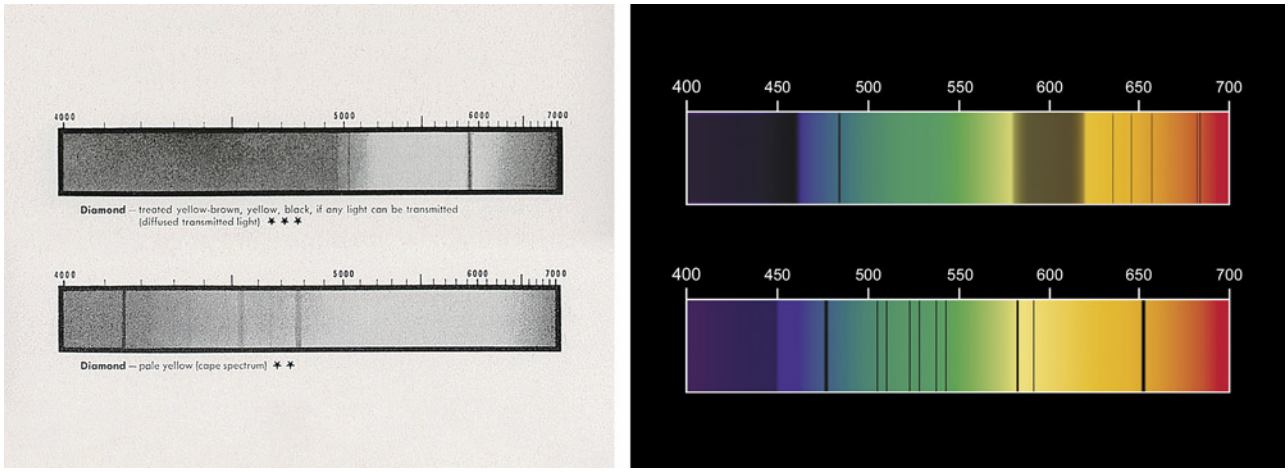


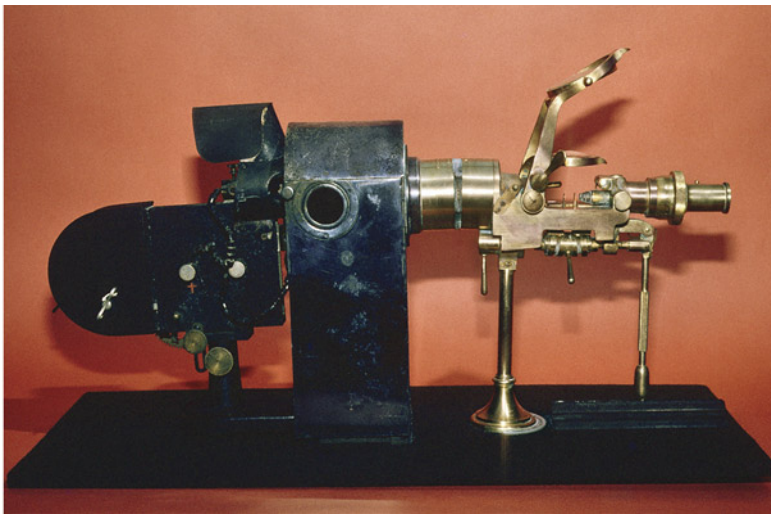

Figure 10. Left: Richard Liddicoat using an endoscope to examine the internal structure of a pearl. Right: A 1979 photo of the same instrument.

In addition to their diagnostic value, spectroscopic methods are also generally nondestructive (although some types of higher-energy ultraviolet illumination can affect a gem's color or other features). However, these methods do present some practical challenges. A gem's facet arrangement and cutting style often affect the amount of light transmission. Faceted gems are optically designed so that incident light enters through the crown facets, is internally reflected by the pavilion facets, and ultimately exits upward back through the crown. To record a visible transmission/absorption spectrum, however, some light signal must pass from the light source through the gem to the instrument detector. Certain facet arrangements provide little if any light transmission. A longer light path within the stone results in stronger selective light absorption and therefore a more intense face-up color.

Polished gems are not parallel-sided flat "windows" with a fixed and straight light path length that can be directly measured—they are multifaceted objects within which light is often internally reflected. As a result, the visible spectrum plot of most gemstones simply shows increasing absorption along the vertical axis. Individual girdle facets can sometimes be parallel to one another, providing a straight light path for spectra collection. The measured spectrum signal results from the combined effects of selective light absorption by optical defects along the light path. The signal is sampling along the light path but not the entire bulk volume of the gem, except when the stone is quite small. Spectroscopic analysis of gems can be quite rapid (requiring only a few seconds), but the methods are performed on one gem at a time. As a result, samples must be placed and removed from the instrument chamber by hand or by an automatic loader.

The spectroscopic techniques most widely used today in GIA laboratories are described in this special issue. For a review of the various forms of spectroscopy and their applications, see Agnello (2021).

IMAGING

Several imaging techniques are used in gem testing, the most important of which is X-ray radiography for distinguishing natural and cultured pearls. Following the discovery of X-rays in 1895, experiments revealed they could penetrate solid material, and by the 1920s these energetic rays were being used for a variety of medical applications. Different materials vary in their relative transparency to X-rays, and this variation is captured as a light/dark pattern on a photographic image.

The introduction of Japanese cultured pearls into the European market by K. Mikimoto in the early 1920s posed a widespread challenge for jewelers, who could not distinguish them from rare natural pearls by simple visual means (Boutan, 1921; Lemaire, 1921; Eunson, 1955; Nagai, 2013). To address this challenge, the first gem testing laboratories were set up in London, Paris, and other locations during the 1920s. Testing was conducted on a larger scale (but only one sample at a time) by viewing a pearl's internal structure using an endoscope or by viewing internal banding of the bead nucleus within the drill hole (Wright, 1923; Szilard, 1925a,b; Michel, 1926;

Figure 11. Robert Crowningshield preparing to X-ray several pearls at GIA's New York laboratory in the early 1950s.

Jardine, 1931; figure 10). This technique was followed in the late 1920s by X-ray radiography (Dubois, 1907; Anderson, 1932; Alexander, 1941a,b; Barnes, 1947a,b,c,d; Webster, 1957a,b; Ogden, 2012; Scarratt and Karampelas, 2020; Ericson, 2021).

The X-ray method was of particular value because a radiograph image could be created for multiple pearls (loose or strung) at the same time. Responding to the jewelry industry's needs, Dr. A.E. Alexander set up a pearl testing office in New York City, which he operated from 1940 until 1949, when it was turned over to GIA and became the GIA Gem Trade Laboratory (Alexander, 1940, 1941a,b; Benson, 1951) (figure 11). Evaluation of pearl radiographs remains the most important imaging technique at GIA.

CHEMICAL ANALYSIS

A gem mineral's composition reflects the chemical elements and conditions in its formation environment. Minerals such as quartz (SiO_2) have a very simple chemical composition. Others have a complex and variable composition. One such mineral is tourmaline, which is actually a group of more than 40 distinct but related mineral species. It has an idealized chemical formula of $XY_3Z_6(T_6O_{18})(BO_3)_3V_3W$, where B = boron, O = oxygen, and the other six letters represent atomic positions or sites in the crystal lattice where various elements can be accommodated. The many possible element substitutions in these sites result in the large number of mineral species within the tourmaline group.

For discussion purposes, the chemical elements in minerals can be categorized by concentration: major elements above about 1 weight percent (10000 parts per million, or ppm), which are essential since they determine the nature of the mineral; minor elements varying from 0.1 to 1 wt.% (1000 to 10000 ppm); and trace elements below approximately 0.1 wt.% (1000 ppm). The minor and trace elements tend to be more variable in concentration. All these elements substitute for one another in the mineral's crystal structure.

Before the 1960s, the chemical analysis of minerals was a complex, time-consuming process. This involved powdering the material and then dissolving it by chemical reaction in an acidic solution, followed by a combination of "wet chemical" methods to detect the major and minor elements present in the solution. Major and minor elements were often precipitated from the solution as oxides, which could then be dried and weighed. These components were reported as weight percent oxides, a convention still used today. The task required a skilled analytical chemist and a sizeable volume of the mineral to be analyzed.

Chemical analysis techniques vary in the sample size they require. Some methods sample the entire

volume of the material, while others focus on small spots. Certain methods are better suited for detecting major and minor chemical elements, while others can detect trace elements at very low concentrations. These trace elements may be randomly distributed within the sample or concentrated along growth structures, so the analysis location is crucial for accurate results. Some analytical methods provide a *qualitative* chemical analysis (identifying which elements are present), while *quantitative* analysis measures the amount of each element. For quantitative analysis, a standard reference material must also be tested. This reference material must contain the elements of interest in known concentrations, which allows the element concentration in the gem sample to be calculated. The most effective reference materials are those that closely match the structural and compositional characteristics of the gem being tested. An example of such a "matrix-matched" material is synthetic corundum doped with elements of interest for the analysis of natural corundum.

Modern chemical analysis often involves focusing an electron beam (or some other type of energy) onto a small spot on the mineral's surface. This causes the elements to emit X-rays at characteristic frequencies, which can be measured by the instrument's detector. The electron microprobe, introduced in the early 1970s, was often used to obtain quantitative compositional data from rocks and minerals. However, the electron microprobe method required a polished surface for analysis. This surface had to be coated with a thin carbon film to conduct away any buildup of electrical charge, and the element measurement results had to be mathematically corrected to yield accurate composition data (Wilson, 1972; Reed and Ware, 1975; Dunn, 1977; Reed, 1989).

Two chemical analysis methods are used today by GIA. The first is energy-dispersive X-ray fluorescence, or EDXRF (Anzelmo et al., 2013). This provides qualitative analysis of the major and minor elements present in the material, although the detection limits vary by element. Elements with a lighter atomic weight than sodium cannot be detected using EDXRF. The only requirement is a polished surface representative of the material. The method produces a bulk analysis to depths of several millimeters below the sample surface.

The other important chemical analysis technique is laser ablation–inductively coupled plasma–mass spectrometry, or LA-ICP-MS (figure 12), which focuses a narrow beam of high-powered laser light on the gir-

Figure 12. GIA's laser ablation–inductively coupled plasma–mass spectrometry (LA-ICP-MS) system for chemical analysis of small spots on the surface of polished gemstones. Photo by Kevin Schumacher.

dle of the gem being tested. Pulsing of the laser energy physically ablates or removes submicroscopic particles to create a tiny pit on the surface that is approximately 50 µm across (which can be removed by minor repolishing). Because this is a point or spot analysis method, several locations typically along the girdle are selected for analysis to obtain a more accurate indication of the material's overall minor and trace element chemistry. The ablated particles are carried by a flowing inert gas into a very high-temperature plasma torch operating at temperatures of up to 10000 K (hotter than the surface of the sun). Passing through the torch, the particles are vaporized, ionized, and broken down into their constituent chemical elements, which can then be analyzed by the instrument's mass spectrometer. This provides a quantitative determination of the minor and trace elements present and their concentrations (Sun et al., 2019; Wang and Krzemnicki, 2021; Yu et al., 2022). LA-ICP-MS can quickly detect a wide range of elements down to a parts-per-billion level with no sample preparation.

LOOKING AHEAD

For gemological laboratories to maintain consumer confidence, identification and reporting on all types of gem materials must remain a central focus. As analytical techniques such as those discussed in this special issue continue to advance, new testing methods will emerge. The nature of gem identification challenges will also evolve, and the gems themselves will have varying degrees of detectability. Some future trends to watch for include:

1. Synthetic gem materials, some of which have been available for more than a century, will remain abundant, with continued improvements in growth methods. However, the development of entirely new synthetic gems seems unlikely. Almost all natural minerals that can be synthesized for gem use have already been produced, and the few that remain (e.g., topaz and tourmaline) are unlikely to be grown since there is no industrial demand for them beyond their use as gems.
2. Mining at most localities produces a range of qualities of gem materials that could find a place in the market if treated to improve their color, durability, or appearance. Gem treatments, which also have a long history, will likely proliferate and improve, with some processes creating less obvious appearance changes and fewer diagnostic features. Multistep treatments may be further developed. There is also a category of processes designed simply to remove evidence of prior treatment. Since most treatments begin with a natural gem material, they often provide fewer diagnostic clues than synthetic gems.
3. Surface coatings, one of the oldest treatment methods, could regain prominence with advances in coating materials. These developments include less noticeable visual effects, selective application to limited portions of the cut stone's surface, and colorless coating materials offering improved durability without being visible.
4. The emergence of new gem-like materials, such as faceted durable glasses or transparent polycrystalline ceramics, should pose limited testing challenges but may initially cause concern.
5. Country of origin reporting on colored stones will remain a focus for gem testing laboratories. The addition of new localities for high-quality colored gemstones, some occurring in geological settings similar to those of older localities, will require continued refinement of testing methods and determination criteria. Determining the origin of polished diamonds remains unlikely (Smith et al., 2022).

Modern gemological laboratories face significant challenges beyond the initial investment in scientific instrumentation. The equipment also requires trained operators, potential modifications for holding samples, costly maintenance contracts, and robust data collection protocols. Perhaps the greatest challenge is creating a searchable database for the vast amounts of data generated by this technology. The University of Arizona's RRUFF project provides a free database of high-quality spectra and other data on thousands of well-characterized minerals (https://rruff.info/; see also Lafuente et al., 2015; Culka and Jehlička, 2019). Similar online databases exist for other materials but often lack data on the gem samples tested (in particular, for synthetic and treated gem materials).

Gem characterization studies featuring the types of analytical data mentioned above are scattered in the gemological literature and vary in usefulness. Gemological laboratory staff often find themselves creating their own in-house databases using their own instrumentation and the best obtainable gem samples. To confront new identification challenges,

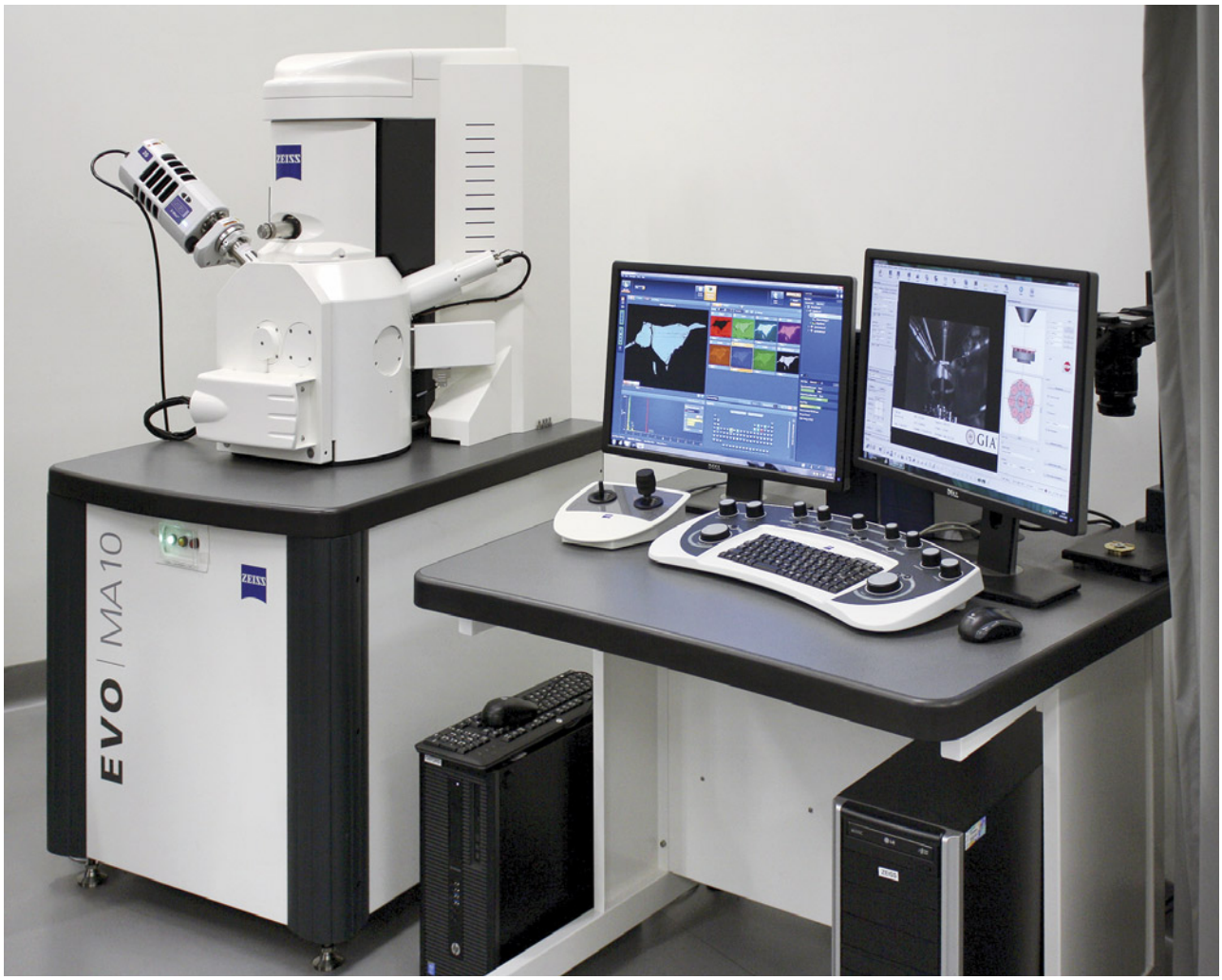

Figure 13. The Zeiss EVO 10 scanning electron microscope used today at GIA in New York. The instrument is capable of magnification up to 100,000×. Photo by Jian Xin (Jae) Liao.

laboratory staff continually search for new analytical techniques and instrumentation that can be adapted for their purposes.

This article began with a photo of the first scanning electron microscope acquired by GIA in 1976 at its former Santa Monica headquarters. Figure 13 shows the newer instrument acquired in 2015 for GIA's New York laboratory. These two photos illustrate the decades-long evolution in analytical instrumentation in major gemological laboratories. The current state of the art in analytical instruments and techniques is described in this special issue.

ABOUT THE AUTHOR
Dr. James Shigley is a distinguished research fellow at GIA in Carlsbad, California.

REFERENCES

Agnello S. (2021) *Spectroscopy for Materials Characterization*. John Wiley & Sons, 496 pp.

Alexander A.E. (1940) The radiography of natural and cultured pearls. *The Gemmologist*, Vol. 10, No. 113, pp. 45–48.

——— (1941a) Natural and cultured pearl identification. *G&G*, Vol. 3, No. 11, pp. 169–172.

——— (1941b) Natural and cultured pearl identification. *G&G*, Vol. 3, No. 12, pp. 184–188.

Anderson B.W. (1932) The use of X-rays in the study of pearls. *British Journal of Radiology*, Vol. 5, No. 49, pp. 57–64.

——— (1944a) Gemstones and the spectroscope. *G&G*, Vol. 4, No. 12, pp. 180–181.

——— (1944b) Gemstones and the spectroscope. *G&G*, Vol. 5, No. 1, pp. 203–204.

Anzelmo J.A., Bouchard M., Provencher M.-E. (2013) X-ray fluorescence spectroscopy, Part 1: The educational essentials. *Spectroscopy*, Vol. 28, No. 7, pp. 16–23.

Barnes W. (1947a) Pearl identification by X-ray diffraction, Part I. *G&G*, Vol. 5, No. 9, pp. 387–391.

——— (1947b) Pearl identification by X-ray diffraction, Part II. *G&G*, Vol. 5, No. 10, pp. 428–429, 440–444, and 446.

——— (1947c) Pearl identification by X-ray diffraction, Part III. *G&G*, Vol. 5, No. 11, pp. 471–474.

——— (1947d) Pearl identification by X-ray diffraction, Part IV. *G&G*, Vol. 5, No. 12, pp. 508–512.

Benson L.B. (1951) Gem Trade Laboratory installs new pearl testing equipment. *G&G*, Vol. 7, No. 4, pp. 107–112.

Boutan L. (1921) Étude sur les perles fines et, en particulier, sur les nouvelles perles complètes de culture japonaise. *Bulletin de la Station Biologique d' Arcachon*, Vol. 18, pp. 5–117.

Crowningshield G.R. (1957) An introduction to spectroscopy in gem testing. *G&G*, Vol. 9, No. 2, pp. 46–55, 62.

Culka A., Jehlička J. (2019) Identification of gemstones using portable sequentially shifted excitation Raman spectrometer and RRUFF online database: A proof-of-concept study. *European Physical Journal Plus*, Vol. 134, No. 4, article no. 130, http://dx.doi.org/10.1140/epjp/i2019-12596-y

Dubois R. (1907) La radiographie appliquée a la recherche des perles fines. *Comptes Rendus Hebdomadaires des Séances et Mémoires de la Société de Biologie*, Vol. 62, pp. 54–55.

Dunn P.J. (1977) The use of the electron microprobe in gemmology. *Journal of Gemmology*, Vol. 15, No. 5, pp. 248–258.

Ericson K.D. (2021) Judging the perle japonaise: The techno-legal separation of culture from nature in 1920s Paris. *Technology and Culture*, Vol. 62, No. 4, pp. 1032–1062, http://dx.doi.org/10.1353/tech.2021.0153

Eunson R. (1955) *The Pearl King: The Story of the Fabulous Mikimoto*. Greenberg Publishers, New York, 243 pp.

Fritsch E., Stockton C. (1987) Infrared spectroscopy in gem identification. *G&G*, Vol. 23, No. 1, pp. 18–26, http://dx.doi.org/10.5741/GEMS.23.1.18

Gübelin E.J. (1945a) Inclusions as a means of identification. *G&G*, Vol. 5, No. 2, pp. 226–231.

——— (1945b) Inclusions as a means of identification. *G&G*, Vol. 5, No. 3, pp. 242–247.

——— (1945c) Inclusions as a means of identification. *G&G*, Vol. 5, No. 4, pp. 270–274.

——— (1948) Gemstone inclusions. *Journal of Gemmology*, Vol. 1, No. 7, pp. 7–39.

Gübelin E.J., Koivula J.I. (1986) *Photoatlas of Inclusions in Gemstones*, Vol. 1, ABC Edition, Zurich, 532 pp.

——— (2005) *Photoatlas of Inclusions in Gemstones*, Vol. 2, Opinio Verlag, Basel, 829 pp.

——— (2008) *Photoatlas of Inclusions in Gemstones*, Vol. 3, Opinio Verlag, Basel, 672 pp.

Gunter M. (2004) The polarized light microscope: Should we teach the use of a 19th century instrument in the 21st century? *Journal of Geoscience Education*, Vol. 52, No. 1, pp. 34–44, http://dx.doi.org/10.5408/1089-9995-52.1.34

Herbert Smith G.F. (1907) *The Herbert-Smith Refractometer and Its Use*. J.H. Steward, London, 28 pp.

Jardine I.G. (1931) The endoscope and its use in pearl testing. *The Gemmologist*, Vol. 1, No. 1, pp. 10–12.

Kane R.E., Boehm E.W., Overlin S.D., Dirlam D.M., Koivula J.I., Smith C.P. (2005) A gemological pioneer: Dr. Edward J. Gübelin. *G&G*, Vol. 41, No. 4, pp. 298–327, http://dx.doi.org/10.5741/GEMS.41.4.298

Kile D.E. (2003) The petrographic microscope: Evolution of a mineralogical research instrument. *Mineralogical Record*, Special Publication Number One, November-December, 96 pp.

Koivula J.I. (2003) Photomicrography for gemologists. *G&G*, Vol. 39, No. 1, pp. 4–23, http://dx.doi.org/10.5741/GEMS.39.1.4

Lafuente B., Downs R.T., Yang H., Stone N. (2015) The power of databases: The RRUFF project. In T. Armbruster and R.M. Danisi, Eds., *Highlights in Mineralogical Crystallography*, De Gruyter, Berlin, pp. 1–30.

Lea I. (1866) Notes on microscopic crystals in some minerals. *Proceedings of the Academy of Natural Sciences of Philadelphia*, Vol. 18, pp. 110–113.

——— (1869) Notes on microscopic crystals included in some minerals. *Proceedings of the Academy of Natural Sciences of Philadelphia*, Vol. 21, pp. 119–121.

——— (1876) Notes on microscopic crystals in some minerals. *Proceedings of the Academy of Natural Sciences of Philadelphia*, Vol. 28, pp. 98–107.

——— (1877) Notes on "inclusions" in gems. *Monthly Microscopical Journal*, Vol. 17, No. 4, pp. 198–205.

Lemaire Y. (1921) La production industrielle des perles fines au Japon – L'oeuvre de M. Mikimoto. *Bulletin de la Société Franco-Japonaise de Paris*, No. 48, pp. 97–107.

Lind T., Schmetzer K. (1983) A method for measuring the infrared spectra of faceted gems such as natural and synthetic amethysts. *Journal of Gemmology*, Vol. 18, No. 5, pp. 411–420.

McMillan P. (1985) Vibrational spectroscopy in the mineral sciences. *Reviews in Mineralogy and Geochemistry*, Vol. 14, pp. 9–63.

McMillan P.F. (1989) Raman spectroscopy in mineralogy and geochemistry. *Annual Review of Earth and Planetary Sciences*, Vol. 17, No. 1, pp. 255–279, http://dx.doi.org/10.1146/annurev.ea.17.050189.001351

McMillan P.F., Hofmeister A.M. (1988) Infrared and Raman spectroscopy. In F.C. Hawthorne, Ed., *Reviews in Mineralogy and Geochemistry*, Vol. 18, Mineralogical Society of America, pp. 99–159.

Michel H. (1926) Die künstlichen Edelsteine: Eine zusammenfassende Darstellung ihrer Erzeugung, ihrer Unterscheidung von den natürlichen Steinen und ihrer Stellung im Handel, Verlag W. Diebener, Leipzig, 477 pp.

Moses T.M., Shigley J.E. (2003) G. Robert Crowningshield: A legendary gemologist. *G&G*, Vol. 39, No. 3, pp. 184–199, http://dx.doi.org/10.5741/GEMS.39.3.184

Nagai K. (2013) A history of the cultured pearl industry. *Zoological Science*, Vol. 30, No. 10, pp. 783–793, http://dx.doi.org/10.2108/zsj.30.783

Nassau K. (1981) Raman spectroscopy as a gemstone test. *Journal of Gemmology*, Vol. 17, No. 5, pp. 306–320.

Ogden J. (2012) Spherical cultured pearls: The early days. *Gems & Jewellery*, Vol. 21, No. 1, pp. 28–30.

Reed S.J.B. (1989) Ion microprobe analysis—A review of geological applications. *Mineralogical Magazine*, Vol. 53, No. 369, pp. 3–24, http://dx.doi.org/10.1180/minmag.1989.053.369.02

Reed S.J.B., Ware N.G. (1975) Quantitative electron microprobe

analysis of silicates using energy dispersive X-ray spectrometry. *Journal of Petrology*, Vol. 16, No. 1, pp. 499–519, http://dx.doi.org/10.1093/petrology/16.1.499
Renfro N. (2015a) Digital photomicrography for gemologists. *G&G*, Vol. 51, No. 2, pp. 144–159, http://dx.doi.org/10.5741/GEMS.51.2.144
——— (2015b) The application of differential interference contrast microscopy to gemmology. *Journal of Gemmology*, Vol. 34, No. 7, pp. 616–620.
Scarratt K., Karampelas S. (2020) Pearls–Evolution in the sector, production, and technology. *InColor*, Spring/Summer, pp. 82–86.
Smith E.M., Smit K.V., Shirey S.B. (2022) Methods and challenges of establishing the geographic origin of diamonds. *G&G*, Vol. 58, No. 3, pp. 270–288, http://dx.doi.org/10.5741/GEMS.58.3.270
Sorby H.C. (1869) On the microscopical structure of some precious stones. *Monthly Microscopical Journal*, Vol. 1, pp. 220–224.
Sorby H.C., Butler P.J. (1869) On the structure of rubies, sapphires, diamonds, and some other minerals. *Proceedings of the Royal Society of London*, Vol. 17, pp. 291–303.
Sun Z.Y., Palke A.C., Breeding C.M., Dutrow B.L. (2019) A new method for determining gem tourmaline species by LA-ICP-MS. *G&G*, Vol. 55, No. 1, pp. 2–17, http://dx.doi.org/10.5741/GEMS.55.1.2
Szilard B. (1925a) Nouvelle methode d'examen de l'intérieur des perles. *Comptes Rendus Hebdomadaires des Séances de l'Académie des Sciences*, Vol. 180, No. 6, pp. 433–436.
——— (1925b) Nouvelle methode d'examen de l'intérieur des perles. *Comptes Rendus Hebdomadaires des Séances de l'Académie des Sciences*, Vol. 181, No. 14, pp. 413–414.
Wang H.A.O., Krzemnicki M.S. (2021) Multi-element analysis of minerals using laser ablation inductively coupled plasma time of flight mass spectrometry and geochemical data visualization using t-distributed stochastic neighbor embedding: Case study on emeralds. *Journal of Analytical Atomic Spectrometry*, Vol. 36, No. 3, pp. 518–527, http://dx.doi.org/10.1039/D0JA00484G
Webster R. (1957a) The detection of cultured pearls: Part I: How it started. *The Gemmologist*, Vol. 26, No. 315, pp. 178–184.
——— (1957b) The detection of cultured pearls: Part II: Further identification methods. *The Gemmologist*, Vol. 26, No. 316, pp. 200–207.
Wilson W.E. (1972) The state of the art: The electron microscopes and electron microprobe. *Mineralogical Record*, Vol. 3, No. 4, pp. 151–164.
Wright F.E. (1923) Methods for distinguishing natural from cultivated pearls. *Journal of the Washington Academy of Sciences*, Vol. 13, No. 13, pp. 282–287.
Yu X.-Y., Long Z.-Y., Zhang Y., Wang G.-Y., Guo H.-S., Zheng Y.-Y. (2022) In-situ micro-analysis and application in gemmology based on LA-(MC)-ICP-MS. *Journal of Gems and Gemmology*, Vol. 24, No. 5, pp. 134–145, http://dx.doi.org/10.15964/j.cnki.027jgg.2022.05.013 [in Chinese].

Application of UV-Vis-NIR Spectroscopy to Gemology

Shiyun Jin, Nathan D. Renfro, Aaron C. Palke, Troy Ardon, and Artitaya Homkrajae

Optical spectroscopy, also known as ultraviolet/visible/near-infrared spectroscopy, measures how electromagnetic radiation around the visible range is preferentially absorbed by a gemstone. A transparent gemstone can absorb certain wavelengths of light that pass through it, creating color in the transmitted light, whereas an opaque gemstone absorbs light on its surface and creates color in the reflected light. The physics of how electromagnetic radiation of different wavelengths interacts with materials is summarized to provide a basic understanding of how electronic transitions in gemstones can cause different colors. The different instruments and configurations suitable for various gemstone types are also explained. Specific routine applications of ultraviolet/visible/near-infrared spectroscopy to colored gemstones, fancy-color diamonds, and saltwater pearls are summarized, showcasing how identifying the chromophores in gemstones can facilitate varietal calls, origin determination, and treatment detection in a gemological laboratory.

The color of a colored gemstone, fancy-color diamond, or pearl is one of the most important aspects determining its desirability and value. Colors can be induced by trace elements, structural defects, or even organic pigments in gemstones, which may be removed, altered, or enhanced through various treatment processes. Even though the average human eye can differentiate millions of colors, the color space is limited to three dimensions, as our eyes only have three different types of cone cells, which are sensitive to different wavelengths of light. Therefore, very similar colors in our vision may be created by completely different chromophores in a gemstone. Moreover, our eyes cannot detect any light beyond the visible range. Therefore, optical spectroscopy in the visible (Vis) spectrum range, along with the adjacent ultraviolet (UV) and near-infrared (NIR), is one of the most important analytical testing techniques in gemology. UV-Vis-NIR spectroscopy, commonly referred to as UV-Vis, measures how light is attenuated by absorption inside or on the surface of a transparent or opaque gemstone, respectively. The details in the absorption spectrum can provide information about the trace element chemistry, defect configurations, and organic pigments that may help identify a gem's species, variety, and potential treatments.

In 1666, Sir Isaac Newton used a glass prism to explore the phenomenon of color in sunlight (Anderson and Payne, 1998), which opened an entirely new physics field of optics. Centuries later, gemologists would regularly use the same principles described by Newton to unravel the origin of color in gemstones. Gemologists have applied spectroscopy to gemstones since the 1930s (Anderson and Payne, 1998). In general, they used handheld spectroscopes to split light into its component colors and observe with their eyes the light not absorbed by the gemstone as bright spectral colors, in contrast to dark bands or sharp black lines representing the areas in the visible spectrum where the gem did absorb light. Many of these

In Brief

- UV-Vis-NIR spectroscopy can resolve the details in the absorption spectrum of gem materials that cannot be detected by the eye.
- Absorption of ultraviolet, visible, and near-infrared radiation is caused mainly by electronic transitions in the outer shells around the atoms in a material.
- UV-Vis-NIR spectroscopy is a quick routine analysis with a wide range of applications in testing colored stones, fancy-color diamonds, and pearls.

See end of article for About the Authors and Acknowledgments.
Gems & Gemology, Vol. 60, No. 4, pp. 456–473,
http://dx.doi.org/10.5741/GEMS.60.4.456

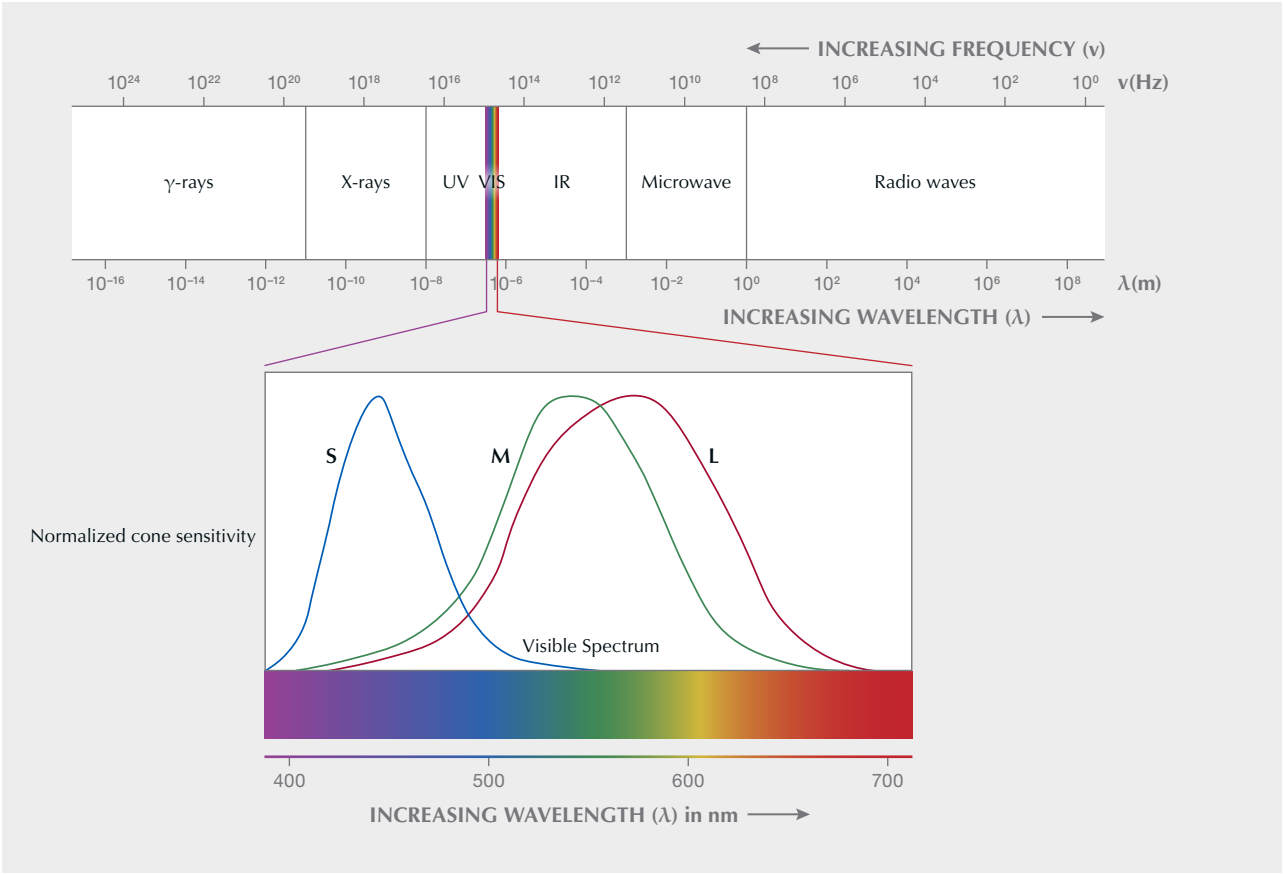

Figure 1. Schematic diagram showing the relation between the visible spectrum and the entire electromagnetic spectrum. The normalized sensitivity curves of three types of cone cells (L: long, M: medium, and S: short) in the human eye are plotted over the visible spectrum.

early observations were documented in articles by Basil Anderson in *The Gemmologist* (see also Anderson et al., 1998). Other references on spectroscopy also became available, such as the 114 spectra recorded by Robert Crowningshield for the 1962 edition of Richard T. Liddicoat's *Handbook of Gem Identification* (Moses and Shigley, 2003). *Gems & Gemology*'s Lab Notes section also became a regular forum for new spectroscopic observations by Crowningshield, who was a pioneer in the field.

In the late 1980s, optical engineers with GIA Gem Instruments developed a digital scanning diffraction grating spectroscope called the DISCAN, which allowed users to precisely measure the position of absorption features (Koivula and Kammerling, 1989). In the early 2000s, advancements in technology led to the development of spectrometers that significantly reduced the measurement time required to collect UV-Vis-NIR spectra, while also making the instruments much more compact and portable (Breeding et al., 2010). While the handheld spectroscope is still widely used in gemology courses, spectrometers have become widely available. In the future, we may see the handheld spectroscope essentially replaced with even smaller compact spectrometers that can quickly measure and record data on gemstones.

THE ELECTROMAGNETIC SPECTRUM AND ITS INTERACTION WITH MATERIALS

Just as ripples spread across the surface of water that has been disturbed, a disturbance in the electromagnetic field can propagate through space as electromagnetic radiation, or an electromagnetic wave. The wavelengths of electromagnetic waves range from ~10^{-15} m to ~10^{5} m. Due to their dramatically different properties, the electromagnetic spectrum is broadly classified into different categories with de-

creasing wavelengths (figure 1): radio waves, microwaves, infrared (IR), visible light, ultraviolet, X-rays, and gamma rays. However, because the electromagnetic spectrum is continuous, the boundaries between two adjacent categories are generally blurred and can vary depending on specific applications. The exception is visible light, which has a well-defined range of 400 to 700 nm (again, see figure 1). The boundary between what a human eye can and cannot see is relatively sharp, although the exact range varies slightly from one individual to another.

The energy of an electromagnetic wave is proportional to its frequency (f) and inversely proportional to its wavelength (λ). This means that shorter wavelengths correspond to higher-energy electromagnetic waves. Because this inverse relation between wavelength and energy is sometimes inconvenient, the quantity wavenumber ($\tilde{\nu}$, in units of cm^{-1}), which is the inverse of wavelength, is often used in spectroscopy, though more commonly for Fourier-transform infrared (FTIR) and Raman spectroscopy (see Breeding and Ahline, 2024, pp. 474–492 of this issue; Jin and Smith, 2024, pp. 518–535 of this issue). The wavelength (in nm) and wavenumber of an electromagnetic wave can be converted between one another using the following equation:

$$\tilde{\nu}\ (cm^{-1}) = \frac{10000000}{\lambda\ (nm)} \quad (1)$$

An electric field exerts a force on a charged particle, causing it to accelerate. An electromagnetic wave, which consists of alternating electric and magnetic fields, makes a charged particle oscillate by moving it back and forth, transferring the energy from the radiation to the charged particle. This is the basic principle of how electromagnetic radiation interacts with materials. All materials in everyday life are composed of charged particles such as electrons and protons, which can be accelerated by electromagnetic radiation. The energy transfer between electromagnetic radiation and a material is most efficient when the wave frequency resonates with the intrinsic frequency of a specific transition in the material—that is, when the energy of the electromagnetic radiation matches the energy difference between two states in the material. For instance, microwaves can excite the low-frequency movements of polar molecules (e.g., water molecules) and thus can be used to heat food. IR radiation has energies similar to vibrations of individual covalent bonds (e.g., OH bonds in water and other hydrous materials) or vibrations of the entire crystal lattice (Breeding and Ahline, 2024); X-rays can excite the high energy electrons in the innermost orbitals of an atom, which is why X-ray fluorescence can be used to analyze the chemical composition of a material (Sun et al., 2024). The most energetic gamma rays, which come from nuclear reactions, are the only photons that can excite the nuclei of atoms.

With energies falling in between X-rays and IR, ultraviolet and visible light mostly interact with the valence and outer-shell electrons of a material. These electronic transitions are very complex quantum mechanical processes that can be described by several different theories, depending on the system (e.g., ligand field theory, molecular orbital theory, crystal field theory, and band theory) (Rossman, 2014). Generally, the electrons in the outer shells of an ion in a material can be excited in several different ways. They may be elevated to a higher energy state around the same ion (i.e., electronic transitions in the transition metals or rare earth elements). They may transfer to orbiting a different ion, such as the charge transfer between an anion and a cation, or the intervalence charge transfer (IVCT) between two cations with variable oxidation states. In a semiconductive material, electrons can be excited all the way up to the conduction band. Electrons in a material can sometimes be displaced and trapped, typically by ionizing radiation (alpha, beta, and gamma rays), which creates electron-hole centers that can be excited by photons in the UV-Vis range.

Various colors are created when certain sections of the visible spectrum are preferentially absorbed by specific electronic transitions. The human eye has only three types of cone cells, each sensitive to a different region of the visible spectrum: red (long wavelength), green (medium wavelength), and blue (short wavelength) (again see figure 1). Color is perceived based on the relative intensities of these three light regions as they excite each type of cone cell in our vision. This is the basis of the RGB color system. Due to the limited number of cone types, different spectral compositions may appear as the same color to our eyes if they excite the same reactions of the cone cells. That is why we need the entire visible absorption spectrum to reveal the color-causing trace element or defect in a gemstone. Although only the absorption features within the visible spectrum can affect the color or appearance of a gemstone, the underlying physical processes could extend beyond the visible spectrum into the UV or IR range. Therefore, optical absorption spectroscopy is not limited only to visible light but includes the ultraviolet and near-infrared as

well, collectively known as UV-Vis-NIR spectroscopy. This is one of the main advantages of an electronic spectrometer over a handheld spectroscope, which only reveals absorption features in the visible range due to the limitations of the human eye.

Note that the light-absorbing electronic transitions are dependent on the valence states or configurations of the trace elements and defects, which are often determined by oxidation conditions or radiation damages. Thus, these transitions can be enhanced, modified, or removed through heat or radiation treatments or by introducing additional chemical components through diffusion (Emmett and Douthit, 1993; Kitawaki et al., 2006; Jollands et al., 2023). These processes may occur either naturally in geological processes or artificially in a gem treatment facility. While UV-Vis-NIR spectroscopy is seldom diagnostic for specific gemstone treatments, it can often help narrow down the number of potential treatments or eliminate the possibility of treatment altogether, expediting testing in a gemological laboratory by removing unnecessary steps.

Adding another layer of complexity, visible light also interacts with nanoscale textures in a material that can create optical and color effects. Conductive nanoparticles can preferentially absorb visible light of certain wavelengths due to the surface plasmon (a quantized collective vibration of electron clouds) on the interface between the particle and the matrix. For instance, the red and green colors of Oregon sunstone are caused by copper nanoparticle inclusions <50 nm (Jin et al., 2022, 2023). Nanoparticles can also preferentially scatter light of specific wavelengths—known as Rayleigh scattering, Mie scattering, or Tyndall scattering depending on the size, shape, or dielectric properties of the particles—which can create opposite colors in transmission and scattered light (Jin et al., 2023). Periodic nanotextures in labradorite, precious opal, or agate can cause an interference effect known as diffraction, which produces iridescent colors that sometimes change with viewing angle (Baier, 1932; Bolton et al., 1966; Heaney, 2021). The color effects created by special nanostructures are known as "structural colors," which are sometimes considered "not real" in comparison to the pigment colors created by electronic transitions and thus sometimes referred to as "pseudochromatic" colors. Except for special research purposes, the structural colors are typically not of interest for UV-Vis-NIR analyses in a gemological laboratory and mostly pose an inconvenience for data collection and interpretation.

The oscillating electric (and magnetic) field in a beam of light can be directional, which is known as its polarization. Similarly, the electronic transitions or nanoscale textures in a material can also be directional, absorbing or scattering photons of different polarization with different efficiencies. Therefore, the optical spectrum may depend on the sample's orientation relative to the polarization of the light source. Optically isotropic (singly refractive) gemstones such as diamond, spinel, garnet, or strain-free glass are not affected by this phenomenon; it is only observed in optically anisotropic (doubly refractive) gemstones, which often display pleochroism and show different colors under the dichroscope. The optical properties of doubly refractive materials such as feldspar, tourmaline, and corundum can be extremely complicated (Dowty, 1978; Dubinsky et al., 2020; Jin et al., 2023) and are beyond the scope of this article. Polarized light is rarely used for qualitative analysis on doubly refractive gems in a gemological laboratory, though multiple measurements along different directions may be performed on intensely pleochroic samples to account for anisotropy.

PRACTICAL APPLICATIONS TO GEMOLOGY

The distinct spectra of colored gemstones, fancy-color diamonds, and pearls can be a powerful tool for identification, origin determination, and treatment detection. The technical details of how UV-Vis-NIR spectra are measured and quantified in a gemological laboratory are described in boxes A and B. As new discoveries about the absorption properties of gemstones emerge, our understanding of gemology continues to evolve. While the applications of UV-Vis-NIR spectroscopy in this field are far too numerous to detail in this article, those most routinely used in GIA laboratories are summarized here.

Colored Stones. Most applications of UV-Vis-NIR spectroscopy for colored stones focus on the identification of specific chromophores. For certain types of gems, the variety can be determined based on specific color-causing agents. The presence or absence of certain spectroscopic features beyond the visible range, in the UV or NIR regions, further assists in identification, making the spectrometer a much more useful tool than a handheld spectroscope.

Copper-Bearing Blue-Green Tourmaline. One of the most common applications of UV-Vis-NIR spectroscopy is the separation between tourmaline

BOX A: ABSORPTION OF LIGHT: MEASUREMENT AND QUANTIFICATION

A light detector, such as a photomultiplier tube or charge-coupled device (CCD) sensor, measures the intensity of light attenuated by the material at each wavelength and compares it to the unattenuated intensity of the light source. The attenuation measured may come from absorption, surface reflection, internal reflection, or scattering from inclusions and other internal textures. These factors can complicate the data interpretation. The simplest way to measure the attenuation spectrum of a transparent material is to use a direct light path. In this approach, the unblocked intensity of the light source is measured as the background, and the attenuated intensity is measured by passing light through the sample (figure A-1A). Transmittance (T) is the fraction of the incident light power that is transmitted through the sample (often expressed as a percentage). It is simply the ratio of the attenuated intensity (I_T) to the unattenuated intensity (I_0) measured by the detector:

$$T = \frac{I_T}{I_0} \quad \text{(A-1)}$$

Absorbance (A) is defined as the negative logarithm of transmittance:

$$A = -\log T = \log \frac{I_0}{I_T} \quad \text{(A-2)}$$

Assuming the contributions from surface reflection and internal scattering are negligible, the absorbance is proportional to the length of the light path in the material (l) and the concentration of the attenuating species (c), such as light-absorbing elements or defects. This linear relationship is known as the Beer-Lambert law:

$$A = \varepsilon l c \quad \text{(A-3)}$$

where ε is the molar absorption coefficient of the absorbing species. In theory, this law can be used to quantify the absolute concentration of certain chromophores in a gemstone (Dubinsky et al., 2020), though in practice it is very difficult due to the irregular shapes, optical anisotropy, and heterogeneity of most gem materials. Except for the special case of copper-colored feldspars (or copper- or gold-colored glass), all the known absorption

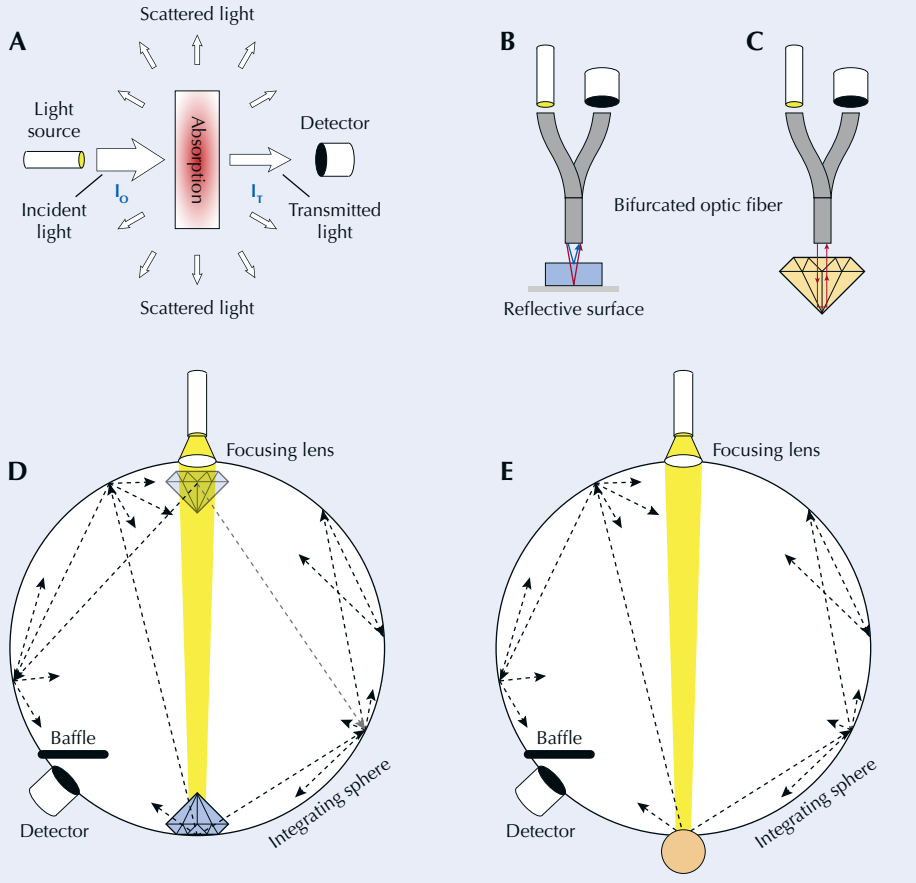

Figure A-1. A: The simplest configuration for measuring transmittance and absorbance with a direct light path through a wafer-shaped sample. B: A reflective configuration with a bifurcated optical fiber, which can be used to measure the surface reflectance of an opaque material (blue path) and transmittance through a wafer placed on a reflective surface (red path). C: Transmittance through a faceted stone can be measured using the internal reflection created by its pavilion facets. D: A common configuration for measuring the absorption of an irregularly shaped transparent sample, which can be placed anywhere inside the integrating sphere as long as it completely covers the incident light. E: A similar configuration as in C, but for measuring the reflectance of opaque samples with irregular or unsmooth surfaces (e.g., pearls) placed outside the sphere.

features (i.e., nonstructural colors) in gemstones are caused by transitions involving valence or outer-shell electrons.

For opaque materials such as pearls that do not transmit light, transmittance or absorbance cannot be measured. Unlike transparent materials, where color is determined by the transmitted light, the light reflected off the surface determines the color and appearance of an opaque material. Rather than the intensity of transmitted light, the intensity of reflected light should be measured for opaque materials. Reflectance (R) is defined as the proportion of incident power that is reflected by the surface:

$$R = \frac{I_R}{I_0} \quad \text{(A-4)}$$

For a well-polished surface that allows specular reflection, reflectance can be measured simply by shining the incident light perpendicular to the surface and collecting the light reflected directly back (figure A-1B, blue path). Due to the different configuration of the spectrometer, the incident intensity I_0 for reflectance cannot be directly measured the same way as for transmittance. A special reflective material that evenly reflects more than 99% of the light back to the detector is needed to acquire the reference background.

Note that the luster of a transparent gemstone comes mainly from its surface reflectance, which is mostly independent of wavelength. Therefore, it is meaningless to measure the surface reflection spectrum of a transparent gemstone. However, if a transparent wafer is placed on top of a reflective surface (figure A-1B, red path), the reflected light measured by the detector will have passed through the wafer twice (before and after reflecting). This allows transmittance and absorbance to be measured using the reflection configuration. In fact, the reflective surface is not even needed for a faceted transparent gemstone cut to maximize light return, because the incident light will reflect back to the detector off the pavilion facets (figure A-1C). This type of measurement is routinely used in gemological laboratories and is particularly useful for mounted stones, through which direct transmittance is impossible to measure.

Accurate quantification of the absorptivity of a specific chromophore in a host material requires creating a wafer-shaped sample with two parallel polished surfaces to ensure a straight light path (with a consistent path length) through the sample (figure A-1A). For anisotropic materials, polarized light aligned with the optical orientation of the analyzed material is also necessary. Such quantitative analysis is obviously infeasible for gemological testing, as it would require destructive reshaping of the material. But due to the linear nature of absorbance, only qualitative analyses are needed for gemological testing, because the overall shape of the absorption spectrum of a gemstone is independent of its size or cut, depending only on the absorptivity ε and relative concentrations of chromophores (if multiple chromophores are involved). Transmittance, on the other hand, is not a linear quantity, so the transmission spectrum will change shape depending on the absolute values of the light path length and chromophore concentrations. As a result, the appearance of a gemstone—its hue, tone, and color saturation, as determined by light transmitted through the stone—may depend considerably on its size and cut. Therefore, the transmission spectrum is needed to calculate the color of a transparent gemstone. Similarly, the reflectance or backscattered spectra are used to calculate the color of an opaque or translucent gemstone.

The facets or curved surfaces of cut stones can refract and reflect light unpredictably, preventing the accurate measurement of transmittance, absorbance, or reflectance. Most gemstones are neither perfectly transparent nor completely opaque but lie somewhere in between. Almost all transparent gemstones contain some inclusions that could distort the measurement of absorption by scattering light away from a straight path. Translucent and semitransparent materials allow some light to transmit through but also scatter or reflect a significant portion of light back. The light transmitted through such materials might be too weak to measure using transmission spectroscopy. Although it may be possible to measure backscattered light using reflection spectroscopy, this technique often lacks the features gemologists need to identify a stone.

To reduce the undesired and unpredictable effects of internal scattering and surface reflections, a special optical device known as an integrating sphere is often used in a UV-Vis-NIR spectrometer (figure A-1, D and E). An integrating sphere is simply a spherical cavity with a diffusively reflective coating on the inside, with a few ports for incident light, detector, and sample placement. Light entering the integrating sphere bounces around randomly multiple times due to the reflective surface before exiting through the detector port, blending the transmitted, scattered, and reflected light together and allowing only the contribution from absorption to be measured. Transparent gemstones must be placed inside the integrating sphere (figure A-1D) to prevent light from leaking out, whereas opaque samples such as pearls can be placed outside the sphere as long as they cover the sample port (figure A-1E). The exact position of the sample inside the integrating sphere does not matter, as long as all incident light is attenuated by the sample before being integrated by the sphere. A lens is often used to focus the incident light through the sample on the opposite side of the integrating sphere so that absorbance and reflectance can be measured using the same configuration (figure A-1, D and E). Positioning the sample on the opposite side of the light source also allows it to be placed on a metal stage cooled by liquid nitrogen, which is often used for testing diamonds.

BOX B: OPTICAL SPECTROMETERS

The equations and measurement configurations explained in box A (figure A-1) consider light as a single entity. However, absorption (or reflection) spectroscopy requires the measuring of absorbance (or reflectance) at each individual wavelength, and this involves splitting light into different wavelengths. There are two physical processes for splitting polychromatic light (light containing multiple colors) into a spectrum of different wavelengths: dispersion and diffraction. The refractive index of a transparent material is often dependent on wavelength, which means light of different wavelengths may be refracted at different angles, allowing light to be dispersed into its spectral components by a prism. (This was how Sir Isaac Newton discovered that white light consists of a mixture of different colors.) Diffraction, on the other hand, takes advantage of how light interferes differently depending on wavelengths and scattering angles. A diffraction grating is an optical device that uses diffraction to split light (Jin and Smith, 2024). Both dispersive prisms and diffraction gratings can be used to make spectroscopes, while diffraction gratings are much more commonly used in spectrometers due to their higher efficiency and accuracy.

A scanning spectrophotometer scans through the spectrum range and measures the light intensity at each wavelength one at a time (figure B-1, top). After the white light source is separated into different wavelengths, only a very narrow range of wavelengths is allowed to pass through a narrow exit slit to the sample and be measured by the detector. The wavelength of light that passes through can be accurately controlled by adjusting the relative angle between the diffraction grating (or optical prism) and the exit slit (the actual optics are much more complicated than shown in figure B-1). This optical device that reduces polychromatic light (consisting of multiple wavelengths) to monochromatic light (of a single wavelength) is called a monochromator. The box with a dashed outline in figure B-1 (top) is a common example. The complete optical spectrum is measured by scanning the monochromator across the desired range. An optional second monochromator tuned to the same wavelength as the incident light can be positioned after the sample and before the detector to filter out any luminescence from the sample, allowing only attenuated light of the same wavelength to pass through to the detector.

In a CCD spectrometer, white light passes directly through the sample before being separated into its spectral components by a stationary dispersion device (figure B-1, bottom). An elongated CCD detector covering the

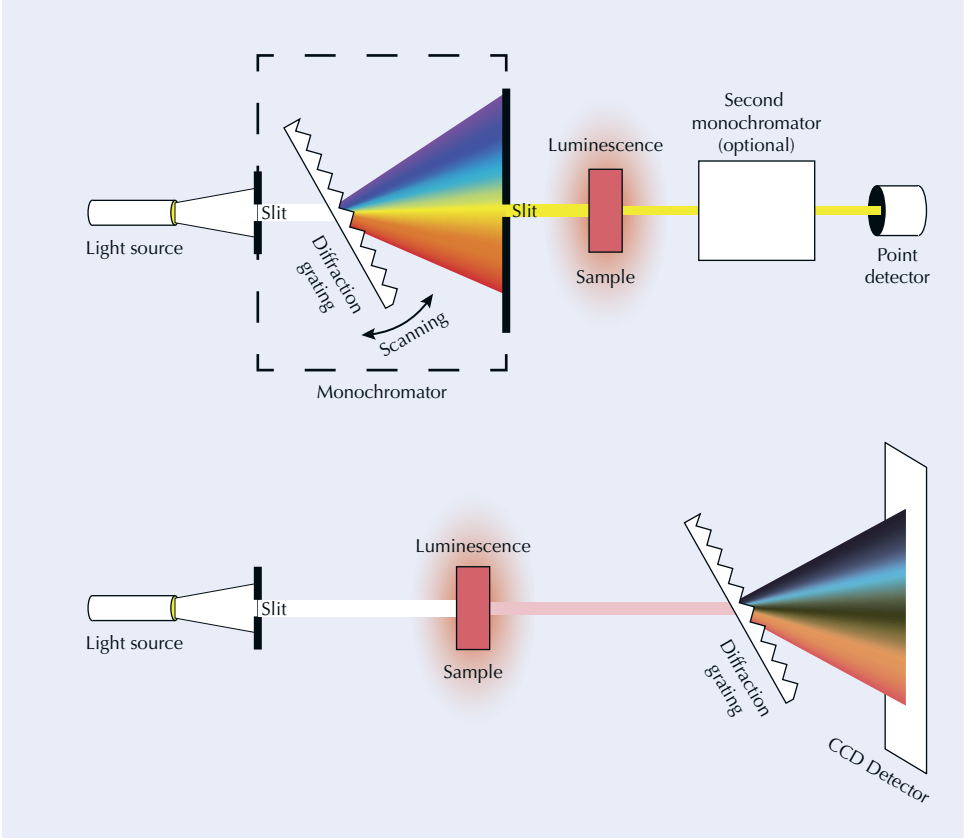

Figure B-1. Schematic comparison of the scanning spectrophotometer (top) and the CCD spectrometer (bottom). The scanning spectrophotometer measures absorbance at each wavelength sequentially, whereas the CCD measures the entire spectrum simultaneously. The CCD detector cannot remove luminescence from the sample excited by the incident light, which may affect the shape of the measured spectrum. Transmission gratings are shown for simplicity, though in reality, reflective gratings are more common in monochromators and CCD spectrometers.

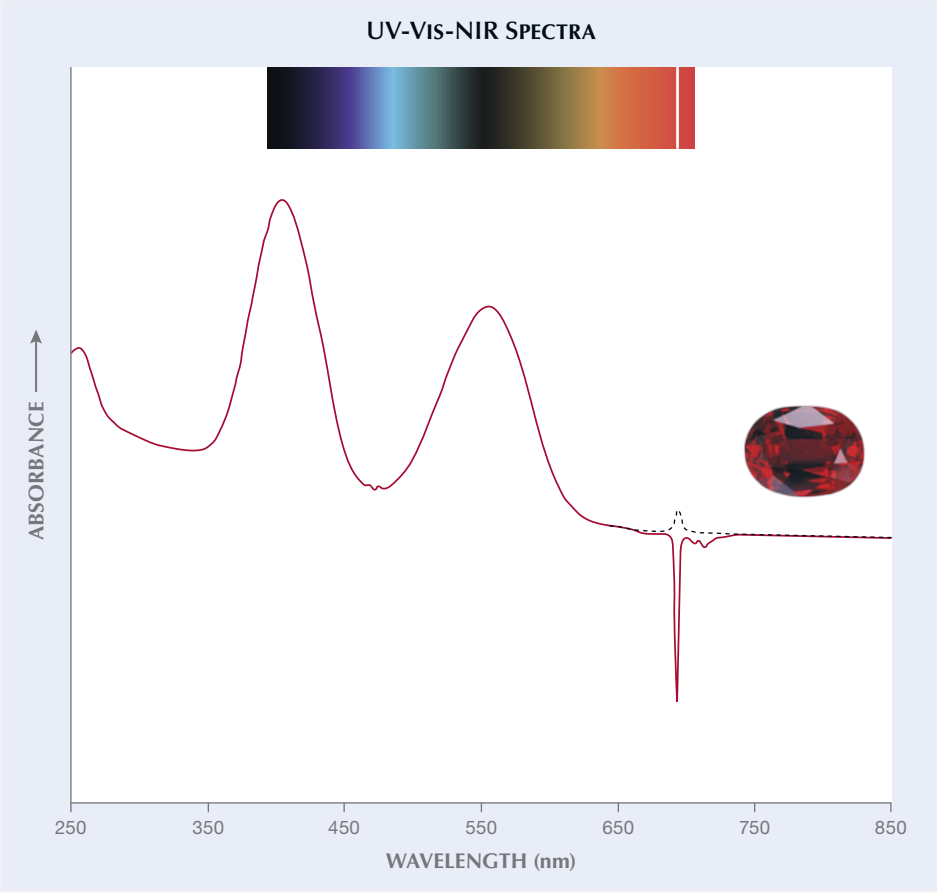

Figure B-2. The absorption spectrum of a synthetic ruby measured using a CCD spectrometer is compared to the view in a spectroscope. Absorption peaks in the spectrum appear as dark bands in the spectroscope. The CCD spectrometer has a much wider range than the spectroscope. A scanning spectrophotometer can have an even wider range, extending from 200 to 2500 nm. The sharp Cr^{3+} fluorescence peak at 694 nm appears as a negative dip, as the "attenuated" light intensity at this wavelength is stronger than the unattenuated incident light. Similarly, a sharp, bright line may be observed in the spectroscope. This type of artifact can be easily recognized for sharp luminescence features but may be overlooked if the luminescence band is broad. A scanning spectrophotometer avoids this artifact by measuring one wavelength at a time, revealing a sharp absorption peak at 694 nm (black dashed line).

entire angle of the dispersed spectrum is positioned at the end. By using well-characterized emission features of known materials, the detector can be calibrated to accurately correlate each pixel on the CCD to a specific wavelength. Note that a handheld spectroscope is essentially a simplified version of a CCD spectrometer, with a human eye in place of the CCD detector. Of course, the human eye can only detect light within the visible spectrum and will miss any features in the UV or NIR range.

The relationship between scanning and CCD spectrometers is analogous to that between the two types of X-ray diffractometers (Jin and Smith, 2024). The scanning spectrophotometer is much more accurate in measuring intensity at each specific wavelength and removes any potential interference from sample luminescence. Light polarizers can be implemented to allow measurement of polarized spectra. However, the geometry of the monochromators before and after the sample significantly limits the flexibility of this device, making it suitable almost exclusively for measuring transparent wafers in a direct light path (figure A-1A). The high-precision optics in the monochromators in scanning spectrophotometers also make them very expensive, limiting their availability to research or industrial facilities. Scanning through a desired range of the spectrum can be time-consuming, especially when high spectral resolution and high accuracy are needed.

The more affordable CCD spectrometers offer a number of advantages. They can make measurements much more rapidly because they capture the entire spectral range simultaneously, and the signal reaching the detector can be integrated repeatedly over a period of time to improve the signal-to-noise ratio. And because unseparated white light is used through most of the optics until the final part before the CCD detector (figure B-1, bottom), the configuration is much more flexible, allowing measurement of opaque and irregularly shaped samples, especially while using integrating spheres (figure A-1, B–E). As a result, CCD spectrometers have become much more widely used for gemological applications. However, one significant disadvantage is that these spectrometers cannot correct for photoluminescence excited by the incident light from the sample (figure B-1, bottom). Sharp-band luminescence features are easily identifiable (e.g., the Cr^{3+} band in ruby, as shown in figure B-2), whereas broad emission

bands can potentially alter the shape of the absorption spectrum in a way that is not noticeable.

It should be noted that the detector in a spectrometer can only measure light intensities within a certain range. Below this range, any signal is indistinguishable from noise. Above it, the detector is saturated and every signal is registered as the same value. The ratio of the maximum value to the minimum value a detector can measure is known as its dynamic range. For a detector with a dynamic range of 1000:1, if the unattenuated intensity of the light source is barely saturating the detector, the lowest transmittance the detector could measure would be 1/1000 (or 0.1%), meaning the largest absorbance that can be measured is 3 (i.e., $\log_{10}1000$). Both the light source intensity and the dynamic range of the detector are wavelength-dependent, which means the measurable range for absorbance by a spectrometer is limited by its weakest point in the spectrum. Most spectrometer software plots unmeasurable absorbance as a constant value above the highest value that can be theoretically measured to avoid confusion, sometimes causing the absorption spectrum to appear as a perfectly flat line when it reaches a certain value. It may be possible to extend the dynamic range by attenuating the light source with a filter of known absorbance or breaking the spectrum into several parts that can be optimized separately. Reducing the light path length (e.g., measuring along a shorter dimension or the edge of the sample) may also help bring the absorbance back to the measurable range of the spectrometer. Weak absorption features (e.g., small sample size, inefficient chromophore) can be enhanced by extending the light path and prolonging the measurement time (i.e., increasing the exposure time or averaging the intensities from multiple measurements).

The ideal light source for a UV-Vis-NIR spectrometer provides white light with a homogeneous intensity across the entire spectrum range, though no single light source fits this criterion yet. LED lights with discontinuous spectra or fluorescent lights with sharp emission peaks are generally not suitable for a UV-Vis-NIR spectrometer. Instead, a tungsten-halogen lamp with a broad emission band spread across 350–1000 nm is typically used to cover the Vis-NIR range, and a deuterium lamp or xenon arc lamp can be used to cover the UV range between 200 and 400 nm. These lamps may operate separately to prolong their lifetime, depending on the range being measured, or together to cover the entire UV-Vis-NIR range. Multiple detector or monochromator types are sometimes used in scanning spectrophotometers to compensate for reduced efficiency or accuracy in different ranges. Switching between these components may introduce step-shaped artifacts in the measured spectrum, though their positions can often be adjusted to avoid significant interference with real features in the data.

dominantly colored by copper (Paraíba tourmaline) and tourmaline colored mainly by iron. Although vividly bright neon blue or green Paraíba tourmaline can often be identified visually, the color of some samples with lower saturation and tone may overlap with tourmaline dominantly colored by iron. UV-Vis-NIR spectroscopy provides a clear distinction: Cu^{2+} in tourmaline has two absorption bands at about 697 and 900 nm (Fritsch et al., 1990; Shigley et al., 2001), while Fe^{2+} has only a single band at about 715 nm (figure 2) within the measured range. Although some tourmalines have comparable color

Figure 2. Absorption spectra of copper-dominant Paraíba tourmaline (left) and iron-dominant tourmaline (right).

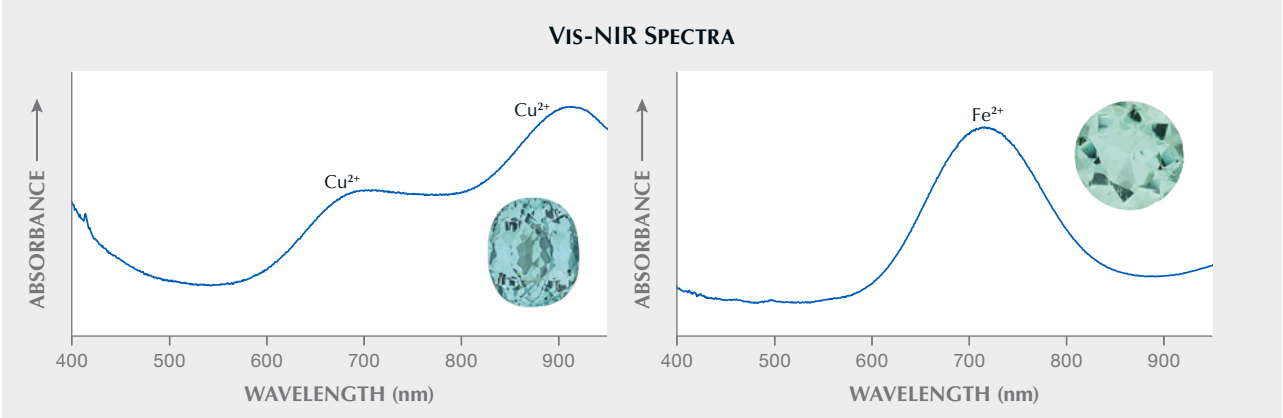

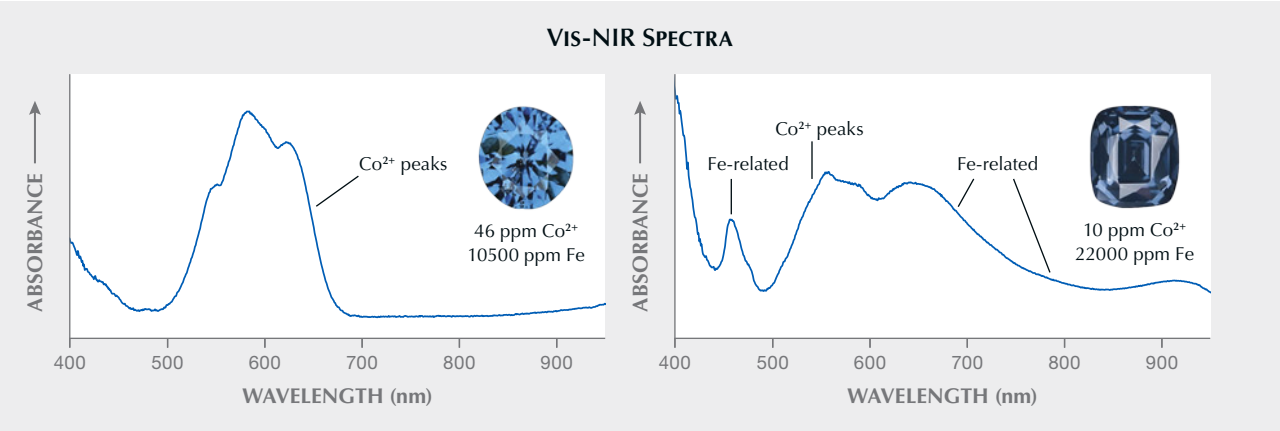

Figure 3. Example absorption spectra of a cobalt spinel (left) and a grayish blue spinel that does not meet the criteria due to its color and the significant influence of iron on its color (right).

contributions from both Cu^{2+} and Fe^{2+}, the end members can be easily separated. Those intermediate stones are a subject of further research that is outside the scope of this article.

Blue Spinel. Another common application of UV-Vis-NIR spectroscopy is distinguishing between blue spinel dominantly colored by cobalt and spinel with a significant iron component. Co^{2+} has a unique spectral pattern, with several peaks from 540 to 622 nm (figure 3, left) (D'Ippolito et al., 2015; Palke and Sun, 2018). Iron also has several possible absorption features in the visible range, including narrow bands at 459 and 473 nm likely related to Fe^{3+}, as well as broad bands around 650 and 900 nm and relatively sharp bands around 555 nm that overlap with Co^{2+} absorption features (figure 3, right). It is important to note that blue color in spinel is caused exclusively by Co^{2+}, while iron-related absorption alters the color by adding gray, purple, or greenish components. Determining whether a blue spinel qualifies as "cobalt spinel" requires a multivariate approach that considers its color, chemistry, and UV-Vis-NIR absorption spectrum together.

Aquamarine vs. Maxixe Beryl. UV-Vis-NIR can also be used to distinguish aquamarine from Maxixe beryl. Aquamarine's blue color is caused by the presence of Fe^{2+}, whose absorption can be intensified by the presence of Fe^{3+} (Taran and Rossman, 2001). Maxixe beryl derives its blue color from radiation. Figure 4 (left) shows a typical aquamarine spectrum, featuring a dominant absorption feature at about 830 nm producing the blue color. This absorption feature is also highly polarizable, with the maximum intensity perpendicular to the *c*-axis (the long dimension of most

Figure 4. Absorption spectra of aquamarine (left) and Maxixe beryl (right).

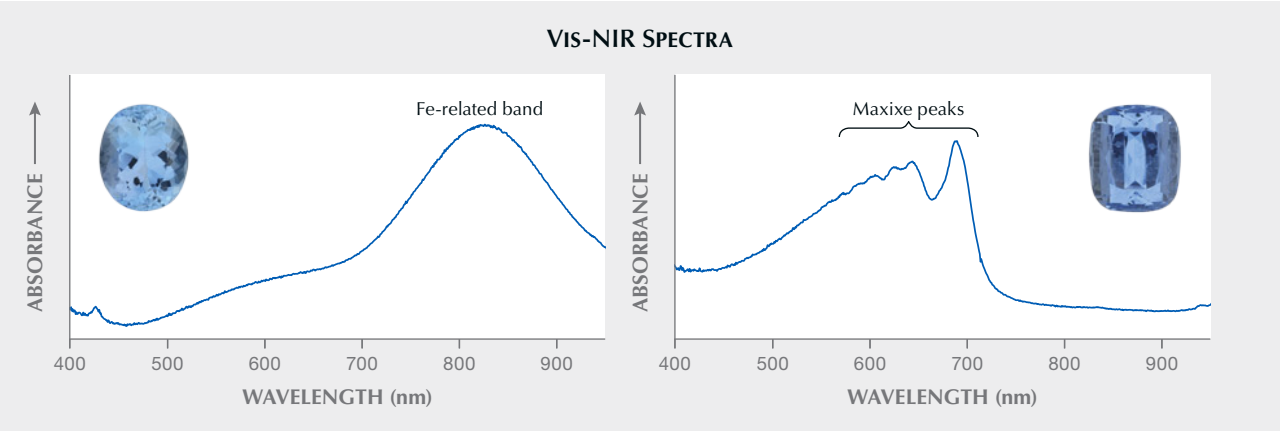

aquamarine crystals). As a result, an aquamarine's blue color appears most intense when the crystal is viewed perpendicular to the *c*-axis; it displays almost no color when viewed along the *c*-axis. In contrast, Maxixe beryl's pleochroic colors are the opposite, with the most intense blue color displayed down the *c*-axis and a weaker blue color perpendicular to the *c*-axis. The distinct UV-Vis-NIR spectrum of Maxixe beryl can also aid in its identification (Adamo et al., 2008). Maxixe beryl has a prominent, fairly narrow peak at about 691 nm, with several smaller peaks at shorter wavelengths of about 646, 630, 607, and 590 nm. These features typically overlay a relatively broad absorption band centered at roughly 620 nm (figure 4, right). It is important to be able to distinguish Maxixe beryl, as its radiation-induced blue color is often unstable and may fade with time.

Magmatic vs. Metamorphic Sapphire. Geographic origin determination for blue sapphire can be an extremely complicated and difficult task. Determining the geological origin of a sapphire, whether metamorphic or magmatic, can be simplified by reducing the number of origins to consider. The UV-Vis-NIR spectrum for sapphires of magmatic origin (e.g., Australia, Thailand, Cambodia, Nigeria, and Ethiopia) shows a pronounced absorption feature at 880 nm. Sapphires of metamorphic origin (e.g., Sri Lanka, Myanmar, Madagascar, and Kashmir) either lack this feature or show an 880 nm band of lower intensity than the Fe^{2+}-Ti^{4+} IVCT band at 580 nm (figure 5) (Palke et al., 2019). The origin of the 880 nm band is unclear but may be related to some combination of iron and titanium ions in corundum (Fritsch and Rossman, 1988; Moon and Phillips, 1994; Hughes et al., 2017). "Nonclassical" sapphire from Tanzania and Montana will show a UV-Vis-NIR spectrum more similar to metamorphic sapphire, lacking the 880 nm feature, but show pronounced Fe^{3+} absorption bands at 378, 388, and 450 nm (Dubinsky et al., 2020). One complication is that some higher-iron metamorphic sapphires may take on a magmatic-looking absorption pattern after low-temperature heating (Hughes and Perkins, 2019).

Jadeite (Natural vs. Dyed Color). The color origin of jadeite (natural or dyed) can also be determined by UV-Vis-NIR spectroscopy. A common cause of green color in jadeite is from Cr^{3+} with broad absorption bands around 454 and 645 nm and a sharp feature around 691 nm (figure 6A). While these can often be observed with a handheld spectroscope, a UV-Vis-NIR spectrometer can be helpful in cases where a jadeite is mounted or it is difficult to transmit light through the piece and into the spectroscope. Fe^{2+} can also cause green color in jadeite, though this green color is never as vibrant and vivid as that in high-quality chromium-colored jadeite. Fe^{2+} bands in jadeite can be seen at around 769 and 940 nm (figure 6B). Fe^{3+} absorption features may also be seen as sharp

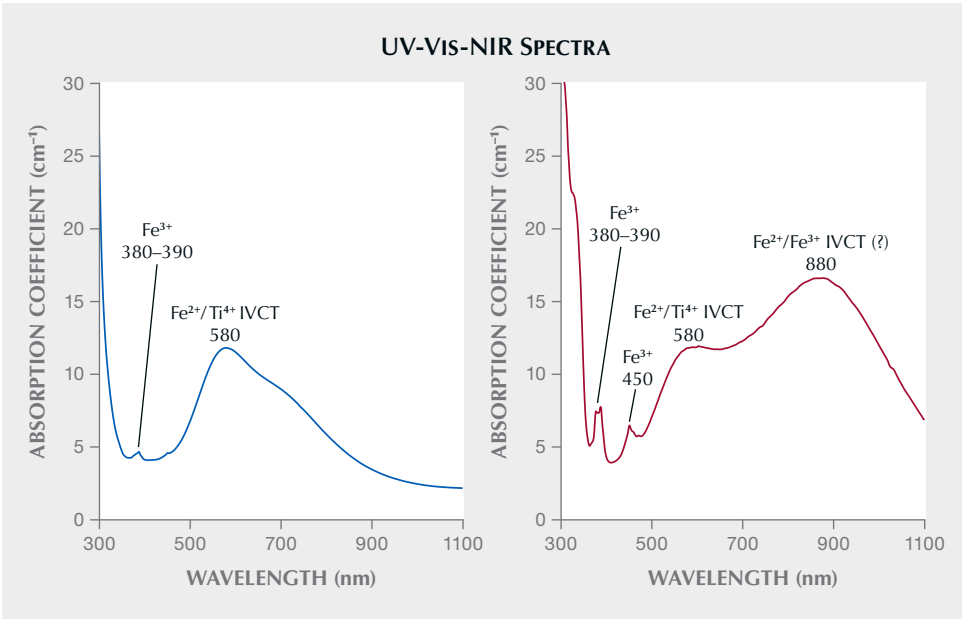

Figure 5. Absorption spectra showing the different intensities of the 880 nm band between metamorphic sapphire (left) and magmatic sapphire (right). From Palke et al. (2019).

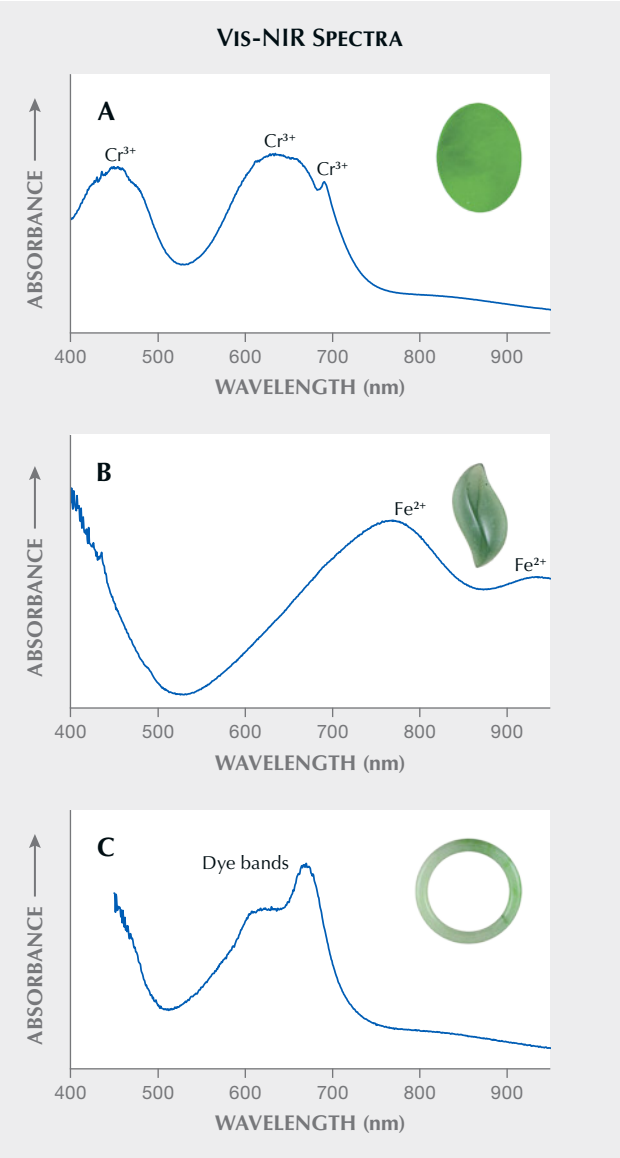

Figure 6. Examples of Vis-NIR spectra of jadeite colored by Cr^{3+} (A), Fe^{2+} (B), and artificial dyes (C).

bands at about 369, 381, 431, and 473 nm, but their effect on color is usually minimal. Dyed green jadeite has an entirely different absorption spectrum, typically displaying a double peak at around 620 and 669 nm (figure 6C). Similar criteria can also be used to separate dyed from natural-color lavender jadeite (Lu, 2012).

Chrome Varieties (Garnet, Tourmaline, Diopside, and Chalcedony). To be considered chrome varieties, the color of garnet, tourmaline, diopside, and chalcedony must be predominantly derived from the presence of chromium (and/or vanadium in the case of some tourmaline and diopside). The presence of chromium is easily confirmed in a UV-Vis-NIR spectrum by the presence of the characteristic Cr^{3+} absorption pattern consisting of two broad peaks. Figure 7 compares two green tourmalines, one colored by Cr^{3+} and the other by Fe^{2+}. Similar absorption patterns have been observed for other chromium-colored gems. Note that V^{3+} often shows an absorption pattern very similar to that of Cr^{3+} for green gems such as emerald or tourmaline, and the so-called chrome variety in the gem trade often includes certain green gemstones predominantly colored by vanadium.

Fancy-Color Diamonds. Because colorless diamonds typically do not show any useful features in the UV-Vis-NIR range, optical spectroscopy is used primarily for testing diamonds with fancy colors. Whereas the colors of colored gemstones can be predicted quite accurately just from their chemical compositions, the light-absorbing features of diamond depend on the exact configurations of defects and defect clusters. Despite the simple chemistry of diamond, it has numerous types of light-absorbing defects and defect clusters, many of which are still poorly understood. Color-causing defects in diamond could easily constitute a set of review articles or even monographs (Zaitsev, 2001; Dischler, 2012; Green et al., 2022). Only a few representative examples will be presented here to showcase the complexity of diamond identification and how it can be facilitated by UV-Vis-NIR spectroscopy.

UV-Vis-NIR spectra of diamonds are typically collected at liquid nitrogen temperatures, as the characteristic sharp absorption features of several defects are temperature sensitive. But the room-temperature spectrum also provides valuable information about the impact of different color centers on the diamond's overall bodycolor. Therefore, the handheld spectroscope can be used to observe many of the spectral features of a diamond, particularly one with strong color.

During crystallization, elements such as nitrogen, boron, and hydrogen can be incorporated into the diamond structure. Annealing at high-pressure, high-temperature (HPHT) conditions, as well as radiation after crystallization, can create new defects, destroy existing ones, or modify them into different configurations. Therefore, identifying the defect types in a diamond helps reveal its temperature, pressure, and radiation history. The different conditions required for each defect to form can potentially distinguish natural colors from colors created by treatment

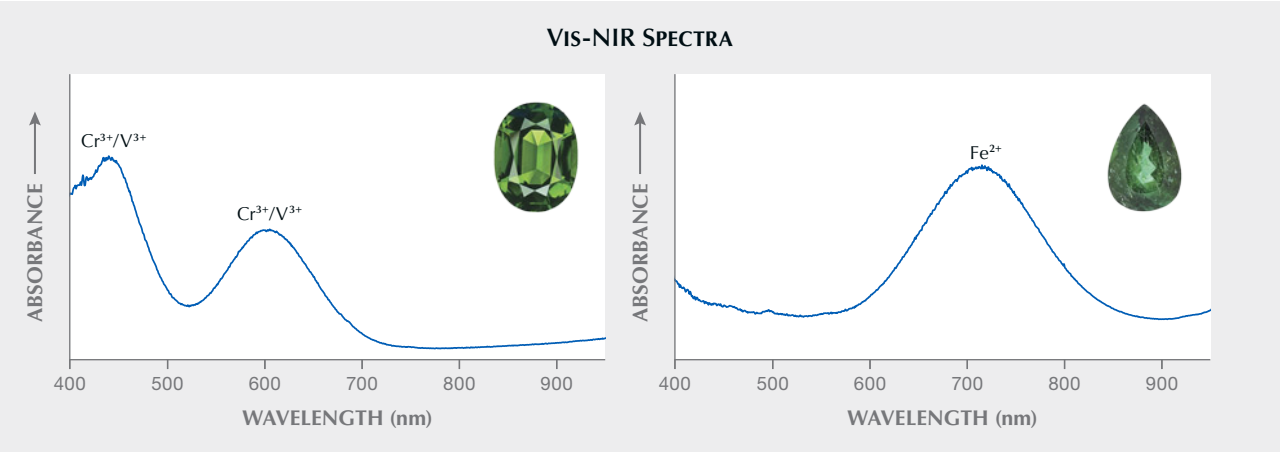

Figure 7. Absorption spectra of chrome tourmaline (left) and iron-colored green tourmaline (right).

processes. Some defects or combinations of defects in diamonds can only form naturally, requiring the extreme temperature-pressure conditions only found deep in the earth, while others require geological timescales for the defects to cluster into certain configurations. These defects may or may not survive certain treatment processes. Some defects are only found in laboratory-grown or treated diamonds, as the conditions needed to create them rarely occur or do not exist in nature. Of course, some defects can be created both naturally and artificially, particularly when the natural conditions responsible are easily replicated in a laboratory.

Fancy Yellow Diamond. Yellow is one of the most common colors in diamond. In fact, many light-colored diamonds are treated to intensify their colors beyond the D-to-Z color scale so they can be graded as fancy-color diamonds with potentially higher value. This yellow hue can be attributed to several types of defects. Four common types are isolated nitrogen defects (C center), the H3 (N_2V^0) defect, the "cape" series defect, and the 480 nm band defect (Breeding et al., 2020).

Isolated nitrogen produces a broad absorption band that peaks in the UV range and extends into the blue region (figure 8). Though all nitrogen-bearing diamonds can contain C centers, those with most nitrogen atoms in isolation, known as type Ib diamonds, are rare in nature, making up only 0.1% of all natural diamonds (Breeding et al., 2020). However, C centers are responsible for the color of most laboratory-grown yellow diamonds. The H3 (N_2V^0) defect consists of two nitrogen atoms surrounding a

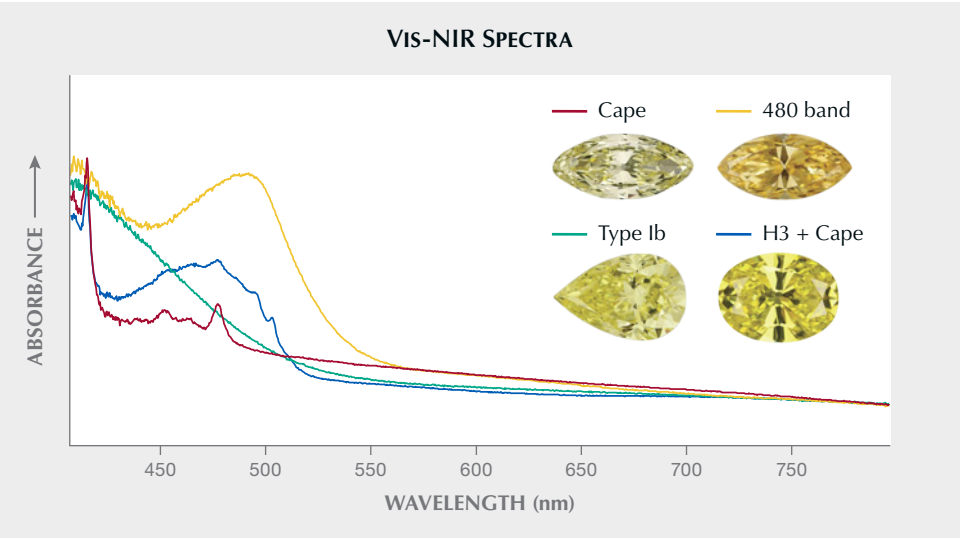

Figure 8. A comparison of four yellow diamonds colored by different defects. The absorption spectra were collected at liquid nitrogen temperature using the configuration shown in figure A-1D. The cape diamond and the 480 band diamond are both natural, while the type Ib diamond is laboratory grown. The H3 + cape diamond was irradiated and annealed to enhance its yellow color.

neutral vacancy with broad absorption in the blue region, characterized by a sharp peak at 503.2 nm (again, see figure 8) (Breeding et al., 2020), which imparts a yellow bodycolor to a diamond. Both C centers and H3 (N_2V^0) defects can be introduced by HPHT treatment to enhance the yellow color. H3 (N_2V^0) defects can also be created by irradiation followed by annealing.

"Cape" series absorption features, named after their original association with South Africa, can occur in diamonds from nearly all deposits. These consist of a series of bands in the blue to UV region, with prominent peaks at 415, 451, and 478 nm (figure 8), mostly related to the N3 (N_3V^0) defect (three nitrogen atoms around a single vacancy) (Mainwood, 1994). Much of the light yellow color in D-to-Z diamonds is due to various concentrations of cape series defects (King et al., 2008).

The defect structure of the wide absorption band centered at 480 nm (figure 8) is unknown, although it has been shown to be related to nickel and nitrogen (Breeding et al., 2020). This band creates yellow to orange color in diamond. Both the cape series and the 480 band are only known to occur naturally and have not been introduced through HPHT treatment.

Other Fancy-Color Diamonds. In addition to yellow, diamonds come in all other colors, each with its own unique defects and UV-Vis-NIR spectra. For instance, blue color can be caused by boron substitution, isolated vacancies, or rarely hydrogen-related defects (Eaton-Magaña et al., 2018). Green color in diamonds is commonly caused by radiation-induced vacancies plus absorption from more complex defects or hydrogen-related defects, though several additional but rarer cases can also produce green color (Breeding et al., 2018). Therefore, UV-Vis-NIR is helpful in identifying the specific defects present (i.e., what "kind" of green diamond). In addition to color-causing defects, there are also defects that contribute little to the color but provide clues as to the radiation and/or annealing history of the stone, indicating possible treatments. UV-Vis-NIR alone is not diagnostic, however, and requires further testing and gemological observation to determine a diamond's color origin with certainty.

Pearls. UV-Vis-NIR reflectance spectroscopy (figure A-1E) can be used to identify biological pigments responsible for natural color in pearls. This helps differentiate between naturally and artificially colored pearls, especially when visual evidence is absent. The untreated colors of pearls, whether natural or cultured, are mainly caused by a mixture of biological pigments associated with the mollusk species producing the pearls. Different mollusk species create pearls in different color ranges. The major pigments across various species are porphyrin and polyenic groups (Iwahashi and Akamatsu, 1994; Karampelas et al., 2007), as well as melanin (Jabbour-Zahab et al., 1992; Wang et al., 2020). And in some cases, unidentified pigments were reported to be responsible for the yellow coloration of saltwater pearls produced from *Pinctada* species (Karampelas et al., 2020).

For pearls, reflection spectra are generally obtained in the 250–800 nm range. It should be noted that reflectance refers to the light not absorbed by the surface, which means a reflection spectrum is interpreted in the opposite way as an absorption spectrum. Absorption features that appear as peaks in an absorption spectrum will appear as dips in a reflection spectrum. The bodycolor of a pearl corresponds to the high-reflectance regions in the reflection spectrum that are less affected by absorption features. Almost all pearls show a common absorption feature at about 280 nm that is associated with conchiolin, a mixture of protein and polysaccharides found in pearls and shells. In the visible range, the spectra for white and very light-colored pearls are relatively featureless due to weak or absent pigmentation, while darker and more saturated pearls exhibit lower reflectance in their spectra and more prominent absorption features. Strong overtone or iridescence colors on the surface may impact the spectrum patterns.

Dark-Colored Nacreous Pearls. Dark, natural-color saltwater nacreous pearls, ranging from light gray, gray, and brown to black with various hues such as green and blue, display characteristic absorption features at 405 and/or 495 nm (Elen, 2002; Karampelas et al., 2011). These features can be used to separate them from artificial dark colors created by dye (figure 9). The 405 nm feature is reported to be from uroporphyrin pigmentation (Iwahashi and Akamatsu, 1994), while the 495 nm feature is possibly related to a type of porphyrin.

Most of the dark-colored pearls on the market are known as Tahitian pearls, produced from *Pinctada margaritifera*. These and the closely related pearls from *P. mazatlanica* display a diagnostic feature at 700 nm (Wada, 1984; Homkrajae, 2016) that can be used to separate them from other natural dark-colored pearls, including other *Pinctada* species (Karampelas, 2012; Homkrajae, 2016; Nilpetploy et al., 2018; Al-

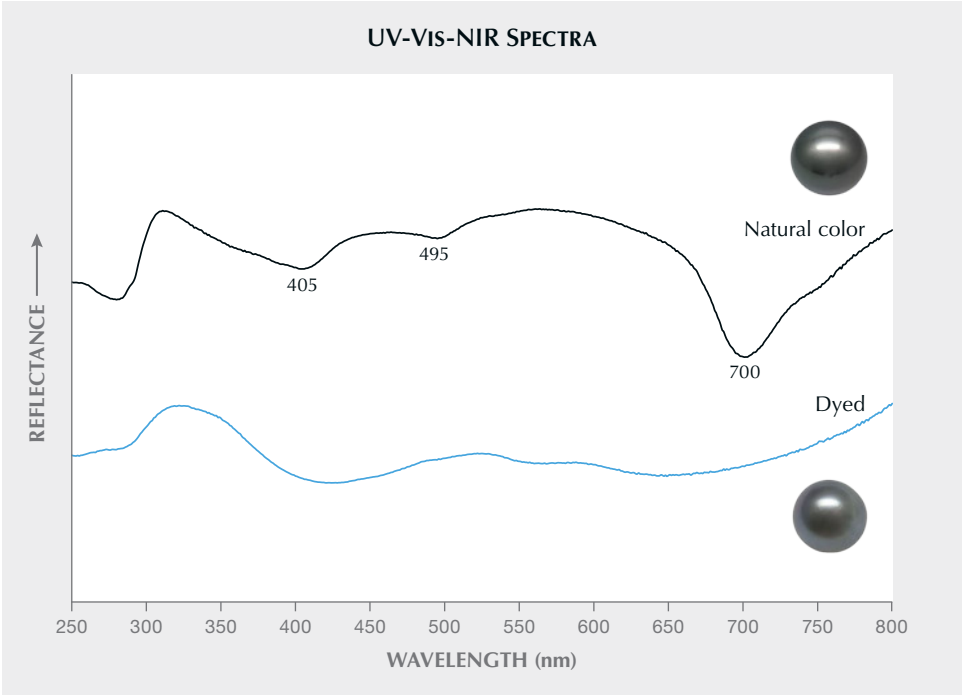

Figure 9. Reflectance spectra of dark gray nacreous pearls, natural and dyed. A natural-color Tahitian pearl exhibits characteristic absorption features at 405 and 495 nm, together with a diagnostic 700 nm feature of the P. margaritifera *mollusk. The natural pigmentation features are absent in the spectra of dyed dark gray pearls.*

Alawi et al., 2020), *Pteria* pearls (Kiefert et al., 2004), and windowpane oyster pearls produced by the Placunidae family (Ho et al., 2024).

Additionally, a series of chemical and physical processes has been reported to lighten naturally gray to dark gray Tahitian pearls to "chocolate" and "pistachio" colors. Since this color alteration is achieved by modifying or removing certain natural pigments, no foreign coloring agent can be detected on the surface. UV-Vis-NIR reflectance spectra obtained from the treated "chocolate" and "pistachio" pearls still show the natural pigment features, but they become

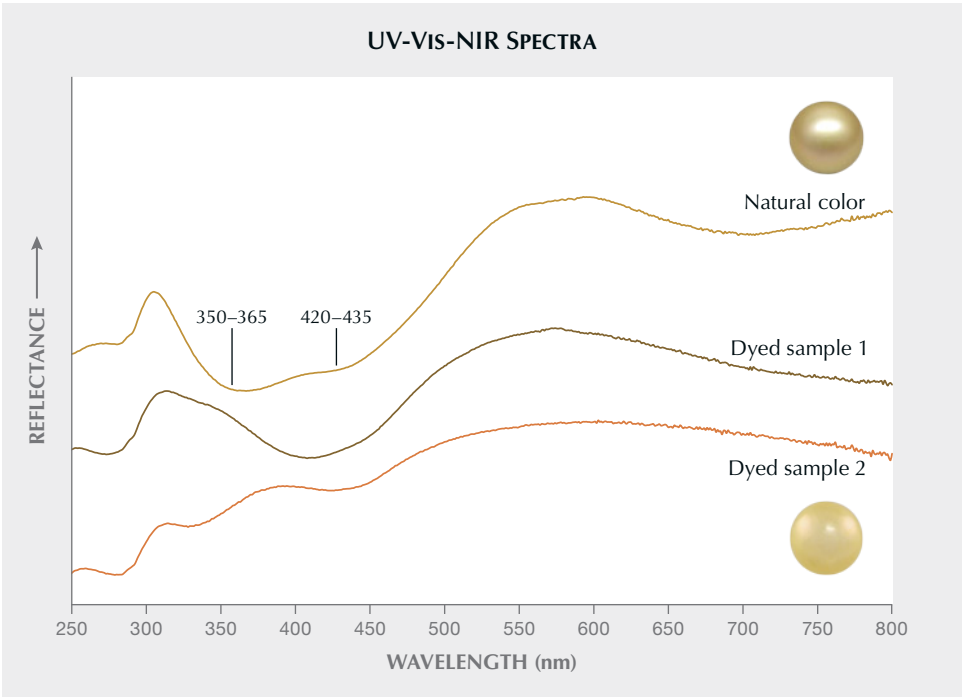

Figure 10. Reflectance spectra of natural and treated yellow nacreous pearls. A natural-color South Sea pearl exhibits a broad absorption region between 330 and 460 nm, consisting of two distinct bands at 350–365 nm and 420–435 nm. Dyed yellow pearls normally have an absence of this characteristic or the presence of different absorption features in the blue region of the spectrum.

broader and the centers are shifted from the 405 and 495 nm positions (Wang et al., 2006; Zhou et al., 2016). The diagnostic 700 nm feature for *P. margaritifera* (Tahitian) remains unchanged in these treated pearls.

Yellow Nacreous Pearls. Yellow colors in pearls are caused by preferential absorbance of light in the long-wave UV to blue region of the spectrum, with most of the green to red light reflected by the surface. Yellow and orangy yellow *Pinctada maxima* pearls, commonly known as golden South Sea pearls, are among the most desirable pearls in the market. Natural-color yellow South Sea pearls typically show a broad absorption region between 330 and 460 nm (figure 10). This broad region usually consists of two absorption features, the first centered between 350 and 365 nm and the second between 420 and 435 nm (Elen, 2001). Similar absorption features have also been observed in yellow-hued pearls produced by other species, including *P. margaritifera* (Karampelas et al., 2011), *P. mazatlanica* (Homkrajae, 2016), and *P. maculata* (Nilpetploy et al., 2018). The absence of this characteristic or the presence of different absorption features in the blue region of the spectrum indicates an unnatural origin for the yellow color (figure 10) (Elen, 2001, 2002; Zhou et al., 2012).

Heat treatment has been reported to create uniform and enhanced colors in cream and light yellow pearls. This process supposedly does not introduce any external dye materials into the pearl. Therefore, the characteristic absorption features observed in natural-color pearls appear much weaker or completely absent in heated yellow pearls with the same color (Elen, 2001; Zhou et al., 2012).

The natural colors in freshwater pearls are caused by a mixture of various polyenic pigments (Karampelas et al., 2009, 2020), which display absorption features in the range of violet to yellow (405–568 nm) of the visible spectrum (Karampelas et al., 2009; Homkrajae et al., 2019). Unfortunately, these features in freshwater pearls are much more complicated and difficult to identify than those in saltwater pearls and thereby not useful for identification purposes. Raman spectroscopy is more useful for identifying the polyenic pigments in freshwater pearls (Jin and Smith, 2024).

CONCLUSIONS

At first glance, the UV-Vis-NIR spectrometer might seem the simplest analytical testing instrument in a gemological laboratory, as it employs the same basic principles as a handheld spectroscope. However, its application to gemology is one of the most far-reaching across all categories of gemstones, since color is such a significant value factor for colored stones, fancy-color diamonds, and pearls. Due to the wide range of size, shape, form, and diaphaneity of gemstones, measuring their UV-Vis-NIR spectra is often challenging. Specialized instruments and configurations have been designed for specific applications, such as mounted jewelry, opaque materials, and even liquid nitrogen measurements, all of which require special procedures for testing. Unlike Raman spectroscopy, which can be automated by computer programs to a great extent, interpreting a UV-Vis-NIR spectrum is not nearly as straightforward. Rigorous training and extensive practice are required for a gemologist to separate the true signals from noise and instrument artifacts and make a correct assessment. As demonstrated by the examples presented in this article, considerable information is hidden behind the striking colors of gemstones. In fact, the mechanisms of many colors in gemstones are still not fully understood. For instance, the exact electronic transition and defect configuration of amethyst, blue zircon, and many light-absorbing features in diamonds are still unknown. The light-absorbing defects in gem materials, as well as their reactions to treatments, are the subject of a very active research field in gemology, and new discoveries constantly emerge. As our understanding of the causes of colors in gems deepens, the utility of UV-Vis-NIR spectroscopy continues to grow.

ABOUT THE AUTHORS

Dr. Shiyun Jin is a research scientist, Nathan Renfro is senior manager of colored stone identification, Dr. Aaron Palke is senior manager of research, Troy Ardon is a senior research engineer, and Artitaya Homkrajae is supervisor of pearl identification at GIA in Carlsbad, California.

ACKNOWLEDGMENTS

The authors thank the peer reviewers for many constructive comments and suggestions.

REFERENCES

Adamo I., Pavese A., Prosperi L., Diella V., Ajò D., Gatta G.D., Smith C.P. (2008) Aquamarine, Maxixe-type beryl, and hydrothermal synthetic blue beryl: Analysis and identification. *G&G*, Vol. 44, No. 3, pp. 214–226, http://dx.doi.org/10.5741/GEMS.44.3.214

Al-Alawi A., Ali Z., Rajab Z., Albedal F., Karampelas S. (2020) Saltwater cultured pearls from *Pinctada radiata* in Abu Dhabi (United Arab Emirates). *Journal of Gemmology*, Vol. 37, No. 2, pp. 164–179.

Anderson B.W., Payne C.J., Mitchell R.K. (1998) *The Spectroscope and Gemmology*. GemStone Press, Woodstock, Vermont.

Baier E. (1932) Die optik der edelopale. *Zeitschrift für Kristallographie - Crystalline Materials*, Vol. 81, No. 1-6, pp. 183–218, http://dx.doi.org/10.1524/zkri.1932.81.1.183

Bolton H.C., Bursill L.A., McLaren A.C., Turner R.G. (1966) On the origin of the colour of labradorite. *Physica Status Solidi (b)*, Vol. 18, No. 1, pp. 221–230, http://dx.doi.org/10.1002/pssb.19660180123

Breeding C.M., Ahline N. (2024) Infrared spectroscopy and its use in gemology. *G&G*, Vol. 60, No. 4, pp. 474–492, http://dx.doi.org/10.5741/GEMS.60.4.474

Breeding C.M., Shen A.H., Eaton-Magaña S., Rossman G.R., Shigley J.E., Gilbertson A. (2010) Developments in gemstone analysis techniques and instrumentation during the 2000s. *G&G*, Vol. 46, No. 3, pp. 241–257, http://dx.doi.org/10.5741/GEMS.46.3.241

Breeding C.M., Eaton-Magaña S., Shigley J.E. (2018) Natural-color green diamonds: A beautiful conundrum. *G&G*, Vol. 54, No. 1, pp. 2–27, http://dx.doi.org/10.5741/GEMS.54.1.2

——— (2020) Naturally colored yellow and orange gem diamonds: The nitrogen factor. *G&G*, Vol. 56, No. 2, pp. 194–219, http://dx.doi.org/10.5741/GEMS.56.2.194

D'Ippolito V., Andreozzi G.B., Hålenius U., Skogby H., Hametner K., Günther D. (2015) Color mechanisms in spinel: Cobalt and iron interplay for the blue color. *Physics and Chemistry of Minerals*, Vol. 42, No. 6, pp. 431–439, http://dx.doi.org/10.1007/s00269-015-0734-0

Dischler B. (2012) *Handbook of Spectral Lines in Diamond*. Springer, Berlin, Heidelberg.

Dowty E. (1978) Absorption optics of low-symmetry crystals—Application to titanian clinopyroxene spectra. *Physics and Chemistry of Minerals*, Vol. 3, No. 2, pp. 173–181, http://dx.doi.org/10.1007/BF00308120

Dubinsky E.V., Stone-Sundberg J., Emmett J.L. (2020) A quantitative description of the causes of color in corundum. *G&G*, Vol. 56, No. 1, pp. 2–28, http://dx.doi.org/10.5741/GEMS.56.1.2

Eaton-Magaña S., Breeding C.M., Shigley J.E. (2018) Natural-color blue, gray, and violet diamonds: Allure of the deep. *G&G*, Vol. 54, No. 2, pp. 112–131, http://dx.doi.org/10.5741/GEMS.54.2.112

Elen S. (2001) Spectral reflectance and fluorescence characteristics of natural-color and heat-treated "golden" South Sea cultured pearls. *G&G*, Vol. 37, No. 2, pp. 114–123, http://dx.doi.org/10.5741/GEMS.37.2.114

——— (2002) Identification of yellow cultured pearls from the black-lipped oyster *Pinctada margaritifera*. *G&G*, Vol. 38, No. 1, pp. 66–72, http://dx.doi.org/10.5741/GEMS.38.1.66

Emmett J.L., Douthit T.R. (1993) Heat treating the sapphires of Rock Creek, Montana. *G&G*, Vol. 29, No. 4, pp. 250–272, http://dx.doi.org/10.5741/GEMS.29.4.250

Fritsch E., Rossman G.R. (1988) An update on color in gems. Part 2: Colors involving multiple atoms and color centers. *G&G*, Vol. 24, No. 1, pp. 3–15, http://dx.doi.org/10.5741/GEMS.24.1.3

Fritsch E., Shigley J.E., Rossman G.R., Mercer M.E., Muhlmeister S.M., Moon M. (1990) Gem-quality cuprian-elbaite tourmalines from São José Da Batalha, Paraíba, Brazil. *G&G*, Vol. 26, No. 3, pp. 189–205, http://dx.doi.org/10.5741/GEMS.26.3.189

Green B.L., Collins A.T., Breeding C.M. (2022) Diamond spectroscopy, defect centers, color, and treatments. *Reviews in Mineralogy and Geochemistry*, Vol. 88, No. 1, pp. 637–688, http://dx.doi.org/10.2138/rmg.2022.88.12

Heaney P.J. (2021) Iris agates and cantor dusts: The textural complexity of agates. In *Seventeenth Annual Sinkankas Symposium—Agate and Chalcedony*. Pala International, Inc., pp. 29–39.

Ho J.W.Y., Lawanwong K., Homkrajae A. (2024) Lab Notes: Pearls from the Placunidae family (windowpane oysters). *G&G*, Vol. 60, No. 1, pp. 69–71.

Homkrajae A. (2016) Gem News International: Spectral characteristics of *Pinctada mazatlanica* and *Pinctada margaritifera* pearl oyster species. *G&G*, Vol. 52, No. 2, pp. 207–208.

Homkrajae A., Sun Z., Shih S.C. (2019) Gem News International: Gemological and chemical characteristics of natural freshwater pearls from the Mississippi River system. *G&G*, Vol. 55, No. 2, pp. 280–285.

Hughes E.B., Perkins R. (2019) Madagascar sapphire: Low-temperature heat treatment experiments. *G&G*, Vol. 55, No. 2, pp. 184–197, http://dx.doi.org/10.5741/GEMS.55.2.184

Hughes R.W., Manorotkul W., Hughes E.B. (2017) *Ruby & Sapphire: A Gemologist's Guide*. RWH Publishing, Bangkok.

Iwahashi Y., Akamatsu S. (1994) Porphyrin pigment in black-lip pearls and its application to pearl identification. *Fisheries Science*, Vol. 60, No. 1, pp. 69–71, http://dx.doi.org/10.2331/fishsci.60.69

Jabbour-Zahab R., Chagot D., Blanc F., Grizel H. (1992) Mantle histology, histochemistry and ultrastructure of the pearl oyster *Pinctada margaritifera* (L.). *Aquatic Living Resources*, Vol. 5, No. 4, pp. 287–298, http://dx.doi.org/10.1051/alr:1992027

Jin S., Smith E.M. (2024) Raman spectroscopy and X-ray diffraction in gemology: Identifying mineral species and other phases. *G&G*, Vol. 60, No. 4, pp. 518–535, http://dx.doi.org/10.5741/GEMS.60.4.518

Jin S., Sun Z., Palke A.C. (2022) Color effects of Cu nanoparticles in Cu-bearing plagioclase feldspars. *American Mineralogist*, Vol. 107, No. 12, pp. 2188–2200, http://dx.doi.org/10.2138/am-2022-8325

Jin S., Palke A.C., Renfro N.D., Sun Z. (2023) Special colors and optical effects of Oregon sunstone: Absorption, scattering, pleochroism, and color zoning. *G&G*, Vol. 59, No. 3, pp. 298–322, http://dx.doi.org/10.5741/GEMS.59.3.298

Jollands M., Ludlam A., Palke A.C., Vertriest W., Jin S., Cevallos P., Arden S., Myagkaya E., D'Haenens-Johannson U., Weeramongkhonlert V., Sun Z. (2023) Color modification of spinel by nickel diffusion: A new treatment. *G&G*, Vol. 59, No. 2, pp. 164–181, http://dx.doi.org/10.5741/GEMS.59.2.164

Karampelas S. (2012) Spectral characteristics of natural-color saltwater cultured pearls from *Pinctada maxima*. *G&G*, Vol. 48, No. 3, pp. 193–197, http://dx.doi.org/10.5741/GEMS.48.3.193

Karampelas S., Fritsch E., Mevellec J.-Y., Gauthier J.-P., Sklavounos S., Soldatos T. (2007) Determination by Raman scattering of the nature of pigments in cultured freshwater pearls from the mollusk *Hyriopsis cumingi*. *Journal of Raman Spectroscopy*, Vol. 38, No. 2, pp. 217–230, http://dx.doi.org/10.1002/jrs.1626

Karampelas S., Fritsch E., Mevellec J.-Y.S., Soldatos T. (2009) Role of polyenes in the coloration of cultured freshwater pearls. *European Journal of Mineralogy*, Vol. 21, No. 1, pp. 85–97, http://dx.doi.org/10.1127/0935-1221/2009/0021-1897

Karampelas S., Fritsch E., Gauthier J.-P., Hainschwang T. (2011) UV-Vis-NIR reflectance spectroscopy of natural-color saltwater cultured pearls from *Pinctada margaritifera*. *G&G*, Vol. 47, No. 1, pp. 31–35, http://dx.doi.org/10.5741/GEMS.47.1.31

Karampelas S., Fritsch E., Makhlooq F., Mohamed F., Al-Alawi A. (2020) Raman spectroscopy of natural and cultured pearls and pearl producing mollusc shells. *Journal of Raman Spectroscopy*, Vol. 51, No. 9, pp. 1813–1821, http://dx.doi.org/10.1002/jrs.5670

Kiefert L., Moreno D.M., Arizmendi E., Hänni H.A., Elen S. (2004)

Cultured pearls from the Gulf of California, Mexico. *G&G*, Vol. 40, No. 1, pp. 26–38, http://dx.doi.org/10.5741/GEMS.40.1.26
King J.M., Geurts R.H., Gilbertson A.M., Shigley J.E. (2008) Color grading "D-to-Z" diamonds at the GIA Laboratory. *G&G*, Vol. 44, No. 4, pp. 296–321, http://dx.doi.org/10.5741/GEMS.44.4.296
Kitawaki H., Abduriyim A., Okano M. (2006) Identification of heat-treated corundum. *G&G*, Vol. 42, No. 3, p. 84.
Koivula J.I., Kammerling R.C. (1989) Gem News: New developments in spectroscopy. *G&G*, Vol. 25, No. 1, pp. 49–50.
Lu R. (2012) Color origin of lavender jadeite: An alternative approach. *G&G*, Vol. 48, No. 4, pp. 273–283, http://dx.doi.org/10.5741/GEMS.48.4.273
Mainwood A. (1994) Nitrogen and nitrogen-vacancy complexes and their formation in diamond. *Physical Review B*, Vol. 49, No. 12, pp. 7934–7940, http://dx.doi.org/10.1103/PhysRevB.49.7934
Moon A.R., Phillips M.R. (1994) Defect clustering and color in Fe,Ti: α-Al_2O_3. *Journal of the American Ceramic Society*, Vol. 77, No. 2, pp. 356–367, http://dx.doi.org/10.1111/j.1151-2916.1994.tb07003.x
Moses T.M., Shigley J.E. (2003) G. Robert Crowningshield: A legendary gemologist. *G&G*, Vol. 39, No. 3, pp. 184–199, http://dx.doi.org/10.5741/GEMS.39.3.184
Nilpetploy N., Lawanwong K., Kessrapong P. (2018) The gemological characteristics of Pipi pearls reportedly from *Pinctada maculata*. *G&G*, Vol. 54, No. 4, pp. 418–427, http://dx.doi.org/10.5741/GEMS.54.4.418
Palke A.C., Sun Z. (2018) What is cobalt spinel? Unraveling the causes of color in blue spinels. *G&G*, Vol. 54, No. 3, p. 262.
Palke A.C., Saeseaw S., Renfro N.D., Sun Z., McClure S.F. (2019) Geographic origin determination of blue sapphire. *G&G*, Vol. 55, No. 4, pp. 536–579, http://dx.doi.org/10.5741/GEMS.55.4.536
Rossman G.R. (2014) Optical spectroscopy. *Reviews in Mineralogy and Geochemistry*, Vol. 78, No. 1, pp. 371–398, http://dx.doi.org/10.2138/rmg.2014.78.9
Shigley J.E., Cook B.C., Laurs B.M., Bernardes M.D.O. (2001) An update on "Paraíba" tourmaline from Brazil. *G&G*, Vol. 37, No. 4, pp. 260–276, http://dx.doi.org/10.5741/GEMS.37.4.260
Sun Z., Jollands M., Palke A. (2024) Chemical analysis in the gemological laboratory: XRF and LA-ICP-MS. *G&G*, Vol. 60, No. 4, pp. 536–559, http://dx.doi.org/10.5741/ GEMS.60.4.536
Taran M.N., Rossman G.R. (2001) Optical spectroscopic study of tuhualite and a re-examination of the beryl, cordierite, and osumilite spectra. *American Mineralogist*, Vol. 86, No. 9, pp. 973–980, http://dx.doi.org/10.2138/am-2001-8-903
Wada K. (1984) Spectral characteristics of pearls. *Hōseki gakkaishi*, Vol. 10, No. 4, pp. 95–103.
Wang W., Scarratt K., Hyatt A., Shen A.H.-T., Hall M. (2006) Identification of "chocolate pearls" treated by Ballerina Pearl Co. *G&G*, Vol. 42, No. 4, pp. 222–235, http://dx.doi.org/10.5741/GEMS.42.4.222
Wang Z., Adzigbli L., Zheng Z., Yang C., Deng Y. (2020) How cultured pearls acquire their colour. *Aquaculture Research*, Vol. 51, No. 10, pp. 3925–3934, http://dx.doi.org/10.1111/are.14765
Zaitsev A.M. (2001) *Optical Properties of Diamond*. Springer, Berlin, Heidelberg.
Zhou C., Homkrajae A., Ho J.W.Y., Hyatt A., Sturman N. (2012) Update on the identification of dye treatment in yellow or "golden" cultured pearls. *G&G*, Vol. 48, No. 4, pp. 284–291, http://dx.doi.org/10.5741/GEMS.48.4.284
Zhou C., Ho J.W.Y., Chan S., Zhou J.Y., Wong S.D., Moe K.S. (2016) Identification of "pistachio" colored pearls treated by Ballerina Pearl Co. *G&G*, Vol. 52, No. 1, pp. 50–59, http://dx.doi.org/10.5741/GEMS.52.1.50

Thank You, Reviewers

GEMS & GEMOLOGY requires each manuscript submitted for publication to undergo a rigorous peer review process, in which each paper is evaluated by at least three experts in the field prior to acceptance. This is essential to the accuracy, integrity, and readability of *G&G* content. In addition to our dedicated Editorial Review Board, we extend many thanks to the following individuals who devoted their valuable time to reviewing manuscripts in 2024.

Non-Editorial Board Reviewers

Abeer Al-Alawi • Alessandra Altieri • Roy Bassoo • Philippe Belley • Thanh Nhan Bui • Athena Chen • Gagan Choudhary • James Conant • Emily Dubinsky • Elliot Entin • Alexander Falster • Hans Albert Gilg • Hertz Hasenfeld • Frank Hawthorne • Shiyun Jin • Michael Jollands • Yusuke Katsurada • Greg and Russell Kwiat • Jose Sasian • Travis Serio • Greg Stopka • Alexandre Zaitsev

Infrared Spectroscopy and Its Use in Gemology

Christopher M. Breeding and Nicole J. Ahline

Since its discovery at the beginning of the nineteenth century, infrared light has proven to be a versatile tool for scientists, industrialists, and consumers. The gem industry has benefited from the power of infrared spectroscopy in gemstone identification for more than 30 years. By measuring the frequencies of vibrations of bonds between atoms in the structure of a gemstone, scientists can determine the composition and atomic arrangement of many important defects that indicate whether a gem is natural, laboratory-grown, or treated. Clever adaptations of instrument hardware and sampling techniques have allowed for efficient and accurate analysis of diamonds and many of the most important colored gems such as ruby, sapphire, emerald, and jadeite. No gemologist's toolbox is complete without an understanding of the power of infrared spectroscopy for gem identification.

The foundations of gemology lie in visual observation and mineral properties. Many basic gemological characteristics including refractive index, specific gravity, pleochroism, fluorescence, optic figure, and color zoning are produced by the specific atomic structure of the gem being examined. Spectroscopy is the tool of choice in gemology for examining atomic structure due to its nondestructive nature and sensitivity. Absorption spectroscopy (measuring the light that is absorbed by a gem) was among the earliest techniques used to evaluate atomic level imperfections (or defects) in gemstones. Depending on the type of absorption spectroscopy used, a laboratory can evaluate the basic identity of a gem, indications of treatment, or the cause of its color. Visible absorption is effective for color investigations and is the subject of another article in this issue of *Gems & Gemology* (see Jin et al., 2024, pp. 456–473). This article focuses on infrared (IR) absorption spectroscopy, a very important tool that measures atomic vibrations to evaluate atomic structure and identify gems and treatments (e.g., Fritsch and Stockton, 1987; Lowry, 2008; Breeding et al., 2010).

In order to understand infrared absorption spectroscopy, a brief discussion of the electromagnetic spectrum is required. In simple terms, the electromagnetic spectrum encompasses all radiation (or "light") in order of increasing frequency/energy and decreasing wavelength: radio waves, microwaves, infrared, visible, ultraviolet, X-rays, and gamma rays (Jenkins and White, 1976; Nassau, 2001) (figure 1). The IR region occurs at slightly lower energies (and longer wavelengths) than the red end of the visible spectrum and is invisible to the human eye. It is used in many heating, imaging, and communication devices, some as simple as television remote controls and other home appliances. The IR region is subdivided by wavelength into near (~0.75–5 µm), mid (~5–30 µm), and far (~30–1000 µm). Most scientists, however, prefer to use wavenumbers (units of 1/cm or cm^{-1}) to describe IR light because the numbers are manageable and linearly correlated with the vibrational energy being measured. It is important to remember that as wavenumbers and the corresponding energy increase, the wavelength decreases. The mid-IR range (~2000–333 cm^{-1}) is most useful in gemol-

In Brief

- Infrared spectroscopy is a key tool for gem identification.
- FTIR measures vibrations of bonds between atoms in minerals.
- Careful analysis of FTIR spectra can help separate natural from laboratory-grown gems as well as identify indications of heating, polymer impregnation, and other gem treatments.

See end of article for About the Authors and Acknowledgments.
Gems & Gemology, Vol. 60, No. 4, pp. 474–492,
http://dx.doi.org/10.5741/GEMS.60.4.474

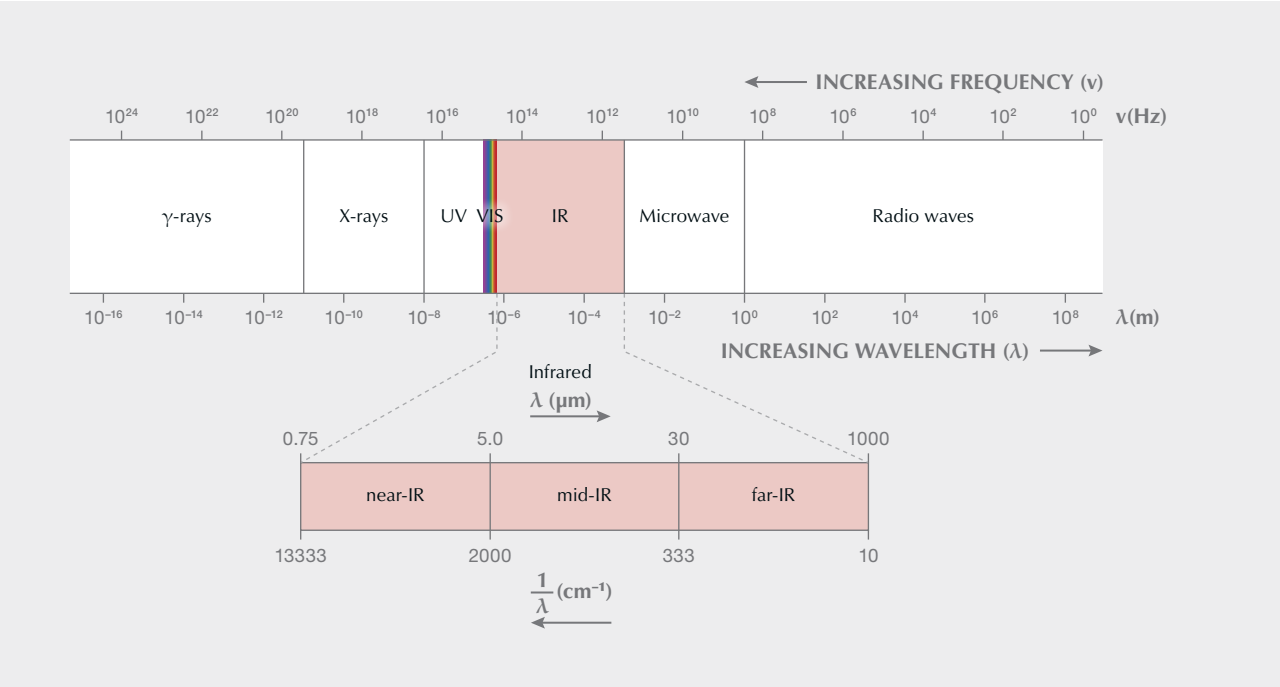

Figure 1. The electromagnetic spectrum represents energy from gamma rays to radio waves and is characterized by both frequency and wavelength. Note that as frequency increases (and wavelength decreases), energy also increases. The infrared region is subdivided into near-, mid-, and far-IR and typically represented by units of wavenumbers (cm^{-1}).

ogy, but some important features also occur in the near-IR (~13333–2000 cm^{-1}).

IR light was first discovered in 1800 by British astronomer Sir William Herschel, using thermometers to measure heat beyond the red part of the visible spectrum (figure 2, left). That same discovery is the underpinning of today's IR thermal imaging devices. The first generation of IR instruments became commercially available in the late 1950s. These instruments were dispersive IR devices (prism or grating monochromators) that required each wavelength of light to be measured individu-

Figure 2. Left: Sir William Herschel discovered infrared light by measuring its heating effect using thermometers. Courtesy of Alamy, Inc. Right: The first IR instruments were dispersive IR involving a diffraction grating that allowed for measurement of single wavelengths at a time.

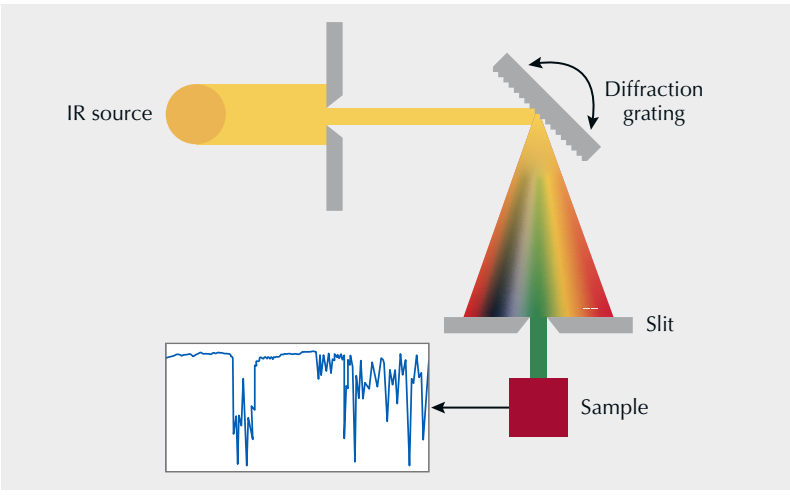

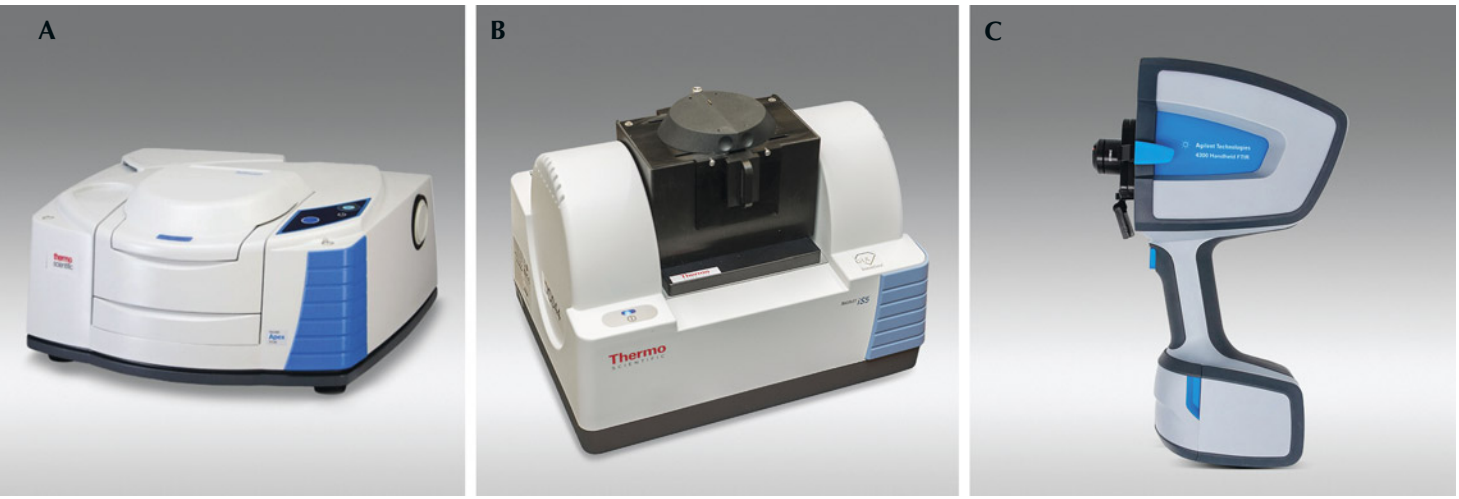

Figure 3. Commercial FTIR instruments include research-grade benchtop devices by manufacturers such as Thermo Fisher (A), Shimadzu, Bruker, and others; smaller and portable desktop instruments such as the GIA DiamondCheck (B); and a few handheld devices such as the one made by Agilent (C). Courtesy of Thermo Fisher Scientific (A) and Agilent Technologies, Inc. (C).

ally, making them very slow and expensive (figure 2, right).

IR spectroscopy as we know it today is almost exclusively performed using the Fourier-transform infrared (FTIR) technique. With the invention of the Michelson interferometer in 1881, it was possible to measure many IR wavelengths at once, but the mathematical transformation of the interferometer data required hours of work on very expensive computers. The first FTIR spectrum was collected in 1949, before dispersive IR instruments became available, but it was not until 1966 that a Fourier-transform algorithm was discovered, which allowed for quick processing and conversion of data to make FTIR viable. The 1970s saw the first commercial FTIR devices, and by the 1990s, FTIR had become mainstream (Becker and Farrar, 1972; Sun, 2009; Smith, 2011).

Gemological laboratories regularly use FTIR for gemstone analysis, and GIA has done so since 1986 (Fritsch and Stockton, 1987). This bulk analysis technique has proven effective for various applications related to diamond and colored stone identification and treatment detection that will be discussed later in this article. It not only allows measurement of subtle details of the atomic structure of gems, such as the presence of hydrogen species in sapphire or individual nitrogen impurity atoms in diamond, but also detects materials that have been mechanically introduced into microscale pores or cracks in gemstones to improve stability and/or clarity (e.g., jadeite, turquoise, and emerald) (Fritsch and Stockton, 1987; Breeding and Shigley, 2009; Thongnopkun et al., 2022). The goal of this article is to introduce readers to the basic concepts of FTIR analysis of gemstones and some of the major applications for which it is currently used. It is not intended as a comprehensive review of IR analysis but as a tool to help readers better understand FTIR and its importance to the gem trade.

INSTRUMENTATION AND DATA COLLECTION

FTIR instruments have been widely commercially available since the 1990s. They range from desktop devices to handheld units and low-resolution, application-specific devices to very expensive, multifunctional research-grade instruments. Well-established manufacturers include Agilent, Bruker, Jasco, Perkin Elmer, Shimadzu, and Thermo Fisher (figure 3). More recently, several smaller companies have also entered the market. While the uses and analytical capabilities of these instruments vary depending on available features and design, all FTIR spectrometers contain the same basic components: IR source, aperture, interferometer (including beam splitter and mirrors), sample introduction system, detector, and processing computer.

The basic principle of FTIR involves a source producing IR light that is directed through an aperture (or controlled opening) into a complex lens called a beam splitter that splits the light into two beams, one of which strikes a fixed-position mirror and the other a moving mirror. The two beams are reflected back into the beam splitter, where they are recombined and directed through the sample to a detector (Smith, 2011)

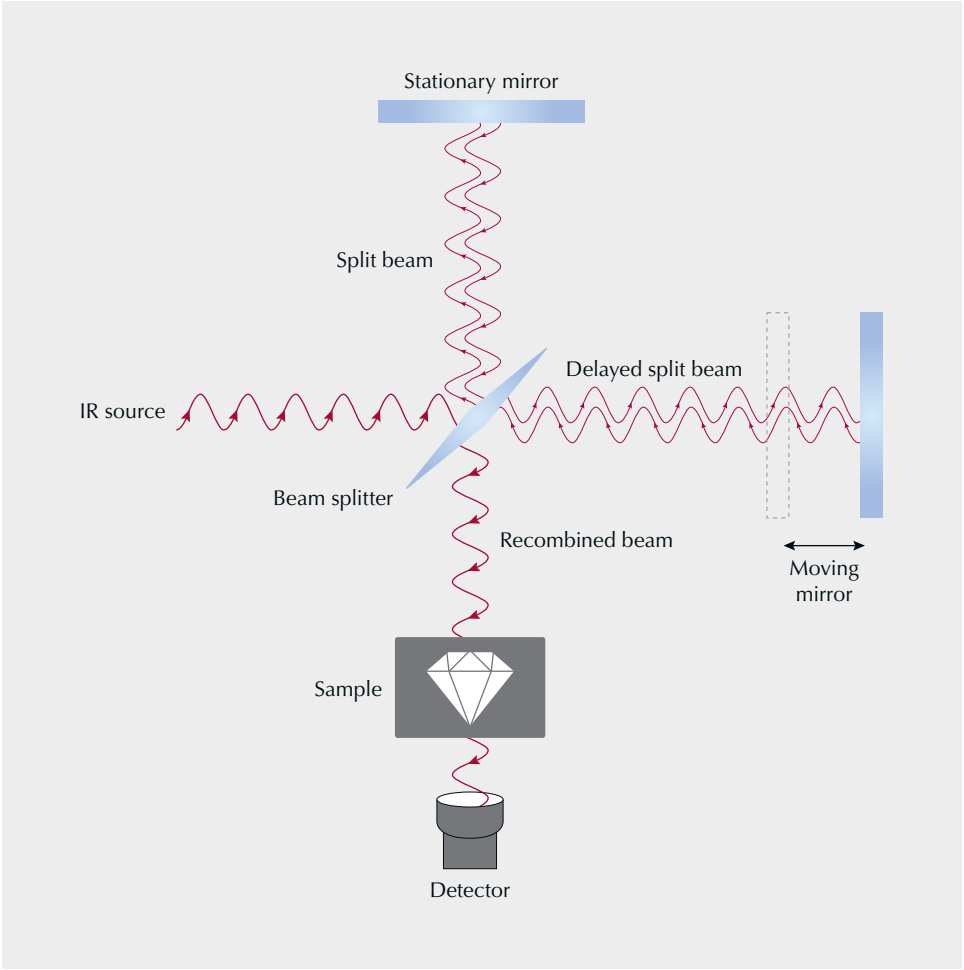

Figure 4. FTIR instruments are based on a Michelson interferometer, which includes two mirrors (one moving) and a beam splitter to split and recombine IR light before sending it through a gemstone to a detector.

(figure 4). The difference in the distance the light travels from each of the two differently positioned mirrors produces a range of constructive and destructive interference of the light waves as the moving mirror travels a designated distance (its position is monitored by a tracking laser at all times). The continuous range of travel of the moving mirror allows for simultaneous collection of the complete spectrum. The atomic structure of the gemstone sample selectively absorbs or attenuates certain wavelengths of IR light. The remaining light hits the detector and is converted into an electronic signal called an interferogram that is mathematically transformed (Fourier transform) as a function of time into an FTIR spectrum (Sun, 2009; Smith, 2011). While the concept sounds complicated, the end result is a graph that shows which IR wavelengths are more strongly and weakly absorbed by the atomic bonds in the gemstone. Gemologists and scientists compare this spectrum to known reference spectra to evaluate the identity of a gem, its impurities, or the presence of treatment.

Gemologists primarily rely on the mid- and near-IR regions, which are more easily measured and contain the information most readily applied to gemstone analysis. The instrument components themselves dictate which of these regions can be measured, as well as the data detail and quality that can be obtained. To collect mid-IR range data, for example, a ceramic IR source (silicon carbide rod electrically heated to >1000°C) is optimal, while a tungsten-halogen lamp is preferable for near-IR. Likewise, different beam splitters are more efficient in different IR regions. For mid-IR, a potassium bromide (KBr) beam splitter is used, while a quartz beam splitter works more efficiently for near-IR. The aperture and interferometer mirror travel distance together determine the resolution of an FTIR spectrum. Resolution refers to a spectrometer's ability to differentiate closely spaced spectral features. Typical FTIR resolutions include 16, 8, 4, 2, or 1 wavenumber (or cm^{-1}) (figure 5). For example, an FTIR resolution of 4 cm^{-1} means that only features separated by four or

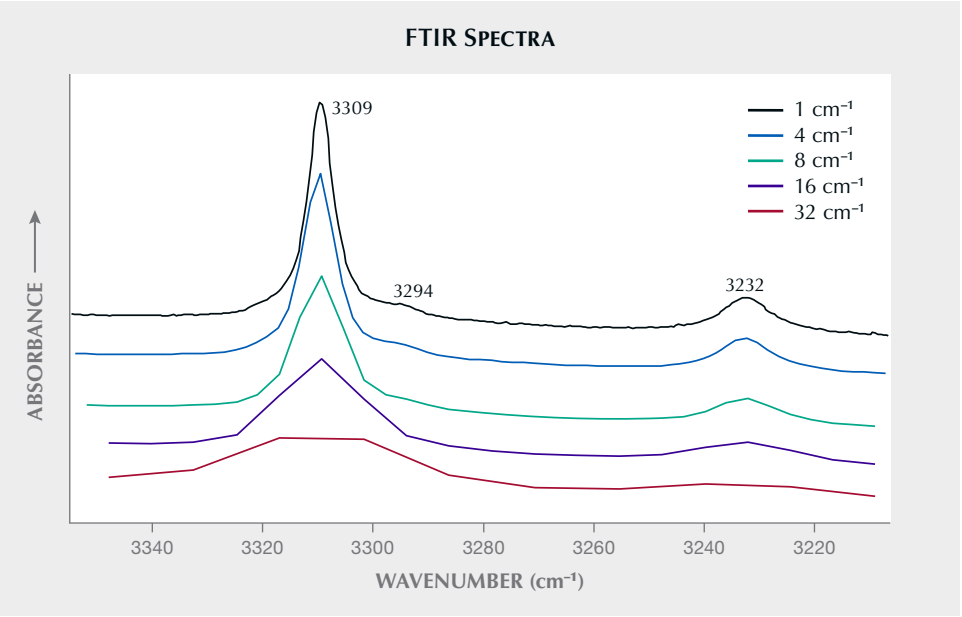

Figure 5. FTIR resolution has a big impact on the peaks in the spectrum and determines whether closely spaced peaks can be seen. For example, the 3309 and 3232 cm^{-1} OH absorptions in corundum become very broad and difficult to distinguish with decreased resolution. The effect of increased resolution is shown by the separation of the 3309 and 3294 cm^{-1} peaks. Spectra are offset vertically for clarity.

more wavenumbers can be separately identified. For most colored gemstones, FTIR features are broad enough that 4 cm^{-1} resolution is adequate. Some diamond defects, however, require 1 cm^{-1} to resolve. The FTIR detector also plays an important role in the data acquired. The two main detectors are mercury cadmium telluride (MCT) and deuterated triglycine sulfate (DTGS). MCT detectors are up to 10× more sensitive and faster, but they often require cooling by liquid nitrogen and are more expensive. DTGS detectors are less expensive and still adequate for many applications (Sun, 2009; Smith, 2011).

A few additional details warrant discussion with FTIR: sample temperature, signal-to-noise ratio, purging, and orientation/polarization. FTIR spectra are collected for all gemstones at room temperature, as there is no distinct advantage in cooling the sample in the IR region. The signal-to-noise ratio is an indicator of how distinguishable small absorptions in the spectrum are from the background noise level (figure 6). The signal-to-noise ratio can be improved with MCT detectors and increasing the number of scans to be averaged for the final spectrum. Other aspects of the Fourier transform, such as the apodiza-

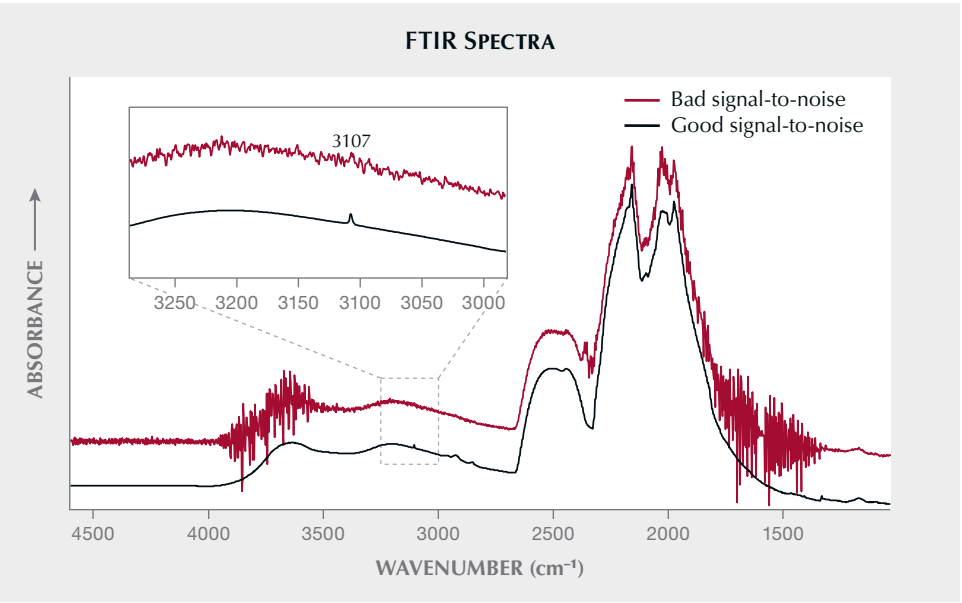

Figure 6. Spectral quality factors such as signal-to-noise ratio are critical for identifying small peaks in FTIR spectra of gems. For example, the tiny 3107 cm^{-1} (N_3VH) defect in diamond is not resolvable with bad signal-to-noise. Spectra are offset vertically for clarity.

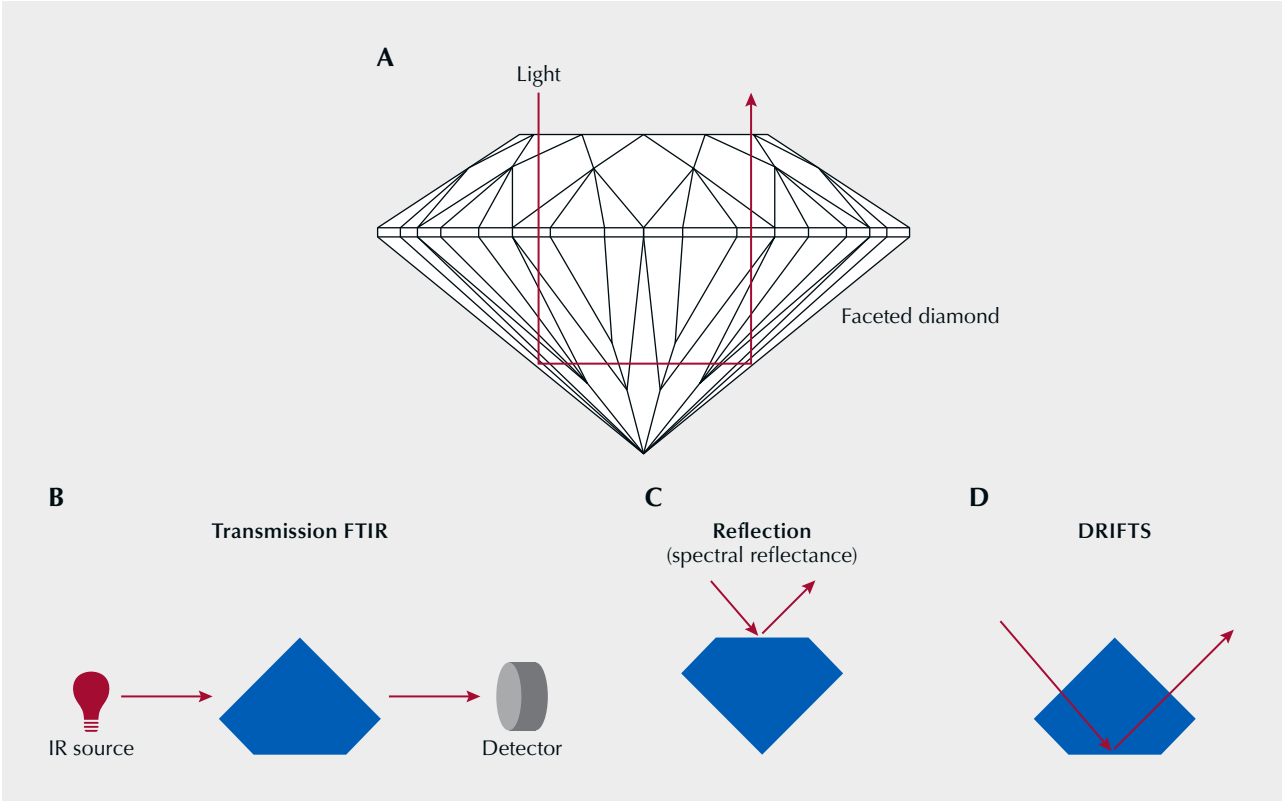

Figure 7. Gemstones are usually faceted to maximize light return through the top and enhance their brilliant appearance (A). This is not ideal for FTIR measurements which are most often collected by transmission (B). Reflection FTIR (C) is easier with faceted gems but provides less information. Gemologists adapted the DRIFTS method (D) to overcome some of these limitations of faceting.

tion function and zero filling (mathematical functions applied to the data during the transform), will also affect the shape of peaks and the appearance of the spectrum but are beyond the scope of this discussion. To avoid atmospheric contaminants (water vapor and carbon dioxide [CO_2] gas) from being measured in an FTIR spectrum, many instruments allow for purging. This procedure involves the continuous cycling of dry air or inert gas (usually nitrogen) through the instrument interior and sample chamber to force out any contaminated air. Finally, IR absorptions are often affected by the crystallographic orientation of a gemstone. While not a common practice in gemology, some mineralogical research requires polarization of the IR beam in order to measure the orientation dependence of features in the spectrum.

One of the most important components of an FTIR instrument is the sample introduction system. Gemstones are faceted to control the movement of light through the stone and to enhance the color or brilliance (figure 7A). The goal of faceting is often counter to the needs of spectroscopy, making it somewhat difficult to obtain good-quality FTIR spectra from gemstones. In gemology, there are three main methods of FTIR sample measurement: transmission, reflection, and diffused reflection (or DRIFTS—diffused reflectance infrared Fourier-transform spectroscopy) (Fritsch and Stockton, 1987; Breeding and Shigley, 2009; Thongnopkun et al., 2022). Another method called attenuated total reflection (ATR), which involves direct physical contact with a sample, is widely used for other industrial applications but has only recently been applied in gemology. This technique does have some potential for the analysis of opaque gemstones that have previously required preparation with KBr, as discussed later in this paper with regard to turquoise and amber.

Transmission FTIR is a basic method of passing the infrared beam directly through a sample and examining the transmitted IR beam to measure absorption. A beam condenser sample stage is often used in transmission FTIR instruments to focus the IR beam to a spot and amplify it using carefully aligned mirrors. The stone is placed at the focal point and the IR beam samples all of the stone area through which it passes, providing a bulk averaged absorption spec-

trum (figure 7B). This method can be difficult for many faceted gems, as direct paths through them are rare. With a carefully constrained beam path length, FTIR data can be quantified using this method.

Reflection FTIR involves reflection of an IR beam off of a flat gem surface (figure 7C). A simple reflection accessory is added to the sample chamber, allowing a gemstone to be placed flat side down on a window. The beam typically does not penetrate below the surface of the gem, and the resultant spectrum is usually different from that measured by transmission. Reflection analysis is very useful for gem identification and for opaque gemstones that cannot be measured by transmission FTIR (Hainschwang and Notari, 2008).

The final technique, DRIFTS, was designed to analyze powders or granular samples by producing multiple internal scattered reflections between the grains. Innovative gemologists, however, modified the technique to allow for efficient FTIR measurements on gems (figure 7D). A faceted stone is placed flat side down on a reflective stage inside a DRIFTS chamber made of multiple mirrors. The mirrors direct the IR beam at a high angle into the side of the gem, causing it to reflect around many times internally and exit through the opposite side at an angle aligned with the mirrors. This clever adaptation allows for bulk sampling of a faceted gem without a straight path through it. The technique may be better described as partial internal reflection, but the resultant FTIR spectrum is identical to a traditional transmission FTIR result.

While nearly all gemological laboratories utilize desktop FTIR instruments, some portable versions are commercially available. These portable FTIRs utilize ATR and reflection FTIR methods to allow for direct sampling of various materials by making physical contact with the instrument's sample port. As mentioned above, ATR is generally not useful for gem analysis except as a replacement in special sample preparation situations involving destruction of parts of the sample. The reflection FTIR spectra obtained from handheld devices tend to be of lower quality and less useful for gemstone analysis due to the limitations of the detectors (DTGS) and other components required to make the instruments portable.

Recently, a new mid-IR spectrometer using upconversion technology has been proposed as an alternative to FTIR. This instrument could provide an opportunity for faster data acquisition in the mid-IR range (Wang and Takahashi, 2023).

ANATOMY OF AN FTIR SPECTRUM

FTIR spectra reveal absorption (or reflection) peaks that represent variations in the atomic structure of a gemstone, such as impurities or atomic lattice disruptions due to atoms simply being out of place. For the most part, IR energy is absorbed by the bonds between atoms or within molecules, causing them to vibrate in distinct and characteristic ways (Becker and Farrar, 1972; Sun, 2009; Smith, 2011). These vibrations are called modes, and each has a frequency that is unique to the particular bonds and atoms within a material (figure 8). Modes may be symmetric or antisymmetric and comprise movements such as stretching, bending, rocking, wagging, and twisting. Sometimes the same bond may have multiple modes that show up simultaneously in an FTIR spectrum as different absorption peaks at different wavenumbers.

An FTIR spectrum is a graph of data with wavenumber units (cm^{-1}) along the horizontal axis representing the range of IR frequencies being measured and units of transmittance, absorbance, or reflectance on the vertical axis (figure 9). FTIR instruments usually make primary measurements as transmittance (usually given as % of total), but those are mathematically converted ($A = -\log T$, where A is absorbance and T is transmittance) into qualitative absorbance (reported as absorbance units or a.u.) if the IR beam path length is unknown. Quantitative absorption coefficient (units of cm^{-1}) is reported if path length has been accounted for ($\alpha = 2.303A/d$, where α is absorption coefficient, A is absorbance, and d is the path length typically in units of cm) (Becker and Farrar, 1972; Fritsch and Stockton, 1987; Breeding and Shigley, 2009; Sun, 2009; Smith, 2011). Reflection is typically reported as reflectance (unitless or as % of total).

In situations where the IR beam path length through a sample is known and absorption coefficients are calculated, the heights of individual peaks in the spectrum represent the concentration of particular defects. If appropriate reference gems with known concentrations of defects or impurities are available for comparison, FTIR spectra can yield quantitative atomic compositional data. For diamond, which has intrinsic absorptions in the mid-IR range, FTIR spectra can be normalized and atomic defect concentrations calculated even when the path length is not measurable (Boyd et al., 1994, 1995; Breeding and Shigley, 2009) (figure 10). While normalization introduces some error, the ability to evaluate chemical composition from a diamond's FTIR spectrum is invaluable to research efforts.

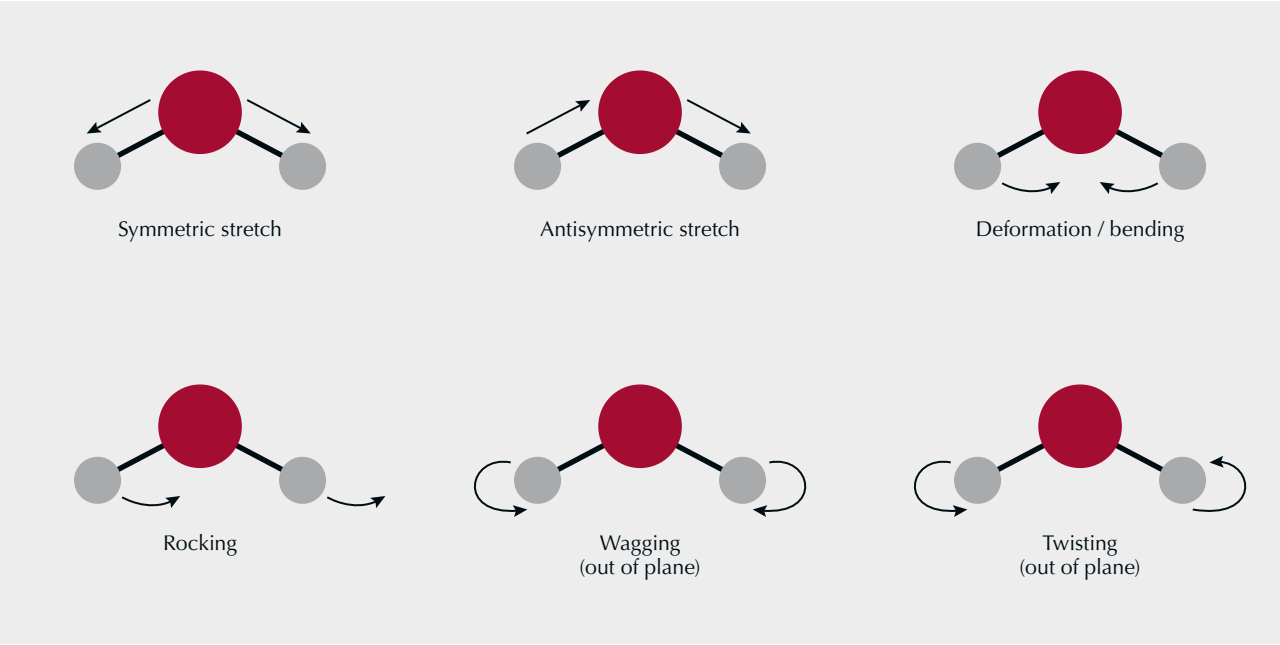

Figure 8. FTIR primarily measures vibrations from different modes of bonds between atoms including stretching, bending, rocking, wagging, and twisting.

Interest in better understanding the spatial distribution of FTIR features sparked the development of instruments capable of rapidly collecting FTIR data in two or even three dimensions across a sample. FTIR mapping is used in gemological research and involves the acquisition of thousands of individual spectra from each point in a map, with the sample moved by a motorized stage (Howell et al., 2019). The time required for mapping can be significant, depending on the user's sample size and spatial resolution needs, but the technique uses the same acquisition parameters defined above. A more recently developed technique is FTIR imaging, which is much faster because it employs a focal plane array (FPA) detector, where a series of arranged detectors are effectively used as pixels in an IR camera, allowing a defined sample area to be mapped almost simultaneously.

In addition to absorption peaks from features within a gemstone, a few other aspects of FTIR spectra are important to understand. Surface or atmos-

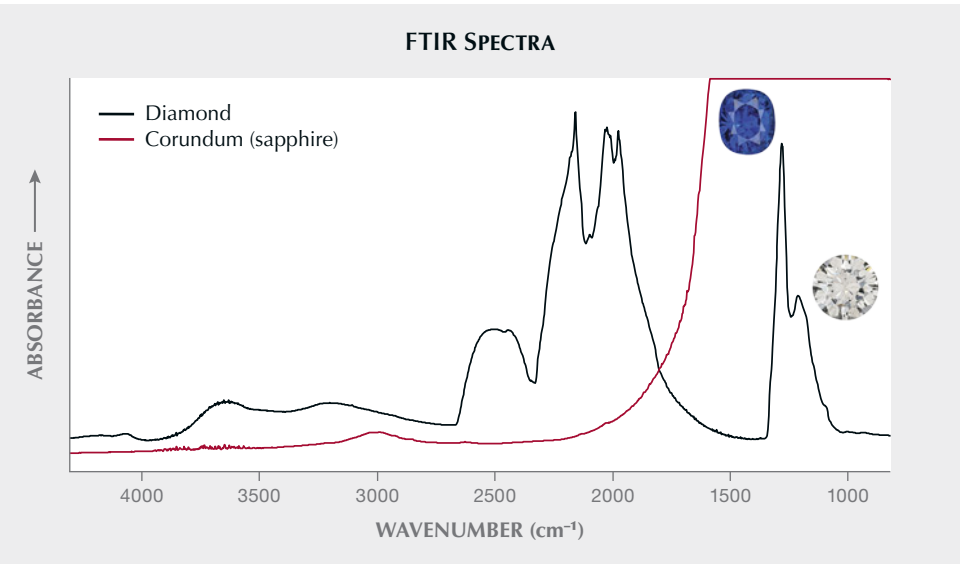

Figure 9. FTIR spectra for most minerals are distinctive, such as those for diamond and corundum. Spectra are offset vertically for clarity.

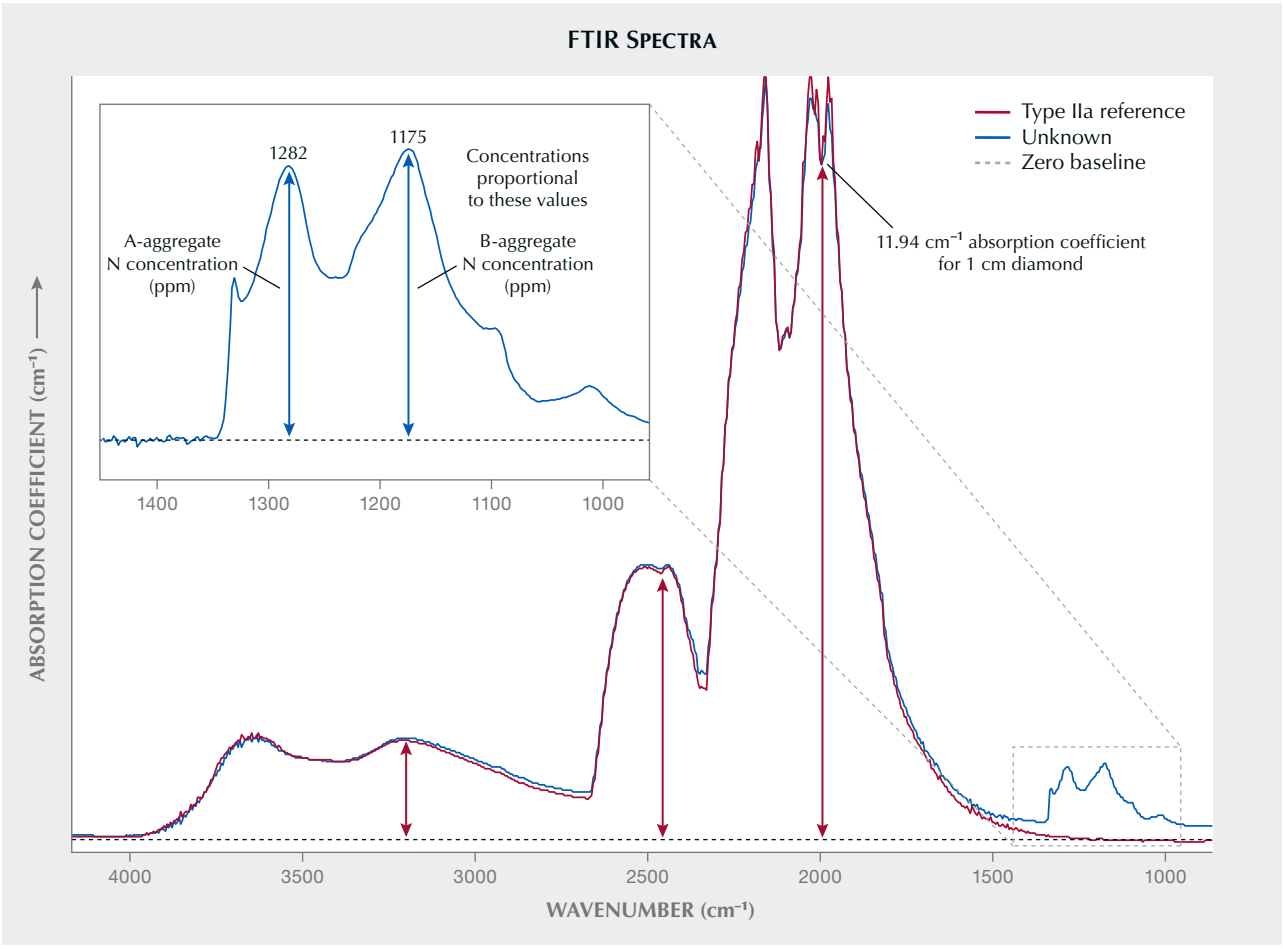

Figure 10. The intrinsic IR absorptions of diamond allow the spectrum to be normalized to a diamond with known path length of 1 cm in order to calculate the atomic concentrations of particular nitrogen defects including A- and B-aggregates. Modified from Breeding and Shigley (2009).

pheric contamination can show up very prominently in a spectrum and, at times, be difficult to differentiate from actual components of a gem. CO_2 occurs as broad, rounded double peaks at ~2200–2400 cm^{-1} in FTIR spectra (figure 11). Water vapor occurs as numerous narrow absorptions concentrated in three regions of the mid-IR: ~1400–1800, 3500–4000, and 5100–5500 cm^{-1} (Smal et al., 2014). CO_2 and water vapor are the most common atmospheric contaminants in FTIR spectra. CO_2 in particular is known to occur in fluid inclusions, and great care must be taken with spectra collection and purging to distinguish gaseous inclusions from contamination. Hydrocarbon surface contamination from finger oils or other organics is also readily observed as three distinctive and broad absorption features between 2830 and 3000 cm^{-1} (figure 11).

Another potentially confusing feature in FTIR spectra is usually termed "saturation." FTIR actually measures the IR light transmitted through a stone, and this information is then converted to absorbance, which is effectively the opposite of transmission. When transmission at particular wavenumbers is too low for the instrument detector to measure (meaning almost all light is absorbed by the gem), the resultant absorbance FTIR spectrum often shows irregular areas of very high noise where the detector has become "saturated" (figure 12). The term is misleading in that these are actually areas of little to no signal, but because we convert to absorbance, the data region is at the top of the limit, implying saturation. The data points in these areas are a byproduct of the instrument's inability to properly represent the data and are thus meaningless other than to indicate very strong absorptions. These areas in an FTIR spectrum should be truncated to avoid confusion and misinterpretation of the data.

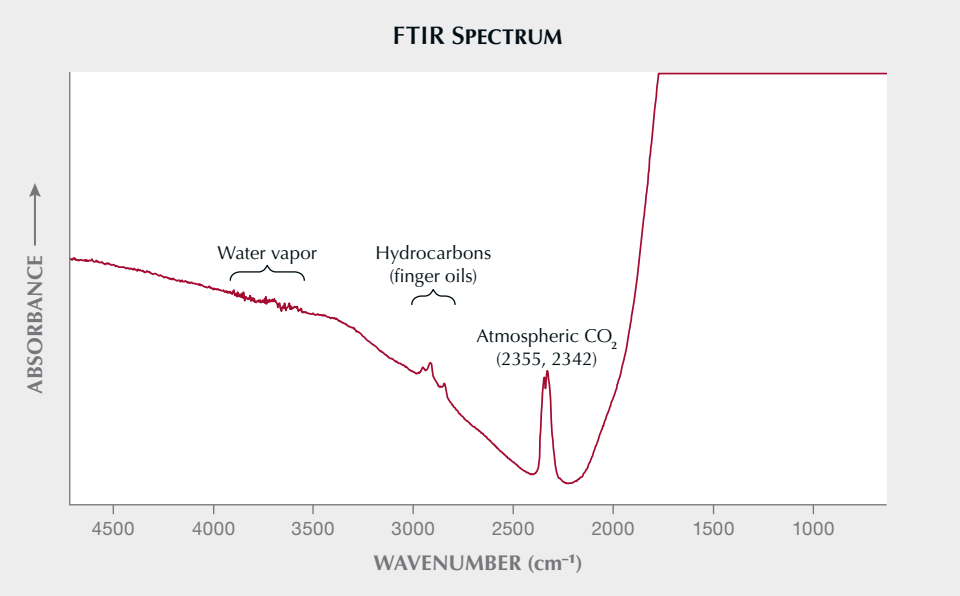

Figure 11. Contaminants in FTIR spectra, as seen here in a corundum spectrum, include atmospheric water vapor and CO_2, as well as hydrocarbons from finger oils on the stone's surface.

MAJOR APPLICATIONS IN GEMOLOGY

FTIR spectroscopy is one of the most common analytical techniques in modern gemology (Fritsch and Stockton, 1987; Breeding and Shigley, 2009; Thongnopkun et al., 2022). Its ability to measure and identify a wide range of gemstones and their treatments at room temperature is particularly valuable for gemologists. Mid-IR spectroscopy is used most often in gemology, and most of the relevant identification features occur in that region. Very little sample preparation is required, and the analysis is rapid and usually provides distinctive results. Its use is most widespread for diamond analysis, as it provides an abundance of information about impurities and their atomic configurations. While IR-related defects in diamonds have been extensively studied and documented, FTIR is also a major analytical tool for ruby, sapphire, emerald, jade, turquoise, amber, and many others. We will review some of the most prominent modern uses of FTIR in gemology below.

At this point, it is helpful to briefly elaborate on the terminology used by scientists and gemologists to describe atomic structures and substitutional elements in minerals. In general, a mineral is considered pure if all of its atoms are in perfect crystallographic positions and no foreign elements have substituted for

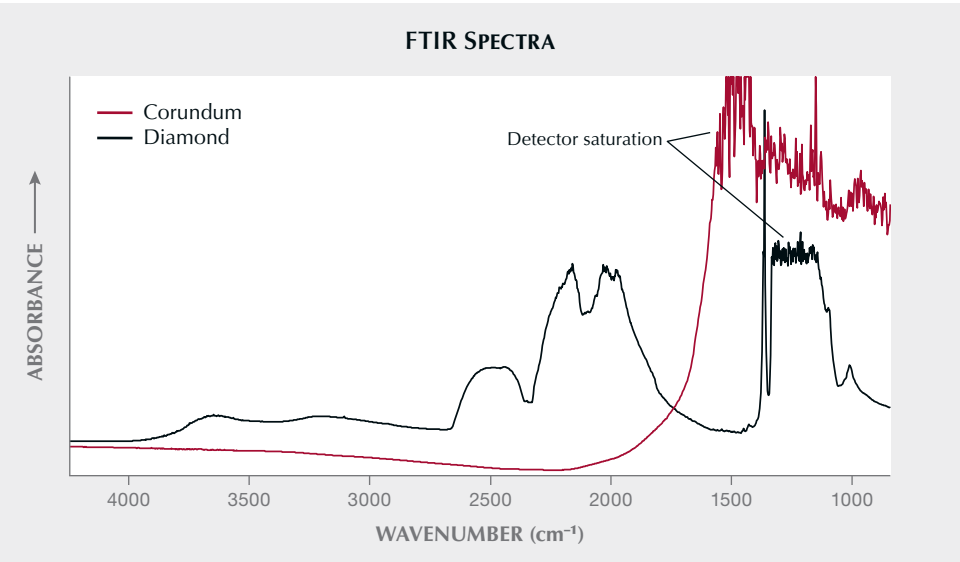

Figure 12. Some parts of FTIR spectra may be "saturated" due to very strong absorptions. These areas do not contain real data and should be truncated from the plot. Spectra are offset vertically for clarity.

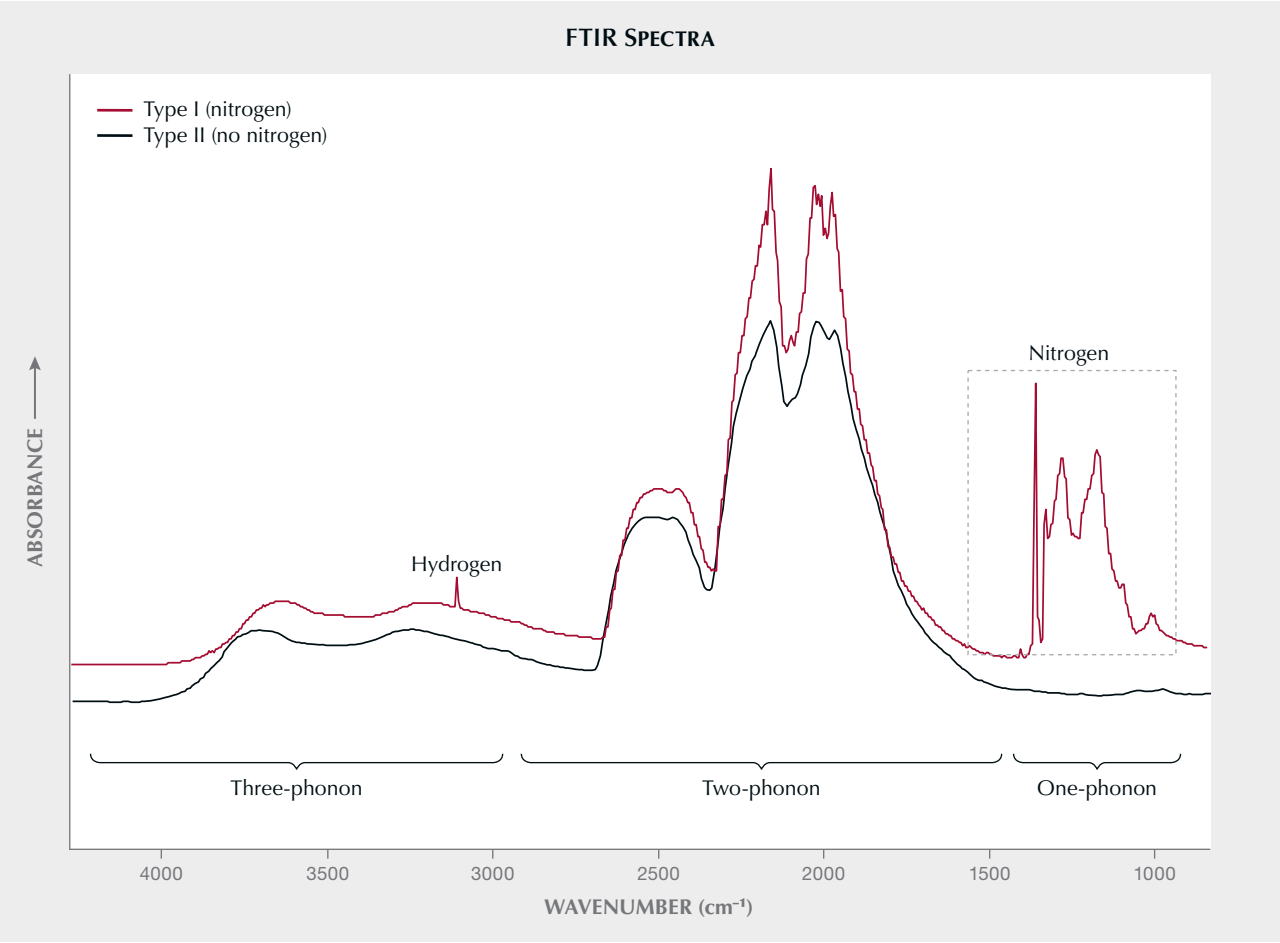

Figure 13. The intrinsic diamond absorptions in IR are subdivided into one-, two-, and three-phonon regions. Absorptions related to nitrogen impurities occur in the one-phonon region and determine whether a diamond is classified as type I or type II. Modified from Breeding and Shigley (2009). Spectra are offset vertically for clarity.

the primary elements (i.e., diamond consisting of only carbon atoms in perfect tetrahedral arrangement). In nature (and in most laboratory crystal growth), some minor or trace amount of a non-native element is nearly always incorporated during mineral growth or treatment. Likewise, some form of deformation, from an environmental condition such as radiation or heating or simply the incorporation of foreign elements of differing atomic sizes or electric charges during growth, can modify the structural alignment or symmetry of the atoms. These deviations from a perfect structure are often termed "defects" or, in the case of foreign elements, "impurities." While these terms have a seemingly negative connotation, defects and impurities are actually the subtle components of a gem that often contribute to its beauty, rarity, and value. For example, minor amounts of chromium in corundum create the red color that makes it a ruby, while a few boron atoms among billions of carbon atoms in diamond produced the stunning blue color of the world-famous Hope diamond.

Diamonds. All diamonds (both natural and laboratory-grown) have a distinctive series of intrinsic absorptions in the multiphonon region of the mid-IR, produced by the vibration of covalently bonded carbon atoms in response to IR energy (Anderson, 1943, 1963; Blackwell and Sutherland, 1949; Davies, 1977; Breeding and Shigley, 2009) (figure 13). Phonons are essentially vibrations of groups of atoms in a crystal lattice. Diamond has three distinctive phonon regions in the IR. The intrinsic absorptions from carbon atoms in diamond comprise the two- and three-phonon IR regions. The one-phonon region has no absorption for completely pure diamond (Wilks and Wilks, 1991; Kiflawi et al., 1994). Diamond usually contains nitrogen or boron as impurities (Kaiser and Bond, 1959). Fortunately for gemologists, nitro-

gen impurities (single, paired, and four N atoms + a vacancy) have distinct absorption features in the one-phonon IR region, while boron (occurring as single atoms only) has distinct peaks across all of diamond's IR phonon regions. These clear features allow diamond to be classified into distinct "types" such as type Ia, Ib, IIa, or IIb (figure 13). For more detailed information about diamond types and their significance in gemology, see Breeding and Shigley (2009). Understanding diamond type is critical for separating laboratory-grown from natural diamonds. Nearly all colorless laboratory-grown diamonds are type IIa, compared to less than 2% of natural diamonds. Additional IR features such as amber centers (produced by plastic deformation in the earth) and particular types of hydrogen-related peaks are unique to natural or laboratory-grown diamonds and provide further help in identification.

FTIR spectra also provide important details of diamond treatment. Irradiation treatment using electron beams creates atomic vacancies and turns diamonds blue or green colors (or yellow or orange or pink with subsequent heating). This produces IR-active atomic defects that can be seen in FTIR spectra, including H1a (1450 cm^{-1}), H1b (4935 cm^{-1}), and H1c (5165 cm^{-1}). These complex interstitial defects are common in irradiation-treated diamonds and much rarer in naturally colored diamonds (Woods, 1984; Collins, 2001; Liggins et al., 2010) (figure 14). High-pressure, high-temperature (HPHT) treatment can be used to either decolorize brown diamonds to make them near-colorless or create substantial color by rearranging existing atomic defects. For all practical purposes, only type IIa brown diamonds (containing few to no nitrogen impurities) can be decolorized, making the IR spectrum and diamond type determination an important tool. Other IR features including a broad 1480 cm^{-1} band and combinations of isolated and aggregated nitrogen defects often indicate HPHT treatment in colored diamonds (Collins et al., 2000). HPHT treatment is also known to reduce the height of platelet peaks (planar bunches of interstitial carbon atoms created as nitrogen aggregates; Woods, 1986; see also figure 15) and destroy plastic deformation features such as amber centers (Massi et al., 2005). While most of these IR peaks can be observed

Figure 14. Irradiation and heat treatment of diamond to enhance its color often produces distinct absorptions in FTIR spectra, including H1a (1450 cm^{-1}), H1b (4935 cm^{-1}), and H1c (5165 cm^{-1}). Spectra are offset vertically for clarity.

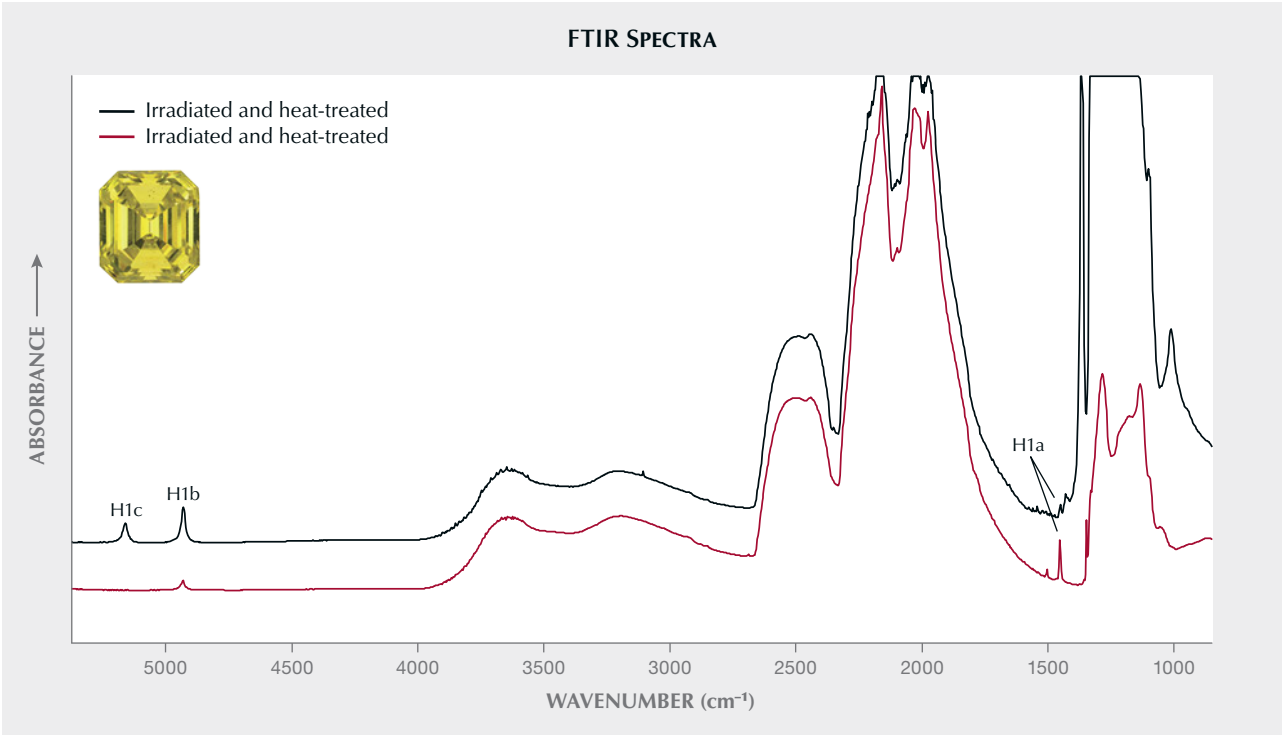

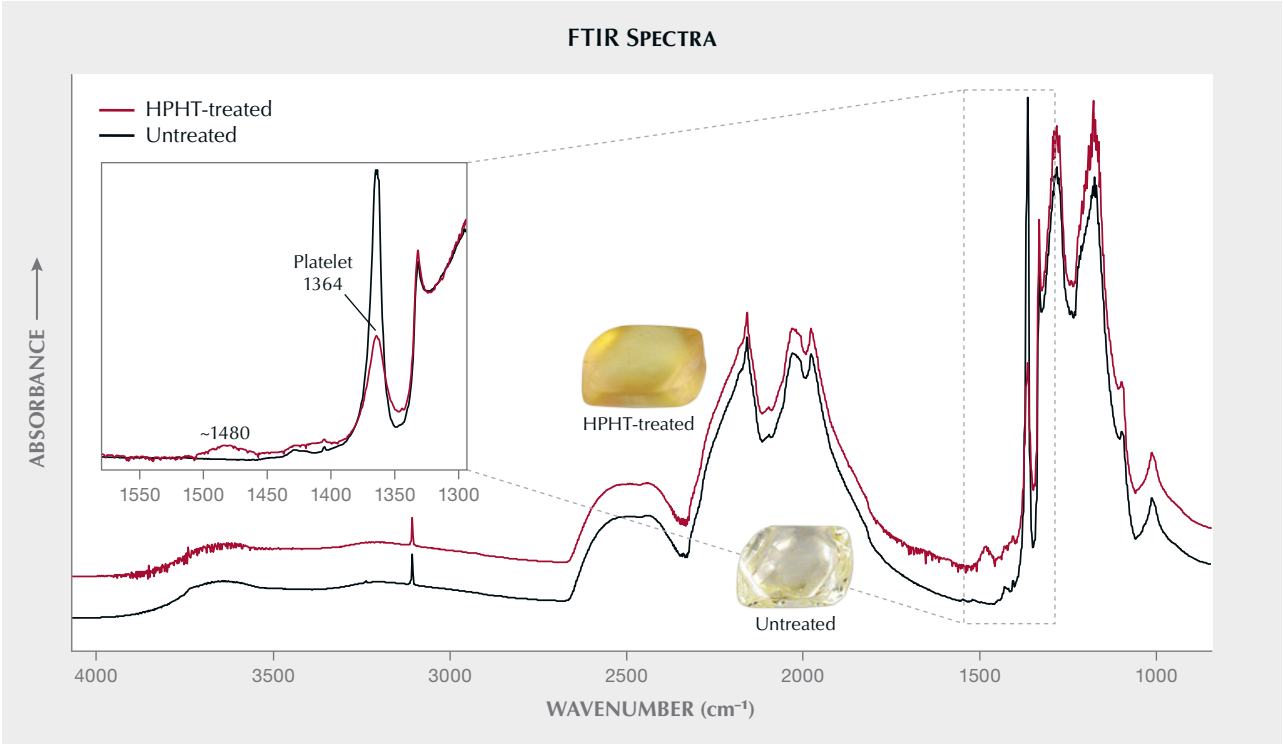

Figure 15. Some FTIR features in diamond are produced or destroyed by HPHT treatment. The platelet peak at 1364 cm^{-1} decreases with treatment, while the broad ~1480 cm^{-1} absorption appears after treatment. Spectra are offset vertically for clarity.

in untreated natural diamonds, they are far more prevalent in treated diamonds. By understanding their occurrence in combination with other defects measured through various types of spectroscopy, gemologists can assess whether a diamond is natural, laboratory-grown, or treated in some way to improve its color.

Ruby and Sapphire. Although ruby and sapphire are gem varieties of the mineral corundum and among the highest-value colored gemstones, not all of them come out of the ground with ideal color. Through extensive experimentation, gem treaters and scientists have learned to improve the color of corundum. Heat treatment (or thermal enhancement) has been used for decades to create a more appealing color in lower-value stones. FTIR analysis has proven to be particularly useful in identifying these treatments. For example, many blue sapphires formed in metamorphic environments that have been heat treated to 1500°C to enhance their color will show IR absorptions related to OH stretching modes of water in the corundum structure at 3309, 3232, and/or 3185 cm^{-1} (figure 16A). Rubies from certain localities such as Mozambique and some pink sapphires from Madagascar show similar features when heat treated at lower temperatures (Smith, 1995; Vertriest and Saeseaw, 2019). While low-temperature and high-temperature heat treatment have been common for ruby and sapphire for decades, a new type of treatment has emerged in the last few years to improve the blue color of sapphires heated in the presence of pressure (~1 kilobar) (PHT). FTIR has once again proven useful, as a broad ~3045 cm^{-1} peak often appears after this treatment (Thanong et al., 2016; Peretti et al., 2018) (figure 16B). It is important to note that the presence of these peaks in FTIR spectra is useful for heat treatment detection, but their absence is not conclusive in any way. Conversely, the presence of a feature at 3161 cm^{-1} is a reliable indicator that a sapphire has not been treated at high temperatures. This peak is particularly valuable in ruling out beryllium diffusion treatment. Another application of FTIR for heat treatment detection in corundum is the identification of mineral inclusions in ruby or sapphire that are unstable at treatment temperatures. Certain secondary minerals in the form of aluminum hydroxides are commonly found in some gem corundum. These minerals (diaspore, gibbsite, and

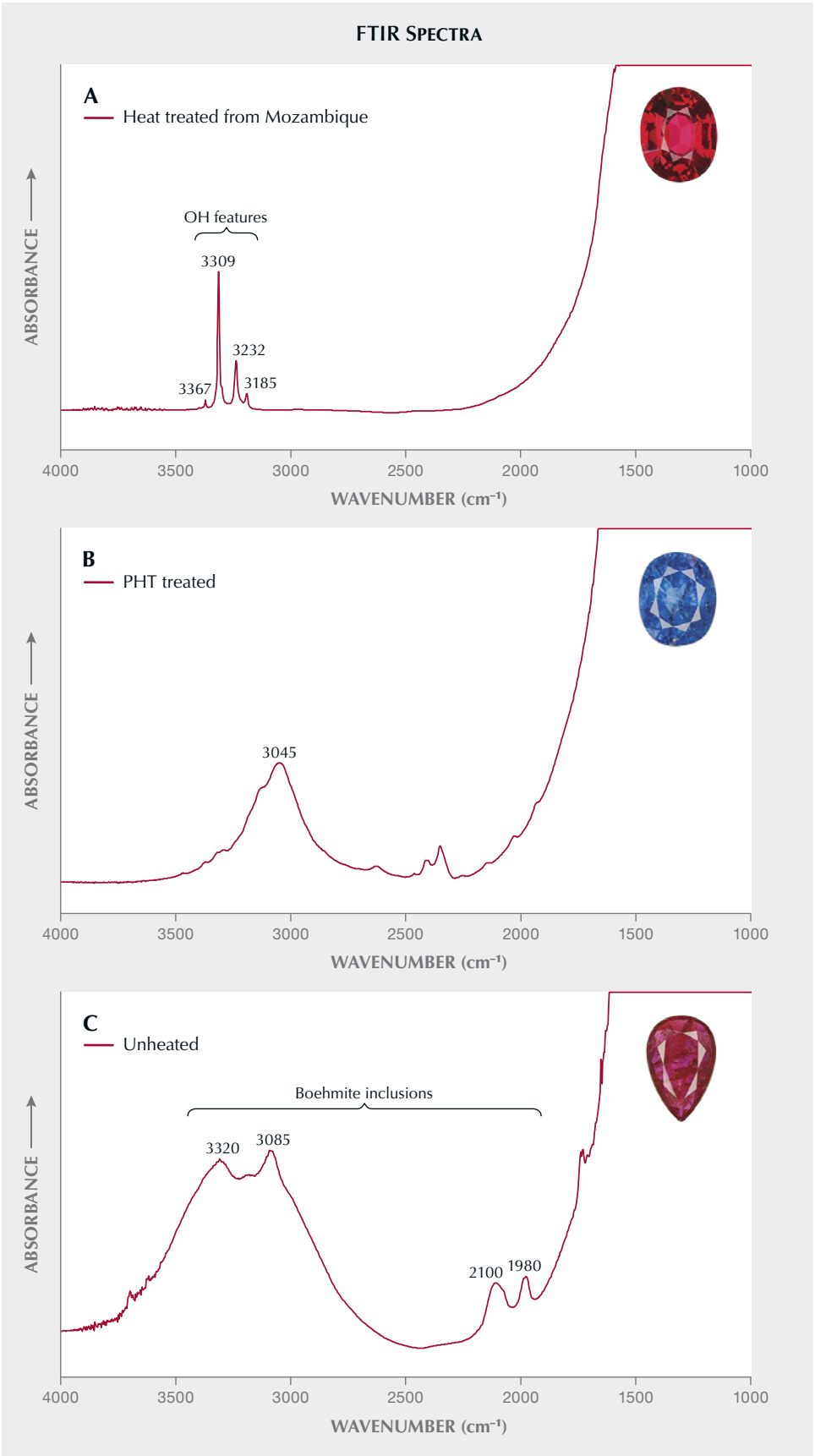

Figure 16. Some corundum, including this ruby from Mozambique (A), develop FTIR absorptions at 3309 cm^{-1}, 3232 cm^{-1}, and others during low-temperature heat treatment to improve their color. Other treatments at high temperatures and elevated pressure (PHT) produce a broad absorption at ~3045 cm^{-1} (B) as they enhance the blue color in this sapphire. Unheated corundum, such as this ruby (C), contain inclusions of minerals that are unstable at higher temperatures. In this case, the presence of boehmite absorption peaks indicates the stone was not heat treated. The fully absorbed region <1600 cm^{-1} is caused by intrinsic Al-O bonds in corundum.

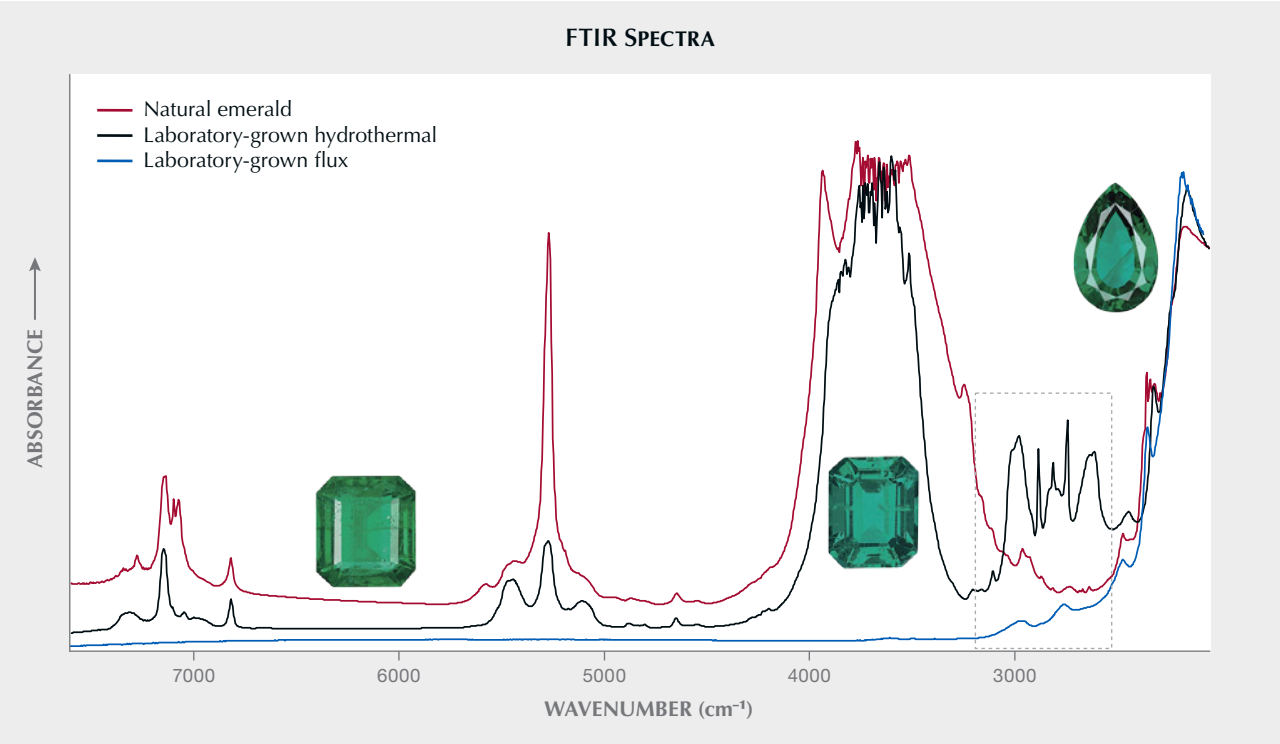

Figure 17. FTIR spectra of natural emerald and those synthesized by flux or hydrothermal growth methods have distinctly different absorptions in the 2400–3100 cm^{-1} region, helping with identification. Spectra are offset vertically for clarity.

boehmite) have distinctive IR absorptions between 2300 and 3800 cm^{-1} in FTIR spectra. When present, they conclusively indicate that the ruby or sapphire has not been heat treated (figure 16C).

Emerald. Emerald is the bluish green to green variety of the mineral beryl. Due to emerald's appeal, scientists began devising ways to grow them in a laboratory as early as 1848 (Koivula and Keller, 1985). There are two main methods to produce laboratory-grown emerald: flux growth and hydrothermal growth. Both types can be difficult to distinguish from natural stones by the untrained eye, and FTIR is a useful tool for distinguishing natural from laboratory-grown emeralds. Flux emeralds are grown from a hot molten metal flux, and their FTIR spectra are easily distinguishable due to the absence of water-related absorptions (~3400–4000, 5000–5500, and 6700–7500 cm^{-1}). Both natural and hydrothermal laboratory-grown emeralds are grown from hot circulating fluids, making their FTIR spectra similar. Fortunately, a series of IR peaks from 2400 to 3100 cm^{-1} attributed to chlorine occur in the most common lab-grown hydrothermal emeralds, making identification possible (Stockton, 1987) (figure 17). FTIR can also aid in identifying fracture-filling materials in emerald (Johnson et al., 1999).

Alexandrite. Alexandrite is a color-change variety of the mineral chrysoberyl. The most sought-after color change is from a greenish hue under daylight or fluorescent lighting to a reddish hue under incandescent light. This dramatic effect has inspired its growth in a laboratory. Alexandrite can be synthesized by three different methods: flux-melt, floating zone, and Czochralski crystal "pulling." All three involve crystallization from a molten liquid and yield comparable FTIR spectra. Conversely, natural alexandrite is formed in a metamorphic geological environment where fluids are abundant. Water-related IR absorptions in the crystal structure distinguish natural alexandrite from its lab-grown counterparts (Stockton and Kane, 1988).

Jadeite. Not all gemstones are single crystals of minerals. The term "jade" refers to two varieties of massive crystal aggregates that are commonly green in color: nephrite (composed of the amphibole minerals actinolite and tremolite) and the more valued and sought-after variety, jadeite. Like many other gem-

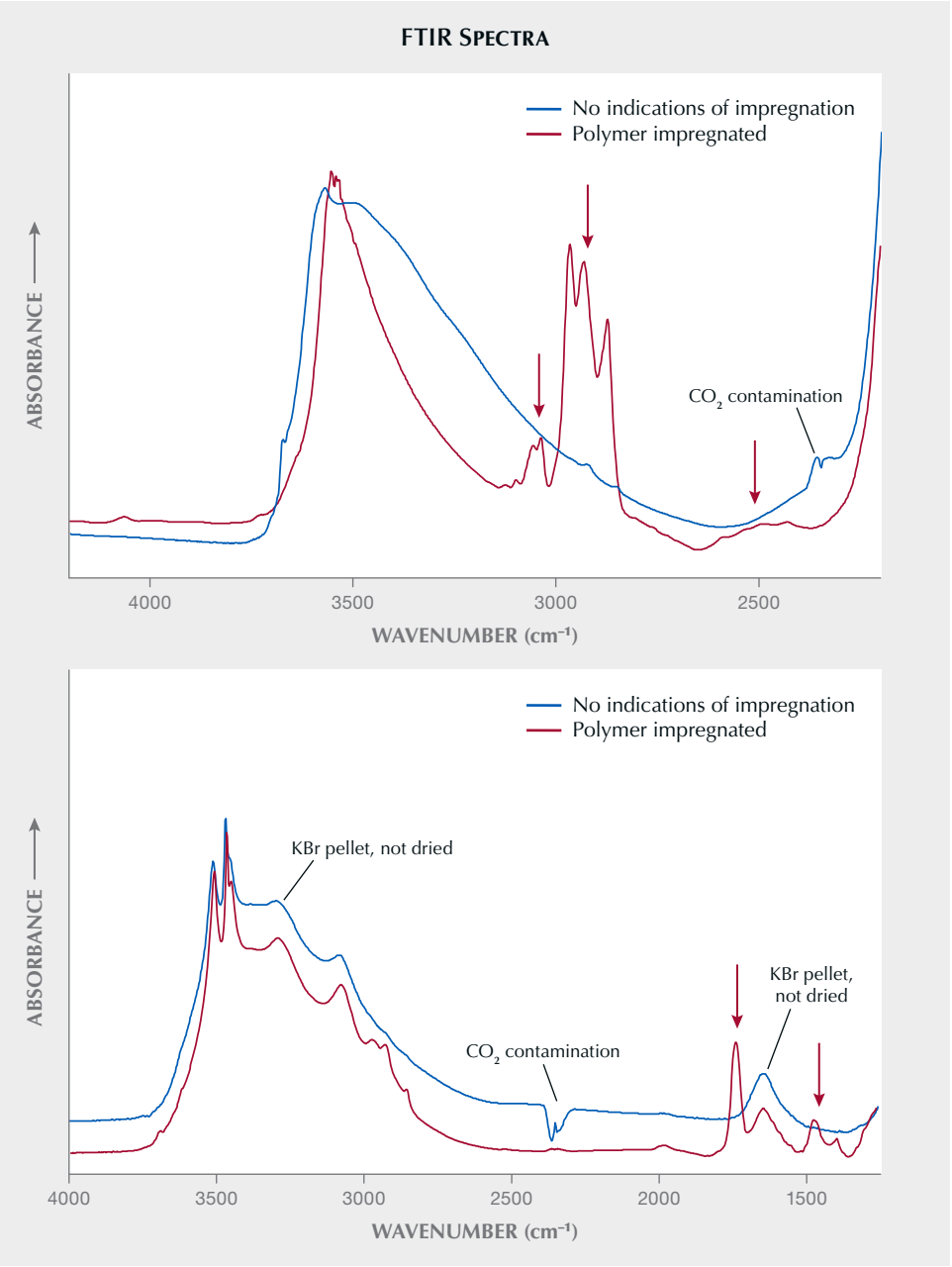

Figure 18. Gemstones such as jadeite (top) and turquoise (bottom) may be naturally fragile and unstable. Treaters sometimes impregnate poor-quality material with polymer resins (and dyes) to improve their stability and appearance. FTIR spectra clearly reveal absorptions related to these treatments (indicated by red arrows). Spectra are offset vertically for clarity.

stones, much of the mined jadeite is not of high quality, containing uneven or little color and brown-stained fractures. As a result, a common practice is to bleach away the brown color using acids and fill the void spaces created with polymer resins to stabilize the stones for cutting and polishing. In some cases, colored dyes are mixed with the polymer to add color throughout the stone. This treatment is known as polymer impregnation with or without dying. While sometimes difficult to see with the untrained eye, the added polymers are readily visible in FTIR spectra, allowing identification of the treatment (Fritsch et al., 1992) (figure 18, top).

Turquoise. Another polymer-impregnated gem material is turquoise, a popular opaque blue to green ornamental gemstone. Finding large, intact pieces of good color is rare because it is a soft, often powdery aggregate of tiny mineral crystals that falls apart easily. To improve its stability, lower-quality turquoise is bonded together at the granular level using polymer resins. Because turquoise is opaque, IR light cannot

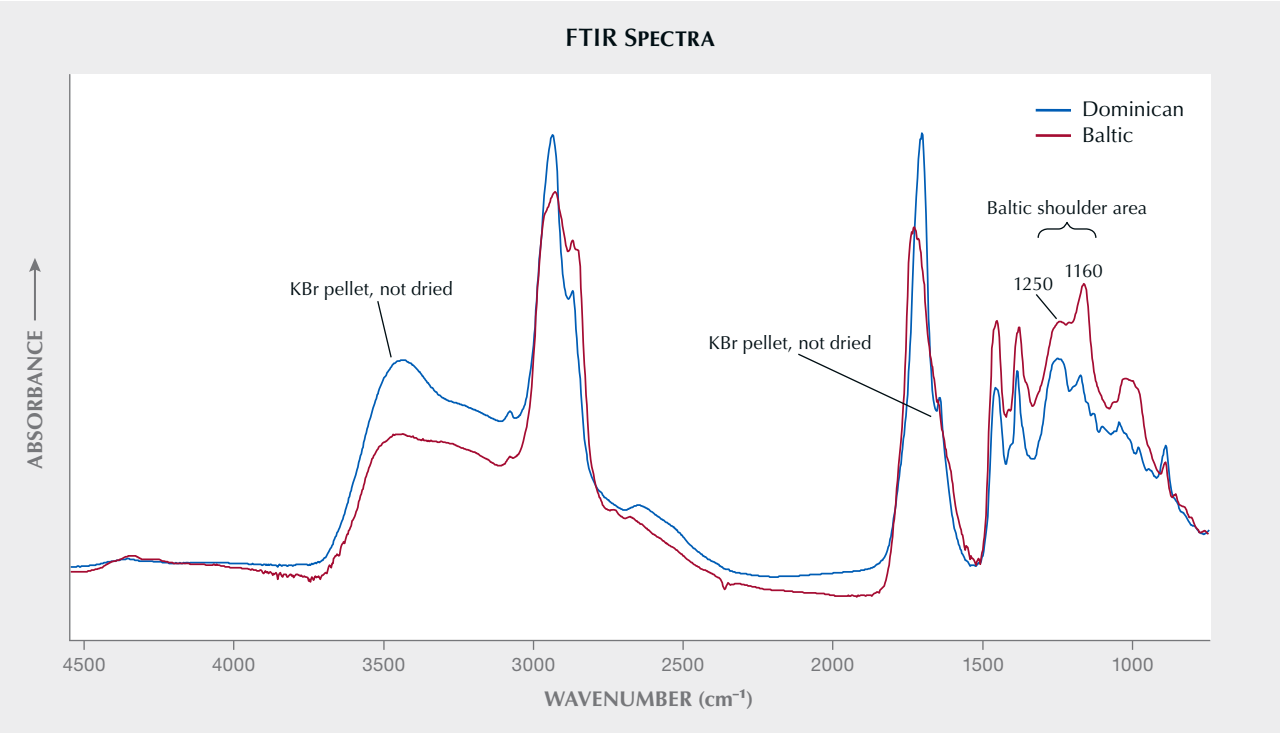

Figure 19. Amber from the Baltic region shows a distinctive pattern of IR absorptions generally between 1160 and 1250 cm^{-1}. These two features, with the 1160 cm^{-1} absorption being higher, are known as the Baltic shoulder in FTIR spectra. Amber from other locations does not show the same pattern. Spectra are offset vertically for clarity.

pass through gem-sized pieces. Industrious gemologists, however, developed a technique to scrape small amounts of powder from the stones and mix them with KBr to form a solid translucent film that can be analyzed using FTIR. In this manner, FTIR spectra clearly identify the presence of polymer resins, even when they are difficult to see using a microscope (Liu et al., 2021) (figure 18, bottom). More recently, ATR FTIR has proven effective in place of KBr for turquoise (Čejka et al., 2015). Turquoise is also often imitated by dyeing common and inexpensive minerals such as howlite or magnesite, and FTIR spectra clearly distinguish turquoise from these imitations.

Other Gemstones. The benefits of FTIR analysis extend to many other gemstones as well. Using the KBr method described above, amber from the Baltic region can be separated from amber from the Dominican Republic and other sources through observation of a unique broad IR absorption around 1250 cm^{-1} (Abduriyim et al., 2009; Khanjian et al., 2013) (figure 19). Rare red beryl can also be differentiated from imitations and other beryl varieties using FTIR. Manufactured glass, which is commonly used as a gemstone, can be distinguished from naturally occurring glasses such as moldavite and obsidian using FTIR analysis (figure 20). Finally, the most abundant mineral on earth, quartz, has many color varieties (amethyst, citrine, rose, smoky) and is one of the most commonly faceted gem materials. FTIR spectra are useful in distinguishing some natural quartz from its lab-grown equivalent (Balitsky et al., 2004; Karampelas et al., 2011). These examples illustrate the wide-ranging role of FTIR analysis in gemology.

Gemstone Identification Using Reflection IR. While most FTIR analysis of gems is performed by some form of absorption spectroscopy, it is important to mention that reflection IR, particularly specular reflection (in which the IR beam simply reflects off of the gem surface rather than sampling the interior), can also be a very useful gem identification tool (Hainschwang and Notari, 2008). These direct reflection IR spectra often show different patterns compared to absorption spectra of the same gem, and they tend to be very distinctive for most gemstones. With consistent sampling protocols and a carefully curated reference library of reflectance spectra of known gemstones, this technique can provide a quick and effective method to identify gem materials. IR absorption

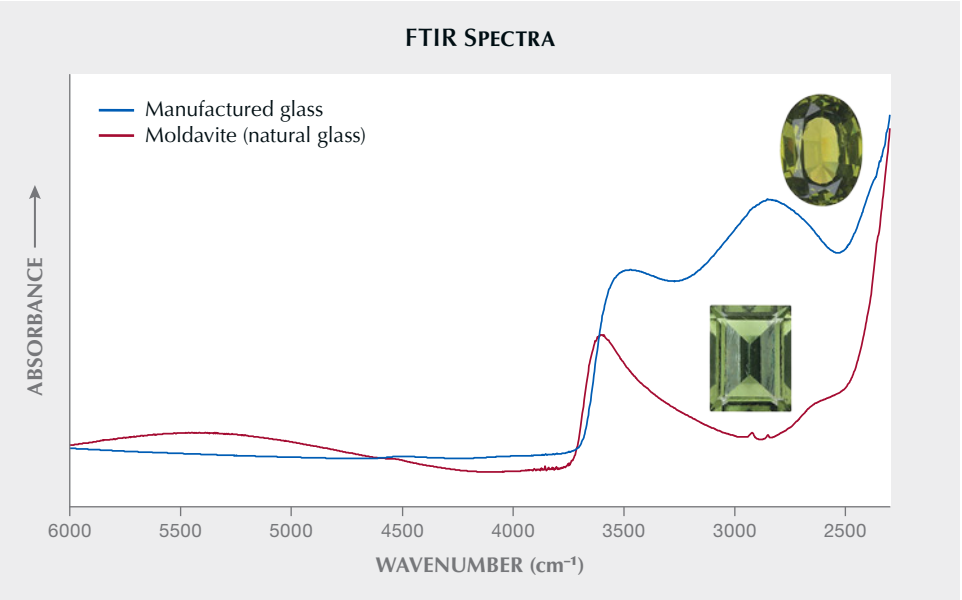

Figure 20. Manufactured glass is commonly used as a gemstone, but some natural glasses, such as moldavite, are also faceted as gems. Fortunately, FTIR spectra are different for both, aiding in identification. Spectra are offset vertically for clarity.

spectroscopy is more useful for treatment detection and separating natural from laboratory-grown gems, but reflection spectroscopy provides a quick and reasonably reliable method to identify the gem mineral being examined.

CONCLUSIONS

Infrared spectroscopy is an indispensable tool for the effective and efficient identification of natural and laboratory-grown gemstones as well as many treatments applied to enhance their color. The vibrational properties of bonds between atoms in a mineral in response to IR energy produce distinctive and consistent absorptions that are easily observed in FTIR spectra taken at room temperature. This analytical technique has been a mainstay in gem laboratories since the 1990s and continues to be a valuable gemological tool. From measuring nitrogen impurities that define diamond type to detecting heat treatment features in ruby and sapphire and polymer impregnation of turquoise and jadeite and beyond, FTIR is an essential resource for gem identification.

ABOUT THE AUTHORS

Dr. Christopher M. Breeding is senior manager of analytics, and Nicole Ahline is supervisor of colored stone identification, at GIA in Carlsbad, California.

ACKNOWLEDGMENTS

We thank Phil Owens and Claire Malaquias for helpful discussions.

REFERENCES

Abduriyim A., Kimura H., Yokoyama Y., Nakazono H., Wakatsuki M., Shimizu T., Tansho M., Ohki S. (2009) Characterization of "green amber" with infrared and nuclear magnetic resonance spectroscopy. *G&G*, Vol. 45, No. 3, pp. 158–177, http://dx.doi.org/10.5741/GEMS.45.3.158

Anderson B.W. (1943) Absorption and luminescence in diamond I. *The Gemmologist*, Vol. 12, No. 138, pp. 21–22.

——— (1963) The classification of diamonds on the basis of their absorption and emission of light. *Journal of Gemmology*, Vol. 9, No. 2, pp. 44–54.

Balitsky V.S., Balitsky D.V., Bondarenko G.V., Balitskaya O.V. (2004) The 3543 cm^{-1} infrared absorption band in natural and synthetic amethyst and its value in identification. *G&G*, Vol. 40, No. 2, pp. 146–161, http://dx.doi.org/10.5741/GEMS.40.2.146

Becker E.D., Farrar T.C. (1972) Fourier transform spectroscopy. *Science*, Vol. 178, No. 4059, pp. 361–368, http://dx.doi.org/10.1126/science.178.4059.361

Blackwell D.E., Sutherland G.B.B.M. (1949) The vibrational spectrum of diamond. *Journal de Chimie Physique et de Physico-Chimie Biologique*, Vol. 46, No. 1, pp. 9–15, http://dx.doi.org/10.1051/jcp/1949460009

Boyd S.R., Kiflawi I., Woods G.S. (1994) The relationship between

infrared absorption and the A defect concentration in diamond. *Philosophical Magazine B*, Vol. 69, No. 6, pp. 1149–1153, http://dx.doi.org/10.1080/01418639408240185
——— (1995) Infrared absorption by the B nitrogen aggregate in diamond. *Philosophical Magazine B*, Vol. 72, No. 3, pp. 351–361, http://dx.doi.org/10.1080/13642819508239089
Breeding C.M., Shigley J.E. (2009) The "type" classification system of diamonds and its importance in gemology. *G&G*, Vol. 45, No. 2, pp. 96–111, http://dx.doi.org/10.5741/GEMS.45.2.96
Breeding C.M., Shen A.H., Eaton-Magaña S., Rossman G.R., Shigley J.E., Gilbertson A. (2010) Developments in gemstone analysis techniques and instrumentation during the 2000s. *G&G*, Vol. 46, No. 3, pp. 241–257, http://dx.doi.org/10.5741/GEMS.46.3.241
Čejka J., Sejkora J., Macek I., Malíková R., Wang L., Scholz R., Xi Y., Frost R.L. (2015) Raman and infrared spectroscopic study of turquoise minerals. *Spectrochimica Acta Part A: Molecular and Biomolecular Spectroscopy*, Vol. 149, pp. 173–182, http://dx.doi.org/10.1016/j.saa.2015.04.029
Collins A.T. (2001) The colour of diamond and how it may be changed. *Journal of Gemmology*, Vol. 27, No. 6, pp. 341–359.
Collins A.T., Kanda H., Kitawaki H. (2000) Colour changes produced in natural brown diamonds by high-pressure, high-temperature treatment. *Diamond and Related Materials*, Vol. 9, No. 2, pp. 113–122, http://dx.doi.org/10.1016/S0925-9635(00)00249-1
Davies G. (1977) The optical properties of diamond. In P.L. Walker Jr. and P.A. Thrower, Eds., *Chemistry and Physics of Carbon*, Vol. 13, Marcel Dekker Inc., New York, pp. 1–143.
Fritsch E., Stockton C.M. (1987) Infrared spectroscopy in gem identification. *G&G*, Vol. 23, No. 1, pp. 18–26, http://dx.doi.org/10.5741/GEMS.23.1.18
Fritsch E., Wu S.T., Moses T., McClure S.F., Moon M. (1992) Identification of bleached and polymer-impregnated jadeite. *G&G*, Vol. 28, No. 3, pp. 176–187, http://dx.doi.org/10.5741/GEMS.28.3.176
Hainschwang T., Notari F. (2008) Specular reflectance infrared spectroscopy – A review and update of a little exploited method for gem identification. *Journal of Gemmology*, Vol. 31, No. 1-2, pp. 23–29.
Howell D., Collins A.T., Loudin L.C., Diggle P.L., D'Haenens-Johansson U.F.S., Smit K.V., Katrusha A.N., Butler J.E., Nestola F. (2019) Automated FTIR mapping of boron distribution in diamond. *Diamond and Related Materials*, Vol. 96, pp. 207–215, http://dx.doi.org/10.1016/j.diamond.2019.02.029
Jenkins F.A., White H.E. (1976) The electromagnetic character of light. In *Fundamentals of Optics*, 4th ed., McGraw-Hill, New York, pp. 423–437.
Jin S., Renfro N., Palke A.C., Ardon T., Homkrajae A. (2024) Application of UV-Vis-NIR spectroscopy to gemology. *G&G*, Vol. 60, No. 4, pp. 456–473, http://dx.doi.org/10.5741/GEMS.60.4.456
Johnson M.L., Elen S., Muhlmeister S. (1999) On the identification of various emerald filling substances. *G&G*, Vol. 35, No. 2, pp. 82–107, http://dx.doi.org/10.5741/GEMS.35.2.82
Kaiser W., Bond W.L. (1959) Nitrogen, a major impurity in common type I diamond. *Physical Review*, Vol. 115, No. 4, pp. 857–863, http://dx.doi.org/10.1103/PhysRev.115.857
Karampelas S., Fritsch E., Zorba T., Paraskevopoulos K.M. (2011) Infrared spectroscopy of natural vs. synthetic amethyst: An update. *G&G*, Vol. 47, No. 3, pp. 196–201, http://dx.doi.org/10.5741/GEMS.47.3.196
Khanjian H., Schilling M., Maish J. (2013) FTIR and PY-GC/MS investigation of archaeological amber objects from the J. Paul Getty Museum. *e-Preservation Science*, Vol. 10, pp. 66–70.
Kiflawi I., Mayer A.E., Spear P.M., Van Wyk J.A., Woods G.S. (1994) Infrared absorption by the single nitrogen and A defect centres in diamond. *Philosophical Magazine B*, Vol. 69, No. 6, pp. 1141–1147, http://dx.doi.org/10.1080/01418639408240184
Koivula J.I., Keller P.C. (1985) Russian flux-grown synthetic emeralds. *G&G*, Vol. 21, No. 2, pp. 79–85, http://dx.doi.org/10.5741/GEMS.21.2.79
Liggins S., Newton M.E., Goss J.P., Briddon P.R., Fisher D. (2010) Identification of the dinitrogen <001> split interstitial H1a in diamond. *Physical Review B*, Vol. 81, No. 8, article no. 085214, http://dx.doi.org/10.1103/PhysRevB.81.085214
Liu L., Yang M., Li Y., Di J., Chen R., Liu J., He C. (2021) Technical evolution and identification of resin-filled turquoise. *G&G*, Vol. 57, No. 1, pp. 22–35, http://dx.doi.org/10.5741/GEMS.57.1.22
Lowry S. (2008) Using FTIR spectroscopy to analyze gemstones. *American Laboratory*, Vol. 40, No. 10, pp. 28–31.
Massi L., Fritsch, E., Collins A.T., Hainschwang T., Notari F. (2005) The "amber centres" and their relation to the brown colour in diamond. *Diamond and Related Materials*, Vol. 14, No. 10, pp. 1623–1629, http://dx.doi.org/10.1016/j.diamond.2005.05.003
Nassau K. (2001) Some fundamentals: Color, light, and interactions. In *The Physics and Chemistry of Color*, 2nd ed., Wiley-Interscience Publication, New York, pp. 1–33.
Peretti A., Musa M., Bieri W., Cleveland E., Ahamed I., Alessandri M., Hahn L. (2018) Identification and characteristics of PHT ('HPHT') – treated sapphires – An update of the GRS research progress. GemResearch SwissLab, https://www.gemresearch.ch/news/2018/11/03/hpht-update
Smal I.M., Yu Q., Veneman R., Fränzel-Luiten B., Brilman D.W.F. (2014) TG-FTIR measurement of CO_2-H_2O co-adsorption for CO_2 air capture sorbent screening. *Energy Procedia*, Vol. 63, pp. 6834–6841, http://dx.doi.org/10.1016/j.egypro.2014.11.717
Smith B.C. (2011) *Fundamentals of Fourier Transform Infrared Spectroscopy*, 2nd ed. CRC Press, Boca Raton, Florida.
Smith C.P. (1995) A contribution to understanding the infrared spectra of rubies from Mong Hsu, Myanmar. *Journal of Gemmology*, Vol. 24, No. 5, pp. 321–335.
Stockton C.M. (1987) The separation of natural from synthetic emeralds by infrared spectroscopy. *G&G*, Vol. 23, No. 2, pp. 96–99, http://dx.doi.org/10.5741/GEMS.23.2.96
Stockton C.M., Kane R.E. (1988) The distinction of natural from synthetic alexandrite by infrared spectroscopy. *G&G*, Vol. 24, No. 1, pp. 44–46, http://dx.doi.org/10.5741/GEMS.24.1.44
Sun D.-W., Ed. (2009) *Infrared Spectroscopy for Food Quality Analysis and Control*. Elsevier, New York, 414 pp.
Thanong L., Nicharee A., Thanapong L., Papawarin O. (2016) Blue sapphire undergone high pressure high temperature enhancement. GIT Gemstone Update, https://git.or.th/th
Thongnopkun P., Wongravee K., Plenpinljtham P., Phlayrahan A. (2022) Application of Fourier-transformed infrared spectroscopy and machine learning algorithm for gem identification. In A.K. Shukla, Ed., *Artificial Intelligence and Spectroscopic Techniques for Gemology Applications*, IOP Series in Spectroscopic Methods and Applications, http://dx.doi.org/10.1088/978-0-7503-3927-8
Vertriest W., Saeseaw S. (2019) A decade of ruby from Mozambique: A review. *G&G*, Vol. 55, No. 2, pp. 162–183, http://dx.doi.org/10.5741/GEMS.55.2.162
Wang Z., Takahashi H. (2023) Development of mid-infrared absorption spectroscopy for gemstone analysis. *Minerals*, Vol. 13, No. 5, article no. 625, http://dx.doi.org/10.3390/min13050625
Wilks E., Wilks J. (1991) *Properties and Applications of Diamond*. Butterworth-Heinemann Ltd., Oxford, UK.
Woods G.S. (1984) Infrared absorption studies of the annealing of irradiated diamonds. *Philosophical Magazine B*, Vol. 50, No. 6, pp. 673–688, http://dx.doi.org/10.1080/13642818408238892
——— (1986) Platelets and the infrared absorption of type Ia diamonds. *Proceedings of the Royal Society of London: Series A, Mathematical and Physical Sciences*, Vol. 407, No. 1832, pp. 219–238, http://dx.doi.org/10.1098/rspa.1986.0094

AMERICAN GEM SOCIETY®
Consumer Protection Since 1934®

GIA®

CONVERGE™

AGS CONCLAVE X GIA SYMPOSIUM

Presenting Sponsor

Jewelers Mutual®
EST 1913

SEPTEMBER 7 - 10, 2025
CARLSBAD, CA

Education. Innovation. Connection.
Join us as GIA's innovative gemological research and industry-leading education converges with the American Gem Society's professional development, networking, and opportunities to connect.

Converge is an exciting opportunity to get inspired by world-class speakers and be a part of important conversations that spark new ideas to lead the industry to new heights of success.

Space is limited, so register today! Attend Converge and be part of the future of gems and jewelry.

Registration, updates, and more at
ConvergeEvent.com

Shining a Light on Gemstone Properties: An Exploration of Photoluminescence Spectroscopy

Sally Eaton-Magaña, Daniel C. Jones, Rachelle B. Turnier, and Christopher M. Breeding

Photoluminescence (PL) spectroscopy is a powerful testing method for gemstones in which absorption of light leads to emission at longer wavelengths, revealing valuable insights into the material's composition, structure, and optical properties. In gemology, PL is a crucial tool for identifying and characterizing gemstones, understanding their geological history, detecting treatments and synthetics, and providing clues about the presence of impurities, defects, and inclusions.

The advantages and disadvantages of PL will be explored along with a survey of its applications among various gemstones including diamonds, pearls, and chromium-containing gems, with a focus on emerging techniques such as PL mapping, fluorescence lifetime, and large-scale statistical analysis. This article highlights the significance of PL spectroscopy applied to gemstones, revealing new insights into these natural wonders and helping distinguish them from their treated and laboratory-grown counterparts.

Defects that occur within the lattice of a gemstone, due to the disruption of the crystal lattice or the introduction of impurity atoms, often give rise to optically detectable features; these are often called "color centers," "optical centers," "optical defects," or simply "defects." In ionic crystals, the term "F-center" is also used. These defects are a gem's storytellers and can reveal much about its history, whether it formed in the earth or in a laboratory. The atomic-level defects preserved in a gem are determined by its growth conditions as well as any subsequent geological or treatment history.

Gemological laboratories rely on nondestructive analytical techniques, usually based on optical methods such as absorption spectroscopy, Raman, and photoluminescence (PL) spectroscopy. With PL and Raman spectroscopy, a material is exposed to laser light (figure 1), typically under a microscope in a gemological laboratory or research setting, and the resulting emission is measured with a high-resolution spectrometer. PL spectroscopy has become an invaluable tool in gemological laboratories. This technique is nondestructive and very sensitive, and in some cases it can detect defects at concentrations lower than 10 parts per billion, or ppb (Wotherspoon et al., 2003). The method has numerous applications and can successfully distinguish some treated and laboratory-grown diamonds from their natural counterparts.

In Brief

- Over the last two decades, PL spectroscopy has become one of the most important analytical methods for gemstone identification, particularly diamond.
- PL spectroscopy, closely related to fluorescence as it is also measuring emission from a gem, is capable of detecting defects at very low concentrations that are not measurable by other methods.
- In recent years, specialized technologies such as spatial PL mapping in two and three dimensions, nanosecond-scale lifetime measurements, and large-dataset statistical analysis have become possible and are now being used.

This article provides a historical overview of PL and its applications (see box A), a detailed look at how PL is used in gemology, and an evaluation of

See end of article for About the Authors and Acknowledgments.
Gems & Gemology, Vol. 60, No. 4, pp. 494–517,
http://dx.doi.org/10.5741/GEMS.60.4.494

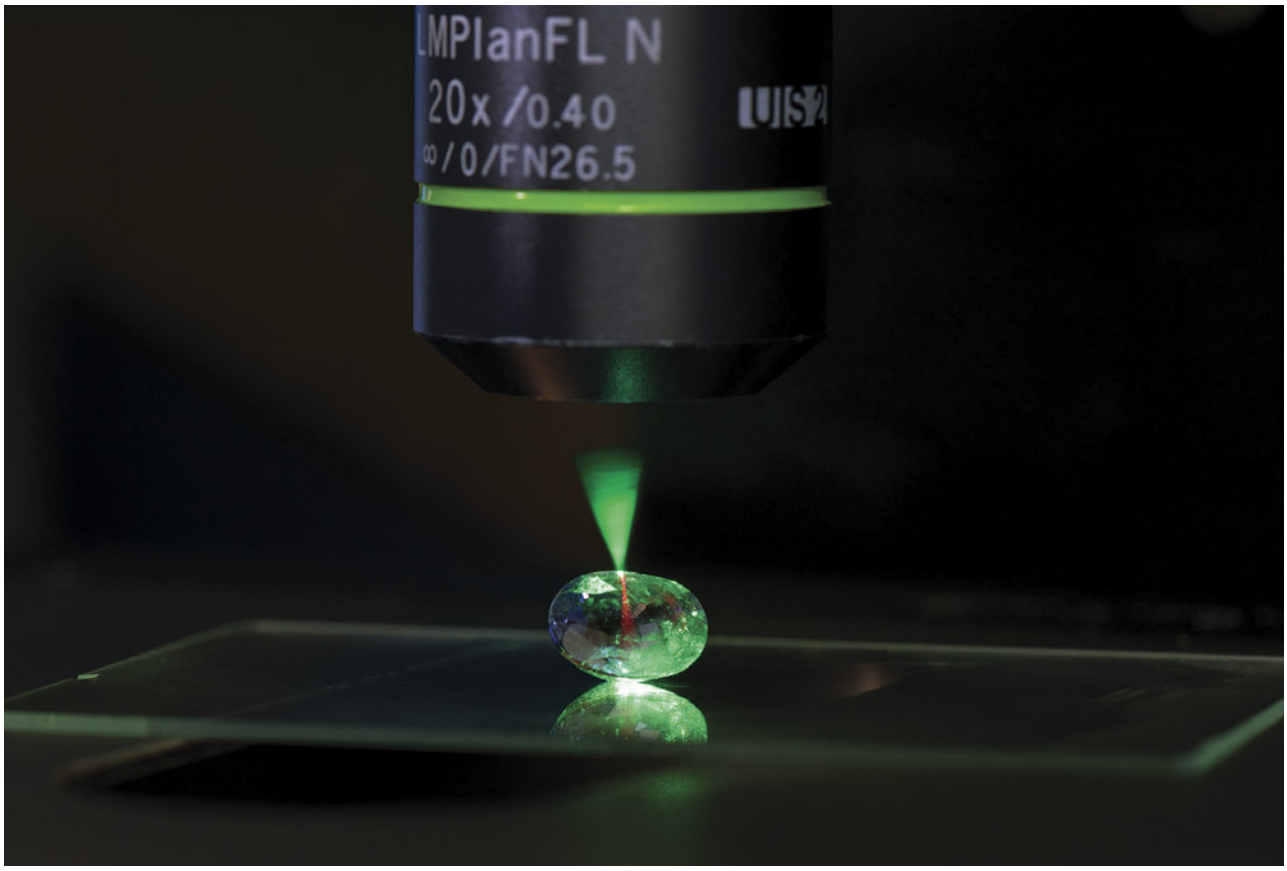

Figure 1. Microscope-assisted photoluminescence spectroscopy is an important technique for collecting data in gemological research and identification. Here, a 514 nm laser illuminates a sapphire sample at room temperature, creating red luminescence caused by trace amounts of chromium. Photo by Kevin Schumacher.

emerging PL-based techniques. For a substantial recounting of the underlying theory of luminescence (e.g., Nasdala et al., 2004; Waychunas, 2014; Eaton-Magaña and Breeding, 2016; Green et al., 2022; Zhang and Shen, 2023) or a compendium of PL features found in gem materials (e.g., Zaitsev, 2003; Gaft et al., 2015; Hughes et al., 2017; D'Haenens-Johansson et al., 2022), please refer to the cited works.

Impurities in gemstones can produce optical phenomena, resulting in characteristic features or peaks in spectroscopic data. Diamond, for instance, is composed primarily of carbon, but it can contain defects such as vacant lattice sites (i.e., vacancies), displaced carbon atoms ("interstitials"), and elemental impurities such as nitrogen, boron, and nickel atoms. Luminescence features arise from several different mechanisms, including transitions between the material's intrinsic electronic states, impurities, and structural defects or disorder. These interactions in gems help reveal the defects and the energy states of the atoms involved, making spectroscopy an accurate and useful identification tool in gemology. While photoluminescence spectroscopy is a more powerful tool than the fluorescence observations that are familiar to those in the trade, both techniques are based on comparable mechanisms and the same emitting defects.

Several important aspects are involved in using PL spectroscopy to detect and identify defects. Along with collecting the spectrum of the emission from the sample (standard PL spectroscopy), additional techniques include (1) cooling the sample to reduce the broadening of spectral features, (2) monitoring photochromic effects, (3) measuring the spatial distribution of the defects across the sample (PL mapping), (4) measuring the fluorescence decay time (time-resolved luminescence, or TRL), and (5) measuring the emission as a function of excitation wavelength (photoluminescence excitation, or PLE). In gemology, technique 1 is regularly used for diamond samples by cooling to liquid nitrogen temperatures (–196°C). Technique 2 can be observed in some PL features due to deep-UV exposure such as with the DiamondView, while techniques 3–5 are only rarely

BOX A: HISTORY OF PL IN GEMOLOGY

Over the past twenty years, PL spectroscopy has become an important tool used by major gemological laboratories to distinguish treated diamonds from their natural counterparts (e.g., Breeding et al., 2010; Lim et al., 2010). Raman analysis, a reliable gem identification tool since the 1930s, employs equipment that is often quite suitable for collecting PL spectra. The application of photoluminescence techniques dates back more than a century, with an early report discussing the photoluminescence of calcite (Nichols et al., 1918). In the latter half of the twentieth century, several dozen articles related to gem materials were published, with most of these focusing on diamond (e.g., Clark and Norris, 1971; Solin, 1972; Walker, 1977; Thomaz and Davies, 1978; Collins et al., 1983b; Collins, 1992; Freitas et al., 1994), along with a few studies on other gem materials such as cinnabar (Simpson et al., 1980), zircon (Shinno, 1987), garnet (O'Donnell et al., 1989), fluorite (Calderon et al., 1990, 1992), forsterite (Glynn et al., 1991), and olivine (Bakhtin et al., 1995).

The adoption of PL spectroscopy as a method of diamond identification began in 1999 when General Electric (GE) announced a high-pressure, high-temperature (HPHT) treatment method for decolorizing type II brown diamonds ("Pegasus Overseas Limited…," 1999; Shigley et al., 1999). Conventional gemological tests could not detect HPHT-treated diamonds, but PL spectroscopy's high sensitivity made identification possible. After the diamond industry's initial alarm following the GE announcement, extensive research showed that PL spectroscopy at liquid nitrogen temperatures was the most effective method for detecting HPHT treatment (Fisher and Spits, 2000; Smith et al., 2000).

When HPHT treatment was first introduced, detecting the presence or absence of specific PL peaks from a single or a few laser wavelengths was sufficient. If more sophisticated analysis was needed, the tools were not available in the early 2000s. For example, measuring the full width at half-maximum (FWHM, a standard method for determining peak width) was accomplished by the rudimentary procedure of printing out the spectrum and using a ruler. Today, that calculation is performed by standard computer algorithms and, in some cases, performed automatically (e.g., Martineau and McGuinness, 2018). As diamond processing and synthesis have advanced, the standard procedure now demands far greater resources.

Therefore, PL spectroscopy has become a vital addition to all gemological laboratories. Along with the hardware, this technique requires infrastructure such as training and the construction of a spectral database of known samples. In addition to detecting HPHT treatment in colorless diamonds, PL spectroscopy is now used to identify growth history and color origin in both colorless and colored diamonds (Wang et al., 2012). The increasing sophistication of treatment and laboratory growth processes has driven the use of complex analytical methods and instruments, such as mapping spectrometers and automated gem testing, in large gemological laboratories. As a result, PL-related applications have expanded far beyond their original purpose.

applied, typically for research or in an academic setting. Nevertheless, methods 3 and 4 provide important information regarding the identity of defects and will be discussed in greater detail in later sections.

In addition, certain natural and laboratory processes can change the structure of a physical material and hence the PL response. Interpreting PL spectra for some gem materials can reveal permanent treatment such as irradiation and/or annealing, changes or variations in applied stresses of the crystal, changes in the isotopic composition of elements used in laboratory growth, and the implantation and/or diffusion of ions of a known element into the atomic structure. However, using this extensive array of attributes and tests is often not possible due to their unavailability, the cost required, or the destructive nature of the measurement process.

In a gemological laboratory where PL data is being gathered on hundreds or thousands of stones, some of the considerations during the data collection process include balancing time and data quality, accounting for the heterogeneity of PL features within the gem, and ensuring consistency between gems. The procedure for client stones often consists of collecting PL spectra with one or more lasers of various wavelengths, typically on one location on the stone, and comparing the resulting spectra against a database of known samples.

Although generally utilized by gemological laboratories, PL spectroscopy can also be used by the trade to screen laboratory-grown diamonds and simulants at room temperature using near-UV (385 nm; Tsai and D'Haenens-Johansson, 2021) or deep-UV excitation (193 nm; Wang et al., 2023) and on mounted jewelry pieces (Tsai and Takahashi, 2022; Tsai, 2023). Screening devices can also be employed by trade professionals to collect PL or Raman measurements for the identification of materials such as

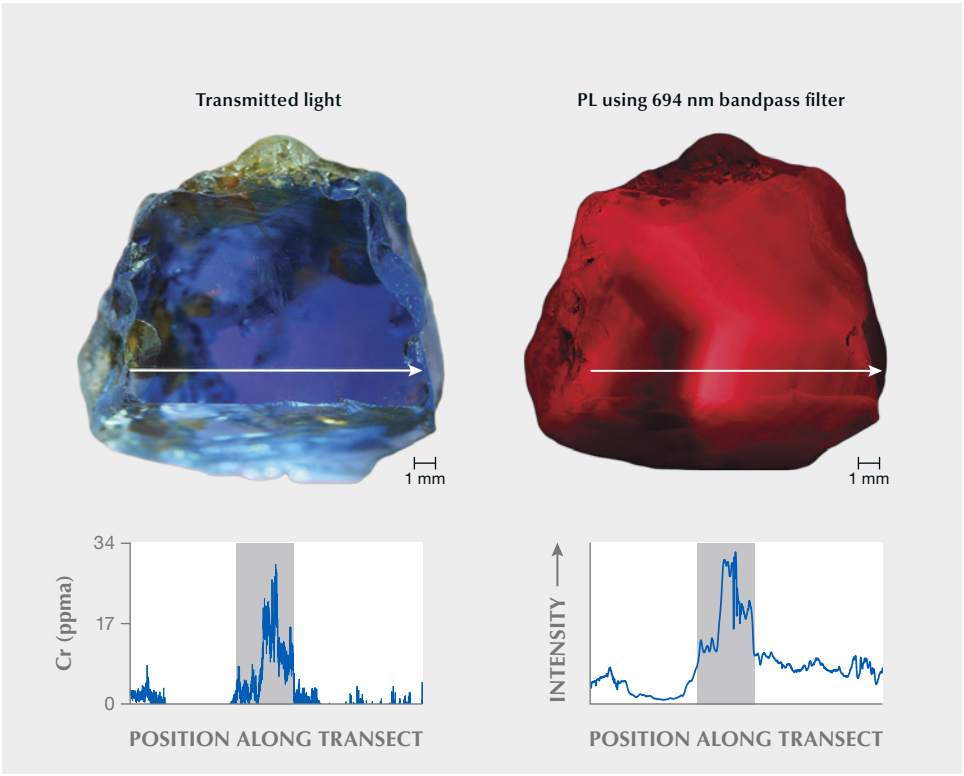

Figure 2. Sri Lankan metamorphic blue sapphire. Left: Shown in transmitted light with an arrow marking a traverse of LA-ICP-MS measurements for chromium. Right: Excited by a 365 nm light source and photographed with a 694 nm bandpass filter attached to a microscope objective, showing the same traverse. The plots show the chromium concentration and PL intensity along the traverse, respectively, with a gray band showing their correlation. Photos by Rachelle Turnier.

beryl, corundum, spinel, and zoisite (Culka et al., 2016; Tsai and D'Haenens-Johansson, 2021). Recent advancements have made PL systems available at a lower cost than full laboratory-grade instruments, assisting the industry in detecting fraudulent gems. While the results may not conclusively determine whether a diamond is natural, treated, or laboratory grown, they can provide helpful screening and identification.

Advantages. One of the hallmarks of PL spectroscopy is the sensitivity it can achieve. It can detect optical peaks indicating concentrations at the ppb level (Iakoubovskii et al., 2001; Wotherspoon et al., 2003). These highly sensitive instruments can identify dozens to hundreds of peaks depending on the material, which can help create a reliable database of distinguishing characteristics for natural, treated, and laboratory-grown gemstones. This sensitivity is generally unmatched by other noninvasive, nondestructive methods, making PL analysis vital for gem identification (Hainschwang et al., 2024).

For example, even in diamonds with no detectable nitrogen impurities by infrared absorption instruments (i.e., type II diamonds; below the detection limit of ~1–5 ppm), PL spectroscopy can detect NV concentrations of 10 ppb or less (Wotherspoon et al., 2003). Therefore, the type II designation does not mean an "absence of nitrogen," but rather that the diamond contains very low concentrations of this impurity. Nitrogen-containing defects (such as H2, H3, H4, N3, and NV centers) are usually the dominant features in the PL spectra of type IIa diamonds. Similarly, in corundum the efficiency of Cr^{3+} luminescence allows concentrations in the ppb range to be detected in sapphires. This is advantageous for using PL maps to characterize chromium zoning in corundum (e.g., figure 2).

With PL spectroscopy, several features in diamond not seen by ultraviolet/visible/near-infrared absorption spectroscopy may be detected consistently due to higher sensitivity (e.g., figure 3). The technique offers not only high detection sensitivity but also high spatial sensitivity when PL measurement is used in conjunction with a microscope, making it possible to create concentration maps showing the spatial distribution of defects (Loudin, 2017) or other parameters such as internal strain (Noguchi et al., 2013). Unlike the visible and infrared absorption measurements typically used in gemological laboratories, which are bulk measurements, PL spectroscopy can perform point measurements and control the activation volume of the material. This

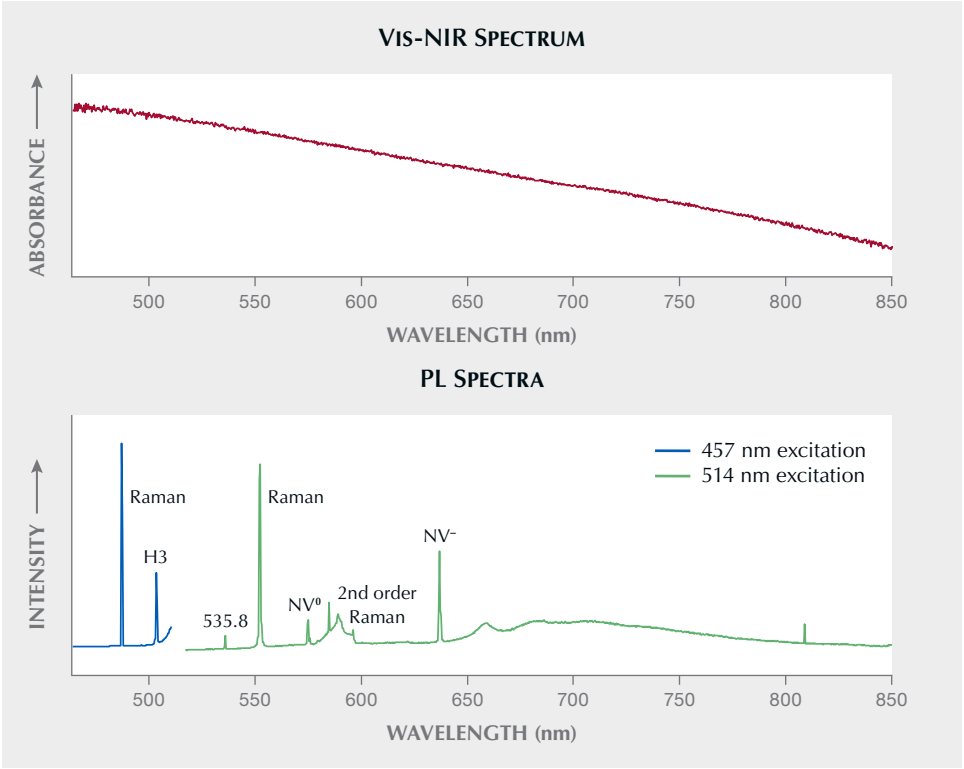

Figure 3. Spectroscopic data for a 10.09 ct H-color type IIa HPHT-treated diamond collected at liquid nitrogen temperature demonstrate the enhanced sensitivity of PL spectroscopy for detecting defects. While the Vis-NIR absorption spectrum is featureless (top), the PL spectra (bottom) show Raman features that identify the sample as diamond along with numerous peaks that aid in identification. Note that the wavelength of Raman lines shifts with the laser excitation wavelength, causing the positions of the diamond Raman lines to differ for spectra collected with 457 and 514 nm excitation.

spatial ability will be discussed further in the section on PL mapping.

PL spectroscopy also has the advantage of not requiring any sample preparation beyond cleaning, and spectra can be collected from rough surfaces as well as irregularly shaped samples such as pearls and carvings. While spectra can be collected from rough surfaces, surface topography does affect the intensity of a PL feature. Thus, PL maps collected from rough samples will show variations in PL intensity that correlate with cracks or surface height, superimposed on PL variations related to changes in defect concentration.

Disadvantages. While PL spectroscopy offers significant advantages, there are also important disadvantages to consider. For high-quality spectra, there are correspondingly high costs. Most PL systems have specialized microscopes, lasers, and spectrometers, costing hundreds of thousands of U.S. dollars along with significant maintenance costs (approximately 10% of the purchase cost annually). While small desktop and portable versions using charge-coupled devices (CCDs) offer some of the features of more expensive systems, they may fall short in other areas such as spectral resolution (the ability to distinguish individual peaks) or spatial resolution (distinguishing variations across a sample).

Operating the device typically requires specially trained users who are knowledgeable about the theory and instrumentation and can ensure that spectra are correctly collected. Operators must also be trained in special safety protocols. Although the devices are generally operated within an enclosure and designated as safe Class I lasers, laser safety training is essential, as is knowledge of safe cryogenic handling when working with diamonds at liquid nitrogen temperatures.

Temperature plays an important role in PL analysis of diamonds, particularly in cooling samples to liquid nitrogen temperatures. The PL features of diamond defects become more pronounced at these very low temperatures. Higher temperatures can reduce, shift, broaden, or eliminate their response. The effect of temperature can be clearly seen in the PL spectrum of a near-colorless, type IIa diamond shown in figure 4 at temperatures ranging from ~80 K (–193°C) to room temperature.

Unlike most gemstones, diamonds can be cooled to liquid nitrogen temperatures to optimize PL spectroscopy results because of their low coefficient of thermal expansion and very high thermal conductivity. Other gems (and heavily included diamonds) have a much greater risk of shattering when cooled. For example, corundum has a coefficient of thermal

expansion five times higher than that of diamond (Fiquet et al., 1999), while its thermal conductivity is 65 times lower (Read, 2008).

Only optically active defects that emit light can be detected with this method, and their detection depends on operating conditions such as temperature, excitation laser, and light wavelength. These limitations affect the detection of all impurities and defects in the stone. For example, Lai et al. (2020) used PL spectroscopy to show that high-pressure, high-temperature (HPHT) annealing of some natural diamonds revealed the creation of previously undetectable SiV^- defects that produce luminescence at 737 nm. The silicon impurities had been present but were not detected because they existed in a form that was not optically active. They required HPHT annealing to transform into optically active centers indicating the presence of silicon. Similarly, boron-related peaks such as the 648.2 nm (B_i) and 776.4 nm (ascribed to a boron-vacancy complex) PL features can be created at moderate annealing temperatures and annihilated at higher temperatures (Green, 2013; Eaton-Magaña and Ardon, 2016). In diamonds where these features cannot be detected and uncompensated boron is not detected by IR absorption spectroscopy, the presence of boron impurities generally cannot be known without chemical analysis. Therefore, PL analysis can often provide a

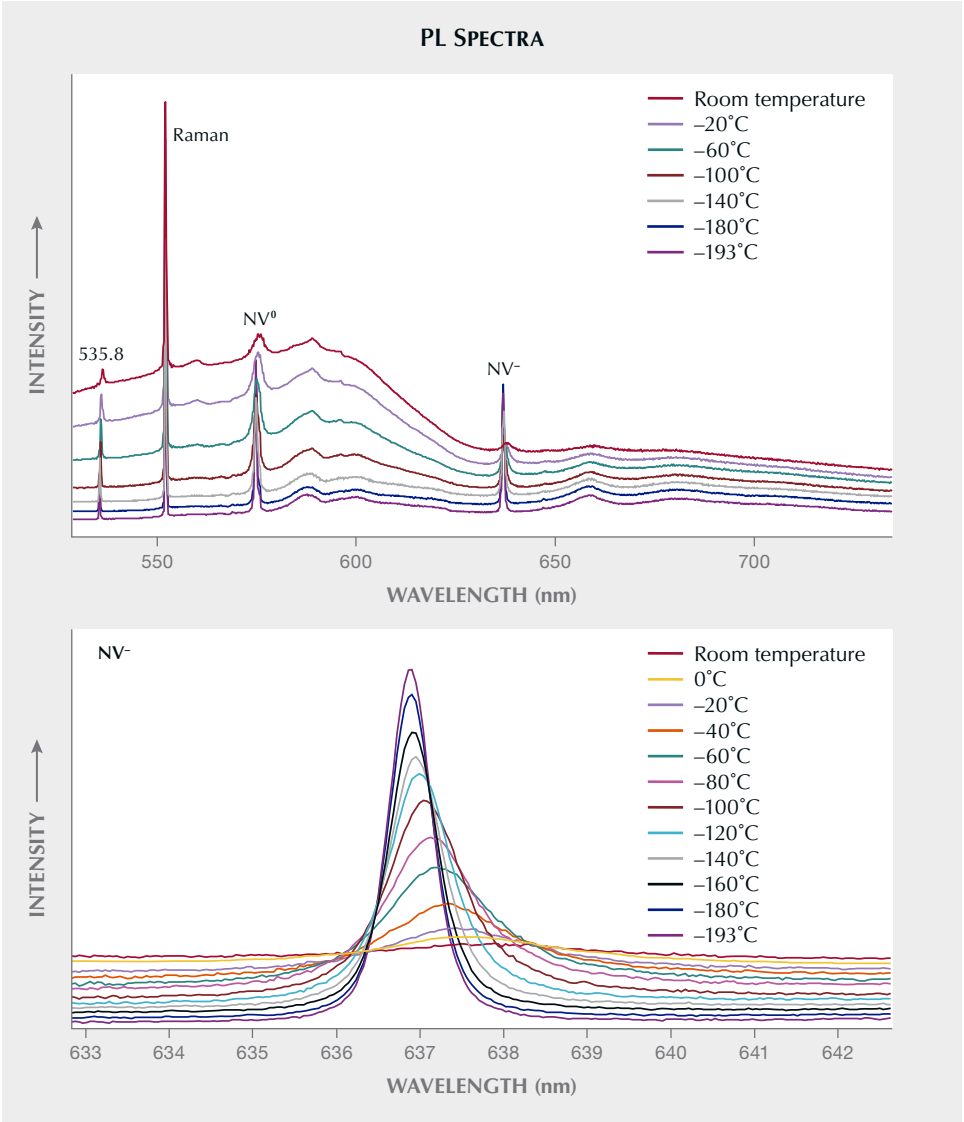

Figure 4. Temperature effect on the 514 nm PL spectra of a near-colorless type IIa diamond from liquid nitrogen temperature to room temperature (–193° to 23°C) across a broad wavelength range (top) and for the NV^- defect (bottom). The NV^- peak is well-defined at low temperature but broadens and decreases in intensity with increasing temperature, becoming much weaker at room temperature. Spectra are offset vertically for clarity and intensities are scaled to the Raman peak.

good indication of impurities in diamonds, but some impurities may go undetected because they are not optically active and can only be identified through destructive tests.

Distinction Between Raman and PL Spectroscopy. Raman spectroscopy is a crucial tool for evaluating and identifying many gems (Bersani and Lottici, 2010; Kiefert and Karampelas, 2011; Groat et al., 2019; Smith et al., 2022; Jin and Smith, 2024, pp. 518–535 of this issue). While instruments configured to detect PL features often detect Raman peaks as well, there are several important differences between these two types of peaks. Photoluminescence emits from a material at a constant energy (or wavelength). For example, the NV^0 defect can, with NV^-, give diamond a pink to orangy pink bodycolor. It has principal absorption and emission at 575 nm, regardless of the nature or the wavelength of the excitation source. The absorption band and the luminescence band do not shift to different wavelengths simply because a different light source is used.

In contrast, the energy *difference* between the Raman peak and the excitation wavelength is constant. Consequently, the absolute energy of the scattered photons depends on the energy of the photons in the excitation source, and so the wavelength of a Raman peak is not constant and varies with the excitation source. In Raman spectroscopy, light interacts with the molecular vibrations, or phonons, of the material. This causes a change in frequency because the material reemits the absorbed light; the resulting peaks indicate the energy change caused by these vibrational (and sometimes rotational) energy levels.

Although this vibrational energy shift occurs in only one out of 10 million photons coming from the sample (Berry et al., 2017), the Raman peak is the dominant feature in most PL spectra of type IIa diamonds. This highlights the very low intensity of the luminescence peaks in type IIa diamonds and the need for very sensitive equipment to accurately measure the PL properties. On the other hand, chromium or iron impurities in corundum can hinder the collection of Raman spectra by producing PL bands that overlap with Raman peaks. Careful selection of laser wavelength is thus an important consideration during experimental design—for example, choosing a blue excitation wavelength to avoid overlap between Cr^{3+} and Raman bands in corundum (Nasdala et al., 2004, 2012; Zeug et al., 2017).

A Raman spectrum can identify a stone as diamond, but the PL spectrum provides additional information that an experienced analyst can interpret to determine if the diamond is natural, treated, or laboratory-grown. Both methods have an important place in gemology: Raman for identifying a material and PL for further evaluating the stone's history. Importantly, the diamond Raman line and the PL features appear in the same spectrum, originating from the same sample volume and dependent on similar laser power (Collins, 1992). This allows semiquantitative comparison of PL features corresponding to lattice defects in different spectra by ratioing the integrated intensity of the PL peak to the area of the diamond Raman line (though the values can still be affected by the presence of other point defects that compete for the laser excitation or quench the luminescence). This normalization procedure is helpful in comparing PL features between samples, after different treatments, or in comparing spatial variations across the gem. Normalization is especially important in cases of mapping rough materials where spatial variations may be obscured when surface topography creates variations in peak intensity.

Effect of Different Excitation Wavelengths of Lasers. Many lasers in the UV-Vis-NIR wavelength range are now necessary, as different laser wavelengths effectively activate different PL features. Common laser excitation wavelengths include 325, 355, 405, 455, 457, 488, 514, 532, 633, 785, and 830 nm for single-point spectroscopy and PL mapping, but any commercially available laser wavelength can be used for either if the necessary laser filters are available. The use of multiple laser wavelengths maximizes the number of PL peaks that can be detected, since certain peaks are more effectively excited by particular wavelengths. Furthermore, some peaks may be obscured at a specific excitation if stronger features occur at a similar wavelength (figure 5).

GEMOLOGICAL APPLICATIONS

Natural Diamond. Aside from nitrogen, boron, hydrogen, nickel, and silicon, few other elements are regularly incorporated into natural diamond due to the high atomic density and charge states of diamond. Nevertheless, this small set of diamond-compatible elements creates a wide range of optical transitions (e.g., Zaitsev, 2001; Ashfold et al., 2020; D'Haenens-Johannson et al., 2022).

All type II diamonds, either D-to-Z or fancy-color, now require low-temperature PL analysis to reliably verify them as natural, treated, or laboratory-grown.

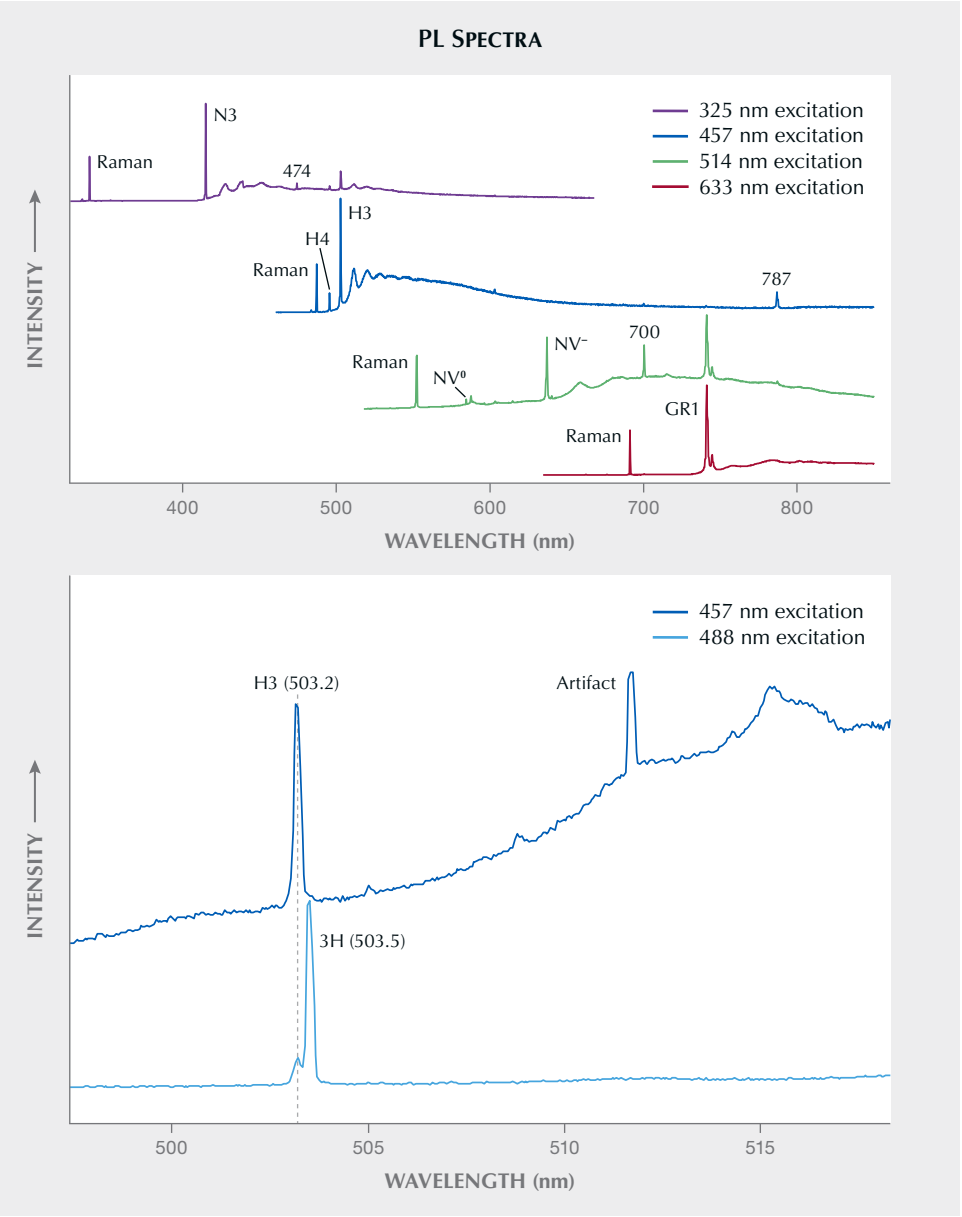

Figure 5. Top: PL spectra of a 1.16 ct Fancy green-gray natural diamond. Across the array of lasers, several peaks are more efficiently detected with one laser over another. For example, NV⁻ centers are best observed with 514 nm excitation, GR1 with 514 and 633 nm excitation, and H3 with 457 nm excitation. The N3 peak could only be detected with the 325 nm laser. Bottom: A 1.10 ct D-color natural diamond shows distinctive features even with lasers of slightly different wavelengths. The H3 peak at 503.2 nm is detected with 457 nm excitation, while the 488 nm laser can detect both the H3 and the 3H peak at 503.5 nm. Spectra are offset vertically for clarity, and the Raman peaks are scaled as equal.

All type IaB diamonds with low nitrogen also require low-temperature PL spectroscopy to distinguish natural color from treated color. For example, type IIa pink and type IIb blue natural diamonds are quite rare, with prices sometimes exceeding US$1 million per carat. The natural origin of such diamonds is almost always confirmed by their PL spectral characteristics.

PL spectroscopy has been useful in characterizing natural diamonds for a wide variety of fundamental research applications. For example, it helps characterize gems from specific geographic locations (Komarovskikh et al., 2020) and from unusual formations such as impact diamonds found in meteor craters (Yelisseyev et al., 2016). Another key application is characterizing PL features associated with optical centers such as boron (Lu et al., 2017), the 550 nm absorption band (Eaton-Magaña et al., 2020), and the 480 nm absorption band (Lai et al., 2024a).

Treatment Identification of Gem Diamond. *HPHT Treatment.* The origin of a diamond (whether mined from the earth or manufactured in a laboratory) and

its subsequent processing are significant factors in a diamond's value. HPHT treatment, regardless of its complexity, is generally quite short (lasting from minutes to hours). The time needed for defects to rearrange in a natural diamond while it resided in the earth at ~1050°–1250°C (Stachel and Luth, 2015) simply cannot be replicated in a laboratory. Therefore, higher treatment temperatures are used to compensate for the shorter time available compared with natural diamonds. These higher temperatures (1800°–2100°C at 5–6 GPa confining pressure) can also create PL features that are telltale signs of the treatment.

While many of the identifying features detected by PL spectroscopy go undisclosed due to proprietary concerns, some have been published. It has been widely reported (e.g., Fisher and Spits, 2000) that after HPHT treatment, the intensity of the PL peak at 637 nm (NV^-) is often stronger than its 514 nm laser-excited counterpart at 575 nm (NV^0). For most natural type II diamonds, this relationship is reversed (figure 6). Under the temperature conditions required to remove the brown color, HPHT treatment typically breaks down the nitrogen aggregates to form isolated nitrogen impurities that act as electron donors. The charge transfer of new electrons causes an increase in the PL intensity of the 637 nm defect compared to the 575 nm peak (Chalain et al., 2000); therefore, most HPHT-treated type IIa diamonds have an intensity ratio of $I_{637}/I_{575} > 1$. Some of the individual vacancies that make up the NV centers are also thought to be liberated from vacancy clusters decorating slip planes during the treatment.

Combined Processed Diamonds. The introduction of HPHT treatment in the late 1990s brought about treatments that combine HPHT annealing with subsequent treatments such as irradiation and lower-temperature annealing. This "stacking" of treatments, often with the intent to obscure earlier color treatment, can make identification more difficult and make the diamond appear more spectroscopically "natural." Multi-treatment processes can also be used to create certain attractive colors such as pink to red. Identifying treated diamonds often requires a combination of advanced testing techniques. It is increasingly important to consider the presence or absence of numerous PL features in addition to information from other spectroscopic and gemological techniques such as UV-Vis-NIR absorption, deep-UV fluorescence imaging, and microscopy. For many high-value diamonds, PL spectra are often the most important piece

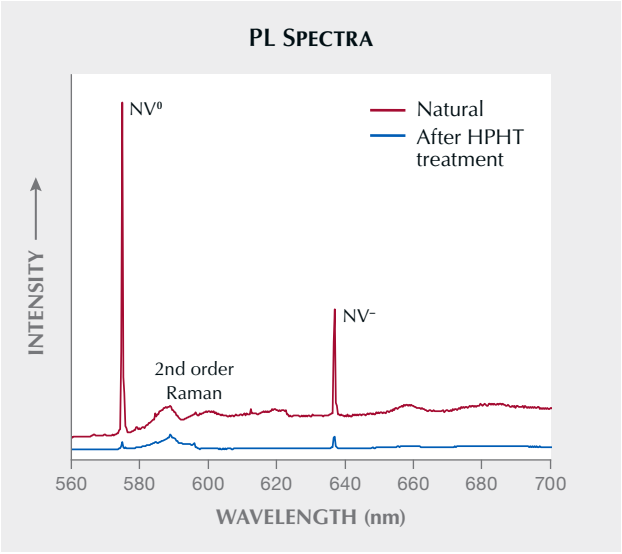

Figure 6. These two PL spectra with 514 nm excitation were collected before and after HPHT treatment of a type IIa diamond. The HPHT treatment caused a reduction in the NV intensities but also shifted the ratio of NV^-/NV^0 from values <1 to >1. The natural diamond weighed 3.07 ct with L color. After treatment, it weighed 3.04 ct with E color.

of evidence, but all tests and data must tell a consistent story. Therefore, gemologists cannot rely solely on a single property or technique. With complex treatments and the evolution of synthetic diamond growth techniques, the accurate assessment of color origin is best left to fully equipped gemological laboratories with knowledgeable, experienced staff.

Laboratory-Grown Diamonds. In recent years, gem-quality laboratory-grown diamonds produced by either chemical vapor deposition (CVD) or HPHT methods have become widely available on the market (Eaton-Magaña and Shigley, 2016; Eaton-Magaña et al., 2017). High-quality PL spectroscopy has proven useful for their identification (e.g., Wang et al., 2007, 2012; Song et al., 2012; D'Haenens-Johansson et al., 2022; Johnson et al., 2023). The rapid development of CVD synthesis techniques over the past two decades has made PL spectroscopy important for accurately verifying CVD origin and detecting post-growth annealing (Hardman et al., 2022b). Impurities rarely found in natural type II diamonds such as nickel (as the 883/885 nm doublet when measured at liquid nitrogen temperature) and silicon (as SiV^- with a 736.6/736.9 nm doublet when measured at liquid nitrogen temperature or as SiV^0 with a zero-phonon line [ZPL] at 946 nm) are often detected in

HPHT-grown and CVD-grown diamonds, respectively. Other PL features, such as the uncharacterized PL peak at 468 nm, are often detected in CVD-grown diamonds (e.g., Zaitsev et al., 2021).

Spinel. PL spectroscopy is most commonly used with diamond analysis, but it has important applications for other gemstones as well. For example, it can be very difficult to distinguish high-clarity natural and laboratory-grown spinel using standard gemological methods. However, synthetic spinel can be distinguished through PL analysis of chromium luminescence (Deeva and Shelementiev, 2002; Kitawaki and Okano, 2006). Natural spinel exhibits a strong ZPL at ~686 nm, along with several other narrow peaks, while their laboratory-grown counterparts show significantly broadened and shifted peaks.

Additionally, PL spectroscopy is helpful in identifying treatment. Sharp chromium peaks verify that the stone is natural and unheated, while heat treatment typically broadens and shifts the position of the PL peaks (Saeseaw et al., 2009; Kondo et al., 2010; Malsy et al., 2012; Liu et al., 2022; Wu et al., 2023).

Corundum. Research on photoluminescence in corundum has been driven by the physics and materials science communities, spurred by the use of corundum as laser crystals (ruby and titanium-doped sapphire). Studying PL in corundum is much more complex than in diamond due to the variety of potential trace element impurities and the difficulty of isolating and identifying the source of various PL bands. The most well-studied emission is Cr^{3+} in corundum, seen as a series of sharp peaks at 692.8 and 694.2 nm, called the R1 and R2 or "R-lines," short for "Raman lines." These are sometimes accompanied by sidebands called N-lines, short for "neighbor lines," in corundum with higher chromium concentrations (Guguschev et al., 2010). Cr^{3+} is very efficient at generating visible luminescence in corundum, even at chromium concentrations around a few ppma (Hughes et al., 2017). Due to the sensitivity of chromium luminescence and the potential for chromium concentrations to vary during the growth of a corundum crystal, PL mapping of the 694 nm luminescence band can reveal internal growth textures. Chromium luminescence is notably quenched by iron impurities (e.g., high-iron rubies with diminished fluorescence). Other trace element substitutions with absorption bands that overlap with either chromium luminescence wavelengths or the excitation wavelength may also affect the resulting luminescence (Yu and Clarke, 2002).

Other luminescence bands in natural corundum are less extensively characterized. The presence of Mn^{4+} can be seen as a sharp peak at ~678 nm, which increases in intensity with manganese content until an inflection and exponential decrease after 0.1 wt.% manganese (Ivakin et al., 2003). A broad band with a peak at 740 nm is thought to be due to Ti^{3+} luminescence (Mikhailik et al., 2005). But different titanium valence states have different luminescence signatures. When Ti^{4+} substitutes for a vacant Al^{3+}, interactions between Ti^{4+} and O^{2-} result in blue to chalky white luminescence. Lower concentrations of Ti^{4+} result in a blue band peaking around 415 nm that shifts to longer wavelengths and whiter luminescence as Ti^{4+} concentrations increase (Wong et al., 1995). This luminescence is rarely seen in natural sapphire because of other divalent trace elements that charge-balance Ti^{4+} (e.g., the Fe^{2+}-Ti^{4+} charge transfer that causes blue coloration in sapphire) and the overlapping charge-transfer band of Fe^{3+}, which is usually present in much greater concentrations compared to Ti^{4+} and is known to quench luminescence. Heat-treated sapphire usually shows blue to chalky white luminescence because the dissolution of rutile silk introduces excess Ti^{4+}, except in high-iron sapphire where Ti^{4+} pairs with iron rather than occurring as isolated Ti^{4+} that can pair with O^{2-} (Hughes et al., 2017). The prevalence of blue to chalky white luminescence in heat-treated corundum and its rarity in untreated corundum make this an important line of evidence for heat treatment. A lesser-studied luminescence band is orange or "apricot"-colored luminescence, likely caused by the combination of F-centers and divalent ions (e.g., Mg^{2+}) in sapphires with iron concentrations <1000 ppm (Vigier et al., 2024). Orange luminescence can occur in all colors of natural or synthetic sapphire and almost all beryllium-diffused corundum (Fritsch et al., 2011).

Pearls. After diamond, pearls are the gem most commonly analyzed using PL spectroscopy. PL features in pearls are generally attributed to organic compounds within the nacre composite material (Karampelas et al., 2007). This technique, especially using a 514 nm laser, makes it possible to distinguish naturally colored pearls from artificially colored pearls (e.g., Wang et al., 2006; Karampelas et al., 2011). This is true for both natural and cultured pearls, as the treatment creates notable differences

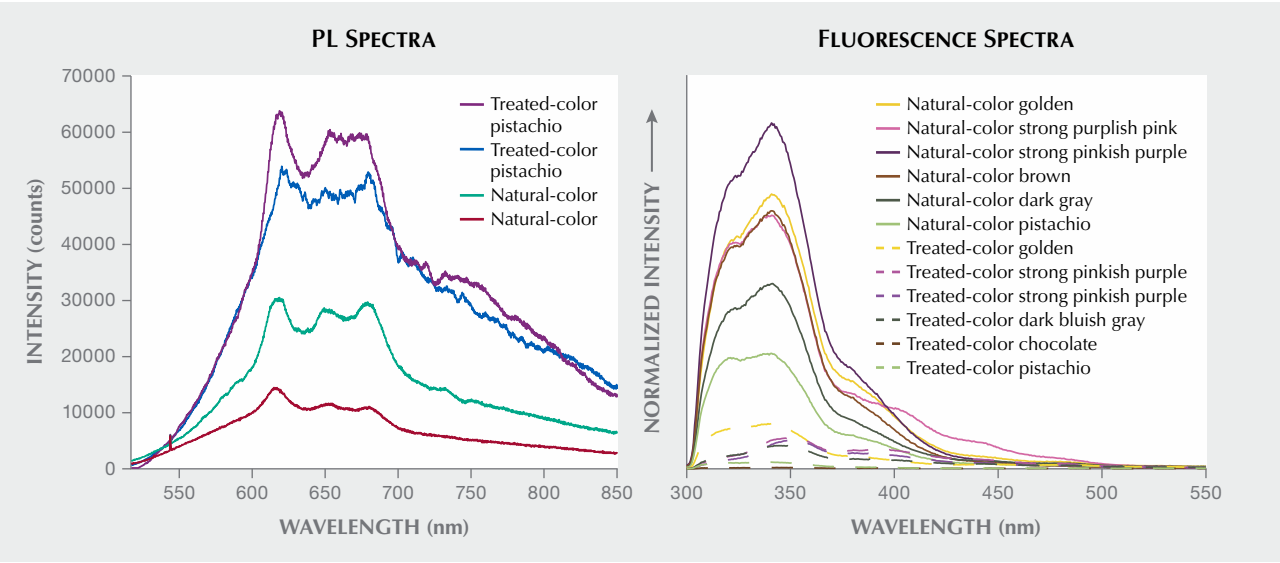

Figure 7. Left: PL spectra obtained for two color-treated "pistachio" pearls and two naturally colored specimens using 514 nm laser excitation. The characteristic feature at around 650 nm becomes less defined in the treated cultured pearls (Zhou et al., 2016). Right: Fluorescence spectra of naturally colored and color-treated pearls (Tsai and Zhou, 2020).

in PL spectra (e.g., figure 7; Zhou et al., 2016; Tsai and Zhou, 2020).

PL spectroscopy can also detect a series of bands positioned at 620, 650, and 680 nm, attributed to porphyrin pigments (Iwahashi and Akamatsu, 1994; Karampelas et al., 2020). These pigments are responsible for the natural gray to black tones in pearls produced by mollusk species such as *Pinctada margaritifera* and *Pteria* species. These bands are lacking in dark-colored pearls dyed with silver nitrate.

Treated "chocolate" and "pistachio" pearls from *P. margaritifera* have been modified from their original gray to dark gray color by a series of chemical and physical processes. These treated pearls retain some porphyrin characteristics in their PL spectra, but the features are less defined and show a higher overall fluorescence intensity (i.e., their F/A ratio). This ratio compares the highest fluorescence intensity in the 600–700 nm region to the main aragonite Raman peak at 545 nm or Raman shift of 1085 cm^{-1} (e.g., figure 7, left; Zhou et al., 2016). In a study on golden South Sea cultured pearls, the broadband fluorescence detected by PL spectroscopy (with a high F/A ratio) effectively separates naturally colored from dyed cultured pearls (Zhou et al., 2012).

Fluorescence spectroscopy using a long-wave UV (385 nm) light-emitting diode (LED) excitation provides a quick and effective method to detect optical whitening and brightening of pearls (Zhou et al., 2020). Short-wave UV (275 nm) LED excitation is used to measure fluorescence features attributed to the amino acid tryptophan within a pearl's nacre (Tsai and Zhou, 2021). Naturally colored and unprocessed pearls show fluorescence signals at least 2.5 times stronger in the UV region compared to treated or processed pearls (e.g., figure 7, right; Tsai and Zhou, 2020).

Other Gemstones. PL methods have benefited fundamental research and identification issues for a number of gems. Chromium-related PL has been useful for gemstones including topaz (Zeug et al., 2022), gahnite (Chen et al., 2024), and emerald. In particular, the position of the R1 line at ~684 nm due to chromium (Thompson et al., 2014, 2017; García-Toloza et al., 2019) is key to distinguishing various origins of emerald. In laboratory-grown emerald, this line is located at shorter wavelengths, and natural emeralds from a non-schist environment have an R1 line position that is comparable. Meanwhile, natural emeralds with schist origins have an R1 position at higher wavelengths (Thompson et al., 2014). This R1 line, particularly when combined with other gemological information, has also proven useful in geographic origin determination between several sources such as Colombia, Afghanistan, and Zambia (Thompson et al., 2017).

PL spectroscopy has been instrumental in detecting other defects measured in gemstones such as the iron-related emission in feldspar (Prasad and Jain, 2018) and irradiated kyanite (Nagabhushana et al., 2008). PL detection is also useful in zircon for detecting rare earth elements (REEs; Vuong et al., 2019) or measuring the transition of crystalline to metamict zircon due to irradiation damage (Lenz et al., 2020).

PL spectroscopy has also proven helpful in the characterization of some organic gems beyond pearls. Paired with Raman spectroscopy, the interpretation of PL spectra can distinguish natural red coral from dyed coral (Smith et al., 2007). PL spectroscopy can help distinguish tortoise shell from some of its imitators; however, the results can be ambiguous, and interpretation must be combined with other gemological techniques (Hainschwang and Leggio, 2006).

RECENT ADVANCEMENTS

PL Mapping. For decades, gemologists have been using Raman and PL spectroscopy to answer the questions "What is the gem?" and "What are the defects?" With the advent of PL mapping in the past decade, we have been able to answer another question: "Where are the defects?"

Raman and PL mapping, sometimes referred to as *hyperspectral imaging*, is a logical extension of the applications described above. These techniques enable spectra to be quickly and automatically collected from an area rather than from a single point (or having to manually move the sample to collect multiple spectra from it). Improvements in the necessary instrumentation, such as computer hardware for data processing, detector efficiencies, and higher-power excitation sources, have made this possible. Therefore, Raman and PL mapping have emerged as preferred methods for analyzing spatial differences. As the computerized microscope stage scans across a gem, thousands of spectra are rapidly collected. This allows gemologists and researchers to piece together a detailed picture showing the areas with high intensities (or concentrations) of optical features. The ability to collect Raman and PL data quickly and easily has permitted fundamental studies of spatial variations within a gem that were not possible just a few years earlier (e.g., Eaton-Magaña et al., 2021; Laidlaw et al., 2021; Lai et al., 2024a). The technique opens many opportunities to explore growth processes and different treatments, as well as wider applications such as determining geological provenance.

Natural growth processes can create pronounced spatial variations of defects across gemstones. For example, yellow to orange diamonds colored by the 480 nm band (Lai et al., 2024b) and pink diamonds colored by the 550 nm band (Eaton-Magaña et al., 2020) have pronounced spatial differences. PL mapping of these gems reveals the defects that correspond to the color zoning.

Corundum. When corundum crystals form at depth, concentrations of chromium and other trace elements vary throughout the crystal in response to geological conditions. These minute variations can be imaged and mapped using PL spectroscopy. The 694 nm luminescence band is related to chromium, with its intensity resulting from a complex interplay between chromium and other trace elements that quench (reduce) or sensitize (increase) the intensity of Cr^{3+} luminescence (Calvo del Castillo et al., 2009). The interactions between quenchers or sensitizers and chromium remain poorly understood due to the variety of trace element substitutions in natural corundum and the difficulty in interpreting their relationships. Complete characterization often requires growing specially doped synthetic corundum crystals to restrict the number of concurrent interactions, or it may involve complex calculations based on crystal field theory. Quantitative determinations of chromium and trace element concentrations in crystal domains require chemical analysis.

Regardless of the specifics of quenchers and sensitizers of chromium luminescence in corundum, PL mapping can be a useful technique for imaging differences in natural versus synthetic corundum, provided the chromium concentrations vary sufficiently within the synthetic crystal. While natural corundum may undergo chaotic and varied growth processes, synthetic corundum is grown under more predictable and consistent conditions that can form regular oscillatory bands or curved striations, often seen as curved color banding when viewed under the microscope with diffused light. If the curvature of these oscillatory bands is not clearly visible, it can be difficult to discriminate from natural corundum. Due to its growth mechanisms, natural corundum displays straight or angular oscillatory bands.

In natural corundum, PL mapping is an important tool for choosing locations of interest to analyze, as both sapphires and rubies can exhibit complex zonation and a range in chemistry through-

out the crystal (figure 8; Turnier, 2022). Zoning in natural corundum is more complex and varied than in synthetic corundum.

3D Mapping. Recent advances in technology and custom instruments have enabled the acquisition of high spectral and spatial resolution, large-volume three-dimensional measurements of gems (Jones et al., 2024a). While two-dimensional PL maps have demonstrated usefulness for a wide variety of gem applications (Eaton-Magaña et al., 2021; Laidlaw et al., 2021) and 2D depth profiling has also shown some promising applications (e.g., Lai et al., 2024b), those provide only a fraction of the available information about a gem. Full 3D spectroscopic imaging allows us to better understand a gemstone's growth history, distribution of defects, and the locations of inclusions. The speed of these systems is achieved through simultaneously collecting information along a line, as opposed to a point, which enables much more efficient 3D data collection.

High-resolution 3D PL mapping using a custom-built device at GIA has been successfully applied to natural and CVD-grown diamond. This technique has provided a wealth of information that was previously unattainable due to instrumentation issues or long collection times (Jones et al., 2024a). Shown in figure 9 are 2D PL images of a natural diamond, captured using 405 nm excitation. These false-color images contain a spectrum at each point, simplified to represent emission from three defects: N3 (blue), H3 (green), and plastic deformation–related features around 700 nm (red). Since data collection took place at room temperature, these spectra overlap. The relative concentrations vary across the sample, mixing to create colors such as yellow and orange, as shown in the core of figure 9A.

One of the challenges of PL mapping is how to best plot the results. Both samples in figure 9 are natural diamonds, cut in half and polished flat on one side. Sample A shows a colorless central region and a brown outer rim, with a different relative combi-

Figure 8. Representative false-color PL maps showing Cr^{3+}-related luminescence in corundum. A: A Cambodian sapphire from Pailin Province with diffuse zoning (yellow and green colors). B: A Thai sample from Kanchanaburi with oscillatory growth zoning that decreases sharply with chromium content toward the rim. C: An Australian sapphire from Inverell shows diffuse core-to-rim zoning (perceived ridges at the yellow-red boundary are due to larger step size during PL mapping, which may also be related to the green linear features down the crystal center). The overlaid circles show the location of oxygen isotope analyses targeting different growth domains in the sapphires (Turnier, 2022).

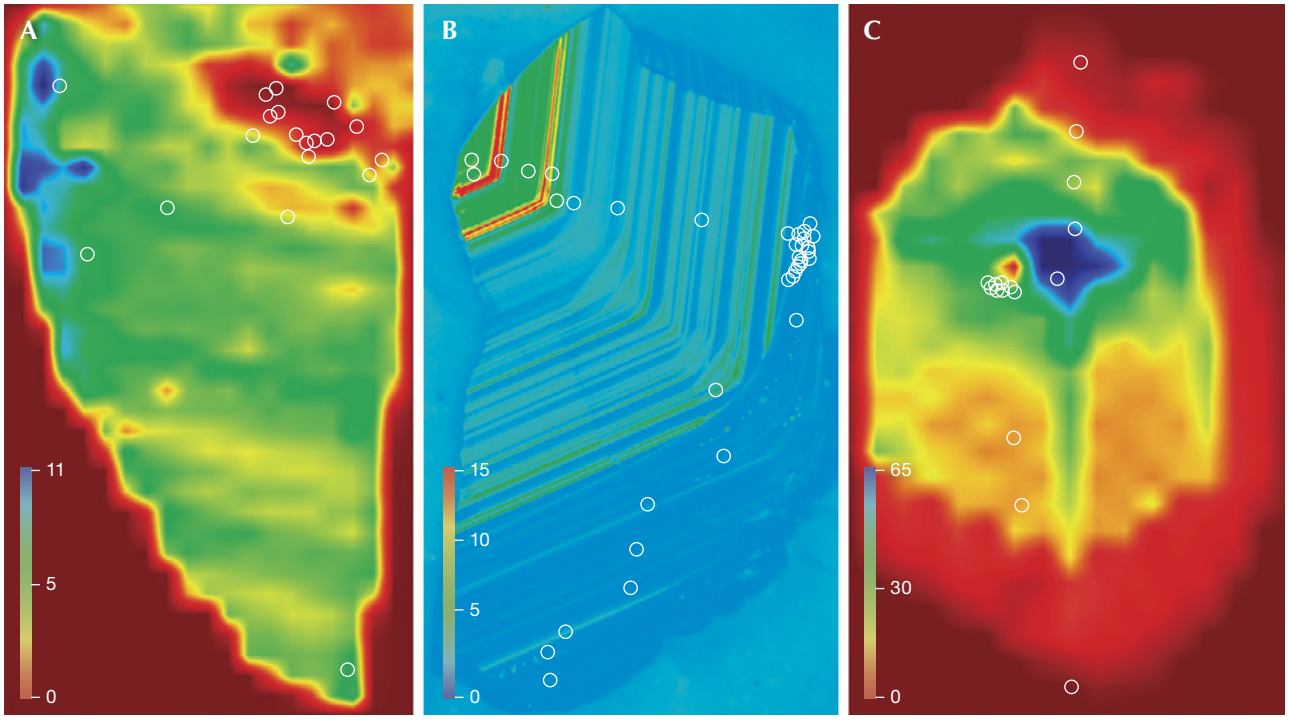

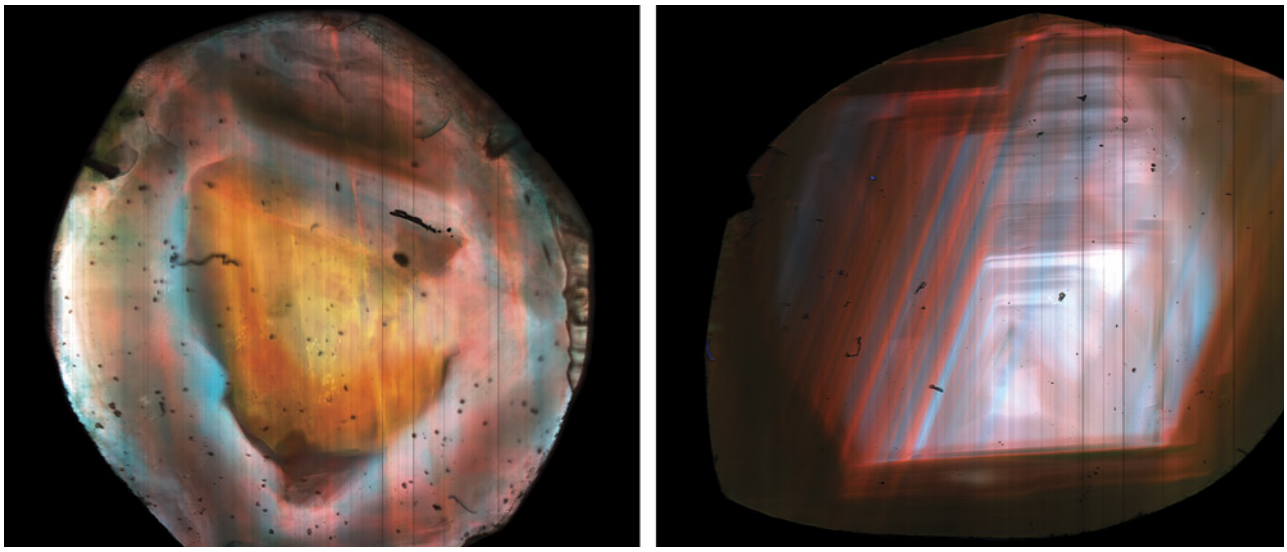

Figure 9. False-color images of two natural rough diamonds, cut in half with one polished face to show their internal growth structures. Broad sections of the spectra from each pixel were separated into blue (N3), green (H3), and red (plastic deformation–related luminescence at ~700 nm). Spectral overlap between features results in colors that represent combinations of defects. Sample A on the left is a natural diamond with two distinct growth phases: a colorless central core region and a brown-colored rim. Sample B on the right is a cross-section of natural diamond showing strong N3 emission with regions of higher H3 (appearing blue-green), with red lines representing plastic deformation throughout the growth structure. Both images are ~5.5 mm across and were acquired with a 4 × 0.16 NA objective lens using 405 nm excitation at room temperature. Images by Daniel Jones.

nation of the three defects. Sample B displays N3-related growth structure near the center of the stone, decreasing in intensity from core to rim. Both samples display plastic deformation–related emission in the red channel, which is sparser in A but follows the growth structure shown in B.

Figure 10 presents a subsect of sample A using a 10 × 0.4 NA (numerical aperture) objective lens, imaged in 3D. Figure 10A shows cross-sectional images of scans along the XY, YZ, and XZ planes. The pink, red, and white areas indicate that the diamond actually experienced three growth events. The plastic deformation–related red emission penetrates in straight lines through the sample from core to rim. The two images shown in figure 10 (B and C) represent the full 3D dataset, which can be freely rotated and scanned at any angle to reveal the internal growth structure. Figure 10B represents the unsliced dataset, while figure 10C shows the same view but with a diagonal slice of the internal structure. This technique can be applied to determining the orientation of samples by identifying features related to specific growth directions. This helps researchers determine growth history to better understand the incorporation of inclusions during natural growth.

Large Databases and Statistics. Gemological laboratories are uniquely positioned to identify large-scale spectral trends from thousands of gemstones. Statistical analysis has been used for PL spectral data and other gem-related applications, including trace element data (e.g., Zhang et al., 2019; Chankhantha et al., 2020). Full use of the information requires automatic software processing to identify and analyze the spectral peaks and incorporate them into a searchable database. Statistical analysis can include factors such as the presence or absence of particular peaks across all selected lasers, the peak areas normalized to the diamond Raman line, and the peak widths. The data can be cross-referenced against color, diamond type, or concluded origin. Developing robust peak-finding and peak-matching algorithms for rapid automatic processing of all collected spectra is nearly as important as the analysis itself. Large-scale spectral data mining also has the potential to reveal new patterns among detected PL features and uncover previously hidden trends and relationships. For example, Hardman et al. (2022a) examined PL spectral differences in more than 2,000 natural green diamonds, correlating the normalized peak intensities with the presence of green and brown radiation

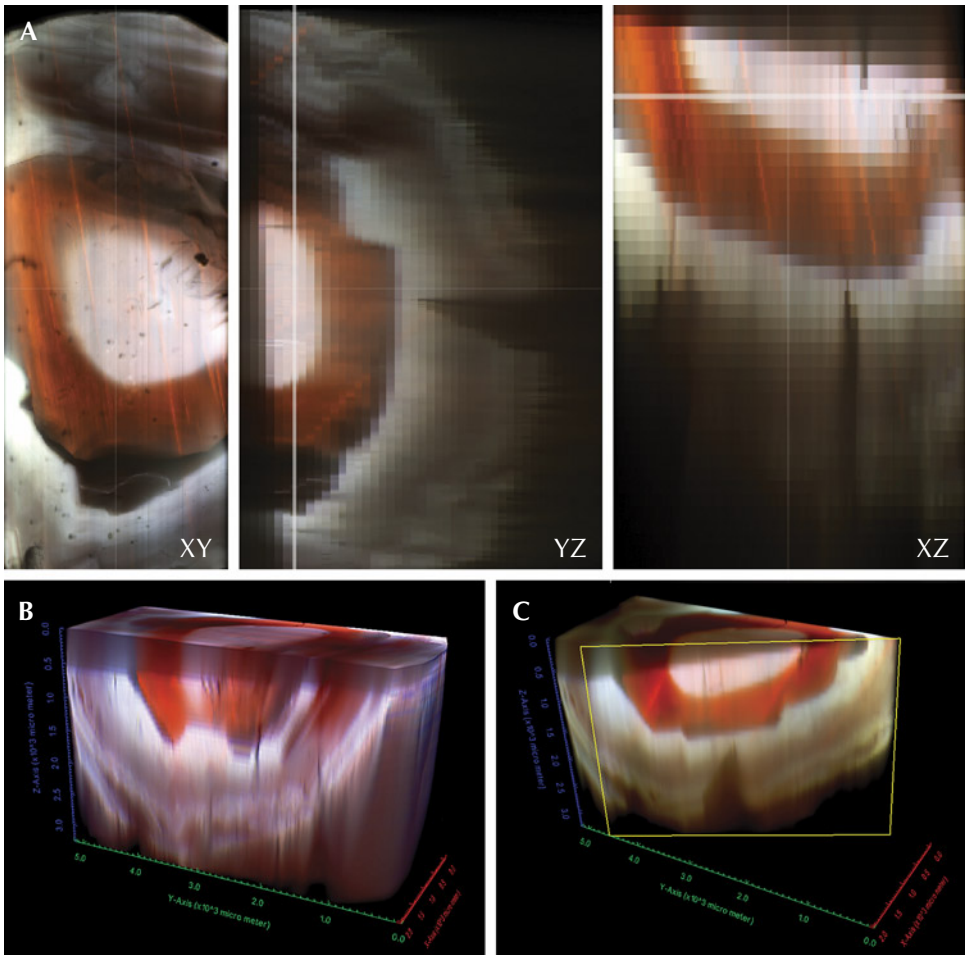

Figure 10. 3D representations of spectra for sample A from figure 9 (left), acquired with 405 nm excitation at room temperature. The spectra associated with each pixel were separated by wavelengths into blue (N3; ZPL = 415.2 nm), green (H3; ZPL = 503.2 nm), and red (plastic deformation–related luminescence at ~700 nm). A: These three images show XY, YZ, and XZ scans of the 3D data cube, indicating three growth events—a central core, another growth rim, and then an outer layer. B and C: Volumetric slices from the full 3D dataset, which can be selectively scanned and freely rotated. Image B is a visualization of the full dataset, while image C shows a diagonal slice through the dataset.

stains. Hardman et al. (2022b) examined the PL spectra of more than 11,000 CVD-grown diamonds to locate statistically significant peak differences between as-grown and HPHT-treated CVD-grown diamonds.

Although the specific details of datasets or computed models may be proprietary, the results can reveal previously unknown links between PL spectral features or between PL features and characteristics such as color or growth history (Hardman et al., 2024). However, machine learning and artificial intelligence methods should be seen as a tool to aid in research or gemological assessment. Statistical analysis should not be considered a replacement for expert judgment and experience that draws upon data from numerous tests and microscopic observations.

Time-Resolved Luminescence. Luminescence from defects does not occur instantaneously—it takes time for the electron to decay from the excited state back to the ground state, either emitting a photon of light or non-radiatively decaying. Broadly, we can consider two types of luminescence: fluorescence and phosphorescence. This is a slight simplification, as there are additional complexities. Fluorescence occurs on pico- and nanosecond timescales, making it very fast and difficult to measure. Phosphorescence generally occurs on longer timescales, milliseconds or longer, and can be caused by several mechanisms within gemstones. Phosphorescence has been measured extensively both for diamond and other colored stones (McGuinness et al., 2020; Zhang and Shen, 2023). The time-domain intensity graphs generated from lifetime data are referred to as a "decay."

Fluorescence is much more difficult to measure, but there are a few methods for measuring on these very fast timescales. Time-resolved luminescence, though not used regularly in gemstone analysis, has been implemented in a few applications (e.g., Liaugaudas et al., 2009, 2012; Monticone et al., 2013; Fisher, 2018; Dupuy and Phillips, 2019; Jones et al., 2019, 2021; McGuinness et al., 2020). The two techniques described here require the use of a pulsed laser, which

emits laser light in pulses less than ~1 nanosecond in duration. The "gold standard" is time-correlated single photon counting (TCSPC), which measures the arrival time of a single photon relative to the triggered pulses from the laser source. This method is slow, limited to a collection rate <5% of the repetition rate of the laser. The second method is time-gated measurement, where temporal gates are rapidly opened and closed to allow light from the emission to be detected. These gates are then moved through time in small increments to measure the full decay.

Data from these decays is typically modeled using an exponential decay model. Most single-defect species emit with a single lifetime, producing a monoexponential decay. When two or more defects overlap in the detection, or if quenching occurs, the decay will be more complex. In these cases, the different components can be fitted by a series of exponentials. Quenching occurs when energy is transferred from a donor defect to a nearby acceptor defect, reducing the emitting light and also the lifetime. A prime example is the interaction between N3 and A-center defects in diamond. The lifetime of N3 will decrease with increasing A-center concentrations, reducing the intensity of the light emitted from N3. This is an interesting mechanism because A-centers are best detected and quantified through IR absorption, which means it may be possible to use the lifetime of the N3 center to measure the concentration of A-centers.

Examining the decay curves of various defects can reveal significant differences between nominally similar gems such as natural and treated diamonds. Ongoing research is investigating the differences in the decay times of various color centers between natural, treated, and laboratory-grown stones to extend beyond standard PL measurements (e.g., Eaton-Magaña, 2015). Each defect has a different characteristic lifetime, which can be used to separate them, and collecting lifetime data per wavelength can reveal the spectra for overlapping components. Lifetime measurements with short timescales require more specialized lab equipment including fast detectors and electronics, pulsed lasers, and spectral blocking mechanisms such as spectrometers and filters. An alternative method for analyzing lifetime data comes from mathematical transformations of the decay data in a phasor plot. More detailed information on its application to gemstones can be found in Jones et al. (2021).

Figure 11 (left) shows data from a CVD-grown diamond containing NV^0 and NV^-, acquired through TCSPC using a 510 nm excitation source. The collected spectrum (generated from the sum of all photons in the decay) is shown in figure 11 (left), and this

Figure 11. A CVD-grown diamond containing both NV charge states was measured using TCSPC with 510 nm excitation, and the sample's luminescence decay was measured every 1 nm for the wavelength range of 540–780 nm (left). Right: Examples of the decays are shown, fitted with a double exponential decay function yielding decay times of 19 ns for NV^0 and 12 ns for NV^-.

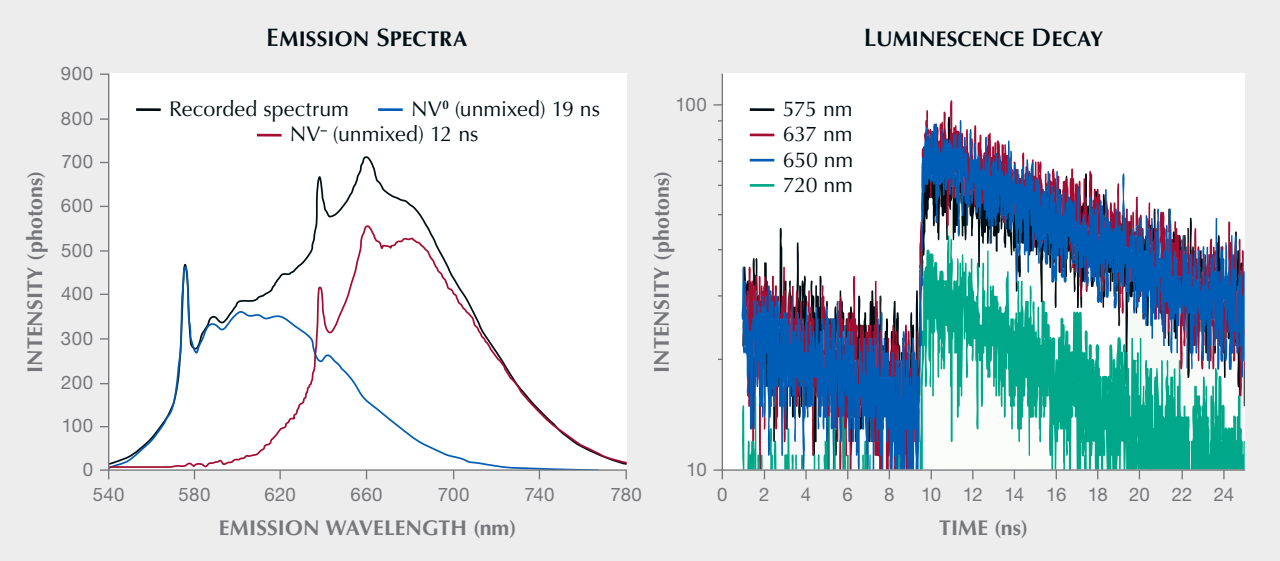

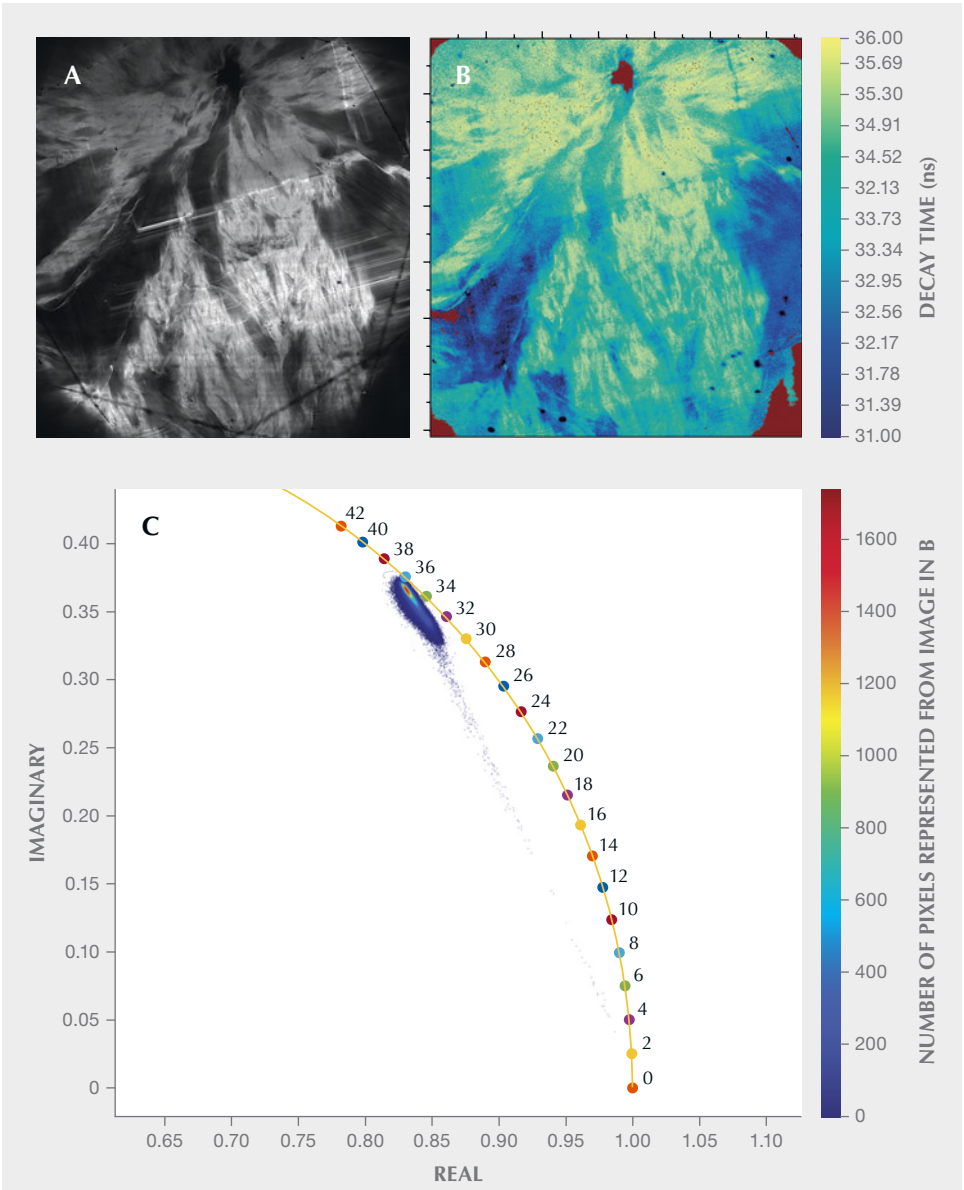

Figure 12. A: The summed intensity image of a natural brown diamond shows unusual cloud-like networks acquired from TCSPC lifetime data using 405 nm excitation. B: The same region of the sample is shown, but with the phase lifetime extracted through phasor analysis of the decays present at each pixel. C: A phasor plot of image B shows decay times (in nanoseconds along the circumference of a section of a circle, called the universal circle; see Jones et al., 2021). The color bar represents the pixels from image B located at that point in the histogram. The data is clustered near the 35 ns datapoint, indicating the predominant decay time.

represents something that can be acquired conventionally. Decays at four wavelengths are shown in figure 11 (right), displaying a subtle variation in the decay. By fitting a double exponential decay model with time constants of 12 and 19 ns, representing NV^- and NV^0, respectively, the two NV spectra can be unmixed from the recorded spectrum (shown in blue and red). This demonstrates that lifetime can be used to separate overlapping spectral features. The fitted lifetimes agree well with those determined on these two centers individually: 13 ± 0.5 ns for NV^0 (Collins et al., 1983a) and 19 ± 2 ns for NV^- (Liaugaudas et al., 2012).

Factors affecting emission are the impurities' valence state, structure, charge, and the appearance of other impurities (Gaft and Panczer, 2013). Previous studies on diamond have shown that the decay time can be reduced by quenching, in which energy transfers to other impurities. This can create several distinct observed lifetimes for an optical center. For example, the intrinsic lifetime of NV^0 (ZPL at 575.0 nm) in high-purity, low-nitrogen samples is given as 19 ± 2 ns (Liaugaudas et al., 2012). However, quenching of the single substitutional nitrogen (N_S^0) can shorten the NV^0 lifetime (Monticone et al., 2013). Therefore, HPHT treatment of diamond can help

shorten the decay time of NV^0 centers by increasing the concentration of N_S^0 (although other factors can complicate the analysis). While many diamond-related defects have been shown to have short decay times on nanosecond timescales, some researchers have shown that other defects yet to be characterized exist for a longer duration, from microseconds to milliseconds, and can also be useful for gemstone identification (Eaton-Magaña et al., 2008; Fisher, 2018).

As mentioned above, PL mapping involves collecting thousands of spectra across a sample's surface. The same can be accomplished for lifetime data in a method called fluorescence lifetime imaging microscopy (FLIM). Lifetime images are shown in figure 12 for a diamond and in figure 13 for a sapphire and emerald. These maps take longer to acquire than PL maps due to the large number of photons needed for a good data fit, which is necessary for accurate lifetime measurement. It is also highly beneficial to detect light only over a narrow, well-selected wavelength range for measuring the lifetime of a single emitter.

The authors measured the N3 lifetime of a natural faceted diamond using 405 nm excitation with 5 µm pixels. The intensity image shown in figure 12A reveals a network of filaments in a cloud-like structure, extending from a core near the top of the image, with bright lines crossing through filaments that resemble standard growth structure. The lifetime map in figure 12B shows a scale from 36 to 31 ns (where the natural lifetime of N3 is reported to be 41 ns; Thomaz and Davies, 1978), which could indicate the presence of A-centers. This map shows that the lower-intensity regions have a shorter lifetime, and the phasor plot in figure 12C indicates that most of the pixels are clustered around 35 ns. Lifetime measurements are very sensitive to weak emission, and even a low concentration of a very different lifetime component can show contrast.

While diamond is often the focus of research on luminescence decay times, studies have also been conducted on other gemstones. Naturally irradiated fluorite exhibits red photoluminescence at 750 and 635 nm with decay times of 20.3 and <5 ns, respec-

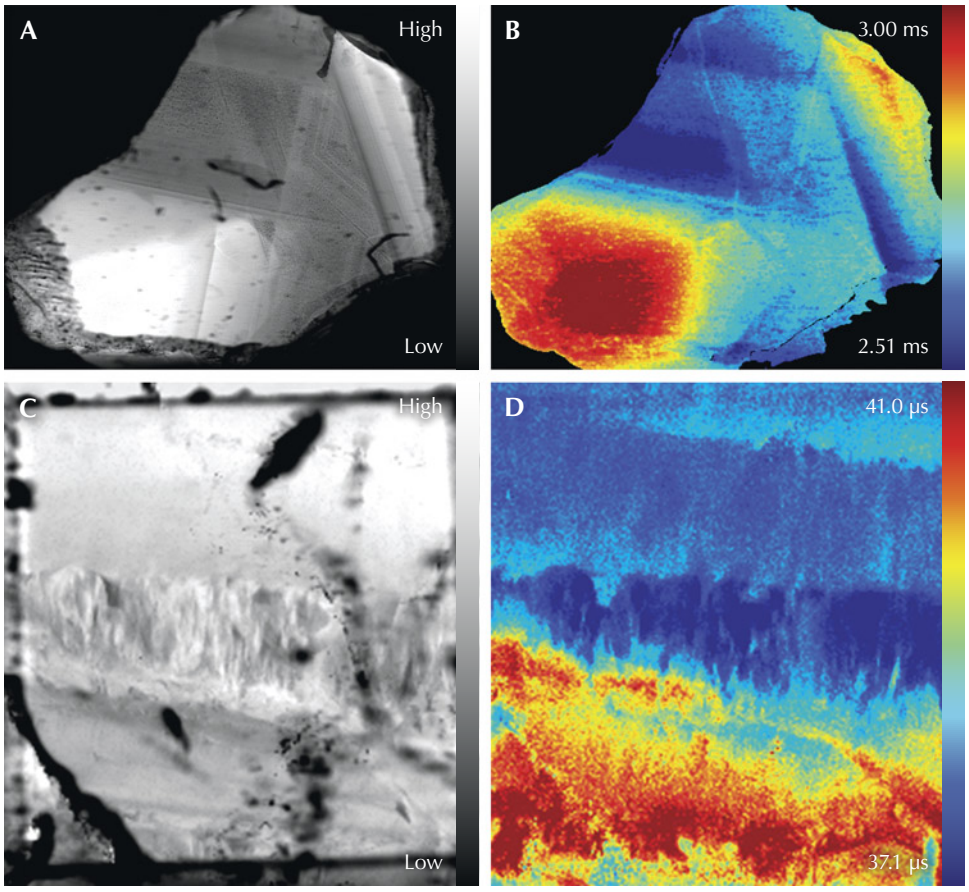

Figure 13. Images A and B show a natural blue sapphire plate measured with TCSPC using 405 nm excitation and detecting the emission band of Cr^{3+}, where A shows the summed intensity and B the weighted mean lifetime. Growth structure is apparent in both images. C and D show a faceted untreated emerald measured using 405 nm excitation with emission centered at 684 nm, where C shows the summed intensity and D the weighted mean lifetime. The summed intensity map is heavily affected by the inclusions and cracks in the sample, but the lifetime map is resistant to these features, revealing various growth structures. Fields of view 6.5 mm (A) and 3.1 mm (C).

tively (Gaft et al., 2020). The photoluminescence features of spinel and alexandrite, with lifetimes on the microsecond timescale, can be more readily detected and chronicled than defects with nanosecond lifetimes. Xu et al. (2023) determined the lifetime for the chromium peak at 685–687 nm as 9–23 µs in spinel and 25–53 µs in alexandrite. Although there was some overlap in lifetimes, the researchers were able to distinguish natural, treated, and laboratory-grown spinel, as well as natural and laboratory-grown alexandrite.

One of the more widely studied lifetimes in gemstones other than diamond is that of Cr^{3+}. In the past, this was because of its viability for a laser gain medium, where lifetime is an important factor, such as ruby. The natural lifetime of Cr^{3+} is 3.43 ms, though this can be reduced by various other defects (Seat and Sharp, 2004; Jones et al., 2024b). Figure 13 (A and B) shows a natural blue sapphire plate measured with TCSPC using 405 nm excitation. The emission was centered on the double Cr^{3+} peaks at 692.8 (R1) and 694.2 nm (R2), and the summed intensity image in figure 13A indicates growth structure. The lifetime map in figure 13B shows very different lifetimes over the sample, indicating the presence of different unknown quenching species.

An untreated faceted emerald was also measured using 405 nm excitation, with an emission band centered at 684 nm. The literature (e.g., Xu et al., 2023) suggests that this is Cr^{3+}, but it possesses a much shorter decay time than chromium in corundum. While the intensity map in figure 13C shows many cracks and inclusions, the lifetime map in figure 13D clearly shows growth structure, with a small variation in lifetime. The clarity of the features shown in the lifetime map contrasts with the large changes in intensity caused by cracks and inclusions, demonstrating one of the advantages of lifetime measurements over intensity maps: their resistance to these types of clarity features.

Time-resolved luminescence has proven useful in resolving PL bands that overlap with very intense luminescence from Cr^{3+}, which has a long decay time of 3.43 ms (Chandler et al., 2006), as well as other PL bands that typically have much shorter lifetimes compared to chromium luminescence.

CONCLUSIONS

As a nondestructive tool, PL spectroscopy is vital in many ways: identifying gemstones, evaluating the origin of their color, and occasionally providing clues about their geographic origin. As treatments become more prevalent and sophisticated, gemologists must look for increasingly subtle clues to distinguish nat-

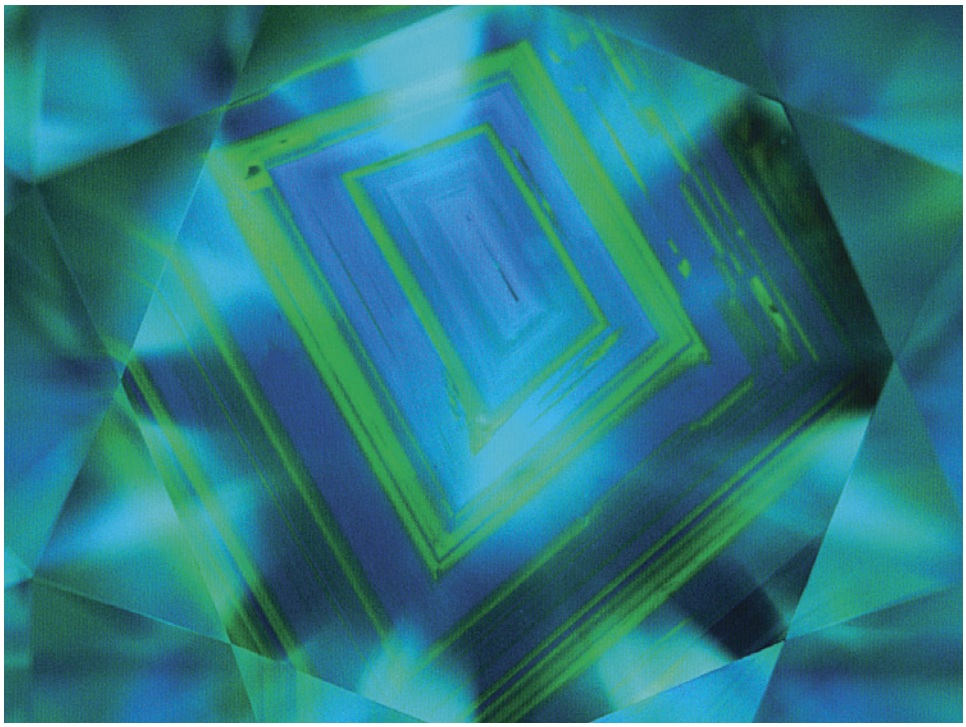

Figure 14. Natural type Ia diamonds often show a growth pattern that has been compared to the growth rings of a tree. However, it is not as common to see the alternating pattern of blue fluorescence (due to the N3 center) and green (due to H3/H4 centers) shown in this 1.83 ct K-color diamond with SI_2 clarity. PL spectroscopy is very useful for confirming these centers and for detecting much weaker optical centers. Image by GIA staff.

ural from laboratory-grown gemstones and untreated from treated gemstones. Therefore, many gemstones are subjected to several types of spectroscopy to reveal histories hidden in defects that occur in very low concentrations.

In recent decades, as the use of PL spectroscopy has become more common in gemological research laboratories, PL analysis itself has become more sophisticated. Every gem, whether natural, laboratory-grown, or treated in some manner, has its own story (e.g., figure 14), and every consumer can learn their gem's story through proper identification. Over the past 25 years, PL analysis has become a powerful, highly sensitive research tool leading to many recent discoveries about diamond and other gemstones, revealing subtle distinctions that can significantly affect commercial value. This helps to ensure public confidence in the gem and jewelry industry.

ABOUT THE AUTHORS

Dr. Sally Eaton-Magaña is senior manager of diamond identification, Dr. Rachelle Turnier is GIA Museum manager, and Dr. Christopher M. Breeding is senior manager of analytics, at GIA in Carlsbad, California. Dr. Daniel Jones is a research scientist at GIA in New Jersey.

ACKNOWLEDGMENTS

The authors would like to thank Andy Shen for his help in collecting the photoluminescence spectra shown in figure 4, which were collected while he was at GIA, and Artitaya Homkrajae (GIA, Carlsbad) for her very helpful suggestions. We also express our gratitude to Adrian Chan (GIA, New Jersey) for cutting and polishing the two natural diamond samples and Aaron Palke (GIA, Carlsbad) for providing the sapphire and emerald plates. We sincerely thank Paul French, Chris Dunsby, Daan Arroo, and Neil Alford (Imperial College London) for providing the sample and equipment for the lifetime measurements of the NV-containing CVD diamond.

REFERENCES

Ashfold M.N.R., Goss J.P., Green B.L., May P.W., Newton M.E., Peaker C.V. (2020) Nitrogen in diamond. *Chemical Reviews*, Vol. 120, No. 12, pp. 5745–5794, http://dx.doi.org/10.1021/acs.chemrev.9b00518

Bakhtin A.I., Denisov I.G., Lopatin O.N. (1995) Photoluminescence of hole centers in olivine crystals. *Optics and Spectroscopy*, Vol. 79, No. 5, pp. 773–777.

Berry R.F., Danyushevsky L.V., Goemann K., Parbhakar-Fox A., Rodemann T. (2017) Micro-analytical technologies for mineral mapping and trace element deportment. In B.G. Lottermoser, Ed., *Environmental Indicators in Metal Mining*, Springer, Switzerland, pp. 55–72.

Bersani D., Lottici P.P. (2010) Applications of Raman spectroscopy to gemology. *Analytical and Bioanalytical Chemistry*. Vol. 397, No. 7, pp. 2631–2646, http://dx.doi.org/10.1007/s00216-010-3700-1

Breeding C.M., Shen A.H., Eaton-Magaña S., Rossman G.R., Shigley J.E., Gilbertson A. (2010) Developments in gemstone analysis techniques and instrumentation during the 2000s. *G&G*, Vol. 46, No. 3, pp. 241–257, http://dx.doi.org/10.5741/GEMS.46.3.241

Calderon T., Millan A., Jaque F., Solé J.G. (1990) Optical properties of Sm^{2+} and Eu^{2+} in natural fluorite crystals. *International Journal of Radiation Applications and Instrumentation. Part D. Nuclear Tracks and Radiation Measurements*, Vol. 17, No. 4, pp. 557–561, http://dx.doi.org/10.1016/1359-0189(90)90016-Q

Calderon T., Khanlary M.-R., Rendell H.M., Townsend P.D. (1992) Luminescence from natural fluorite crystals. *International Journal of Radiation Applications and Instrumentation. Part D. Nuclear Tracks and Radiation Measurements*, Vol. 20, No. 3, pp. 475–485, http://dx.doi.org/10.1016/1359-0189(92)90033-R

Calvo del Castillo H., Deprez N., Dupuis T., Mathis F., Deneckere A., Vandenabeele P., Calderón T., Strivay D. (2009) Towards the differentiation of non-treated and treated corundum minerals by ion-beam-induced luminescence and other complementary techniques. *Analytical and Bioanalytical Chemistry*, Vol. 394, No. 4, pp. 1043–1058, http://dx.doi.org/10.1007/s00216-009-2679-y

Chalain J.-P., Fritsch E., Hänni H.A. (2000) Identification of GE POL diamonds: A second step. *Journal of Gemmology*, Vol. 27, No. 2, pp. 73–78.

Chandler D.E., Majumdar Z.K., Heiss G.J., Clegg R.M. (2006) Ruby crystal for demonstrating time- and frequency-domain methods of fluorescence lifetime measurements. *Journal of Fluorescence*, Vol. 16, No. 6, pp. 793–807, http://dx.doi.org/10.1007/s10895-006-0123-7

Chankhantha C., Amphon R., Rehman H.U., Shen A.H. (2020) Characterisation of pink-to-red spinel from four important localities. *Journal of Gemmology*, Vol. 37, No. 4, pp. 393–403.

Chen Y., Zheng J., Lu M., Liu Z., Zhou Z. (2024) Gemological and spectral characteristics of gem-quality blue gahnite from Nigeria. *Journal of Spectroscopy*, article no. 6693346, http://dx.doi.org/10.1155/2024/6693346

Clark C.D., Norris C.A. (1971) Photoluminescence associated with the 1.673, 1.944 and 2.498 eV centres in diamond. *Journal of Physics C: Solid State Physics*, Vol. 4, No. 14, pp. 2223–2229, http://dx.doi.org/10.1088/0022-3719/4/14/036

Collins A.T. (1992) The characterisation of point defects in diamond by luminescence spectroscopy. *Diamond and Related Materials*, Vol. 1, No. 5-6, pp. 457–469, http://dx.doi.org/10.1016/0925-9635(92)90146-F

Collins A.T., Thomaz M.F., Jorge M.I.B. (1983a) Luminescence decay time of the 1.945 eV centre in type Ib diamond. *Journal of Physics C: Solid State Physics*, Vol. 16, No. 11, pp. 2177–2181, http://dx.doi.org/10.1088/0022-3719/16/11/020

Collins A.T., Thomaz M.F., Jorge M.I.B. (1983b) Excitation and decay of H4 luminescence in diamond. *Journal of Physics C:*

Solid State Physics, Vol. 16, No. 28, pp. 5417–5425, http://dx.doi.org/10.1088/0022-3719/16/28/009
Culka A., Hyršl J., Jehlička J. (2016) Gem and mineral identification using GL gem Raman and comparison with other portable instruments. *Applied Physics A*, Vol. 122, No. 11, article no. 959, http://dx.doi.org/10.1007/s00339-016-0500-2
Deeva V.A., Shelementiev Y.B. (2002) Gemological properties of synthetic flux spinel. *Gemmological Bulletin*, No. 6, pp. 9–17.
D'Haenens-Johansson U.F.S., Butler J.E., Katrusha A.N. (2022) Synthesis of diamonds and their identification. *Reviews in Mineralogy and Geochemistry*, Vol. 88, No. 1, pp. 689–753, http://dx.doi.org/10.2138/rmg.2022.88.13
Dupuy H., Phillips J.C. (2019) Selecting a diamond verification instrument based on the results of the Assure Program: An initial analysis. *Journal of Gemmology*, Vol. 36, No. 7, pp. 606–619.
Eaton-Magaña S. (2015) Comparison of luminescence lifetimes from natural and laboratory irradiated diamonds. *Diamond and Related Materials*, Vol. 58, pp. 94–102, http://dx.doi.org/10.1016/j.diamond.2015.06.007
Eaton-Magaña S., Ardon T. (2016) Temperature effects on luminescence centers in natural type IIb diamonds. *Diamond and Related Materials*, Vol. 69, pp. 86–95, http://dx.doi.org/10.1016/j.diamond.2016.07.002
Eaton-Magaña S., Breeding C.M. (2016) An introduction to photoluminescence spectroscopy for diamond and its application in gemology. *G&G*, Vol. 52, No. 1, pp. 2–17, http://dx.doi.org/10.5741/GEMS.52.1.2
Eaton-Magaña S.C, Shigley J.E. (2016) Observations on CVD-grown synthetic diamonds: A review. *G&G*, Vol. 52, No. 3, pp. 222–245, http://dx.doi.org/10.5741/GEMS.52.3.222
Eaton-Magaña S., Post J.E., Heaney P.J., Freitas J., Klein P., Walters R., Butler J.E. (2008) Using phosphorescence as a fingerprint for the Hope and other blue diamonds. *Geology*, Vol. 36, No. 1, pp. 83–86, http://dx.doi.org/10.1130/G24170A.1
Eaton-Magaña S.C., Shigley J.E., Breeding C.M. (2017) Observations on HPHT-grown synthetic diamonds: A review. *G&G*, Vol. 53, No. 3, pp. 262–284, http://dx.doi.org/10.5741/GEMS.53.3.262
Eaton-Magaña S., McElhenny G., Breeding C.M., Ardon T. (2020) Comparison of gemological and spectroscopic features in type IIa and Ia natural pink diamonds. *Diamond and Related Materials*, Vol. 105, article no. 107784, http://dx.doi.org/10.1016/j.diamond.2020.107784
Eaton-Magaña S., Breeding C.M., Palke A.C., Homkrajae A., Sun Z., McElhenny G. (2021) Raman and photoluminescence mapping of gem materials. *Minerals*, Vol. 11, No. 2, article no. 177, http://dx.doi.org/10.3390/min11020177
Fiquet G., Richet P., Montagnac G. (1999) High-temperature thermal expansion of lime, periclase, corundum and spinel. *Physics and Chemistry of Minerals*, Vol. 27, pp. 103–111, http://dx.doi.org/10.1007/s002690050246
Fisher D. (2018) Addressing the challenges of detecting synthetic diamonds. *G&G*, Vol. 54, No. 3, pp. 263–264.
Fisher D., Spits R.A. (2000) Spectroscopic evidence of GE POL HPHT-treated natural type IIa diamonds. *G&G*, Vol. 36, No. 1, pp. 42–49, http://dx.doi.org/10.5741/GEMS.36.1.42
Freitas J.A. Jr., Klein P.B., Collins A.T. (1994) Evidence of donor–acceptor pair recombination from a new emission band in semiconducting diamond. *Applied Physics Letters*, Vol. 64, No. 16, pp. 2136–2138, http://dx.doi.org/10.1063/1.111710
Fritsch E., Massuyeau F., Rondeau B., Segura O., Hainschwang T. (2011) Advancing the understanding of luminescence in gem materials. *G&G*, Vol 47, No. 2, p. 123.
Gaft M., Panczer G. (2013) Laser-induced time-resolved luminescence spectroscopy of minerals: A powerful tool for studying the nature of emission centres. *Mineralogy and Petrology*, Vol. 107, No. 3, pp. 363–372, http://dx.doi.org/10.1007/s00710-013-0293-3
Gaft M., Reisfeld R., Panczer G. (2015) *Modern Luminescence Spectroscopy of Minerals and Materials*. Springer International Publishing, Berlin, 606 pp.
Gaft M., Waychunas G.A., Rossman G.R., Nagli L., Panczer G., Cheskis D., Raichlin Y. (2020) Red photoluminescence and purple color of naturally irradiated fluorite. *Physics and Chemistry of Minerals*, Vol. 47, No. 11, article no. 46, http://dx.doi.org/10.1007/s00269-020-01116-4
García-Toloza J., Herreño-Daza M.J., González-Durán A.F., Cedeño-Ochoa C.J., Angarita-Sarmiento L.G. (2019) Photoluminescence analysis to determine the origin of emeralds from the Eastern and Western belts in Colombia. *In Proceedings of the 15th Biennial Meeting SGA, Glasgow, Scotland*, Vol. 2, pp. 931–934.
Glynn T.J., Imbusch G.F., Walker G. (1991) Luminescence from Cr^{3+} centres in forsterite (Mg_2SiO_4). *Journal of Luminescence*, Vol. 48-49, pp. 541–544, http://dx.doi.org/10.1016/0022-2313(91)90188-2
Green B. (2013) Optical and magnetic resonance studies of point defects in single crystal diamond. PhD thesis, University of Warwick, UK.
Green B.L., Collins A.T., Breeding C.M. (2022) Diamond spectroscopy, defect centers, color, and treatments. *Reviews in Mineralogy and Geochemistry*, Vol. 88, No. 1, pp. 637–688, http://dx.doi.org/10.2138/rmg.2022.88.12
Groat L.A., Giuliani G., Stone-Sundberg J., Sun Z., Renfro N.D., Palke A.C. (2019) A review of analytical methods used in geographic origin determination of gemstones. *G&G*, Vol. 55, No. 4, pp. 512–535, http://dx.doi.org/10.5741/GEMS.55.4.512
Guguschev C., Götze J., Göbbels M. (2010) Cathodoluminescence microscopy and spectroscopy of synthetic ruby crystals grown by the optical floating zone technique. *American Mineralogist*, Vol. 95, No. 4, pp. 449–455, http://dx.doi.org/10.2138/am.2010.3291
Hainschwang T., Leggio L. (2006) The characterization of tortoise shell and its imitations. *G&G*, Vol. 42, No. 1, pp. 36–52, http://dx.doi.org/10.5741/GEMS.42.1.36
Hainschwang T., Fritsch E., Gaillou E., Shen A. (2024) Analysing the luminescence of gems. *Elements*, Vol. 20, No. 5, pp. 312–317, http://dx.doi.org/10.2138/gselements.20.5.312
Hardman M.F., Eaton-Magaña S., Breeding C.M., Bassoo R. (2022a) Evaluating the effects of natural radiation exposure on green diamonds. Presented at the 2022 Goldschmidt Conference, Honolulu, http://dx.doi.org/10.46427/gold2022.13133
Hardman M.F., Eaton-Magaña S.C., Breeding C.M., Ardon T., D'Haenens-Johansson U.F.S. (2022b) Evaluating the defects in CVD diamonds: A statistical approach to spectroscopy. *Diamond and Related Materials*, Vol. 130, article no. 109508, http://dx.doi.org/10.1016/j.diamond.2022.109508
Hardman M.F., Homkrajae A., Eaton-Magaña S., Breeding C.M., Palke A.C., Sun Z. (2024) Classification of gem materials using machine learning. *G&G*, Vol. 60, No. 3, pp. 306–329, http://dx.doi.org/10.5741/GEMS.60.3.306
Hughes R.W., Manorotkul W., Hughes E.B. (2017) *Ruby & Sapphire: A Gemologist's Guide*. RWH Publishing, Bangkok, 733 pp.
Iakoubovskii K., Adriaenssens G.J., Vohra Y.K. (2001) Nitrogen incorporation in CVD diamond. *Diamond and Related Materials*, Vol. 10, No. 3-7, pp. 485–489, http://dx.doi.org/10.1016/S0925-9635(00)00436-2
Ivakin U.D., Danchevskaya M.N., Muravieva G.P., Ovchinnikova O.G. (2003) Physiochemical properties of corundum doped in supercritical water. *High Pressure Science and Technology*, Joint 19th AIRAPT and 41st EHPRG Conference, Bordeaux.
Iwahashi Y., Akamatsu S. (1994) Porphyrin pigment in black-lip pearls and its application to pearl identification. *Fisheries Science*, Vol. 60, No. 1, pp. 69–71, http://dx.doi.org/10.2331/fishsci.60.69
Jin S., Smith E.M. (2024) Raman spectroscopy and X-ray diffraction in gemology: Identifying mineral species and other phases. *G&G*, Vol. 60, No. 4, pp. 518–535, http://dx.doi.org/10.5741/GEMS.60.4.518

Johnson P., Moe K.S., Persaud S., Odake S., Kazuchits N.M., Zaitsev A.M. (2023) Spectroscopic characterization of yellow *gem* quality CVD diamond. *Diamond and Related Materials*, Vol. 140, article no. 110505, http://dx.doi.org/10.1016/j.diamond.2023.110505

Jones D.C., Kumar S., Lanigan P.M.P., McGuinness C.D., Dale M.W., Twitchen D.J., Fisher D., Martineau P.M., Neil M.A.A., Dunsby C., French P.M.W. (2019) Multidimensional luminescence microscope for imaging defect colour centres in diamond. *Methods and Applications in Fluorescence*, Vol. 8, No. 1, article no. 014004, http://dx.doi.org/10.1088/2050-6120/ab4eac

Jones D.C., Alexandrov Y., Curry N., Kumar S., Lanigan P.M.P., McGuinness C.D., Dale M.W., Twitchen D.J., Fisher D., Neil M.A.A., Dunsby C., French P.M.W. (2021) Multidimensional spectroscopy and imaging of defects in synthetic diamond: Excitation-emission-lifetime luminescence measurements with multiexponential fitting and phasor analysis. *Journal of Physics D: Applied Physics*, Vol. 54, No. 4, article no. 045303, http://dx.doi.org/10.1088/1361-6463/abbde2

Jones D.C., Jollands M.C., D'Haenens-Johansson U.F.S., Muchnikov A.B., Tsai T.H. (2024a) Development of a large volume line scanning, high spectral range and resolution 3D hyperspectral photoluminescence imaging microscope for diamond and other high refractive index materials. *Optics Express*, Vol. 32, No. 9, pp. 15231–15242, http://dx.doi.org/10.1364/OE.516046

Jones D.C., Jollands M.C., Jin S., Stewart-Barry S.S., Dale M.W., Green B.L. (2024b) Resolving and imaging ultra-low H concentrations in partially protonated Mg:α Al_2O_3 using FRET and the luminescence lifetime of Cr^{3+}. *Journal of Materials Chemistry C*, Vol. 12, No. 39, pp. 16004–16014, http://dx.doi.org/10.1039/D4TC02646B

Karampelas S., Fritsch E., Mevellec J.-Y., Gauthier J.-P., Sklavounos S., Soldatos T. (2007) Determination by Raman scattering of the nature of pigments in cultured freshwater pearls from the mollusk *Hyriopsis cumingi*. *Journal of Raman Spectroscopy*, Vol. 38, No. 2, pp. 217–230, http://dx.doi.org/10.1002/jrs.1626

Karampelas S., Fritsch E., Hainschwang T., Gauthier J.-P. (2011) Spectral differentiation of natural-color saltwater cultured pearls from *Pinctada margaritifera* and *Pteria sterna*. *G&G*, Vol. 47, No. 2, p. 117.

Karampelas S., Fritsch E., Makhlooq F., Mohamed F., Al-Alawi A. (2020) Raman spectroscopy of natural and cultured pearls and pearl producing mollusc shells. *Journal of Raman Spectroscopy*, Vol. 51, No. 9, pp. 1813–1821, http://dx.doi.org/10.1002/jrs.5670

Kiefert L., Karampelas S. (2011) Use of the Raman spectrometer in gemmological laboratories: Review. *Spectrochimica Acta Part A: Molecular and Biomolecular Spectroscopy*, Vol. 80, No. 1, pp. 119–124, http://dx.doi.org/10.1016/j.saa.2011.03.004

Kitawaki H., Okano M. (2006) Spinel up to date. GAAJ Research Lab Report, https://grjapan.ddo.jp/gaaj_report/2006/2006_03-01en.html

Komarovskikh A., Rakhmanova M., Yuryeva O., Nadolinny V. (2020) Infrared, photoluminescence, and electron paramagnetic resonance characteristic features of diamonds from the Aikhal pipe (Yakutia). *Diamond and Related Materials*, Vol. 109, article no. 108045, http://dx.doi.org/10.1016/j.diamond.2020.108045

Kondo D., Befi R., Beaton D. (2010) Lab Notes: Heat-treated spinel. *G&G*, Vol. 46, No. 2, pp. 145–146.

Lai M.Y., Breeding C.M., Stachel T., Stern R.A. (2020) Spectroscopic features of natural and HPHT-treated yellow diamonds. *Diamond and Related Materials*, Vol. 101, article no. 107642, http://dx.doi.org/10.1016/j.diamond.2019.107642

Lai M.Y., Hardman M.F., Eaton-Magaña S., Breeding C.M., Schwartz V.A., Collins A.T. (2024a) Spectroscopic characterization of diamonds colored by the 480 nm absorption band. *Diamond and Related Materials*, Vol. 142, article no. 110825, http://dx.doi.org/10.1016/j.diamond.2024.110825

Lai M.Y., Myagkaya E., Hardman M.F., Eaton-Magaña S., Breeding C.M., Sohrabi S., Collins A.T. (2024b) Spectroscopic characterization of rare natural pink diamonds with yellow color zones. *Diamond and Related Materials*, Vol. 148, article no. 111428, http://dx.doi.org/10.1016/j.diamond.2024.111428

Laidlaw F.H.J., Diggle P.L., Breeze B.G., Dale M.W., Fisher D., Beanland R. (2021) Spatial distribution of defects in a plastically deformed natural brown diamond. *Diamond and Related Materials*, Vol. 117, article no. 108465, http://dx.doi.org/10.1016/j.diamond.2021.108465

Lenz C., Belousova E., Lumpkin G.R. (2020) The in-situ quantification of structural radiation damage in zircon using laser-induced confocal photoluminescence spectroscopy. *Minerals*, Vol. 10, No. 1, article no. 83, http://dx.doi.org/10.3390/min10010083

Liaugaudas G., Collins A.T., Suhling K., Davies G., Heintzmann R. (2009) Luminescence-lifetime mapping in diamond. *Journal of Physics: Condensed Matter*, Vol. 21, No. 36, article no. 364210, http://dx.doi.org/10.1088/0953-8984/21/36/364210

Liaugaudas G., Davies G., Suhling K., Khan R.U.A., Evans D.J.F. (2012) Luminescence lifetimes of neutral nitrogen-vacancy centres in synthetic diamond containing nitrogen. *Journal of Physics: Condensed Matter*, Vol. 24, No. 43, article no. 435503, http://dx.doi.org/10.1088/0953-8984/24/43/435503

Lim H., Park S., Cheong H., Choi H.-M., Kim Y.C. (2010) Discrimination between natural and HPHT-treated type IIa diamonds using photoluminescence spectroscopy. *Diamond and Related Materials*, Vol. 19, No. 10, pp. 1254–1258, http://dx.doi.org/10.1016/j.diamond.2010.06.007

Liu Y., Qi L., Schwarz D., Zhou Z. (2022) Color mechanism and spectroscopic thermal variation of pink spinel reportedly from Kuh-i-lal, Tajikistan. *G&G*, Vol. 58, No. 3, pp. 338–353, http://dx.doi.org/10.5741/GEMS.58.3.338

Loudin L.C. (2017) Photoluminescence mapping of optical defects in HPHT synthetic diamond. *G&G*, Vol. 53, No. 2, pp. 180–188, http://dx.doi.org/10.5741/GEMS.53.2.180

Lu H.C., Peng Y.C., Lin M.Y., Chou S.L., Lo J.I., Cheng B.M. (2017) Analysis of boron in diamond with UV photoluminescence. *Carbon*, Vol. 111, pp. 835–838, http://dx.doi.org/10.1016/j.carbon.2016.10.082

Malsy A.-K., Karampelas S., Schwarz D., Klemm L., Armbruster T., Tuan D.A. (2012) Orangey-red to orangey-pink gem spinels from a new deposit at Lang Chap (Tan Huong-Truc Lau), Vietnam. *Journal of Gemmology*, Vol. 33, No. 1-4, pp. 19–27.

Martineau P.M., McGuinness C.D. (2018) De Beers consumer confidence technical research and diamond verification instruments. In *Diamonds–Source to Use Conference* pp. 35–43, https://www.saimm.co.za/Conferences/Diamonds2018/035-Martineau.pdf

McGuinness C.D., Wassell A.M., Lanigan P.M.P., Lynch S.A. (2020) Separation of natural from laboratory-grown diamond using time-gated luminescence imaging. *G&G*, Vol. 56, No. 2, pp. 220–229, http://dx.doi.org/10.5741/GEMS.56.2.220

Mikhailik V.B., Kraus H., Wahl D., Mykhaylyk M.S. (2005) Luminescence studies of Ti-doped Al_2O_3 using vacuum ultraviolet synchrotron radiation. *Applied Physics Letters*, Vol. 86, No. 10, article no. 101909, http://dx.doi.org/10.1063/1.1880451

Monticone D.G., Quercioli F., Mercatelli R., Soria S., Borini S., Poli T., Vannoni M., Vittone E. Olivero P. (2013) Systematic study of defect-related quenching of NV luminescence in diamond with time-correlated single-photon counting spectroscopy. *Physical Review B*, Vol. 88, No. 15, article no. 155201, http://dx.doi.org/10.1103/PhysRevB.88.155201

Nagabhushana H., Prashantha S.C., Lakshminarasappa B.N., Singh F. (2008) Ionoluminescence and photoluminescence studies of Ag^{8+} ion irradiated kyanite. *Journal of Luminescence*, Vol. 128, No. 1, pp. 7–10, http://dx.doi.org/10.1016/j.jlumin.2007.04.010

Nasdala L., Götze J., Hanchar J.M., Gaft M., Krbetschek R. (2004) Luminescence techniques in earth sciences. In A. Beran and E. Libowitzky, Eds., *Spectroscopic Methods in Mineralogy*. European Mineralogical Union, Vol. 6, pp. 43–92.

Nasdala L., Beyssac O., Schopf W., Bleisteiner B. (2012) Application of Raman-based images in the earth sciences. In A. Zoubir, Ed.,

Raman Imaging—Techniques and Applications. Springer Series in Optical Sciences, No. 168, Springer-Verlag, Berlin and Heidelberg, pp. 145–187.
Nichols E.L., Howes H.L., Wilber D.T. (1918) The photoluminescence and kathodo-luminescence of calcite. *Physical Review*, Vol. 12, No. 5, pp. 351–367, http://dx.doi.org/10.1103/PhysRev.12.351
Noguchi N., Abduriyim A., Shimizu I., Kamegata N., Odake S., Kagi H. (2013) Imaging of internal stress around a mineral inclusion in a sapphire crystal: Application of micro-Raman and photoluminescence spectroscopy. *Journal of Raman Spectroscopy*, Vol. 44, No. 1, pp. 147–154, http://dx.doi.org/10.1002/jrs.4161
O'Donnell K.P., Marshall A., Yamaga M., Henderson B., Cockayne B. (1989) Vibronic structure in the photoluminescence spectrum of Cr^{3+} ions in garnets. *Journal of Luminescence*, Vol. 42, No. 6, pp. 365–373, http://dx.doi.org/10.1016/0022-2313(89)90081-1
Pegasus Overseas Limited, Lazare Kaplan International, General Electric Company—press release (1999) Diamonds.net, March 25.
Prasad A.K., Jain M. (2018) Dynamics of the deep red Fe^{3+} photoluminescence emission in feldspar. *Journal of Luminescence*, Vol. 196, pp. 462–469, http://dx.doi.org/10.1016/j.jlumin.2017.11.051
Read P.G. (2008) *Gemmology*, 3rd ed. Elsevier Butterworth-Heinemann, Oxford, UK.
Saeseaw S., Wang W., Scarratt K., Emmett J.L., Douthit T.R. (2009) Distinguishing heated spinels from unheated natural spinels and from synthetic spinels. *GIA Research News*, http://www.gia.edu/gia-news-research-NR32209A
Seat H.C., Sharp J.H. (2004) Dedicated temperature sensing with c-axis oriented single-crystal ruby (Cr^{3+}: Al_2O_3) fibers: Temperature and strain dependences of R-line fluorescence. *IEEE Transactions on Instrumentation and Measurement*, Vol. 53, No. 1, pp. 140–154, http://dx.doi.org/10.1109/TIM.2003.822010
Shigley J., Moses T., McClure S., Van Dael M. (1999) GIA reports on GE POL diamonds. *Rapaport Diamond Report*, Vol. 22, No. 36, pp. 1, 11, 14, 18.
Shinno I. (1987) Color and photo-luminescence of rare earth element-doped zircon. *Mineralogical Journal*, Vol. 13, No. 5, pp. 239–253, http://dx.doi.org/10.2465/minerj.13.239
Simpson C.T., Imaino W., Becker W.M. (1980) Photoluminescence, optical absorption, and excitation spectra of cinnabar (α-HgS). *Physical Review B*, Vol. 22, No. 2, pp. 911–920, http://dx.doi.org/10.1103/PhysRevB.22.911
Smith C.P., Bosshart G., Ponahlo J., Hammer V M., Klapper H., Schmetzer K. (2000) GE POL diamonds: Before and after. *G&G*, Vol. 36, No. 3, pp. 192–215, http://dx.doi.org/10.5741/GEMS.36.3.192
Smith C.P., McClure S.F., Eaton-Magaña S., Kondo D.M. (2007) Pink-to-red coral: A guide to determining origin of color. *G&G*, Vol. 43, No. 1, pp. 4–15, http://dx.doi.org/10.5741/GEMS.43.1.4
Smith E.M., Krebs M.Y., Genzel P.T., Brenker F.E. (2022) Raman identification of inclusions in diamond. *Reviews in Mineralogy and Geochemistry*, Vol. 88, pp. 451–473, http://dx.doi.org/10.2138/rmg.2022.88.08
Solin S.A. (1972) Photoluminescence of natural type I and type IIb diamonds. *Physics Letters A*, Vol. 38, No. 2, pp. 101–102, http://dx.doi.org/10.1016/0375-9601(72)90506-3
Song Z., Lu T., Lan Y., Shen M., Ke J., Liu J., Zhang Y. (2012) The identification features of undisclosed loose and mounted CVD synthetic diamonds which have appeared recently in the NGTC laboratory. *Journal of Gemmology*, Vol. 33, No. 1-4, pp. 45–48.
Stachel T., Luth R.W. (2015) Diamond formation—Where, when and how? *Lithos*, Vol. 220-223, pp. 200–220, http://dx.doi.org/10.1016/j.lithos.2015.01.028
Thomaz M.F., Davies G. (1978) The decay time of N3 luminescence in natural diamond. *Proceedings of the Royal Society A*, Vol. 362, No. 1710, pp. 405–419, http://dx.doi.org/10.1098/rspa.1978.0141
Thompson D.B., Kidd J.D., Åström M., Scarani A., Smith C.P. (2014) A comparison of R-line photoluminescence of emeralds from different origins. *Journal of Gemmology*, Vol. 34, No. 4, pp. 334–343.
Thompson D.B., Bayens C.J., Morgan M.B., Myrick T.J., Sims N.E. (2017) Photoluminescence spectra of emeralds from Colombia, Afghanistan, and Zambia. *G&G*, Vol. 53, No. 3, pp. 296–311, http://dx.doi.org/10.5741/GEMS.53.3.296
Tsai T.-H. (2023) Imaging-assisted Raman and photoluminescence spectroscopy for diamond jewelry identification and evaluation. *Applied Optics*, Vol. 62, No. 10, pp. 2587–2594, http://dx.doi.org/10.1364/AO.484366
Tsai T.-H., D'Haenens-Johansson U.F.S. (2021) Rapid gemstone screening and identification using fluorescence spectroscopy. *Applied Optics*, Vol. 60, No. 12, pp. 3412–3421, http://dx.doi.org/10.1364/AO.419885
Tsai T.-H., Takahashi H. (2022) Automatic jewelry identification and evaluation based on imaging-assisted Raman spectroscopy. In C.F. Hahlweg and J.R. Mulley, Eds., *Novel Optical Systems, Methods, and Applications XXV*. SPIE, Bellingham, Washington, pp. 49–57.
Tsai T.-H., Zhou C. (2020) Lab Notes: Fluorescence spectroscopy for colored pearl treatment screening. *G&G*, Vol. 56, No. 1, pp. 136–137.
——— (2021) Rapid detection of color-treated pearls and separation of pearl types using fluorescence analysis. *Applied Optics*, Vol. 60, No. 20, pp. 5837–5845, http://dx.doi.org/10.1364/AO.427203
Turnier R.B. (2022) Views on corundum genesis from zircon inclusions, SIMS oxygen isotope analyses, geochronology, trace elements, and spectroscopy. PhD thesis, University of Wisconsin-Madison.
Vigier M., Massuyeau F., Fritsch E. (2024) Orange luminescence of α-Al_2O_3 related to clusters consisting of F centers and divalent cations. *Luminescence*, Vol. 39, No. 5, article no. e4757, http://dx.doi.org/10.1002/bio.4757
Vuong B.T.S., Osanai Y., Lenz C., Nakano N., Adachi T., Belousova E., Kitano I. (2019) Gem-quality zircon megacrysts from placer deposits in the central highlands, Vietnam—Potential source and links to Cenozoic alkali basalts. *Minerals*, Vol. 9, No. 2, article no. 89, http://dx.doi.org/10.3390/min9020089
Walker J. (1977) An optical study of the TR12 and 3H defects in irradiated diamond. *Journal of Physics C: Solid State Physics*, Vol. 10, No. 16, pp. 3031–3037, http://dx.doi.org/10.1088/0022-3719/10/16/013
Wang W., Scarratt K., Hyatt A., Shen A.H.-T., Hall M. (2006) Identification of "chocolate pearls" treated by Ballerina Pearl Co. *G&G*, Vol. 42, No. 4, pp. 222–235, http://dx.doi.org/10.5741/GEMS.42.4.222
Wang W., Hall M.S., Moe K.S., Tower J., Moses T.M. (2007) Latest-generation CVD-grown synthetic diamonds from Apollo Diamond Inc. *G&G*, Vol. 43, No. 4, pp. 294–312, http://dx.doi.org/10.5741/GEMS.43.4.294
Wang W., D'Haenens-Johansson U.F.S., Johnson P., Moe K.S., Emerson E., Newton M.E., Moses T.M. (2012) CVD synthetic diamonds from Gemesis Corp. *G&G*, Vol. 48, No. 2, pp. 80–97, http://dx.doi.org/10.5741/GEMS.48.2.80
Wang Z., Tsai T.-H., Wang W. (2023) Excimer laser based photoluminescence device for diamond identification. In *Novel Optical Systems, Methods, and Applications XXVI*, Vol. 12665. SPIE, pp. 118–122, http://dx.doi.org/10.1117/12.2672542
Waychunas G.A. (2014) Luminescence spectroscopy. In G.S. Henderson et al., *Reviews in Mineralogy and Geochemistry*, Vol. 78. Mineralogical Society of America, Chantilly, Virginia, pp. 175–211.
Wong W.C., McClure D.S., Basun S.A., Kokta M.R. (1995) Charge-exchange processes in titanium-doped sapphire crystals. I. Charge-exchange energies and titanium-bound excitations. *Physical Review B*, Vol. 51, No. 9, pp. 5682–5698, http://dx.doi.org/10.1103/PhysRevB.51.5682
Wotherspoon A., Steeds J.W., Catmull B., Butler J. (2003) Photolu-

minescence and positron annihilation measurements of nitrogen doped CVD diamond. *Diamond and Related Materials*, Vol. 12, pp. 652–657, http://dx.doi.org/10.1016/S0925-9635(02)00229-7

Wu J., Sun X., Ma H., Ning P., Tang N., Ding T., Li H., Zhang T., Ma Y. (2023) Purple-violet gem spinel from Tanzania and Myanmar: Inclusion, spectroscopy, chemistry, and color. *Minerals*, Vol. 13, No. 2, article no. 226, http://dx.doi.org/10.3390/min13020226

Xu W., Tsai T.-H., Palke A. (2023) Study of 405 nm laser-induced time-resolved photoluminescence spectroscopy on spinel and alexandrite. *Minerals*, Vol. 13, No. 3, article no. 419, http://dx.doi.org/10.3390/min13030419

Yelisseyev A.P., Khrenov A.Y., Afanasiev V.P. (2016) Photoluminescence spectra of impact diamonds formed by solid-state graphite-to-diamond transition. *Journal of the Optical Society of America B*, Vol. 33, No. 3, pp. B43–B48, http://dx.doi.org/10.1364/JOSAB.33.000B43

Yu H., Clarke D.R. (2002) Effect of codoping on the R-line luminescence of Cr^{3+}-doped alumina. *Journal of the American Ceramic Society*, Vol. 85, No. 8, pp. 1966–1970, http://dx.doi.org/10.1111/j.1151-2916.2002.tb00389.x

Zaitsev A.M. (2001) *Optical Properties of Diamond: A Data Handbook*. Springer-Verlag, Berlin.

Zaitsev A.M., Kazuchits N.M., Moe K.S., Butler J.E., Korolik O.V., Rusetsky M.S., Kazuchits V.N. (2021) Luminescence of brown CVD diamond: 468 nm luminescence center. *Diamond and Related Materials*, Vol. 113, article no. 108255, http://dx.doi.org/10.1016/j.diamond.2021.108255

Zeug M., Vargas A.I.R., Nasdala L. (2017) Spectroscopic study of inclusions in gem corundum from Mercaderes, Cauca, Colombia. *Physics and Chemistry of Minerals*, Vol. 44, No. 3, pp. 221–233, http://dx.doi.org/10.1007/s00269-016-0851-4

Zeug M., Nasdala L., Chutimun C.N., Hauzenberger C. (2022) Gem topaz from the Schneckenstein Crag, Saxony, Germany: Mineralogical characterization and luminescence. *G&G*, Vol. 58, No. 1, pp. 2–17, http://dx.doi.org/10.5741/GEMS.58.1.2

Zhang Z., Ye M., Shen A.H. (2019) Characterisation of peridot from China's Jilin Province and from North Korea. *Journal of Gemmology*, Vol. 36, No. 5, pp. 436–446.

Zhang Z., Shen A. (2023) Fluorescence and phosphorescence spectroscopies and their applications in gem characterization. *Minerals*, Vol. 13, No. 5, article no. 626, http://dx.doi.org/10.3390/min13050626

Zhou C., Homkrajae A., Ho J.W.Y., Hyatt A., Sturman N. (2012) Update on the identification of dye treatment in yellow or "golden" cultured pearls. *G&G*, Vol. 48, No. 4, pp. 284–291, http://dx.doi.org/10.5741/GEMS.48.4.284

Zhou C., Ho J.W.Y., Chan S., Zhou J.Y., Wong S.D., Moe K.S. (2016) Identification of "pistachio" colored pearls treated by Ballerina Pearl Co. *G&G*, Vol. 52, No. 1, pp. 50–59, http://dx.doi.org/10.5741/GEMS.52.1.50

Zhou C., Tsai T.-H., Sturman N., Nilpetploy N., Manustrong A., Lawanwong K. (2020) Optical whitening and brightening of pearls: A fluorescence spectroscopy study. *G&G*, Vol. 56, No. 2, pp. 258–265, http://dx.doi.org/10.5741/GEMS.56.2.258

Raman Spectroscopy and X-Ray Diffraction: Phase Identification of Gem Minerals and Other Species

Shiyun Jin and Evan M. Smith

One of the fundamental tasks in a modern gemological laboratory is identifying the species of a gemstone. Laboratories apply many different approaches, from routine methods used for almost every gemstone to more advanced techniques on a case-by-case basis. While standard gemological testing can accurately identify the most common gemstone species, additional testing is often required for unusual or rare stones. Two advanced analytical tools for phase identification are reviewed in this article: Raman spectroscopy and X-ray diffraction. Both methods harness photon scattering to characterize the atomic-scale structures of materials. Raman spectroscopy relies on inelastic light scattering from crystal lattice or molecular vibrations. X-ray diffraction relies on constructive interference of X-rays "reflected" from regularly spaced atomic layers of a crystal lattice. In addition to identifying mineral species, these techniques can capture information about composition, degree of crystallinity, strain, and other factors that affect a material's structure. The applications of these techniques are summarized first, followed by technical details regarding the underlying physics and instrumentation.

While testing or grading a gemstone, the first and perhaps most critical step is gem identification. Gem species are primarily defined as the mineral species that the gems belong to, which can be further divided into different gem varieties based on colors and phenomena. A mineral species is defined by both its chemical composition and specific crystal structure, which means chemical analysis techniques alone (e.g., X-ray fluorescence, electron probe microanalysis, and mass spectrometry) may be insufficient for a conclusive species identification. Furthermore, light elements such as carbon, beryllium, lithium, and hydrogen may be difficult to detect and analyze using common chemical analysis methods, leading to an uncertain chemical formula for the tested material. Techniques that can characterize the crystal structure of a solid material may therefore be necessary.

For colored stones, gemological laboratories mainly see ruby, sapphire, and emerald—the most popular gemstones. The vast majority of well-known gems can be accurately identified using standard gemological testing, including measurements of refractive index (RI) and specific gravity. Sometimes, however, a laboratory encounters unusual or rare gemstone species that require advanced analytical techniques. One of the most important categories of analytical techniques is spectroscopy, which characterizes how a solid responds to electromagnetic radiation of various wavelengths. Most spectroscopic

In Brief

- Gem species identification is the first test in a gemological laboratory.
- Raman spectroscopy and X-ray diffraction are two methods that can identify the atomic structure of materials.
- Raman spectra are easy to collect but occasionally ambiguous to interpret.
- XRD is not as convenient as Raman spectroscopy but can be more conclusive in identifying crystalline solids.

See end of article for About the Authors and Acknowledgments.
Gems & Gemology, Vol. 60, No. 4, pp. 518–535,
http://dx.doi.org/10.5741/GEMS.60.4.518

methods analyze either absorption or emission spectra, which reflect the material's chemistry and chemical bonding but do not reveal the overall structure. When characterizing the structure of a material, the electromagnetic waves scattered by the material must be analyzed. *Scattering* is a term used in physics to describe how moving particles (including photons) are deflected from a straight path by localized nonuniformities in the medium through which they pass.

Raman spectroscopy and X-ray diffraction (XRD) are the two methods commonly used for identifying unknown materials based on their crystalline or atomic structures. Both are scattering techniques, but they operate on dramatically different physical principles. The similarities in data presentation and overlapping applications in a gemological laboratory make it useful to discuss and compare the two methods together.

DATA INTERPRETATION OF RAMAN SPECTRA AND X-RAY DIFFRACTOGRAMS

Both Raman spectra and X-ray diffractograms (XRD patterns) are presented as intensity plots. The difference is that a Raman spectrum is plotted against wavenumber (figure 1, top), whereas an XRD pattern is plotted against diffraction angle (figure 1, bottom). Identification using either Raman spectroscopy or XRD involves comparing the band positions, intensities, and shapes of a collected spectrum against those of known materials. This process requires a database containing the reference spectra or diffraction patterns of all possible materials.

The most comprehensive database of powder X-ray diffraction patterns used for phase identification is the Powder Diffraction File (PDF), with more than one million entries. The International Centre for Diffraction Data (ICDD) maintains the PDF, which is accessible through a paid subscription (Kabekkodu et al., 2024). Several free but less comprehensive databases, such as the Crystallography Open Database (COD; Grazulis et al., 2009) or the Cambridge Structure Database (CSD; Groom et al., 2016), are also available for specific fields.

However, there is no comprehensive Raman spectra database for phase identification, due to the impracticality of tracking more than 170 million known chemical substances (a rapidly growing number as new substances are created). Instead, small field-specific databases (such as RRUFF for minerals) are maintained for specialized applications. While manual search-and-match processes can be tedious and time-consuming, modern computer programs make it possible to match experimental data with known spectra in a database within seconds.

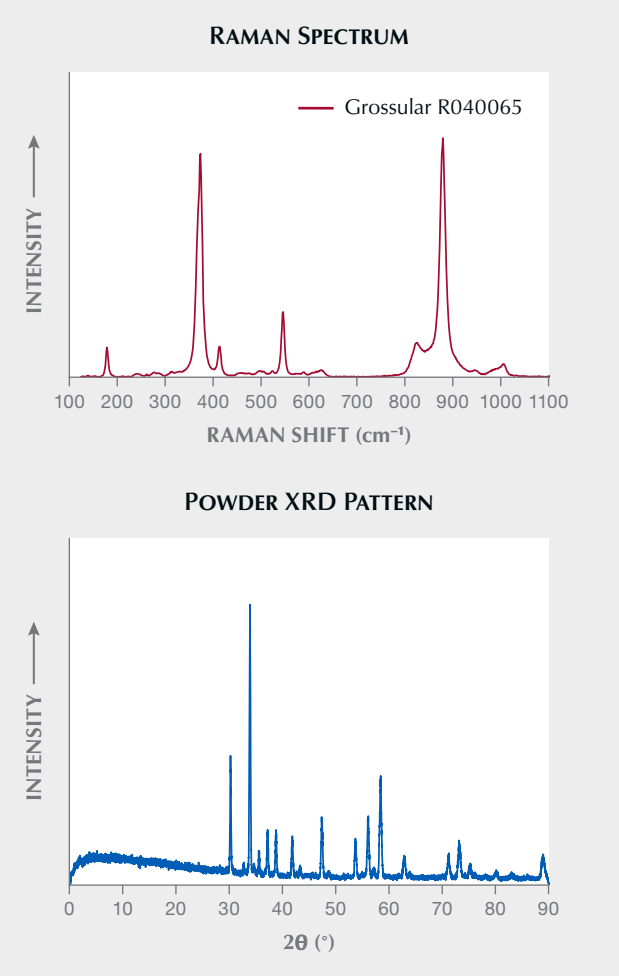

Figure 1. Top: A Raman spectrum of grossular garnet from the RRUFF database (Lafuente et al., 2015). Bottom: A powder XRD pattern of a hydrogrossular garnet.

The peaks in a Raman spectrum are often broader and more variable, which can make it challenging to match them with reference spectra, especially when peaks from multiple phases are present or the background is high. Software can only provide the user with a constrained list of possible matches, sometimes with a numerical score for the closeness of the match, which leaves the final decision with the user. It is important to keep in mind that band positions, intensities, and shapes can vary as a function of many different factors, including composition, strain, degree of crystallinity, or instrumental parameters

such as excitation wavelength or laser polarization relative to the sample. Therefore, human judgment remains essential to a conclusive analysis.

In contrast, the peaks in XRD patterns of crystalline materials are much sharper and better separated. In fact, the peak sharpness of an XRD pattern is limited mainly by the instrument rather than the intrinsic properties of the analyzed sample. Therefore, XRD's algorithm for phase identification is more straightforward, focusing solely on the positions and relative intensities of a handful of the strongest peaks without considering peak shapes and broadness. This approach is especially advantageous when diffraction data is collected on a mixture of multiple phases, as peaks from individual phases show less overlap. Nonetheless, the exact peak positions and intensities in an XRD pattern are affected by the composition, strain, and ordering states of the structure, again making human judgment necessary for the final decision.

For both methods, the complexity of the spectrum or diffraction pattern tends to decrease with increasing symmetry of the crystal structure. Because Raman scattering is an indirect probe of the crystal structure, calculating the theoretical Raman spectrum of a known structure is a very complicated quantum mechanical computation, the result of which almost never matches experimental data perfectly (e.g., Maschio et al., 2013, 2014). As a result, it is impossible to deduce the crystal structure from a given Raman spectrum, with the exception of some general qualitative speculations. An XRD pattern, on the other hand, is a direct reflection of the crystal structure, allowing straightforward calculation even by hand. In fact, many complicated crystal structures were solved by XRD before the advent of the computer. This direct relationship makes it possible to refine the details in a crystal structure—e.g., lattice parameters, atomic coordinates, occupancies, and displacements—by fine-tuning the parameters and matching the computed pattern to the experimental data. With high-quality diffraction data, it is even possible to solve the crystal structure of a completely new or unknown material.

APPLICATIONS OF RAMAN SPECTROSCOPY AND X-RAY DIFFRACTION IN GEMOLOGY

The applications of Raman and XRD are presented here first, to avoid overwhelming the reader with the technical details of each method. Despite the convoluted physical principles and technical complications, computer programs make their use quite straightforward. However, a deeper understanding of the technical details is often required to correctly interpret the data, which is why we take the opportunity to explain the physical principles and data collection of these techniques toward the end of this article. Raman and XRD largely serve the same function, which is to identify the characteristic structure of a material. Although not all crystalline materials are Raman-active (most gem minerals are), they always diffract X-rays to produce a unique pattern. Conversely, Raman spectroscopy is not limited to crystalline structures: It can also identify bond vibrations in polymers or small molecules in liquid and gaseous materials. XRD cannot identify molecular materials unless they are crystallized.

There have been several review articles and book chapters on applications of Raman spectroscopy to gemology (Kiefert et al., 2001; Bersani and Lottici, 2010; Fritsch et al., 2012; Eaton-Magaña et al., 2021), though almost no publications mention XRD in a gem laboratory. Nonetheless, to avoid repeating previous works, this article will broadly summarize how Raman and XRD assist in testing gem materials. Readers should refer to the referenced articles for the details in each specific application. Given that XRD is less commonly used in a gemological laboratory, Raman spectroscopy will be emphasized.

Gem Species Identification. Gem species identification is obviously the most basic application of Raman spectroscopy and XRD. Both Raman spectra and XRD patterns serve as signatures or fingerprints of specific material species. As explained earlier, identification of a gem species requires comparing the experimental data with spectra of known materials in a database. While there is a comprehensive XRD database for crystalline materials, it is excessive for gem identification purposes. The most commonly used option in a gemological laboratory is the XRD data of minerals in the RRUFF project (Lafuente et al., 2015). When Raman or XRD is needed to confirm a gemstone's identity in a laboratory, it always follows other tests, such as chemical analyses, that have already narrowed down the possibilities.

Given that a Raman spectrum can be collected on a faceted crystal very quickly (within seconds, depending on the instrument), it is routinely used for rapid gem species identification, especially when a fast turnaround is required. Small portable Raman spectrometers (box A) are also useful as a simple way to confirm the identity of gemstones when other testing methods are not easily accessible. Furthermore, a Raman spectrometer would undoubtedly be

an important component of any automated system designed to sort large quantities of small gemstones.

Raman spectroscopy is ideally suited for common gem species such as corundum, beryl, chrysoberyl, feldspar, tourmaline, spinel, and garnet (Jenkins and Larsen, 2004). While XRD is always more reliable for identifying gem or mineral species, it is often considered a destructive analytical method in which samples are crushed into a fine powder. However, modern area detectors using Debye-Scherrer diffractometers have made it possible to collect powder XRD patterns directly from single crystals such as faceted gemstones with pointed culets using a Gandolfi stage (Gandolfi, 1967; Schmidt, 2019). Cabochon-cut aggregate gemstones made up of many small crystals (e.g., jadeite, nephrite, chalcedony, turquoise, and hydrogrossular) can also be directly analyzed by XRD in either the Bragg-Brentano or Debye-Scherrer geometry with the appropriate sample stage (see the "X-Ray Instrumentation and Data Collection" section below). While Raman is much more efficient and user-friendly, XRD is occasionally used in the gemological laboratory when Raman spectroscopy together with chemical analysis cannot conclusively identify an obscure specimen. For instance, the recently discovered mineral johnkoivulaite was identified in GIA's laboratory when its Raman spectrum and XRD pattern did not match any known mineral species (Palke et al., 2021). Characterizing the crystal structure using XRD (either single-crystal or powder diffraction) is often a prerequisite for proposing a new mineral species to the International Mineralogical Association (IMA) (Nickel and Grice, 1998).

The subtle differences in peak positions and shapes in Raman spectra and XRD patterns reflect variations in the crystal structures of the tested material, providing additional structural information beyond phase identification. For instance, Raman spectroscopy can separate beryl into different groups based on alkali content, and it can identify molecule species such as carbon dioxide and water in structural channels. This information aids in determining geographic origin or distinguishing natural from synthetic emerald (Łodziński et al., 2005; Huong et al., 2010). The ordering state of spinel is reflected in its Raman spectrum (and XRD pattern), assisting in heat treatment detection. Peak positions in the Raman spectrum have even been proposed as a means to calculate the chemical composition of a garnet (Bersani et al., 2009), though the results are too inaccurate for practical applications.

Raman and XRD can also be applied to certain amorphous materials. Without the long-range ordering of a well-defined crystal structure, amorphous materials do not show sharp peaks in their Raman spectra or X-ray diffraction patterns but display broad bands determined by short-range local structures. The various categories of opal (opal-A, opal-CT, and opal-C), which can also be distinguished to some extent by Raman spectroscopy (Smallwood et al., 1997; Ilieva et al., 2007; Sodo et al., 2016), are defined by their distinct XRD patterns showing bands with various positions and sharpness (Jones and Segnit, 1975). The C-C, C-O, or C-H bonds in some polymeric chains of purely organic gems such as amber and copal can also be identified and characterized by Raman spectroscopy (Verkhovskaia and Prokopenko, 2020; Karolina et al., 2022).

Inclusion Identification. While most gemstones submitted to a gemological laboratory are valued for their high clarity and lack of inclusions, these tiny trapped materials can provide crucial insights into the geological and treatment history of a gemstone. Therefore, identifying and characterizing inclusions is sometimes a critical test in gemological analysis. The confocal mode in a Raman microscope makes it possible to analyze inclusions measuring only a few micrometers.

Primary inclusions reflect the geological conditions in which gemstones were formed, with certain mineral inclusions or inclusion combinations serving as characteristic fingerprints for a specific locality. Inclusion identification using Raman spectroscopy has emerged as a valuable tool in determining the geographic origin of corundum (Dele et al., 1997; Garnier et al., 2008; Graham et al., 2008; Palanza et al., 2008; Xu and Krzemnicki, 2021). This technique can also identify the liquid and gas species trapped inside fluid inclusions in gemstones. In practice, however, origin determination using inclusions relies largely on their visual appearance, without the need for Raman spectroscopy (Palke et al., 2019a,b).

Characterizing certain mineral inclusions may also help detect treatment processes. For instance, goethite and diaspore dehydrate at low temperatures (<600°C), so identifying them proves the host corundum has not been subjected to heat treatment (Krzemnicki et al., 2023). Other inclusions, such as zircon in corundum, may decompose or melt when heated at high temperatures, and thus their decomposition product (baddeleyite in the case of zircon) indicates high-temperature heat treatment (Rankin and Edwards, 2003; Wang et

Box A: Portable Raman Spectrometers

Raman spectroscopy offers a fast, simple, and nondestructive means of identifying phases of molecular or crystalline materials, making it valuable across a wide range of scientific and industrial applications. These include pharmaceuticals, narcotics, biopsy, nanotechnology, chemical engineering, material design, explosives detection, and the study of art and cultural heritage artifacts. Its versatility has led nearly all spectrometer manufacturers to offer portable, general-purpose Raman devices that range in size from a smartphone to a small briefcase.

As illustrated in figure 5, the basic configuration of a Raman spectrometer is quite simple, consisting of a laser source, a spectrometer, and optics to direct the laser and scattered light. This simplicity enables the design of compact Raman spectrometers. In fact, the display and controls are often the size-limiting components for a fully integrated, stand-alone instrument with its own system (Crocombe et al., 2023). Compared to a research-grade Raman spectrometer, these portable devices are equipped with much weaker single-laser sources and

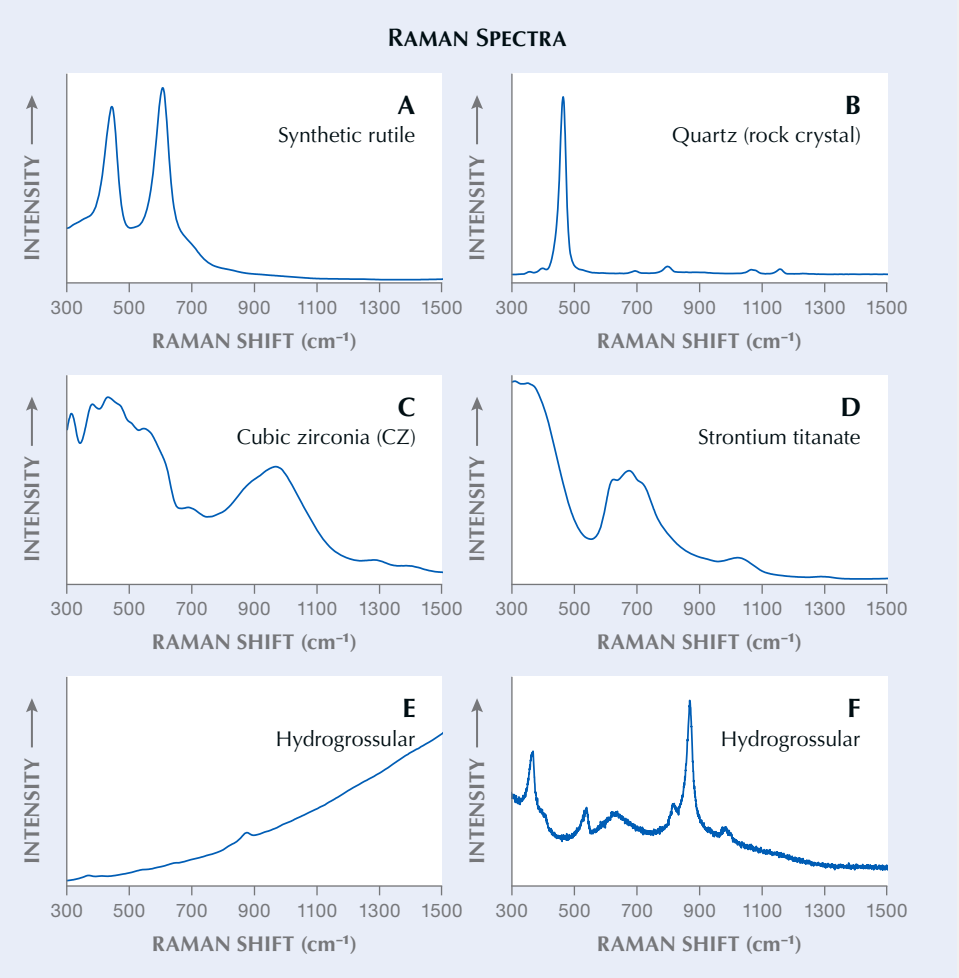

Figure A-1. Raman spectra of various gem materials. Spectra A–E were collected with a MagiLabs GemmoRaman-532 (using a 532 nm green laser), and spectrum F was collected with a Renishaw inVia confocal Raman microscope (figure 6) using an 830 nm infrared laser. Materials with sharp and distinct peaks, such as rutile and quartz (A and B), are easiest to identify, while materials with broad and overlapping bands, such as CZ and strontium titanate (C and D), are challenging due to the lack of individual peaks. Minerals such as hydrogrossular (E), feldspar, and corundum can show intense fluorescence bands when excited by a green laser, and these bands can overwhelm the Raman scattering signal. Avoiding this requires the use of a laser with a different wavelength. Note that the Raman peaks are much more prominent using an 830 nm laser (F) compared to the spectrum collected on the sample using a 532 nm laser (E).

al., 2006). Radiation-damaged zircons can recrystallize during annealing at relatively low temperatures (Zhang et al., 2000a,b; Ende et al., 2021), which means characterizing the peak sharpening and positional shift of zircon inclusions in corundum may help detect low-temperature heat treatment as well.

Inclusions in diamonds are scientifically valuable, as these often fully enclosed materials contain information from deep inside the earth that would be impossible to obtain otherwise. Raman spectroscopy and XRD are the primary methods for studying these samples in geological research (Angel et al., 2022;

much lower-resolution spectrometers. The optics are also much simpler, directing the laser and collecting the scattered light from a much larger area on the sample. Nonetheless, they offer the benefits of affordability, convenience, and fewer safety restrictions, making Raman spectroscopy accessible to less-experienced users.

Although a few devices on the market are specifically designed for gemological use, there are some significant limitations the buyer needs to be aware of before applying them to gem identification. Not all gemstones exhibit Raman spectra with sharp, distinct peaks; some may show broad overlapping bands instead (figure A-1, A–D). Some gemstones are weak Raman scatterers that require intense laser power or long exposure time to acquire usable data. Some gem materials have strong fluorescence, which can saturate the detector and overwhelm Raman signals, requiring lasers of longer wavelength to reduce the photoluminescence (figure A-1, E and F). No single laser wavelength or power is suitable for all materials, so research-grade Raman spectrometers are equipped with multiple laser sources and adjustable power output. A portable Raman device, on the other hand, is only equipped with a single weaker laser source (usually a green laser for gemological applications), which could significantly limit its use on challenging gem materials with a weak Raman signal or strong fluorescence.

Moreover, phase identification using Raman spectroscopy requires comparing the collected data with a reference database, but this is not always straightforward or conclusive. Gem materials encompass a wide range of drastically different materials, including natural and synthetic single crystals, polycrystalline rocks, organic or composite materials, and even amorphous materials such as plastic and glass. There is still no comprehensive Raman database for quick and accurate gem species identification. The best available option is the Raman spectra data of minerals from the RRUFF project (Lafuente et al., 2015). However, most minerals are not gemstones, which means this database contains many irrelevant references that could slow down the identification rate or lead to errors. Most Raman devices designed for gem identification come with custom-built databases, but their completeness and accuracy for challenging or obscure gem materials are difficult to assess.

Raman spectroscopy is generally more effective and efficient when the range of potential matches is limited, minimizing the chance of misidentification. This is why portable Raman devices excel at quickly detecting explosives or toxic substances. Despite some advertising claims that these portable devices can instantly identify a gemstone species with 100% accuracy, a Raman spectrometer is not a stand-alone gem identification method—it should be used as confirmation after standard gemological tests have eliminated all but a few possibilities. It is best suited for identifications within subcategories of gem materials where the possibility pool is limited, such as a trader or appraiser who exclusively deals with diamond and diamond simulants or a ruby miner who wants to quickly separate garnet from corundum. It should be noted that these specialized applications may require a custom database for the device to be most efficient.

CHECKLIST FOR PURCHASING A PORTABLE RAMAN DEVICE

Self-Assessment

- What is my primary need for this equipment?
- Is this equipment best for my particular applications?
- Can I justify the cost based on the additional information I can expect from this equipment?

Questions for the Manufacturer

- What is the laser wavelength and power?
- What is the laser safety classification, and does it meet local regulations or require special training to operate safely?
- What is the expected learning curve to operate this equipment?
- What support does the manufacturer offer users?
- What warranty is provided?
- Is there dedicated software specific to gemology?
- How often is the software updated?
- How many gemstones are included in the software database?
- Is the database customizable for special applications?

Smith et al., 2022). The recently discovered mineral crowningshieldite was identified and characterized as an inclusion in a type IIa diamond using both methods (Smith et al., 2021). Although inclusion identification may help separate natural gemstones from synthetics, inclusions do not routinely undergo Raman spectroscopy, since other testing methods are more effective at achieving the same goal.

Testing Pearls and Other Biogenic Carbonate Gems. Biogenic gems are discussed separately because they often contain composite materials rather than a sin-

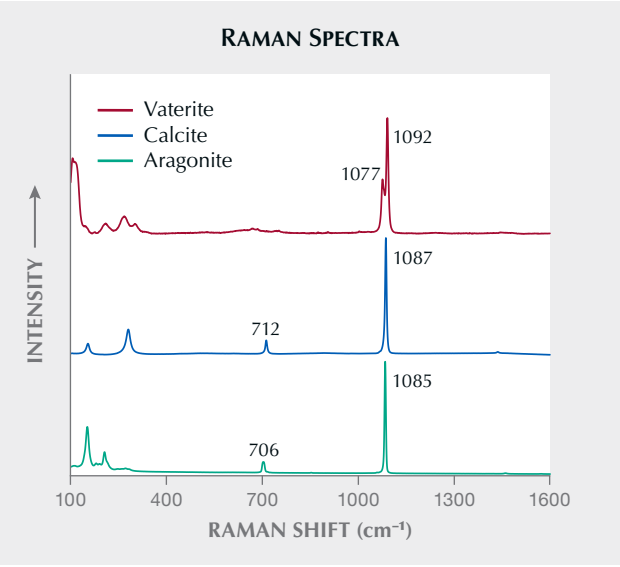

Figure 2. Raman spectra of vaterite, calcite, and aragonite collected from pearls. The peak positions at ~710 and ~1090 cm^{-1} can be used to identify the calcite polymorph of calcium carbonate. Spectra are offset vertically for clarity.

gle mineral. Pearls (and shells) are composed mainly of biomineralized calcium carbonate in organic matrices. Calcium carbonate has three known polymorphs (minerals with the same chemical formula but different crystal structures)—aragonite, calcite, and vaterite (figure 2)—and all three can be found in pearls. More than one polymorph (and sometimes all three) can be found in pearls from the same species, or even within the same sample.

Most pearls, both nacreous and non-nacreous, are made up mostly of aragonite. Calcite frequently occurs in low-quality nacreous pearls accompanying aragonite, and it is the main component of some non-nacreous pearls produced by a few special mollusk species. Vaterite, an unstable polymorph of calcium carbonate, does not occur regularly in pearls but has been reported in certain growth zones or sectors of freshwater cultured pearls (Qiao et al., 2007; Wehrmeister et al., 2007; Soldati et al., 2008). The factors that determine the carbonate species found in a given pearl are not fully understood, but the mollusk species and the environment (temperature and chemistry) undoubtedly play crucial roles. Therefore, identifying the calcium carbonate polymorph is an important test for determining the mollusk species and origin of certain pearl types (Eaton-Magaña et al., 2021). The same test applies to corals, which may comprise aragonite, calcite, or almost purely organic matter depending on the type. One notable example (Karampelas et al., 2009) is separating the endangered and internationally protected *Stylaster* corals (aragonite with carotenoid pigment) from the highly valued red coral from the *Corallium* genus (calcite with parrodiene pigment).

Besides identifying the specific carbonate polymorph, Raman spectroscopy and XRD can also reveal information about the chemistry, which may also help in separating pearls from different species or environments. The exact position of the calcite Raman peak at ~710 cm^{-1} is sensitive to magnesium content (Kim et al., 2021). Disordered dolomite (calcite with almost half of the calcium substituted by magnesium) was recently discovered in the center of a natural *Cassis* pearl using Raman spectroscopy and XRD (Zhou et al., 2023).

One complication in pearl analysis is the orientation effect. Unlike faceted single-crystal gemstones with sharp points, which can either be tested on different facets or randomized using a Gandolfi stage, the surface of a nacreous pearl is always perpendicular to the *c*-axis of the aragonite due to the orderly packing of platelets in the nacre (Yoshimi et al., 2004). A similar orientation can be observed in some calcite pearls (Okumura et al., 2010; Pérez-Huerta et al., 2014). The restricted orientation may result in spectra or diffraction patterns that differ significantly from the reference, in which the peak positions remain the same but the relative intensities of the peaks are different due to the biased orientation during analysis (e.g., Friedmann, 1957; Yoshimi et al., 2004; Lu, 2009; Gao et al., 2023). This orientation effect does not affect qualitative phase identification, especially when the possibilities are limited to carbonates, but quantification may be impossible without destructive testing, which is only applied for research purposes.

Treatment Identification. Besides identifying altered (or unaltered) natural inclusions, Raman spectroscopy can help identify foreign materials introduced during treatment. Since materials introduced by treatment are often highly localized and amorphous, the applications discussed in this section mostly pertain to Raman spectroscopy and do not apply to XRD.

One common clarity enhancement for colored stones and diamonds is the filling of fractures using RI-matching materials such as glass or epoxy. Raman spectroscopy can detect the lead glass fillers in fracture-filled rubies and the flux in fracture-healed rubies (McClure et al., 2006; Calvo del Castillo et al.,

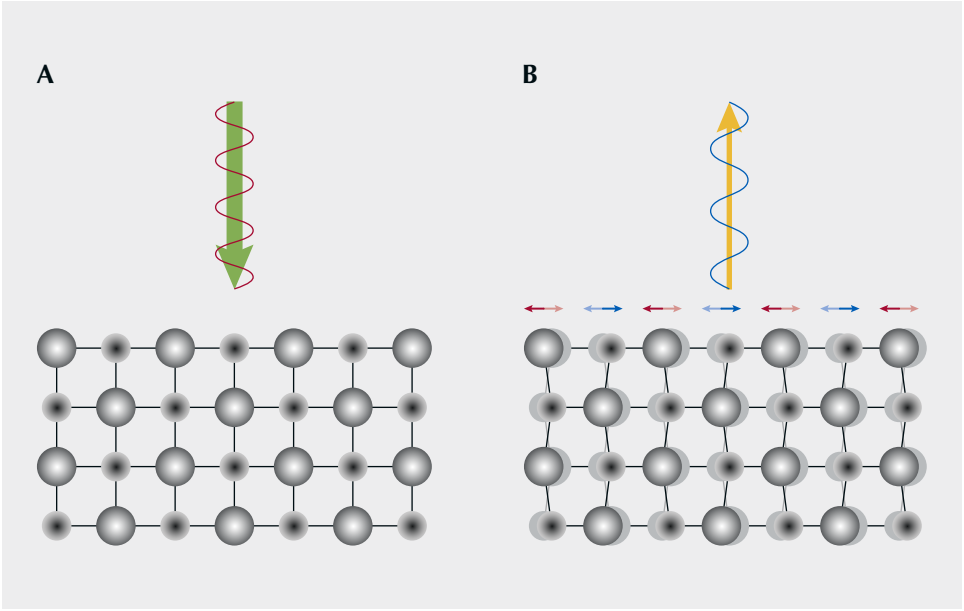

Figure 3. Light striking a crystalline material (A) may excite certain vibration modes of the crystal lattice (B). The scattered light has a slightly lower energy (longer wavelength) due to the energy transferred to the lattice. This process is known as Stokes Raman scattering. The reverse process, though less likely, is known as anti-Stokes Raman scattering (B to A with reversed light directions), where the incident light takes energy away from the vibrating lattice, resulting in scattered light with shorter wavelength (higher frequency and higher energy).

2009; Fan et al., 2009). The organic materials used to fill gems of lower RI, such as jadeite and emerald, can also be identified by their various Raman-active C-C, C-O, and C-H bonds (Johnson et al., 1999; Kiefert et al., 1999, 2000). This test is especially useful for emeralds, as the acceptability of a permanent filler (epoxy) versus a removable filler (oil) may vary depending on customer preference.

Coating of faceted surfaces is another treatment sometimes used for luster enhancement, color alteration, or protection from scratches. Certain coating materials, such as diamond films, are also easily identified by Raman spectroscopy (Fritsch et al., 1989). Notably, Raman spectroscopy is only applicable when a significant amount of a new phase is introduced by the treatment. The claim suggesting that beryllium diffusion (or any diffusion treatment) can be detected by Raman (Sastry et al., 2009) contradicts the basic principle of Raman scattering and is completely unsupported by any empirical evidence.

Raman spectroscopy can also help distinguish natural-color pearls and corals from color-treated or dyed material. Many natural-color pearls and corals derive their color from polyenic pigments (Karampelas et al., 2007). If a pearl or coral displays a color known to be from a polyenic pigment in nature but does not show any polyenic peaks in its Raman spectrum, the color must be the result of treatment. Certain dyes used to enhance the color of pearls, such as silver nitrate for blackening freshwater pearls, show distinct peaks in their Raman spectra, making identification even simpler.

PRINCIPLES OF RAMAN SCATTERING

Scattering of visible light occurs everywhere in the world around us. Thin clouds and snow appear white because of the non-selective scattering of the visible spectrum by water droplets or ice flakes. Scattering is almost always *elastic*, meaning the light's wavelengths remain unchanged. Imagine a bright green spot that appears from shining a green laser pointer at the wall. The wavelength and color of the bright spot are exactly the same as the laser beam because almost all the light is scattered elastically. However, if our eyes were supersensitive detectors of both intensity and wavelength, we would see that the bright spot on the wall actually contains tiny amounts of light of different colors (wavelengths). Some of this *inelastic* scattering of light, about 10 million times weaker than elastic scattering (Pasteris and Beyssac, 2020), is called Raman scattering, named after Sir C.V. Raman, the Indian physicist who received the Nobel Prize in 1930 for recognizing it. The spectrum of Raman-scattered light contains information from the light-scattering medium, which can be used to identify and characterize materials.

Most introductions to Raman spectroscopy focus on inelastic scattering by molecules, in the manner of its original discovery (Raman, 1922). In the context of gemology, however, we need to consider inelastic scattering from solids, often crystalline. In this case, Raman scattering also occurs as incoming photons exchange energy with the entire crystal structure. For example, if an incident photon excites

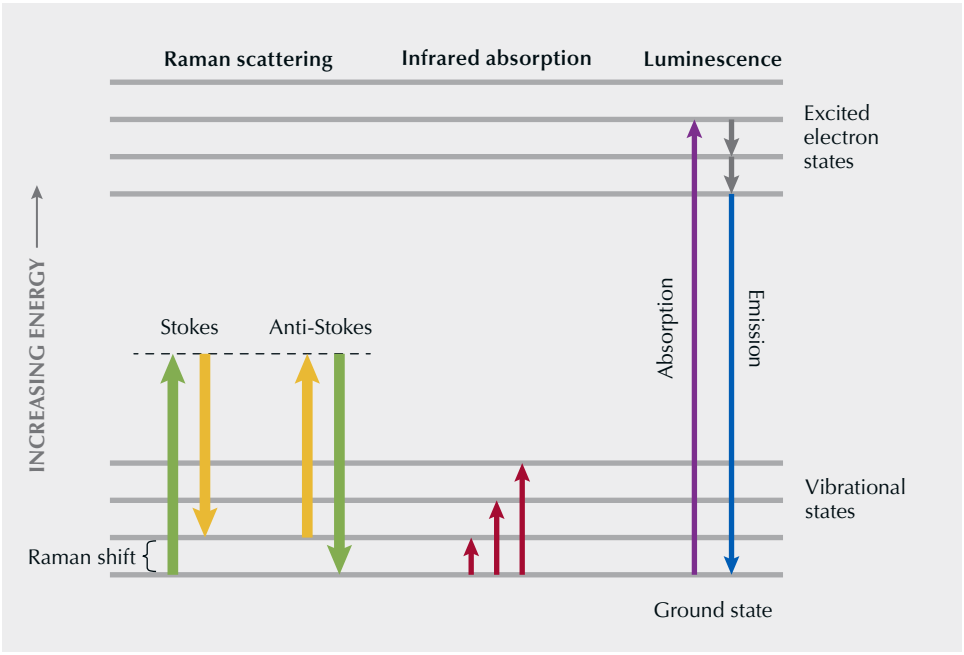

Figure 4. Energy level diagram illustrating Raman scattering, as well as other phenomena for context. As a quantum mechanical system, only discrete amounts of energy are allowed, represented by the horizontal lines. The lower energy states at the bottom correspond to different vibrations in the molecules or crystal lattice. Only a finite number of vibrations are allowed, each with its own distinct frequency or energy. Energy can be transferred between a photon and the vibration states, resulting in a scattered photon of a different energy. This energy change is called the Raman shift.

a particular crystal lattice vibration, it will lose some specific amount of energy, resulting in a scattered photon of longer wavelength (lower energy) (figure 3). This process is known as Stokes Raman scattering. The amount of energy lost is called the Raman shift, as illustrated in the energy level diagram in figure 4, and it is characteristic for the scattering material. The reverse process, called anti-Stokes Raman scattering, where photons gain specific amounts of energy from the vibrating lattice, can also occur but tends to be weaker and harder to detect. Therefore, Raman spectroscopy typically focuses on Stokes Raman scattering.

Figures 3 and 4 depict just one Raman shift, but materials usually have multiple available vibrational modes with different energies that can inelastically scatter photons, depending on the bonding structure and symmetry. The spectrum of Raman-scattered light can therefore exhibit bands or peaks at various energies, together providing structural (and to some extent chemical) information. It is often possible to identify and characterize a material based on its Raman spectrum. However, some materials, such as metals and table salt, are Raman-inactive because they cannot scatter light inelastically due to symmetry constraints. Raman spectroscopy is often considered complementary to infrared absorption (IR) spectroscopy, as they both involve observations of vibrational energy states (figure 4), although they often do not activate the same vibration modes.

A key feature of Raman spectroscopy is that it detects small "shifts" in the light energy between the excitation and scattered radiation. For any given Raman-active feature (mode), the wavelength of the scattered light depends on the wavelength of the incident light (e.g., the laser wavelength). This differs from methods such as IR spectroscopy or luminescence spectroscopy, where we associate particular wavelengths of light with particular molecules or defects. This is why Raman spectra are plotted on a wavenumber-shift scale (in units of cm^{-1}) instead of a wavelength scale, as wavelength values are inversely proportional to the photon energies and thus cannot be directly added or subtracted. Note that the units used in Raman and IR spectroscopy, which are both conventionally plotted in wavenumbers (in units of cm^{-1}), are not equivalent. In Raman spectroscopy, a spectrum shows the relative energy, plotted as the Raman shift compared to the laser excitation, which sits at 0 cm^{-1}. In IR spectroscopy, a spectrum shows the absolute energy in wavenumbers.

RAMAN SPECTROSCOPY INSTRUMENTATION AND DATA COLLECTION

There are many different instrument designs and variations on the technique, serving different purposes, ranging from small handheld devices that can fit in a pocket (box A) to large research-grade instruments equipped with multiple laser sources and powerful optical microscopes that take up an entire desk. Regardless of the size or application, the basic

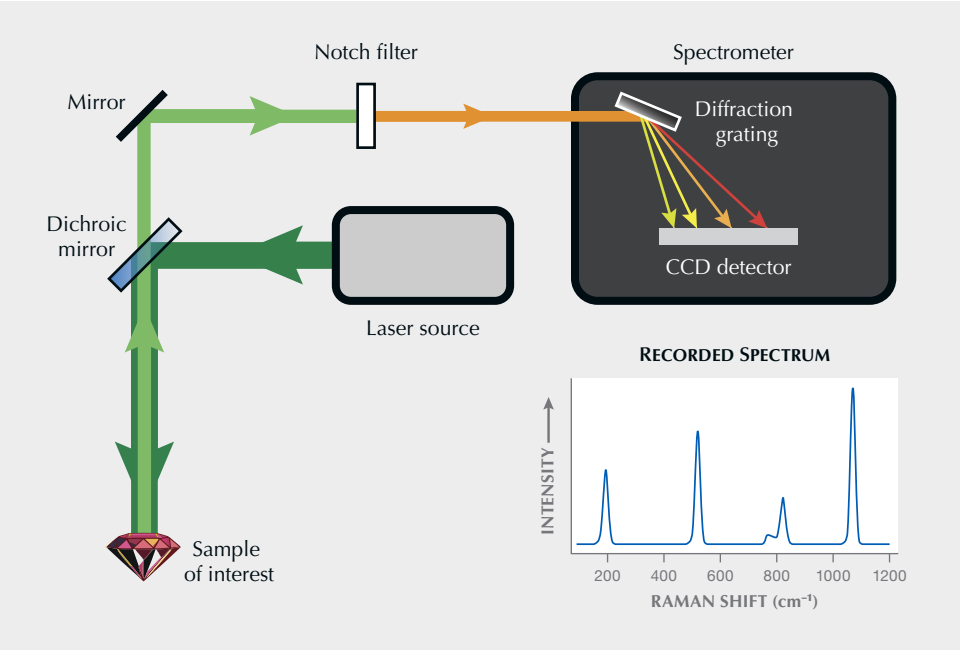

Figure 5. Schematic diagram of a basic Raman spectrometer. The light produced by a laser source is directed to the sample by optical fibers or mirrors. Scattered light is directed back to the spectrometer via a notch filter, which blocks the elastically scattered light and allows only the much weaker Raman-scattered light to pass through. The diffraction grating in the spectrometer disperses the scattered light into a spectrum of wavelengths, and the detector records this dispersed light. A computer reads and displays the spectrum.

configuration of a Raman spectrometer is always the same (figure 5): a laser source to provide intense incident monochromatic light (light of a single wavelength), optics to direct and collect light to and from the sample of interest, and a spectrometer to measure the Raman-scattered light. This section focuses on

Figure 6. The Renishaw inVia confocal Raman microscope is a popular research-grade Raman spectrometer. Samples are placed on the microscope stage under the objective lens for analysis. The protective doors are open here to show the internal path of the laser beam. The green light is scattered light along the optical path of the 514.5 nm argon laser, which is mounted behind the instrument. Photo by Kevin Schumacher.

the more powerful and versatile research-grade instruments that best represent the technical capabilities of Raman spectroscopy.

Figure 6 shows an example of a Raman microscope, with the doors opened to reveal the green glow of scattered light from the 514.5 nm laser source. The user views the specimen through the microscope eyepieces or uses a digital camera, bringing the desired point of analysis into focus and moving it under the crosshairs to center it in the focal point of the laser, which is aligned to be coaxial with the objective lens. The same instrument can also be used for photoluminescence spectroscopy (to measure the emission light, as in figure 4). In this case, the recorded spectrum is simply plotted in wavelength (in nanometers) instead of being expressed as a Raman shift (Eaton-Magaña and Breeding, 2016).

Modern Raman spectroscopy owes its success as a practical analytical technique to the development of powerful monochromatic laser sources and sensitive detectors. One important refinement is the use of confocal optics, which blocks out-of-focus light and improves the spatial resolution of the analyzed volume (e.g., Everall, 2009). Confocality is achieved by focusing the collected light through a pinhole or a slit using a more adjustable quasi-confocal arrangement. The spatial resolution also depends on the numerical aperture (NA) of the microscope objective lens and the laser wavelength (λ) and is proportional to λ/NA.

With confocal optics, it is possible to characterize relatively small regions of a gem, such as internal inclusions. For example, a 100× objective lens with a 0.9 NA used in combination with a 514.5 nm laser can achieve a spatial resolution of approximately $1 \times 1 \times 5$ μm^3, elongated along the optical axis (i.e., the direction of the incident laser beam). Note, however, that there are many additional factors affecting the spatial resolution (e.g., Kim et al., 2020). Focusing the laser inside a crystal to examine inclusions or other internal features will further distort the light and affect the spatial resolution. Conventional microscope lenses have short working distances, which can become a limiting factor when attempting to analyze inclusions inside a gemstone or when more clearance is needed to work around a jewelry setting. Lenses with a long working distance offer a practical solution, but the tradeoff is a lower NA, which means the light is not as tightly focused and the analyzed volume is larger.

Another important consideration is the choice of laser wavelength. Raman spectrometers are sometimes equipped with multiple interchangeable lasers. A shorter wavelength (e.g., blue 488 nm laser) generally leads to more intense Raman scattering and a slightly smaller spot size. However, it also increases the likelihood of luminescence from the gemstone or other target material. Luminescence (particularly fluorescence) is problematic because it can drown out the Raman signal and decrease spectral resolution (e.g., figure A-1E). For this reason, longer wavelengths such as red (e.g., 633 nm) or even infrared lasers (e.g., 830 or 1064 nm) can be a more practical choice for Raman spectroscopy because they are less likely to excite luminescence. A green laser (e.g., 514 or 532 nm) can offer a good compromise (again, see figure 6). Ultimately, the problem of luminescence depends on the sample and atomic scale defects within it.

Laser power is another variable to consider. Benchtop Raman microscopes often employ lasers in the range of a few to hundreds of milliwatts. Ideally, the laser power that actually reaches the sample after passing through the various internal components can be measured with a laser power meter. Although higher power generally yields a stronger Raman signal, it also increases the risk of altering the sample and obtaining poor-quality data. An intense laser focused down to a spot can produce enough heat to damage sensitive materials, especially if they are dark or opaque. When attempting to collect a Raman spectrum from magnetite (Fe_3O_4), localized heating from the beam often alters the specimen at the small surface region where the laser is focused, resulting in a spectrum that corresponds to hematite (de Faria et al., 1997). In such cases, the solution is to use a lower laser power, and many instruments allow the option to step down the laser power. Starting at a low laser power and gradually increasing it until obtaining an acceptable Raman signal is a good approach.

Figure 5 shows Raman analysis at a single point. With computer-controlled motorized stages, moving optics, and faster detectors, an increasing number of instruments can collect data from multiple points in succession to achieve two-dimensional and three-dimensional Raman maps. Mapping can be very helpful in rapidly visualizing or imaging heterogeneities that might otherwise be invisible (Eaton-Magaña et al., 2021). As technology continues to advance, Raman spectroscopy will become an even more powerful technique whose applications will continue to expand.

PRINCIPLES OF X-RAY DIFFRACTION

Diffraction is the phenomenon in which a wave is redirected around an obstacle or aperture. While very

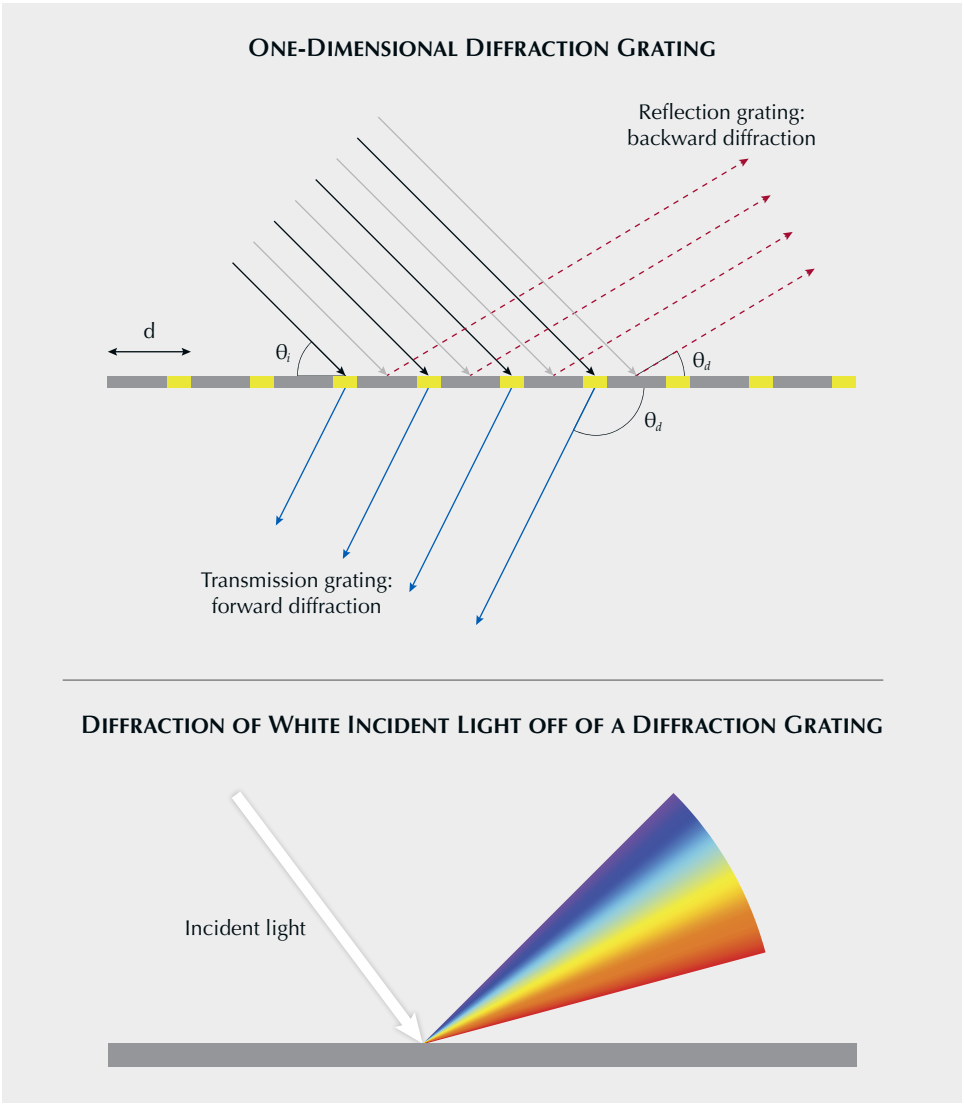

Figure 7. Top: The light scattered (either transmitted through or reflected back) by different sections of the one-dimensional diffraction grating travels varying distances. Constructive interference (diffraction) occurs only when the wavelength (λ), periodicity (d), and incident (θ_i) and diffraction (θ_d) angles satisfy a certain condition. Bottom: Because of the varying diffraction angles for different wavelengths, an incident beam of white light is dispersed by the diffraction grating into a spectrum.

similar to scattering, diffraction differs in that it applies to waves instead of particles. Since photons demonstrate wave-particle duality, the same physical process involving electromagnetic waves can often be described as both scattering and diffraction. As a wave phenomenon, diffraction does not change the energy or wavelength (being elastic by default) and is often accompanied by interference, especially when the diffracting obstacle or aperture has a periodic structure. The amplitude (or intensity) of the diffracted wave can be recorded by a detector positioned far from the diffracting object (with the detector distance much larger than the size of the diffracting object). This far-field distribution of the diffracted wave amplitude, often expressed in terms of diffraction angle, is known as a diffraction pattern. Diffraction is encountered in everyday life, with the most noticeable examples involving visible light. The striking iridescent colors of butterfly wings and iris agates are examples of naturally occurring diffraction phenomena.

A diffraction grating is an optical grating with a periodic structure that bends light into different directions. The light rays scattered by different slits or grooves in a diffraction grating with a periodicity of d will constructively interfere with each other when the optical path differences between them are integer n multiples of the wavelength (λ):

$$d(\cos\theta_i - \cos\theta_d) = n\lambda \quad (1)$$

in which θ_i represents the incident angle and θ_d the diffraction angle relative to the grating plane (figure 7, top). The diffraction angle is dependent on the wavelength of the incident light, which means incident light containing a range of different wavelengths

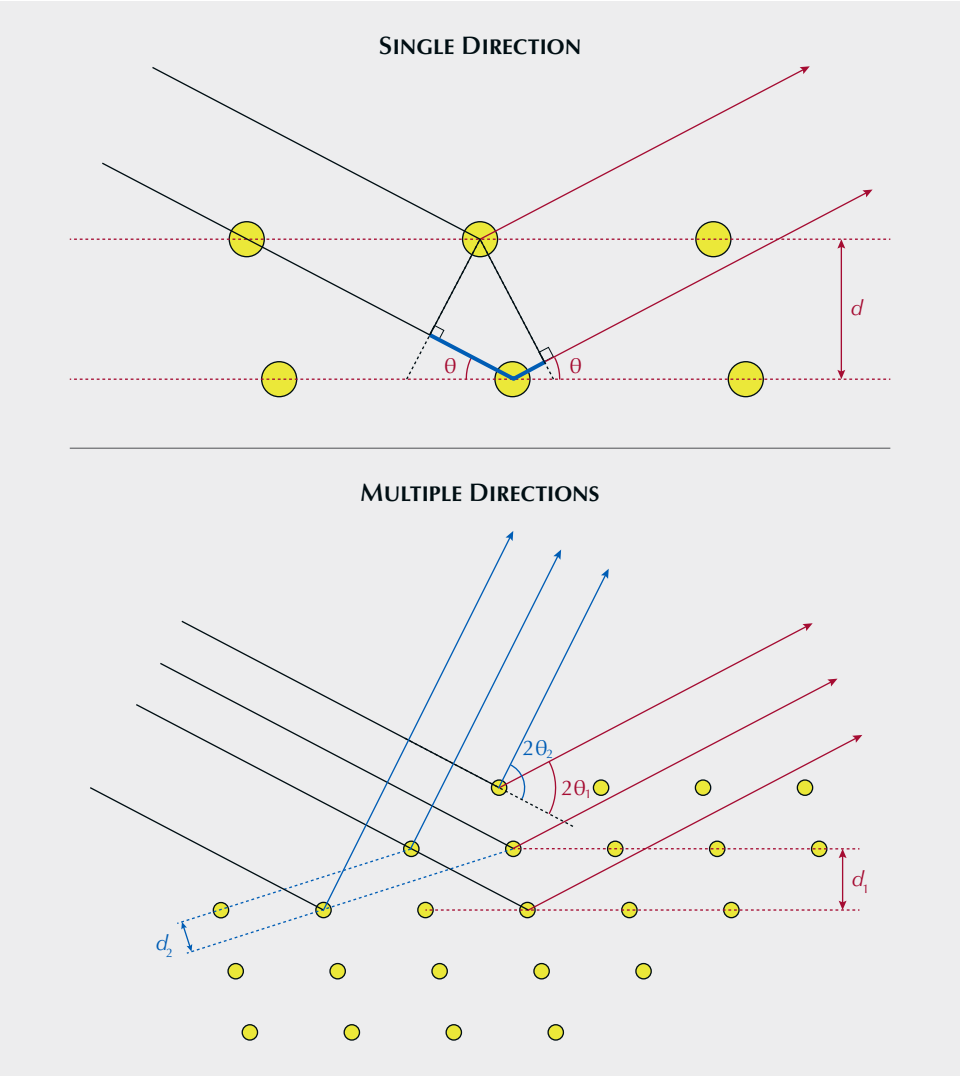

Figure 8. Top: This simple diagram illustrates Bragg's law. The X-ray "reflected" by the second layer of atoms travels an extra distance of 2dsinθ *(the blue section of the path) compared to the first layer. X-rays "reflected" by different layers (lattice planes) will constructively interfere when the optical path differences equal integer* n *multiples of the wavelength (i.e.,* nλ*). Bottom: Bragg's law may be satisfied in more than one way, allowing the X-ray to be diffracted in several directions simultaneously. However, the only experimentally measurable angle is between the diffracted beam and the incident beam, which is 2θ rather than* θ*.*

can be dispersed by a diffraction grating into a spectrum (figure 7, bottom). This principle is the basis for how most optical spectrometers, such as the one used in Raman spectroscopy, separate light of different wavelengths (again, see figure 5).

For a diffraction grating to effectively bend and disperse the incident light, its periodicity must be larger than, and on the same scale as, the wavelengths of the incident light. For instance, a diffraction grating that effectively disperses the visible spectrum (~400–700 nm; figure 7) typically has a period of a few micrometers. In contrast, a diffraction grating with a nanometer-scale periodicity (i.e., a crystal structure) can only bend electromagnetic waves of shorter wavelengths, which are X-rays. Equation 1 above is known as the first Laue equation in X-ray crystallography (Hammond, 2015), named after Max von Laue (Friedrich et al., 1913). Because crystals are three-dimensional periodic structures, three Laue equations in three different directions must be satisfied simultaneously for diffraction to occur. The three combined Laue equations can be simplified into the more commonly known Bragg's law (Bragg and Bragg, 1913):

$$2d_{hkl} \sin\theta = n\lambda \quad (2)$$

in which the d_{hkl} represents the spacing between lattice planes with a Miller index of *hkl*.

Bragg's law can be intuitively explained as a calculation of the optical path difference between X-rays "reflected" by different layers of lattice planes that are integer multiples of the wavelength, allowing constructive interference (figure 8, top). However, this is a simplification, because the lattice planes cannot truly "reflect" X-rays like a mirror—they are not real physical planes but imaginary ones in the crystal structure. The experimentally meas-

urable angle is 2θ between the incident beam and the diffracted beam, instead of θ relative to the lattice plane (figure 8, bottom). Moreover, Bragg's law can be satisfied in multiple ways at once, which means the incident X-ray beam can be diffracted into multiple directions in three dimensions by a single crystal. Bragg's law determines the diffraction angles but does not reveal anything about the intensities of the diffraction peaks. A two-dimensional XRD pattern, known as a diffractogram, combines peak positions (diffraction angles) and peak intensities (figure 1, bottom). Peak positions are determined by the unit cell geometry (lattice parameters). Peak intensities depend on the detailed atomic arrangement within the unit cell.

A crystal structure diffracts not only X-rays but also any form of wave with similar wavelengths as X-rays. Physical particles such as electrons and neutrons can also behave like waves. Known as matter waves or de Broglie waves, they are also commonly used to analyze crystal structures through diffraction.

XRD is not typically considered a spectroscopic method, since a spectrum requires a range of continuously varying wavelengths (or frequencies). Technically, though, its principle is closely related to spectroscopic methods. If the angle θ in Bragg's law is fixed (equation 2) but the wavelength λ is variable, the X-ray diffraction pattern would indeed become a spectrum. In practice, it is much easier to generate monochromatic X-rays and measure the diffraction angle than to resolve the energy of the diffracted X-rays from a white incident X-ray beam. In fact, the most accurate way to resolve an X-ray spectrum is by using a perfect crystal with known lattice parameters as a diffraction grating to disperse the different wavelengths. In other words, an X-ray diffractometer is essentially an X-ray spectrometer in which the diffraction grating itself is the test subject.

X-RAY INSTRUMENTATION AND DATA COLLECTION

A single small crystal diffracts X-rays in three-dimensional space. This diffraction can be fully characterized using a single-crystal X-ray diffractometer to study the crystal structure in 3D space. However,

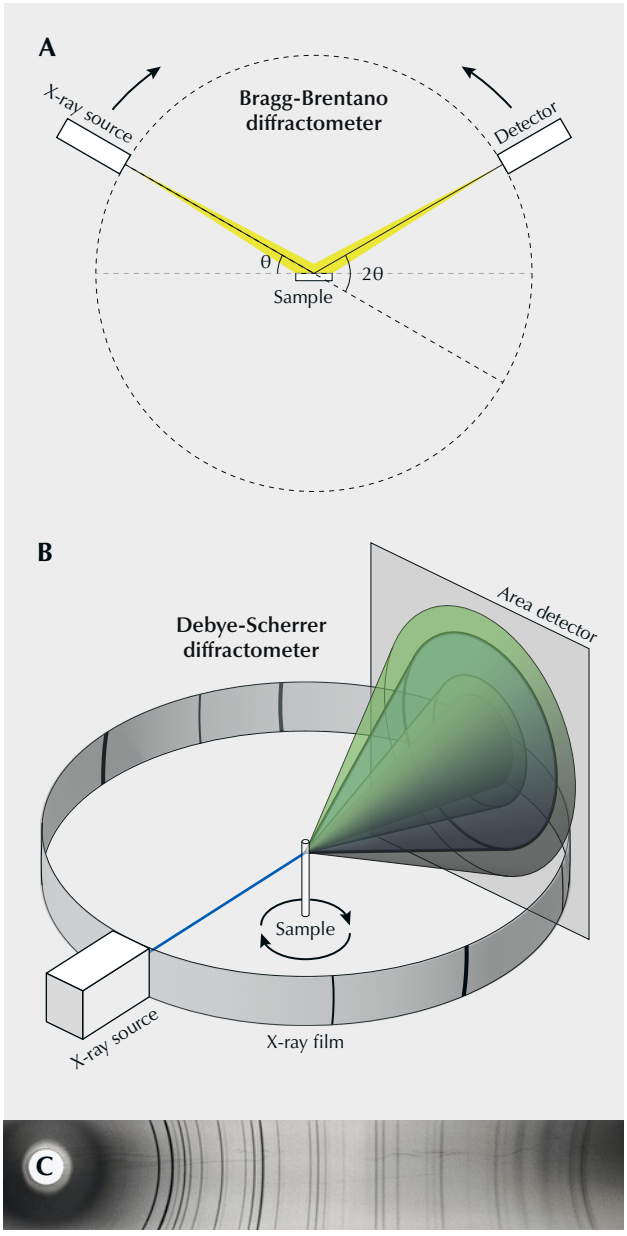

Figure 9. Diagrams showing two different geometries for powder XRD. A: The Bragg-Brentano diffractometer uses a point detector that moves in a circular path to measure the X-rays at different diffraction angles. The X-ray source (or sample stage) rotates together with the detector to maintain a "reflective" geometry that optimizes detection efficiency. B: The Debye-Scherrer diffractometer uses a stationary X-ray source and an area detector or X-ray film. Either a section or the entire diffraction pattern can be collected without moving the detector. The powdered sample is in the center. A smaller amount of sample is required, and it is often rotated during data collection to best randomize the orientation. C: An example XRD pattern of grossular garnet collected on X-ray film using a Debye-Scherrer camera, as illustrated in B. Similar 2D diffraction patterns collected on digital area detectors can be converted to the 1D intensity vs. 2θ plot, as shown in figure 1B.

without any modifications, XRD is assumed to be powder X-ray diffraction, the most widely used diffraction technique. The powder XRD pattern comprises diffracted X-rays from millions of randomly oriented crystal grains. In this process, the orientational information is completely omitted and only the intensity as a function of diffraction angle remains. The most common X-ray diffractometer uses the Bragg-Brentano geometry (figure 9A), in which the powdered sample is spread on a plate as a flat surface. A point or line detector on a moving goniometer arm measures the intensity over a range of diffraction angles. The X-ray source moves on a separate goniometer arm to keep the incident angle to the sample surface the same as the diffraction angle. In some instruments, the X-ray source is stationary but the sample plate rotates along with the detector arm at a $\theta/2\theta$ relation to maintain the same "mirror reflection" geometry. The Bragg-Brentano geometry optimizes the efficiency and accuracy of a line detector by allowing the diffracted X-ray to be focused on the detector circle.

However, XRD is not a symmetrical process (figure 8, bottom), contrary to what the Bragg-Brentano geometry suggests (figure 9A). The Debye-Scherrer geometry provides a more complete picture of the diffraction process. Instead of using a point or line detector, it employs an area detector or X-ray film to measure diffracted X-rays in all directions simultaneously, without moving the detector. The sample is often placed in a capillary made of polymers or glass that do not diffract or fluoresce X-rays. The X-ray diffracted by the sample forms concentric cones with half-angles of 2θ as defined by Bragg's law.

XRD typically employs an X-ray tube as the X-ray source. In this tube, high-energy electrons (accelerated by high voltage) strike an anode material, typically copper or molybdenum, causing it to emit characteristic X-rays. This is essentially the same mechanism Wilhelm Conrad Roentgen used in 1895 to discover X-ray radiation. A rotating anode source, where the anode can be cooled more easily, can produce more intense X-rays, such as those used for medical imaging. A substantially more powerful source, known as a synchrotron, uses a cyclic particle accelerator. High-energy electrons are bent by a magnetic field, emitting electromagnetic radiation of various wavelengths, including X-rays.

With more powerful X-ray sources and more sensitive area detectors becoming increasingly accessible, Debye-Scherrer diffractometers are gaining popularity due to their versatility. Data collection is much faster since the entire diffraction pattern is collected simultaneously, without having to wait for the detector to sweep the necessary angles. Additionally, much smaller sample amounts are required. With a

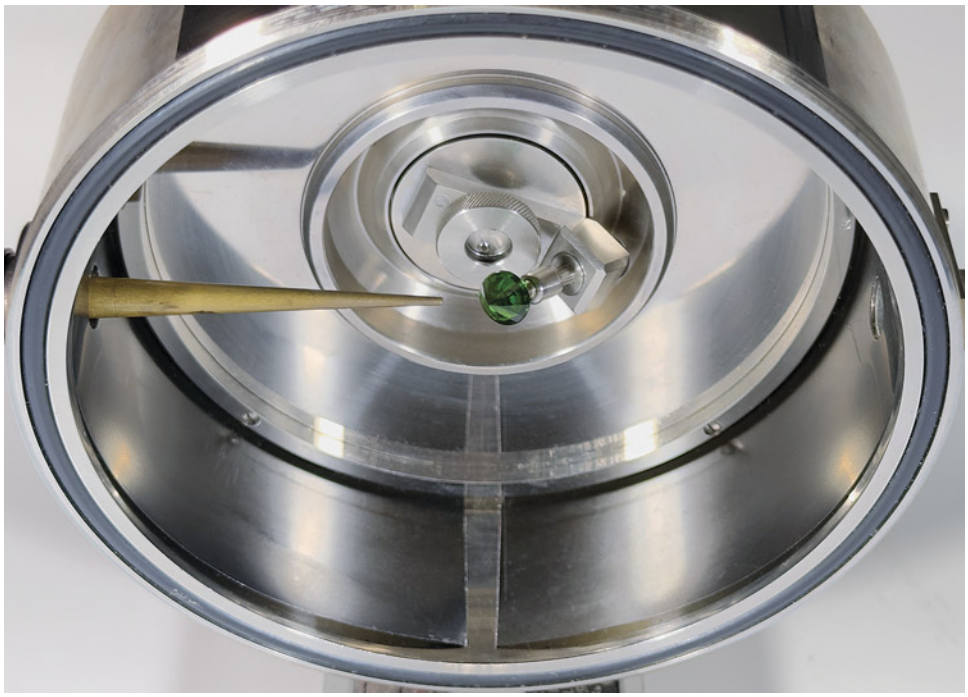

Figure 10. An old Debye-Scherrer camera formerly used at GIA. A faceted chrome diopside is mounted on a Gandolfi stage that rotates the gem around two intersecting axes to randomize its orientation during data collection. The X-ray beam is directed to the culet of the gemstone by the collimator on the left. A strip of X-ray film lines the inside of the camera to collect the diffraction pattern from the gemstone. The XRD pattern shown in figure 9C was taken using a similar device. Photo by Kevin Schumacher.

rotating Gandolfi stage (figure 10), even a single crystal grain can be used to generate a simulated powder diffraction pattern by randomizing its orientation in three dimensions (Gandolfi, 1967; Schmidt, 2019). The angular resolution and precision of the Bragg-Brentano geometry are generally better due to the well-focused X-ray beam. However, other factors such as detector distance, beam convergence, and bandwidth are more critical in determining the accuracy of the XRD data.

CONCLUSIONS

Raman spectroscopy and X-ray diffraction are perhaps the most overlooked methods in a gemological laboratory, since they are not always part of routine testing procedures. In many cases, the information they provide is already known or can be acquired through other methods such as standard gemological testing, infrared absorption, photoluminescence, or chemical analysis. However, these phase identification methods become a necessity when testing an obscure gem sample that cannot be conclusively identified by other means. While these materials may only represent a fraction of samples submitted, they are often the ones that require a positive test result. Most gem laboratories can detect diffusion treatment of corundum or identify the origin of an emerald, but recognizing a new mineral species previously unknown to geologists requires additional expertise. The ability to accurately identify atypical or uncommon gem materials is what truly differentiates gemological laboratories by their technical capabilities and depth of knowledge.

ABOUT THE AUTHORS

Dr. Shiyun Jin is a research scientist at GIA in Carlsbad, California. Dr. Evan M. Smith is a senior research scientist at GIA in New York.

ACKNOWLEDGMENTS

The authors would like to thank Artitaya Homkrajae for sharing her expertise on the application of Raman spectroscopy to biogenic carbonates in pearls and shells. The authors also thank the reviewers for many constructive comments and suggestions.

REFERENCES

Angel R.J., Alvaro M., Nestola F. (2022) Crystallographic methods for non-destructive characterization of mineral inclusions in diamonds. *Reviews in Mineralogy and Geochemistry*, Vol. 88, No. 1, pp. 257–305, http://dx.doi.org/10.2138/rmg.2022.88.05

Bersani D., Andò S., Vignola P., Moltifiori G., Marino I.-G., Lottici P.P., Diella V. (2009) Micro-Raman spectroscopy as a routine tool for garnet analysis. *Spectrochimica Acta Part A: Molecular and Biomolecular Spectroscopy*, Vol. 73, No. 3, pp. 484–491, http://dx.doi.org/10.1016/j.saa.2008.11.033

Bersani D., Lottici P.P. (2010) Applications of Raman spectroscopy to gemology. *Analytical and Bioanalytical Chemistry*, Vol. 397, No. 7, pp. 2631–2646, http://dx.doi.org/10.1007/s00216-010-3700-1

Bragg W.H., Bragg W.L. (1913) The reflection of X-rays by crystals. *Proceedings of the Royal Society of London, Series A,* Vol. 88, No. 605, pp. 428–438, http://dx.doi.org/10.1098/rspa.1913.0040

Calvo del Castillo H., Deprez N., Dupuis T., Mathis F., Deneckere A., Vandenabeele P., Calderón T., Strivay D. (2009) Towards the differentiation of non-treated and treated corundum minerals by ion-beam-induced luminescence and other complementary techniques. *Analytical and Bioanalytical Chemistry*, Vol. 394, No. 4, pp. 1043–1058, http://dx.doi.org/10.1007/s00216-009-2679-y

Crocombe R.A., Kammrath B.W., Leary P.E. (2023) Portable Raman spectrometers: How small can they get? *Raman Technology for Today's Spectroscopists*, Vol. 38, No. S6, pp. 32–40, http://dx.doi.org/10.56530/spectroscopy.cn5172t4

de Faria D.L.A., Venâncio Silva S., de Oliveira M.T. (1997) Raman microspectroscopy of some iron oxides and oxyhydroxides. *Journal of Raman Spectroscopy*, Vol. 28, No. 11, pp. 873–878, http://dx.doi.org/10.1002/(SICI)1097-4555(199711)28:11<873::AID-JRS177>3.0.CO;2-B

Dele M.L., Dhamelincourt P., Poirot J.P., Dereppe J.M., Moreaux C. (1997) Use of spectroscopic techniques for the study of natural and synthetic gems: Application to rubies. *Journal of Raman Spectroscopy*, Vol. 28, No. 9, pp. 673–676, http://dx.doi.org/10.1002/(SICI)1097-4555(199709)28:9<673::AID-JRS158>3.0.CO;2-H

Eaton-Magaña S., Breeding C.M. (2016) An introduction to photoluminescence spectroscopy for diamond and its applications in gemology. *G&G*, Vol. 52, No. 1, pp. 2–17, http://dx.doi.org/10.5741/GEMS.52.1.2

Eaton-Magaña S., Breeding C.M., Palke A.C., Homkrajae A., Sun Z., McElhenny G. (2021) Raman and photoluminescence mapping of gem materials. *Minerals*, Vol. 11, No. 2, article no. 177, http://dx.doi.org/10.3390/min11020177

Ende M., Chanmuang N.C., Reiners P.W., Zamyatin D.A., Gain S.E.M., Wirth R., Nasdala L. (2021) Dry annealing of radiation-damaged zircon: Single-crystal X-ray and Raman spectroscopy study. *Lithos*, Vol. 406–407, article no. 106523, http://dx.doi.org/10.1016/j.lithos.2021.106523

Everall N.J. (2009) Confocal Raman microscopy: Performance, pitfalls, and best practice. *Applied Spectroscopy*, Vol. 63, No. 9, pp. 245A–262A, http://dx.doi.org/10.1366/000370209789379196

Fan J.-L., Guo S.-G., Liu X.-L. (2009) The application of confocal micro-Raman spectrometer to nondestructive identification of filled gemstones. *Spectroscopy Letters*, Vol. 42, No. 3, pp. 129–135, http://dx.doi.org/10.1080/00387010902729112

Friedmann G.B. (1957) The relative intensities of the polarized components of the symmetric Raman line of calcite. PhD thesis, University of British Columbia.

Friedrich W., Knipping P., Laue M. (1913) Interferenzerscheinungen bei Röntgenstrahlen. *Annalen der Physik*, Vol. 346, No. 10,

pp. 971–988, http://dx.doi.org/10.1002/andp.19133461004
Fritsch E., Conner L., Koivula J.I. (1989) A preliminary gemological study of synthetic diamond thin films. *G&G*, Vol. 25, No. 2, pp. 84–90, http://dx.doi.org/10.5741/GEMS.25.2.84
Fritsch E., Rondeau B., Hainschwang T., Karampelas S. (2012) Raman spectroscopy applied to gemmology. In J. Dubessy et al., Eds., *Raman Spectroscopy Applied to Earth Sciences and Cultural Heritage*. European Mineralogical Union, pp. 455–489, http://dx.doi.org/10.1180/EMU-notes.12.13
Gandolfi G. (1967) Discussion upon methods to obtain X-ray powder patterns from a single crystal. *Acta Mineralogica-Petrografica*, Vol. 13, p. 67.
Gao J., Zhang J., Wu W., Yen C.-K., Su W. (2023) Polarized Raman spectroscopy reveals unaligned orientation in pearls. *Journal of Raman Spectroscopy*, Vol. 54, No. 4, pp. 371–378, http://dx.doi.org/10.1002/jrs.6492
Garnier V., Giuliani G., Ohnenstetter D., Fallick A.E., Dubessy J., Banks D., Vinh H.Q., Lhomme T., Maluski H., Pêcher A., Bakhsh K.A., Long P.V., Trinh P.T., Schwarz D. (2008) Marble-hosted ruby deposits from Central and Southeast Asia: Towards a new genetic model. *Ore Geology Reviews*, Vol. 34, No. 1-2, pp. 169–191, http://dx.doi.org/10.1016/j.oregeorev.2008.03.003
Graham I., Sutherland L., Zaw K., Nechaev V., Khanchuk A. (2008) Advances in our understanding of the gem corundum deposits of the West Pacific continental margins intraplate basaltic fields. *Ore Geology Reviews*, Vol. 34, No. 1-2, pp. 200–215, http://dx.doi.org/10.1016/j.oregeorev.2008.04.006
Grazulis S., Chateigner D., Downs R., Yokochi A.T., Quiros M., Lutterotti L., Manakova E., Butkus J., Moeck P., Le Bail A. (2009). Crystallography Open Database – An open access collection of crystal structures. *Journal of Applied Crystallography*, Vol. 42, No. 4, pp 726–729, http://dx.doi.org/10.1107/S0021889809016690
Groom C.R., Bruno J., Lightfoot M.P., Ward S.C. (2016) The Cambridge Structural Database. *Acta Crystallographica*, Vol. 72, No. 2, pp. 171–179, http://dx.doi.org/10.1107/S2052520616003954
Hammond C. (2015) X-ray diffraction: The contributions of Max von Laue, W.H. and W.L. Bragg and P.P. Ewald. In C. Hammond, Ed., *The Basics of Crystallography and Diffraction*. Oxford University Press, pp. 198–209.
Huong L.T.-T., Häger T., Hofmeister W. (2010) Confocal micro-Raman spectroscopy: A powerful tool to identify natural and synthetic emeralds. *G&G*, Vol. 46, No. 1, pp. 36–41, http://dx.doi.org/10.5741/GEMS.46.1.36
Ilieva A., Mihailova B., Tsintsov Z., Petrov O. (2007) Structural state of microcrystalline opals: A Raman spectroscopic study. *American Mineralogist*, Vol. 92, No. 8-9, pp. 1325–1333, http://dx.doi.org/10.2138/am.2007.2482
Jenkins A., Larsen R. (2004) Gemstone identification using Raman spectroscopy. *Spectroscopy*, Vol. 19, No. 4, pp. 20–25.
Johnson M.L., Elen S., Muhlmeister S. (1999) On the identification of various emerald filling substances. *G&G*, Vol. 35, No. 2, pp. 82–107, http://dx.doi.org/10.5741/GEMS.35.2.82
Jones J.B., Segnit E.R. (1975) Nomenclature and the structure of natural disordered (opaline) silica. *Contributions to Mineralogy and Petrology*, Vol. 51, No. 3, pp. 231–234, http://dx.doi.org/10.1007/BF00372083
Kabekkodu S., Dosen A., Blanton T. (2024) PDF-5+: A comprehensive Powder Diffraction File™ for materials characterization. *Powder Diffraction*, Vol. 39, No. 2, pp. 47–59, http://dx.doi.org/10.1017/S0885715624000150
Karampelas S., Fritsch E., Mevellec J.-Y., Gauthier J.-P., Sklavounos S., Soldatos T. (2007) Determination by Raman scattering of the nature of pigments in cultured freshwater pearls from the mollusk *Hyriopsis cumingi*. *Journal of Raman Spectroscopy*, Vol. 38, No. 2, pp. 217–230, http://dx.doi.org/10.1002/jrs.1626
Karampelas S., Fritsch E., Rondeau B., Andouche A., Métivier B. (2009) Identification of the endangered pink-to-red *Stylaster* corals by Raman spectroscopy. *G&G*, Vol. 45, No. 1, pp. 48–52, http://dx.doi.org/10.5741/GEMS.45.1.48
Karolina D., Maja M.-S., Magdalena D.-S., Grażyna Ż. (2022) Identification of treated Baltic amber by FTIR and FT-Raman – A feasibility study. *Spectrochimica Acta Part A: Molecular and Biomolecular Spectroscopy*, Vol. 279, article no. 121404, http://dx.doi.org/10.1016/j.saa.2022.121404
Kiefert L., Hänni H.A., Chalain J.-P. (2000) Identification of gemstone treatments with Raman spectroscopy. In *Optical Devices and Diagnostics in Materials Science*. Presented at the International Symposium on Optical Science and Technology, San Diego, California, pp. 241–251, http://dx.doi.org/10.1117/12.401634
Kiefert L., Hänni H.A., Chalain J.-P., Weber W. (1999) Identification of filler substances in emeralds by infrared and Raman spectroscopy. *Journal of Gemmology*, Vol. 26, No. 8, pp. 501–520.
Kiefert L., Hänni H.A., Ostertag T., Lewis I.R., Edwards H.G.M. (2001) Raman spectroscopic applications to gemmology. In *Handbook of Raman Spectroscopy: From the Research Laboratory to the Process Line*. Marcel Dekker, New York, pp. 469–490.
Kim Y., Caumon M.-C., Barres O., Sall A., Cauzid J. (2021) Identification and composition of carbonate minerals of the calcite structure by Raman and infrared spectroscopies using portable devices. *Spectrochimica Acta Part A: Molecular and Biomolecular Spectroscopy*, Vol. 261, article no. 119980, http://dx.doi.org/10.1016/j.saa.2021.119980
Kim Y., Lee E.J., Roy S., Sharbirin A.S., Ranz L.-G., Dieing T., Kim J. (2020) Measurement of lateral and axial resolution of confocal Raman microscope using dispersed carbon nanotubes and suspended graphene. *Current Applied Physics*, Vol. 20, No. 1, pp. 71–77, http://dx.doi.org/10.1016/j.cap.2019.10.012
Krzemnicki M.S., Lefèvre P., Zhou W., Braun J., Spiekermann G. (2023) Dehydration of diaspore and goethite during low-temperature heating as criterion to separate unheated from heated rubies and sapphires. *Minerals*, Vol. 13, No. 12, article no. 1557, http://dx.doi.org/10.3390/min13121557
Lafuente B., Downs R.T., Yang H., Stone N. (2015) The power of databases: The RRUFF project. In T. Armbruster and R.M. Danisi, Eds., *Highlights in Mineralogical Crystallography*. W. de Gruyter GmbH, Berlin, pp. 1–29.
Łodziński M., Sitarz M., Stec K., Kozanecki M., Fojud Z., Jurga S. (2005) ICP, IR, Raman, NMR investigations of beryls from pegmatites of the Sudety Mts. *Journal of Molecular Structure*, Vol. 744-747, pp. 1005–1015, http://dx.doi.org/10.1016/j.molstruc.2004.12.042
Lu R. (2009) Crystallographic orientation of biogenic aragonite in pearls. *GIA Research News*, April 8, https://www.gia.edu/ongoing-research/crystallographic-orientation-of-biogenic-aragonite-in-pearls
Maschio L., Demichelis R., Orlando R., De La Pierre M., Mahmoud A., Dovesi R. (2014) The Raman spectrum of grossular garnet: A quantum mechanical simulation of wavenumbers and intensities. *Journal of Raman Spectroscopy*, Vol. 45, No. 8, pp. 710–715, http://dx.doi.org/10.1002/jrs.4527
Maschio L., Kirtman B., Salustro S., Zicovich-Wilson C.M., Orlando R., Dovesi R. (2013) Raman spectrum of pyrope garnet. A quantum mechanical simulation of frequencies, intensities, and isotope shifts. *The Journal of Physical Chemistry A*, Vol. 117, No. 45, pp. 11464–11471, http://dx.doi.org/10.1021/jp4099446
McClure S.F., Smith C.P., Wang W., Hall M. (2006) Identification and durability of lead glass–filled rubies. *G&G*, Vol. 42, No. 1, pp. 22–34, http://dx.doi.org/10.5741/GEMS.42.1.22
Nickel E.H., Grice J.D. (1998) The IMA Commission on New Minerals and Mineral Names: Procedures and guidelines on mineral nomenclature, 1998. *Mineralogy and Petrology*, Vol. 64, No. 1-4, pp. 237–263, http://dx.doi.org/10.1007/BF01226571
Okumura T., Suzuki M., Nagasawa H., Kogure T. (2010) Characteristics of biogenic calcite in the prismatic layer of a pearl oyster, *Pinctada fucata*. *Micron*, Vol. 41, No. 7, pp. 821–826, http://dx.doi.org/10.1016/j.micron.2010.05.004
Palanza V., Di Martino D., Paleari A., Spinolo G., Prosperi L. (2008)

Micro-Raman spectroscopy applied to the study of inclusions within sapphire. *Journal of Raman Spectroscopy*, Vol. 39, No. 8, pp. 1007–1011, http://dx.doi.org/10.1002/jrs.1939
Palke A.C., Henling L.M., Ma C., Rossman G.R., Sun Z., Renfro N., Kampf A.R., Thu K., Myo N., Wongrawang P., Weeramonkhonlert V. (2021) Johnkoivulaite, $Cs(Be_2B)Mg_2S_{16}O_{18}$, a new mineral of the beryl group from the gem deposits of Mogok, Myanmar. *American Mineralogist*, Vol. 106, No. 11, pp. 1844–1851, http://dx.doi.org/10.2138/am-2021-7785
Palke A.C., Saeseaw S., Renfro N.D., Sun Z., McClure S.F. (2019a) Geographic origin determination of ruby. *G&G*, Vol. 55, No. 4, pp. 580–613, http://dx.doi.org/10.5741/GEMS.55.4.580
——— (2019b) Geographic origin determination of blue sapphire. *G&G*, Vol. 55, No. 4, pp. 536–579, http://dx.doi.org/10.5741/GEMS.55.4.536
Pasteris J.D., Beyssac O. (2020) Welcome to Raman spectroscopy: Successes, challenges, and pitfalls. *Elements*, Vol. 16, No. 2, pp. 87–92, http://dx.doi.org/10.2138/gselements.16.2.87
Pérez-Huerta A., Cuif J.-P., Dauphin Y., Cusack M. (2014) Crystallography of calcite in pearls. *European Journal of Mineralogy*, Vol. 26, No. 4, pp. 507–516, http://dx.doi.org/10.1127/0935-1221/2014/0026-2390
Qiao L., Feng Q.-L., Li Z. (2007) Special vaterite found in freshwater lackluster pearls. *Crystal Growth & Design*, Vol. 7, No. 2, pp. 275–279, http://dx.doi.org/10.1021/cg060309f
Raman C.V. (1922) *Molecular Diffraction of Light*. University of Calcutta, Kolkata, India.
Rankin A.H., Edwards W. (2003) Some effects of extreme heat treatment on zircon inclusions in corundum. *Journal of Gemmology*, Vol. 28, No. 5, pp. 257–264.
Sastry M.D., Mane S.N., Gaonkar M.P., Bagla H., Panjikar J., Ramachandran K.T. (2009) Evidence of colour-modification induced charge and structural disorder in natural corundum: Spectroscopic studies of beryllium treated sapphires and rubies. *IOP Conference Series: Materials Science and Engineering*, Vol. 2, No. 1, article no. 012007, http://dx.doi.org/10.1088/1757-899X/2/1/012007
Schmidt G. (2019) The Gandolfi stage: A novel approach for the analysis of single crystals and small volume samples. *IUCr Newsletter*, Vol. 27, No. 1, p. A28.
Smallwood A.G., Thomas P.S., Ray A.S. (1997) Characterisation of sedimentary opals by Fourier transform Raman spectroscopy. *Spectrochimica Acta Part A: Molecular and Biomolecular Spectroscopy*, Vol. 53, No. 13, pp. 2341–2345, http://dx.doi.org/10.1016/S1386-1425(97)00174-1
Smith E.M., Krebs M.Y., Genzel P.-T., Brenker F.E. (2022) Raman identification of inclusions in diamond. *Reviews in Mineralogy and Geochemistry*, Vol. 88, No. 1, pp. 451–473, http://dx.doi.org/10.2138/rmg.2022.88.08
Smith E.M., Nestola F., Pasqualetto L., Zorzi F., Secco L., Wang W. (2021) The new mineral crowningshieldite: A high-temperature NiS polymorph found in a type IIa diamond from the Letseng mine, Lesotho. *American Mineralogist*, Vol. 106, No. 2, pp. 301–308, http://dx.doi.org/10.2138/am-2020-7567
Sodo A., Casanova Municchia A., Barucca S., Bellatreccia F., Della Ventura G., Butini F., Ricci M.A. (2016) Raman, FT-IR and XRD investigation of natural opals. *Journal of Raman Spectroscopy*, Vol. 47, No. 12, pp. 1444–1451, http://dx.doi.org/10.1002/jrs.4972
Soldati A.L., Jacob D.E., Wehrmeister U., Hofmeister W. (2008) Structural characterization and chemical composition of aragonite and vaterite in freshwater cultured pearls. *Mineralogical Magazine*, Vol. 72, No. 2, pp. 579–592, http://dx.doi.org/10.1180/minmag.2008.072.2.579
Verkhovskaia I., Prokopenko V. (2020) Raman scattering spectra of amber. *E3S Web of Conferences*, Vol. 164, article no. 14003, http://dx.doi.org/10.1051/e3sconf/202016414003
Wang W., Scarratt K., Emmett J.L., Breeding C.M., Douthit T.R. (2006) The effects of heat treatment on zircon inclusions in Madagascar sapphires. *G&G*, Vol. 42, No. 2, pp. 134–150, http://dx.doi.org/10.5741/GEMS.42.2.134
Wehrmeister U., Jacob D.E., Soldati A.L., Häger T., Hofmeister W. (2007) Vaterite in freshwater cultured pearls from China and Japan. *Journal of Gemmology*, Vol. 31, No. 7-8, pp. 399–412.
Xu W., Krzemnicki M.S. (2021) Raman spectroscopic investigation of zircon in gem-quality sapphire: Application in origin determination. *Journal of Raman Spectroscopy*, Vol. 52, No. 5, pp. 1011–1021, http://dx.doi.org/10.1002/jrs.6092
Yoshimi K., Shoji M., Ogawa T., Yamauchi A., Naganuma T., Muramoto K., Hanada S. (2004) Microstructure and orientation distribution of aragonite crystals in nacreous layer of pearl shells. *Materials Transactions*, Vol. 45, No. 4, pp. 999–1004, http://dx.doi.org/10.2320/matertrans.45.999
Zhang M., Salje E.K.H., Capitani G.C., Leroux H., Clark A.M., Schlüter J., Ewing R.C. (2000a) Annealing of α-decay damage in zircon: A Raman spectroscopic study. *Journal of Physics: Condensed Matter*, Vol. 12, No. 13, article no. 3131, http://dx.doi.org/10.1088/0953-8984/12/13/321
Zhang M., Salje E.K.H., Farnan I., Graeme-Barber A., Daniel P., Ewing R.C., Clark A.M., Leroux, H. (2000b) Metamictization of zircon: Raman spectroscopic study. *Journal of Physics: Condensed Matter*, Vol. 12, No. 8, pp. 1915–1925, http://dx.doi.org/10.1088/0953-8984/12/8/333
Zhou C., Jin S., Sun Z., Homkrajae A., Myagkaya E., Nilpetploy N., Lawanwong K. (2023) Disordered dolomite as an unusual biomineralization product found in the center of a natural *Cassis* pearl. *PLOS One*, Vol. 18, No. 4, article no. e0284295, http://dx.doi.org/10.1371/journal.pone.0284295

CHEMICAL ANALYSIS IN THE GEMOLOGICAL LABORATORY: XRF AND LA-ICP-MS

Ziyin Sun, Michael Jollands, and Aaron C. Palke

The modern gem trade faces challenges that require sophisticated analytical instrumentation beyond what was needed in the early days of gemological laboratories. Several identification problems can only be solved through precise measurements of the chemical composition of a gemstone. The two techniques used most commonly in an advanced gemological laboratory are energy-dispersive X-ray fluorescence (EDXRF, or XRF) and laser ablation–inductively coupled plasma–mass spectrometry (LA-ICP-MS). XRF was initially introduced for general identification purposes and detection of some treatments such as lead glass filling in rubies. LA-ICP-MS, a much more sensitive technique, emerged in the detection of beryllium-diffused sapphires but has become an invaluable tool for determining the geographic origin of many colored stones. This contribution provides a technical overview of both techniques and presents several examples of how they are employed in the laboratory for gemstone identification.

This contribution describes two analytical techniques: X-ray fluorescence (XRF) and laser ablation–inductively coupled plasma–mass spectrometry (LA-ICP-MS). Both are instrumental in gemological testing, as they enable the chemical composition of a stone (usually a colored stone) to be determined either nondestructively (XRF) or by sampling only minimal amounts of the stone (LA-ICP-MS). These analytical methods are essential tools in the modern gemological laboratory for gemstone identification, geographic origin determination, and detecting certain treatments. With XRF, a gemstone is bombarded with high-energy X-rays, causing the atoms in the stone to emit characteristic X-rays that can be measured with a spectrometer to establish its elemental composition. LA-ICP-MS uses a focused laser to microsample a gemstone (typically on the girdle) with a very small amount of material delivered into an inductively coupled plasma (ICP) and then transferred into a mass spectrometer (MS) for chemical analysis. LA-ICP-MS offers greater sensitivity, lower detection limits, and the capacity to detect a wider range of elements (including those lighter than sodium). The laser-induced breakdown spectroscopy (LIBS) technique will also be briefly introduced. LIBS and LA-ICP-MS are both microanalytical techniques, and the two share some similarities.

Together, XRF and LA-ICP-MS form a powerful arsenal for gemologists seeking to unravel the chemical mysteries of some of the world's most captivating gemstones. Whether used singly or in combination, these techniques have vastly expanded our knowledge of gemstone composition, provenance, and treatment history, and they will undoubtedly continue to play a pivotal role in advancing the field of gemological research.

TECHNICAL BACKGROUND

X-Ray Fluorescence (XRF) Spectrometry. This was one of the first chemical analysis techniques adopted by gemological laboratories. Prior to the 1980s, standard gemological testing was generally sufficient for routine gem species identification. However, as new challenges arose—distinguishing natural from synthetic stones, detecting lead glass filling in rubies, and separating low- and high-iron rubies for origin determination, to name a few—gemological laboratories needed to expand their analytical capabilities to include measurement of a stone's chemical composition. XRF spectrometers were introduced to gemological labs in the 1980s and were, at the time, the most accessible instruments for conducting nondestructive chemical testing of gemstones.

X-rays are electromagnetic waves with short wavelength and high energy, falling between ultra-

See end of article for About the Authors and Acknowledgments.
GEMS & GEMOLOGY, Vol. 60, No. 4, pp. 536–559,
http://dx.doi.org/10.5741/GEMS.60.4.536

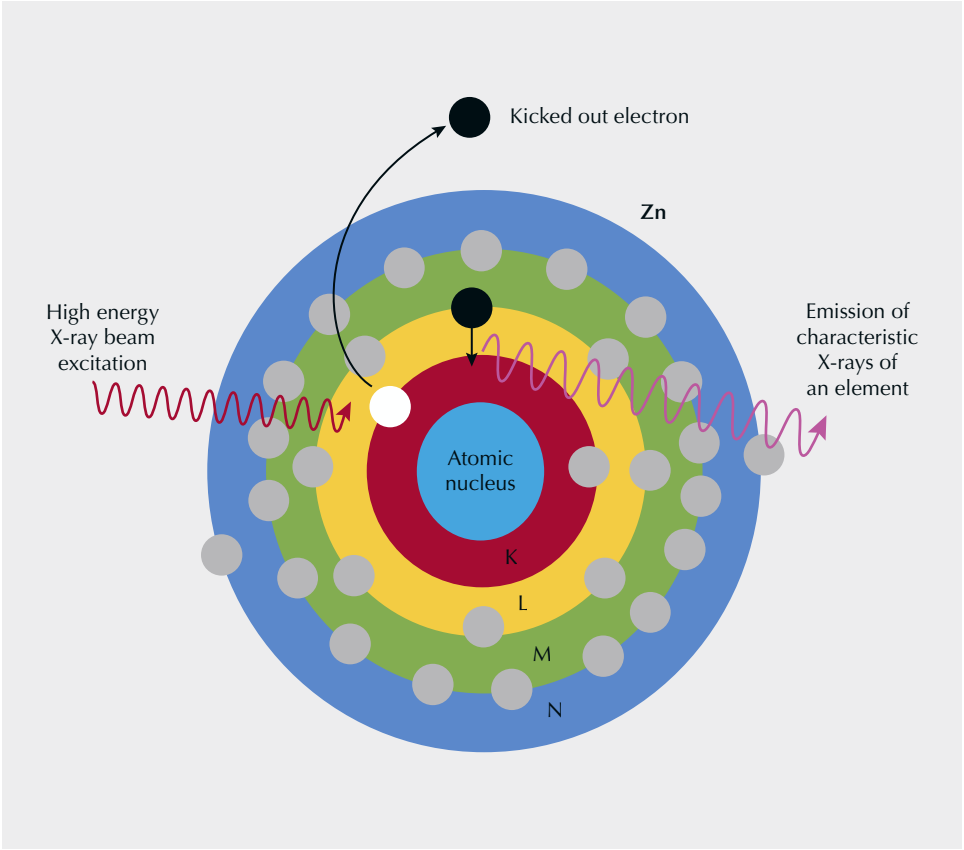

Figure 1. The principle of fluorescent X-ray emission. An X-ray tube directs high-energy X-rays at the sample, some of which penetrate atoms in the sample and can knock out inner-shell electrons. These atoms then emit characteristic X-rays when an outer-shell electron falls in to replace the ejected electron. These characteristic X-rays can be measured to fingerprint the elements present in the sample.

violet rays and gamma rays on the electromagnetic spectrum. In an XRF unit, a sample such as a gemstone is bombarded with a stream of X-rays generated by passing a current through a metal filament, which then emits electrons that are accelerated toward a metal target, often rhodium, molybdenum, tungsten, or copper. When the electrons strike this metal target, it emits a stream of X-rays directed at the gemstone to be analyzed. The X-rays are usually directed at the table of a faceted stone or either the dome or base of a cabochon. Upon striking the gem's surface, the X-rays interact with its constituent atoms. While many of the X-rays are scattered away, some will penetrate into the inner electron shells of the atoms, knocking out an electron (as long as the incident X-ray has energy greater than the binding energy of these inner electrons) (figure 1). This creates an electron hole, which is then filled by an electron from an outer electron shell. Each electron shell in an atom has a discrete, well-defined energy level. When an outer shell electron falls into an inner shell, it releases energy in the form of an X-ray whose energy corresponds to the difference in energy levels between the two shells. This phenomenon is known as fluorescence and is similar, at least in principle, to photoluminescence, described by Eaton-Magaña et al. (2024), pp. 494–517 of this issue.

Each atom has a unique "fingerprint" of electron shell energy levels. This means that each type of atom in a material will emit its own characteristic pattern (spectrum) of X-rays corresponding to the differences in energy levels between its inner and outer electron shells. In other words, the pattern of energies (or wavelengths) of emitted X-rays measured by an

In Brief

- Many gemological questions require accurate and precise measurements of a gemstone's chemistry.
- X-ray fluorescence spectroscopy is a relatively simple technique to measure chemistry, but it has largely been supplanted by laser ablation–inductively coupled plasma–mass spectrometry, which has better precision and measures a wider range of elements.
- While both techniques are used in identification challenges, one main focus for chemical measurements is geographic origin determination.

Box A: Portable XRF Devices

Since XRF was first used for elemental analysis in 1913, the technology and the device have continued to advance. Around the mid-1960s, portable XRF devices started to enter the market. The early versions consisted of at least two units: a probe with a measurement head and a processing/display unit connected to the probe. Although these instruments still lacked true mobility and a user-friendly interface, they did allow for on-site analyses with reasonable results. Industries began to realize that this category of devices could lower the cost of sampling, transportation, and analyzing, reducing operational downtime.

With increasing demand from multiple industries, the first fully handheld single-unit XRF analyzer was introduced in 1994. Niton, which later became part of Thermo Fisher Scientific, released the XL-309. This device weighed only 1.13 kg (2.5 lbs.) and featured enhanced analytical performance, at a much lower price point than its predecessors.

With the publication of the U.S. Environmental Protection Agency's Standard Method 6200 in 1996, field-portable XRF was recognized as an elemental analytical method. Since then, the portable XRF landscape has evolved rapidly. Miniaturized X-ray tubes have replaced radioactive isotope emitters to make portable devices much smaller, more affordable, better-performing, and safer. Desktop and handheld devices alike are widely applied in numerous industries: mining, agriculture, art conservation, archaeology, forensics, petroleum, aerospace, nanotechnology, food and beverage, consumer goods, and jewelry, to name a few.

As the demand for portable XRF units continues to grow and new markets develop globally, nearly all instrumentation companies offer their own product line. Key players in this field include Thermo Fisher Scientific, Bruker, Rigaku, Olympus, Fischer Technologies, Shimadzu, Spectro Analytical Instruments, Horiba, Hitachi High-Tech, and Oxford Instruments. These manufacturers offer multiple models of portable XRF devices to cater to different users. The price of a unit today can range from thousands to tens of thousands of U.S. dollars. While most portable devices are not designed specifically for the gem and jewelry industry, many can easily tackle precious metal analysis and be adapted to gem identification.

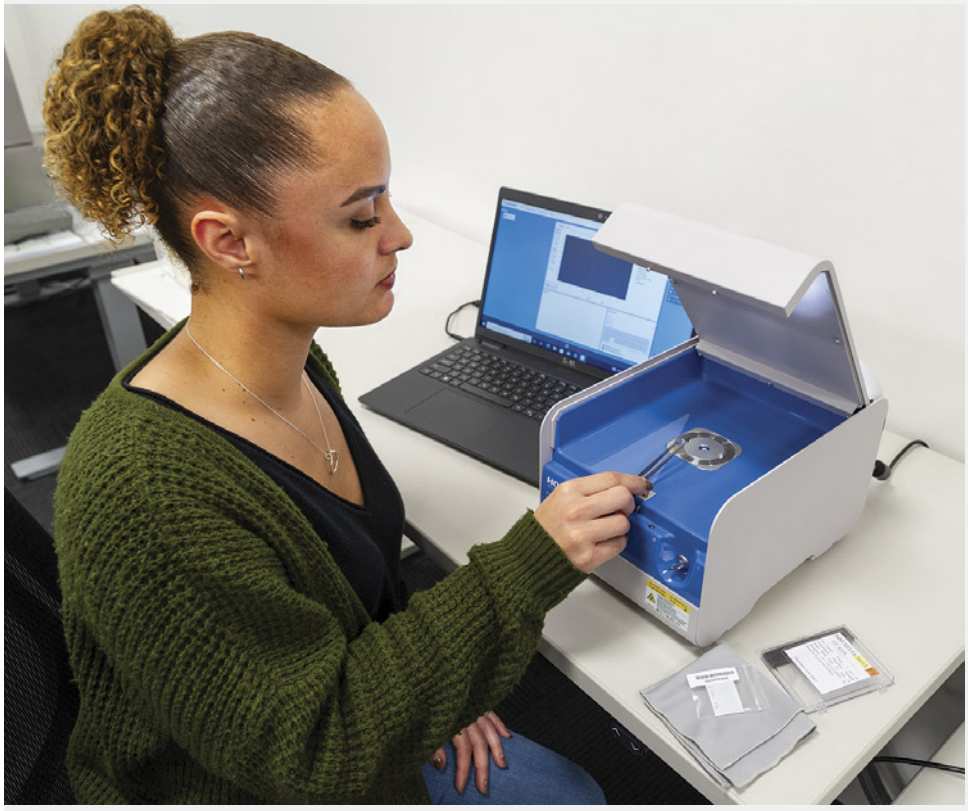

Figure A-1. The Horiba Mesa-50 XRF is used by GIA's laboratories. Gemstones and jewelry pieces can be placed on top of the testing window. A laptop is connected to the testing unit, and the system also has a built-in camera that allows the user to adjust the position of the X-ray beam on the sample. Photo by Kevin Schumacher.

Figure A-2. The Thermo Scientific Niton XL2 is the portable XRF device used by GIA to quickly test precious metals. Photo by Emily Lane; courtesy of Hallock Coin.

One key consideration in using a portable XRF apparatus is safety. Regulations on X-ray usage can vary by country and jurisdiction. Before buying and using any X-ray generating device, a user must complete required training and adopt defined safety protocols. If using these devices for teaching or allowing others to operate them, the required training and protection must be provided.

One of the units at GIA is the Horiba Mesa-50, a compact desktop XRF that can be moved from one place to another or transported off-site if needed (figure A-1). Instruments like this are designed to be very user-friendly. There is no sample preparation required other than cleaning the surface. Many of these instruments have built-in cameras to allow users to target a specific area of the material being tested. The use of the fundamental parameters method for calculating concentrations further streamlines operations and allows data to be collected without the use of external standards, which can yield greater accuracy but are cumbersome to set up and may be unnecessary for routine identification and characterization. These desktop instruments share many of the same capabilities as more robust lab units, including detection of silver in color-treated pearls, detection of coatings on zoisite, and gemstone identification, among others. The Horiba Mesa-50 also has a "recipe" procedure where users can quickly create new methods and train them with known samples for rapid identification. Some disadvantages of desktop units include their inability to draw a vacuum in the sample chamber and the weaker signals produced from the analyzed gemstones.

In recent years, companies have released compact, handheld XRF units designed for field use. Of particular interest for the gem and jewelry industry are handheld XRF units optimized for precious metals testing, allowing rapid measurement of gold, silver, and platinum contents in jewelry in an office setting or in the field (figure A-2).

CHECKLIST FOR PURCHASING A PORTABLE XRF DEVICE

Self-Assessment

- Do I need elemental analysis for my precious metals and gemstones?
- What types of elements do I need to detect or analyze?
- What detection limit is needed for the elements I want to focus on?
- Do I have the ability to build a database for gem identification?
- What is the mobility requirement of this device?
- What is my budget?

Questions for the Manufacturer

- What is the device designed for?
- What types of samples can be tested?
- Is special sample preparation needed?
- What is the lightest element the device can analyze?
- What is the safety standard of the device?

Additional Reading

https://www.portaspecs.com/the-evolution-of-portable-xrf-instruments/ (timeline of portable XRF)
https://www.azonano.com/article.aspx?ArticleID=6531
https://www.thermofisher.com/blog/materials/understanding-the-journey-from-lab-based-to-handheld-xrf-technology

XRF is specific to each element. By measuring the X-ray energies across a broad energy range, one can identify not only single elements but also the majority of elements that make up a gem (excluding very light elements; see below). Most XRF systems use a type of detector that sorts X-rays by their energy, and this is known as an energy-dispersive XRF (EDXRF). The output is a spectrum plot with energy on the x-axis and intensity on the y-axis. Taking this a step further, the intensities of the peaks are proportional to the concentrations of those elements. Higher relative fluorescence intensity indicates a higher concentration, enabling quantitative analysis of the elements (Johnson and King, 1987). By calibrating the XRF detector using well-characterized reference standards, it is possible to quantify the concentrations of various major and minor trace elements in an unknown material. While most XRF units are desktop units, several portable and even handheld units are available in the market. These are often used on-site in mining or industrial applications or in jewelry stores or pawn shops for precious metals testing (box A).

EDXRF can measure most elements in the periodic table either semiquantitatively or quantitatively. However, it cannot measure elements with an atomic number less than 11, that of sodium. For instance, EDXRF cannot detect beryllium in corundum (He and Van Espen, 1991). A related technique, wavelength-dispersive XRF (WDXRF), is able to measure beryllium, at least at higher concentrations in the wt.% range, but these instruments are less efficient and more costly than EDXRF systems. For the remainder of this paper, "XRF" will refer specifically to EDXRF. The XRF instruments typically found in gemological laboratories consist of an X-ray generator, a sample chamber, a detector, and a data processing system that outputs the concentrations of measurable elements in the sample. XRF can measure lighter elements from magnesium to calcium in the wt.% range, transition metals around the 0.1 wt.% range, and many heavier elements down to the 0.01 wt.% range.

Micro-Analytical Techniques for Gemstone Trace Element Chemistry: LA-ICP-MS. The term *LA-ICP-MS* describes two separate but interconnected parts of a system. "LA" stands for laser ablation, a technique that allows very small amounts of material to be removed from a sample. This can be thought of as a micrometer-scale microdrill, but with the physical drill bit replaced by a pulsing laser. "ICP-MS" stands for inductively coupled plasma–mass spectrometry, which determines the chemical composition of the ablated material by atomizing and ionizing it in a plasma and filtering the charged particles by mass through a mass spectrometer.

ICP-MS systems first became commercially available in the early 1980s, and the first demonstration of coupling ICP-MS to a laser ablation system followed shortly after (Gray, 1985). Since then, the technique has improved continuously (Sylvester and Jackson, 2016), although the fundamental concept remains basically the same. The lasers now use shorter, faster pulses of light with shorter wavelengths and higher energy. Different carrier gases are used, while optical components and sample holding methods have been modified. With these refinements, ICP-MS systems have been improved to maximize, among other factors, speed and sensitivity.

The LA-ICP-MS technique was adopted by gemological laboratories in the early 2000s. This was driven largely by the need to detect beryllium in response to the emerging problem of beryllium-diffused corundum (Emmett et al., 2003). Until then, the most common microanalytical technique applied to gemstones was electron probe microanalysis (EPMA) (e.g., Rinaldi and Llovet, 2015). EPMA is similar in principle to XRF, but with a focused electron beam as the excitation source for obtaining characteristic X-rays from the sample. Applications of LA-ICP-MS have since expanded to include such treatments as cobalt diffusion of spinel (Saeseaw et al., 2015) and, significantly, geographic origin determination (Pornwilard et al., 2011; Palke et al., 2019 a,b).

For similar reasons, the related technique of LIBS was being adopted in gemological testing at about the same time (Krzemnicki et al., 2004, 2006; McMillan et al., 2006). In this method, the laser ablation system is not interfaced to an ICP-MS. Rather, the small amount of light created as a result of the laser ablation is recorded using an optical spectrometer. The wavelengths of this emitted light can be used to determine, at least in part, the composition of the stone.

Colored stones submitted for analysis to a major gemological laboratory such as GIA often undergo LA-ICP-MS. The only evidence of this analysis consists of small holes, normally placed on the girdle and generally tens of micrometers wide and a few micrometers deep, that are essentially invisible to the unaided eye (figure 2). In the following section, we describe the complex analysis process and the vast amount of information that can be revealed.

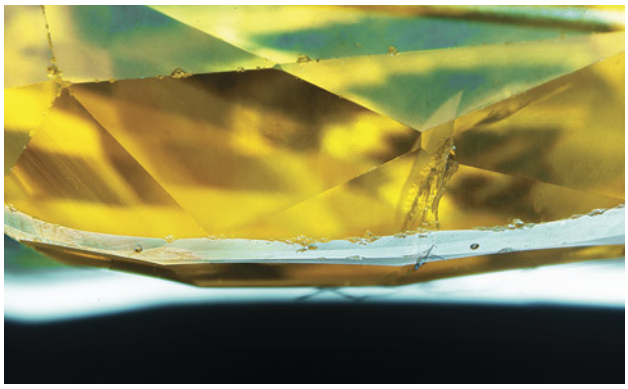

Figure 2. The appearance of laser ablation spots on a faceted yellow sapphire. There are two ablation pits on the girdle, located left and right of center. They are 55 µm in diameter and essentially undetectable without a microscope or loupe. Photomicrograph by Aaron Palke; field of view 5.21 mm.

How Do LA-ICP-MS Systems Work? Starting with the LA system, the laser is its most important component. The lasers typically used in modern laser ablation systems for LA-ICP-MS operate in the ultraviolet range, using 193, 213, or 266 nm light. The latter two are solid-state lasers produced using a crystal medium and additional frequency-doubling crystals, while the former is generated from a precise and potentially hazardous mix of gases containing fluorine. The 213 nm systems provide a compromise between ablation quality (generally better at shorter wavelengths) and user-friendliness (better at longer wavelengths), and these are used at GIA's global laboratories. Figure 3 shows the laser head of one of these systems. It houses a Nd:YAG laser rod inside a xenon flash lamp that uses ultraviolet light to stimulate fluorescence in the laser rod. Nd:YAG can produce intense infrared light with a wavelength of 1064 nm, which is then frequency-quintupled (i.e., the frequency is increased by a factor of five and the wavelength decreased by the same factor) to a wavelength of 213 nm using special nonlinear optical crystals.

The laser light is then passed through an optical channel consisting of a series of mirrors, lenses, apertures, and other optical components. The last part of the optical channel is a microscope objective, which focuses the beam onto the sample. The optical channel creates a small (tens of micrometers), well-defined beam of light that can ablate material from the sample.

The samples are loaded into a cell (effectively a closed box) that has a controlled stream of gas, usually pure helium, flowing in and out. The cells used in gemstone analysis must be deep enough to hold large, loose stones or even mounted jewelry.

The laser is then focused onto the surface of the stone and pulsed, typically between 5 and 20 Hz (pulses per second). When the laser strikes the sample with high enough energy, ablation will occur. In other words, the bonds holding the atoms together in the crystal can be broken, allowing the atoms to

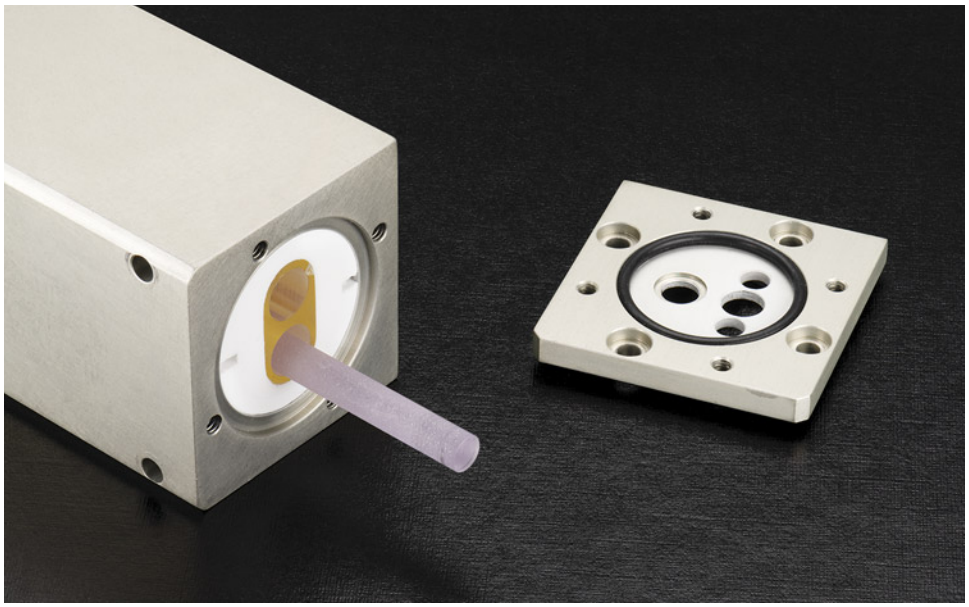

Figure 3. The laser head of one of the 213 nm laser ablation systems used at GIA. In this system, a Nd:YAG rod is housed in a chamber along with a xenon flash lamp that stimulates the production of 1064 nm fluorescence from the Nd:YAG. This fluorescence is frequency-quintupled to 213 nm light and focused into a laser. Photo by Emily Lane.

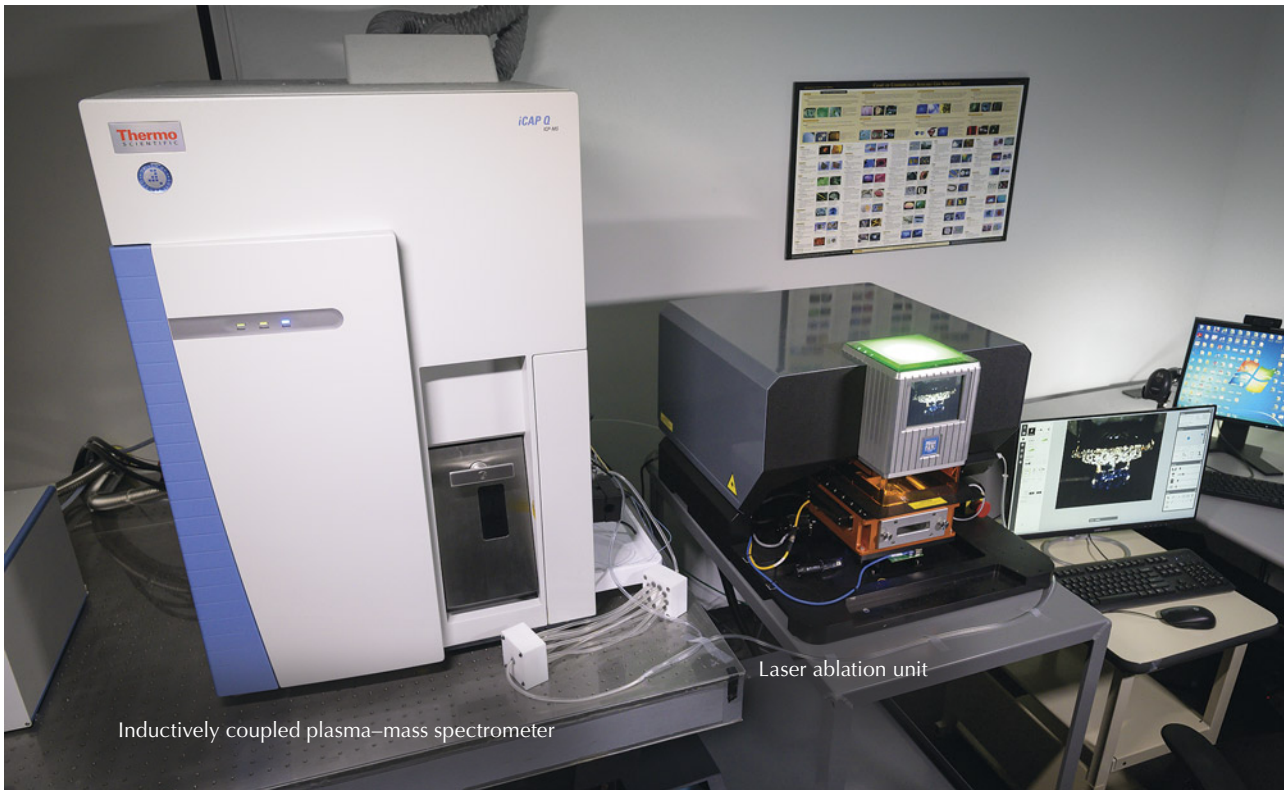

Figure 4. The LA-ICP-MS system at GIA's Carlsbad laboratory, consisting of a New Wave Research ESI NWR 213 laser ablation system and a Thermo Fisher Scientific iCAP-Q inductively coupled plasma–mass spectrometer. Photo by Kevin Schumacher.

be freed from the solid. These evaporated atoms form a plasma, which can be considered a highly energetic gas. As the plasma loses energy, the ablated material condenses into droplets that are rapidly swept away from the site of ablation by the helium carrier gas, toward the ICP-MS.

The helium is generally mixed with argon gas and passed together into an argon plasma (the ICP), which converts the material coming from the laser into ions. This ionization is necessary because the mass spectrometer does not measure mass, but rather the ratio of mass to charge. This means that an electron, or multiple electrons, must be stripped from the atoms being analyzed. The ionized material from the plasma, which is at atmospheric pressure, then moves through small orifices into the high-vacuum body of the mass spectrometer.

At this point, the stream of ions of ablated material also contains contaminants such as nitrogen, oxygen, and carbon from the atmosphere and argon from the plasma. The next step is to separate the ions based on their mass-to-charge ratio, which is accomplished in most LA-ICP-MS systems used in gemological laboratories through a quadrupole mass analyzer. The quadrupole consists of four cylindrical rods that selectively allow only species with a certain mass-to-charge ratio to pass through, by applying oscillating electric fields. Ions that are too heavy or too light are filtered out. Ions that have successfully passed through the quadrupole are then detected, typically with an "electron multiplier" that converts the number of ions that have exited the quadrupole into an electrical current, which can be recorded by a computer.

As with XRF, periodically analyzing materials with well-known concentrations (i.e., standards) establishes the relationship between the recorded signal and the concentration of a given element. This allows the concentration of elements in the gemstone to be determined.

The full LA-ICP-MS system used at GIA is shown in figure 4, and a diagram illustrating the general process of analyzing a gemstone by LA-ICP-MS is shown in figure 5. One of the major advantages of LA-ICP-MS is the ability to analyze nearly the entire periodic table, including particularly important elements in the gemological laboratory such as beryllium.

The LIBS technique also relies on the use of a laser ablation unit, but its principle of measuring chemistry is fundamentally different. In the process of laser ablation, a small plasma is generated at the surface of the material being analyzed. As the plasma cools and condenses, light is emitted within micro- to milliseconds after the laser pulse. Similar to XRF, the light's wavelength is related to the energy levels in the atoms that have been ablated, which is different for each element. By pointing a fiber-optic probe at the ablation site and connecting this to one or more spectrometers, the spectrum of light emitted following ablation is monitored. Every ablation shot yields an emission spectrum, which contains information regarding the composition of the material being ablated. In general, LIBS is very powerful at detecting the major elements in a sample, as well as light elements (such as hydrogen, lithium, beryllium, and sodium) at low concentrations (parts-per-million levels or lower). The intensities of the element-specific emission lines are a function of the concentration of the element, so LIBS data can, in some cases, be turned into quantitative data. In other cases, it can be used for a rapid presence/absence decision, such as the presence of beryllium in corundum.

TRACE AND MAJOR ELEMENT CHEMISTRY IN THE GEMOLOGICAL LABORATORY

Qualitative XRF Applications. Some of the most basic applications of XRF in a gemological laboratory involve simple qualitative analysis to ascertain the presence or absence of certain chemical elements that can identify treatments.

Glass-Filled Rubies. One of the most common applications of XRF is the detection of lead glass–filled rubies. Highly fractured and included ruby can be treated with lead glass, which fills fractures and effectively hides them by closely matching the refractive index of corundum. Lead glass filling can often be detected using a gemological microscope

Figure 5. The process of chemical analysis using an LA-ICP-MS system, shown from right to left. Material is laser-ablated from a gemstone in the sample chamber. The ablated material is carried to the argon plasma (temperature of around 10000 K) by helium gas, where it is atomized and ionized. Positively charged ions from the sample pass through a series of cones and are focused into a beam electronically through a series of ion optics. A tunable quadrupole magnet selectively filters the isotope of interest by targeting a specific mass-to-charge ratio (m/z), delivering all ions with that value to the detector.

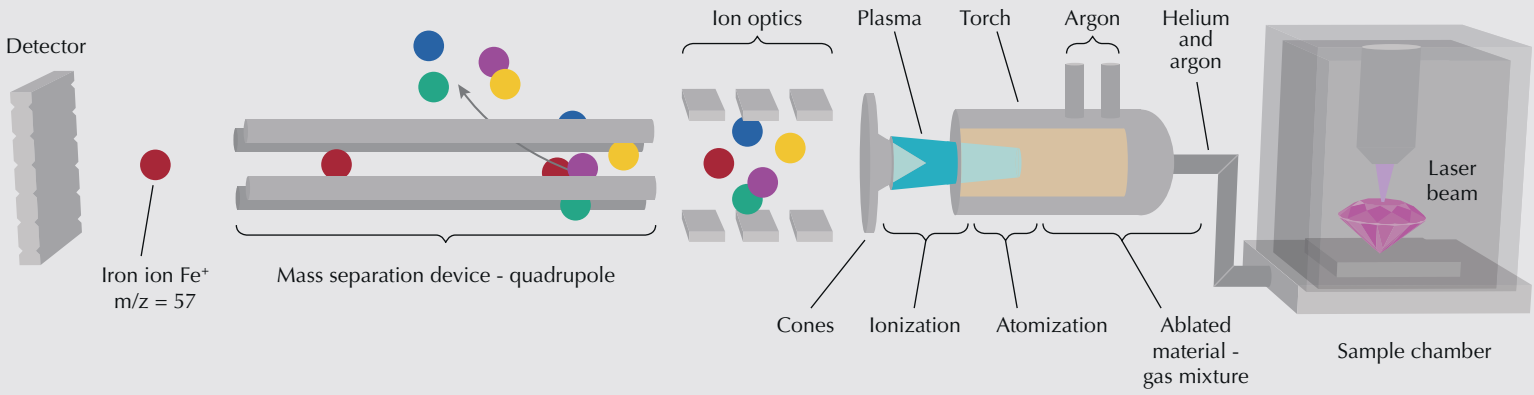

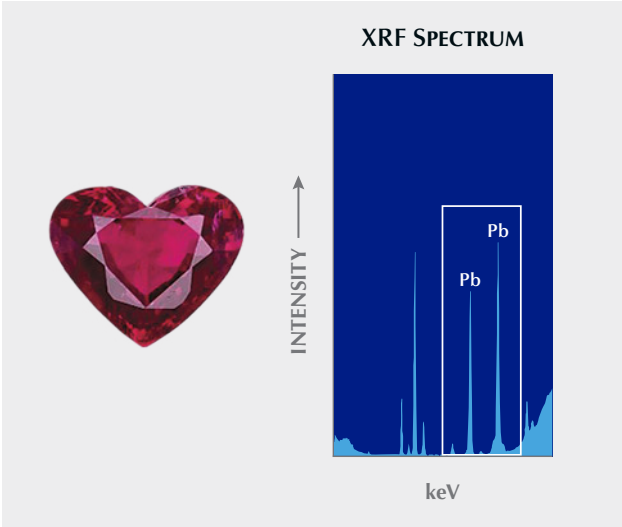

Figure 6. This lead glass–filled ruby displayed the characteristic X-ray fluorescence of lead in its XRF spectrum, indicating the presence of the treatment.

to observe gas bubbles in the glass-filled fractures, luster differences at the surface of the stone, or blue or orange flashes. However, glass-filled rubies often have significant clarity issues which can make these microscopic observations difficult, driving the need for chemical analysis. With XRF, this is done by simply observing the emission associated with lead, which is readily detected in the XRF spectrum (figure 6). Additionally, some recent clarity treatments use glasses with heavy metals other than lead, such as zinc (Sohrabi and Cooper, 2023). In these cases, XRF's ability to identify specific elements becomes even more important.

Coated Tanzanite. Another qualitative application of XRF is the detection of coatings on tanzanite (McClure and Shen, 2008). Some tanzanite or zoisite with low color saturation can undergo significant color enhancement by adding a thin layer of cobalt or titanium on the stone's pavilion. While the coating is not permanent and can often be detected by observing visible wear in the microscope, any fresh, unworn applications of this coating can be confirmed by testing the pavilion with XRF (figure 7). High intensities of titanium or cobalt provide definitive proof of this treatment, as natural tanzanite has low concentrations of these elements. A similar treatment determination that relies on qualitative XRF is the detection of strong potassium peaks in Zachery-treated turquoise (Fritsch et al., 1999).

Other qualitative applications of XRF include the detection of color-causing elements in stones where certain variety designations require that the color be caused by specific chromophores. XRF analysis is important for verifying the presence of copper in tourmaline. This separates Paraíba-type tourmaline from iron-colored indicolite, which sometimes has similar colors at lower levels of blue saturation.

Quantitative Applications of XRF. While XRF is often described as semiquantitative, proper calibration of the instrument using well-characterized standards can

Figure 7. XRF can detect cobalt- or titanium-coated tanzanite. The presence of characteristic X-ray fluorescence of cobalt (left) or titanium (right) provides strong evidence that the stone has been coated with these elements.

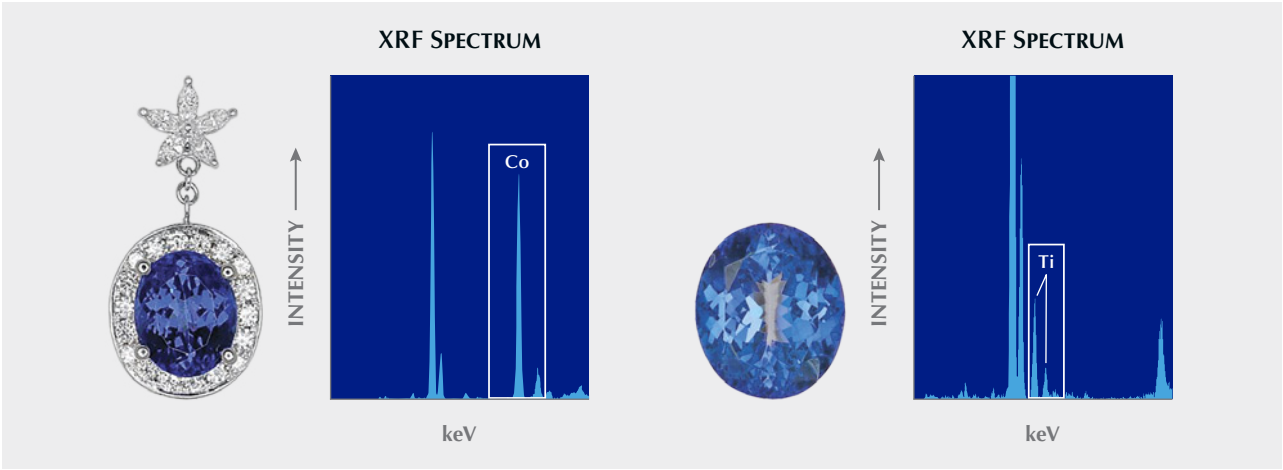

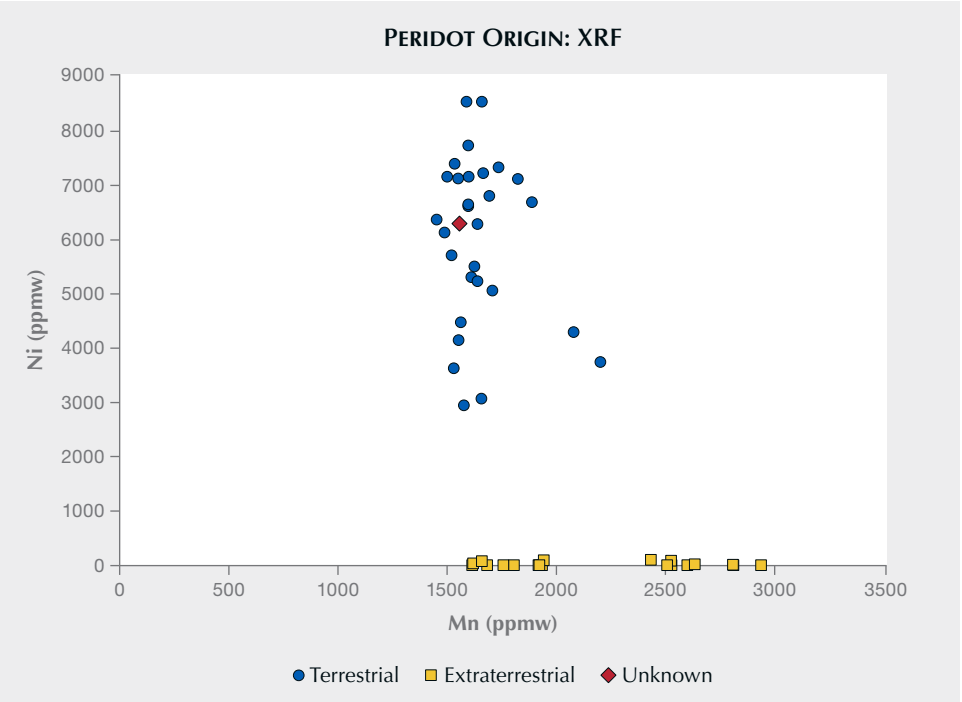

Figure 8. Comparison of nickel vs. manganese in terrestrial and extraterrestrial gem-quality peridot tested by GIA, generated using XRF data. This plot shows that peridot from pallasitic meteorites contains much less nickel than terrestrial peridot. The red diamond shape represents a peridot of unknown origin submitted to the lab. The peridot's placement in the terrestrial peridot field confirms its origin.

allow fully quantitative chemical analyses. XRF does not cover the entire periodic table, but it is frequently used for quantitative analyses, especially for geochemical testing facilities providing whole-rock analysis for mineral exploration and academic studies.

Pallasitic Peridot. Pallasitic meteorites consist of a matrix of iron-nickel metal with gemmy peridot that can be extracted and is sometimes faceted as a collector stone. Shen et al. (2011) demonstrated that LA-ICP-MS could be used to separate extraterrestrial pallasitic peridot from terrestrial peridot based on lithium, vanadium, manganese, cobalt, nickel, and zinc concentrations. XRF can also be used to identify pallasitic peridot and separate it from terrestrial peridot by measuring the nickel content (figure 8). Terrestrial, gem-quality green peridot tested by GIA to date contains nickel above ~3000 ppmw, though some terrestrial skarn-related near-colorless gem-quality forsterite contains lower nickel. However, the iron-nickel metal in pallasitic meteorites sequesters most of the nickel, effectively leaving the pallasitic peridot nickel-free.

Geographic Origin by XRF. One of the most important uses of XRF and LA-ICP-MS in gemological laboratories is in determining the geographic origin of gemstones. LA-ICP-MS, which will be discussed in more detail below, is generally the preferred method due to its higher precision, lower detection limits, potentially greater accuracy, and ability to detect light elements. In some cases, however, XRF can be used for geographic origin calls. Although XRF data does not distinguish between as many emerald localities as LA-ICP-MS, it has proven highly effective in identifying emeralds from Colombia and Zambia, which represent the majority submitted to GIA.

Colombian emerald often displays distinct inclusion scenes, especially jagged three-phase fluid inclusions but sometimes pyrite, carbonaceous shale, and rare but diagnostic parisite. However, there is some overlap in their inclusions with other lower-iron metamorphic- or metasomatic-type emeralds from Afghanistan, China, and Musakashi (a Zambian deposit). Likewise, emerald from the major Zambian deposit at Kafubu shows overlap with the inclusion scenes in Brazil, Russia, Ethiopia, and others (Saeseaw et al., 2019). While LA-ICP-MS measurements can confidently identify these and most other origins, XRF can distinguish two major sources by their low iron content (Colombia) or their high iron and cesium contents (Kafubu). For all other origins besides Colombia and Kafubu, there is significant overlap in the XRF trace element data. These other origin calls require the higher precision and lower detection limits for other elements afforded by LA-ICP-MS.

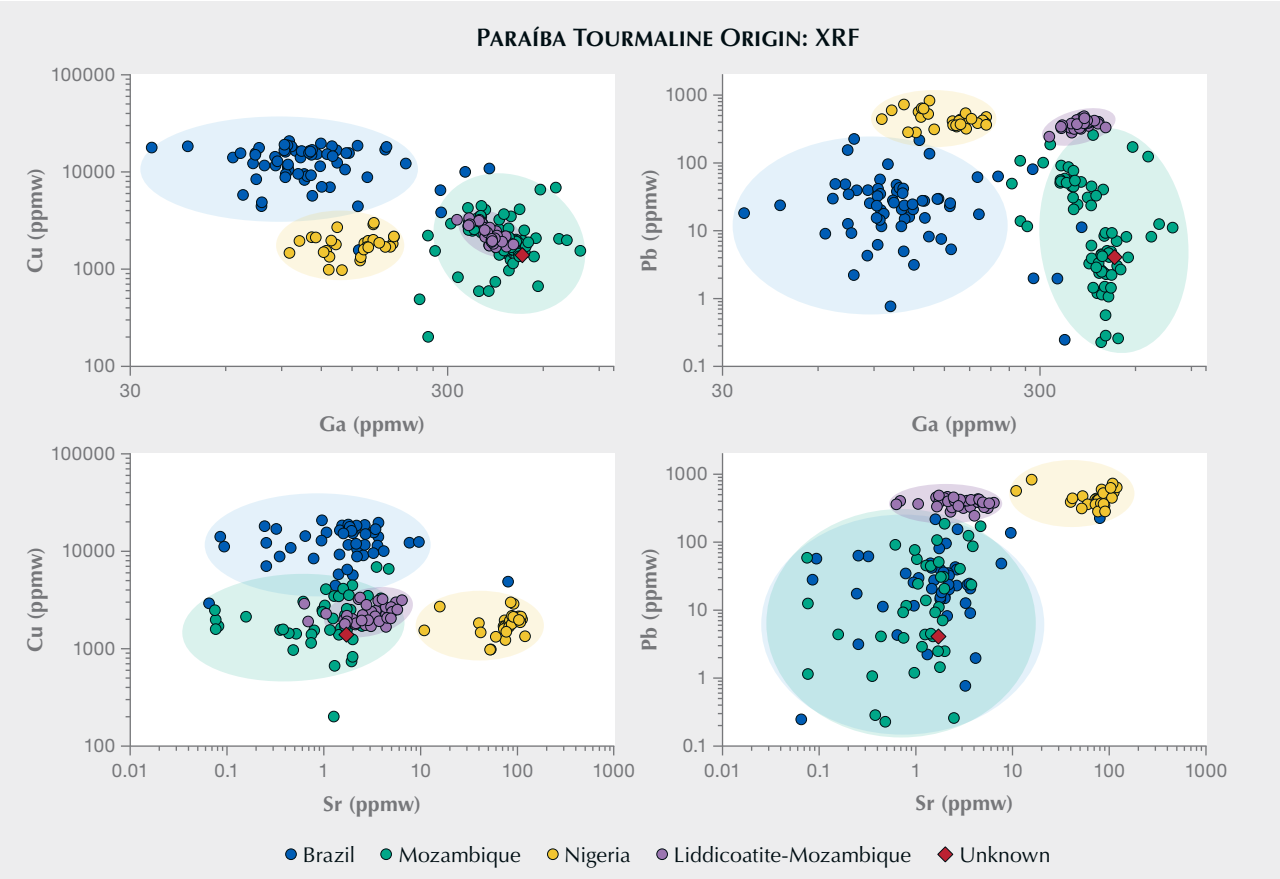

Figure 9. 2D scatter plots of trace elements, generated using XRF, can distinguish the majority of Paraíba tourmalines mined in Brazil, Mozambique, and Nigeria. In these plots, the red diamond shape represents the analysis of a Paraíba tourmaline of unknown origin. Its position in the plots confirms a Mozambique origin.

Although geographic origin determination of Paraíba-type tourmaline is often done by LA-ICP-MS, figure 9 shows that measuring their copper, gallium, and strontium contents using XRF can also be useful. In general, Paraíba tourmaline from Brazil contains higher concentrations of copper and lower concentrations of gallium, strontium, and lead. Non-liddicoatite Paraíba tourmaline from Mozambique contains higher concentrations of gallium and lower concentrations of copper, strontium, and lead. Liddicoatite Paraíba tourmaline from Mozambique contains higher concentrations of lead and gallium and lower concentrations of copper and strontium. Nigerian Paraíba tourmaline contains higher concentrations of strontium and lead and lower concentrations of copper and gallium. The four 2D scatter plots in figure 9 effectively separate the majority of Paraíba tourmaline from different localities.

Pearl Identification with XRF. Research has shown that strontium and manganese are excellent discriminators for distinguishing saltwater from freshwater natural and cultured pearls using LA-ICP-MS data (Karampelas et al., 2019). These elements can also be measured accurately using XRF, offering a fast, non-destructive, and reliable alternative to LA-ICP-MS for differentiation. Figure 10 illustrates the strontium vs. manganese distribution in saltwater and freshwater pearls. Freshwater pearls typically exhibit higher manganese and lower strontium concentrations, while saltwater pearls show lower manganese and higher strontium. A decision boundary generated using machine learning algorithms ensures reliable and efficient separation during the analytical process.

Precious Metal Testing. Quantitative XRF is widely used to verify precious metal content in jewelry and even to detect plating. Alloys used in jewelry primarily consist of gold, platinum, silver, copper, nickel, cobalt, and zinc, with minor additions of palladium, rhodium, ruthenium, and iridium as coatings or alloy components. Other elements may be incorporated

into alloys to enhance their chemical and physical properties, including corrosion resistance, ductility, hardness, and surface quality.

XRF can accurately measure the major components of common gold alloys (Mercer, 1992). XRF can also detect gold plating, often through measurement of the base metal being plated or other metals plated between the gold and base metal such as nickel. Additionally, different X-rays emitted by the gold in a piece of jewelry are absorbed differently by gold and other metals in an alloy. X-rays from a thin layer of gold will travel through less gold before leaving the sample. This means there will be a difference between the spectrum for gold in a thin layer (i.e., a plating) and the spectrum for a solid piece of gold, which can also be used as an indicator of plating.

Applications of LA-ICP-MS in Gemological Testing. While XRF offers rapid data acquisition, ease of use, and fully nondestructive analysis, LA-ICP-MS has major advantages over XRF in a gemological laboratory. The first is significantly increased sensitivity for essentially all trace elements. In other words, LA-ICP-MS can detect much smaller concentrations of trace elements with greater analytical precision across the periodic table. Detection limits for XRF

Figure 10. Plot distinguishing saltwater from freshwater pearls, generated using XRF data, in which a decision boundary has been determined using machine learning algorithms. Data points to the right of the red line (0.9) are classified as freshwater pearls, with a probability greater than 90%. Data points to the left of the blue line (0.1) are classified as saltwater pearls, with a less than 10% probability of being freshwater. Data points between the red and blue lines are considered questionable and require further examination. The red diamond shape represents a pearl of unknown origin; its position confirms a saltwater origin. Note that the data points in a straight vertical line on the left side contain no detectable manganese; their manganese values were assigned as the assumed detection limit for XRF (1 ppmw) so that these data could be visualized using a log base 2 scale.

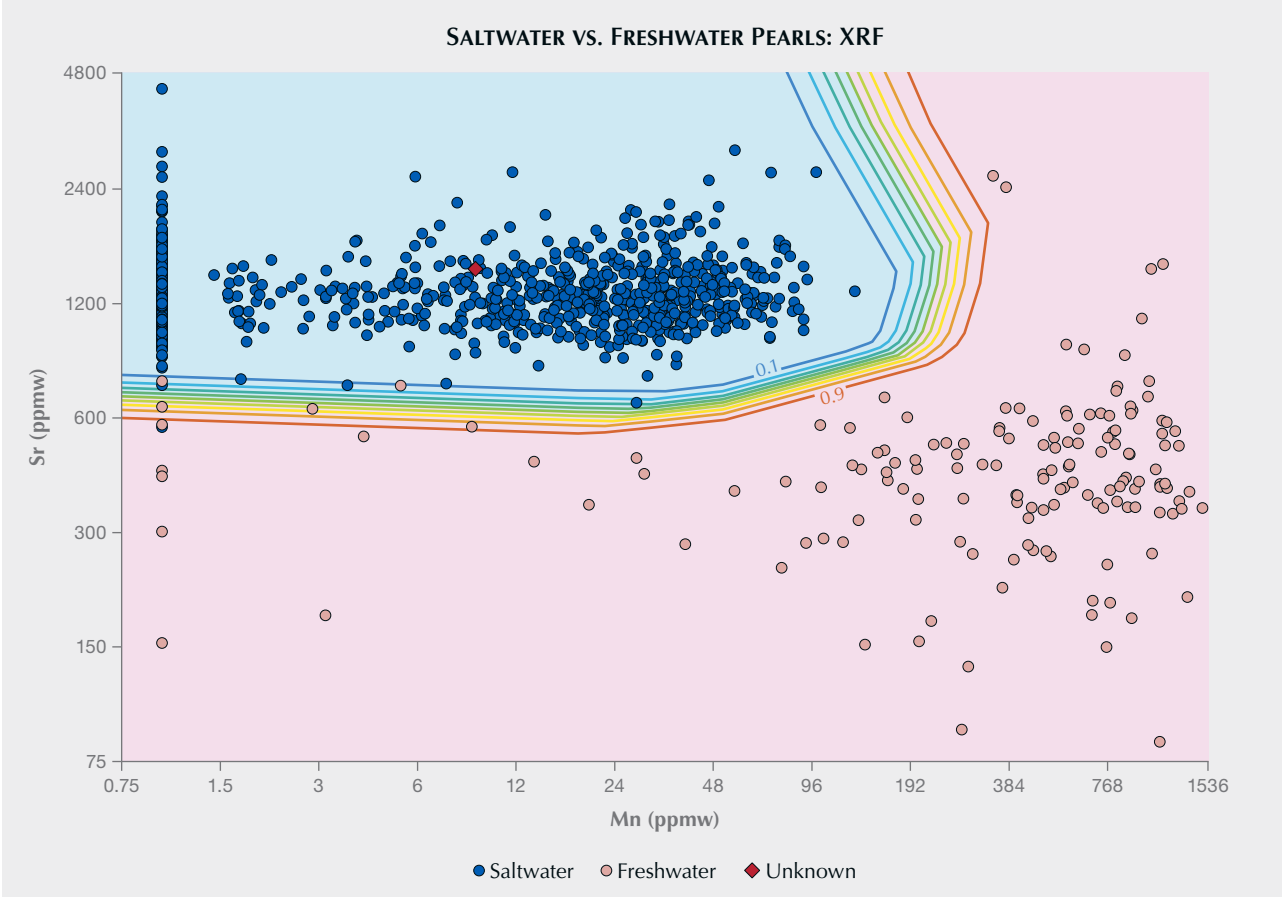

generally range from around 1000 ppm for lighter elements to tens of ppm for mid-range elements and around 1 ppm for very heavy elements. Detection limits with LA-ICP-MS are generally below 1 ppm for most elements and down to several parts per billion (ppb) for many of the heavier elements. Another advantage is the ability of LA-ICP-MS to measure light elements that simply cannot be detected by XRF. Light elements such as lithium and beryllium emit lower-energy characteristic X-rays that either cannot reach the XRF detector due to scattering or fall below the low-energy limit of the detector. Even elements like sodium and magnesium can generally only be measured at weight % levels (greater than approximately 10000 ppm) due to these restrictions. LA-ICP-MS, on the other hand, is capable of measuring light elements down to lithium at ppm or sub-ppm levels.

One major distinction from XRF is that LA-ICP-MS is a microanalytical technique that samples very small areas around tens of micrometers. On the other hand, XRF is more of a bulk analysis method that samples much larger surface areas, typically on the order of 1–5 mm^2, so care must be taken in choosing the technique that provides the appropriate level of spatial analysis. This could be an important consideration in the analysis of single-crystal gemstones with little or no chemical zoning or when analyzing opaque or translucent gems composed of individual cryptocrystalline grains and multiple different minerals in a mechanical mixture.

Beryllium Diffusion Detection. In the early 2000s, the colored stone market saw a dramatic influx of sapphire with a pinkish orange to orangy pink "padparadscha"-like color. Given the rarity of natural-color padparadscha sapphire, this new supply raised suspicion in the trade. Subsequent research demonstrated that beryllium diffusion treatment was being used to add an orange or yellow color to pink sapphire by heating these stones at high temperatures in the presence of an external source of beryllium. This produces trapped hole coloration and a padparadscha-like color for pink sapphire (Emmett et al., 2003). Colorless or pale colored sapphire can also be turned to a yellow/orange color, and the color of dark blue sapphires can be lightened significantly with beryllium diffusion. In some of the early production of beryllium-diffused sapphire, orange rims could be identified around the outside of the stone (figure 11). However, beryllium can diffuse very rapidly in corundum at the temperatures used in this process (often up to 1800°C), so microscopy cannot identify this treatment in many cases.

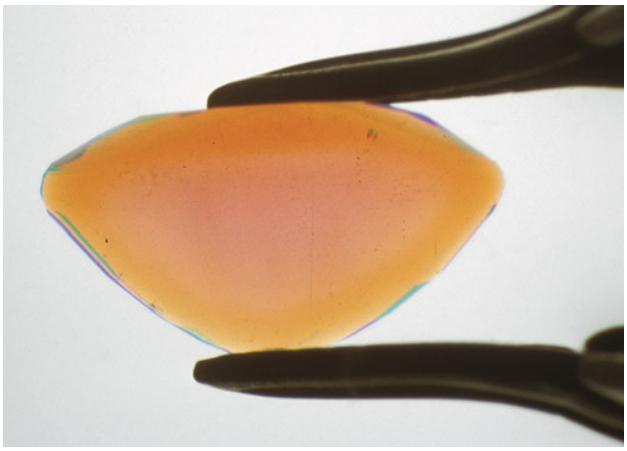

Figure 11. A cross section of a beryllium-diffused sapphire showing a purplish pink core and an orangy pink rim caused by the introduction of beryllium to the corundum structure.

The only means of analyzing the chemistry of a sapphire in the gem laboratory when this treatment was introduced was by XRF, which cannot detect light elements such as beryllium. Commercially available techniques being used in other fields at the time included LA-ICP-MS and secondary ion mass spectrometry (SIMS). While SIMS is capable of producing exceptionally high-quality data with detection limits much lower than LA-ICP-MS, analysis is very time-consuming and these instruments are very complicated, often requiring a PhD-level scientist just for daily operation of the instrument. SIMS is also a much more significant investment, easily costing over $1 million just to purchase the instrument.

For this reason, LA-ICP-MS, which can routinely detect beryllium at levels down to 0.1 ppma, was introduced into many gemological laboratories for the sole purpose, at least initially, of identifying beryllium diffusion in ruby and sapphire. Figure 12 shows a laser ablation profile seen when processing LA-ICP-MS data for a beryllium-diffused sapphire with about 10 ppma of beryllium present at the stone's girdle. LIBS can also be used for beryllium detection, as it is particularly well suited for the light elements. LIBS has the advantage of being less destructive than LA-ICP-MS, as less ablation is required, but it has poorer detection limits and quantification is more challenging.

Geographic Origin Determination. LA-ICP-MS is also an exceptional tool in establishing geographic

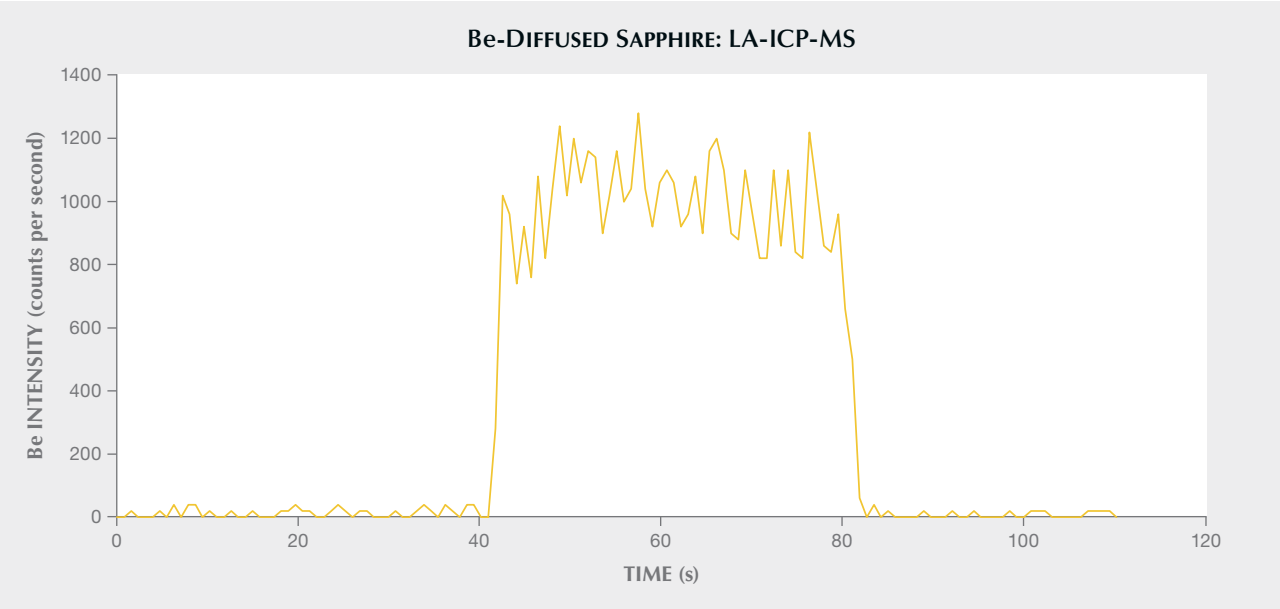

Figure 12. Laser ablation profile of an LA-ICP-MS analysis of a beryllium-diffused sapphire. Ablation begins at the 40 s mark, indicated by a significant increase in beryllium intensity as the laser shutter opens and the laser begins to interact with the stone. Ablation ceases at the 80 s mark, indicated by a rapid decline in the beryllium signal to the gas background level. The intervals from 0 to 40 s and from 80 to 120 s represent the gas background.

origin. The major origin applications currently involve sapphire (Palke et al., 2019a), ruby (Palke et al., 2019b), emerald (Saeseaw et al., 2019), Paraíba tourmaline (Katsurada et al., 2019), alexandrite (Sun et al., 2019a), and red/pink spinel. Research is ongoing to expand the use of LA-ICP-MS for origin analysis of demantoid, blue spinel, peridot, and opal.

Figure 13 shows 2D plots of various trace elements used for geographic origin determination of Paraíba tourmaline. Samples sourced from Brazil, Mozambique, and Nigeria often have similar colors and inclusions, making it essentially impossible to pinpoint their origin using conventional gemological instruments. While the origin of some Paraíba tourmaline can be identified with quantitative XRF analysis (see above), in many cases LA-ICP-MS is needed. The higher precision of LA-ICP-MS affords a higher confidence in trace element measurements, allowing a conclusive origin call for some borderline cases. In addition to the main trace elements used for Paraíba origin determination (copper, gallium, lead, and strontium), other trace elements such as tin and zinc can be useful. These are usually at concentrations too low to be detected by XRF. The chemical trends distinguishing these geographic origins are shown in figure 13. Generally, Paraíba tourmaline from Brazil is characterized by higher concentrations of copper and zinc and lower concentrations of gallium, strontium, and lead. In contrast, Paraíba tourmaline from Mozambique exhibits higher concentrations of gallium and lower concentrations of copper, zinc, and strontium. Tourmaline from Nigeria shows elevated levels of strontium and lead and reduced levels of copper and gallium. The violet dots in figure 13 represent a separate species of tourmaline, liddicoatite, from Mozambique.

Emerald geographic origin determination is heavily reliant on trace element analysis by LA-ICP-MS. As with Paraíba tourmaline, some emerald origins—specifically those from Colombia and Kafubu, Zambia—can be confidently identified using only XRF. While XRF trace element data is similar in some ways to that obtained by LA-ICP-MS, XRF detects far fewer trace elements in emerald and at much lower precision. For this reason, LA-ICP-MS is necessary to establish origin for emerald from sources other than Colombia and Kafubu. Trace elements measured by LA-ICP-MS for emerald origin primarily include lithium, potassium, vanadium, chromium, iron, rubidium, and cesium, and many of these cannot be measured by XRF with sufficient precision at the concentrations required for accurate origin determination. In almost all cases, an accurate origin conclusion is possible for all major emerald sources using LA-ICP-MS (Saeseaw et al., 2019).

The geographic origin of alexandrite is also largely determined using trace element analysis by

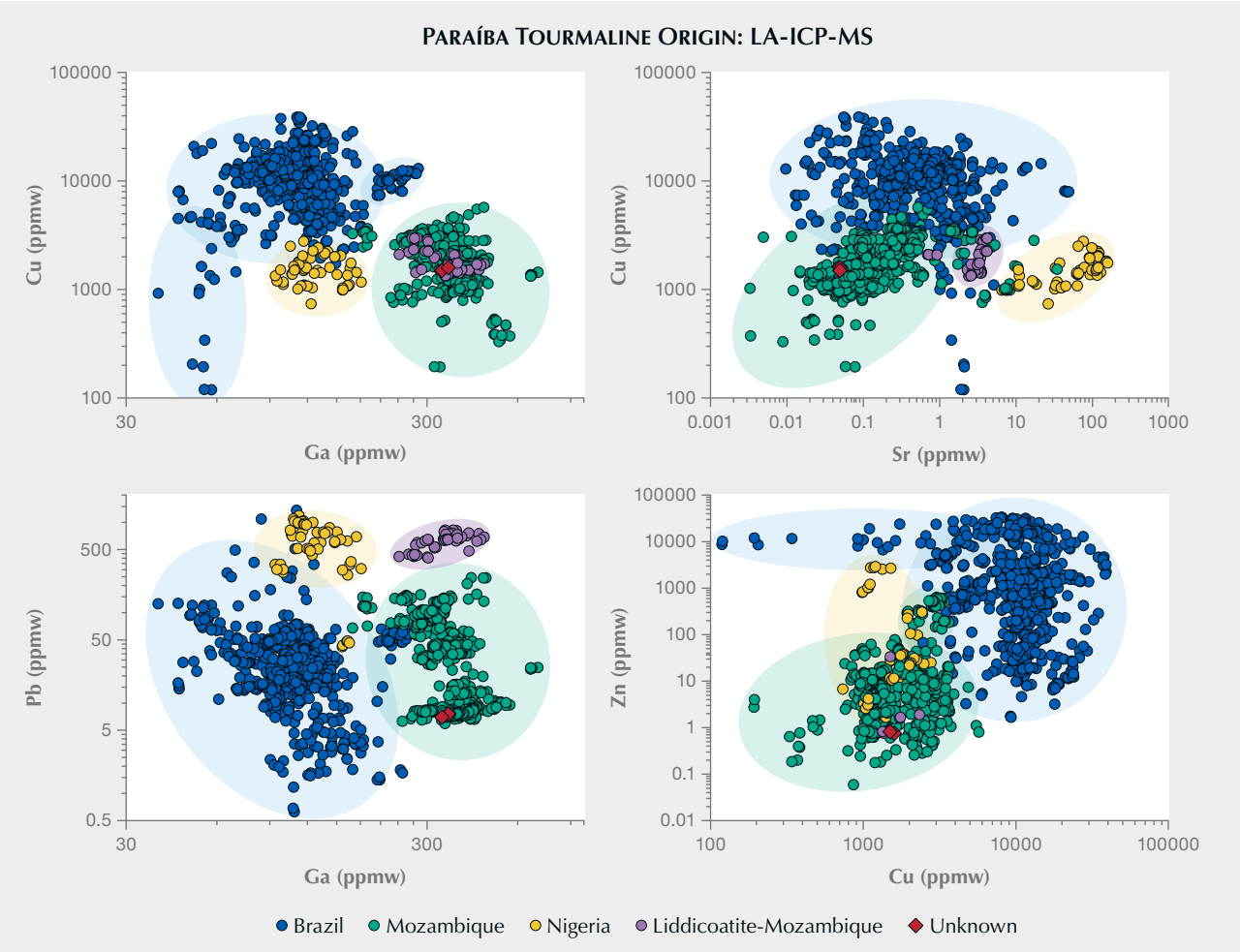

Figure 13. 2D scatter plots of trace elements, generated using LA-ICP-MS, can distinguish the majority of Paraíba tourmalines mined in Brazil, Mozambique, and Nigeria. In these plots, each red diamond shape represents the analysis of a Paraíba tourmaline of unknown origin. Their position in the plots confirms a Mozambique origin.

LA-ICP-MS (Sun et al., 2019a). While there are some general differences in warm/cool color ranges (e.g., incandescent vs. daylight colors) and inclusions between alexandrite from some deposits, there is generally too much overlap to determine origin through standard gemological testing. For instance, Brazilian alexandrite typically occurs with more highly saturated colors, while Sri Lankan has less-saturated colors. But most deposits, including those in Sri Lanka, India, Russia, Tanzania, and Madagascar, can have similar warm/cool colors. The key trace elements for distinguishing alexandrite from different geographic locations by LA-ICP-MS include magnesium, iron, gallium germanium, tin, boron, vanadium, and chromium. Some of these trace elements are undetectable by XRF (boron and magnesium, except at very high concentrations). Other trace elements *may* be detected in some alexandrite, but their concentrations are often too low for accurate XRF analysis. Alexandrite from various countries exhibits distinctive chemical profiles (figure 14). Russian, Zambian, and Zimbabwean alexandrite generally have medium to high concentrations of germanium. Brazilian samples are characterized by high levels of tin and lower concentrations of magnesium and gallium, with some exhibiting extremely low boron levels. Sri Lankan alexandrite is known for its very high gallium concentrations. Tanzanian stones typically show low gallium and medium levels of magnesium and tin. Indian alexandrites are marked by low tin and high vanadium concentrations, while alexandrite from Madagascar is distinguished by low germanium and medium concentrations of gallium and tin. In figure 14, the red

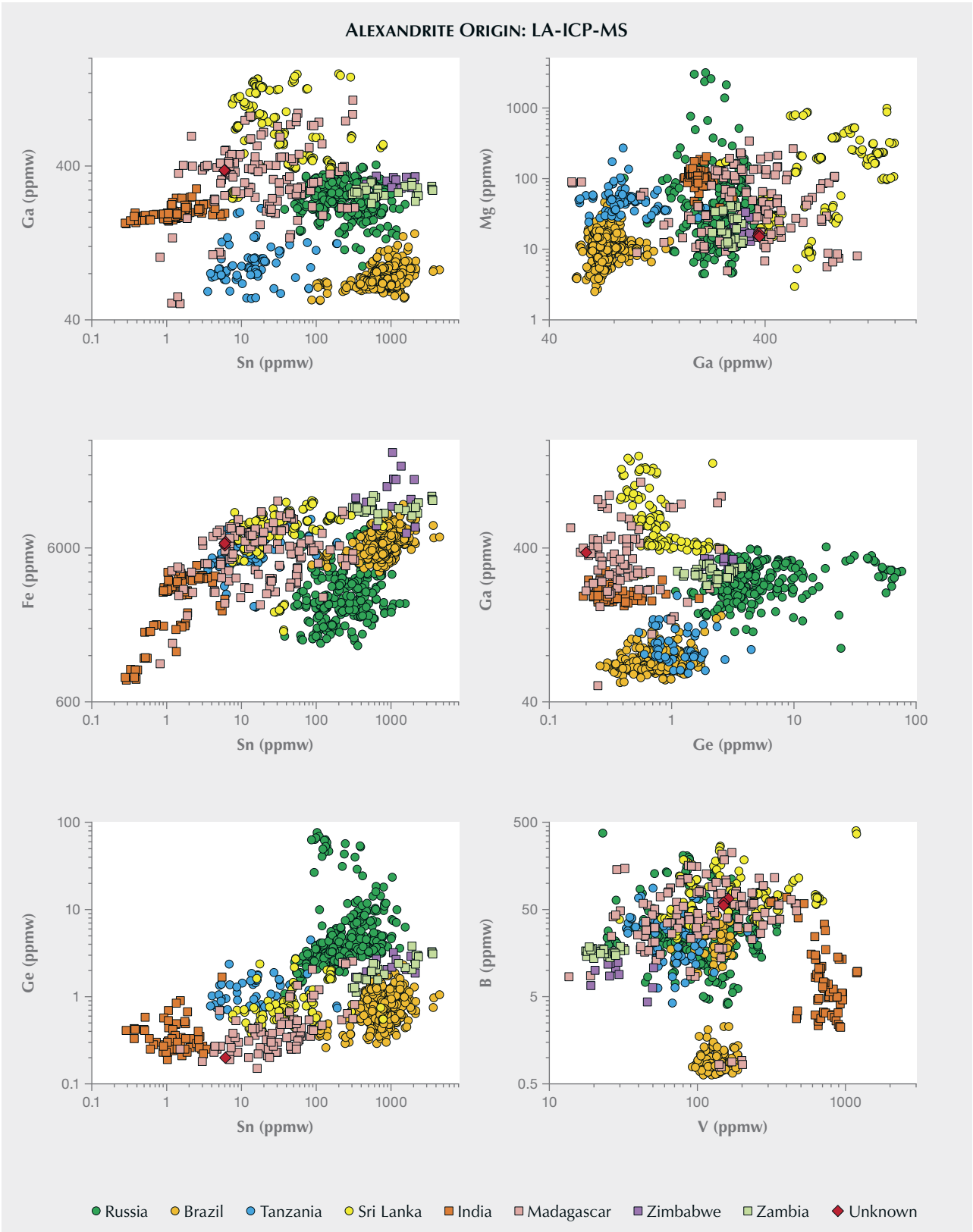

Figure 14. 2D scatter plots of trace elements, generated using LA-ICP-MS, can distinguish the majority of alexandrites mined from different countries. The red diamond shape represents the analysis of an alexandrite of unknown origin. Its position in the plots confirms a Madagascar origin.

diamond shape representing a stone of unknown origin is identified as alexandrite from Madagascar based on the analysis of all six plots.

Ruby and Sapphire Origin Determination. LA-ICP-MS is a powerful tool for establishing the geographic origin of rubies and sapphires. In many of the examples above (emerald, tourmaline, and tanzanite), there was a clear distinction between the chemical composition of stones from different deposits. For gem corundum (ruby and sapphire), however, trace element chemistry often strongly overlaps between different deposits. This is especially apparent in standard two-dimensional plots where trace element substitution is more limited and constrained to a smaller set of elements (typically magnesium, titanium, vanadium, iron, and gallium for ruby and sapphire). For most ruby and sapphire, microscopic observation of inclusion scenes (and sometimes analyzing spectroscopic features) carries greater weight in geographic origin determination than trace element chemistry. Nonetheless, trace element chemistry can still play an important role in many cases, and various techniques have been developed to enhance the use of trace element chemistry to complement origin data from inclusion features.

Consider a complex magnesium-gallium 2D plot of metamorphic blue sapphires. The data points for the unknown stone are obscured among numerous reference data points, which complicates the stone's origin. To simplify a complex magnesium-gallium 2D plot, additional elements such as vanadium, iron, and titanium are utilized as supplementary dimensions for data filtering.

At GIA's laboratory, the approach to simplifying the comparison with reference data for sapphire and ruby origin is essentially a variation of the k-nearest neighbor statistical approach, in which an unknown is classified by determining which reference data points are closest to it in multidimensional trace element space. This is helpful because humans cannot visualize more than three dimensions. Because we can only see three trace elements at a time in these plots, there is a potential risk of missing valuable information from other trace elements. GIA's approach, referred to as the selective plotting method, essentially reverses the k-nearest neighbor process, allowing simpler visualization of which geographic origins are consistent with the unknown data, with the hope that only one origin will be a strong match (Palke et al., 2019b).

The method is illustrated in figure 15. Using vanadium as the third dimension, we can expand the data from the magnesium-gallium 2D plot into magnesium-gallium-vanadium 3D space. Then we can decide to compare only against data with similar vanadium concentrations by drawing a window around the unknown data in the vertical dimension and excluding reference data outside this window. Then the 3D plot can be projected back onto the magnesium-gallium plot with the data outside the window excluded. The magnesium-gallium plot has far fewer data points than before, making it easier to compare the unknown against our reference data. This process can be repeated by expanding the magnesium-gallium 2D plot into the third dimension with iron and then titanium, again creating windows around the vertical dimension and excluding data in each iteration. The resulting projection back onto the magnesium-gallium plot again has far fewer data points.

The example in figure 15 still does not exclude any origins or produce a "preferred" origin call for this unknown data. However, the process can be repeated, each time with a smaller window around the unknown data in the expanded third dimension. The process used by GIA utilizes coarse, medium, and fine windows that progressively filter the data each time (figure 16). In this example, the unknown sapphire clearly matches our Sri Lankan reference data more closely than any other source when filtering down to the "fine" screen. This process, described in greater detail in Palke et al. (2019a), is used by GIA for ruby, sapphire, emerald, alexandrite, and spinel.

Origin Determination of Freshwater Pearls Using LA-ICP-MS. LA-ICP-MS excels at quantifying both light elements (e.g., sodium and magnesium) as well as heavier elements (e.g., barium), making it an ideal tool for pearl analysis. LA-ICP-MS can distinguish the origins of various freshwater pearls, including American natural pearls, American cultured pearls, and Chinese cultured pearls, by analyzing trace elements such as sodium, magnesium, manganese, strontium, and barium (Homkrajae et al., 2019). As illustrated in figure 17 (A and B), American natural pearls typically exhibit lower concentrations of manganese, sodium, strontium, and barium compared to other freshwater pearls, while American cultured pearls are characterized by higher levels of manganese, strontium, and barium

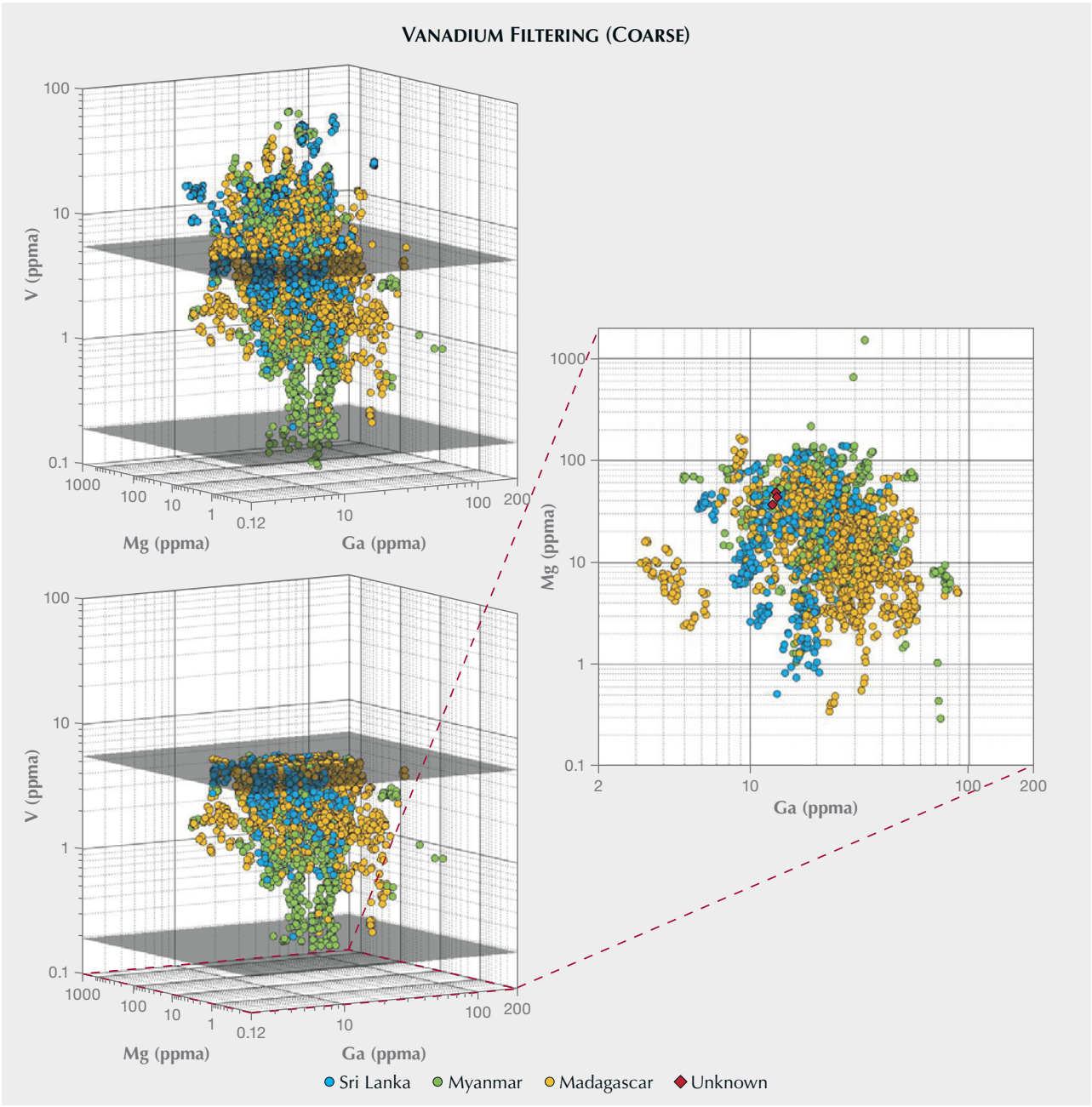

Figure 15. Data filtered using vanadium as the third dimension with a coarse (large) filtering window, simplifying projections back onto the magnesium-gallium 2D plot.

as well as moderate levels of sodium. Chinese cultured pearls, on the other hand, show elevated sodium and strontium levels but lower manganese and barium.

A practical method to clearly visualize and easily interpret this data employs a combination of machine learning techniques. By using principal component analysis (PCA; Abdi and Williams, 2010) for dimension reduction and a feed-forward neural network (Mishra and Gupta, 2017) for classification, the five-dimensional data space—comprising the elements sodium, magnesium, manganese, strontium, and barium—can be effectively projected into a two-dimensional space. This approach not only simplifies the data but also defines clear decision regions for more straightforward data interpretation. Tech-

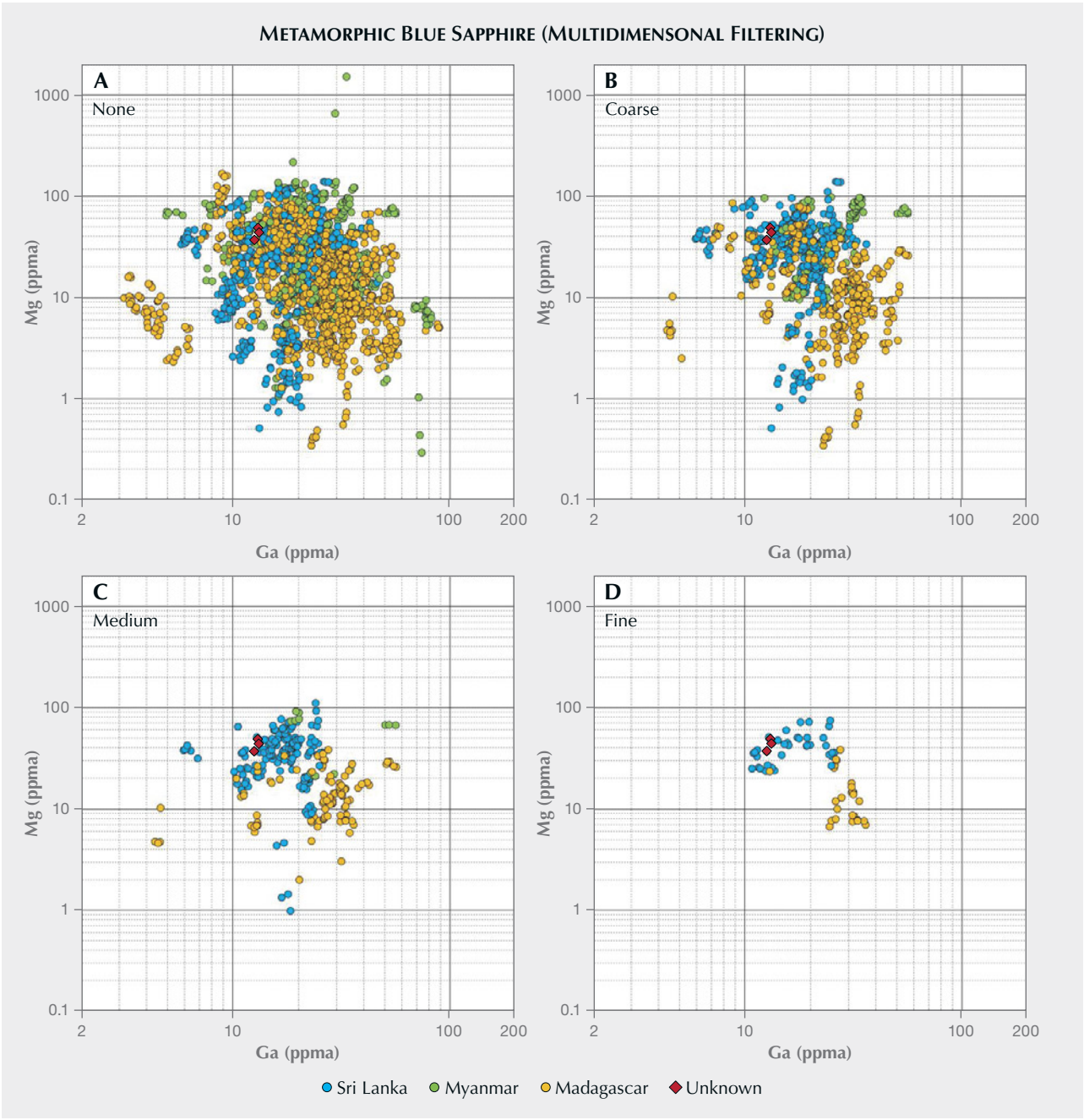

Figure 16. Visualization of the simultaneous multidimensional filtering process for metamorphic blue sapphire plots. A: The initial magnesium-gallium 2D plot prior to filtering. B: The magnesium-gallium 2D plot after coarse filtering using vanadium, iron, and titanium. C: The magnesium-gallium 2D plot after medium filtering. D: The magnesium-gallium 2D plot after fine filtering.

niques like PCA are another way of approaching the problem of visualization of multidimensional data, similar to the selective plotting method described above. Figure 17C displays the decision regions for reference freshwater pearl data mapped onto two principal component axes. Data points within the light red region are likely classified as American natural pearls. Similarly, data points within the light green region are likely classified as American cultured pearls and those within the yellow region as

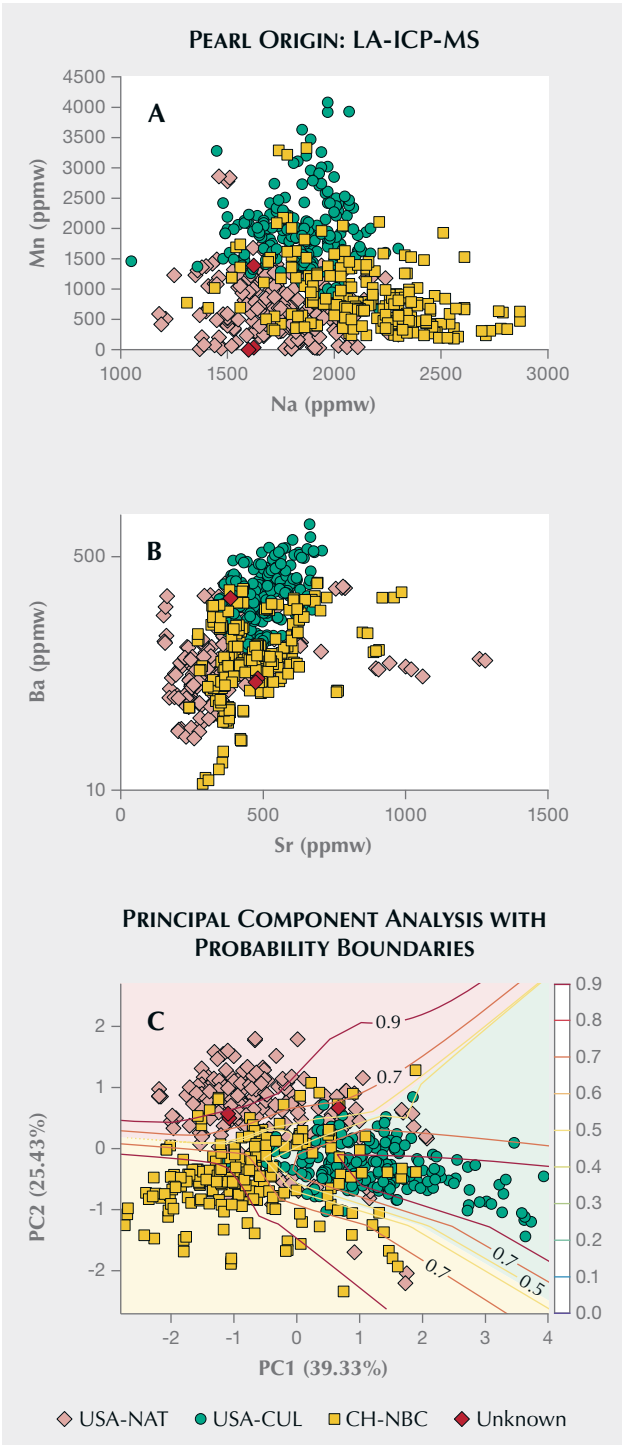

Figure 17. A and B: 2D scatter plots of pearls from three origins: American natural (USA-NAT), American cultured (USA-CUL), and Chinese cultured (CH-NBC) (Homkrajae et al., 2019). C: Principal component analysis, achieved by transforming five-dimensional data (representing five elements) using a projection matrix onto a two-dimensional subspace. The x-axis (first principal component) accounts for 39.33% of the information ("explained variance") from the original dataset, while the y-axis (second principal component) captures an additional 25.43%. The plot incorporates probability decision boundaries. For each pearl type, data points within the orange to red line boundary (indicating a 0.7–0.9 threshold) are classified as belonging to their respective categories, with a classification probability exceeding 70–90%. Three red diamond shapes represent chemical data points for an unclassified pearl.

Chinese. The unknown pearls, represented by red diamond shapes across the plots, are classified as American natural pearls.

While the combined use of machine learning methods enhances the interpretability of results, it is important to acknowledge that this approach introduces certain trade-offs. The reduction in dimensionality through principal component analysis, for example, does not preserve the full variance of the original data structure, capturing only 64.76% of the total variance as shown in figure 17C. Because principal component analysis is restricted to linear transformations, it does not capture complex nonlinear patterns present in the data. An alternative approach involves applying a different machine learning technique called a deep feed-forward neural network directly to the original dataset. This method can potentially improve classification accuracy but at the expense of interpretability and the ease of visualization.

Chemical Mapping on Gemstones with LA-ICP-MS. LA-ICP-MS is typically used for localized analysis, obtaining elemental information from a microscopic area on a gemstone. However, this technique can also be utilized to characterize the distribution of chemical elements over larger areas, thereby enhancing the comprehensive study of gemstones (Zaw et al., 2015).

For instance, by ablating along parallel lines to cover a substantial rectangular area, one can examine the distribution of associated chemical elements (titanium, tantalum, niobium, tungsten, and thorium) within the cloud-like inclusions of a metamorphic blue sapphire. This approach aids in understanding the sapphire's growth process and environment and helps identify the nature of the inclusions. Similarly, elemental mapping of a cultured pearl's cross section can reveal variations in

elemental density across different concentric growth layers (see figure 18), offering valuable insights into the pearl's growth process and potentially the geographic environment in which it grew. Note, however, that this mapping would leave significant, eye-visible marks on a stone and is not suitable for gems submitted to the lab for reports.

Materials Identification. LA-ICP-MS and even XRF can be very useful for identifying gem materials that are challenging to determine using standard gemological techniques. For instance, LA-ICP-MS can separate various garnet species such as pyrope, pyrope-almandine, almandine, almandine spessartine, spessartine, and pyrope-spessartine by accurately measuring the mixture of pyrope-almandine-spessartine end members in the stone. A similar process can be followed for tourmaline species, as described by Sun et al. (2019b).

In some cases, gem species are encountered that do not match any known gem materials based on results from standard gemological testing. In these situations, LA-ICP-MS can provide a relatively quick chemical measurement to help identify the gem's species. For instance, LeCroy and Palke (2024) recently used the technique to identify a faceted stone submitted to GIA as titanoholtite, a member of the dumortierite supergroup heretofore observed only as small, non-gemmy crystals from a pegmatite in Poland. XRF can achieve similar results in many cases, but its inability to measure light elements makes LA-ICP-MS the more reliable tool.

LA-ICP-MS also excels at measuring both trace, minor, and major element concentrations in inclusions when they are exposed at the surface. For instance, identifying the various inclusions in the black topaz shown in figure 19A can be particularly challenging. Raman spectroscopy can effectively identify certain inclusions in this mineral specimen, such as colorless fluorite, reddish brown flaky mica, and magnetite, as shown in figure 19B. However, some inclusions are so rare that their Raman spectra are not well established for comparison, as is the case with the black inclusions from the same specimen shown in figure 19C. In this case, LA-ICP-MS can be employed to conduct precise chemical element analysis of these inclusions. The computed chemical molecular formula of the inclusion is quite complex: $(Ca_{0.07}, Ti_{0.07}, Mn_{0.19}, Fe^{3+}_{0.62}, Zr_{0.04}, Nb_{0.46}, Mo_{0.02}, Ta_{0.01}, W_{0.43}, others_{0.03})_{1.95}O_4$. When combined with Raman spectroscopy, this analysis identifies the inclusion as a variety of the mineral ixiolite, sometimes informally referred to as wolframoixiolite, a mineral primarily composed of manganese, niobium, and tungsten. While LA-ICP-MS is not expected to give results as accurate as EPMA due to difficulties with non-matrix-matched standardization, in most cases mineral formulas are produced that closely match the expected stoichiometry constraints for the expected mineral, improving confidence in the accuracy of chemical measurements.

Comparison of LA-ICP-MS, LIBS, and XRF. LA-ICP-MS and XRF are both widely used in gemological laboratories. A less commonly used technique is LIBS, which shares some similarities with LA-ICP-MS and is even built into some of those systems. Each technique has some advantages and disadvantages. In terms of being able to accurately and precisely determine concentrations of most elements with high spatial resolution, LA-ICP-MS is by far the best tool. XRF has the advantage of being the only of these

Figure 18. LA-ICP-MS elemental maps of a cross section of a cultured pearl. The red rectangle indicates the area mapped, measuring 1200 × 3400 µm.

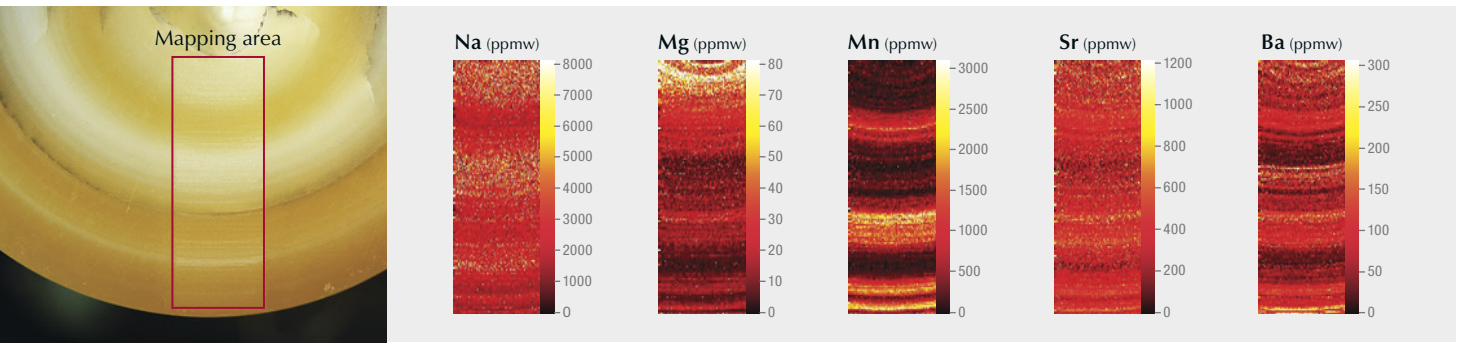

Figure 19. A: A black topaz crystal specimen from the Thomas Mountains in Utah, measuring 24.80 × 17.92 × 12.29 mm. Photo by Kevin Schumacher. B: Inclusions of black magnetite, colorless fluorite, and flaky mica in the black topaz. C: Clusters of tabular ixiolite. From Muyal et al. (2019); fields of view 0.288 mm (B) and 0.36 mm (C).

methods that is truly nondestructive. LIBS offers the same spatial resolution advantages as LA-ICP-MS but is considerably faster, with less stringent requirements for laboratory conditions.

On the other hand, LA-ICP-MS systems are the most expensive to purchase and operate, with a potentially five to ten times higher cost than LIBS and XRF systems. LIBS data are considerably more

challenging to quantify than LA-ICP-MS, and the usefulness of LIBS for trace element analysis is limited to light elements. The XRF systems typically employed at gemological laboratories, as described above, cannot perform microanalytical analysis and struggle with lighter elements. There are, however, some micro-XRF instruments available on the market that can scan with a spatial resolution of approximately 20 µm.

Detection limits are also significantly lower for LA-ICP-MS measurements than for XRF. LIBS may have fairly low detection limits in the ppm range for light elements, close to but generally higher than LA-ICP-MS measurements. However, detection limits for heavier elements can be closer to hundreds or thousands of ppm for LIBS, putting the technique at a disadvantage compared to LA-ICP-MS.

SUMMARY

As identification demands have grown more complex over the last few decades, gemological laboratories have had to adopt progressively more advanced analytical instrumentation. Measurements of a gemstone's chemical composition have proven to be of paramount importance in many ways. XRF was the first chemical analysis technique introduced to most gemological laboratories. Later, chemical measurement techniques were supplemented with LIBS and more importantly LA-ICP-MS with the introduction of beryllium-diffused corundum and the growing importance of geographic origin determination. While LA-ICP-MS can be a challenging instrument to operate and maintain, the modern gem trade often relies on laboratories to use this technology for accurate gemstone identification.

ABOUT THE AUTHORS

Ziyin Sun is a senior research associate, and Dr. Aaron Palke is senior manager of research, at GIA in Carlsbad. Dr. Michael Jollands is a senior research scientist at GIA in New York.

ACKNOWLEDGMENTS

The authors are deeply indebted to many years of guidance and collaboration with many researchers and gemologists while working at GIA, including Shane McClure, Nathan Renfro, John Emmett, George Rossman, Artitaya Homkrajae, Tom Moses, and Sudarat Saeseaw, among others, as well as GIA's field gemology department for providing access to samples with known provenance that has made all of this research possible. Many thanks to Chunhui Zhou for providing the pearl sample for elemental mapping using LA-ICP-MS.

REFERENCES

Abdi H., Williams L.J. (2010) Principal component analysis. *WIREs Computational Statistics*, Vol. 2, No. 4, pp. 433–459, http://dx.doi.org/10.1002/wics.101

Abduriyim A., Kitawaki H. (2006) Applications of laser ablation-inductively coupled plasma-mass spectrometry (LA-ICP-MS) to gemology. *G&G*, Vol. 42, No. 2, pp. 98–118, http://dx.doi.org/10.5741/GEMS.42.2.98

Eaton-Magaña S., Jones D.C., Turnier R.B., Breeding C.M. (2024) Shining a light on gemstone properties: An exploration of photoluminescence spectroscopy. *G&G*, Vol. 60, No. 4, pp. 494–517, http://dx.doi.org/10.5741/GEMS.60.4.494

Emmett J.L., Scarratt K., McClure S.F., Moses T., Douthit T.R., Hughes R., Novak S., Shigley J.E., Wang W., Bordelon O., Kane R.E. (2003) Beryllium diffusion of ruby and sapphire. *G&G*, Vol. 39, No. 2, pp. 84–135, http://dx.doi.org/10.5741/GEMS.39.2.84

He F., Van Espen P.J. (1991) General approach for quantitative energy dispersive X-ray fluorescence analysis based on fundamental parameters. *Analytical Chemistry*, Vol. 63, No. 20, pp. 2237–2244, http://dx.doi.org/10.1021/ac00020a009

Fritsch E., McClure S.F., Ostrooumov M., Andres Y., Moses T., Koivula J.I., Kammerling R.C. (1999) The identification of Zachery-treated turquoise. *G&G*, Vol. 35, No. 1, pp. 4–16, http://dx.doi.org/10.5741/GEMS.35.1.4

Gray A.L. (1985) Solid sample introduction by laser ablation for inductively coupled plasma source mass spectrometry. *Analyst*, Vol. 110, No. 5, pp. 551–556, http://dx.doi.org/10.1039/an9851000551

Homkrajae A., Sun Z., Blodgett T., Zhou C. (2019) Provenance discrimination of freshwater pearls by LA-ICP-MS and linear discriminant analysis (LDA). *G&G*, Vol. 55, No. 1, pp. 47–60, http://dx.doi.org/10.5741/GEMS.55.1.47

Johnson R.G., King B.S. (1987) Energy-dispersive X-ray fluorescence spectrometry. In P.A. Baedecker, Ed., *U.S. Geological Survey Bulletin 1770: Methods for Geochemical Analysis*, pp. F1–F5.

Karampelas S., Mohamed F., Abdulla H., Almahmood F., Flamarzi L., Sangsawong S., Alalawi A. (2019) Chemical characteristics of freshwater and saltwater natural and cultured pearls from different bivalves. *Minerals*, Vol. 9, No. 6, article no. 357, http://dx.doi.org/10.3390/min9060357

Katsurada Y., Sun Z., Breeding C.M., Dutrow B.L. (2019) Geographic origin determination of Paraíba tourmaline. *G&G*, Vol. 55, No. 4, pp. 648–659, http://dx.doi.org/10.5741/GEMS.55.4.648

Krzemnicki M.S., Hänni H.A., Walters R.A. (2004) A new method for detecting Be diffusion-treated sapphires: Laser-induced breakdown spectroscopy (LIBS). *G&G*, Vol. 40, No. 4, pp. 314–322, http://dx.doi.org/10.5741/GEMS.40.4.314

Krzemnicki M.S., Pettke T., Hänni H.A. (2006) Perspectives of LIBS in gemstone testing: Analysis of light elements such as beryllium, boron, lithium. GIT International Gem & Jewelry Conference (GIT 2006).

LeCroy B., Palke A. (2024) Lab Notes: Exceptionally rare titanoholtite. *G&G*, Vol. 60, No. 1, pp. 71–72.

McClure S.F., Shen A.H. (2008) Coated tanzanite. *G&G*, Vol. 44, No. 2, pp. 142–147, http://dx.doi.org/10.5741/GEMS.44.2.142

McMillan N.J., McManus C.E., Harmon R.S., De Lucia F.C. Jr., Miziolek A.W. (2006) Laser-induced breakdown spectroscopy analysis of complex silicate minerals—beryl. *Analytical and Bioanalytical Chemistry*, Vol. 385, No. 2, pp. 263–271, http://dx.doi.org/10.1007/s00216-006-0374-9

Mercer M.E. (1992) Methods for determining the gold content of jewelry metals. *G&G*, Vol. 28, No. 4, pp. 222–233, http://dx.doi.org/10.5741/GEMS.28.4.222

Mishra C., Gupta D.L. (2017) Deep machine learning and neural networks: An overview. *IAES International Journal of Artificial Intelligence*, Vol. 6, No. 2, pp. 66–73, http://dx.doi.org/10.11591/ijai.v6.i2.pp66-73

Muyal J., Sun Z., Shigley J. (2019) *G&G* Micro-World: Inclusion-rich black topaz from the Thomas Mountains, Utah. *G&G*, Vol. 55, No. 2, pp. 266–269.

Palke A.C., Saeseaw S., Renfro N.D., Sun Z., McClure S.F. (2019a) Geographic origin determination of ruby. *G&G*, Vol. 55, No. 4, pp. 580–612, http://dx.doi.org/10.5741/GEMS.55.4.580

——— (2019b) Geographic origin determination of blue sapphire. *G&G*, Vol. 55, No. 4, pp. 536–579, http://dx.doi.org/10.5741/GEMS.55.4.536

Pornwilard M.-M., Hansawek R., Shiowatana J., Siripinyanond A. (2011) Geographical origin classification of gem corundum using elemental fingerprint analysis by laser ablation inductively coupled plasma mass spectrometry. *International Journal of Mass Spectrometry*, Vol. 306, No. 1, pp. 57–62, http://dx.doi.org/10.1016/j.ijms.2011.06.010

Rinaldi R., Llovet X. (2015) Electron probe microanalysis: A review of the past, present, and future. *Microscopy and Microanalysis*, Vol. 21, No. 5, pp. 1053–1069, http://dx.doi.org/10.1017/S1431927615000409

Saeseaw S., Weeramonkhonlert V., Khowpong C., Ng-Pooresatien, N., Sangsawong S., Raynaud V., Ito C. (2015) Cobalt diffusion of natural spinel: A report describing a new treatment on the gem market. *GIA Research News*, June 3, https://www.gia.edu/doc/Cobalt-Diffusion-in-Spinel-v2.pdf

Saeseaw S., Renfro N.D., Palke A.C., Sun Z., McClure S.F. (2019) Geographic origin determination of emerald. *G&G*, Vol. 55, No. 4, pp. 614–646, http://dx.doi.org/10.5741/GEMS.55.4.614

Shen A.H., Koivula J.I., Shigley J.E. (2011) Identification of extra-terrestrial peridot by trace elements. *G&G*, Vol. 47, No. 3, pp. 208–213, http://dx.doi.org/10.5741/GEMS.47.3.208

Sohrabi S., Cooper A. (2023) Lab Notes: Translucent ruby filled with zinc glass. *G&G*, Vol. 59, No. 3, pp. 368–369.

Sun Z., Palke A.C., Muyal J., DeGhionno D., McClure S.F. (2019a) Geographic origin determination of alexandrite. *G&G*, Vol. 55, No. 4, pp. 660–681, http://dx.doi.org/10.5741/GEMS.55.4.660

Sun Z., Palke A.C., Breeding C.M., Dutrow B.L. (2019b) A new method for determining gem tourmaline species by LA-ICP-MS. *G&G*, Vol. 55, No. 1, pp. 2–17, http://dx.doi.org/10.5741/GEMS.55.1.2

Sylvester P. J., Jackson S.E. (2016) A brief history of laser ablation inductively coupled plasma mass spectrometry (LA–ICP–MS). *Elements*, Vol. 12, No. 5, pp. 307–310, http://dx.doi.org/10.2113/gselements.12.5.307

Zaw K., Sutherland L., Yui T.F., Meffre S., Thu K. (2015) Vanadium-rich ruby and sapphire within Mogok Gemfield, Myanmar: Implications for gem color and genesis. *Mineralium Deposita*, Vol. 50, No. 1, pp. 25–39, http://dx.doi.org/10.1007/s00126-014-0545-0

Glowing Gems: Fluorescence and Phosphorescence of Diamonds, Colored Stones, and Pearls

Ulrika F.S. D'Haenens-Johansson, Sally Eaton-Magaña, W. Henry Towbin, and Elina Myagkaya

The use of photoluminescence imaging for gemstone characterization is reviewed, considering both fluorescence and its time-delayed counterpart, phosphorescence. Luminescence results from the excitation of atomic impurities and defects by an external source. Fluorescence can be excited by ultraviolet, visible, or infrared light, or even X-rays. Fluorescence to long-wave UV light is a characteristic included in diamond grading reports issued by major gemological laboratories. This article provides a comprehensive overview of the principles, mechanisms, and characteristics of luminescence that create the impressive and memorable glow of gemstones. Although diamond is the focus, a variety of colored stones and pearls are reviewed as well. This article is intended to foster a deeper appreciation of the complexity necessary to understand these natural wonders.

Have you ever wondered why certain materials appear to glow from within when exposed to ultraviolet light? Luminescence, the emission of energy as light following the absorption of applied energy, is a fascinating and often beautiful property of many minerals and gemstones (figure 1). Luminescence phenomena can be classified according to the excitation source, such as: incident light or photons (photoluminescence, PL), an electron beam (cathodoluminescence), heat (thermoluminescence), electric currents (electroluminescence), and friction (triboluminescence). Luminescence signals can be detected through visual inspection, camera imaging, or spectroscopic means. This review will focus on photoluminescence, further separated into fluorescence or phosphorescence (within gemology defined as during or following excitation, respectively), as well as observations and imaging as routes to explore luminescent defects in gem materials. The luminescence energies or wavelengths (which are inversely proportional to one another) of a suitably excited gemstone can reveal a wealth of information related to its chemical and structural identity and purity. Additionally, the spatial distribution of luminescence features can elucidate a gem's unique growth and potential treatment history. Although applications for colored stones and pearls will be discussed, diamond will be the primary example presented. The detailed multidisciplinary study of diamond's luminescence has captivated gemologists, geologists, and physicists for centuries since Robert Boyle's first reported observation in 1664 (Boyle, 1664).

In Brief

- Ultraviolet light can excite fluorescence and phosphorescence in many gems, providing insights into the material's chemical and structural identity.
- The luminescence response depends on the excitation wavelength. Deep-UV illumination (<225 nm) will induce fluorescence from practically all diamonds, even if inert to long- or short-wave UV.
- The luminescence colors observed depend on the impurity and structural defect structures present in the crystal lattice.
- The spatial distribution of luminescence features can reveal whether a gem is natural or laboratory-grown, and may also indicate treatment, coating, dyeing, and fracture filling.

See end of article for About the Authors and Acknowledgments.
Gems & Gemology, Vol. 60, No. 4, pp. 560–580,
http://dx.doi.org/10.5741/GEMS.60.4.560

Figure 1. Burmese ruby and diamond necklace and earrings under daylight-equivalent (left) and long-wave ultraviolet (right, ~365 nm) illumination, revealing an alluring fluorescence response. Several of the diamonds show blue fluorescence attributed to the N3 (N_3V^0) defect, whereas trivalent chromium ions (Cr^{3+}) produce red fluorescence in the rubies. Intense red fluorescence is particularly common in Burmese rubies, though not exclusive to them (Webster, 1975; Fritsch and Waychunas, 1994). Courtesy of a private collector and Mona Lee Nesseth, Custom Estate Jewels. Photos by Robert Weldon.

PRINCIPLES OF LUMINESCENCE

A deeper understanding and appreciation of luminescence requires the consideration of the electronic states of the species within a material being excited (e.g., a structural defect or impurity) and where they lie relative to the electronic band structure of the crystal. The electronic band structure of a solid describes the energy ranges or levels that its electrons may have according to the principles of quantum mechanics. This model lays the foundation for explaining many of the electronic and optical properties of insulating and semiconducting materials such as gemstones.

Diamond, for instance, consists of carbon atoms in a tetrahedral configuration, with each atom covalently bonded to four neighboring atoms. The interaction between the carbon atoms results in diamond's characteristic electronic band structure, illustrated in figure 2. The outermost electrons of the carbon atoms that are involved in the chemical bonding occupy the valence band, which is separated from the empty, electronically allowed conduction band by the forbidden band gap, with energy E_g. Diamond is classified as either an insulator or a wide-band gap semiconductor with an indirect band gap energy E_g ~5.49 eV (Clark et al., 1964)—practically too wide to conduct through thermal energy alone. However, if an electron in a perfect defect-free diamond is exposed to light with energy $>E_g$, the electron-pair bonds can be successfully broken and the electron can be excited into the conduction band, resulting in intrinsic edge absorption (Collins, 1992, 1993; Green et al., 2022). The excited electron leaves behind a hole in the valence band, conceptually a positively charged electron void. Together, the electron-hole pair is known as an exciton and can move through the crystal as a unit. As the electron deexcites back to the valence band, it releases energy in the form of a photon—i.e., creating luminescence and recombining with the hole. Since diamond is an indirect semiconductor, the excitation of electrons into the lowest energy level of the conduction band also involves lattice vibrational waves known as phonons, that are affected by the sample's temperature (Collins et al., 1990a; Collins, 1993; Barjon, 2017). The loss of energy through nonradiative processes means that the

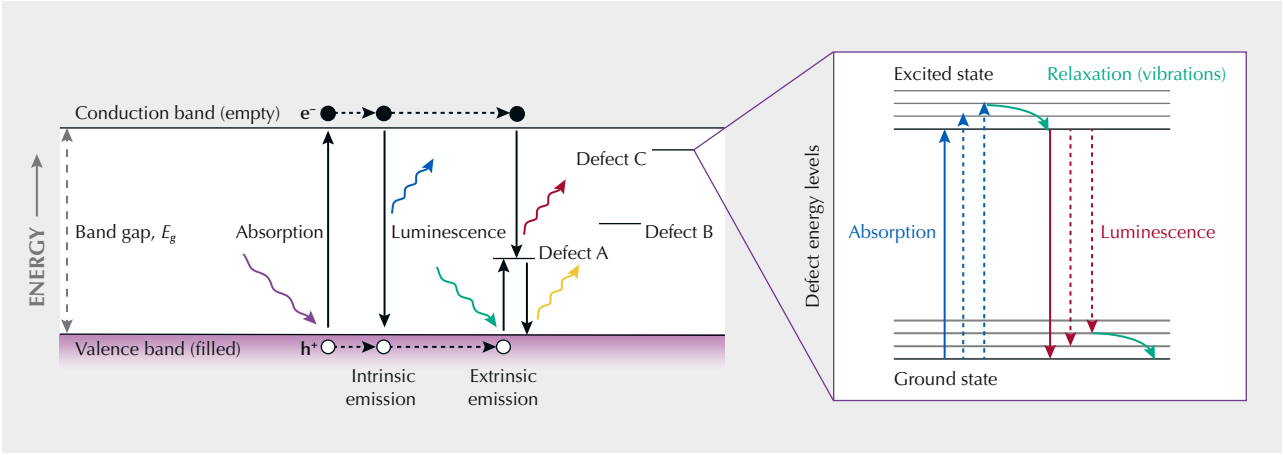

Figure 2. The filled valence band and empty conduction band in a semiconductor and insulator are separated by the band gap energy (E_g). Intrinsic luminescence can occur when incident photons (light) or electrons of energies greater than the band gap excite valence electrons (e^-) into the conduction band, leaving behind holes (h^+). In the absence of any defects, the electrons and holes may recombine, emitting intrinsic luminescence. Defects introduce energy levels within the band gap that can trap the electrons, resulting in extrinsic emission. Each defect has its own characteristic energy level structure that can also lead to absorption and emission processes at lower excitation energies. Nonradiative relaxation processes can also occur, producing vibronic structure in both the absorption and emission spectra (e.g., figure 3).

emitted light has a lower energy E (i.e., longer wavelength λ) than the light that was originally absorbed. In this ideal, defect-free diamond, the resulting emitted light is its intrinsic edge emission (Collins, 1992, 1993; Barjon, 2017).

Luminescence becomes significantly more interesting—and informative—if we move away from a perfect crystal. Crystalline gems can contain a variety of atomic-scale irregularities, scientifically termed *point defects*, in their crystal lattice due to their unique formation and post-growth environmental histories. For diamond, these point defects include missing carbon atoms (vacancies), displaced atoms (interstitials), and impurity complexes based on elements including nitrogen, boron, nickel, silicon, and hydrogen. Extended defects such as dislocations also exist. Their presence disturbs the host lattice, introducing additional energy levels within the band gap (figure 2). Defects introduce alternative relaxation pathways following exposure to above band gap excitation energies, leading to extrinsic emission with characteristic energies that allow the defects to be identified. Furthermore, these defects open up the possibility that incident light with energies smaller than the band gap energy (longer wavelengths) may be absorbed and subsequently emitted if the photon energy lies within a defect's absorption band. Thus, diamonds with defects can support vibronic transitions of electrons—combining vibrational and electronic interactions—between the valence band, defect energy levels, and the conduction band, leading to a rich combination of absorption and luminescence features (Collins, 1992, 1993).

In colored stones such as rubies, sapphires, and emeralds, it is the electrons in trace amounts of the metallic ions (e.g., Cr^{3+}, V^{3+}, and/or $Mn^{3+/2+}$) or rare earth elements in the host lattice that are excited and subsequently luminesce (Fritsch and Waychunas, 1994; Ponahlo, 2000; Waychunas and Kempe, 2024). These are often called activators. In some cases, sensitizers or coactivators, such as Pb^{2+} for Mn^{2+}, facilitate fluorescence by strongly absorbing the incident light and transferring the energy to the activator. Waychunas and Kempe (2024) present a detailed review of activators, sensitizers, and electronic defects and their roles in the luminescence of minerals.

The spectroscopic signatures of these luminescence features for diamond and other gemstones have been tabulated and described in several publications (e.g., Collins, 1982, 1992; Ponahlo, 2000; Zaitsev, 2001; Gaft and Panczer, 2013; Luo and Breeding, 2013; Shigley and Breeding, 2013; Gaft et al., 2015; Green et al., 2022; Zhang and Shen, 2023). Identifying the structural defects associated with these features is a nontrivial matter that combines rigorous experimental and theoretical work that may span several decades. Importantly, *correlation does not imply causation*. Somewhat confusingly, features may be referred to by their most recognizable energy or wavelength of absorption or emission

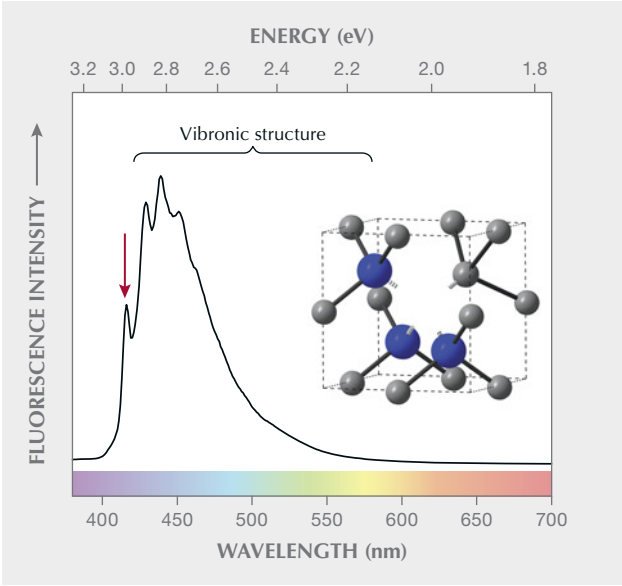

Figure 3. The blue fluorescence commonly observed for natural diamonds (e.g., figure 1) is attributed to emission from the N3 defect (inset), consisting of three nitrogen atoms surrounding a vacancy, N_3V^0. Its characteristic spectrum has a zero-phonon line at 415 nm (arrow) and vibronic structure extending to longer wavelengths.

(often the zero-phonon line [ZPL] for vibronic defects), by a nickname, or by their structural identity (if determined). For example, blue luminescence from diamond is often associated with the N3 defect (as pictured in figure 1) (Clark et al., 1956). It is characterized by a ZPL at 415 nm (2.985 eV), with vibronic structure extending to higher or lower wavelengths for emission and absorption, respectively (e.g., Davies et al., 1978). During room temperature luminescence, the vibronic structure of N3—peaking at ~450 nm—dominates (figure 3), resulting in visible blue emission. The N3 defect has been conclusively identified as three nitrogen atoms surrounding a vacancy, N_3V^0 (when considering diamond defects, "V" stands for a vacancy instead of the element vanadium) (Davies et al., 1978; van Wyk and Loubser, 1993; Green et al., 2017).

When multiple luminescing defect species are present, they may be excited simultaneously, depending on the incident energy. For energies above the band gap ($>E_g$), emission at defects can be induced by the capture of the exciton. Spectroscopically, each defect's contribution can be distinguished. Yet during visual or imaging-based observations, the overlapping luminescence features cannot be separated and instead the combined color is perceived. These contributions can be separated by optical filtering of the emission signal. Deliberate tuning of the excitation energy can also lead to selective excitation of defects, depending on their energy structure and absorption. If the incident energy of the photons ($<E_g$) matches the absorption spectrum of one or more defects, electron excitation may occur at those defects, followed by emission. If the energy does *not* coincide with the absorption of one or more of the defect species, those defects will remain inert and the overall luminescence response will instead be based on that of the other defects present.

Whereas the absorption of light by a defect is proportional to its concentration, the potential presence of other nonradiative relaxation pathways means that luminescence is only semiquantitative. A sufficient concentration of the defect must be present for significant absorption of the incident radiation, yet the subsequent emission may be weak if the energy is instead transferred nonradiatively to another defect, effectively quenching the defect's luminescence. For instance, the luminescence of N3 (N_3V^0), H3 (N_2V^0), and GR1 (V^0) defects in diamond can be quenched by A-centers (nitrogen pairs) (Davies and Crossfield, 1973; Crossfield et al., 1974; Thomaz and Davies, 1978; Davies et al., 1987), while the transition metal ions Fe^{+3}, Fe^{+2}, Co^{+2}, and Ni^{+2} are common quenchers in colored stones (Ponahlo, 2000; Fritsch and Waychunas, 1994; Yu and Clarke, 2002; Waychunas, 2014; Waychunas and Kempe, 2024). Other forms of quenching are concentration quenching, where high concentrations of activators in colored stones result in the fluorescence being absorbed by neighboring ions of the same species, and thermal quenching, where a temperature increase results in increasing lattice vibrations that carry off the excitation energy (Fritsch and Waychunas, 1994).

EVOLUTION OF FLUORESCENCE AND PHOSPHORESCENCE OBSERVATION METHODS

In 1852, the Irish physicist George Stokes created the term "fluorescence" to refer to the visible light reaction seen in objects when illuminated by ultraviolet light. In his magnum opus (Stokes, 1852), he added a footnote: "I am almost inclined to coin a word and call the appearance fluorescence, from fluor-spar [fluorite], as the analogous term opalescence is derived from the name of a mineral." The excitation ranges associated with the term have expanded over time to encompass short-lived luminescence excited by electromagnetic radiation from X-rays, ultraviolet, visi-

ble, and infrared sources. This feature is commonly observed in gemstones and minerals, and its measurement has become standard practice in gemology.

Gemologists typically observe fluorescence using long-wave (defined as 365 nm emission) and short-wave (254 nm) UV excitations, based on the filtered output from readily available and inexpensive mercury-vapor discharge lamps. Unfortunately, the band-pass filters in these portable lights deteriorate over time, allowing additional mercury emissions to slip through and leading to variability in the observed fluorescence (Williams, 2007; Pearson, 2011; Luo and Breeding, 2013). Filtering or monochromating the broadband emission of a xenon arc lamp is also an option (e.g., Hainschwang et al., 2013). Currently, long- and short-wave UV light is frequently produced for fluorescence applications using LEDs, or light-emitting diodes (Luo and Breeding, 2013).

In 1996, De Beers launched the DiamondView instrument, which illuminates samples using ultra-short wave or deep-UV illumination ($\lambda < 225$ nm, $E > 5.51$ eV) generated by filtering the output from a xenon flash lamp (Welbourn et al., 1996). Targeting diamond, this wavelength results in excitation with above band gap energy, inducing fluorescence from practically all diamonds, including those that are inert to long-wave and short-wave UV. As diamond is strongly absorbing of light with $E > E_g$, the fluorescence is generated close to the sample surface, resulting in sharp patterns that can be used as evidence of the diamond's identity (natural or laboratory-grown), as well as possible dissolution and treatment, as described later in this article. In a fully enclosed system, digital images of sample fluorescence and phosphorescence can be collected under either optical or digital magnification (original and current design, respectively). A selection of optical filters (blue = 390 nm band-pass, green = 475 nm long-pass, orange = 550 nm long-pass, and red = 725 nm long-pass) can be placed in the detection path to restrict the detected wavelengths, enabling more detailed inspection of the spatial distribution of otherwise overlapping emissions. The DiamondView rapidly established itself as a popular tool for diamond identification, and images collected from it are frequently included in diamond studies. Deep-UV fluorescence imaging studies of other gemstone materials are limited, though this energy can effectively excite common fluorescence features and provide the magnification necessary to observe their distribution.

UV lamp output can significantly affect the observed fluorescence and phosphorescence color and intensities for gemstones. Pearson (2011) and Luo and Breeding (2013) present emission spectra for common UV light sources used by the jewelry industry and hobbyists. Observation, whether unaided or using a microscope, should include light filtration through appropriate engineering controls and/or the use of UV goggles to avoid eye and skin damage. Color cameras can be used to safely capture and store fluorescence and phosphorescence images for subsequent analysis. Although most fluorescence testing in gemology today is still based on visual observation and imaging, technological developments and lower equipment costs have made fluorescence spectroscopy a much more widely used tool for rapid analysis (e.g., Hainschwang et al., 2013, 2024; Tsai and D'Haenens-Johansson, 2021; Zhang and Shen, 2023; Tsai et al., 2024).

There have been several compilations of fluorescence and phosphorescence observations across various gems (e.g., Kunz and Baskerville, 1903; De Ment, 1949; Webster, 1983; Fritsch and Waychunas, 1994; Hainschwang et al., 2024). These works established the definitions of fluorescence and phosphorescence still used by gemologists today. Namely, fluorescence is "luminescence lasting only during the direct influence of the exciting agent," and phosphorescence is the "emission or propagation of ethereal stresses, which affect the optical centers, producing light, white or colored, which persists after the removal of the cause" (Kunz and Baskerville, 1903).

FLUORESCENCE AND PHOSPHORESCENCE OBSERVATIONS OF DIAMONDS

Short-Wave and Long-Wave UV Excited Luminescence of Diamonds. The luminescence of diamonds has long captured the interest of the scientific community and the jewelry industry. One of the first documented instances was by the famous Irish scientist Robert Boyle, who noted that a flash of light was released when a diamond broke, a phenomenon now known as triboluminescence (Boyle, 1664). In 1813, the English mineralogist John Mawe discussed the luminescence of diamonds exposed to sunlight and also to electricity (electroluminescence) (Mawe, 1813). Since then, numerous publications have documented observations of fluorescence and, less commonly, phosphorescence in gem diamond (e.g., Anderson, 1943; Dyer and Matthews, 1958; Moses et al., 1997; Eaton-Magaña et al., 2007; Luo and Breeding, 2013; Breeding and Eaton-Magaña, 2019).

Among natural colorless to faint yellow colored diamonds on the D-to-Z scale, approximately 35% fluoresce when exposed to long-wave UV light (Moses et al., 1997). While a rainbow of fluorescence colors are possible, the overwhelmingly most common color is blue (97%) due to emission by the N3 (N_3V^0) defect, as shown in figures 1, 3, and 4 (Moses et al., 1997; Luo and Breeding, 2013). Green fluorescence is usually caused by the H4 (ZPL at 496.2 nm, $N_4V_2^0$) or H3 (ZPL at 503.2 nm, N_2V^0) defects, but it can occasionally arise from the nickel-nitrogen-related S2 and S3 defects (ZPLs at 489.2 and 496.7 nm, respectively) (Clark et al., 1956; Collins, 1982, 1992; Eaton-Magaña et al., 2007; Yelisseyev and Kanda, 2007; Luo and Breeding, 2013). An overlapping combination of unidentified broad emission bands in the ~500–700 nm range are responsible for yellow to orange fluorescence (e.g., figure 4), most clearly detected in diamonds with 480 nm band absorption and in color-changing "chameleon" diamonds, though notably the fluorescence is not directly caused by the 480 nm band defect (Hainschwang et al., 2005; Eaton-Magaña et al., 2007; Fritsch et al., 2007; Luo and Breeding, 2013; Byrne et al., 2018; Lai et al., 2024). Finally, orange to red fluorescence can be produced by $NV^{0/-}$ defects (ZPLs at 575 and 637 nm, respectively) (Davies and Hamer, 1976; Collins, 1992; Eaton-Magaña et al., 2007; Luo and Breeding, 2013). This list is not exhaustive, and Shigley and Breeding (2013) provided a convenient diamond defect reference chart showing representative fluorescence images under long-wave and deep-UV (DiamondView) excitations. For natural diamonds, the fluorescence response is generally stronger to long-wave compared to short-wave UV, though there are exceptions.

The scientific definition of phosphorescence is complex, linked to the luminescence lifetime and the types of transitions that produce it (Nasdala and Fritsch, 2024). In practical terms, it is typically considered the emission of light after excitation is turned off (i.e., an "afterglow"). As a general guide, any emission lasting longer than 100 ns following excitation can be classified as phosphorescence. Most of the famous natural diamond examples are boron-contain-

Figure 4. Representative long-wave, short-wave, and deep-UV excited fluorescence and phosphorescence responses for D-to-Z color natural and laboratory-grown diamonds. Diamond origin details: blue-fluorescing natural (A), yellow-fluorescing natural (B), untreated CVD-grown (C), HPHT-annealed CVD-grown (D), and HPHT-grown (E). White light, long- and short-wave fluorescence, and phosphorescence images by Towfiq Ahmed. Deep-UV fluorescence and phosphorescence images by Ulrika F.S. D'Haenens-Johansson.

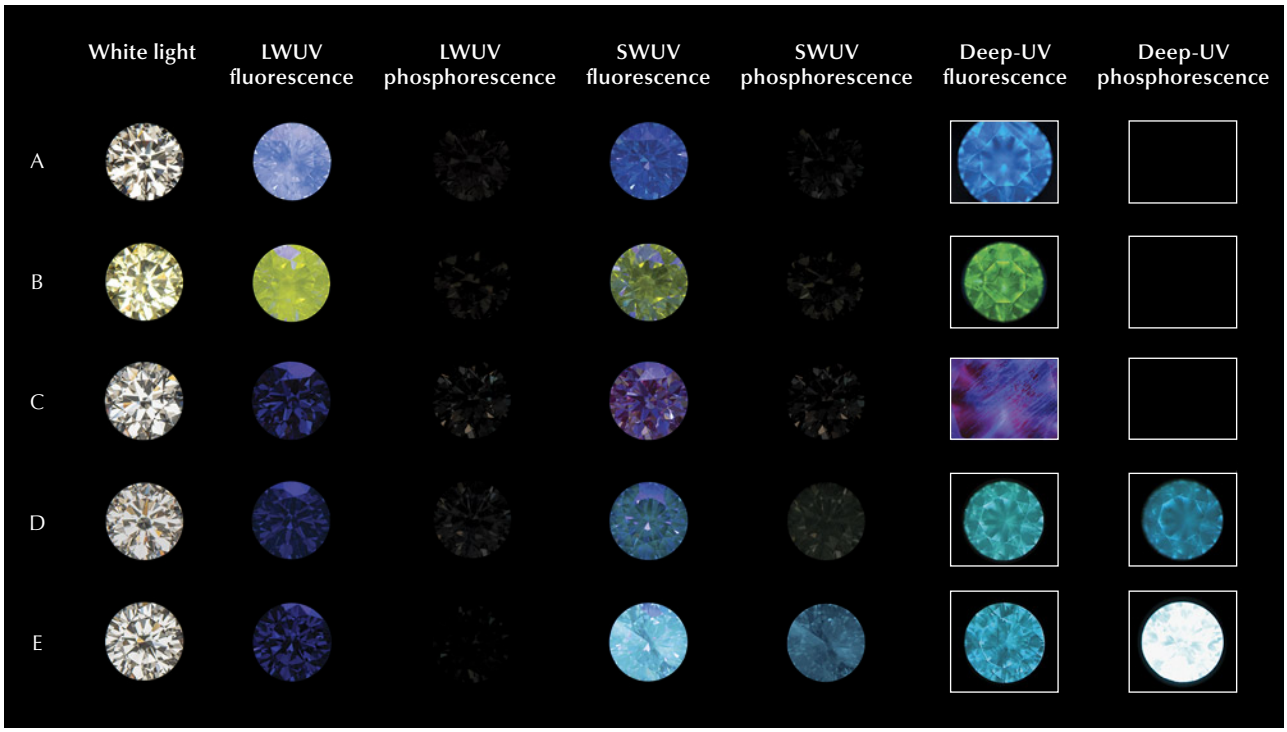

ing type IIb diamonds, which can show chalky blue to green, or rarely red or orangy red, phosphorescence following exposure to short-wave UV (Eaton-Magaña et al., 2008; Gaillou et al., 2010a). The phosphorescence can last from a few seconds to typically under a minute, though rare longer-lived natural examples exist (Shen and Eaton-Magaña, 2011). The phosphorescence is produced by two emission bands centered at 500 nm (blue-green) and 660 nm (red); the relative intensities and lifetimes determine the dominant phosphorescence color and its possible color evolution with time (Eaton-Magaña et al., 2008; Gaillou et al., 2010b; Eaton-Magaña and Lu, 2011). The mechanism used to explain the broad blue-green band is donor-acceptor pair recombination (DAP), where electrons bound to substitutional nitrogen defects (N_S^0, the donors) and holes bound to substitutional boron defects (B_S^0, the acceptors) are excited by the ultraviolet light, emitting phosphorescence as they recombine (Dean, 1965; Watanabe et al., 1997; Eaton-Magaña et al., 2008; Eaton-Magaña and Lu, 2011; Zhao et al., 2023). The detailed origin of the red band remains unexplained. Phosphorescence has also been reported for type I diamonds. Weak yellow and blue phosphorescence can be observed in strongly blue-fluorescing (N3) diamonds (Chandrasekharan, 1946a,b). Yellow phosphorescence following short-wave UV excitation, with a band centered at 550 nm, is considered a defining characteristic of color-changing "chameleon" diamonds (Hainschwang et al., 2005; Byrne et al., 2018; Lai et al., 2024).

The luminescence behavior of laboratory-grown diamonds produced by the high-pressure, high-temperature (HPHT) and chemical vapor deposition (CVD) methods has been studied extensively since their inception in the 1950s. For recent detailed reviews on the synthesis of diamond using these techniques, see Palyanov et al. (2015), Arnault et al. (2022), and D'Haenens-Johansson et al. (2022). These diamonds' fluorescence and phosphorescence properties, along with the distributions of the associated defects (discussed later in this article), have been exploited for diamond screening to separate natural from laboratory-grown diamonds, resulting in an assortment of device designs and approaches (Welbourn et al., 1996; Martineau et al., 2004; Hainschwang et al., 2013; Lan et al., 2016; Dupuy and Phillips, 2019; McGuinness et al., 2020; Tsai and D'Haenens-Johansson, 2021; Tsai et al., 2024).

Shigley et al. (2004a) and D'Haenens-Johansson et al. (2022) tabulated common fluorescence and phosphorescence characteristics for HPHT-grown diamonds produced with a range of bodycolors. Eaton-Magaña et al. (2017) analyzed several thousand HPHT-grown diamonds submitted to GIA from 2007 to 2016 and found that those showing fluorescence generally had a stronger reaction to short-wave UV than to long-wave UV, in contrast with most natural fluorescing diamonds. Since the majority of HPHT-grown diamond gemstones in the market today are colorless, including >90% of those submitted to GIA, it is appropriate to highlight their luminescence characteristics here (Eaton-Magaña et al., 2024). Among colorless and near-colorless HPHT-grown diamonds, the vast majority are inert to long-wave UV, with a yellow or orange emission if observed, while ~90% show yellow or yellow-green fluorescence to short-wave UV (Eaton-Magaña et al., 2017). Short-wave UV also induces an often strong and long-lived blue, yellow, or green-yellow phosphorescence that is associated with boron (Watanabe et al., 1997; Eaton-Magaña and Lu, 2011; Zhao et al., 2023). The range of phosphorescence colors observed are influenced by the intensities and lifetimes of a boron-related blue emission band centered at 500 nm and an orange or yellowish orange emission band whose center can range from 575 to 590 nm (Watanabe et al., 1997; Eaton-Magaña et al., 2008; Eaton-Magaña and Lu, 2011; D'Haenens-Johansson et al., 2015; Zhao et al., 2023). Figure 4 shows an example of the fluorescence and phosphorescence response of a colorless HPHT-grown diamond compared to that for natural and CVD-grown diamonds. It is, however, possible to reduce and even remove the phosphorescence through irradiation treatment, leaving screening instruments that rely on this feature vulnerable (Robinson, 2018; Dupuy and Phillips, 2019; Eaton-Magaña et al., 2024).

CVD-grown diamonds dominate the non-melee-sized laboratory-grown gem market; they currently account for ~80% of laboratory-grown diamond submissions to GIA (Eaton-Magaña et al., 2024). Of those, ~80% are graded as colorless. To achieve such high colors, CVD-grown diamonds are regularly subjected to HPHT or LPHT (low-pressure, high-temperature) annealing treatments, in which less desirable brown hues are reduced or removed (e.g., Martineau et al., 2004; Meng et al., 2008; Wang et al., 2012; Eaton-Magaña et al., 2021, 2024; D'Haenens-Johansson et al., 2022). These treatments modify the relative concentrations of defects in the material, resulting in changes to the fluorescence behavior. Early "as-grown" (untreated) CVD diamonds sometimes showed orange, orange-yellow, or yellow fluorescence

to both long- and short-wave UV (with a stronger response to the latter) from high concentrations of $NV^{0/-}$ defects (Martineau et al., 2004; Wang et al., 2007). Yet, as the colors and purity levels of as-grown products have improved, they are now nearly all inert under both long- and short-wave UV illumination (Eaton-Magaña et al., 2021); see, for instance, the sample shown in figure 4. Decolorizing annealing treatments reduce the relative concentration of NV centers while introducing green fluorescence from H3 (N_2V^0) defects or an unidentified defect with a ZPL at 499 nm and a complex vibronic band centered at ~550 nm; these treatments are most easily detected using short-wave UV (Martineau et al., 2004; Wang et al., 2012; Wassell et al., 2018; McGuinness et al., 2020). Weak blue-green phosphorescence associated with trace amounts of boron may also be introduced (Wang et al., 2012). The fluorescence and phosphorescence behavior for an HPHT-annealed colorless CVD diamond using long-wave, short-wave, and deep-UV illumination is shown in figure 4.

Spatial Distribution of Fluorescent and Phosphorescent Defects in Diamond: Analysis Using Deep-UV. Natural diamond can be pictured as growing outward from a nucleating core, supplied with carbon atoms from melts and fluids, deep in the earth's mantle at the high temperatures and pressures at which diamond—rather than its allotrope graphite—is stable. Sunagawa (1984) and Harris et al. (2022) presented comprehensive reviews of natural diamond *morphology*, or crystal shape. The ideal natural diamond rough morphology is octahedral: two square-based pyramids connected at the base with {111}-oriented faces.[1] The second most common morphology has well-developed, gently curved, and hummocky square faces that are approximately {100}-oriented. As they are not true {100} cubic faces, the preferred name for this morphology is *cuboid*. Diamonds can also experience mixed habit growth, though rarely observed, developing both octahedral and cuboid faces. By the time the diamond is recovered, the external morphology could be dramatically modified through geological processes, leading to rounded and irregular shapes. Furthermore, in the gem trade, the external surfaces are removed through polishing. Yet all is not lost: Conditions of natural diamond formation, their residence in the mantle, and subsequent transportation to the surface combine to leave an imprint.

Diamond growth progresses through a series of episodes, experiencing changes in the growth environment and the source fluid composition. Additionally, diamonds can potentially go through periods during which their surfaces are attacked by aggressive fluids, removing atoms and leading to crystal dissolution and resorption (Fedortchouk, 2019; Fedortchouk et al., 2019; Smit and Shirey, 2020; Harris et al., 2022). Diamonds may also be subjected to plastic deformation, introducing extended defects such as dislocations and glide planes (Evans and Wild, 1965; Willems et al., 2006; Laidlaw et al., 2020, 2021). As a result, the distributions, combinations, and relative concentrations of defects present in the crystal are heterogeneous, and every diamond has a unique and complex internal growth structure that reveals a fascinating history. One can think of these patterns as analogous to the growth rings present within a tree trunk, with variations caused by cyclical environmental changes as well as stressing conditions such as disease or insect infestations.

Since many diamond defects are luminescent, their distribution may be observed through fluorescence and phosphorescence, as well as electron-beam excited cathodoluminescence imaging (e.g., Welbourn et al., 1996; Harris et al., 2022). Although growth structure can occasionally be perceived through long-wave or short-wave UV illumination, the preferred excitation energy of incident photons is greater than diamond's band gap energy, here termed deep-UV, resulting in surface-specific emission from practically all diamonds (Welbourn et al., 1996). The characteristic fluorescence colors associated with specific luminescing defects described in the previous section remain unchanged, though the emission efficiency is generally improved using deep-UV illumination. Additionally, deep-UV illumination is able to excite blue to green "band A" emission (Dean, 1965; Ruan et al., 1992; Green et al., 2022). Recent high-resolution multi-technique studies by Laidlaw et al. (2020, 2021) have shown that band A originates from unidentified defects in the material adjacent to dislocations and grain boundaries, which themselves act as nonradiative recombination centers (i.e., they are dark). Importantly, the fundamental growth structure of a diamond, whether natural

[1]In crystallography, the Miller indices *h*, *k*, and *l* are used to mathematically define crystal planes and directions, enveloped by different forms of brackets and parentheses. Briefly, the notation is as follows: {*hkl*} represents planes that are symmetrically equivalent to a specific plane (*hkl*). [*hkl*] is a specific direction lying perpendicular to (*hkl*), whereas <*hkl*> is a group of directions that are equivalent to [*hkl*] by symmetry. For diamond, key crystallographic faces are the {111} octahedral, {100} cubic, and {110} dodecahedral faces.

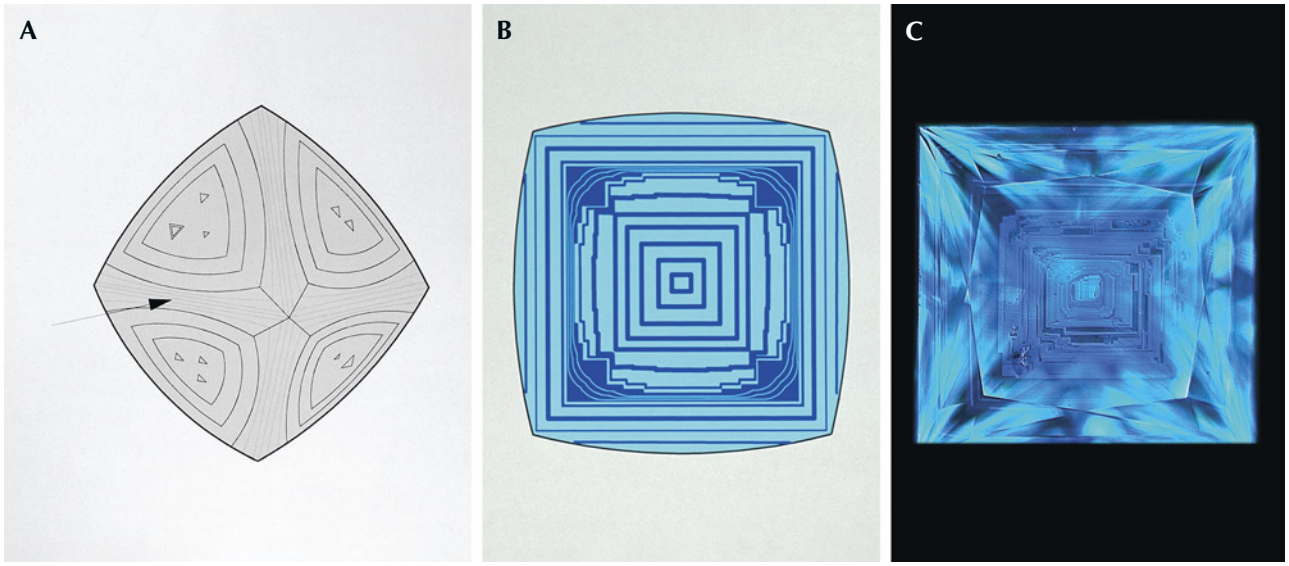

Figure 5. A: A representative illustration of a natural octahedral type Ia diamond crystal, showing rounded edges from resorption, as well as trigon etch pits. B: If the crystal was sliced along the central cubic {100} plane, the resulting distribution of fluorescent defects may show a series of concentric rectangles and hillocky rounded regions of cuboid growth. C: This 1.18 ct diamond displays an octahedral growth pattern when illuminated under deep-UV. Illustrations A and B are from Welbourn et al. (1996), and image C is from Chan (2009).

or laboratory-grown, cannot be changed by treatment, though the fluorescing colors can potentially be modified.

Internal growth patterns associated with natural octahedral diamond growth present themselves as a series of concentric squares or rectangles with varying luminescence, as shown in figure 5 (e.g., Welbourn et al., 1996; Harris et al., 2022). Depending on the crystallographic orientations of a polished diamond's facets and the viewing angle, the pattern may deviate from this ideal and appear truncated. Figure 6 shows a selection of natural diamond fluorescence patterns collected under deep-UV illumination. Cuboid growth introduces curved and hummocky growth horizons (figure 6A; Moore and Lang, 1972; Lang, 1974, 1979; Suzuki and Lang, 1976; Welbourn et al., 1989; Harris et al., 2022). Sometimes the internal growth patterns in natural diamond can be highly irregular or show multiple nucleation sites (figure 6B). Additionally, plastic deformation can introduce luminescent glide planes or dislocations (figure 6, C and D). Luminescence patterns in high-purity type IIa and boron-containing type IIb diamonds are typically dominated by polygonized dislocation networks (e.g., Hanley et al., 1977; De Corte et al., 2006; Smith et al., 2016, 2017; Smith, 2023), often emitting blue band A emission (figure 6E). High levels of natural irradiation can create structural damage to the diamond lattice, quenching luminescence, resulting in localized dark regions in fluorescence images, as shown in figure 6F (Schulze and Nasdala, 2016; Breeding et al., 2018; Smit et al., 2018; Breeding and Eaton-Magaña, 2019). Diamonds that phosphoresce under conventional UV excitation wavelengths, such as type IIb diamonds (e.g., figure 7), will also phosphoresce under deep-UV (e.g., Gaillou et al., 2010a; Eaton-Magaña and Lu, 2011; Eaton-Magaña et al., 2018). The response is typically more pronounced. With practice, these patterns can be recognized as natural, though complementary data is occasionally necessary for conclusive identification. Notably, treatments may or may not create changes in the fluorescence or phosphorescence colors, depending on the starting material and the treatment recipe (e.g., Hainschwang et al., 2008, 2009; Nasdala et al., 2013; Eaton-Magaña and Ardon, 2016; Wang et al., 2018; Breeding and Eaton-Magaña, 2019; Eaton-Magaña, 2020). Due to this variability, discussion is beyond the scope of this article.

The growth morphology of HPHT-grown diamonds is typically cuboctahedral, with well-developed cube {100} and octahedral {111} faces, with minor dodecahedral {110} and trapezohedral {113} faces (illustrated in figure 8), the balance of which can be affected by the growth temperatures (Strong and Chrenko, 1971; Kanda et al., 1980, 1989; Sunagawa, 1984, 1995; Satoh et al., 1990; Burns et al., 1999; Sumiya et al., 2002; D'Haenens-Johansson et

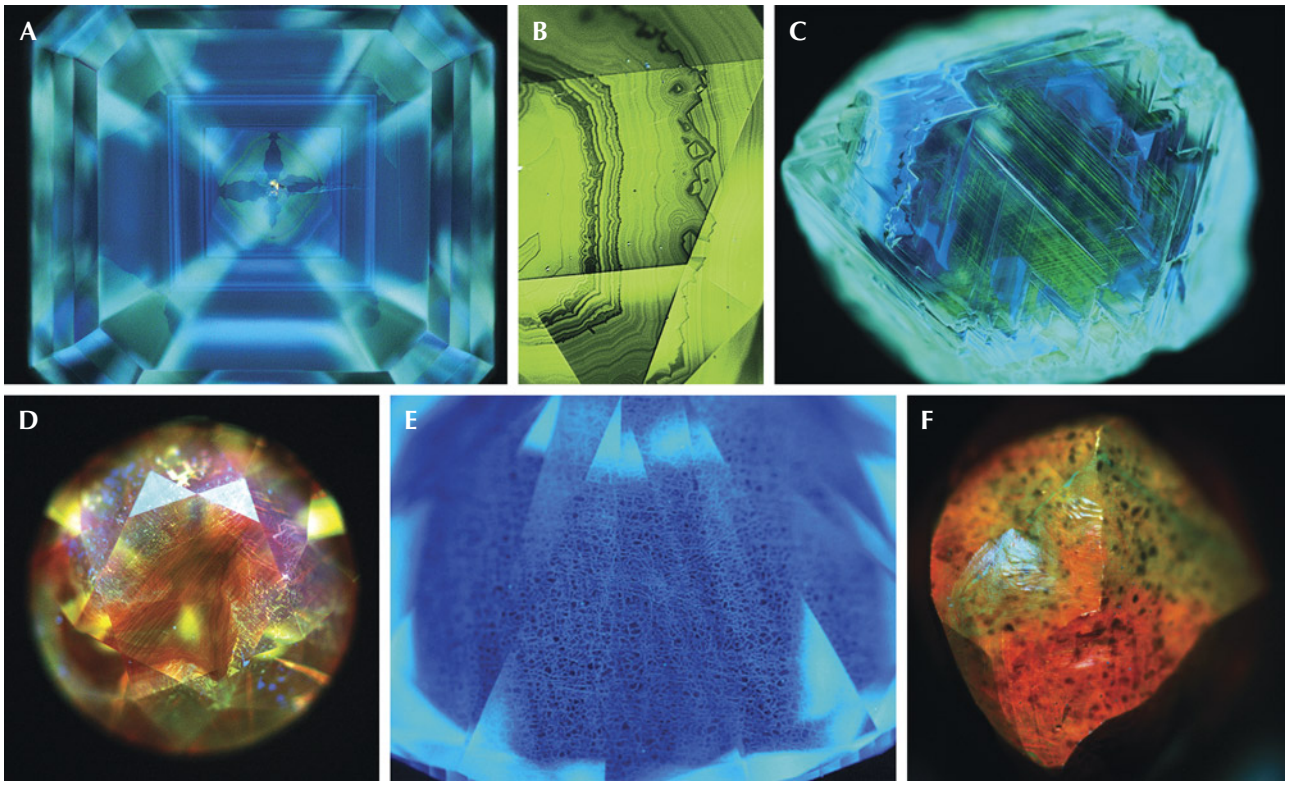

Figure 6. This selection of deep-UV fluorescence images of natural diamonds highlights the wide range of potential emission patterns and colors that can be observed, evidence of diamond's unique growth and residence history. E: Most natural type II diamonds show blue fluorescence with mosaic-like polygonized dislocation patterns, differing from characteristic type II CVD- or HPHT-grown diamond patterns (compare with figures 8–10). Images by Garrett Koneval (A), Najmeh Anjomani (B), Wuyi Wang (C), Christopher Vendrell (D), Ulrika F.S. D'Haenens-Johansson (E), and Sandeep Kabariya (F).

al., 2022). The uptake of impurities is strongly sector-dependent and sensitive to growth rates and temperatures (Strong and Chrenko, 1971; Burns et al., 1990, 1999; Satoh et al., 1990; Kiflawi et al., 2002). Boron concentrations are typically highest in {111} growth sectors, followed by {110} sectors; nitrogen concentrations follow a different order: {111} > {100} > {113} > {110} (Burns et al., 1990). The incorporation of nickel- and cobalt-related defects is also sector-dependent (Collins et al., 1990b; Lawson et al., 1996).

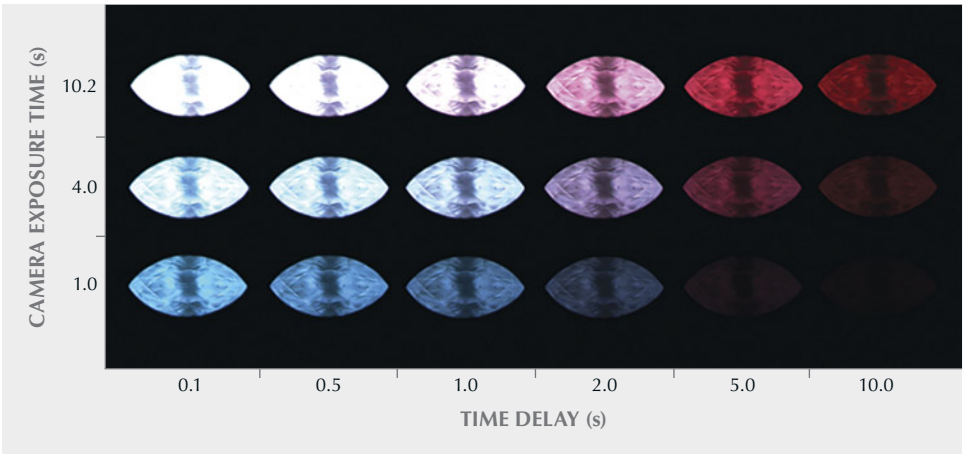

Figure 7. Following deep-UV illumination, the overall phosphorescence of natural type IIb diamonds may appear blue, gray, violet, or red due to emission bands centered at about 500 nm and/or 660 nm. From Moe and Johnson (2007).

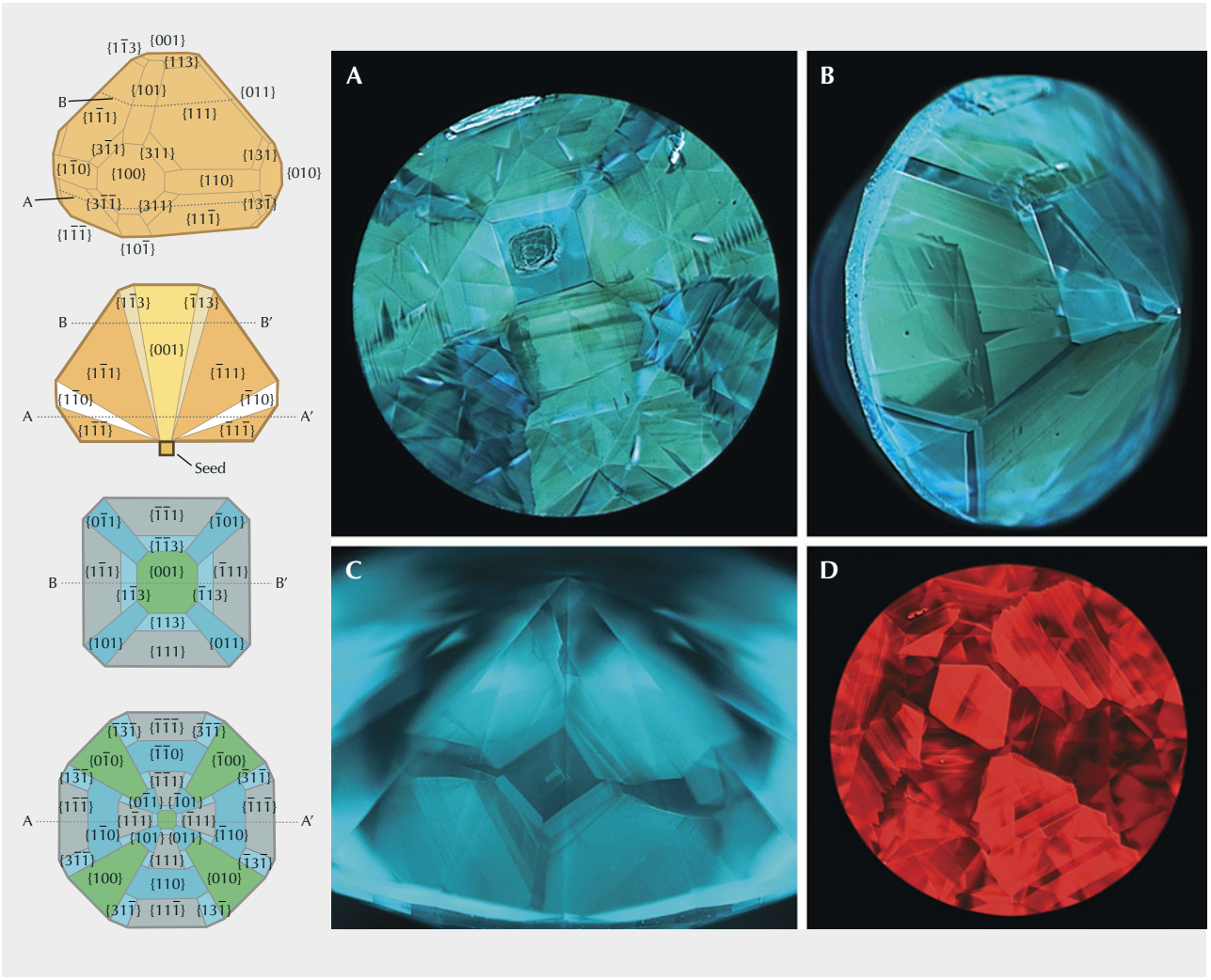

Figure 8. HPHT growth of diamonds typically results in crystals with a cuboctahedral morphology (top illustration), showing dominant octahedral {111} and cube {100} growth faces and minor dodecahedral {110} and trapezohedral {113} faces. The distribution of defects is highly heterogeneous, incorporating preferentially in certain growth sectors, shown as changing colors in the illustrations. The resulting characteristic sharp geometric growth patterns are apparent in deep-UV fluorescence images (A–D, where A and B are of the same sample), showing a range of fluorescence colors depending on growth chemistry and treatments. Colorless and near-colorless HPHT-grown diamonds, like this 4.07 ct E-color oval brilliant (C), typically show green-to-blue fluorescence followed by strong, long-lived phosphorescence. Illustrations from Welbourn et al. (1996).

In fancy-color HPHT-grown diamonds, the cuboctahedral distribution of defects may be noticeable under visible light, short-wave, and/or long-wave UV (e.g., Shigley et al., 2004a,b). Using deep-UV, the characteristic cuboctahedral growth patterns are enhanced (figure 8); this feature was largely the driving force for the development of the DiamondView instrument for diamond identification (Welbourn et al., 1996). The fluorescence colors depend on the concentration of defects, as summarized by Eaton-Magaña et al. (2017) and D'Haenens-Johansson et al. (2022). Colorless type II specimens fluoresce blue-green to green-blue, followed by remarkably long-lived green-blue (500 nm band) and/or yellow-orange (575 nm) phosphorescence, as shown in figure 8 (Watanabe et al., 1997; Eaton-Magaña et al., 2008, 2017; Eaton-Magaña and Lu, 2011; D'Haenens-Johansson et al., 2014, 2015; Zhao et al., 2023). The combination of the characteristic growth zonation, fluorescence color, and phosphorescence is recognizably different from what is observed for similarly colored natural and CVD-grown diamonds, making this a powerful tech-

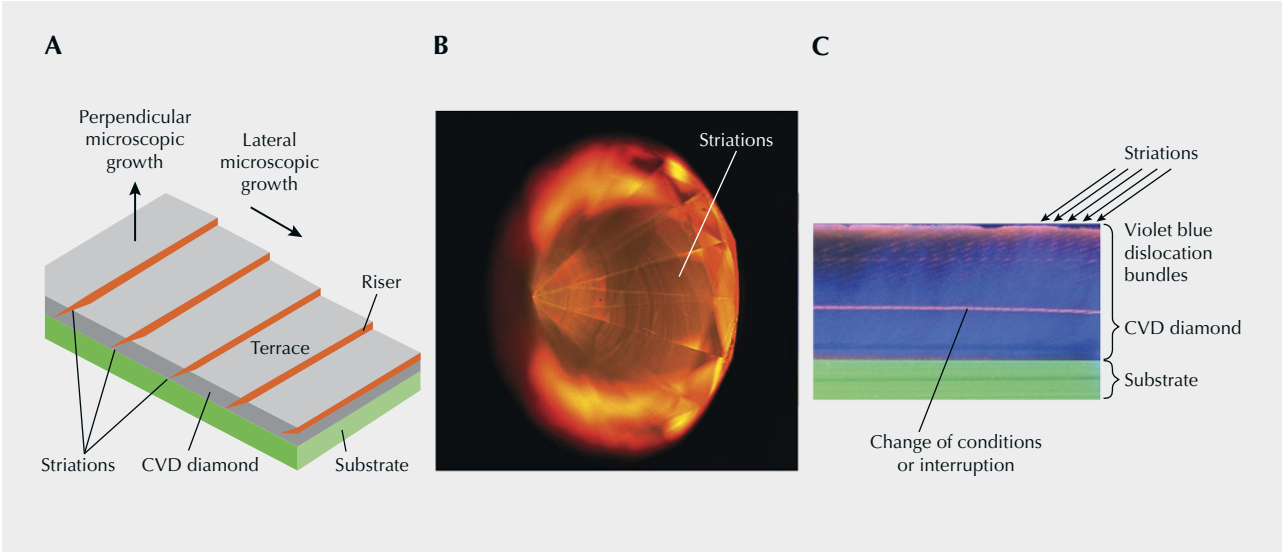

Figure 9. A: During the CVD growth process, diamond is deposited on a sacrificial diamond substrate as a series of flowing steps. Differences in defect incorporation between the risers and terraces form a pattern of tightly spaced striations. B: This 0.53 ct Fancy brownish pink untreated CVD-grown diamond shows a classic striation pattern, fluorescing orange from NV^0 defects under deep-UV illumination. C: Interruptions or changes in growth conditions can form either sharp or gradual interfaces that lie parallel to the main growth plane. Images A and C adapted from Martineau et al. (2004, 2009).

nique to differentiate between HPHT-grown and other diamond materials.

The CVD growth method is based on careful control of the gas-phase chemistry of a carbon-containing plasma that has been activated by a source of energy (typically microwaves), leading to diamond deposition on diamond seeds that act as the template for crystal growth. High-quality CVD diamond deposition usually occurs on (001)-oriented diamond seeds (also referred to as substrates), following what is known as "step-flow growth," with microscopic riser and terrace segments oriented along [001] and [101] directions, respectively (Martineau et al., 2004; 2009). The ensuing idealized layer-by-layer deposition produces a crystal with a cubic growth morphology. The different impurity uptake in the risers and terraces results in a heterogeneous incorporation of defects, creating a characteristic fluorescence pattern of tightly spaced striations that can be observed by deep-UV illumination (figure 9) (Martineau et al., 2004, 2009). Furthermore, any modifications to the growing conditions, whether unintentional or caused by planned interruptions, result in changes to the defect content in a plane parallel to the substrate, creating a layered appearance that depends on the viewing angle. This is a feature often observed in the deep-UV fluorescence images for large CVD-grown diamonds, presenting clear evidence they are produced through multiple-stage growth (e.g., Dieck et al., 2015; Law and Wang, 2016; Tam and Poon, 2023; Eaton-Magaña et al., 2024). Blue-fluorescing threading dislocations and bundles can also be observed, oriented in a direction approximately parallel to the main macroscopic growth direction, with deviations caused by the step-flow growth (Martineau et al., 2004, 2009). Notably, these dislocations may have a recognizably linear appearance when viewed along directions that transect the growth planes but can look patchy and nearly polygonized when the viewing angle is parallel to the main growth direction (Martineau et al., 2004, 2009; Dieck et al., 2015).

The fluorescence colors can span the entire visible spectrum, even for samples that are colorless. As-grown CVD diamonds generally show red, orange, or pink fluorescence colors from NV^0 defects, whereas the fluorescence colors of these nitrogen-containing CVD diamonds progress from yellow to green to turquoise with higher annealing temperatures (Martineau et al., 2004; Wang et al., 2012; Eaton-Magaña and Shigley, 2016; Wassell et al., 2018). Many annealed CVD diamonds also show green-blue phosphorescence (e.g., Wang et al., 2012). Eaton-Magaña and Myagkaya (2024) recently compared changes to the deep-UV images for a CVD-grown diamond that was

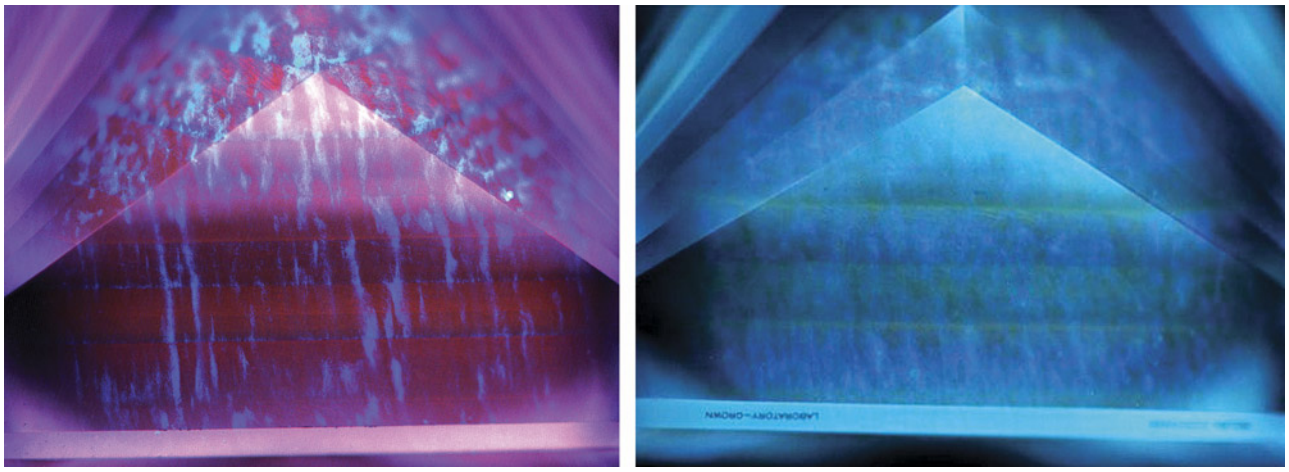

Figure 10. This CVD-grown diamond was examined before and after HPHT annealing treatments. Deep-UV fluorescence imaging highlights the changes in defect concentrations. Left: Untreated, it showed red emission from NV^0 defects. Right: After treatment, the fluorescence was dominated by shades of blues and greens from band A associated with dislocations and H3 (N_2V^0) defects, respectively. Notably, the layered pattern indicative of multi-stage CVD growth, as well as the violet blue–fluorescing dislocations, remain after treatment. The square modified brilliant sample was repolished, changing the weight from 16.41 ct to 15.73 ct. From Eaton-Magaña and Myagkaya (2024).

submitted to GIA before and after HPHT annealing (figure 10). The deep-UV fluorescence images illustrate luminescent defect concentration changes, highlighting that the sample's intrinsic growth pattern, characteristic of multi-stage CVD growth, was unaffected. CVD-grown diamonds that have been treated to produce blue, pink, or yellow bodycolors display similar characteristic patterns, but with different fluorescent colors depending on the defect content of the starting material and the treatment sequence (e.g., Wang et al., 2010; Moe et al., 2015; Eaton-Magaña and Shigley, 2016; Johnson et al., 2023).

Deep-UV imaging has also proven to be an invaluable tool in detecting rare CVD diamonds that are grown on natural diamonds, creating a "hybrid" natural/laboratory-grown diamond product (Fritsch and Phelps, 1993; Moe et al., 2017; Tang et al., 2018; Ardon and McElhenny, 2019). These examples were apparently produced to increase the sample weight or to create a potentially more valuable color, such as the blue hues introduced by type IIb CVD overgrowth layers. When exposed to deep-UV, the hybrid diamonds studied thus far have shown distinctive fluorescence patterns. The natural regions fluoresce blue due to N3 defects, while the CVD layers fluoresce red due to high NV^0 concentrations or, for cases of type IIb diamond deposition, fluoresce green-blue with similarly colored phosphorescence.

FLUORESCENCE AND PHOSPHORESCENCE BEHAVIOR OF OTHER GEMSTONES

Corundum. Lecoq de Boisbaudran (1887) demonstrated that pure alumina (i.e., corundum) was not luminescent but did show a red luminescence after doping with a small amount of chromium. This observation was later confirmed by several other researchers, including Nichols and Howes (1929). The red Cr^{3+} luminescence seen in ruby (e.g., figure 1) has been the subject of extensive research in the scientific and gemological literature (Ponahlo, 2000; Fritsch and Waychunas, 1994; Gaft and Panczer, 2013; Gaft et al., 2015). Ruby lasers, for instance, are based on the emission of chromium at 692.9 and 694.3 nm. Although this luminescence is commonly referred to as "fluorescence" in gemology and elsewhere, the excitation pathway for this feature means it should technically be classified as phosphorescence (Nasdala and Fritsch, 2024).

Fluorescence can be a useful tool for separating natural from synthetic rubies and identifying heat treatment in some rubies and sapphires (Hainschwang et al., 2013, 2024; Hughes et al., 2017; Mauthner, 2020). For instance, synthetic rubies are usually more strongly fluorescent than many natural rubies, as they generally lack iron. Synthetic rubies typically have strong red chromium-related fluorescence in long-wave UV and moderate to strong red

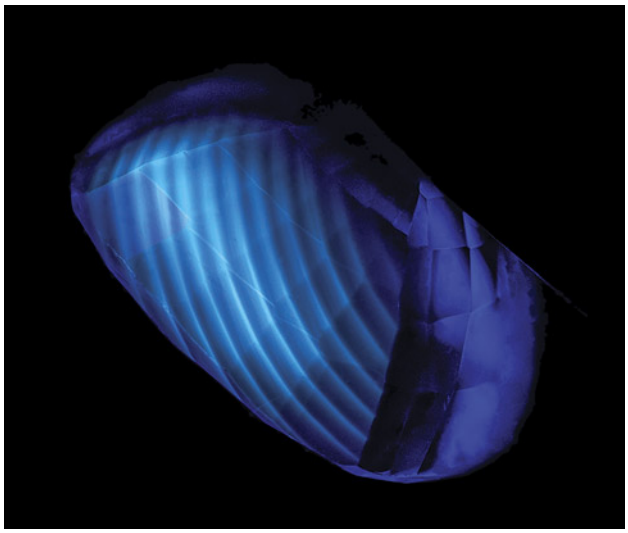

Figure 11. The curved banding in this flame-fusion synthetic blue sapphire is revealed by deep-UV illumination. From Hughes (2019); field of view ~10.4 mm.

fluorescence in short-wave UV. However, low-iron rubies from marble deposits such as Myanmar can show similar fluorescence intensities. Therefore, this test may support a natural versus synthetic determination, but it is insufficient on its own to fully separate these materials. Short-wave and deep-UV excitation can also provide insights into the growth structure of corundum. For example, they can enhance characteristic curved banding in flame-fusion synthetic sapphire, as shown in figure 11, which differs markedly from the angular growth patterns in natural stones (Hughes et al., 2017; Hughes, 2019; Zandi, 2021; Sohrabi and Anjomani, 2022; Hainschwang et al., 2024).

Fluorescence observations may also be helpful for identifying heat treatment. Many heat-treated low-iron sapphires and rubies show a chalky blue fluorescence under short-wave UV (figure 12) (Hughes and Emmett, 2005; Hughes et al., 2017; Hughes and Perkins, 2019; Hughes and Vertriest, 2022; Hainschwang et al., 2024). However, careful observation is needed, as red Cr^{3+} fluorescence can mask the chalky fluorescence (Mauthner, 2020). Notably, synthetic ruby and sapphire will often display this chalky fluorescence as well, although it can be masked by red fluorescence in some synthetic rubies. This bluish fluorescence often occurs in the wavelength range of 410–420 nm and is ascribed to the $O^{2-} \rightarrow Ti^{4+}$ charge-transfer transition (Evans, 1994; Wong et al., 1995a,b; Tsai et al., 2024). When heated, exsolved rutile (TiO_2) in corundum undergoes dissolution, creating Ti^{4+} ions and Ti-Al vacancies. The chalky bluish fluorescence coincides with rutile-containing zones but can be quenched by high iron concentrations (Hughes et al., 2017; Hughes and Perkins, 2019). This chalky reaction in heated corundum is almost never detected in natural corundum and was first documented by Crowningshield (1966, 1970). However, an inert reaction does not confirm that the stone is unheated, as the fluorescence bands can be destroyed at annealing temperatures above ~1500°C. The chalky reaction can be intensified if observed under deep-UV illumination

Figure 12. Left: A ruby sample tested by Hughes and Vertriest (2022) showed a strong red fluorescence in short-wave UV before heat treatment. Its appearance remained unchanged after heating to 600°, 750°, 900°, and 1100°C. Right: Zoned chalky fluorescence appeared following heating to 1500°C. From Hughes and Vertriest (2022).

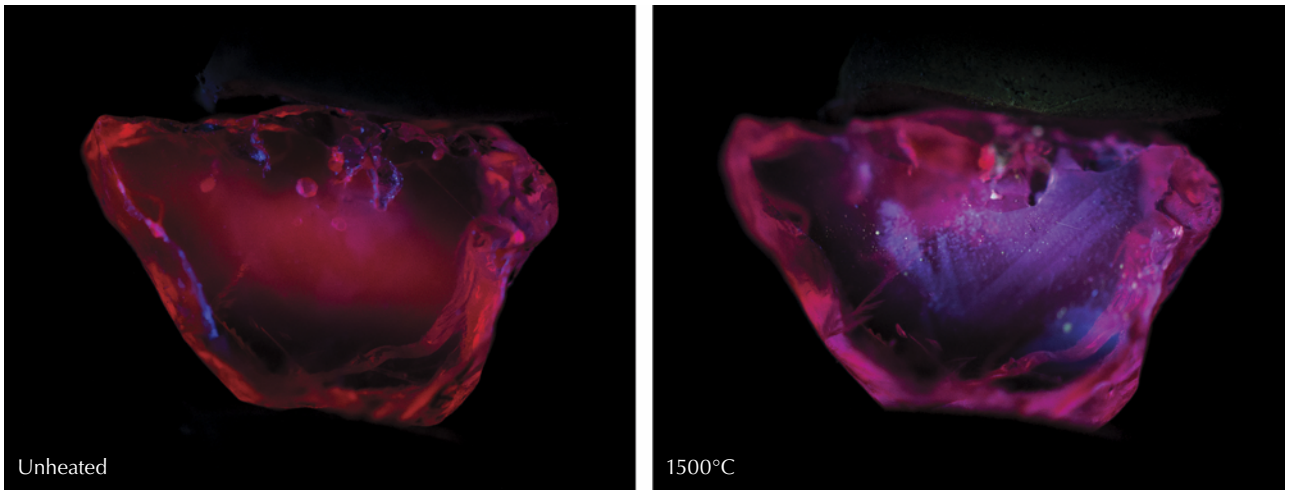

compared to short-wave UV, and it is possible that it can reveal lower-temperature annealing treatments (Hughes and Perkins, 2019).

Colored Stone Fracture Filling and Coatings. Although it is used far less commonly for colored stones than for diamonds, deep-UV fluorescence has proven useful in revealing different types of fracture-filling materials and potentially in estimating the degree of clarity enhancement. For example, surface-reaching glass filler in clarity-enhanced rubies can fluoresce blue, in sharp contrast to the red Cr^{3+} emission from the host (Lai, 2018a). Filtering the emission signal using a blue band-pass filter reduces the intensity of the red background emission, facilitating detection of the filler's fluorescence. Similar results were found for emeralds that had been clarity enhanced with epoxy resin fillers or oils, with the fluorescence color providing clues to the filler's identity (Notari et al., 2002; Hainschwang et al., 2013; Droux and Fritsch, 2015; Lai, 2018b; Gaievskyi, 2022). Fluorescence from fillers may also be observed in emeralds using long-wave UV illumination due to the mineral's often weak to undetectable Cr^{3+} fluorescence, as shown in figure 13 (e.g., Tsai, 2021). Untreated jadeite is typically inert, but fluorescence testing can provide evidence of coating, dyeing, and impregnation (Lu, 2012; Zhang and Shen, 2023). Waxes and epoxy resins used to impregnate jadeite may fluoresce blue under long-wave UV illumination (Lai, 2016, 2018c); the response can be more pronounced using deep-UV excitation, with epoxy resin forming a complex weblike fluorescence pattern. Coated jadeite may also be identified by differences in fluorescence color and intensity between the coating and any exposed jadeite (Zhang et al., 2013).

Figure 13. The epoxy filling of this clarity-enhanced emerald fluoresces blue under 365 nm illumination. From Tsai (2021).

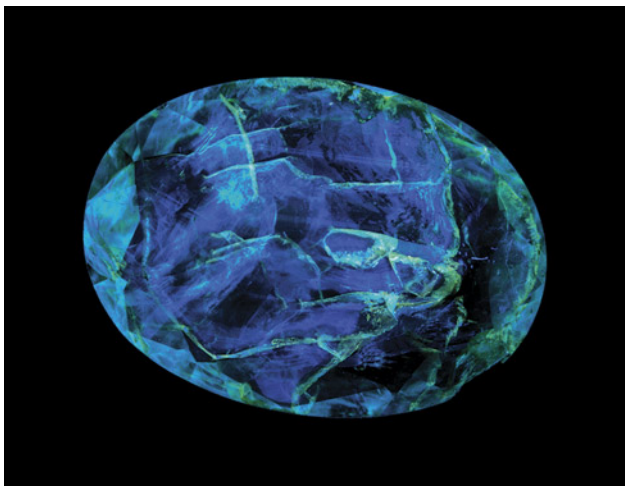

Pearls. Pearls are organic gemstones produced by various saltwater and freshwater mollusk species, with radial layers consisting of calcium carbonate crystals held together by a mixture of organic matrix that is often referred to as conchiolin. Most are nacreous, where the calcium carbonate is in the form of aragonite platelets, while the less common non-nacreous pearls have a different aragonite structure or, in some cases, are composed of calcite instead of aragonite (figure 14). Pearls can be natural or cultured and may undergo a range of treatments to improve their appearance, including dyeing, bleaching, optical brightening, irradiation, or *maeshori* luster enhancement.

UV fluorescence analysis of pearls is neither straightforward nor conclusive (Fritsch and Waychunas, 1994). Pearls may fluoresce under long-wave UV, with a rainbow of colors and intensities that are influenced by several factors, including treatments and the intensity of bodycolor (Elen, 2001; Kiefert et al., 2004; Wang et al., 2006; Sturman et al., 2014, 2019; Zhou et al., 2012, 2016, 2020, 2021; Tsai and Zhou, 2021). Generally, darker or more saturated colors fluoresce more weakly. Untreated white to cream-colored pearls often show blue or greenish blue fluorescence, yet processed pearls such as akoya and cultured freshwater pearls can fluoresce a strong bluish white (Zhou et al., 2020). Strong bluish fluorescence to long-wave UV also raises the suspicion that a pearl has been subjected to optical brightening, where an optical brightening agent (OBA) has been added to counteract less valuable yellow hues by intensifying or introducing blue fluorescence (~430 nm) (Zhou et al., 2020, 2021). Fluorescence from OBAs is not as efficiently excited by short-wave UV. Yet short-wave UV can induce fluorescence from the naturally occurring amino acid tryptophan (Trp or W) that is present in pearl nacre, and its intensity may be reduced by color treatments and processing (Tsai and Zhou, 2021; Tsai et al., 2024). As its emission is centered at ~340 nm, with a higher wavelength tail ending at ~450 nm, its fluorescence is only weakly blue and difficult to detect visually.

The range of fluorescence behaviors observed for pearls and their overlapping emissions makes visual analysis challenging. Fluorescence spectroscopy using

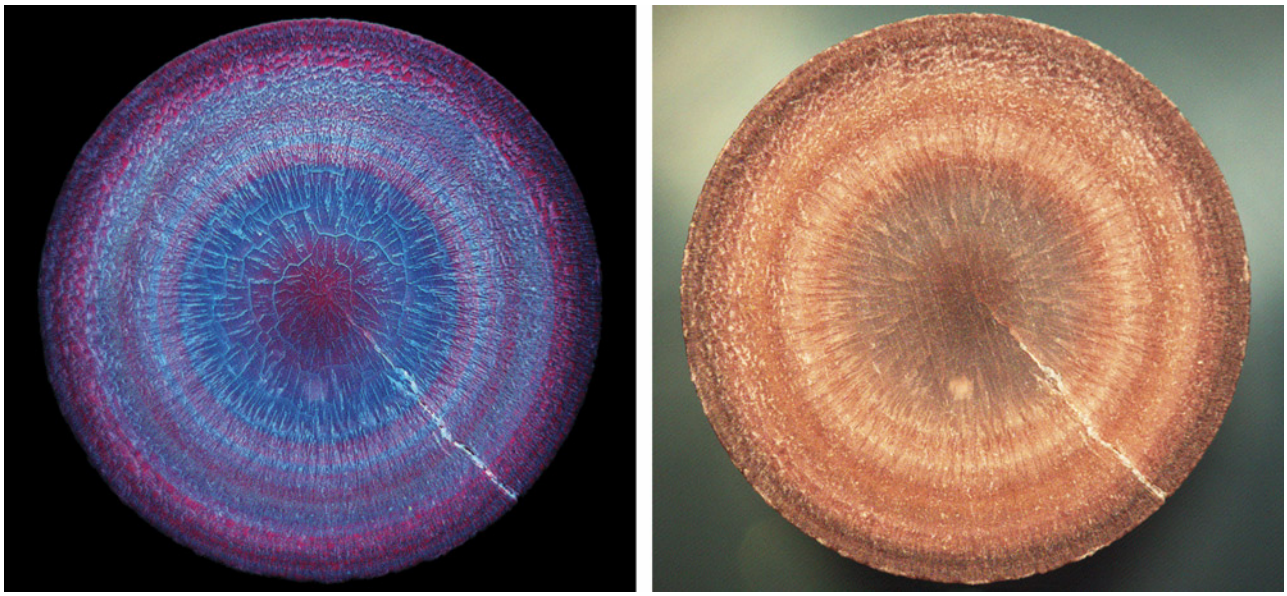

Figure 14. Left: Deep-UV fluorescence of this 0.51 ct non-nacreous natural pearl cross section (~6.57 mm diameter) reveals its concentric calcite growth structure, held together by inert conchiolin. Right: The fluorescence colors are associated with variations in the natural pigments, seen under white light. The original pearl weighed 2.18 ct and was reportedly from a Pinctada radiata *mollusk from the waters off Kuwait. Images by Ravenya Atchalak.*

different excitation sources shows promise for gemological applications, as it allows separation and identification of the fluorescing components, though a comprehensive assessment still requires multi-technique analysis (Miyoshi et al., 1987; Miyoshi, 1992; Iwahashi and Akamatsu, 1994; Ju et al., 2011; Shi et al., 2018; Zhou et al., 2016, 2020, 2021; Tsai and Zhou, 2021; Tsai et al., 2024).

CONCLUSIONS

Luminescence analysis can elucidate much about a gemstone's history and whether it is natural, laboratory-grown, or treated. The luminescence arises from impurity and defect structures in the crystal lattice and can be detected even at concentrations as low as a few parts per billion. Imaging methods based on photoluminescence, comprising fluorescence and phosphorescence, are particularly powerful analytical tools because they reveal characteristic luminescent defect distributions using simple ultraviolet light sources. This has made it a valuable technique for gemologists and scientists alike.

For example, the distribution of luminescent defects in gem diamond can help distinguish between natural and laboratory-grown crystals. It can also provide clues into any post-growth processes the diamond may have undergone, either naturally or through artificial treatment. Phosphorescence is rare enough in natural diamonds that any phosphorescent diamond should be fully analyzed to determine its method of formation. Although most commonly used for diamond research, fluorescence and phosphorescence investigations of other gemstones are also plentiful.

Natural and synthetic growth structures for other materials, including corundum and pearls, have also been revealed under UV illumination. Furthermore, any treatments applied to these gems may alter their fluorescence. Coatings, dyes, and fracture filling of corundum, emerald, and jade can be highlighted using fluorescence imaging, as these foreign substances have fluorescence responses that differ from the host gem. A deeper understanding of fluorescing materials, and their corresponding spectra, has resulted in key advances in instrumentation, optimizing illumination wavelengths to selectively enhance certain features. Consequently, luminescence imaging has become an indispensable tool for material analysis, one that is routinely used in gemological laboratories. The largely straightforward interpretation of gemstone fluorescence and phosphorescence behaviors, coupled with their distinctive patterns, makes these techniques valuable for those in the trade as well. The low cost and ease of operating fluorescence and phosphorescence imaging systems compared to alternative luminescence techniques such as cathodoluminescence further increase their accessibility and appeal.

ABOUT THE AUTHORS
Dr. Ulrika D'Haenens-Johansson is senior manager of diamond research, Dr. W. Henry Towbin is a postdoctoral research associate, and Elina Myagkaya is a research associate, at GIA in New York. Dr. Sally Eaton-Magaña is senior manager of diamond identification at GIA in Carlsbad, California.

ACKNOWLEDGMENTS
Dr. Towbin is supported by the Richard T. Liddicoat Postdoctoral Research Associate Fellowship at GIA. We would like to thank Christopher M. Welbourn, Simon C. Lawson, James E. Butler, and Aaron C. Palke for their manuscript feedback, as well as Chunhui Zhou and Tsung-Han Tsai for their illuminating comments on pearl luminescence. Rachelle Turnier is acknowledged for identifying some relevant references on colored stone fluorescence. We are also grateful to Christopher M. Breeding for providing the N3 fluorescence data presented in figure 3. Finally, we are thankful to the GIA identification and analytics teams who have collected countless fluorescence and phosphorescence images over the years, providing the backbone for this article.

REFERENCES

Anderson B.W. (1943) Absorption and luminescence of diamonds. *The Gemmologist*, Vol. 12, No. 138, pp. 21–22; No. 139, pp. 25–27; No. 141, pp. 33–35.

Ardon T., McElhenny G. (2019) Lab Notes: CVD layer grown on natural diamond. *G&G*, Vol. 55, No. 1, pp. 97–99.

Arnault J.-C., Saada S., Ralchenko V. (2022) Chemical vapor deposition single-crystal diamond: A review. *Physica Status Solidi Rapid Research Letters*, Vol. 16, No. 1, article no. 2100354, http://dx.doi.org/10.1002/pssr.202100354

Barjon J. (2017) Luminescence spectroscopy of bound excitons in diamond. *physica status solidi (a)*, Vol. 214, No. 11, article no. 1700402, http://dx.doi.org/10.1002/pssa.201700402

Boyle R. (1664) *Experiments and Considerations Touching Colours: First Occasionally Written, Among Some Other Essays to a Friend, and Now Suffer'd to Come Abroad as the Beginning of an Experimental History of Colours*. Herringman, London.

Breeding C.M., Eaton-Magaña S. (2019) Fluorescence of natural and synthetic gem diamond: Mechanism and applications. In R.A. Meyers, Ed., *Encyclopedia of Analytical Chemistry*, Wiley & Sons, pp. 1–24, https://doi.org/10.1002/9780470027318.a9670

Breeding C.M., Eaton-Magaña S., Shigley J.E. (2018) Natural-color green diamonds: A beautiful conundrum. *G&G*, Vol. 54, No. 1, pp. 2–27, http://dx.doi.org/10.5741/GEMS.54.1.2

Burns R.C., Cvetkovic V., Dodge C.N., Evans D.J.F., Rooney M.L.T., Spear P.M., Welbourn C.M. (1990) Growth-sector dependence of optical features in large synthetic diamonds. *Journal of Crystal Growth*, Vol. 104, No. 2, pp. 257–279, http://dx.doi.org/10.1016/0022-0248(90)90126-6

Burns R.C., Hansen J.O., Spits R.A., Sibanda M., Welbourn C.M., Welch D.L. (1999) Growth of high purity large synthetic diamond crystals. *Diamond and Related Materials*, Vol. 8, No. 8-9, pp. 1433–1437, http://dx.doi.org/10.1016/S0925-9635(99)00042-4

Byrne K.S., Butler J.E., Wang W., Post J.E. (2018) Chameleon diamonds: Thermal processes governing luminescence and a model for the color change. *Diamond and Related Materials*, Vol. 81, pp. 45–53, http://dx.doi.org/10.1016/j.diamond.2017.10.014

Chan S. (2009) Lab Notes: Unusual trigon-shaped clouds indicate two diamonds cut from the same piece of rough. *G&G*, Vol. 45, No. 4, p. 291–292.

Chandrasekharan V. (1946a) The thermoluminescence of diamond. *Proceedings of the Indian Academy of Sciences – Section A*, Vol. 24, No. 1, article no. 187, http://dx.doi.org/10.1007/BF03170755

——— (1946b) The phosphorescence of diamond. *Proceedings of the Indian Academy of Sciences – Section A*, Vol. 24, No. 1, article no. 193, http://dx.doi.org/10.1007/BF03170756

Clark C.D., Ditchburn R.W., Dyer H.B. (1956) The absorption spectra of natural and irradiated diamonds. *Proceedings of the Royal Society of London, Series A*, Vol. 234, No. 1198, pp. 365–381, http://dx.doi.org/10.1098/rspa.1956.0040

Clark C.D., Dean P.J., Harris P.V. (1964) Intrinsic edge absorption in diamond. *Proceedings of the Royal Society of London, Series A*, Vol. 277, No. 1370, pp. 312–329, http://dx.doi.org/10.1098/rspa.1964.0025

Collins A.T. (1982) Colour centres in diamond. *Journal of Gemmology*, Vol. 18, No. 1, pp. 37–75.

——— (1992) The characterisation of point defects in diamond by luminescence spectroscopy. *Diamond and Related Materials*, Vol. 1, No. 5-6, pp. 457–469, http://dx.doi.org/10.1016/0925-9635(92)90146-F

——— (1993) Intrinsic and extrinsic absorption and luminescence in diamond. *Physica B: Condensed Matter*, Vol. 185, No. 1-4, pp. 284–296, http://dx.doi.org/10.1016/0921-4526(93)90250-A

Collins A.T., Lawson S.C., Davies G., Kanda H. (1990a) Indirect energy gap of ^{13}C diamond. *Physical Review Letters*, Vol. 65, No. 7, pp. 891–894, http://dx.doi.org/10.1103/PhysRevLett.65.891

Collins A.T., Kanda H., Burns R.C. (1990b) The segregation of nickel-related optical centres in the octahedral growth sectors of synthetic diamond. *Philosophical Magazine B*, Vol. 61, No. 5, pp. 797–810, http://dx.doi.org/10.1080/13642819008207562

Crossfield M.D., Davies G., Collins A.T., Lightowlers E.C. (1974) The role of defect interactions in reducing the decay time of H3 luminescence in diamond. *Journal of Physics C: Solid State Physics*, Vol. 7, No. 10, pp. 1909–1917, http://dx.doi.org/10.1088/0022-3719/7/10/018

Crowningshield R. (1966) Developments and Highlights at the Gem Trade Lab in New York: Unusual items encountered [sapphire with unusual fluorescence]. *G&G*, Vol. 12, No. 3, p. 73.

——— (1970) Developments and Highlights at GIA's Lab in New York: Unusual fluorescence. *G&G*, Vol. 13, No. 4, pp. 120–122.

Davies G., Crossfield M. (1973) Luminescence quenching and zero-phonon line broadening associated with defect interactions in diamond. *Journal of Physics C: Solid State Physics*, Vol. 6, No. 5, pp. L104–L108, http://dx.doi.org/10.1088/0022-3719/6/5/007

Davies G., Hamer M.F. (1976) Optical studies of the 1.945 eV vibronic band in diamond. *Proceedings of the Royal Society of London A*, Vol. 348, No. 1653, pp. 285–298, http://dx.doi.org/10.1098/rspa.1976.0039

Davies G., Welbourn C.M., Loubser J.H.N. (1978) Optical and electron paramagnetic effects in yellow type Ia diamonds. In P. Daniel, Ed., *Diamond Research*, Industrial Diamond Information Bureau, Ascot, UK, pp. 23–30.

Davies G., Thomaz M.F., Nazare M.H., Martin M.M., Shaw D. (1987) The radiative decay time of luminescence from the vacancy in diamond. *Journal of Physics C: Solid State Physics*, Vol. 20, No. 1, pp. L13–L17, http://dx.doi.org/10.1088/0022-3719/20/1/003

Dean P.J. (1965) Bound excitons and donor-acceptor pairs in natural and synthetic diamond. *Physical Review*, Vol. 139, No. 2A, article no. A588, http://dx.doi.org/10.1103/PhysRev.139.A588

De Corte K., Anthonis A., Van Royen J., Blanchaert M., Barjon J., Willems B. (2006) Overview of dislocation networks in natural type IIa diamonds. *G&G*, Vol. 42, No. 3, pp. 122–123.
De Ment J. (1949) *Handbook of Fluorescent Gems and Minerals – An Exposition and Catalog of the Fluorescent and Phosphorescent Gems and Minerals, Including the Use of Ultraviolet Light in the Earth Sciences*. Mineralogist Publishing Company, Portland, Oregon.
D'Haenens-Johansson U.F.S., Moe K.S., Johnson P., Wong S.Y., Lu R., Wang W. (2014) Near-colorless HPHT synthetic diamonds from AOTC Group. *G&G*, Vol. 50, No. 1, pp. 30–45, http://dx.doi.org/10.5741/GEMS.50.1.30
D'Haenens-Johansson U.F.S., Katrusha A., Moe K.S., Johnson P., Wang W. (2015) Large colorless HPHT-grown synthetic gem diamonds from New Diamond Technology. Russia. *G&G*, Vol. 51, No. 3, pp. 260–279, http://dx.doi.org/10.5741/GEMS.51.3.260
D'Haenens-Johansson U.F.S., Butler J.E., Katrusha A.N. (2022) Synthesis of diamonds and their identification. *Reviews in Mineralogy & Geochemistry*, Vol. 88, No. 1, pp. 689–753, http://dx.doi.org/10.2138/rmg.2022.88.13
Dieck C., Loudin L., D'Haenens-Johansson U.F.S. (2015) Lab Notes: Two large CVD-grown synthetic diamonds tested by GIA. *G&G*, Vol. 51, No. 4, pp. 437–439.
Droux A., Fritsch E. (2015) Gem News International: An unusual filled ruby. *G&G*, Vol. 51, No. 2, pp. 206–208.
Dupuy H., Phillips J.C. (2019) Selecting a diamond verification instrument based on the results of the Assure Program: An initial analysis. *Journal of Gemmology*, Vol. 36, No. 7, pp. 606–619.
Dyer H.B., Matthews I.G. (1958) The fluorescence of diamond. *Proceedings of the Royal Society of London A*, Vol. 243, No. 1234, pp. 320–335, http://dx.doi.org/10.1098/rspa.1958.0002
Eaton-Magaña S. (2020) Lab Notes: Irradiated blue diamond with interesting DiamondView image. *G&G*, Vol. 56, No. 2, p. 283.
Eaton-Magaña S., Ardon T. (2016) Temperature effects on luminescence centers in natural type IIb diamonds. *Diamond and Related Materials*, Vol. 69, pp. 86–95, http://dx.doi.org/10.1016/j.diamond.2016.07.002
Eaton-Magaña S., Lu R. (2011) Phosphorescence in type IIb diamonds. *Diamond and Related Materials*, Vol. 20, No. 7, pp. 983–989, http://dx.doi.org/10.1016/j.diamond.2011.05.007
Eaton-Magaña S., Myagkaya E. (2024) Lab Notes: Large CVD-grown diamond resubmitted after HPHT treatment. *G&G*, Vol. 60, No. 1, pp. 61–63.
Eaton-Magaña S., Shigley J.E. (2016) Observations on CVD-grown synthetic diamonds: A review. *G&G*, Vol. 52, No. 3, pp. 222–245, http://dx.doi.org/10.5741/GEMS.52.3.222
Eaton-Magaña S., Post J.E., Heaney P.J., Walters R.A., Breeding C.M., Butler J.E. (2007) Fluorescence spectra of colored diamonds using a rapid, mobile spectrometer. *G&G*, Vol. 43, No. 4, pp. 332–351, http://dx.doi.org/10.5741/GEMS.43.4.332
Eaton-Magaña S., Post J.E., Heaney P.J., Freitas J., Klein P., Walters R., Butler J.E. (2008) Using phosphorescence as a fingerprint for the Hope and other blue diamonds. *Geology*, Vol. 36, No. 1, pp. 83–86, http://dx.doi.org/10.1130/G24170A.1
Eaton-Magaña S., Shigley J.E., Breeding C.M. (2017) Observations on HPHT-grown synthetic diamonds: A review. *G&G*, Vol. 53, No. 3, pp. 262–284, http://dx.doi.org/10.5741/GEMS.53.3.262
Eaton-Magaña S., Breeding C.M., Shigley J.E. (2018) Natural-color blue, gray, and violet diamonds: Allure of the deep. *G&G*, Vol. 54, No. 2, pp. 112–131, http://dx.doi.org/10.5741/GEMS.54.2.112
Eaton-Magaña S., Ardon T., Breeding C.M. (2021) Laboratory-grown diamond: A gemological laboratory perspective. *Journal of Gems & Gemmology*, Vol. 23, No. 6, pp. 25–39.
Eaton-Magaña S., Hardman M.F., Odake S. (2024) Laboratory-grown diamonds: An update on identification and products evaluated at GIA. *G&G*, Vol. 60, No. 2, pp. 146–167, http://dx.doi.org/10.5741/GEMS.60.2.146
Elen S. (2001) Spectral reflectance and fluorescence characteristics of natural-color and heat-treated "golden" South Sea cultured pearls. *G&G*, Vol. 37, No. 2, pp. 114–123, http://dx.doi.org/10.5741/GEMS.37.2.114
Evans B.D. (1994) Ubiquitous blue luminescence from undoped synthetic sapphires. *Journal of Luminescence*, Vol. 60–61, pp. 620–626, http://dx.doi.org/10.1016/0022-2313(94)90233-X
Evans T., Wild R.K. (1965) Plastic bending of diamond plates. *Philosophical Magazine*, Vol. 12, No. 117, pp. 479–489, http://dx.doi.org/10.1080/14786436508218894
Fedortchouk Y. (2019) A new approach to understanding diamond surface features based on a review of experimental and natural diamond studies. *Earth Science Review*, Vol. 193, pp. 45–65, http://dx.doi.org/10.1016/j.earscirev.2019.02.013
Fedortchouk Y., Liebske, C., McCammon C. (2019) Diamond destruction and growth during mantle metasomatism: An experimental study of diamond resorption features. *Earth and Planetary Science Letters*, Vol. 506, pp. 493–506, http://dx.doi.org/10.1016/j.epsl.2018.11.025
Fritsch E., Phelps A.W. (1993) Type IIb diamond thin films deposited onto near-colorless natural gem diamonds. *Diamond and Related Materials*, Vol. 2, No. 2-4, pp. 70–74, http://dx.doi.org/10.1016/0925-9635(93)90033-X
Fritsch E., Massi L., Rossman G.R., Hainschwang T., Jobic S., Dessapt R. (2007) Thermochromic and photochromic behaviour of "chameleon" diamonds. *Diamond and Related Materials*, Vol. 16, No. 2, pp. 401-408, http://dx.doi.org/10.1016/j.diamond.2006.08.014
Fritsch E., Waychunas G.A. (1994) Gemstones. In M. Robbins, Ed., *Fluorescence: Gems and Minerals Under Ultraviolet Light*, Geoscience Press Inc., Phoenix.
Gaft M., Panczer G. (2013) Laser-induced time-resolved luminescence spectroscopy of minerals: A powerful tool for studying the nature of emission centres. *Mineralogy and Petrology*, Vol. 107, No. 3, pp. 363–372, http://dx.doi.org/10.1007/s00710-013-0293-3
Gaft M., Reisfeld R., Panczer G. (2015) *Modern Luminescence Spectroscopy of Minerals and Materials*, 2nd ed., Springer-Verlag, Berlin and Heidelberg.
Gaievskyi I. (2022) Gem News International: Unusual repair of a natural emerald. *G&G*, Vol. 58, No. 1, pp. 118–120.
Gaillou E., Wang W., Post J.E., King J.M., Butler J.E., Collins A.T., Moses T.M. (2010a) The Wittelsbach-Graff and Hope diamonds: Not cut from the same rough. *G&G*, Vol. 46, No. 2, pp. 80–88, http://dx.doi.org/10.5741/GEMS.46.2.80
Gaillou E., Post J.E., Bassim N.D., Zaitsev A.M., Rose T., Fries M.D., Stroud R.M., Steele A., Butler J.E. (2010b) Spectroscopic and microscopic characterizations of color lamellae in natural pink diamonds. *Diamond and Related Materials*, Vol. 19, No. 10, pp. 1207–1220, http://dx.doi.org/10.1016/j.diamond.2010.06.015
Green B.L., Breeze B.G., Newton M.E. (2017) Electron paramagnetic resonance and photochromism of N_3V^0 in diamond. *Journal of Physics: Condensed Matter*, Vol. 29, No. 22, article no. 225701, http://dx.doi.org/10.1088/1361-648X/aa6c89
Green B.L., Collins A.T., Breeding C.M. (2022) Diamond spectroscopy, defect centers, color, and treatments. *Reviews in Mineralogy and Geochemistry*, Vol. 88, No. 1, pp. 637–688, http://dx.doi.org/10.2138/rmg.2022.88.12
Hainschwang T., Simic D., Fritsch E., Deljanin B., Woodring S., DelRe N. (2005) A gemological study of a collection of chameleon diamonds. *G&G*, Vol. 41, No. 1, pp. 2–17, http://dx.doi.org/10.5741/GEMS.41.1.20
Hainschwang T., Notari F., Fritsch E., Massi L. Rondeau B., Breeding C.M., Vollstaedt H. (2008) HPHT treatment of CO_2 containing and CO_2-related brown diamonds. *Diamond and Related Materials*, Vol. 17, No. 3, pp. 340–351, http://dx.doi.org/10.1016/j.diamond.2008.01.022
Hainschwang T., Respinger A., Notari F., Hartmann H.J., Günthard C. (2009) A comparison of diamonds irradiated by high fluence neutrons or electrons, before and after annealing. *Diamond and Related Materials*, Vol. 18, No. 10, pp. 1223–1234,

http://dx.doi.org/10.1016/j.diamond.2009.04.011
Hainschwang T., Karampelas S., Fritsch E., Notari F. (2013) Luminescence spectroscopy and microscopy applied to study gem materials: A case study of C centre containing diamonds. *Mineralogy and Petrology*, Vol. 107, No. 3, pp. 393–413, http://dx.doi.org/10.1007/s00710-013-0273-7
Hainschwang T., Fritsch, E., Gaillou E., Shen A. (2024) Analysing the luminescence of gems. *Elements*, Vol. 20, No. 5, pp. 312–317, http://dx.doi.org/10.2138/gselements.20.5.312
Hanley P.L., Kiflawi I., Lang A.R. (1977) On topographically identifiable sources of cathodoluminescence in natural diamonds. *Philosophical Transactions of the Royal Society – Series A*, Vol. 284, No. 1324, pp. 329–368, http://dx.doi.org/10.1098/rsta.1977.0012
Harris J.W., Smit K.V., Fedortchouk Y., Morre M. (2022) Morphology of monocrystalline diamond and its inclusions. *Reviews in Mineralogy and Geochemistry*, Vol. 88, No. 1, pp. 119–166, http://dx.doi.org/10.2138/rmg.2022.88.02
Hughes E.B. (2019) Micro-World: Curved banding in flame-fusion synthetic sapphires. *G&G*, Vol. 55, No. 2, pp. 264–265.
Hughes E.B., Perkins R. (2019) Madagascar sapphire: Low-temperature heat treatment experiments. *G&G*, Vol. 55, No. 2, pp. 184–197, http://dx.doi.org/10.5741/GEMS.55.2.184
Hughes E.B., Vertriest W. (2022) A canary in the ruby mine: Low-temperature heat treatment experiments on Burmese ruby. *G&G*, Vol. 58, No. 4. pp. 400–423, http://dx.doi.org/10.5741/GEMS.58.4.400
Hughes R.W., Emmett J.L. (2005) Heat seeker | UV fluorescence as a gemological tool. LotusGemology.com, https://www.lotusgemology.com/resources/articles/156-heat-seeker-uv-fluorescence-as-a-gemological-tool
Hughes R.W., Manorotkul W., Hughes E.B. (2017) *Ruby & Sapphire: A Gemologist's Guide*; RWH Publishing/Lotus Publishing: Bangkok, 732 pp.
Iwahashi Y., Akamatsu S. (1994) Porphyrin pigment in black-lip pearls and its application to pearl identification. *Fisheries Science*, Vol. 60, No. 1, pp. 69–71, http://dx.doi.org/10.2331/fishsci.60.69
Johnson P., Moe K.S., Persaud S., Odake S., Kazuchits N.M., Zaitsev A.M. (2023) Spectroscopic characterization of yellow *gem* quality CVD diamond. *Diamond and Related Materials*, Vol. 140, Part B, article no. 110505, http://dx.doi.org/10.1016/j.diamond.2023.110505
Ju M.J., Lee S.J., Kim Y., Shin J.G., Kim H.Y., Lim Y., Yasuno Y., Lee B.H. (2011) Multimodal analysis of pearls and pearl treatments by using optical coherence tomography and fluorescence spectroscopy. *Optics Express*, Vol. 19., No. 7, pp. 6420–6432, http://dx.doi.org/10.1364/OE.19.006420
Kanda H., Akaishi M., Setaka N., Yamaoka S., Fukunaga O. (1980) Surface structures of synthetic diamonds. *Journal of Materials Science*, Vol. 15, No. 11, pp. 2743–2748, http://dx.doi.org/10.1007/BF00550541
Kanda H., Ohsawa T., Fukunaga O., Sunagawa I. (1989) Effect of solvent metals upon the morphology of synthetic diamonds. *Journal of Crystal Growth*, Vol. 94, No. 1, pp. 115–124, http://dx.doi.org/10.1016/0022-0248(89)90610-6
Kiefert L., McLaurin Moreno D., Arizmendi E., Hänni H.A., Elen S. (2004) Cultured pearls from the Gulf of California, Mexico. *G&G*, Vol. 40, No. 1, pp. 26–38, http://dx.doi.org/10.5741/GEMS.40.1.26
Kiflawi I., Kanda H., Lawson S.C. (2002) The effect of the growth rate on the concentration of nitrogen and transition metal impurities in HPHT synthetic diamonds. *Diamond and Related Materials*, Vol. 11, No. 2, pp. 204–211, http://dx.doi.org/10.1016/S0925-9635(01)00569-6
Kunz G.F., Baskerville C. (1903) The action of radium, roentgen rays and ultra-violet light on minerals and gems. *Science*, Vol. 18, No. 468, pp. 769–783, http://dx.doi.org/10.1126/science.18.468.769
Lai L.T.-A. (2016) Gem News International: Application of the DiamondView in separating impregnated jadeite. *G&G*, Vol. 52, No. 3, pp. 327–328.
——— (2018a) Gem News International: Separating glass-filled rubies using the DiamondView. *G&G*, Vol. 54, No. 2, pp. 458–459.
——— (2018b) Gem News International: Emeralds filled with epoxy resin: DiamondView observations. *G&G*, Vol. 54, No. 4, pp. 250–251.
——— (2018c) Gem News International: Strong fluorescence in B-jade impregnated with wax. *G&G*, Vol. 54, No. 2, pp. 251–252.
Lai M.Y., Hardman M.F., Eaton-Magaña S., Breeding C.M., Schwartz V.A., Collins A.T. (2024) Spectroscopic characterization of diamonds colored by the 480 nm absorption band. *Diamond and Related Materials*, Vol. 142, article no. 110825, http://dx.doi.org/10.1016/j.diamond.2024.110825
Laidlaw F.H.J., Beanland R., Fisher D., Diggle P.L. (2020) Point defects and interstitial climb of 90° partial dislocations in brown type IIa natural diamond. *Acta Materialia*, Vol. 201, pp. 494–503, http://dx.doi.org/10.1016/j.actamat.2020.10.033
Laidlaw F.H.J., Diggle P.L., Breeze B.G., Dale M.W., Fisher D., Beanland R. (2021) Spatial distribution of defects in a plastically deformed natural brown diamond. *Diamond and Related Materials*, Vol. 117, article no. 108465, http://dx.doi.org/10.1016/j.diamond.2021.108465
Lan Y., Lu T., Zhang C., Liang R., Ding T., Chen H., Ke J., Bi L. (2016) Development of a new multi-spectral induced luminescence imaging system (GV5000) and its application in screening melee-sized near-colorless synthetic diamonds and natural diamonds. *Rock and Mineral Analysis*, Vol. 35, No. 5, pp. 505–512 (in Chinese with English abstract).
Lang A.R. (1974) On the growth-sectorial dependence of defects in natural diamonds. *Proceedings of the Royal Society of London. Series A*, Vol. 340, No. 1621, pp. 233–248, http://dx.doi.org/10.1098/rspa.1974.0150
——— (1979) Internal structure. In J.E. Field, Ed., *The Properties of Diamond*, Academic Press, London, pp. 425–469.
Law B.P.L., Wang W. (2016) Lab Notes: CVD synthetic diamond over 5 carats identified. *G&G*, Vol. 52, No. 4, pp. 414–416.
Lawson S.C., Kanda H., Watanabe K., Kiflawi I., Sato Y., Collins A.T. (1996) Spectroscopic study of cobalt-related optical centers in synthetic diamond. *Journal of Applied Physics*, Vol. 79, No. 8, pp. 4348–4357, http://dx.doi.org/10.1063/1.361744
Lecoq de Boisbaudran P.E. (1887) Sur la fluorescence rouge de l'alumine. *Comptes Rendus Hebdomadaires des Séances de l'Académie des Sciences*, Vol. 104, pp. 330–334.
Lu R. (2012) Color origin of lavender jadeite: An alternative approach. *G&G*, Vol. 48, No. 4, pp. 273–283, http://dx.doi.org/10.5741/GEMS.48.4.273
Luo Y., Breeding C.M. (2013) Fluorescence produced by optical defects in diamond: Measurement, characterization, and challenges. *G&G*, Vol. 49, No. 2, pp. 82–97, http://dx.doi.org/10.5741/GEMS.49.2.82
Martineau P.M., Lawson S.C., Taylor A.J., Quinn S.J., Evans D.J.F., Crowder M.J. (2004) Identification of synthetic diamond grown using chemical vapor deposition (CVD). *G&G*, Vol. 40, No. 1, pp. 2–25, http://dx.doi.org/10.5741/GEMS.40.1.2
Martineau P., Gaukroger M., Khan R., Evans D. (2009) Effect of steps on dislocations in CVD diamond grown on {001} substrates. *physica status solidi c*, Vol. 6, No. 8, pp. 1953–1957, http://dx.doi.org/10.1002/pssc.200881465
Mauthner M. (2020) Fluorescence in gems. *Rocks & Minerals*, Vol. 96, No. 1, pp. 38–43, http://dx.doi.org/10.1080/00357529.2021.1827909
Mawe J. (1813) *A Treatise on Diamonds and Precious Stones: Including Their History – Natural and Commercial. To which is Added, Some Account of the Best Methods of Cutting and Polishing Them*. Longman, Hurst, Rees, Orme, and Brown, London.
McGuinness C.D., Wassell A.M., Lanigan P.M.P., Lynch S.A.

(2020) Separation of natural from laboratory-grown diamond using time-gated luminescence imaging. *G&G*, Vol. 56, No. 2, pp. 220–229, http://dx.doi.org/10.5741/GEMS.56.2.220
Meng Y.F., Yan C.S., Lai J., Krasnicki S., Shu H., Yu T., Liang Q., Mao H.K., Hemley R.J. (2008) Enhanced optical properties of chemical vapor deposited single crystal diamond by low-pressure/high-temperature annealing. *Proceedings of the National Academy of Sciences*, Vol. 105, No. 46, pp. 17620–17625, http://dx.doi.org/10.1073/pnas.0808230105
Miyoshi T. (1992) Effect of light irradiation on fluorescence and optical reflectance of pearls. *Technology Reports of Yamaguchi University*, Vol. 5, No. 1, pp. 23–30.
Miyoshi T., Matsuda Y., Komatsu H. (1987) Fluorescence from pearls and shells of black lip oyster, *Pinctada margaritifera*, and its contribution to the distinction of mother oysters used in pearl culture. *Japanese Journal of Applied Physics*, Vol. 26, No. 7, pp. 1069–1072.
Moe K.S., Johnson P. (2007) Lab Notes: Blue diamonds showing multiple colors of phosphorescence. *G&G*, Vol. 43, No. 1, pp. 47–48.
Moe K.S., D'Haenens-Johansson U., Wang W. (2015) Lab Notes: Irradiated green-blue CVD synthetic diamonds. *G&G*, Vol. 51, No. 3, pp. 320–321.
Moe K.S., Johnson P., D'Haenens-Johansson U., Wang W. (2017) Lab Notes: A synthetic diamond overgrowth on a natural diamond. *G&G*, Vol. 53, No. 2, pp. 237–239.
Moore M., Lang A.R. (1972) On the internal structure of natural diamonds of cubic habit. *Philosophical Magazine*, Vol. 26, No. 6, pp. 1313–1325, http://dx.doi.org/10.1080/14786437208220345
Moses T.M., Reinitz I.M., Johnson M.L., King J.M., Shigley J.E. (1997) A contribution to understanding the effect of blue fluorescence on the appearance of diamonds. *G&G*, Vol. 33, No. 4, pp. 244–259, http://dx.doi.org/10.5741/GEMS.33.4.244
Nasdala L., Fritsch E. (2024) Luminescence: The "cold glow" of minerals. *Elements*, Vol. 20, No. 5, pp. 287–292, http://dx.doi.org/10.2138/gselements.20.5.287
Nasdala L., Grambole D., Wildner M., Gigler A.M., Hainschwang T., Zaitsev A.M., Harris J.W., Milledge J., Schulze D.J., Hofmeister W., Balmer W.A. (2013) Radio-colouration of diamond: A spectroscopic study. *Contributions to Mineralogy and Petrology*, Vol. 165, No. 5, pp. 843–861, http://dx.doi.org/10.1007/s00410-012-0838-1
Nichols E.L., Howes H.L. (1929) The transformation spectrum of the ruby. *Proceedings of the National Academy of Sciences*, Vol. 15, No. 2, pp. 139–146, http://dx.doi.org/10.1073/pnas.15.2.139
Notari F., Grobon C., Fritsch E. (2002) Observation des émeraudes traitées en luminescence UVISIO® Quelle mention attribuer aux émeraudes après suppression des résines synthétiques de leurs fissures? *Revue de Gemmologie AFG*, Vol. 144, pp. 27–31 (in French).
Palyanov Y.N., Kupriyanov I.N., Khokhryakov A.F., Ralchenko V.G. (2015) Crystal growth of diamond. In P. Rudolph, Ed., *Handbook of Crystal Growth*, Elsevier, Boston, pp. 671–713.
Pearson G. (2011) Review of ultraviolet sources for gem fluorescence and testing. *Journal of Gemmology*, Vol. 32, No. 5-8, pp. 211–222.
Ponahlo J. (2000) Cathodoluminescence as a tool for gemstone identification. In M. Pagel et al., Eds., *Cathodoluminescence in Geosciences*, Springer, Berlin, pp. 479–500.
Robinson A. (2018) Irradiated HPHT-grown diamonds might escape detection as synthetics, says lab. *IDEX Online*, http://www.idexonline.com/FullArticle?Id=43871
Ruan J., Kobashi K., Choyke W.J. (1992) On the "band-A" emission and boron related luminescence in diamond. *Applied Physics Letters*, Vol. 60, No. 25, pp. 3138–3140, http://dx.doi.org/10.1063/1.106748
Satoh S., Sumiya H., Tsuji K., Yazu S. (1990) Differences in nitrogen concentration and aggregation among {111} and {100} growth sectors of large synthetic diamonds. In S. Saito, Eds., *Science and Technology of New Diamond*, KTK Scientific Publishers/Terra Scientific Publishing Co., Tokyo, pp. 351–355.
Schulze D.J., Nasdala L. (2016) Unusual paired pattern of radiohaloes on a diamond crystal from Guaniamo (Venezuela). *Lithos*, Vol. 265, pp. 177–181, http://dx.doi.org/10.1016/j.lithos.2016.09.024
Shen A., Eaton-Magaña S. (2011) Lab Notes: Type IIb diamond with long phosphorescence, *G&G*, Vol. 47, No. 4, pp. 308–315.
Shi L., Wang Y., Liu X., Mao J. (2018) Component analysis and identification of black Tahitian cultured pearls from the oyster *Pinctada margaritifera* using spectroscopic techniques. *Journal of Applied Spectroscopy*, Vol. 85, No. 1, pp. 98–102, http://dx.doi.org/10.1007/s10812-018-0618-4
Shigley J.E., Breeding C.M. (2013) Optical defects in diamond: A quick reference chart. *G&G*, Vol. 49, No. 2, pp. 107–111, http://dx.doi.org/10.5741/GEMS.49.2.107
Shigley J.E., Breeding C.M., Shen A.H.T. (2004a) An updated chart on the characteristics of HPHT-grown synthetic diamonds. *G&G*, Vol. 40, No. 4, pp. 303–313, http://dx.doi.org/10.5741/GEMS.40.4.303
Shigley J.E., McClure S.F., Breeding C.M., Shen A.H.T., Muhlmeister S.M. (2004b) Lab-grown colored diamonds from Chatham Created Gems. *G&G*, Vol. 40, No. 2, pp. 128–145, http://dx.doi.org/10.5741/GEMS.40.2.128
Smit K.V., Shirey S.B. (2020) Diamonds from the Deep: Diamonds are not forever! Diamond dissolution. *G&G*, Vol. 56, No. 1, pp. 148–155.
Smit K.V., Myagkaya E., Persaud S., Wang W. (2018) Black diamonds from Marange (Zimbabwe): A result of natural irradiation and graphite inclusions. *G&G*, Vol. 54, No. 2, pp. 132–148, http://dx.doi.org/10.5741/GEMS.54.2.132
Smith E.M. (2023) Diamond Reflections: Plastic deformation: How and why are most diamonds slightly distorted? *G&G*, Vol. 59, No. 1, pp. 94–99.
Smith E.M., Shirey S.B., Nestola F., Bullock E.S., Wang J., Richardson S.H., Wang W. (2016) Large gem diamonds from metallic liquid in Earth's deep mantle. *Science*, Vol. 354, No. 6318, pp. 1403–1405, http://dx.doi.org/10.1126/science.aal1303
Smith E.M., Shirey S.B., Wang W. (2017) The very deep origin of the world's biggest diamonds. *G&G*, Vol. 53, No. 4, pp. 388–403, http://dx.doi.org/10.5741/GEMS.53.4.388
Sohrabi S., Anjomani N. (2022) Lab Notes: Hydrothermal synthetic ruby. *G&G*, Vol. 58, No. 1, pp. 57–58.
Stokes G.G. (1852) On the change of refrangibility of light. *Philosophical Transactions of the Royal Society of London*, Vol. 142, pp. 463–562, http://dx.doi.org/10.1098/rstl.1852.0022
Strong H.M., Chrenko R.M. (1971) Further studies on diamond growth rates and physical properties of laboratory-made diamond. *Journal of Physical Chemistry*, Vol. 75, No. 12, pp. 1838–1843, http://dx.doi.org/10.1021/j100681a014
Sturman N., Homkrajae A., Manustrong A., Somsa-ard N. (2014) Observations on pearls reportedly from the Pinnidae family (pen pearls). *G&G*, Vol. 50, No. 3, pp. 202–215, http://dx.doi.org/10.5741/GEMS.50.3.202
Sturman N., Otter L.M., Homkrajae A., Manustrong A., Nilpetploy N., Lawanwong K., Kessrapong P., Jochum K.P., Stoll B., Götz H., Jacob D.E. (2019) A pearl identification challenge. *G&G*, Vol. 55, No. 2, pp. 229–243, http://dx.doi.org/10.5741/GEMS.55.2.229
Sumiya H., Toda N., Satoh S. (2002) Growth rate of high-quality large diamond crystals. *Journal of Crystal Growth*, Vol. 237–239, pp. 1281–1285, http://dx.doi.org/10.1016/S0022-0248(01)02145-5
Sunagawa I. (1984) Morphology of natural and synthetic diamond crystals. In I. Sunagawa, Ed., *Materials Science of the Earth's Interior*, Terra Scientific Publishing Co., Tokyo, pp. 303–330.
——— (1995) The distinction of natural from synthetic diamond. *Journal of Gemmology*, Vol. 24, No. 7, pp. 485–499.
Suzuki S., Lang A.R. (1976) Internal structures of natural diamonds revealing mixed-habit growth. In P. Daniel, Ed., *Diamond Re-*

search, Industrial Diamond Information Bureau, Ascot, UK, pp. 39–47.
Tam K.W., Poon T.P.Y. (2023) Lab Notes: CVD diamond over 34 carats. *G&G*, Vol. 59, No. 2, pp. 213–214.
Tang S., Su J., Lu T., Ma Y., Ke J., Song Z., Zhang J., Liu H. (2018) A thick overgrowth of CVD synthetic diamond on a natural diamond. *Journal of Gemmology*, Vol. 36, No. 2, pp. 134–141.
Thomaz M.F., Davies G. (1978) The decay time of N3 luminescence in natural diamond. *Proceedings of the Royal Society of London. Series A*. Vol. 362, No. 1710, pp. 405–419, http://dx.doi.org/10.1098/rspa.1978.0141
Tsai T.-H. (2021) Multi-excitation fluorescence imaging for identifying clarity enhancement in gemstones. *Proceedings SPIE 11815, Novel Optical Systems, Methods, and Applications XXIV*, article no. 1181505, http://dx.doi.org/10.1117/12.2592939
Tsai T.-H., D'Haenens-Johansson U.F.S. (2021) Rapid gemstone screening and identification using fluorescence spectroscopy. *Applied Optics*, Vol. 60, No. 12, pp. 3412–3421, http://dx.doi.org/10.1364/AO.419885
Tsai T.-H., Zhou C. (2021) Rapid detection of color-treated pearls and separation of pearl types using fluorescence analysis. *Applied Optics*, Vol. 60, No. 20, pp. 5837–5845, http://dx.doi.org/10.1364/AO.427203
Tsai T.-H., D'Haenens-Johansson U.F.S., Smith T., Zhou C., Xu W. (2024) Multi-excitation photoluminescence spectroscopy system for gemstone analysis. *Optics Express*, Vol. 32, No. 14, pp. 24839–24855, http://dx.doi.org/10.1364/OE.525832
Wang M., Shi G., Yuan J.C.C., Han W., Bai Q. (2018) Spectroscopic characteristics of treated-color natural diamonds. *Journal of Spectroscopy*, Vol. 2018, article no. 81532941, http://dx.doi.org/10.1155/2018/8153941
Wang W., Scarratt K., Hyatt A., Shen A.H.-T., Hall M. (2006) Identification of "chocolate pearls" treated by Ballerina Pearl Co. *G&G*, Vol. 42, No. 4, pp. 222–235, http://dx.doi.org/10.5741/GEMS.42.4.222
Wang W., Hall M.S., Moe K.S., Tower J., Moses T.M. (2007) Latest-generation CVD-grown synthetic diamonds from Apollo Diamond Inc. *G&G*, Vol. 43, No. 4, pp. 294–312, http://dx.doi.org/10.5741/GEMS.43.4.294
Wang W., Doering P., Tower J., Lu R., Eaton-Magaña S., Johnson P., Emerson E., Moses T.M. (2010) Strongly colored pink CVD lab-grown diamonds. *G&G*, Vol. 46, No. 1, pp. 4–17, http://dx.doi.org/10.5741/GEMS.46.1.4
Wang W., D'Haenens-Johansson U.F.S., Johnson P., Moe K.S., Emerson E., Newton M.E., Moses T.M. (2012) CVD synthetic diamond from Gemesis Corp. *G&G*, Vol. 48, No. 2, pp. 80–97, http://dx.doi.org/10.5741/GEMS.48.2.80
Wassell A.M., McGuinness C.D., Hodges C., Lanigan P.M.P., Fisher D., Martineau P.M., Newton M.E., Lynch S.A. (2018) Anomalous green luminescent properties in CVD synthetic diamonds. *physica status solidi (a)*, Vol. 215, No. 22, article no. 1800292, http://dx.doi.org/10.1002/pssa.201800292
Watanabe K., Lawson S.C., Isoya J., Kanda H., Sato Y. (1997) Phosphorescence in high-pressure synthetic diamond. *Diamond and Related Materials*, Vol. 6, No. 1, pp. 99–106, http://dx.doi.org/10.1016/S0925-9635(96)00764-9
Waychunas G.A. (2014) Luminescence spectroscopy. *Reviews in Mineralogy and Geochemistry*, Vol. 78, No. 1, pp. 175–217, http://dx.doi.org/10.2138/rmg.2014.78.5
Waychunas G., Kempe U. (2024) Activators in minerals and the role of electronic defects. *Elements*, Vol. 20, No. 5, pp. 293–298, http://dx.doi.org/10.2138/gselements.20.5.293
Webster R. (1975) *Gems: Their Sources, Descriptions and Identification*, 3rd ed. Archon Books, Butterworth & Co., London.
——— (1983) *Gems: Their Sources, Descriptions and Identification*, 4th ed. Butterworths, London.
Welbourn C.M., Rooney M.-L.T., Evans D.J.F. (1989) A study of diamonds of cube and cube-related shape from the Jwaneng mine. *Journal of Crystal Growth*, Vol. 94, No. 1, pp. 229–252, http://dx.doi.org/10.1016/0022-0248(89)90622-2
Welbourn C.M., Cooper M., Spear P.M. (1996) De Beers natural versus synthetic diamond verification instruments. *G&G*, Vol. 32, No. 3, pp. 156–169, http://dx.doi.org/10.5741/GEMS.32.3.156
Willems B., Martineau P.M., Fisher D., Van Royen J., Van Tendeloo G. (2006) Dislocation distributions in brown diamond. *physica status solidi (a)*, Vol. 203, No, 12, pp. 3076–3080, http://dx.doi.org/10.1002/pssa.200671129
Williams B. (2007) Technology update—Ultraviolet light. *Gem Market News*, Vol. 26, pp. 8–11.
Wong W.C., McClure D.C., Basun S.A., Kokta M.R. (1995a) Charge-exchange processes in titanium-doped sapphire crystals. I. Charge-exchange energies and titanium-bound excitons. *Physical Review B*, Vol. 51, No. 9, pp. 5682–5692, http://dx.doi.org/10.1103/PhysRevB.51.5682
——— (1995b) Charge-exchange processes in titanium-doped sapphire crystals. II. Charge-transfer transition states, carrier trapping, and detrapping. *Physical Review B*, Vol. 51, No. 9, pp. 5693–5698, http://dx.doi.org/10.1103/PhysRevB.51.5693
van Wyk J.A., Loubser J.H.N. (1993) ENDOR of the P2 centre in type-Ia diamonds. *Journal of Physics: Condensed Matter*, Vol. 5, No. 18, pp. 3019–3026, http://dx.doi.org/10.1088/0953-8984/5/18/024
Yelisseyev A., Kanda H. (2007) Optical centers related to 3d transition metals in diamond. *New Diamond and Frontier Carbon Technology*, Vol. 17, pp. 127–178.
Yu H., Clarke D.R. (2002) Effect of codoping on the R-line luminescence of Cr^{3+}-doped alumina. *Journal of the American Ceramic Society*, Vol. 85, No. 8, pp. 1966–1970, http://dx.doi.org/10.1111/j.1151-2916.2002.tb00389.x
Zaitsev A.M. (2001) *Optical Properties of Diamond: A Data Handbook*. Springer, Berlin.
Zandi F. (2021) Lab Notes: Lead glass-filled laboratory-grown ruby. *G&G*, Vol. 57, No. 1, pp. 61–62.
Zhang J., Lu T., Chen H. (2013) Characteristics of coated jadeite jade. *G&G*, Vol. 49, No. 4, pp. 246–251, http://dx.doi.org/10.5741/GEMS.49.4.246
Zhang Z., Shen A. (2023) Fluorescence and phosphorescence spectroscopies and their applications in gem characterization. *Minerals*, Vol. 13, No. 5, article no. 626, http://dx.doi.org/10.3390/min13050626
Zhao J., Green B.L., Breeze B.G., Newton M.E. (2023) Phosphorescence and donor-acceptor pair recombination in laboratory-grown diamond. *Physical Review B*, Vol. 108, No. 16, article no. 165203, http://dx.doi.org/10.1103/PhysRevB.108.165203
Zhou C., Homkrajae A., Ho J.W.Y., Hyatt A., Sturman N. (2012) Update on the identification of dye treatment in yellow or "golden" cultured pearls. *G&G*, Vol. 48, No. 4, pp. 284–291, http://dx.doi.org/10.5741/GEMS.48.4.284
Zhou C., Ho J.W.Y., Chan S., Zhou J.Y., Wong S.D., Moe K.S. (2016) Identification of "pistachio" colored pearls treated by Ballerina Pearl Co. *G&G*, Vol. 52, No. 1, pp. 50–59, http://dx.doi.org/10.5741/GEMS.52.1.50
Zhou C., Tsai T.-H., Sturman N., Nilpetploy N., Manustrong A., Lawanwong K. (2020) Optical whitening and brightening of pearls: A fluorescence spectroscopy study. *G&G*, Vol. 56, No. 2, pp. 258–265, http://dx.doi.org/10.5741/GEMS.56.2.258
Zhou C., Ho J.W.Y., Shih S.C., Tsai T.-H., Sun Z., Persaud S., Qi L.-J. (2021) Detection of color treatment and optical brightening in Chinese freshwater "Edison" pearls. *G&G*, Vol. 57, No. 2, pp. 124–134, http://dx.doi.org/10.5741/GEMS.57.2.124

Protect Your Customers and Your Business.

GIA®

The most effective defense against diamond deception.

In under two seconds, the easy-to-use **GIA iD100®** can identify a diamond as natural with 100% accuracy.

Speed, precision, and convenience – the ideal tool to add to your protocol.

Learn More

GIA.edu/iD100

Applications of X-Ray Radiography and X-Ray Computed Microtomography In Gemology

Chunhui Zhou and W. Henry Towbin

X-ray radiography and X-ray computed microtomography are two imaging techniques with far-reaching applications in many fields. In gemology, they play a crucial role in the identification of pearl, a unique biogenic gem material. This article offers a brief history of pearl testing by X-ray imaging, as well as basic instrumental theory, examples of different types of pearls that can be separated with X-ray imaging, and examples of its other uses in gemology and mineralogy. The aim of this paper is to provide readers with a basic understanding of these methods and the importance of these devices in a gemological setting, particularly for pearl testing.

In 1895, Wilhelm Conrad Roentgen captured the first X-ray image, which showed the bones inside his wife's hand and the ring on her finger (Roentgen, 1896). This discovery revolutionized how scientists probe the human body and the structure of crystals and atoms (Assmus, 1995). Just two years prior, in 1893, Kokichi Mikimoto had begun experimenting with culturing pearls using the so-called akoya pearl oyster (*Pinctada fucata*) in Japan. Mikimoto succeeded in culturing hemispherical shell blisters and subsequently gem-quality spherical cultured pearls that would forever change the pearl industry (Nagai, 2013). These two seemingly unrelated events would eventually meet, as X-ray imaging technology became an essential part of pearl testing worldwide.

Natural pearls have been cherished since the dawn of civilization. Many mollusk species from the Bivalvia and Gastropoda classes are known to produce pearls naturally, often as a response to a foreign particle irritant in their soft mantle tissue. This tissue is responsible for the biomineralization of shells by producing calcium carbonate. Before the advent of pearl culturing, gem-quality pearls were extremely rare and expensive, reserved almost exclusively for the wealthy elites globally. By the beginning of the twentieth century, pearl oyster beds and freshwater mussel populations around the world had been depleted significantly by overharvesting. (Later, the discovery of oil in the Persian [Arabian] Gulf caused further reduction of natural pearl production.) Mikimoto's successful commercial production of akoya cultured pearls had a profound impact, providing an affordable alternative that was almost indistinguishable from natural pearls. This shift created an urgent need for new technologies that could distinguish between natural and cultured pearls.

Several major gemological laboratories were established in the early twentieth century. These included the gem testing laboratory of the London Chamber of Commerce (which later became the laboratory of the Gemmological Association of Great Britain) in 1925, the Laboratoire Français de Gemmologie (LFG) in 1929, and the Gemological Institute of America (GIA) in 1931. All of them initially focused their efforts on the identification of natural and cultured pearls. At first, Laue diffraction using X-ray (along with endoscope analysis using optic light) played an important role in separating natural pearls from akoya cultured pearls containing a shell bead nucleus (Anderson, 1932; Shipley Jr., 1934; Bloch, 1937; Alexander, 1941; Barnes, 1946, 1947; Scarratt and Karampelas, 2020). It was found that the X-ray diffraction patterns obtained are due to the presence of aragonite crystals. Natural pearls displayed the typical spoke-like diffraction pattern (also known as a six-spot pattern), while cultured pearls produced a "Maltese" cross pattern (also known as a four-spot pattern) (Alexander, 1941;

See end of article for About the Authors.
Gems & Gemology, Vol. 60, No. 4, pp. 582–595,
http://dx.doi.org/10.5741/GEMS.60.4.582

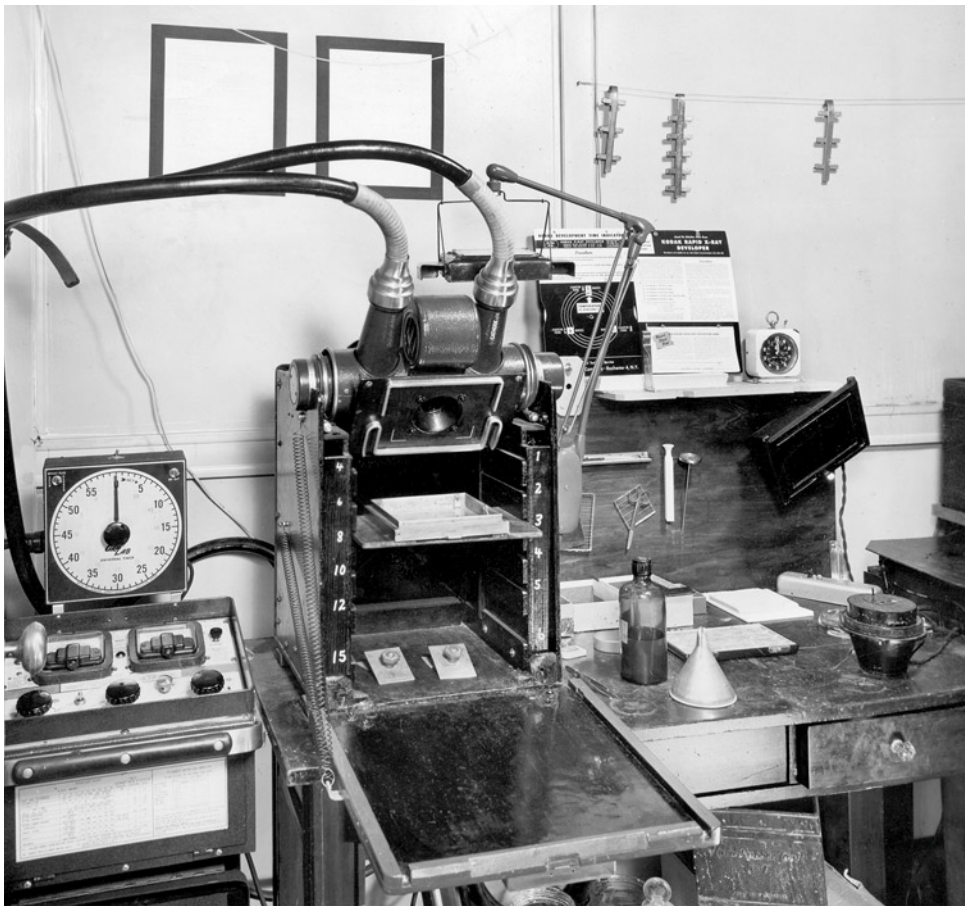

Figure 1. This specially adapted X-ray medical unit used by GIA during the 1950s features an automatic timer, a pearl tray, a lead glass protective cover, and accessories used in X-ray radiography.

Scarratt and Karampelas, 2020). While the diffraction patterns of saltwater natural pearls and some bead cultured akoya pearls are distinctly different, some cultured akoya pearls with thick nacre (containing a small bead nucleus inside) can produce the same pattern found in a natural pearl, which is misleading. In addition, some freshwater natural pearls may exhibit diffraction patterns similar to those of bead cultured pearls. Furthermore, the relatively long exposure time of X-ray diffraction and its inability to examine multiple pearls at the same time eventually led to the adoption of X-ray radiography in pearl testing.

In the early twentieth century, gemologists began using X-ray radiography to detect pearls inside mollusk shells and distinguish natural and cultured pearls (Kempton, 1922; Alexander, 1941). While X-ray diffraction was used to analyze the crystal structure and atomic arrangement within a pearl's nacre layers, X-ray radiography creates a 2D image of the internal structures of a pearl by measuring the attenuation of X-rays as they pass through it. Because of technology limitations, the images obtained during that time often failed to clearly show the difference in density between the nacre and the nucleus of a cultured pearl. In 1950, a newly designed X-ray instrument was introduced by the Gemmological Laboratory of the London Chamber of Commerce. This apparatus, slightly larger than a household refrigerator, was capable of producing both radiography images and readily observable luminescence (Webster, 1950). X-ray luminescence marked a significant advancement, as it could separate saltwater pearls from either freshwater pearls or pearls cultured with freshwater shell bead nuclei, based on differences in luminescence caused by trace element concentrations of manganese (Hänni et al., 2005).

The following year, the GIA Gem Trade Laboratory in New York installed a similar instrument specially adapted and designed for pearl testing (figure 1) with the ability to generate radiography images and readily observable luminescence. It generated detailed images of the concentric nacreous layers surrounding the nucleus of a cultured pearl. The basic operating procedure of these early machines was to direct a beam of X-rays at a specimen with X-ray sensitive film placed directly behind it. The pearls were

sometimes immersed in carbon tetrachloride to minimize traces of surface reflection and refraction. After exposure to the X-rays, any differences in the structural density of the specimen would cause uneven absorption of the X-ray beam, and the resultant image recorded on film would show these characteristics (Benson, 1951). The entire process of capturing a single X-ray image often required 15 to 20 minutes. As more modern X-ray units were introduced in the decades that followed, the underlying concept of radiography remained an essential method for differentiating natural and cultured pearls (Zhou, 2019).

In recent decades, digital X-ray equipment has largely replaced film-based systems in gemological laboratories. The transition from image intensifiers to flat-panel detectors and the adoption of X-ray computed microtomography (μ-CT) have further enhanced image resolution, allowing the detection of fine growth features inside a pearl (Karampelas et al., 2010, 2017; Krzemnicki et al., 2010). These more advanced instruments are also used by GIA for pearl identification services in various laboratory locations (figure 2).

This article reviews general theories of X-ray radiography and μ-CT and explains their working mechanisms. While the main application of these techniques in gemology is to separate natural and cultured pearls, we will briefly cover their use in examining other gems and minerals. Examples of 3D reconstruction of μ-CT data further demonstrate the capability of such instrumentation in revealing the secrets hidden inside these unique biogenic gems, such as unusual materials used as nuclei in the culturing process.

X-RAY IMAGING THEORY

X-ray radiography is a powerful tool for visualizing the internal structures of an object based on the differential absorption of X-ray photons. A basic X-ray imaging system consists of three components:

1. An X-ray source that emits a beam of X-ray photons
2. A sample that absorbs X-rays; this absorption is dependent on the material's composition and density.
3. A detector that enables X-rays to be imaged. Modern systems typically use a special digital image sensor, but X-ray film or a fluorescent screen could also be used.

Figure 3 shows an illustration of these basic components. To optimize image quality, it is important to understand how each component works. The following sections explain the principles of each component and how they operate in modern X-ray radiography. Rather than an exhaustive explanation of the underlying physics, this article will focus on practical aspects of X-ray and μ-CT data collection and interpretation. For a more comprehensive overview of the theory and physics of X-ray generation, refer to Als-Nielsen and McMorrow (2011). A review of X-ray imaging is available in Ou et al. (2021). For a review of μ-CT imaging, refer to Molteni (2020) and Withers et al. (2021).

X-Ray Generation. Most commercial systems generate X-rays using an electrically driven X-ray tube. A user can control two parameters: voltage (kV) and current (mA) of the X-ray source. Voltage has the greatest impact, determining the energy distribution and overall number of X-ray photons emitted. Current influences the number of X-ray photons produced but has a less dramatic effect than voltage.

In Brief

- X-ray radiography and X-ray computed microtomography are two essential imaging techniques used by gemological laboratories to separate natural and cultured pearls.
- X-ray radiography produces a flat, two-dimensional image, while CT scans create three-dimensional images by rotating the specimen and converting them into a digital 3D representation.
- A basic X-ray imaging system consists of three components: an X-ray source that emits a beam of X-ray photons, a sample that absorbs different amounts of X-rays depending on the material's composition and density, and a detector that enables X-rays to be imaged.

There are many different designs of X-ray tubes, but all operate based on the same fundamental principle. X-rays are generated by shooting a focused, high-energy electron beam onto a metal "target." The electrons in the beam are accelerated toward the target by applying a high voltage (10–300 kV) between the anode and cathode of the X-ray tube, based on the voltage applied; the energy of these electrons is measured in thousands of electron volts (keV). When the electrons strike the target, this generates either continuum X-ray emission (photons

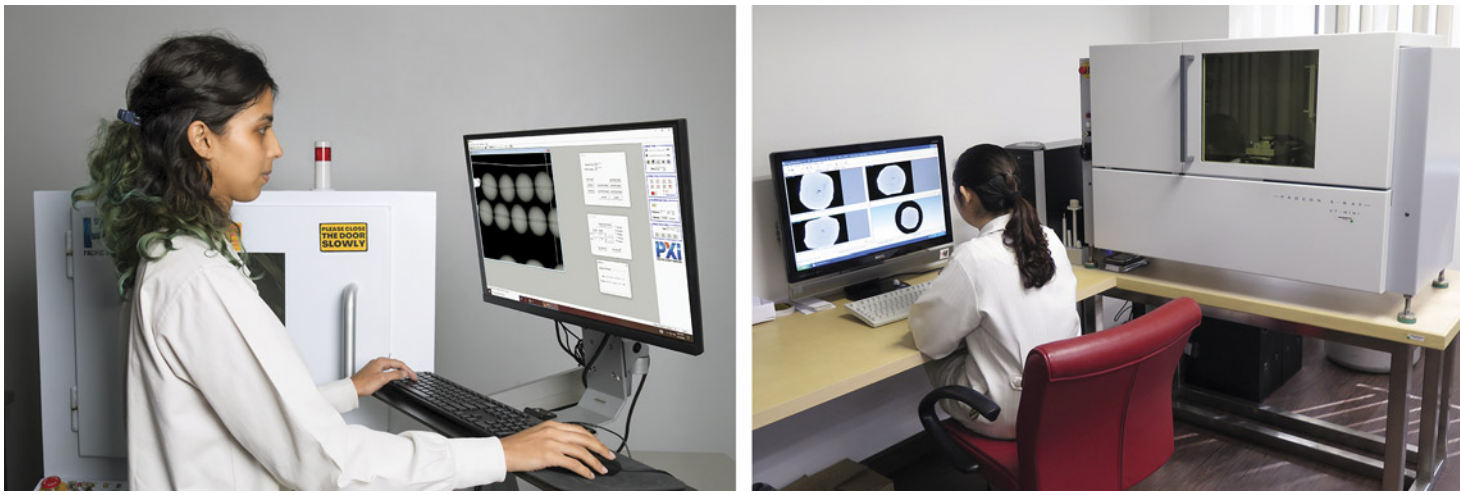

Figure 2. An X-ray microradiography unit in GIA's Mumbai laboratory (left) and an X-ray computed microtomography unit at GIA's Bangkok laboratory (right). Both are used mainly for pearl testing. Photos by Gaurav Bera (left) and GIA staff (right).

emitted over a broad continuous energy range) or characteristic X-ray emission (photons with a fixed energy level specific to the target material's elemental composition). In both cases, X-rays are produced when electrons lose their kinetic or potential energy and emit photons with energy corresponding to the difference in electron energy level. These photons are also measured in electron volts. In modern laboratory X-ray imaging systems, the target material is usually either tungsten for high-energy X-rays ($K_{\alpha 1}$ = 59.3 keV), suitable for imaging denser materials, or molybdenum for lower-energy X-rays ($K_{\alpha 1}$ = 17.5 keV) suitable for high-contrast imaging of low-density materials. X-ray generation takes place under a vacuum since electrons are deflected and lose energy interacting with gas molecules. The X-rays lack an electric charge and thus pass through air unimpeded. They are directed out of the vacuum tube through a low X-ray absorbing "window" and toward a sample.

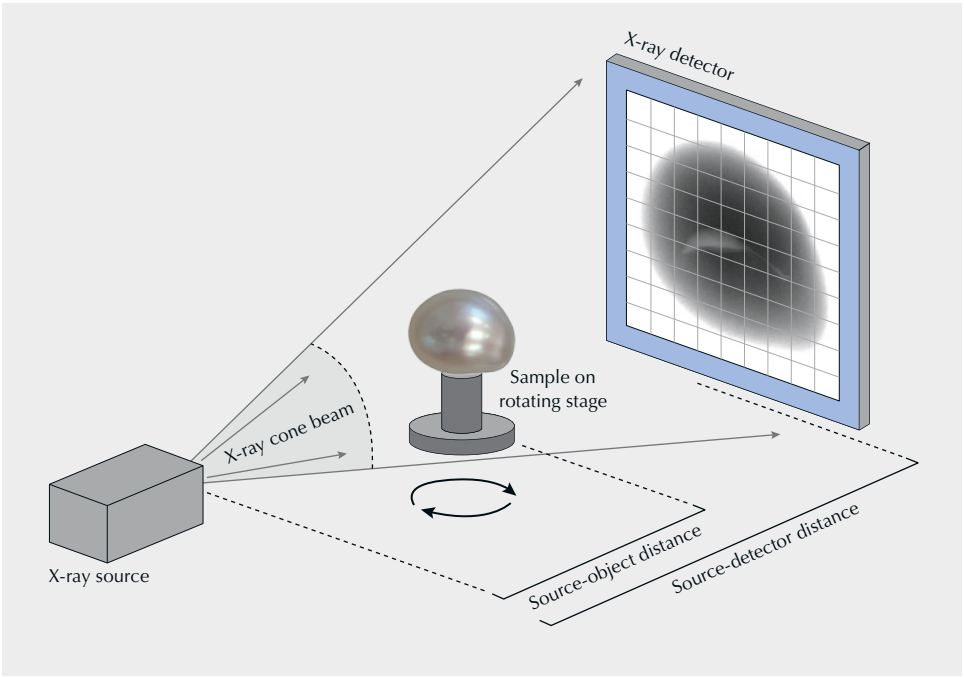

Figure 3. Basic components of a laboratory X-ray imaging system. The X-ray source emits a cone-shaped beam of X-ray photons. The beam is partially absorbed by the sample (a non-bead cultured pearl with an irregular-shaped void feature in this case), projecting a shadow onto the X-ray detector. The magnification of the radiograph is determined by the distance from the X-ray source to the detector, divided by the distance between the source and the object. The pixel size of the image corresponds to the pixel size of the detector divided by the magnification. Illustration by Henry Towbin.

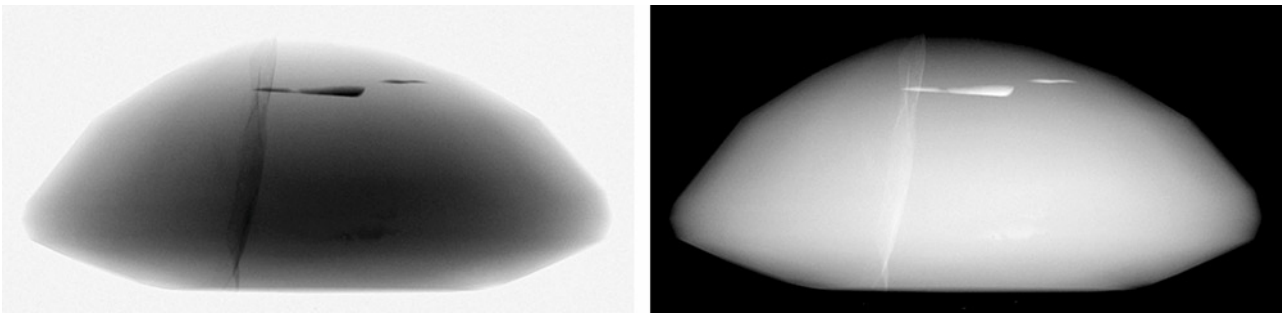

Figure 4. X-ray images of an oval ruby with lead glass–filled fractures, viewed from the girdle. Left: The image collected by digital X-ray imaging. The lead glass is seen as the darker marks. The vertical fracture is narrower and has lower contrast than the horizontal fractures, which are thicker and absorb more X-rays. Right: The same image with inverted grayscale. This contrast is also conventionally used in medical X-ray imaging, where denser, more absorbing structures such as bone are typically white. This is a relic from when X-rays were recorded on photosensitive film as negative images. Many gemological X-ray systems use inverted contrast.

X-Ray Absorption. Differences in a sample's X-ray absorbance provide the contrast within an image. X-ray absorption is sensitive to the chemical composition, the amount (thickness and density) of material between the X-ray source and the detector, and the energy of the X-rays. Materials with heavier elements (higher average atomic number) will absorb more X-rays. This absorption is proportional to the average atomic number to the third power (z^3) (Hubbell and Seltzer, 1995). For a material with a uniform density, the X-ray absorption will follow the Beer-Lambert law, meaning the absorption is proportional to the thickness of the material. Roughly speaking, the more atoms there are and the higher their atomic number, the greater the likelihood the X-rays will be absorbed (transferring their energy to the material's atomic structure).

The example in figure 4 (left) shows an X-ray image of an oval-cut ruby with lead glass–filled fractures viewed from the side of the stone. In an X-ray image, the darker-looking structures absorb more X-rays (i.e., fewer photons pass through the material). The lead glass appears as dark, distinct structures within the body of the ruby. The sharp contrast is due to the difference in the chemical composition of the materials—the lead in the glass has higher absorption than ruby, which is made of lighter elements aluminum and oxygen. The thin, wispy vertical fractures are not as dark as the thick horizontal fractures toward the top of the image. This difference in absorbance is due to the difference in material thickness along the path of the X-rays through the sample and to the detector. If the ruby were imaged at a different orientation, the pattern would change. If it were oriented so that the plane of the crack was perfectly aligned to the X-ray path, the lead glass along that path would be thicker than the horizontal features and thus absorb more X-rays. The ruby also shows differences in X-ray absorption depending on its thickness. The center of the ruby (where the cross section is thickest) is darkest, with decreasing absorption toward the rim where there is less material for the X-rays to penetrate. In gemology, it is customary to collect X-ray images with inverted contrast (also called negative imaging) (figure 4, right), as shown in the rest of the X-ray images in this article.

Absorption is also sensitive to the energy of the X-ray photons. Lower-energy photons are more easily absorbed than high-energy photons, which pass through the material with less likelihood of being absorbed. This differential absorption allows high-energy X-rays to penetrate dense objects better, while lower-energy X-rays provide better contrast between materials. A user generally controls the energy of the X-ray beam by adjusting the voltage applied to the X-ray tube. This sets the maximum energy of the X-rays being emitted. To reduce the energy of X-rays, users can "filter" the beam by using a thin sheet of metal to block low-energy X-rays. This can narrow the energy range of the X-ray beam, helping minimize artifacts due to the differential absorption of X-ray energy.

X-Ray Detection. In much the same way a digital camera operates, a digital X-ray image sensor converts X-ray photons into a digital image. A grid of pixels measures the relative number of photons that hit the detector within a set exposure time and reads out the signal as an image. The X-rays first pass through a material called a scintillator, which fluoresces visible light in response to X-ray excitation. The visible light is then measured by an imaging detector and converted to a digital signal. The more X-rays hitting

the scintillator, the greater the signal. By default, this creates images with contrast opposite to older X-ray sensitive film, which creates negative images based on a photochemical reaction that leaves the areas exposed to the most X-ray photons darker than areas exposed to fewer. This means that structures with higher absorption will appear brighter on a film X-ray image. Due to the longtime use of film X-rays in medical imaging, most people think of more highly X-ray absorbing structures, such as bones, as appearing white in X-rays. To maintain consistency with this convention, many digital X-ray systems invert the contrast on the image to show areas with less X-ray signal as brighter than those with more.

In digital X-ray imaging, the user sets the exposure time for each image to ensure enough signal is being collected to avoid underexposure or overexposure. Underexposing means there are not enough photons passing through the sample to provide adequate contrast in the image. This can often be the result of image noise, due to random fluctuations in the number of photons traveling through the material or electrical signals in the detector. Overexposure occurs when too many photons strike the detector and overwhelm the detector's ability to measure additional signals. This results in an image that appears washed out and overly bright, with reduced contrast in the sample.

Two main types of X-ray detectors are used in modern digital X-ray imaging. X-ray image intensifiers are vacuum tubes that convert X-rays into visible light, creating an image. First, the incoming X-ray photons are converted to light photons using a phosphorescent material, and then they are further converted to electrons via the photoelectric effect inside a photocathode. These electrons are accelerated and focused toward the output phosphor using an electron optic system. At the end, the output electrons are converted back to visible light, which can be captured by a camera. In recent years, flat-panel detectors have become the state of the art in X-ray detector technology for radiography and µ-CT applications. Introduced in the mid-1990s, they offer a direct digital readout of the X-ray image and an increased spatial resolution (Berger et al., 2018). GIA currently utilizes X-ray imaging devices containing both types of X-ray detectors at various global laboratory locations, mainly for pearl identification services.

Basics of µ-CT. X-ray computed microtomography is a technique that combines X-ray images of a specimen from multiple perspectives, collected either by rotating the specimen or alternatively the X-ray source and detector, and converts them into a digital 3D representation. These 3D representations are typically viewed as cross-sectional images. Sir Godfrey N. Hounsfield created the first computed tomography scan of a human brain in 1971 and a full-body computed tomography device in 1975, breakthroughs that earned him (with Allan M. Cormack) a Nobel Prize in 1979. Cross-sectional images obtained by µ-CT are in terms of micrometer scale, which has a higher spatial resolution in the range of 1–10 µm for better detecting internal structures and geometries of tiny features in small objects, such as growth features in a pearl. The main components of the microtomography device are the X-ray tube, a computer-driven step motor that intermittently rotates the mounted sample, a radiation filter and collimator (which focuses the beam geometry to either a fan- or cone-beam projection), a specimen stand, and a scintillator-coupled digital X-ray detector. Microtomography was regarded as a revolutionary development (Boerckel et al., 2014; Orhan, 2020).

Data acquisition using µ-CT involves consideration of several factors, including sample size, resolution, voxel size (the 3D analog of a pixel), scan time, number of images, and rotation options. The X-ray source needs to be aligned with and centered on the X-ray detector. Total acquisition time is a balance between the number of images collected and the time it takes to collect a single image. The major consideration for scan time is the acquisition time of single projection images, which can vary from system to system due to detector sensitivity and dynamic range differences, X-ray tube brightness differences, and differences in physical distance from source to detector (du Plessis et al., 2017). The quality of a single image, particularly the contrast between features of interest and noise level, will determine much of the contrast in the final 3D images. The number of images taken at different rotational positions will affect the geometric accuracy of the 3D cross sections as well as the image quality. For pearl testing at GIA, a quick µ-CT scan of a median-sized pearl (around 7 mm) takes as little as 20 minutes to complete.

After data acquisition, the next step is the reconstruction of all 2D image projections into a 3D volume and the rendering and segmentation of the 3D volume using special software. Reconstruction produces 2D cross-sectional images or "slices" perpendicular to the rotational axis, and rendering converts these images to 3D objects that can be digitally manipulated. The data can be crosscut in different orientations to reveal

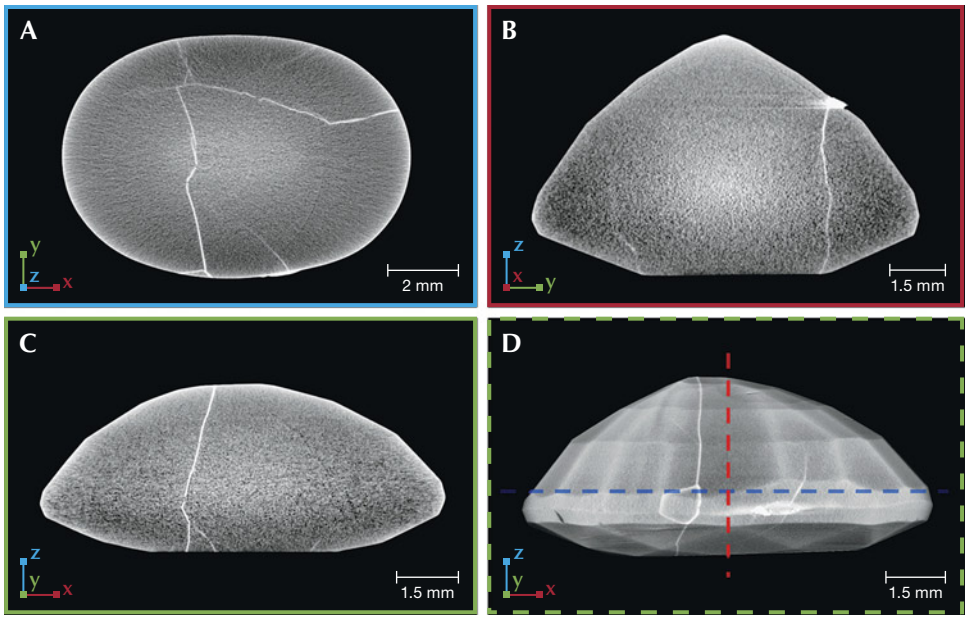

Figure 5. µ-CT reconstruction of a lead glass–filled ruby seen in cross section (A–C) and a 3D reconstruction (D). The orientation of the cross sections is shown in the bottom left corner. The colored boundaries show which plane the cross section is parallel to. In D, the z (blue) and x (red) section locations are marked on the 3D visualization; the y (green) section is perpendicular to the viewing direction and crosscuts through the midline of the sample. Note that the contrast between the lead glass and the ruby correlates to density, not absorbance.

alternate views of the material's interior. This is seen in figure 5, which shows various cross sections of a lead glass–filled ruby. Note that in the µ-CT reconstruction, the contrast between the lead glass and the ruby correlates to material density and chemistry, not the absorbance seen in 2D X-ray radiographs. This is because the 3D reconstruction algorithm corrects the path length of the absorbance by combining the 2D radiographs of the sample from different angular positions. Ideally, the contrast of the 2D cross-sections would only relate to the sample's material properties, but there are several artifacts that can distort the final images. Some of these include shadowing or bright streaking caused by very dense objects; ringed artifacts surrounding the axis of rotation; and so-called beam-hardening from the higher absorption of lower-energy X-rays in the thickest part of the sample which can make objects appear more absorbing than they actually are. For a more complete description and examples of µ-CT artifacts, refer to figure 7 in Withers et al. (2021).

The µ-CT data can be rendered and viewed in 3D; a user can also digitally segment the data to highlight different structures and features of interest. This is demonstrated in figure 6, where the lead glass within the ruby seen in figure 5 has been exposed by reducing the opacity (alternatively referred to as transparency) of the surrounding ruby in the 3D rendering. This powerful research tool makes it possible to virtually explore, manipulate, extract, and reconstruct specific areas of an object for analysis. It also gives researchers the ability to enhance existing µ-CT data to see details more clearly.

APPLICATIONS IN PEARL TESTING

Since the 1950s, X-ray radiography has been the main method to separate cultured and natural pearls, as the examiner is able to observe the internal growth structures below the nacre. Pearl imitations such as coated glass or plastic beads can also be detected

Figure 6. 3D rendering of a lead glass–filled ruby, with different contrast highlighting the opaque lead glass areas inside the gem.

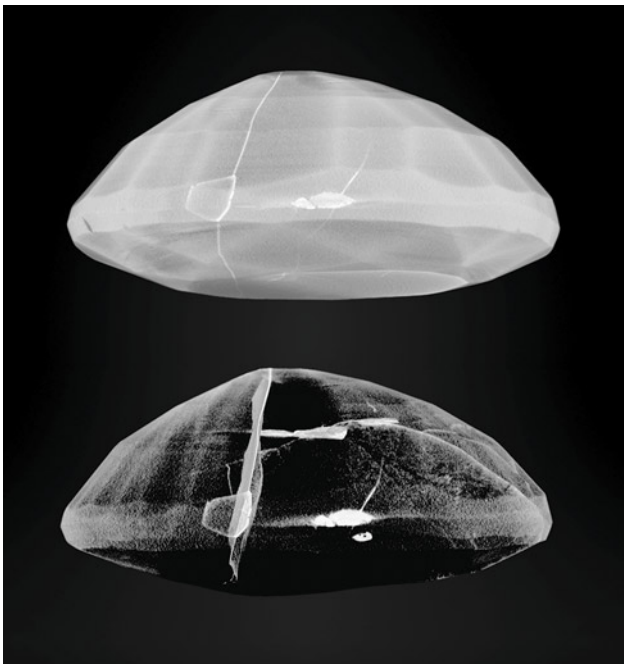

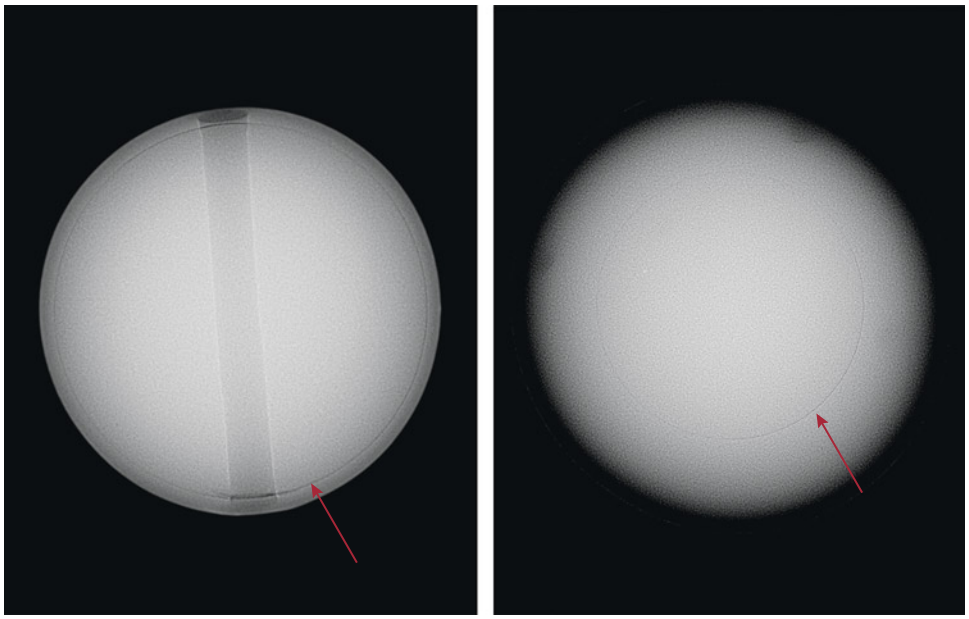

Figure 7. X-ray microradiographs of a 6.85 mm akoya bead cultured pearl and an 11.15 mm South Sea bead cultured pearl. Left: The akoya pearl has a relatively thin nacre, with an approximate thickness of 0.34 mm. A drill hole can also be seen in the middle. The white outline around the edge is due to contrast adjustment to better show the bead demarcation. Right: The South Sea pearl shows a relatively thick nacre, measuring approximately 1.92 mm thick. The demarcations between the shell bead nucleus and nacre in both pearls are transparent to X-rays and indicated by the arrows.

through this method. In the realm of testing, pearls can be broadly separated into three major groups: bead cultured, non-bead cultured, and natural.

To create bead cultured pearls, a skilled technician takes mantle tissue from a donor mollusk of the same species and inserts a shell bead along with it into a host mollusk's gonad. The mantle tissue grows and forms a sac around it and secretes nacre inward and onto the bead to eventually form a bead cultured pearl (Strack, 2006). These pearls are relatively straightforward to identify under X-ray radiography, as their internal structure usually shows a clear and continuous demarcation line that separates the shell bead nucleus and nacre layers that cover the bead, with no additional growth features inside the shell bead structure. Gemologists are able to gauge and measure the nacre thickness using X-ray radiography. An example can be seen in figure 7, which shows two bead cultured pearls of different size and nacre thickness. The pearls are created by different *Pinctada* species mollusks, which in turn affects the size of the pearl. Pearl size also depends on the size of the shell bead nucleus inserted and the duration of the culturing period.

While bead cultured pearls are relatively simple to identify, cultured pearls that do not contain a bead nucleus, known as non-bead cultured pearls (or beadless cultured pearls), can be more challenging. These usually occur as byproducts of bead culturing practices but can also result from intentional culturing (particularly freshwater cultured pearls). The internal structures of non-bead cultured pearls can vary significantly, often featuring irregular linear features, irregular void features, or evenly spaced alternating nacre and organic layers with a white core in

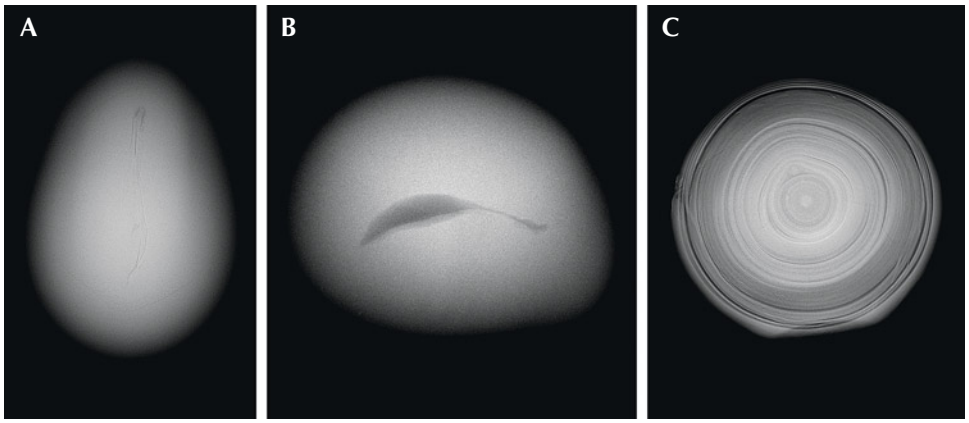

Figure 8. X-ray microradiographs of three saltwater non-bead cultured pearls obtained from Pinctada maxima *pearl oysters (Homkrajae et al., 2021b). These pearls show central irregular linear structure (A), central irregular void structure (B), and evenly spaced alternating nacre and organic layers with a white core in the center (C).*

the center (Scarratt et al., 2000; Krzemnicki, 2010; Sturman et al., 2016a,b; Nilpetploy et al., 2018; Al-Alawi et al., 2020; Homkrajae et al., 2021b). Examples of these structures are shown in figure 8.

Unlike cultured pearls, natural pearls are formed by various saltwater and freshwater mollusk species inside a natural pearl sac, without human intervention. Each natural pearl exhibits unique internal growth features when examined under X-ray radiography, such as the classic "onion ring" or "tree ring" concentric growth structure. However, examination using both destructive and nondestructive methods has revealed that the growth patterns inside natural pearls are much more complicated than typically described. These involve intricate building blocks from various polymorphs of calcium carbonate and complex mixtures of organic compounds (Vasiliu, 2016; Homkrajae et al., 2021a).

Examples of typical internal growth structures of natural pearls are seen in figure 9, which shows a section of a multi-strand necklace containing natural saltwater pearls formed by a *Pinctada* species mollusk. These structures include minimal growth arcs, concentric growth arcs, and some organic-rich light gray or dark gray cores. While these growth structures are relatively straightforward, it is important to note that natural pearls may exhibit additional growth patterns resembling those found in non-bead cultured pearls, such as linear, void, or evenly spaced growth rings in the center. Some structures fall into the borderline region between natural and non-bead cultured pearls, requiring additional information such as mollusk species, surface or age condition, and trace element chemistry to help with the identification.

In addition to separating three major types of pearls, the X-ray radiographic technique can also be used in detecting other features or unusual culturing methods, such as silver nitrate treatment to darken the color (Segura and Fritsch, 2014), imitation products such as Majorica imitation pearls (Hanano et al., 1990), and pearls that have been filled or plugged internally (Wong and Ho, 2013). While 2D microradiographs are essential for the identification of pearls, they can only provide overall growth structural information. It is often necessary to examine pearls from different directions to better visualize growth patterns. An attempt to create "3D X-ray radiography"

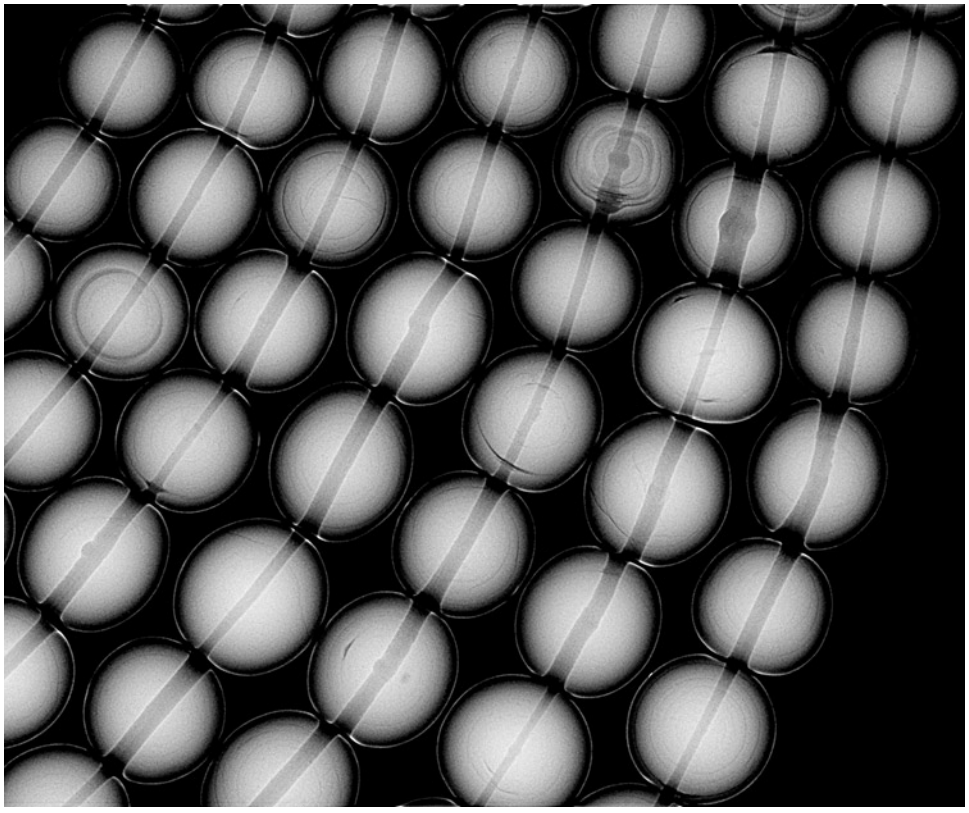

Figure 9. A section of a multi-strand necklace containing natural saltwater pearls from Pinctada *species. Various natural growth structures can be found inside these pearls with X-ray microradiography.*

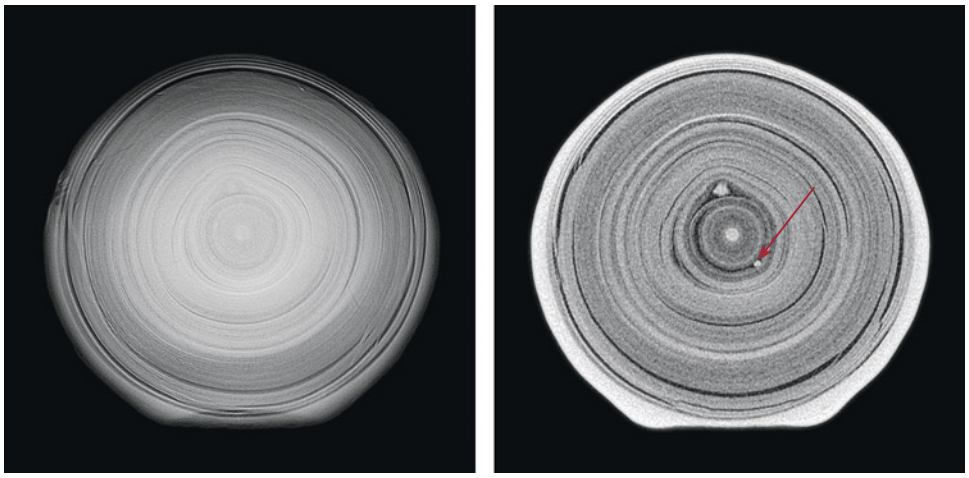

Figure 10. Compared to X-ray microradiography (left), additional fine details of a pearl's internal growth structure such as small "seeds" (indicated by the arrow) can be detected by µ-CT (right). From Homkrajae et al. (2021b).

using a conventional radiographic system has also been made (Hainschwang, 2011). In recent years, µ-CT analysis has become more common and is often needed to conclude a pearl's identity. High-resolution scans of a sample can reveal fine details of its growth structures, including fine linear structures or other small growth features that are otherwise difficult to observe. When the non-bead cultured pearl shown in figure 8C was subjected to µ-CT analysis, one of the images revealed additional "seed" features in its center, which supported the conclusion of a non-bead cultured pearl; compare figure 10 (right) to figure 10 (left). Conventionally, µ-CT analysis is limited to loose pearls or unobstructed mounted pearls, and it is relatively time-consuming to examine each pearl individually. However, recent advances make it possible to examine multiple pearls in a strand simultaneously using this technique (Rosc et al., 2016).

Another advantage of µ-CT is its ability to reconstruct a pearl's internal structures into 3D models using specialized software. This provides better visualization of internal structures, especially for pearls that contain unusual nuclei. Pearls cultured using atypical materials, producing unique shapes and morphologies, are excellent examples of this use (figure 11) (Zhou et al., 2016; Scarratt et al., 2017; Yazawa and Zhou, 2018).

While these X-ray techniques undoubtedly play a critical role in the characterization of pearls, there are several limitations. Pearls mounted in jewelry are often blocked by a metal setting, which prevents X-rays from penetrating and reaching the target. Certain

Figure 11. 3D reconstructions of the internal structures of two bead cultured pearls with atypical nuclei. Left: A flower-shaped bead nucleus in a freshwater cultured pearl. Right: A small gastropod shell used as a nucleus in a pearl from Pinctada maxima*. From Yazawa and Zhou (2018).*

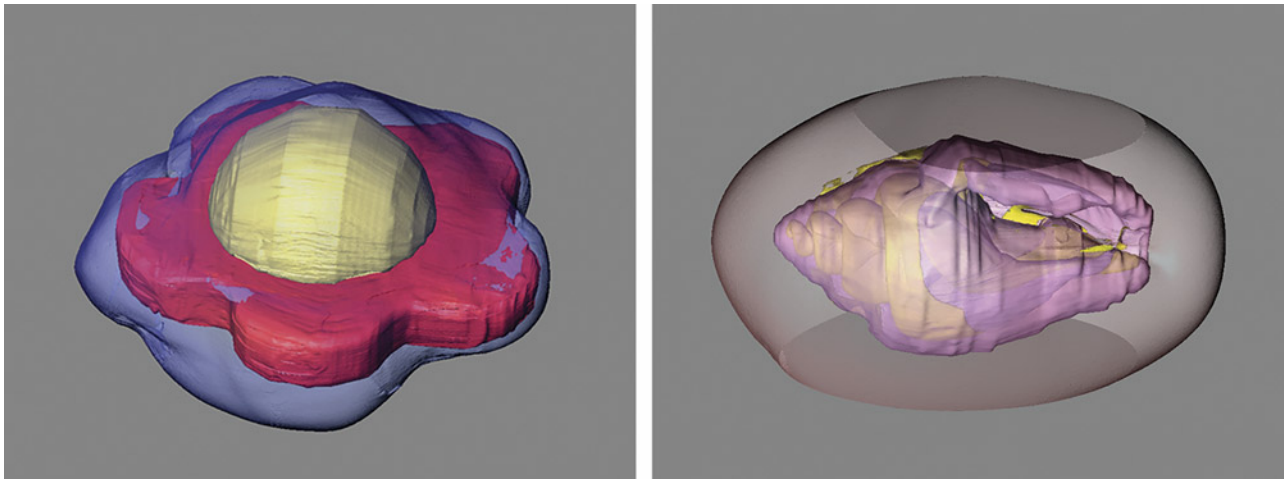

Figure 12. Sections of a multi-strand necklace containing natural saltwater pearls. X-ray radiographs of some of the pearls in this necklace were shown in figure 9. Photo by Gaurav Bera.

colored pearls such as Queen conch pearls are unstable under extended X-ray exposure, causing an unwanted discoloration of their pink color, which may impact their value (Hyatt et al., 2020). Moreover, the cost of a modern µ-CT unit and the time needed to acquire high-quality data may be prohibitive.

Finally, there have been novel techniques involving various X-ray imaging methods applied to pearl analysis in recent years, but these are not routinely used and fall beyond the scope of this article. These techniques include using simultaneous X-ray radiography, phase-contrast and darkfield imaging to separate natural from cultured pearls (Krzemnicki et al., 2017), and the attempt to use neutron radiography to investigate internal structures (Hanser et al., 2018; Micieli et al., 2018).

APPLICATIONS IN GEMSTONE TESTING AND MINERALOGY

µ-CT has a wide range of applications in gemology and mineralogy. Perhaps the most compelling use is documenting rare and unique samples in 3D. One recent example was the analysis of the Matryoshka diamond, a 0.62 ct green crystal with cavities and a freely moving inclusion within it. Wang et al. (2020) used µ-CT to observe how the morphology of the internal cavity related to that of the exterior diamond. This technology

is well suited for examining an array of inclusions trapped within other minerals. Nimis et al. (2016) used µ-CT to study mineral inclusions in diamonds and found a very thin (<1 µm thick) layer of hydrosilicic fluid surrounding many of these inclusions. This layer appeared to have a lower density than the host diamond and the mineral inclusions. Linzmeyer et al. (2024) used µ-CT to image clouds of nickel-rich microinclusions captured along the cuboid growth sectors of two large diamonds. The individual inclusions were too small to be seen directly in the µ-CT reconstruction, but inclusion clouds provided a very subtle difference in X-ray absorbance that allowed for 3D imaging of the included growth sectors. Gao et al. (2022) used high-resolution µ-CT on an emerald with a special trapiche pattern containing a colorless core, solid minerals, and fluids to visualize the distribution of these inclusions within the gem host.

In the field of paleontology, µ-CT is widely used to image fossils. For example, Watanabe et al. (2015) studied the air-filled sacs in dinosaur vertebrae, which contributed to their respiratory system similarly to the bones of modern birds. Barta et al. (2018) studied the evolution of dinosaur hand anatomy. Fossils in amber were studied by Barden and Grimaldi (2012), who documented an ant with sharp tusk-like mandibles in 98-million-year-old amber from Myanmar.

X-ray radiography and µ-CT are powerful tools for detecting and analyzing fracture filling in gems such as diamonds, rubies, and sapphires. An X-ray radiograph of a 0.90 ct Yehuda-treated diamond showed the filled areas as opaque, unexposed white patches (Koivula et al., 1989). Jia and Sit (2020) used 2D X-ray imaging to visualize bismuth-glass filling in Burmese rubies. An unusual tin-glass filling in ruby was also reported in which X-ray radiography of the ruby revealed slightly lighter-appearing patchy areas corresponding to the location of the filler in surface-reaching fissures (Sun et al., 2023). Similarly, Sahoo et al. (2016) used 2D and 3D X-ray imaging to analyze the structure of lead glass–filled fractures in rubies. They coupled this method with electron microprobe analysis to determine the chemical composition of the filler. In addition, X-ray imaging techniques can be used to pinpoint filled laser drill holes in diamonds (Hainschwang, 2011) and even aid in the identification of ivory products (Karampelas and Kiefert, 2010). Finally, X-ray radiography can be a supplemental method in identifying composite gemstones such as the lead glass–filled corundum doublet reported by Promwongnan et al. (2016). A study on a range of gems using µ-CT analysis, focusing on fracture filling but also investigating any color change due to X-ray exposure, found that most of the gems recovered their original color with time. However, one sky blue topaz lost all color, and it did not return even after months (Heyn et al., 2021).

CONCLUSIONS

Both X-ray radiography and X-ray computed microtomography have a wide range of applications. In the field of gemology, these two techniques are commonly used to distinguish natural and cultured pearls, though they have also been used to characterize other gem materials. With the continuous development of pearl culturing methods and the complexity of natural pearl formation, these techniques will play a more critical role in the identification of these beautiful yet mysterious biogenic gemstones (figure 12). Although most cultured and natural pearls can be reliably separated with X-ray microradiography alone, their internal growth features are better visualized with µ-CT. In certain cases, high-resolution µ-CT is required to distinguish some natural and non-bead cultured pearls. While X-ray radiography and µ-CT are not generally used in the routine analysis of non-pearl gems, these methods could be more widely applied to study fracture filling in gems and to document and visualize the interiors of rare and interesting samples.

ABOUT THE AUTHORS

Dr. Chunhui Zhou is senior manager of pearl identification, and Dr. W. Henry Towbin is a postdoctoral research associate, at GIA in New York.

REFERENCES

Al-Alawi A., Ali Z., Rajab Z., Albedal F., Karampelas S. (2020) Saltwater cultured pearls from *Pinctada radiata* in Abu Dhabi (United Arab Emirates). *Journal of Gemmology*, Vol. 37, No. 2, pp. 164–179.

Als-Nielsen J., McMorrow D. (2011) *Elements of Modern X-ray Physics*, 2nd ed. John Wiley & Sons, New York.

Alexander A.E. (1941) Natural and cultured pearl differentiation. *G&G*, Vol. 3, No. 11, pp. 169–172.

Anderson B.W. (1932) The use of X rays in the study of pearls. *British Journal of Radiology*, Vol. 5, No. 49, pp. 57–64.

Assmus A. (1995) Early history of X rays. *Beam Line*, Vol. 25, No. 2, pp. 10–24.

Barden P., Grimaldi D. (2012) Rediscovery of the bizarre cretaceous ant *Haidomyrmex* Dlussky (Hymenoptera: Formicidae), with two new species. *American Museum Novitates*, No. 3755, pp. 1–16, http://dx.doi.org/10.1206/3755.2

Barnes W.H. (1946) Radiographic examination of pearl. *G&G*, Vol. 5, No. 8, pp. 359–362, 376.

——— (1947) Pearl identification by X-ray diffraction, Part I. *G&G*, Vol. 5, No. 9, pp. 387–391.

——— (1947) Pearl identification by X-ray diffraction, Part II. *G&G*, Vol. 5, No. 10, pp. 428–429, 440–444, 446.

——— (1947) Pearl identification by X-ray diffraction, Part III. *G&G*, Vol. 5, No. 11, pp. 471–474.

——— (1947) Pearl identification by X-ray diffraction, Part IV. *G&G*, Vol. 5, No. 12, pp. 508–512.

Barta D.E., Nesbitt S.J., Norell M.A. (2018) The evolution of the manus of early theropod dinosaurs is characterized by high inter- and intraspecific variation. *Journal of Anatomy*, Vol. 232, No. 1, pp. 80–104, http://dx.doi.org/10.1111/joa.12719

Benson L.B. (1951) Gem Trade Laboratory installs new pearl testing equipment. *G&G*, Vol. 7, No. 4, pp. 107–112.

Berger M., Yang Q., Maier A. (2018) X-ray imaging. In A. Maier et al., Eds., *Medical Imaging Systems: An Introductory Guide*. Springer Open, Cham, Switzerland, pp. 119–145, http://dx.doi.org/10.1007/978-3-319-96520-8_7

Bloch O.F. (1937) Applications of photography to scientific and technical problems. *Journal of the Royal Society of Arts*, Vol. 85, No. 4410, pp. 651–672.

Boerckel J.D., Mason D.E., McDermott A.M., Alsberg E. (2014) Microcomputed tomography: Approaches and applications in bioengineering. *Stem Cell Research & Therapy*, Vol. 5, No. 6, article no. 144, http://dx.doi.org/10.1186/scrt534

Gao Y., He M., Li X., Lin M., Sun X., Zhang Y. (2022) Gemstone inclusion study by 3D Raman-mapping and high-resolution X-ray computed tomography: The case of trapiche emerald from Swat, Pakistan. *Crystals*, Vol. 12, No. 12, article no. 1829; http://dx.doi.org/10.3390/cryst12121829

Hainschwang T. (2011) Three-dimensional X-ray radiography. *Gems & Jewellery*, Vol. 20, No. 1, pp. 11–14.

Hanano J., Wildman M., Yurkiewicz P.G. (1990) Majorica imitation pearls. *G&G*, Vol, 26, No. 3, pp. 178–188, http://dx.doi.org/10.5741/GEMS.26.3.178

Hänni H.A., Kiefert L., Giese P. (2005) X-ray luminescence, a valuable test in pearl identification. *Journal of Gemmology*, Vol. 29, No. 5-6, pp. 325–329.

Hanser C.S., Krzemnicki M.S., Grünzweig C., Harti R.P., Betz B., Mannes D. (2018) Neutron radiography and tomography: A new approach to visualize the internal structures of pearls. *Journal of Gemmology*, Vol. 36, No. 1, pp. 54–63.

Heyn R., Rozendaal A., du Plessis A., Mouton C. (2021) Characterization of coloured gemstones by X-ray micro computed tomography. *Minerals*, Vol. 11, No. 2, article no. 178, http://dx.doi.org/10.3390/min11020178

Homkrajae A., Manustrong A., Nilpetploy N., Sturman N., Lawanwong K., Kessrapong P. (2021a) Internal structures of known *Pinctada maxima* pearls: Natural pearls from wild marine mollusks. *G&G*, Vol. 57, No. 1, pp. 2–21, http://dx.doi.org/10.5741/GEMS.57.1.2

Homkrajae A., Nilpetploy N., Manustrong A., Sturman N., Lawanwong K., Kessrapong P. (2021b) Internal structures of known *Pinctada maxima* pearls: Cultured pearls from operated marine mollusks. *G&G*, Vol. 57, No. 3, pp. 186–205, http://dx.doi.org/10.5741/GEMS.57.3.186

Hubbell J.H., Seltzer S.M. (1995) Tables of X-ray mass attenuation coefficients and mass energy-absorption coefficients 1 keV to 20 MeV for elements Z = 1 to 92 and 48 additional substances of dosimetric interest. NISTIR 5632, https://nvlpubs.nist.gov/nistpubs/Legacy/IR/nistir5632.pdf

Hyatt A., Ho J.W.Y., Yazawa E., Zhou C. (2020) Color classification and stability of Queen conch pearls. *GIA Research News*, March 4, https://www.gia.edu/gia-news-research/queen-conch-pearls-color-stability

Jia X., Sit M.M. (2020) Lab Notes: Bismuth glass-filled Burmese star ruby. *G&G*, Vol. 56, No. 1, p. 139.

Karampelas S., Kiefert L. (2010) Organic gems protected by CITES. *InColor*, No. 15, pp. 20–23.

Karampelas S., Michel J., Zheng-Cui, M., Schwarz J-O., Enzmann F., Fritsch E., Leu L., Krzemnicki M.S. (2010) X-ray computed microtomography applied to pearls: Methodology, advantages, and limitations. *G&G*, Vol. 46, No. 2, pp. 122–127, http://dx.doi.org/10.5741/GEMS.46.2.122

Karampelas S., Al-Alawi A.T., Al-Attawi A. (2017) Real-time microradiography of pearls: A comparison between detectors. *G&G*, Vol. 53, No. 4, pp. 452–456, http://dx.doi.org/10.5741/GEMS.53.4.452

Kempton P.H.S. (1922) *The Industrial Applications of X-rays: An Introduction to the Apparatus and Methods Used in the Production and Application of X-rays for the Examination of Materials and Structures, with Many Examples from Practice*. Sir I. Pitman & Sons, Ltd., London.

Koivula J.I., Kammerling R.C., Fritsch E., Fryer C.W., Hargett D., Kane R.E. (1989) The characteristics and identification of filled diamonds. *G&G*, Vol. 25, No. 2, pp. 68–83, http://dx.doi.org/10.5741/GEMS.25.2.68

Krzemnicki M.S. (2010) Trade alert: "Keshi" cultured pearls are entering the natural pearl trade. *SSEF Newsletter*, May.

Krzemnicki M.S., Friess S.D., Chalus P., Hänni H.A., Karampelas S. (2010) X-ray computed microtomography: Distinguishing natural pearls from beaded and non-beaded cultured pearls. *G&G*, Vol. 46, No. 2, pp. 128–134, http://dx.doi.org/10.5741/GEMS.46.2.128

Krzemnicki M.S., Hanser C.S., Revol V. (2017) Simultaneous X-radiography, phase-contrast and darkfield imaging to separate natural from cultured pearls. *Journal of Gemmology*, Vol. 35, No. 7, pp. 628–638.

Linzmeyer T., Towbin H., Eaton-Magaña S. (2024) Lab Notes: Large natural diamonds with asteriated cloud inclusions. *G&G*, Vol. 60, No. 2, pp. 212–214.

Micieli D., Di Martino D., Musa M., Gori L., Kaestner A., Bravin A., Mittone A., Navone R., Gorini G. (2018) Characterizing pearls structures using X-ray phase-contrast and neutron imaging: A pilot study. *Scientific Reports*, Vol. 8, No. 1, article no. 12118, http://dx.doi.org/10.1038/s41598-018-30545-z

Molteni R. (2020) X-ray imaging: Fundamentals of X-ray. In K. Orhan, Ed., *Micro-Computed Tomography (Micro-CT) in Medicine and Engineering*. Springer, Cham, Switzerland, pp. 7–19.

Nagai K. (2013) A history of the cultured pearl industry. *Zoological Science*, Vol. 30, No. 10, pp. 783–793, http://dx.doi.org/10.2108/zsj.30.783

Nilpetploy N., Lawanwong K., Kessrapong P. (2018) Non-bead-cultured pearls from *Pinctada margaritifera*. *GIA Research News*, April 27, https://www.gia.edu/gia-news-research/non-bead-cultured-pearls-from-pinctada-margaritifera

Nimis P., Alvaro M., Nestola F., Angel R.J., Marquardt K., Rustioni G., Harris J.W., Marone F. (2016) First evidence of hydrous silicic fluid films around solid inclusions in gem-quality diamonds. *Lithos*, Vol. 260, pp. 384–389, http://dx.doi.org/10.1016/j.lithos.2016.05.019

Orhan K. (2020) Introduction to micro-CT imaging. In K. Orhan, Ed., *Micro-Computed Tomography (Micro-CT) in Medicine and Engineering*. Springer, Cham, Switzerland, pp. 1–5.

Ou X., Chen X., Xu X., Xie L., Chen X., Hong Z., Bai H., Liu X., Chen Q., Li L., Yang H. (2021) Recent development in X-ray imaging technology: Future and challenges. *Research*, Vol. 2021, article no. 9892152, http://dx.doi.org/10.34133/2021/9892152

du Plessis A., Broeckhoven C., Guelpa A., le Roux S.G. (2017) Laboratory x-ray micro-computed tomography: A user guideline for biological samples. *GigaScience*, Vol. 6, No. 6, pp. 1–11, http://dx.doi.org/10.1093/gigascience/gix027

Promwongnan S., Leelawatanasuk T., Saengbuangamlam S. (2016) A lead-glass-filled corundum doublet. *Journal of Gemmology*, Vol. 35, No. 1, pp. 64–68.

Roentgen W.C. (1896) On a new kind of rays. *Science*, Vol. 3, No. 59, pp. 227–231, http:dx.doi.org/10.1126/science.3.59.227

Rosc J., Hammer V.M.F., Brunner R. (2016) X-ray computed tomography for fast and non-destructive multiple pearl inspection. *Case Studies in Nondestructive Testing and Evaluation*, Vol. 6, Part A, pp. 32–37, http://dx.doi.org/10.1016/j.csndt.2016.08.002

Sahoo R.K., Singh S.K., Mishra B.K. (2016) Surface and bulk 3D analysis of natural and processed ruby using electron probe micro analyzer and X-ray micro CT scan. *Journal of Electron Spectroscopy and Related Phenomena*, Vol. 211, pp. 55–63, http://dx.doi.org/10.1016/j.elspec.2016.06.004

Scarratt K., Karampelas S. (2020) Pearls – Evolution in the sector, production and technology. *InColor*, No. 46, pp. 82–86.

Scarratt K., Moses T.M., Akamatsu S. (2000) Characteristics of nuclei in Chinese freshwater cultured pearls. *G&G*, Vol. 36, No. 2, pp. 98–109, http://dx.doi.org/10.5741/GEMS.36.2.98

Scarratt K., Sturman N., Tawfeeq A., Bracher P., Bracher M., Homkrajae A., Manustrong A., Somsa-ard N., Zhou C. (2017) Atypical "beading" in the production of cultured pearls from Australian *Pinctada maxima*. *GIA Research News*, February 13, https://www.gia.edu/gia-news-research/atypical-beading-production-cultured-pearls-australian-pinctada-maxima

Segura O., Fritsch E. (2014) Aging silver-treated cultured pearl. *Journal of Gemmology*, Vol. 34, No. 3, p. 203.

Shipley Jr. R. (1934) Pearl tests. *G&G*, Vol. 1, No. 5, p. 136.

Strack E. (2006) *Pearls*. Rühle-Diebener-Verlag, Stuttgart, Germany.

Sturman N., Bergman J., Poli J., Homkrajae A., Manustrong A., Somsa-ard N. (2016a) Bead-cultured and non-bead-cultured pearls from Lombok, Indonesia. *G&G*, Vol. 52, No. 3, pp. 288–297, http://dx.doi.org/10.5741/GEMS.52.3.288

Sturman N., Manustrong A., Pardieu V. (2016b) The cultured pearls of Mergui with an emphasis on their internal structures. *Proceedings: The 5th GIT International Gem and Jewelry Conference*, Pattaya, Thailand, pp. 143–145.

Sun X., Gao Y., Huang T. (2023) An unusual tin glass-filled ruby. *Journal of Gemmology*, Vol. 38, No. 5, pp. 442–443.

Vasiliu A. (2016) Natural pearls. *Key Engineering Materials*, Vol. 672, pp. 80–102, http://dx.doi.org/10.4028/www.scientific.net/KEM.672.80

Wang W., Yazawa E., Persaud S., Myagkaya E., D'Haenens-Johansson U., Moses T.M. (2020) Lab Notes: Formation of the "Matryoshka" diamond from Siberia. *G&G*, Vol. 56, No. 1, pp. 127–129.

Watanabe A., Gold M.E.L., Brusatte S.L., Benson R.B.J., Choiniere J., Davidson A., Norell M.A. (2015) Vertebral pneumaticity in the ornithomimosaur *Archaeornithomimus* (Dinosauria: Theropoda) revealed by computed tomography imaging and reappraisal of axial pneumaticity in Ornithomimosauria. *PLOS One*, Vol. 10, No. 12, article no. e0145168, http://dx.doi.org/10.1371/journal.pone.0145168

Webster R. (1950) London laboratory's new X-ray equipment. *G&G*, Vol. 6, No. 9, pp. 279–281.

Withers P.J., Bouman C., Carmignato S., Cnudde V., Grimaldi D., Hagen C.K., Maire E., Manley M., Du Plessis A., Stock S.R. (2021) X-ray computed tomography. *Nature Reviews Methods Primers*, Vol. 1, No. 1, article no. 18, http://dx.doi.org/10.1038/s43586-021-00015-4

Wong S.D., Ho J.W.Y. (2013) Lab Notes: Enormous South Sea cultured pearl filled with cultured pearls. *G&G*, Vol. 49, No. 3, pp. 172–173.

Yazawa E., Zhou C. (2018) 3D reconstruction of the internal structures of pearls. Poster Presentations, Sixth International Gemological Symposium, *G&G*, Vol. 54, No. 3, p. 294.

Zhou C. (2019) A brief history of pearl testing through *Gems & Gemology*. In *Sixteenth Annual Sinkankas Symposium—Pearl*. Gemological Society of San Diego and Gemological Institute of America, pp. 74–83.

Zhou C., Yazawa E., Sturman N. (2016) New 3-D software expands GIA's pearl identification capabilities. *GIA Research News*, May 13, https://www.gia.edu/gia-news-research/3d-software-expands-pearl-identification-capabilities

METROLOGY AT GIA

David P. Nelson and Ilene M. Reinitz

Metrology, the science of measurement and its application, plays a critical role in the accuracy of GIA's research and laboratory services. The metrology team closely monitors the performance of instruments and devices in all global laboratory locations, assessing accuracy (within the established measurement uncertainty of each parameter), repeatability, and reproducibility. Calibration objects traceable to a national standards agency (such as the National Institute of Standards and Technology) and working references traceable to those calibration objects provide benchmarks for these performance criteria. Instruments that do not meet these criteria are removed from service until repair and recalibration have been performed to restore measurement validity.

Throughout GIA laboratories, both instruments and scientific equipment are used to collect data on gemstones. These data include physical measurements recorded as numerical values, graphical charts or plots, and various types of images. In each case, this information must be accurate and reproducible. This article outlines fundamental metrology concepts and the rigorous program used daily to ensure all measuring instruments are operating within tolerance across all of GIA's global laboratories. This program is vital for maintaining the accuracy and integrity of the gemological data contained in GIA laboratory reports.

Measurement of various properties has been important throughout human history. The concept of establishing a reference object to assess accuracy dates back to ancient Egypt (Ferrero, 2015; MSC Training Symposium, 2022). Accurate measurements are critical in most industries. In construction, mistakes lead to unstable buildings. In medicine, inaccurate test results can result in misdiagnosis and improper treatment. In the gem trade, even a small discrepancy in carat weight can significantly affect the value of a gemstone.

Many assume that the measurement of a property is absolute—that each measured value is exact and every measurement of that property for a given object produces the same value. However, every physical measurement has an associated uncertainty, or tolerance, due to small, uncontrollable variations in the environment or in measurement recording procedures.

Consider the example of measuring human body temperature. In the 1860s, Carl Wunderlich used a primitive thermometer to measure the temperature of a group of subjects once per day. He recorded values between 36.5°C and 37.5°C and reported an average value of 37.0°C, which converts to the familiar 98.6°F. When we express this with measurement uncertainty, we understand the whole range: 37.0°C ± 0.5°C, or 98.6°F ± 0.9°F. More recent measurements (Mackowiak et al., 1992) found an average body temperature of 36.8°C (98.2°F), well within the uncertainty of the much older measurements but also revealing a diurnal variation in core temperature of about 1.2°C. Consideration of measurement uncertainty and measurement variance provides a different perspective on what constitutes a "low" fever.

Repeated measurements of well-characterized reference objects are central to establishing the uncertainty for any type of measurement. These objects can be traceable measurement standards or reference materials. In either case, "well-characterized" means that the property of interest has been measured independently (sometimes by several methods) from the current measurement device (or method or process). This provides a consistent basis for comparison. When that independent measurement links to a traceable measurement standard, the objects can then be used to maintain the calibration of a measuring tool or process over time or to ensure consistent results across different locations.

See end of article for About the Authors and Acknowledgments.
GEMS & GEMOLOGY, Vol. 60, No. 4, pp. 596–603,
http://dx.doi.org/10.5741/GEMS.60.4.596

BOX A: DEFINING MASS: THE EXAMPLE OF THE KILOGRAM

The kilogram is the fundamental unit of mass in the International System of Units (SI). Originally known as the "Kilogram of the Archives" and defined as the mass of one cubic decimeter of water at the temperature of maximum density, the unit was redefined after the International Metric Convention in 1875. The International Prototype Kilogram (IPK), a cylinder of platinum and iridium, replaced the Kilogram of the Archives. The kilogram was now defined as being exactly equal to the mass of the IPK, which was locked in a vault of the International Bureau of Weights and Measures (BIPM) on the outskirts of Paris in the town of Sèvres. The accuracy of every measurement of mass (or weight) depended on how closely the reference masses used could be linked to the mass of the IPK. To ensure accurate measurements, mass standards used in countries around the world were, in theory, to be directly compared to the IPK. This was impossible in practice, so many countries maintained one or more of their own 1 kilogram standards (e.g., the National Institute of Standards and Technology, or NIST, which is part of the U.S. Department of Commerce). These national standards were periodically adjusted or calibrated using the IPK. Countries developed additional working standards that could be connected through the national standards back to the IPK using a carefully recorded series of comparison measurements.

This system of multiple standards used within countries was not without its problems. Not the least of these was the difficulty of relating the mass of a 1 kilogram standard to that of a much smaller standard, such as the mass standard for 1 milligram, which is one million times smaller. The need for a new system in which scaling of large to small masses did not introduce uncertainty became widely recognized.

In November 2018, a group of 60 nations voted to redefine the kilogram. No longer tied to the mass of a physical object, it was now related to the mathematical value of an invariant constant of nature, known as Planck's constant (h). This followed the earlier redefinition of the meter (as the distance light travels in a vacuum in 1/299,792,458 of a second) and the second itself (in terms of the frequency, ν, of a forced transition in ^{133}Cs atoms). Two fundamental physics equations could then be applied to redefine the kilogram.

The Planck-Einstein equation tells us that a photon's energy is related to its frequency by Planck's constant: $E = h\nu$. Einstein's famous equation of special relativity, $E = mc^2$, tells us that energy is related to mass by the square of the speed of light. Setting these two expressions equal to each other, $h\nu = mc^2$, or $m = h\nu/c^2$. The units for Planck's constant are joule-seconds (J·s), or $kg{\cdot}m^2s^{-1}$; the units for frequency are hertz, or s^{-1}; and the units for the speed of light are meters/second ($m{\cdot}s^{-1}$). Simple units analysis shows how a definition for the kilogram is derived: $(kg{\cdot}m^2s^{-1}) \times (s^{-1})/m^2s^{-2} = kg$. An instrument called a Kibble balance provides the extreme sensitivity and stability required to measure mass or Planck's constant precisely enough to support this change in the definition of the kilogram. According to this new agreement, the fixed numerical value of Planck's constant h is $6.62607015 \times 10^{-34}$ J·s.

As the reestablished kilogram is put into general practice, NIST continues to store a platinum-iridium cylinder called the Prototype Kilogram 20 and working copies of it. GIA uses mass standards that are traceable to the Prototype Kilogram 20 to calibrate its balances, ensuring that every gemstone weight is accurately described on GIA Diamond Grading and Gem Identification Reports.

THE SCIENCE OF METROLOGY

Background. Metrology is the science of measurement and its application (Brown, 2021; www.nist.gov/metrology). It encompasses both the theoretical and practical aspects of measurement, which are at the core of all scientific endeavors. Three activities are essential to metrology: the definition of the units of measurement, the practical realization of measurements and their uncertainties, and documenting the traceability of measurements to reference standards. These activities fall into three basic subfields: fundamental metrology to establish new units of measurement, applied metrology in manufacturing and other processes in society, and legal metrology covering the regulation and statutory requirements for measuring instruments and methods. GIA applies metrology principles to a variety of instruments and processes to ensure the accuracy of measurements and to fully understand measurement uncertainties, instrument reproducibility (for each device and across devices in different locations), and maintenance requirements.

Carat weight, or mass, is just one of many gemstone properties measured at GIA (box A). Measurements of physical dimensions and facet angles of polished gemstones, assessment of color and quantification of fluorescence intensity, as well as spectral data and chemical analyses, all rely on traceable standards. GIA's metrology team performs calibration and regular control checks of measurements for each of these factors.

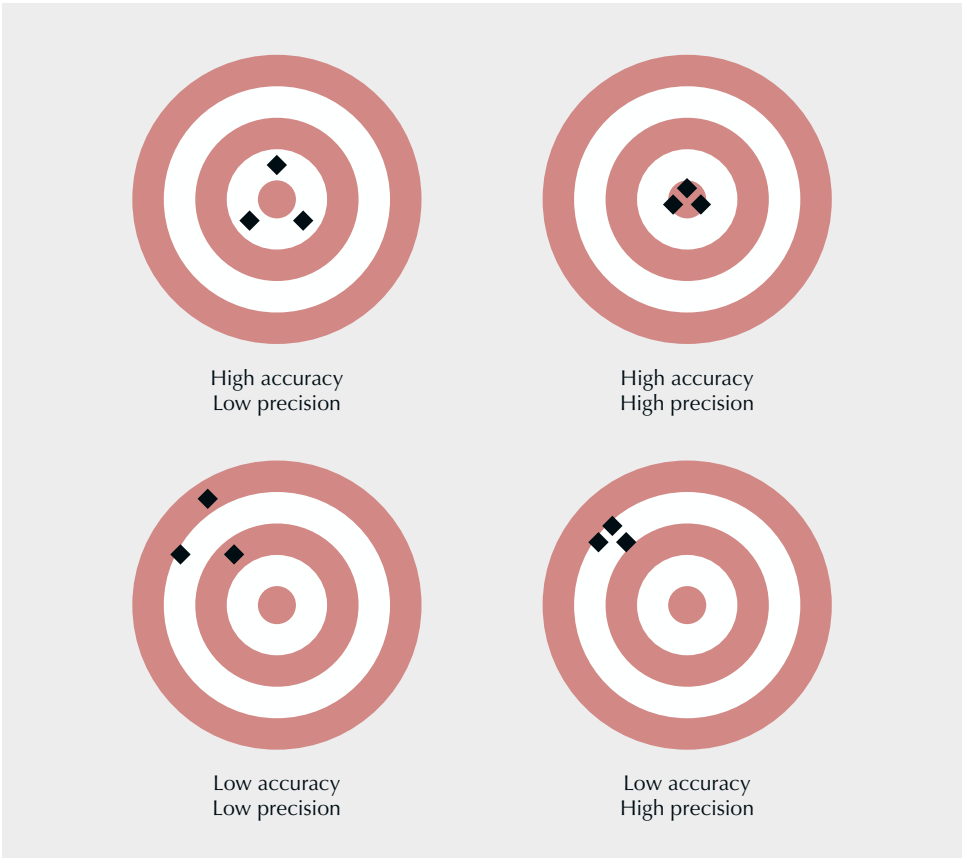

Figure 1. This diagram shows how precision and accuracy differ. Accuracy describes how closely the average of multiple measurements compares to the target value, typically known by other measuring methods. Precision describes how closely those multiple measurement values cluster together. Either aspect can be high or low, but the goal is to achieve both high accuracy (a correct result) and high precision (low uncertainty).

Qualitative and Quantitative Measurement. Some gemological questions can be answered by qualitative measurement, which establishes the presence of a particular feature but does not assess the intensity of that feature. For example, infrared spectroscopy of an emerald can identify fracture filling, but it does not quantify the extent of the treatment. Other gemological questions can only be resolved with quantitative measurements, where the amount of signal is the deciding factor. One such case is a method used to separate terrestrial peridot from extraterrestrial peridot in which nickel concentration is measured at the parts per million by weight (ppmw) level. High concentrations of nickel, above 2000 ppmw, indicate a terrestrial origin (Shen et al., 2011; Sun et al., 2024). The concepts below apply to quantitative measurements.

Measurement Accuracy and Precision. Two key aspects of a measurement result are accuracy and precision. Accuracy describes how close the measured value is to the true value of the quantity being measured. Establishing such a true value often requires multiple methods and traceable standards (see again box A). Precision expresses how well multiple measurements of the same quantity agree with each other (an expression of the measurement uncertainty). As shown in figure 1, either aspect can be low or high.

Another perspective of accuracy and precision is to view them in terms of random error and systematic error (figure 2). Random error takes its name from the mathematical use of the word, and these deviations occur in all directions around the true value. Small fluctuations in environment or power supply or minor variations in operation can produce random

In Brief

- GIA applies metrology principles and methods to achieve consistently accurate measurements from a variety of devices in all laboratory locations and to minimize measurement uncertainty.
- Repeated measurements of reference objects are used to assess uncertainty, repeatability, and reproducibility of each measuring device or method.
- Verification of measurement accuracy requires calibration standards traceable to NIST or other national standards agencies. Working references traceable to those standards are used for ongoing monitoring of instrument performance.

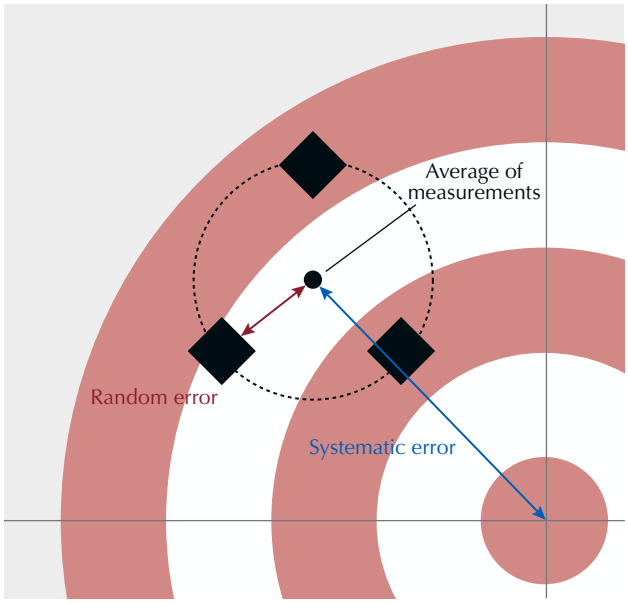

Figure 2. The inherent uncertainty of measurement, even for a well-maintained measuring instrument, contributes random error to multiple measurements of a reference object. When the average of those values deviates from the expected value for the measured property, that systematic error indicates a need for further investigation (and possible recalibration).

error. Systematic error describes deviations that all lie in a common direction away from the true value, which suggests an issue with the device or environment that requires correction in order to obtain more accurate measurements.

Systematic error reduces accuracy, even when multiple measurements are averaged. Random error leads to lower precision (and higher uncertainty), even when the average of multiple measurements produces an accurate value. Among the four categories of results shown in figure 1, the goal of measurement is to achieve both high accuracy (the correct result) and high precision (low uncertainty).

Precision, Repeatability, and Estimates of Measurement Uncertainty. The intrinsic precision of a simple tool, such as a ruler, depends on the spacing of its measurement divisions. Any additional measurement uncertainty arises from the minor fluctuations of the operator as the ruler is applied and the value is read from the printed divisions. Underlying sources of uncertainty are much more challenging to find in a complex measuring tool, such as a spectrometer or polished gemstone scanner, so uncertainty is typically assessed through repeatability. This involves measuring a reference object many times, sometimes in sets under slightly different conditions, and analyzing this group of measurements with appropriate statistical tools (e.g., mean and standard deviation). Unlike accuracy, which requires traceable standards, precision and measurement uncertainty can be determined from any reference object that exhibits the property one wants to measure.

A large number of repeated measurements yields a distribution offering good statistical confidence for both the average value and the total spread of values. Most statistics textbooks describe methods for analyzing measurements. Both the National Institute of Standards and Technology (NIST) in the United States and the National Physical Laboratory in the United Kingdom offer convenient online references that also discuss estimation of error and propagation of uncertainty (Goldsmith, 2010; NIST/SEMATEC, n.d.). In a typical production process, however, it is preferable to make as few measurements of each item as possible while still achieving sufficient confidence in the results. In such cases, the particular purpose of the measurement becomes an important factor in using the overall measurement uncertainty to set a tolerance, the range within which two measured values are considered equivalent.

For example, a carpenter uses a tape measure to mark a piece of wood for cutting five boards of equal width. If the boards are mounted as separate shelves, differences in width of ⅛ in. to ¼ in. (3 mm to 6 mm) might be fully acceptable. But if these boards are to be used to support a load on a platform, a much tighter tolerance (about 1 mm) is required to keep the platform level. This might require a metric tape measure and additional measurements before making the final markings.

In applying metrology to a specific task, one goal is to reduce measurement uncertainty to levels below what the task demands. This can involve taking multiple measurements of each object to minimize inherent measurement uncertainty or developing more precise instruments. Regardless of the approach, uncertainty must be accounted for when comparing different measurements.

The number of digits reported for a measured value is constrained by the precision of the measuring device and should also correspond to the overall measurement uncertainty. This acknowledgment of significant figures also applies to calculations involving measured values. The general rule is that the least certain measurement limits the maximum precision of the calculated result (Yale Department of Astronomy, n.d.). A calculator may supply many digits for a calcu-

lation, but the number of significant figures and uncertainty for each measurement in the calculation dictates how many of those digits are truly supported by the measurement. Additional digits are described as "false precision," and they obscure the true meaning of the measurement.

Consider the reporting of the length-to-width ratio (L:W) of a rectangular gemstone, which uses two decimal places by trade convention. A ratio of 1.05 or less supports describing the gemstone as square. A stone's owner uses a micrometer with readability to 0.01 mm (and similar uncertainty), and measures 8.45 × 8.01 mm for length and width, for a ratio of 1.054931336. But because the input precision is only two decimal places, the result is rounded to 1.05. The owner thinks that the shape will be classified as square but does not factor in the measurement uncertainty or how close the ratio is to the boundary between square and rectangle. When that gemstone arrives at a laboratory, the scanning system measures 8.454 × 8.014 mm (with an uncertainty of ±0.005 mm), well within the uncertainty of the micrometer values. Now the calculated L:W is 1.054903918 and rounds to 1.06 ± 0.001 (for propagation of error, see again NIST/SEMATECH, n.d.), making use of the additional precision of the laboratory's measuring device. The owner will be disappointed when the laboratory report lists the stone as a rectangle.

Reproducibility. Manufacturers of measuring tools and analytical devices strive to build each instrument consistently, but the reproducibility of measurements from one device to another cannot be presumed. This is especially true when instruments operate in locations with different environmental conditions, which requires checking for consistency. GIA's laboratory locations cover both temperate and tropical climates, with wide variations in moisture. Although staff members in these locations are well trained in the established protocols for each measuring device, minor differences among device operators highlight the importance of assuring reproducibility.

Reproducibility measurements allow metrologists to track the performance of each device and assess whether any of them need extra attention. Figure 3 illustrates reproducibility results from measuring the maximum diameter of the same round gemstone several times on four different devices. Although all four devices give average values within tolerance of the target value (6.451 ± 0.010 mm), the results for devices 3 and 4 indicate that individual measurements have lost the desired reliability.

Regular circulation of various reference objects is necessary to monitor reproducibility for the various instrumentation used at GIA. Ideal reference objects are "blind," meaning the operators do not recognize the reference objects as different from regular production work. However, obvious reference materials can also be useful, such as the synthetic crystals and glasses measured along with samples during each quantitative chemical analysis. Behind the scenes, metrologists analyze the data from these reference objects to ensure that every device in each GIA location produces results within the established tolerance for each property measured. GIA uses polished gemstones to track weight, dimensions, and color evaluation; polished oriented plates of various materials for spectral measurements; and solid-state references for X-ray fluorescence (XRF) and laser ablation–inductively coupled plasma–mass spectrometry (LA-ICP-MS).

Standards for Calibration and Measurement. Many measurements of interest to the gem industry are governed by specific international and national standards (figure 4). These standards cover length, weight, volume, angle, elemental concentration in solution or a solid matrix, and the color rendering index of light sources. Implementing such standards in daily practice involves both calibration objects and measurement reference objects.

Calibration objects are typically purchased with a report of the actual value and its uncertainty for one or more measurable properties, tightly traceable to a national or international standards agency. They can be used to check the performance of a device and to adjust that device until it produces the actual value (figure 5). For example, GIA uses three traceable mass standards: 2 grams (10 ct), 500 milligrams (2.5 ct), and 100 milligrams (0.5 ct)—independently measured with seven decimal places of precision.

However, such objects may be of an inconvenient size or only available with higher concentrations than typical samples. Measurement references, or working standards, can be chosen for ease of use, and their values are tied to a calibration standard. When evaluating the practicality of a working standard, important considerations include:

1. Will the object fit within a device?
2. Will it remain stable over time?
3. Can it be easily transported between locations?
4. Will the measurement result be clear and unambiguous?

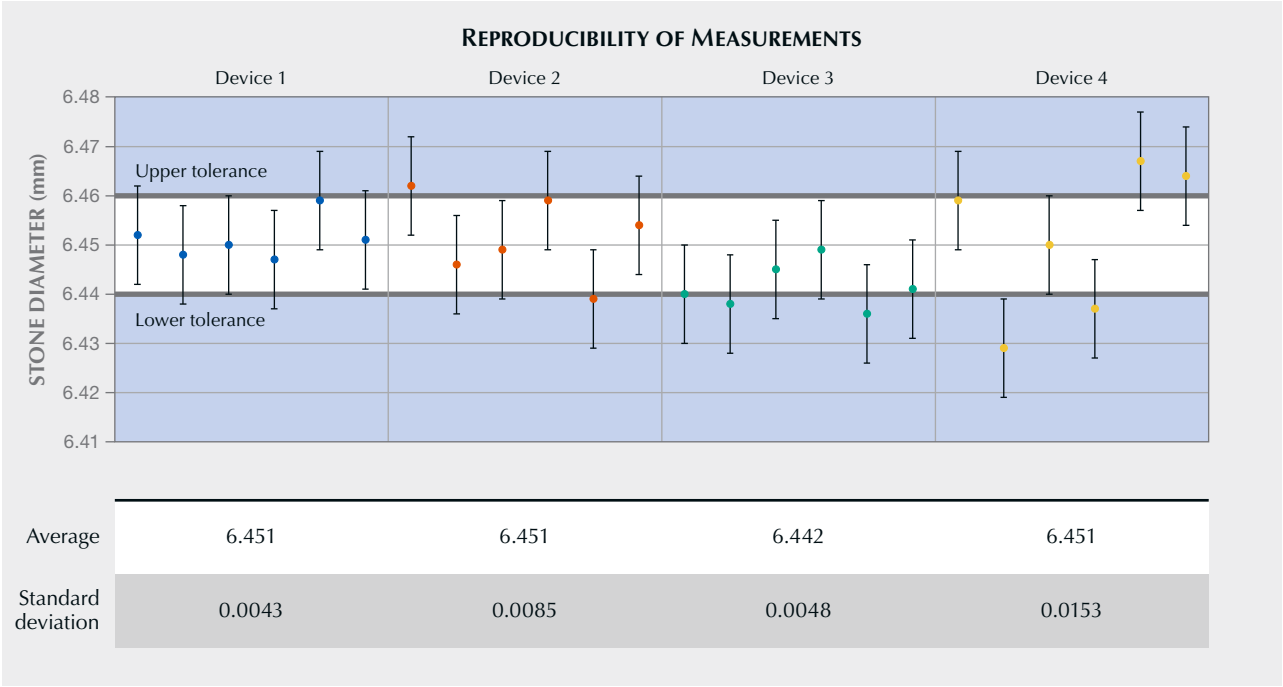

Figure 3. These four examples demonstrate the reproducibility of measurements for the maximum diameter of the same reference stone. Each device yields the same average value (within tolerance), but the four devices are not equally reliable. For Device 1, all six measurements are within the set tolerance of ±0.010. Device 2 shows greater variability and might need attention if the issue persists. Device 3 shows a small standard deviation, but the noticeable decline in the values suggests a calibration problem. For Device 4, the variability is unacceptably large.

Ideally, reference objects are similar to the samples that will be measured. In the gem trade, diamonds and colored stones should be used as references whenever possible.

To ensure confidence in the accuracy of measurements, working standards must be traceable to national or international standards. To be traceable, a result must be linked to a reference through a documented,

Figure 4. LA-ICP-MS analyses are standardized with NIST glass standard reference material (the blue and colorless pieces in yellow epoxy) for a variety of elements. Also shown is our internally developed matrix-matched corundum standard (colorless epoxy with four variously colored sapphires) used specifically for ruby and sapphire analysis. Photo by Kevin Schumacher.

Figure 5. A GIA metrologist uses a calibrated standard to verify instrument performance. Photo by Kevin Schumacher.

unbroken chain of calibrations, each contributing to the measurement uncertainty (https://www.nist.gov/standards). Traceability to NIST means that measurements are directly or indirectly linked to the NIST's own calibration and measurement standards, which are themselves traceable to international sys-

TABLE 1. GIA's instrument verification protocols.

Device	Property measured	Readability	Frequency of reference checks	Number of references per check
Mettler balance	Weight	0.00001 ct	Daily	3
Helium Polish	Dimensions and angles	0.001 mm, 0.01°, 0.1%	Daily	3
Diavision HD	Dimensions and angles	0.001 mm, 0.01°, 0.1%	Daily	3
Micrometer	Dimensions	0.001 mm	Monthly	3
Colorimeter	Color coordinates	0.01 Chroma	Daily	4
Accufluor	Color coordinates	0.01 Lightness	Daily	3
DiamondCheck	Peak ratio and intensity	Pass/Refer	Daily	5
FTIR	Peak ratio and intensity	1 cm^{-1}	Weekly	1
DPL	Peaks detected	Pass/Refer	Daily	1
VisiCheck	Peaks detected	Pass/Refer	Daily	1
Raman/PL	Peak width	0.1 nm	Weekly	1
EDXRF	Characteristic energy	0.01 keV	Weekly	1
LA-ICP-MS	Elemental detection limits	0.001–10 ppmw[a]	Several times per day	1–5

[a]*Sensitivity varies with the element detected.*

tems such as the International System of Units (SI). This connection provides a high level of confidence in the accuracy and consistency of measurements.

SUMMARY

Metrology is a mature field with a wide body of work on fundamental and applied measurement that can be applied to specific measuring needs. One of the ways GIA ensures quality measurements is by verifying all of its instruments prior to measuring diamonds, colored stones, or pearls submitted to the laboratory for evaluation (table 1). Measurement references (many of which are gemstones) are measured periodically to ensure the results are within tolerance; some references are checked daily, others at the time of measurement. This process creates a record of measurements that GIA metrologists can use to observe trends, inform adjustments to instruments, or take instruments offline if their performance falls below standards for accuracy or precision. Monitoring this data from instruments worldwide provides a deep understanding of GIA's capabilities to produce accurate and consistent measurements across all laboratory locations.

An internal team of metrologists, technicians, and engineers work on-site to actively monitor and adjust measuring devices. Robust validation, verification, and calibration processes result from collaboration within this global group. Senior team members routinely travel to each laboratory location to perform validation activities using master references, enhancing the alignment of GIA's measurement equipment worldwide.

Color measurement of a faceted diamond, for example, is particularly sensitive and complex. The results must be accurate and reproducible regardless of the diamond's color, fluorescence characteristics, size, or shape. GIA ensures alignment across the many colorimeters at each laboratory location using a reference set of diamonds representing the potential range of these attributes. Numerous measurements of these reference stones provide the statistical data needed to validate a colorimeter for use.

In addition to periodic validation, the metrology group regularly reviews daily verification data. Measurement trends are analyzed alongside instrument parameters and environmental factors such as temperature, humidity, and air circulation. Adjustments to instruments are performed based on these evaluations. This frequent monitoring also allows the metrologists to investigate measurement outliers and take corrective action.

GIA's reports provide many details about the properties of a gemstone. Each detail is important for evaluating quality and documenting the nature of that gem. GIA invests substantial effort to ensure every measurement is made with the highest precision and accuracy, supporting its mission to ensure the public trust in gems and jewelry.

ABOUT THE AUTHORS

David Nelson is a senior metrologist at GIA in Carlsbad, California. Dr. Ilene Reinitz is a senior research scientist at GIA in New York.

ACKNOWLEDGMENTS

We would like to thank Jim Shigley for inspiring this article and Yun Luo for her leadership of GIA's metrology team.

REFERENCES

Brown R.J.C. (2021) Measuring measurement – What is metrology and why does it matter? *Measurement*, Vol. 168, article no. 108408, http://dx.doi.org/10.1016/j.measurement.2020.108408

Ferrero A. (2015) The pillars of metrology. *IEEE Instrumentation & Measurement Magazine*, Vol. 18, No. 6, pp. 7–11, http://dx.doi.org/10.1109/MIM.2015.7335771

Goldsmith M. (2010) *Good Practice Guide No.118: A Beginner's Guide to Measurement*, Version 3, National Physical Laboratory, https://www.npl.co.uk/special-pages/guides/gpg118_begguide2measure

Mackowiak P.A., Wasserman S.S., Levine M.M. (1992) A critical appraisal of 98.6°F, the upper limit of the normal body temperature, and other legacies of Carl Reinhold August Wunderlich. *Journal of the American Medical Association*, Vol. 268, No. 12, pp. 1578–1580, http://dx.doi.org/10.1001/jama.1992.03490120092034

MSC Training Symposium (2022) History of metrology. Measurement Science Conference, https://msc-conf.com/history-of-metrology/

NIST/SEMATECH (n.d.) *e-Handbook of Statistical Methods*, https://doi.org/10.18434/M32189

Shen A.H., Koivula J.I., Shigley J.E. (2011) Identification of extraterrestrial peridot by trace elements. *G&G*, Vol. 47, No. 3, pp. 208–213, http://dx.doi.org/10.5741/GEMS.47.3.208

Sun Z., Jollands M., Palke A. (2024) Chemical analysis in the gemological laboratory: XRF and LA-ICP-MS. *G&G*, Vol. 60, No. 4, pp. 536–559, http://dx.doi.org/10.5741/GEMS.60.4.536

Yale Department of Astronomy (n.d.) A short guide to significant figures. http://www.astro.yale.edu/astro120/SigFig.pdf

Analysis of Gemstones at GIA Laboratories

Nicole J. Ahline and Jessa Rizzo

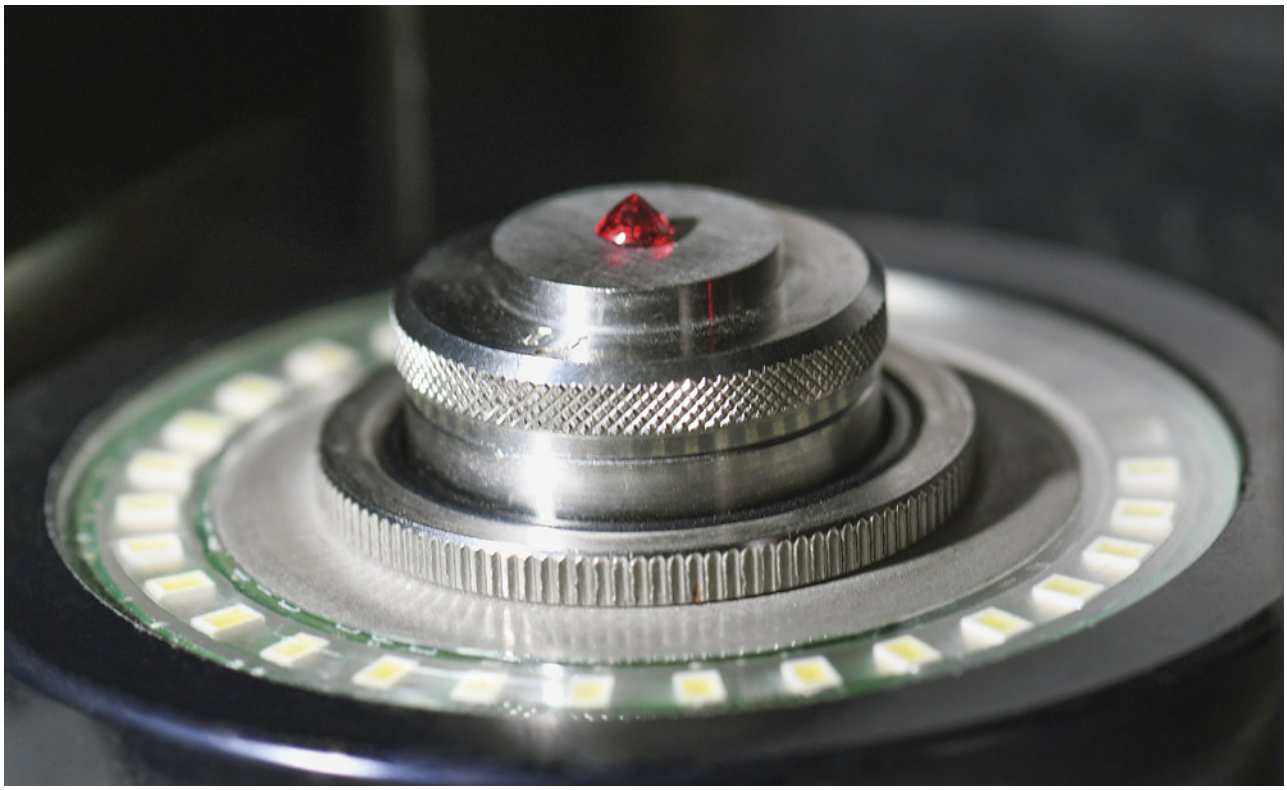

Figure 1. A red gemstone set table-down in a noncontact optical measurement device. Photo by Annie Haynes.

With decades of expertise and laboratory locations worldwide, GIA uses more advanced instrumentation that extends far beyond the boundaries of standard gemological testing. The comprehensive analysis of gemstones submitted to the laboratory ensures accurate identification and grading reports. These gemstones fall under five different categories: natural diamonds, natural colored diamonds, laboratory-grown diamonds, colored stones, and pearls.

GENERAL PROCEDURES

Once a stone is submitted, client information is withheld from the non-client-facing staff who conduct the analysis. This measure helps ensure an unbiased report. Before undergoing examination, each item is weighed and measured. All loose, faceted stones are assessed with a noncontact optical measurement device (figure 1) that projects the stone's shadow to obtain exact measurements of angles and facets. If the stone is mounted, not faceted, or exceeds the device's capacity, it is weighed and measured by hand.

Based on accurate measurements from the noncontact optical measurement device, the stone's volume can be calculated. This provides the information needed to calculate the specific gravity. When this calculation is not possible for a loose stone, GIA gemologists turn to hydrostatic measurement as needed, using the weight of the stone in air and the

weight of the stone suspended in water. After all necessary information related to weights and measurements has been obtained, the item is directed to the next required analysis for that material.

DIAMONDS

Stones submitted as diamonds are examined to verify whether they are natural or laboratory-grown. At this initial stage, a stone with a specific gravity of 3.52 is presumed to be diamond and analyzed using the GIA DiamondCheck. This device, created specifically for the laboratory, detects the presence or absence of nitrogen impurities in the stone's infrared spectrum (figure 2). It separates diamonds into two categories: "Pass" (type I diamonds) or "Refer" (type II diamonds and laboratory-grown diamonds) (Breeding and Shigley, 2009).

Items that do not fall within the "Pass" or "Refer" categories are classified as "non-diamonds" and routed to the identification department for analysis. For example, topaz has a specific gravity of 3.52, the same as diamond. If a topaz were submitted for a diamond report, it would not pass the DiamondCheck step, as it has a different intrinsic infrared spectrum.

Referred diamonds are analyzed by senior gemologists who specialize in detecting laboratory-grown diamonds and potential treatments. Photoluminescence (PL) spectroscopy is used to assist with the identification of laboratory-grown diamonds manufactured by chemical vapor deposition (CVD) or high-pressure, high-temperature (HPHT) methods, as well as the detection of post-growth treatment. PL can also determine whether a colorless natural diamond has undergone HPHT treatment (Eaton-Magaña and Breeding, 2016).

Referred diamonds may also undergo DiamondView screening. This instrument uses ultraviolet light with a wavelength below 225 nm to excite luminescence. The luminescence emitted by the diamonds reveals growth structure characteristics that distinguish natural growth from laboratory growth using CVD or HPHT methods (McGuinness et al., 2020).

Both passed and referred diamonds are then evaluated by GIA graders in controlled environments that are standard across every GIA location. Multiple graders independently examine each diamond through a GIA gemological microscope and a 10× loupe (figure 3). They evaluate clarity by assessing the size, location, and visibility of all internal and external features. A clarity grade is ultimately assigned based on the GIA Clarity Scale. During clarity examination, the graders also confirm the presence or absence of treatments such as internal laser drilling, laser drill holes, and fracture filling (figure 4).

Diamonds are also evaluated for their color using the universal grading scale developed by GIA. This is done under controlled lighting using master stones with established color grades for reference. Diamonds without color are compared against the master stones using GIA's D-to-Z color grading scale, in which "D" denotes colorless, with yellow, brown, or gray color saturation increasing to Z. (Color grades of S to Z can

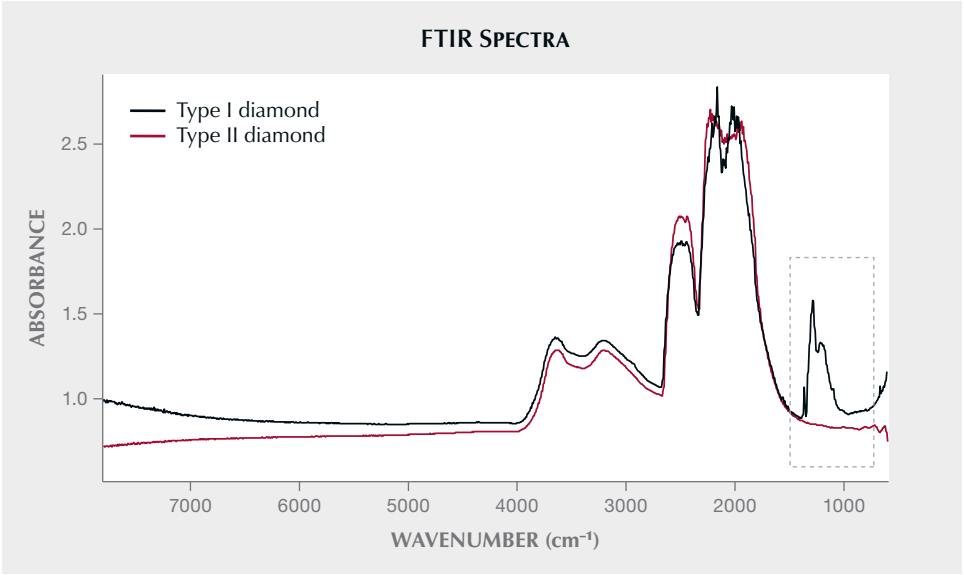

Figure 2. Fourier-transform infrared (FTIR) spectra of diamonds, revealing the presence or absence of nitrogen in the one-phonon region (1400–1000 cm^{-1}).

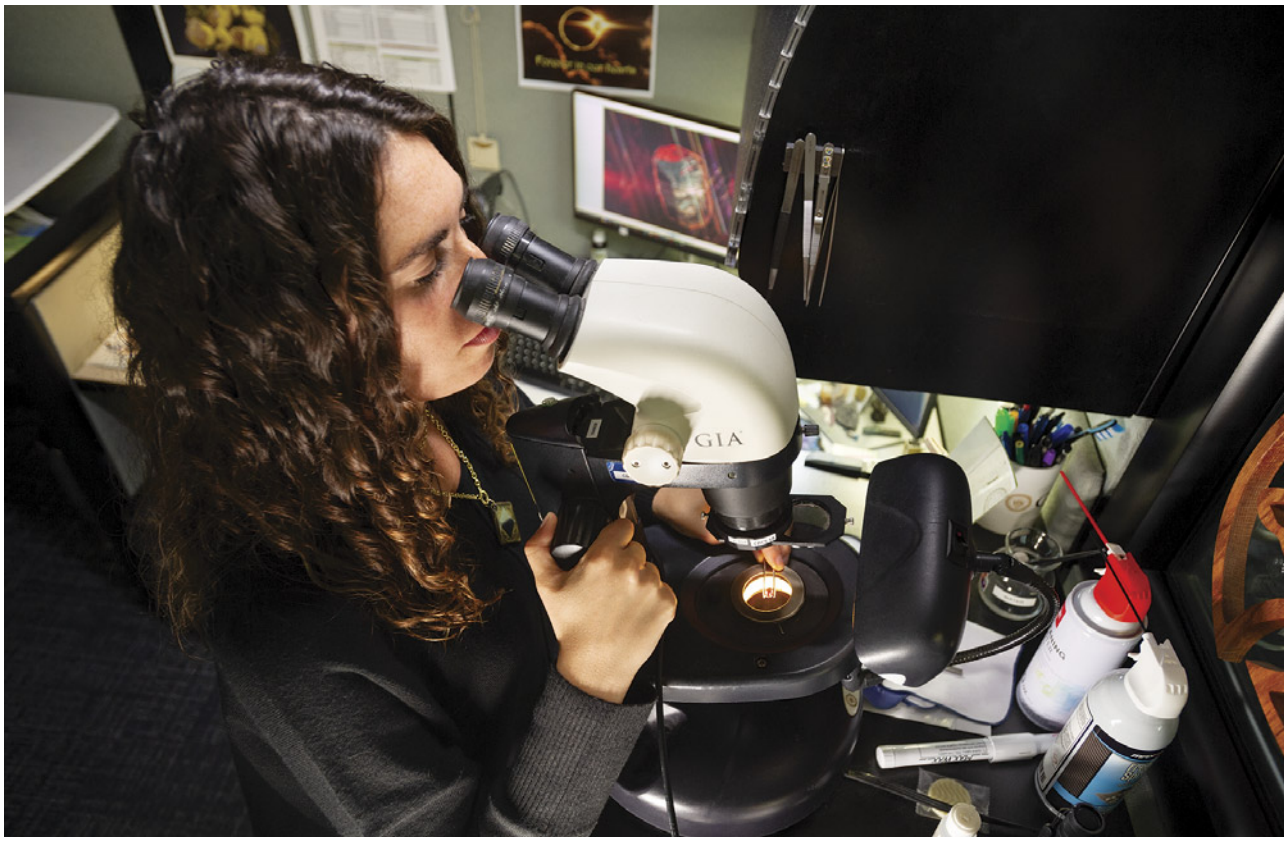

Figure 3. A GIA gemologist examines a diamond's internal and external clarity characteristics using a gemological microscope. Photo by Kevin Schumacher.

also be graded as light yellow, light brown, or light gray.) Colored diamonds with a saturated hue (e.g., yellow, pink, blue, and green) are graded against master stones to analyze the tone and saturation.

Diamonds that receive a W–Z color grade, as well as all colored diamonds, are examined by GIA gemologists to determine the origin of this color. Using analytical techniques, they can distinguish between

Figure 4. Examples of treatments documented in diamond. Left: Fracture filling in a feather on the table of a laboratory-grown diamond. Right: Reflective lighting displaying numerous laser drill holes in the table of a diamond. Photomicrographs by Nicole Ahline; fields of view 3.57 mm (left) and 4.79 mm (right).

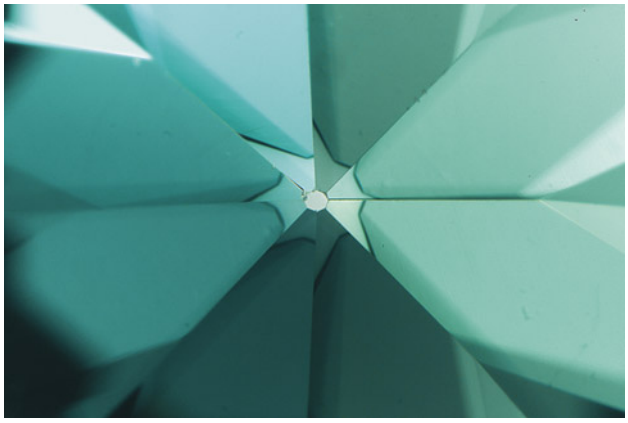

Figure 5. This "umbrella effect" at the culet of a diamond was created by cyclotron treatment, a type of artificial irradiation. Photomicrograph by Nicole Ahline; field of view 2.90 mm.

natural color and color produced by artificial irradiation, HPHT treatment, or a combination of the two (figure 5). These techniques include ultraviolet/visible/near-infrared (UV-Vis-NIR) spectroscopy, Fourier-transform infrared (FTIR) spectroscopy, and photoluminescence (PL) spectroscopy.

UV-Vis-NIR spectroscopy measures absorption patterns within the ultraviolet to visible light range and into the near-infrared. As one of the initial tests, it plays a crucial role in color origin determination (see Jin et al., 2024, pp. 456–473 of this issue). Diamonds are cooled with liquid nitrogen to produce a clean spectrum, revealing optical defects that influence a diamond's color (Shigley and Breeding, 2015). For example, a band at 550 nm is linked to plastic deformation, potentially causing pink or brown bodycolor (Eaton-Magaña et al., 2018). "Cape" features (N3 defect at 415.2 nm, along with N2 at 478 nm and two absorption peaks at 451 and 463 nm) contribute to a yellow color (Breeding et al., 2020). The interpretation of various optical defects, combined with input from other types of data, can help determine a diamond's color origin.

FTIR spectroscopy measures absorption in the infrared region. For diamonds, it is mainly used to classify diamond type, which corresponds to the presence or absence of nitrogen and boron in the crystal lattice (see Breeding and Ahline, 2024, pp. 474–492 of this issue). Certain diamond types, as well as other features found in an IR spectrum, are associated with specific diamond colors or lattice defects (Breeding and Shigley, 2009). For example, isolated nitrogen appears in the infrared as C-centers that contribute a yellow to orange bodycolor (Breeding et al., 2020). FTIR also detects the presence of defects such as H1a, H1b, and H1c (1450, 4935, and 5165 cm^{-1}), which commonly occur in type Ia yellow diamonds that have been exposed to either natural or artificial irradiation and annealing (Wang et al., 2005).

PL spectroscopy measures the fluorescence from a gemstone, typically when stimulated with lasers of various wavelengths (see Eaton-Magaña et al., 2024, pp. 494–517 of this issue). PL spectroscopy is a valuable tool for identifying certain gemstones such as ruby and sapphire. These have characteristic fluorescence spectra related to the presence of Cr^{3+}, which fluoresces at a specific wavelength of 694 nm. The natural or laboratory-grown origin of diamonds can also be reliably determined using PL spectroscopy. In most cases, PL spectroscopy is also crucial for identifying the natural color origin of diamonds or potential treatments applied to enhance their appearance.

GIA gemologists collect all the data provided by advanced gemological testing and analyze it comprehensively. This information, along with the diamond's suite of inclusions, enables them to reach a unanimous conclusion on the color origin.

COLORED STONES

All colored stones are routed to GIA's identification department, where gemologists assess each stone's identity and potential treatments. Not every colored stone requires advanced gemological testing, which is used judiciously to support standard gemological testing as needed. The size and transparency of a gemstone will also determine which instruments are appropriate for its analysis. The stone must be able to fit within the machine and provide reliable data.

Standard gemological testing is the foundation of colored stone identification, using the methods taught in GIA's Graduate Colored Stones program: the refractometer, polariscope, dichroscope, and handheld spectroscope (figure 6). Not all of these tests are applicable for every stone. In addition, gemologists test the stone's specific gravity.

Colored stones are also assessed for their response to UV radiation, the portion of the electromagnetic spectrum from 10 to 400 nm. When UV radiation interacts with some gemstones, it causes them to emit visible light in the form of fluorescence or phosphorescence. This effect can be linked to the gemstone's chemical composition, providing insights into its identity and any potential treatments applied. GIA uses two standardized UV lamps: a long-wave UV light with a wavelength of 365 nm and a short-wave light at 254 nm.

Figure 6. Clockwise from top left: A polariscope, refractometer, dichroscope, and spectroscope are shown with a gem cloth and tweezers. Photo by Emily Lane.

Two gemstones routinely checked under UV light are emerald and blue sapphire. Some fillers used for clarity enhancement of emeralds can fluoresce bright yellow to blue under long-wave UV light (figure 7, left). This can reveal the location of the filler in emeralds, especially in stones that are mounted in jewelry and cannot be fully viewed in the microscope.

One of the most common inclusions in corundum, an aluminum oxide (Al_2O_3), is rutile silk, a titanium dioxide (TiO_2). In natural blue sapphires heated above 1000°C, rutile can start to break down, causing Ti^{4+} ions to dissolve into the corundum and creating titanium-aluminum vacancies (Hughes and Perkins, 2019). These vacancies have a chalky fluorescence under short-wave UV light, providing evidence of heat treatment (figure 7, right).

GIA gemologists also assign a color to the stone. This call is an overall impression of the stone in the "face-up" position, which can be challenging for colored stones given the differences in cutting styles, the impact of pleochroism, and possible phenomenal optical effects (play-of-color in opal, for instance). To keep calls consistent, all GIA laboratories use color chips from the Munsell Book of Color and a standard

Figure 7. Left: An emerald seen in long-wave UV, highlighting the filled fractures in the stone. Photomicrograph by Nicole Ahline; field of view 19.27 mm. Right: A heated natural blue sapphire emits chalky blue to green fluorescence in short-wave UV. Photo by Nicole Ahline and Jessa Rizzo.

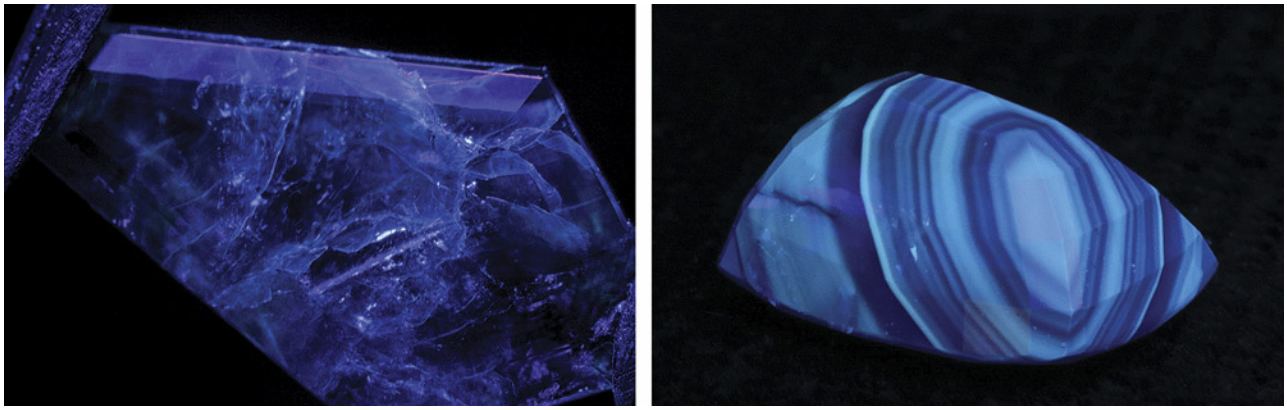


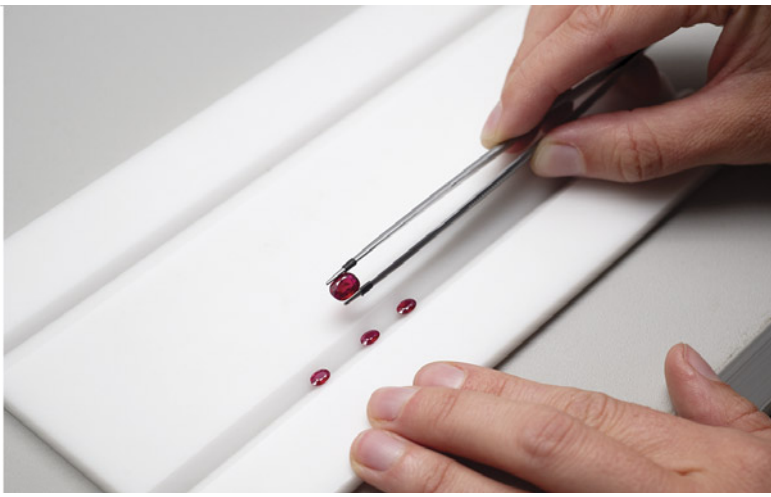

Figure 8. Left: Orangy pink to pinkish orange "padparadscha" sapphires being compared to Munsell color chips. Right: A gemologist comparing a ruby to "pigeon's blood" master stones. Photos by Annie Haynes (left) and Kevin Schumacher (right).

light box. Master stones are also used for comparison of specific color calls (figure 8).

The GIA Identification Report may also include color calls that align with certain color designations used in the trade. Corundum has two of these. "Royal blue" is reserved for sapphires with a highly saturated blue color. Rubies with a vivid red color that have low iron content and a strong red fluorescence under long-wave and short-wave UV light are known in the trade as "pigeon's blood" rubies. Stones with these designations must not be laboratory-grown, treated by a diffusion process, dyed, or assembled.

GIA gemologists select the appropriate analytical instrumentation for each colored stone's identification, treatment detection, and/or geographic origin determination (table 1). These methods consist of UV-Vis-NIR and FTIR spectroscopy (both presented earlier in the "Diamonds" section), Raman spectroscopy, energy-dispersive X-ray fluorescence (EDXRF) spectroscopy, and laser ablation–inductively coupled plasma–mass spectrometry (LA-ICP-MS).

FTIR data can assist with natural vs. laboratory-grown determinations for alexandrite and emerald and detect certain treatments such as polymer impregnation and heat treatment. Colored stones that routinely undergo FTIR analysis include corundum, chrysoberyl, jade, and quartz (Breeding and Ahline, 2024). GIA gemologists use UV-Vis-NIR data to better understand the cause of a stone's color (or lack of color). UV-Vis-NIR is routinely applied to sapphire, emerald, tourmaline, and cobalt spinel (see Jin et al., 2024, pp. 456–473 of this issue).

EDXRF and LA-ICP-MS are used to look at a stone's elemental makeup. EDXRF offers nondestructive analysis, either qualitative or quantitative, of a stone's chemical composition. This can aid in the identification of color-enhancing coatings and other treatments, the presence of certain elements indicating a natural or laboratory-grown origin, and geographic origin (see Sun et al., 2024, pp. 536–559 of this issue). Gems routinely analyzed by EDXRF include turquoise, tourmaline, corundum, and tanzanite.

LA-ICP-MS is a highly sensitive instrument that rapidly and precisely analyzes the quantitative chemical composition of a gem. It is minimally destructive, requiring a very small sample—from a pit roughly 50 µm wide and 50 µm deep (the diameter of a human hair). This pit is not visible without the use of a microscope or gemological loupe. LA-ICP-MS assists with geographic origin determination, the separation of natural and laboratory-grown gems, and detecting certain forms of treatment (Sun et al., 2024). Since LA-ICP-MS is capable of measuring more trace elements with lower detection limits than EDXRF, this data is used extensively for trace element plots when making geographic origin determinations. The sample's chemistry is compared against samples of known origin to narrow down the list of potential geographic origins (refer to *G&G*'s Winter 2019 special issue on geographic origin).

TABLE 1. Comparison of advanced gemological testing performed for various colored stones seen at GIA.

	FTIR	UV-Vis-NIR	Raman/PL	EDXRF	LA-ICP-MS
Sapphire	✓	✓		✓*	✓
Ruby	✓			✓*	✓
Spinel		✓**	✓		✓
Opal	✓			✓	
Turquoise	✓			✓	
Chrysoberyl	✓*			✓	✓**
Emerald	✓*	✓		✓	✓
Rough topaz	✓		✓		
Jade	✓	✓	✓		
Tourmaline		✓		✓	✓**
Feldspar				✓	✓

**For natural vs. laboratory-grown confirmation*
***Only for certain varieties within the group or species*

Raman spectroscopy is also commonly employed to identify colored stones. Monochromatic light in the form of a laser interacts with a gemstone, creating vibrations in the atomic structure. Some of the laser's energy is absorbed by the material to produce these vibrations, and photons are re-emitted or scattered from the material with lower energies corresponding to its vibrational modes. The resulting scattered light is plotted in a spectrum that serves as a fingerprint for identifying the gemstone or an inclusion within it (Eaton-Magaña and Breeding, 2016; Jin and Smith, 2024, pp. 518–535 of this issue). Note that the incident monochromatic light can also interact with vibrations in the gem and scatter light with higher energy, though this higher-energy scattered light is not routinely used in practice; again, see Jin and Smith (2024). Raman analysis is useful in identifying rough or aggregated material when the surface does not allow clean refractive index readings or when other standard gemological tools do not provide precise data. Many inclusions, once identified, can narrow down the potential geographic origins of a given gemstone species and, in some cases, reveal a natural or laboratory-grown origin. Raman data are collected on the same instrument that measures PL spectra. For colored stones, PL spectroscopy is mostly used for detecting heat treatment in spinel (Saeseaw et al., 2009).

Beyond these techniques, a gemologist's most valuable tool is the microscope. However, the microscope's effectiveness depends on the user's knowledge—not just of the instrument itself, but also in interpreting the information they gather. Each gemologist builds their own "internal database," obtained through years of studying reference gemstones of known origin and treatment status.

Each GIA laboratory gemologist uses a GIA gemological microscope with 50× magnification. These microscopes are equipped to view a stone's internal and external characteristics using numerous lighting techniques to highlight different aspects. These techniques include darkfield, brightfield, diffused, reflected, and polarized lighting as well as fiber-optic illumination (figure 9).

Darkfield illumination enters a transparent stone from the sides, making inclusions appear bright against a dark background. Brightfield illumination shows inclusions as dark shapes against a bright background. With transmitted light, the opaque shield is removed to create brightfield light and the microscope stage is covered with a white translucent filter. This is ideal for observing color zoning. Reflected light

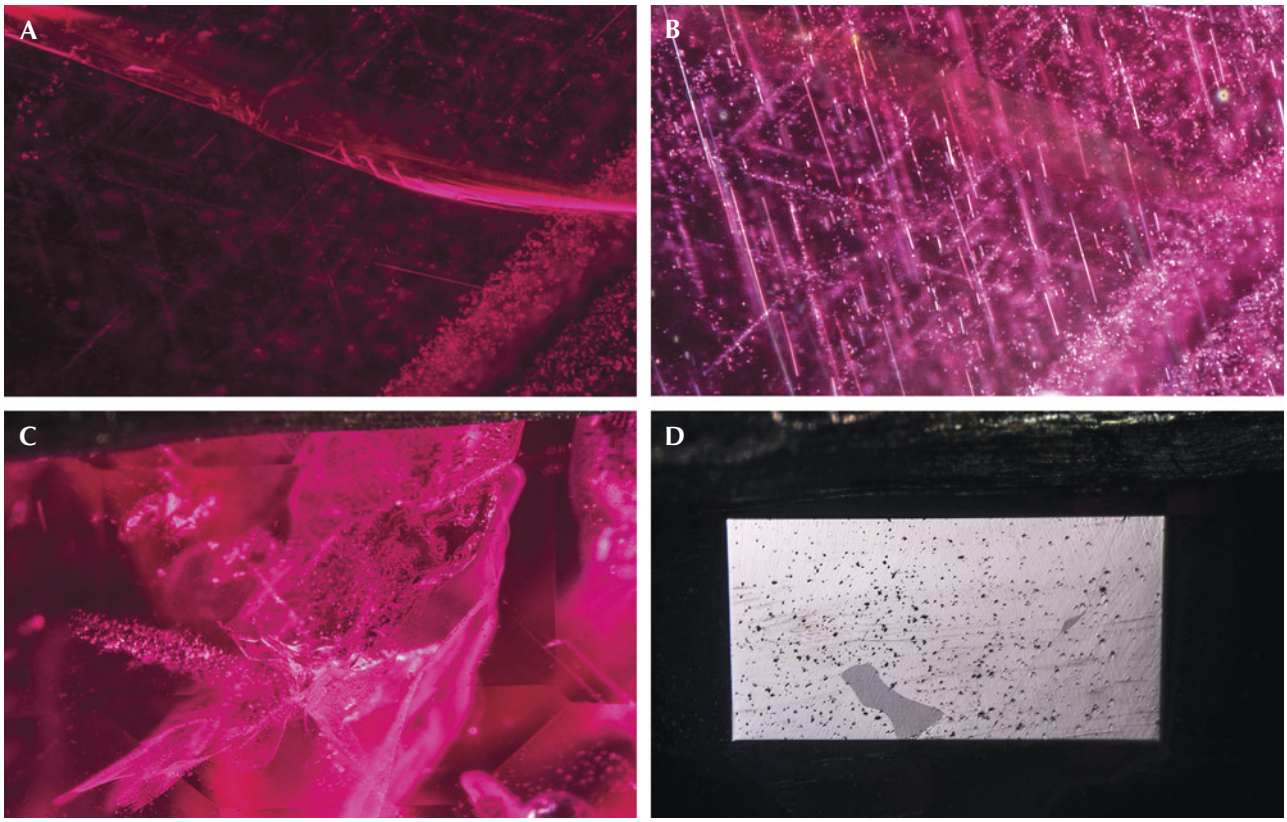

Figure 9. Two different rubies showing features under two different light sources. Top ruby: Darkfield lighting displays a feather (A), and fiber-optic lighting shows fine rutile silk (B). Bottom ruby: Darkfield and fiber-optic lighting reveals residue from heat treatment (C), and reflective lighting displays a cavity filled with a glass residue (D). Photomicrographs by Nicole Ahline; fields of view 1.42 mm (A and B) and 3.57 mm (C and D).

comes from a light source above the stone and reflects off the surface, allowing easier examination of the stone's external characteristics. Polarized light is produced by placing a polarizing filter on the stage in brightfield and an analyzer (a second polarizing filter) above the stage in a crossed position. Viewing through these crossed polarizers provides insight into optically aligned and unaligned features in the stone. Fiber-optic light is a pinpoint light source that provides illumination from any angle, making it effective and versatile for examining both loose and mounted gemstones that are transparent to opaque (Renfro, 2015).

In performing their analyses, GIA staff use various light sources to examine the external and internal features of the gemstone, as well as the mounting if necessary. External features include coatings, indications of assemblage, evidence of repair or damage, and surface remnants from heat treatment. Internally, they examine inclusions that support a natural or laboratory-grown origin, evidence of clarity enhancement or dye, and inclusion suites that point to a specific geographic origin.

Once all data is collected and documented, it must be evaluated together. Gemologists in the identification department are trained extensively on more than 60 gemstone species, their varieties, and the treatments associated with each. They develop the skill to accurately and consistently determine the geographic origin of natural corundum, emerald, Paraíba-type tourmaline, red spinel, and alexandrite. This expertise comes from years of training the eye, examining countless samples, and interpreting accurate data.

The foundation of accurate classification is a reliable research collection, especially when determining geographic origin. GIA's field gemology team has conducted more than 100 field expeditions, collecting samples at mines, trading centers, and international trade shows. These samples undergo extensive analysis by GIA's research team using all available standard gemological tools and analytical techniques (Vertriest et al., 2019). This data is shared globally with GIA gemologists to enhance their knowledge and proficiency.

TABLE 2. Comparison of advanced gemological testing performed for different types of pearls at GIA.

	RTX	XRF imaging	EDXRF	Raman	UV-Vis-NIR	PL
White to cream nacreous	✓	✓	✓			
Colored nacreous	✓	✓	✓	✓	✓	✓
White non-nacreous	✓		✓	✓	✓	
Colored non-nacreous	✓		✓	✓	✓	✓
Porcelaneous	✓			✓	✓	✓

PEARLS

The first step in examining pearls is surface observation, followed by various advanced testing techniques (table 2) that reveal growth structures, surface structure, and any sign of treatment such as artificial color concentrations or a worked surface. Pearls can be classified as either whole or blister pearls based on their growth formation. A shell blister may resemble a blister pearl, but they have a different internal structure and can be separated using X-ray imaging techniques (Lawanwong et al., 2019). Since a shell blister is not considered a true pearl, the result issued on an identification report will be the same as for any shell material.

Pearls come from various mollusk species, and the visible differences in surface structure and color are related mainly to their producing mollusks. Pearls can be classified as nacreous or non-nacreous depending on their surface structures. Most commercially available pearls are nacreous, constructed from layers of stacked aragonite tablets. They often resemble a fingerprint when viewed under magnification. Non-nacreous pearls can display a variety of surface structures due to the diversity of mollusk species. Those with a porcelain-like luster and flame structure, such as conch and melo pearls, are referred to as porcelaneous (figure 10) (Hänni, 2010; see also Zhou and Towbin, 2024, pp. 582–595 of this issue).

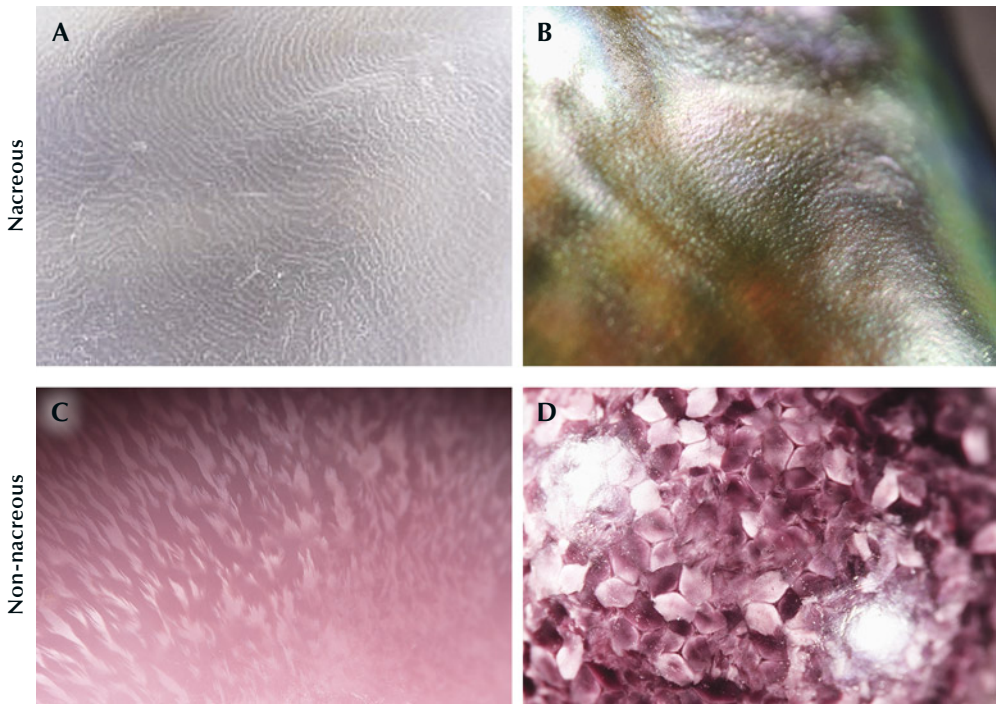

Figure 10. Nacreous vs. non-nacreous surface structures seen in various types of pearls. A: Platy structure patterns on pearls from Pinctada *species mollusk. B: Patches of color and a botryoidal-like subsurface structure on the nacreous surface of an abalone pearl. C: Flame structures seen on a Queen conch pearl. D: Patchwork cells and sheen appearance of a scallop pearl. Photomicrographs by GIA staff; fields of view 0.83 mm (A), 3.9 mm (B), and 0.72 mm (C and D).*

Figure 11. A mixed strand of 79 pearls ranging from 11.8 to 14.8 mm, consisting of pink Chinese freshwater, black Tahitian, golden Indonesian, and white Australian bead cultured pearls. Also pictured is an exceptionally large 20.4 mm South Sea bead cultured pearl weighing 12 g. Photo by Robert Weldon; courtesy of Yoko London.

Digital real-time X-ray microradiography (RTX) is an important technique for analyzing a pearl's internal structure and determining whether it is natural or cultured, which is further classified into bead cultured or non-bead cultured (Sturman, 2009; Karampelas et al., 2017). Interpretation of the results is based on GIA reference samples collected over many years (Homkrajae et al., 2021; see figure 11). When RTX analysis cannot provide sufficient details for the determination, X-ray computed microtomography (μ-CT) can be used to view the internal structure in greater detail through high-resolution 3D imaging. However, the μ-CT technique works best with loose pearls; those mounted in jewelry must be unmounted and unstrung. Furthermore, metal remnants inside a drill hole may cause artifacts that obscure parts of the pearl's internal structure (Karampelas et al., 2010; Krzemnicki et al., 2010).

Pearls form in either saltwater or freshwater environments, and identifying the origin environment involves two advanced techniques: EDXRF and X-ray fluorescence (XRF) imaging. EDXRF analysis is particularly useful for detecting the levels of manganese and strontium within a sample. Manganese is generally high in freshwater pearls but very low or even absent in saltwater pearls. Saltwater pearls display higher strontium levels compared to freshwater pearls. LA-ICP-MS may be used to investigate other trace elements when EDXRF and X-ray fluorescence imaging cannot conclusively separate freshwater and saltwater pearls (Sturman et al., 2019; Homkrajae et al., 2019; Sun et al., 2024). Under X-ray fluorescence, most freshwater pearls exhibit moderate to strong greenish yellow fluorescence due to trace amounts of manganese, while saltwater pearls are generally

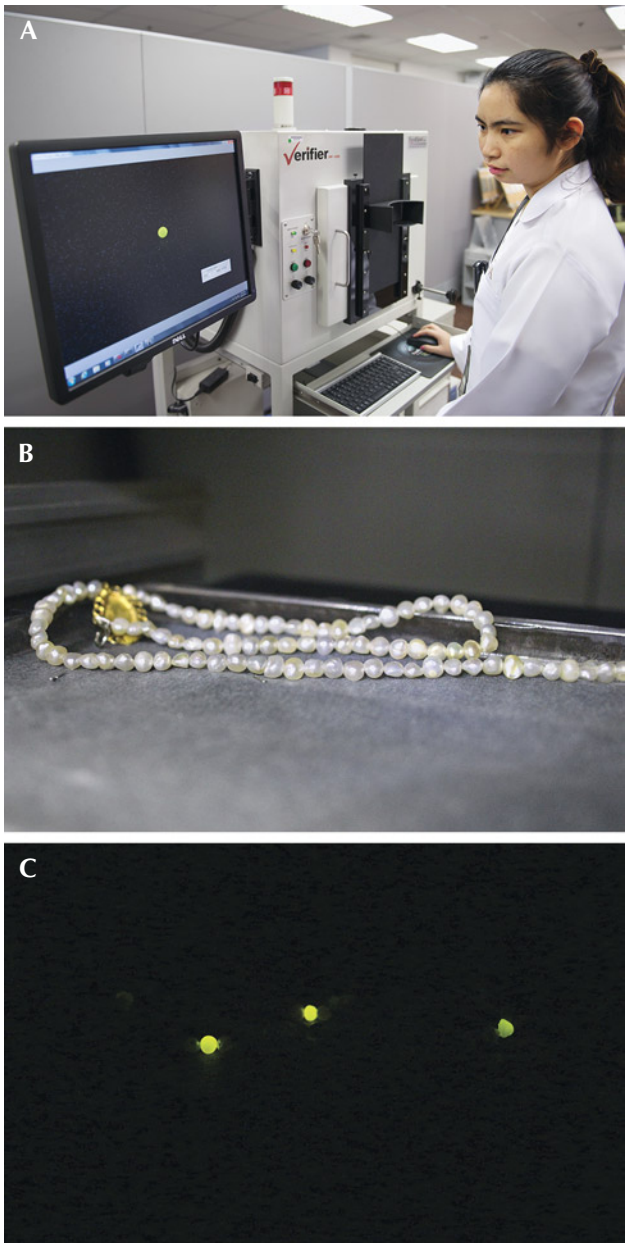

Figure 12. A and B: Pearl necklace being tested by X-ray fluorescence. C: Most of the pearls in the necklace are saltwater in origin and therefore inert when exposed to X-rays. The three pearls that show a moderate greenish yellow reaction are freshwater pearls.

inert (Sturman et al., 2019; Homkrajae et al., 2019). XRF imaging is normally done on multiple pearls in an item such as the pearl necklace shown in figure 12.

Raman photoluminescence spectroscopy is used to identify the calcium carbonate ($CaCO_3$) polymorphs forming the pearls and determine the color origin (Karampelas et al., 2020; Eaton-Magaña et al., 2021). Most pearls available in the market are composed of aragonite. However, some non-nacreous varieties form from calcite, such as scallop pearls (Pectinidae family) and pen pearls (Pinnidae family). UV-Vis-NIR reflectance spectroscopy is another essential technique for color origin determination (Iwahashi and Akamatsu, 1994; Elen, 2001; Karampelas et al., 2011). Some white and lighter-colored pearls have been chemically processed to whiten or brighten their surface appearance. This treatment can be detected using long-wave UV (385 nm) or short-wave UV (275 nm) fluorescence spectroscopy (Zhou et al., 2020; Tsai and Zhou, 2020; Zhou and Towbin, 2024).

CONCLUSIONS

The rigorous testing and analysis conducted by gemological laboratories play a crucial role in ensuring the authenticity and quality of gemstones. Through advanced gemological technologies and expert evaluation, GIA's laboratory provides accurate assessments of diamonds, colored stones, and pearls that contribute to the integrity of the gemstone market by offering consumers and professionals confidence in their purchases and appraisals. The work done in the laboratory not only reinforces trust but also advances the science of gemology.

For this reason, GIA offers an array of reports for colored stones, pearls, and diamonds intended to protect consumers of fine jewelry and enhance trust in the market for gemstone dealers. The case studies at the end of this article show examples of the grading methodologies used. More details of reports offered by GIA can be found online at www.gia.edu/gem-lab.

As the gem and jewelry industry continues to evolve, so does GIA's laboratory, adapting to meet the industry's ever-changing needs. Through continuous research and the use of advanced gemological testing, GIA maintains a high degree of accuracy that defines its grading and identification reports.

ABOUT THE AUTHORS

Nicole Ahline is supervisor of colored stone identification, and Jessa Rizzo is a senior staff gemologist, at GIA in Carlsbad, California.

ACKNOWLEDGMENTS

The authors wish to express their deepest gratitude to Artitaya Homkrajae for her pearl expertise. They would also like to thank their colleagues for sharing countless years of knowledge and skills within the gemstone industry, including Shane McClure, Nathan Renfro, Mike Breeding, Troy Ardon, Aaron Palke, and David Nelson.

REFERENCES

Breeding C.M., Shigley J.E. (2009) The "type" classification system of diamonds and its importance in gemology. *G&G*, Vol. 45, No. 2, pp. 96–111, http://dx.doi.org/10.5741/GEMS.45.2.96

Breeding C.M., Ahline N. (2024) Infrared spectroscopy and its use in gemology. *G&G*, Vol. 60, No. 4, pp. 474–492, http://dx.doi.org/10.5741/GEMS.60.4.474

Breeding C.M., Eaton-Magaña S., Shigley J.E. (2020) Naturally colored yellow and orange gem diamonds: The nitrogen factor. *G&G*, Vol. 56, No. 2, pp. 194–219, http://dx.doi.org/10.5741/GEMS.56.2.194

Eaton-Magaña S., Breeding C.M. (2016) An introduction to photoluminescence spectroscopy for diamond and its applications in gemology. *G&G*, Vol. 52, No. 1, pp. 2–17, http://dx.doi.org/10.5741/GEMS.52.1.2

Eaton-Magaña S., Ardon T., Smit K.V., Breeding C.M., Shigley J.E. (2018) Natural-color pink, purple, red, and brown diamonds: Band of many colors. *G&G*, Vol. 54, No. 4, pp. 352–377, http://dx.doi.org/10.5741/GEMS.54.4.352

Eaton-Magaña S., Breeding C.M., Palke A.C., Homkrajae A., Sun Z., McElhenny G. (2021) Raman and photoluminescence mapping of gem materials. *Minerals*, Vol. 11, No. 2, p. 177, http://dx.doi.org/10.3390/min11020177

Eaton-Magaña S., Jones D.C., Turnier R.B., Breeding C.M. (2024) Shining a light on gemstone properties: An exploration of photoluminescence spectroscopy. *G&G*, Vol. 60, No. 4, pp. 494–517, http://dx.doi.org/10.5741/GEMS.60.4.494

Elen S. (2001) Spectral reflectance and fluorescence characteristics of natural-color and heat-treated "golden" South Sea cultured pearls. *G&G*, Vol. 37, No. 2, pp. 114–123, http://dx.doi.org/10.5741/GEMS.37.2.114

Hänni H.A. (2010) Explaining the flame structure of non-nacreous pearls. *Australian Gemmologist*, Vol. 24, No. 4, pp. 85–88.

Homkrajae A., Sun Z., Blodgett T., Zhou C. (2019) Provenance determination of freshwater pearls by LA-ICP-MS and linear discriminant analysis (LDA). *G&G*, Vol. 55, No. 1, pp. 47–60, http://dx.doi.org/10.5741/GEMS.55.1.47

Homkrajae A., Manustrong A., Nilpetploy N., Sturman N., Lawanwong K., Kessrapong P. (2021) Internal structures of known *Pinctada maxima* pearls: Natural pearls from wild marine mollusks. *G&G*, Vol. 57, No. 1, pp. 2–21, http://dx.doi.org/10.5741/GEMS.57.1.2

Hughes E.B., Perkins R. (2019) Madagascar sapphire: Low-temperature heat treatment experiments. *G&G*, Vol. 55, No. 2, pp. 184–197, http://dx.doi.org/10.5741/GEMS.55.2.184

Iwahashi Y., Akamatsu S. (1994) Porphyrin pigment in black-lip pearls and its application to pearl identification. *Fisheries Science*, Vol. 60, No. 1, pp. 69–71, http://dx.doi.org/10.2331/fishsci.60.69

Jin S., Smith E.M. (2024) Raman spectroscopy and X-ray diffraction in gemology: Identifying mineral species and other phases. *G&G*, Vol. 60, No. 4, pp. 518–535, http://dx.doi.org/10.5741/GEMS.60.4.518

Jin S., Renfro N., Palke A.C., Ardon T., Homkrajae A. (2024) Application of UV-Vis-NIR spectroscopy to gemology. *G&G*, Vol. 60, No. 4, pp. 456–473, http://dx.doi.org/10.5741/GEMS.60.4.456

Karampelas S., Michel J., Zheng-Cui M., Schwarz J.-O., Enzmann F., Fritsch E., Leu L., Krzemnicki M.S. (2010) X-ray computed microtomography applied to pearls: Methodology, advantages, and limitations. *G&G*, Vol. 46, No. 2, pp. 122–127, http://dx.doi.org/10.5741/GEMS.46.2.122

Karampelas S., Fritsch E., Gauthier J.-P., Hainschwang T. (2011) UV-Vis-NIR reflectance spectroscopy of natural-color saltwater cultured pearls from *Pinctada margaritifera*. *G&G*, Vol. 47, No. 1, pp. 31–35, http://dx.doi.org/10.5741/GEMS.47.1.31

Karampelas S., Al-Alawi A.T., Al-Attawi A. (2017) Real-time microradiography of pearls: A comparison between detectors. *G&G*, Vol. 53, No. 4, pp. 452–456, http://dx.doi.org/10.5741/GEMS.53.4.452

Karampelas S., Fritsch E., Makhlooq F., Mohamed F., Al-Alawi A. (2020) Raman spectroscopy of natural and cultured pearls and pearl producing mollusc shells. *Journal of Raman Spectroscopy*, Vol. 51, No. 9, pp. 1813–1821, http://dx.doi.org/10.1002/jrs.5670

Krzemnicki M.S., Friess S.D., Chalus P., Hänni H.A., Karampelas S. (2010) X-Ray computed microtomography: Distinguishing natural pearls from beaded and non-beaded cultured pearls. *G&G*, Vol. 46, No. 2, pp. 128–134, http://dx.doi.org/10.5741/GEMS.46.2.128

Lawanwong K., Nilpetploy N., Manustrong A., Homkrajae A. (2019) Natural shell blisters and blister pearls: What's the difference? *GIA Research News*, August 26, https://www.gia.edu/gia-news-research/natural-shell-blisters-and-blister-pearls

McGuinness C.D., Wassell A.M., Lanigan P.M.P., Lynch S.A. (2020) Separation of natural laboratory-grown diamond using time-gated luminescence imaging. *G&G*, Vol. 56, No. 2, pp. 220–229, http://dx.doi.org/10.5741/GEMS.56.2.220

Renfro N. (2015) Digital photomicrography for gemologists. *G&G*, Vol. 51, No. 2, pp. 144–159, http://dx.doi.org/10.5741/GEMS.51.2.144

Saeseaw S., Wang W., Scarratt K., Emmett J.L., Douthit T.R. (2009) Distinguishing heated spinels from unheated natural spinels and from synthetic spinels. *GIA Research News*, April 2, https://www.gia.edu/gia-news-research-NR32209A

Shigley J.E., Breeding C.M. (2015) Visible absorption spectra of colored diamonds. *G&G*, Vol. 51, No. 1, pp. 41–43, http://dx.doi.org/10.5741/GEMS.51.1.41

Sturman N. (2009) The microradiographic structures of non-bead cultured pearls. *GIA Research News*, November 20, https://www.gia.edu/gia-news-research-NR112009

Sturman N., Otter L.M., Homkrajae A., Manustrong A., Nilpetploy N., Lawanwong K., Kessrapong P., Jochum K.P., Stoll B., Götz H., Jacob D.E. (2019) A pearl identification challenge. *G&G*, Vol. 55, No. 2, pp. 229–243, http://dx.doi.org/10.5741/GEMS.55.2.229

Sun Z., Jollands M., Palke A.C. (2024) Chemical analysis in the gemological laboratory: XRF and LA-ICP-MS. *G&G*, Vol. 60, No. 4, pp. 536–559, http://dx.doi.org/10.5741/GEMS.60.4.536

Tsai T.-H., Zhou C. (2020) Rapid detection of color-treated pearls and separation of pearl types using fluorescence analysis. *Novel Optical Systems, Methods, and Applications*, SPIE Proceedings, article no. 1148307, http://dx.doi.org/10.1117/12.2566590

Vertriest W., Palke A.C., Renfro N.D. (2019) Field gemology: Building a research collection and understanding the development of gem deposits. *G&G*, Vol. 55, No. 4, pp. 490–511, http://dx.doi.org/10.5741/GEMS.55.4.490

Wang W., Smith C.P., Hall M.S., Breeding C.M., Moses T.M. (2005) Treated-color pink-to-red diamonds from Lucent Diamonds Inc. *G&G*, Vol. 41, No. 1, pp. 6–19, http://dx.doi.org/10.5741/GEMS.41.1.6

Zhou C., Towbin W.H. (2024) Applications of X-ray radiography and X-ray micro-computed microtomography in gemology. *G&G*, Vol. 60, No. 4, pp. 582–595, http://dx.doi.org/10.5741/GEMS.60.4.582

Zhou C., Tsai T.-H., Sturman N., Nilpetploy N., Manustrong A., Lawanwong K. (2020) Optical whitening and brightening of pearls: A fluorescence spectroscopy study. *G&G*, Vol. 56, No. 2, pp. 258–265, http://dx.doi.org/10.5741/GEMS.56.2.258

Case Study: Ruby

1. Item Description

Transparent cushion mixed cut weighing 3.00 ct. Red color confirmed with Munsell chips.

2. Standard Gemological Testing

- Specific gravity of 4.00
- Diagnostic ruby spectrum in the handheld spectroscope

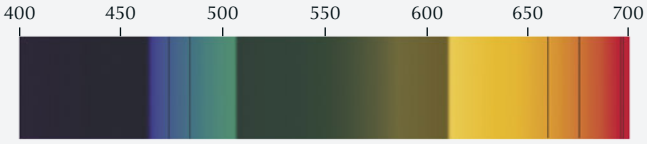

3. Analytical Testing

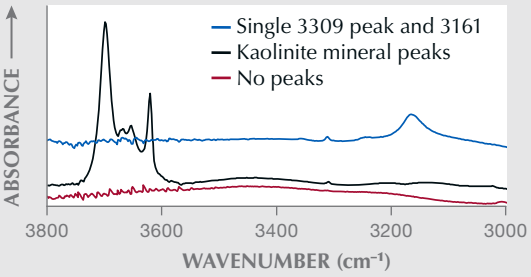

FTIR spectra taken in three different orientations showing no indications of treatment, given the absence of a 3232 cm^{-1} peak. Spectra offset for clarity.

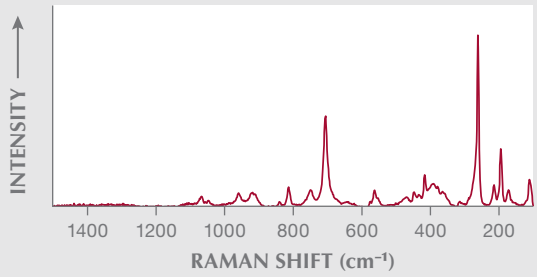

Raman spectrum of an inclusion consistent with mica, commonly documented in Mozambique rubies.

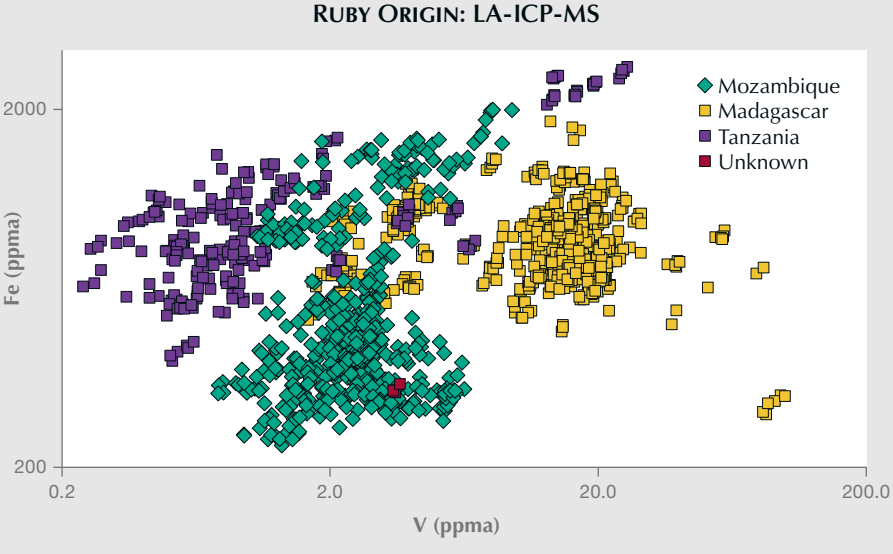

LA-ICP-MS trace element chemistry consistent with a Mozambique origin.

4. Microscopic Examination

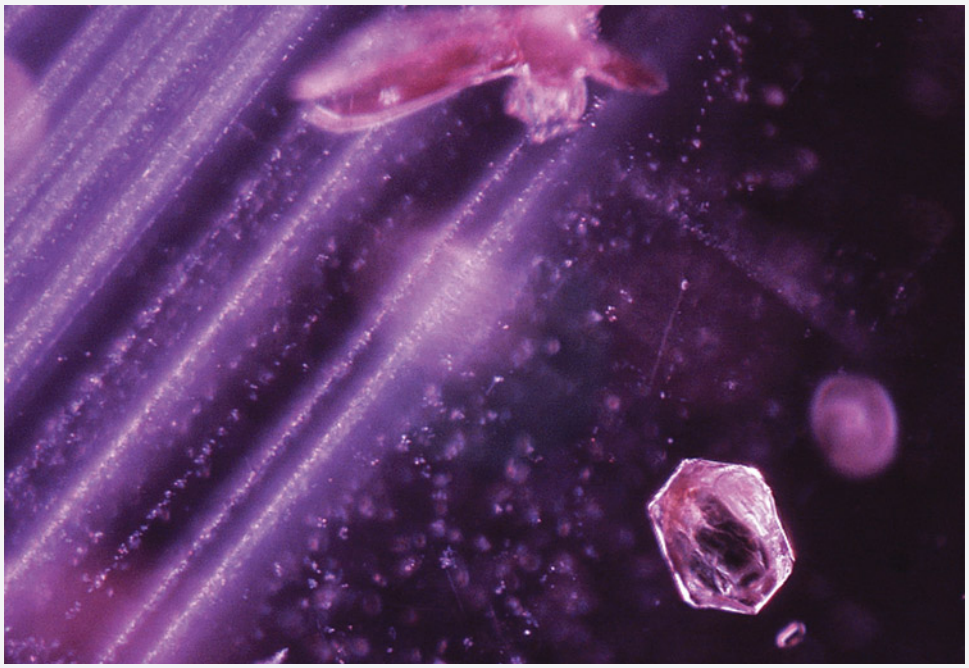

Angular particle clouds associated with white hexagonal mica crystals and amphiboles; field of view 1.42 mm.

5. Report Preview

RUBY ORIGIN REPORT

GIA REPORT 0123456789

DETAILS

Shape..... **Cushion**
Cutting Style: Crown ..... **Brilliant Cut**
Cutting Style: Pavilion ..... **Step Cut**
Transparency ..... **Transparent**
Color..... **Red**

RESULTS

Species..... **Natural Corundum**
Variety..... **Natural Ruby**
Geographic Origin ..... **Mozambique**

TREATMENT

No Indications of Heating

Item Description: One loose stone
Weight: **3.00 carats**
Measurements: **8.43 x 7.57 x 5.31 mm**
Comments: Any statement on geographic origin is an expert opinion based on a collection of observations and analytical data.

Case Study: Emerald

1. Item Description

Transparent octagonal step cut weighing 5.00 ct. Green color confirmed with Munsell chips.

2. Standard Gemological Testing

- Specific gravity of 2.72
- Refractive index of 1.579–1.589
- Chromium-related features in the handheld spectroscope

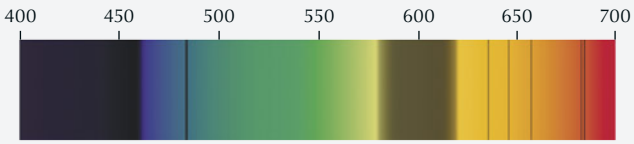

3. Analytical Testing

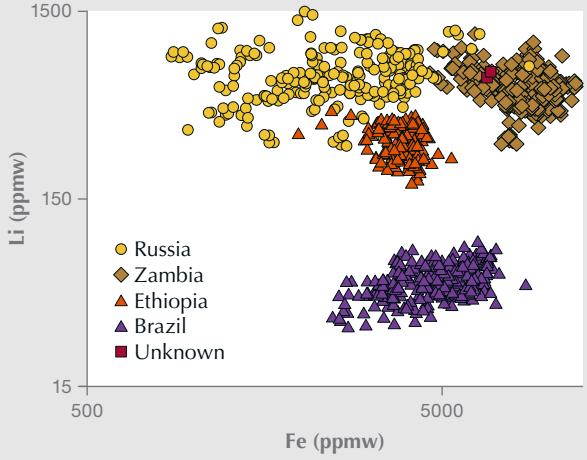

LA-ICP-MS trace element chemistry consistent with a Zambian origin.

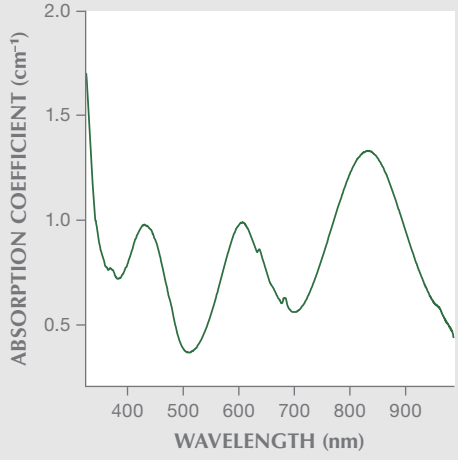

UV-Vis-NIR spectrum indicating a higher-iron geographic origin.

4. Microscopic Examination

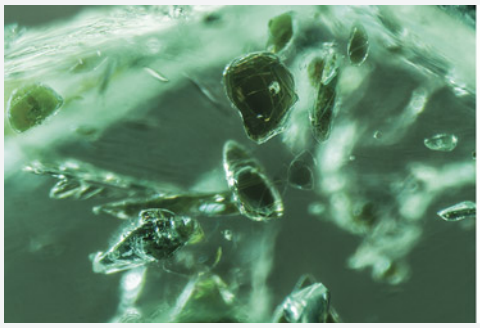

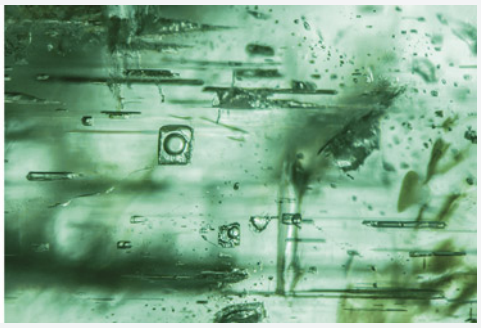

A suite of mica platelets (left) and blocky multi-phase inclusions (right), consistently found in higher-iron emerald sources; fields of view 1.58 and 1.76 mm.

Flash effect seen in feathers, providing evidence of clarity enhancement; field of view 2.90 mm.

5. Report Preview

EMERALD ORIGIN REPORT

GIA REPORT 0123456789

DETAILS

Shape..... Octagonal
Cutting Style ..... Step Cut
Transparency ..... Transparent
Color..... Green

RESULTS

Species..... Natural Beryl
Variety..... Emerald
Geographic Origin ..... Zambia

TREATMENT (Scan QR code for more information)

Clarity Enhanced (F2)

Item Description: One loose stone
Weight: **5.00 carats**
Measurements: **10.15 x 9.50 x 7.18 mm**
Comments: Any statement on geographic origin is an expert opinion based on a collection of observations and analytical data. Due to their growth conditions in nature and recovery methods, most emeralds contain surface reaching features. For this reason, clarity enhancement is a common trade practice.

CLARITY ENHANCEMENT

NO FISSURES PRESENT	NO OR INSIGNIFICANT CLARITY ENHANCEMENT	QUANTIFICATION OF CLARITY ENHANCEMENT		
NONE	NO INDICATIONS OF CLARITY ENHANCEMENT	F1	F2	F3
		MINOR CLARITY ENHANCEMENT	MODERATE CLARITY ENHANCEMENT	SIGNIFICANT CLARITY ENHANCEMENT

Case Study: Colored Diamond

1. Item Description

Transparent round brilliant weighing 0.50 ct. GIA color grade of Fancy Deep yellow-orange on GIA's colored diamond scale.

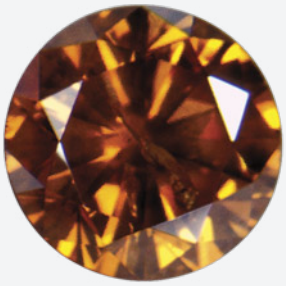

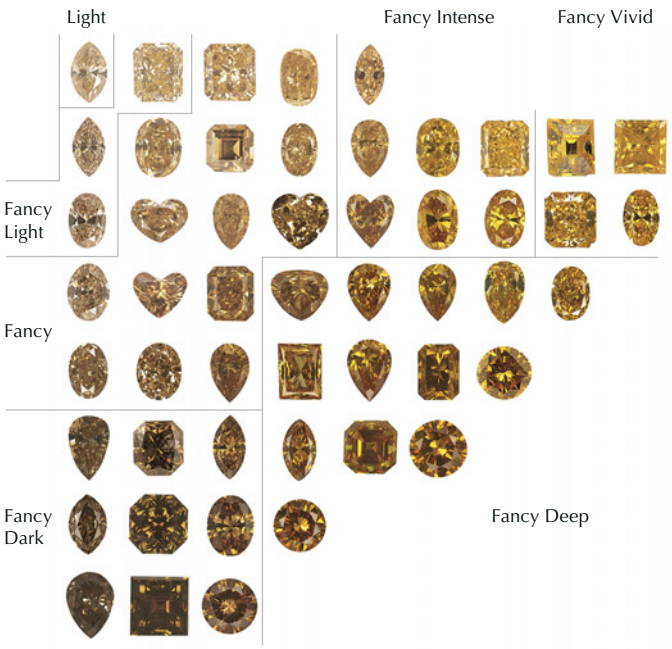

2. Analytical Testing

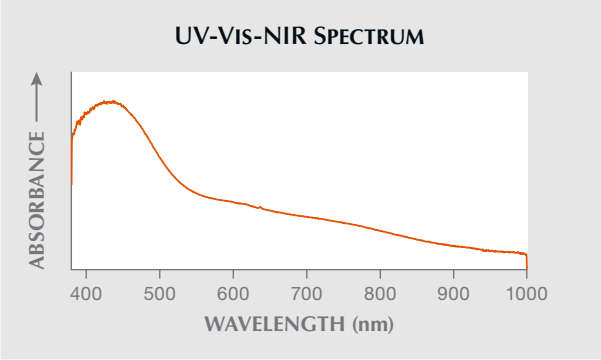

UV-Vis-NIR spectrum with a 637 nm peak (NV^-), indicating type Ib diamond.

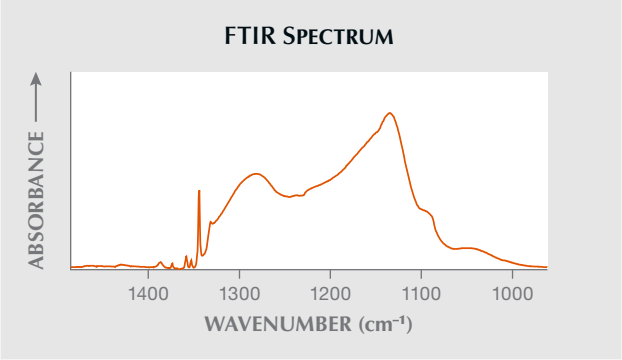

FTIR spectrum of type Ib diamond colored by isolated nitrogen.

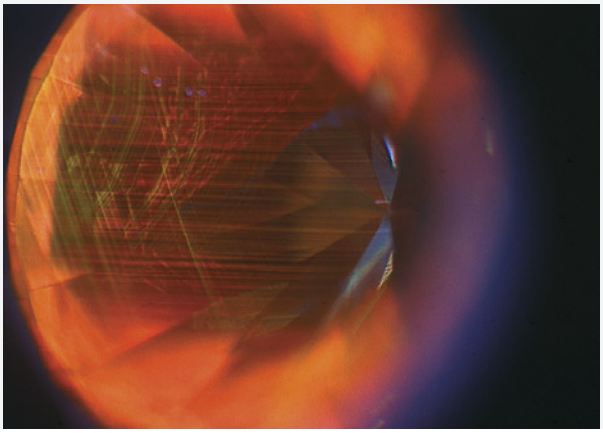

DiamondView image showing the natural growth structure of type Ib diamond.

3. Microscopic Examination

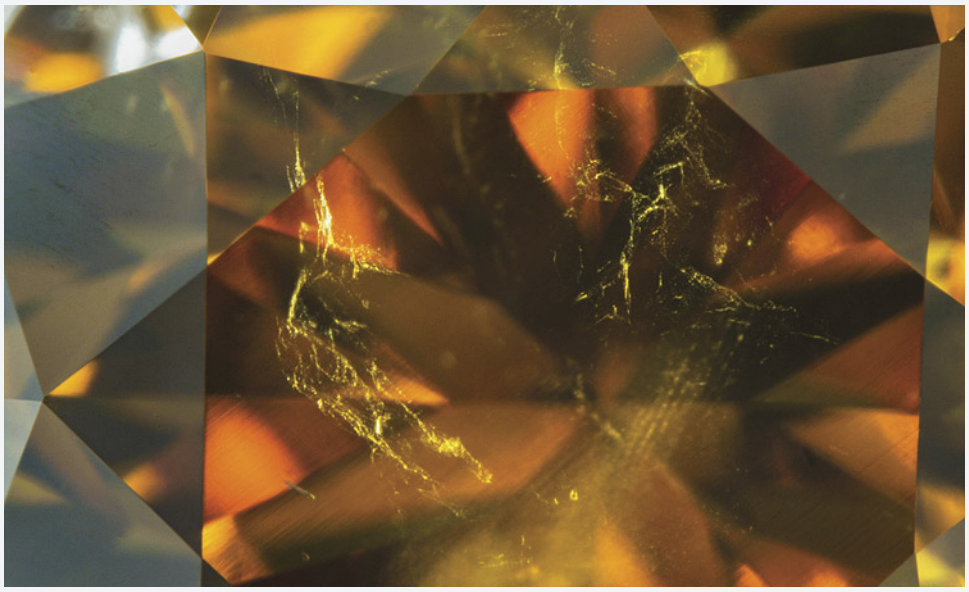

Wispy clouds found in type Ib diamond; field of view 7.19 mm.

4. Report Preview

Report Type ..... Identification and Origin Report
GIA Report Number 0123456789
Shape and Cutting Style ..... Round Brilliant
Measurements ..... 4.81 - 4.84 x 3.35 mm

Carat Weight ..... 0.50 carat
Color Grade ..... Fancy Deep Yellow-Orange
Color Origin ..... Natural
Color Distribution ..... Even

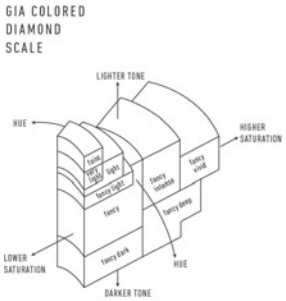

Illustration of GIA fancy color grade interrelationships

Case Study: Cultured Pearl

1. Item Description

Undrilled round measuring 9.81 mm with a strong orangy yellow bodycolor assigned with pearl masters.

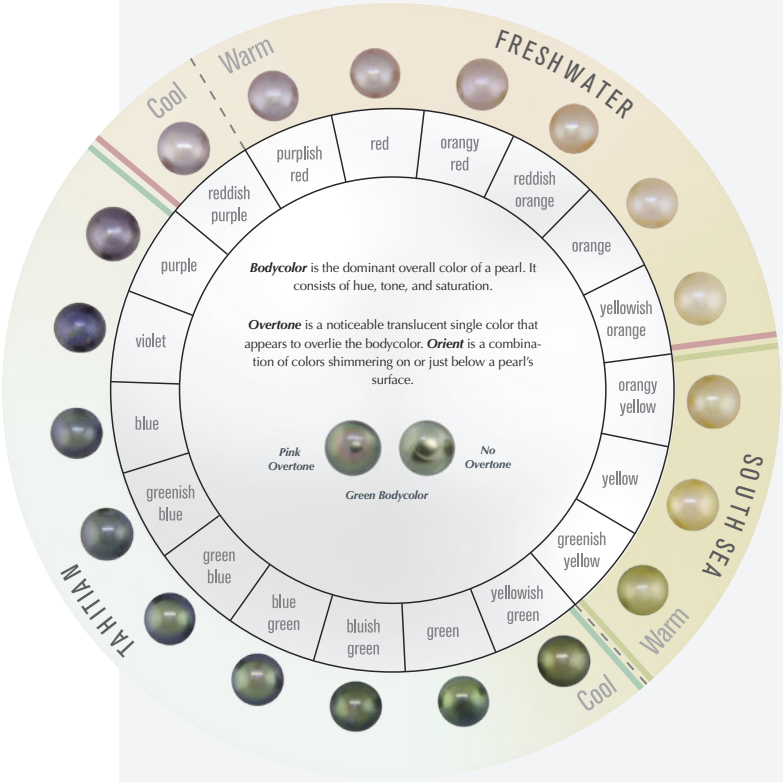

2. Analytical Testing

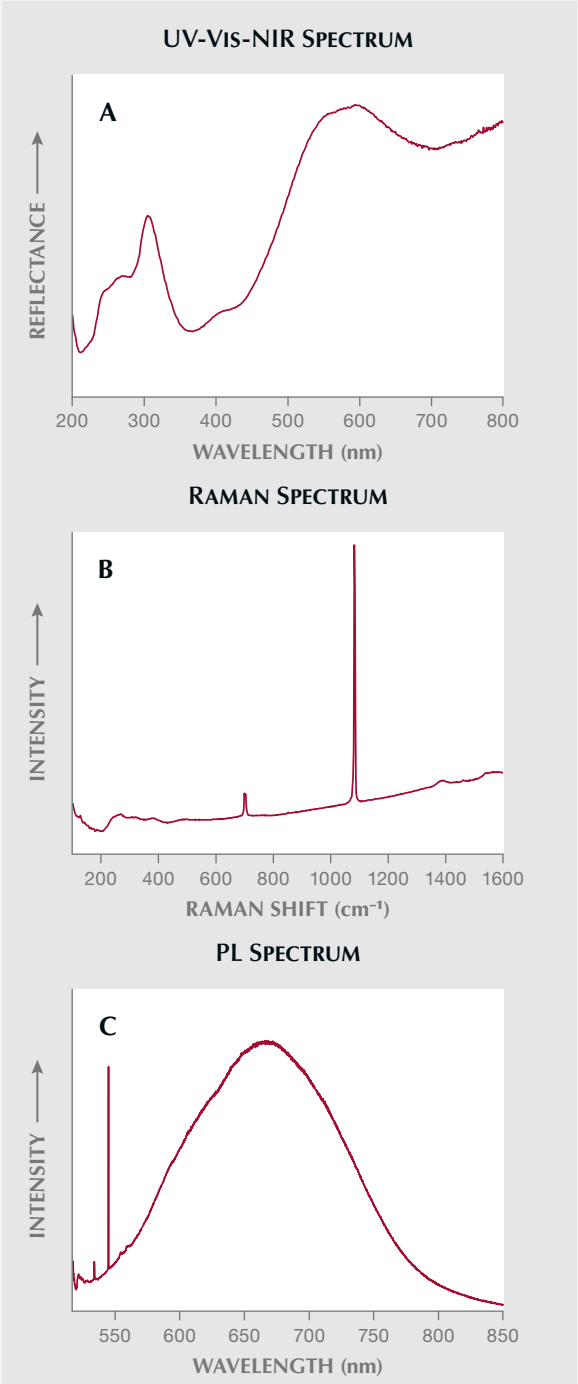

A: UV-Vis-NIR spectrum indicating natural bodycolor of a golden South Sea pearl. B: Raman spectrum confirming the presence of aragonite. C: 514 PL spectrum consistent with a brownish color modifier due to porphyrin protein.

2. Analytical Testing (continued)

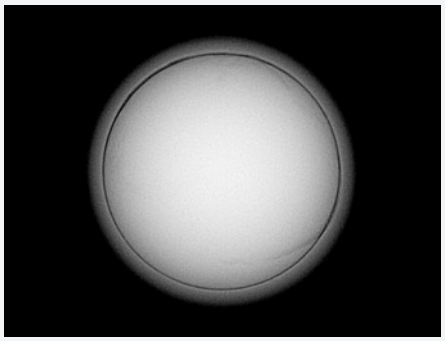

RTX image indicating a bead cultured pearl.

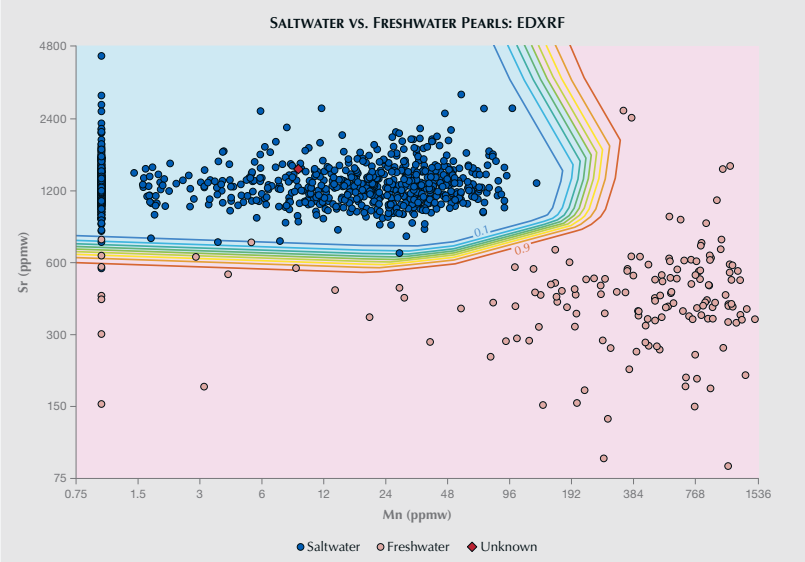

EDXRF chemistry plots identifying a saltwater origin.

3. Microscopic Examination

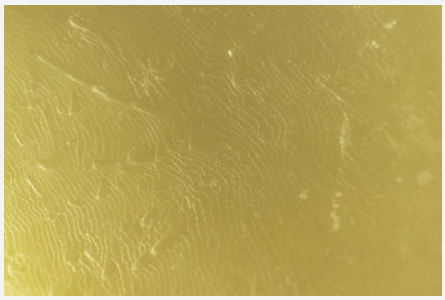

Surface of a Pinctada maxima *pearl; field of view 4.79 mm.*

4. Report Preview

PEARL IDENTIFICATION REPORT

GIA REPORT 0123456789

DETAILS

Shape ..... Round
Bodycolor ..... Strong Orangy Yellow, Natural
Overtone ..... None

RESULTS

Identification ..... Bead cultured pearl
Environment ..... Saltwater
Mollusk ..... Pinctada maxima (gold-lipped pearl oyster)

TREATMENT

No indications of treatment

Item Description: One (1) loose undrilled pearl.
Weight: 6.72 carats
Measurements: 9.81 mm
Comments: This pearl is often referred to as a "South Sea" cultured pearl in the trade, and it falls into the select color range that is known as "golden".
Mollusk identification is an expert opinion based on a collection of observations and analytical data.

In Memoriam

Alan Hodgkinson (1937–2024). The gemological community mourns the loss of Scottish gemologist Alan Hodgkinson, who died in early October at the age of 87 following a brief illness. Known for his extensive use of visual optics in gem identification, Hodgkinson was a jeweler, appraiser, instructor, lecturer, and author.

Alan Hodgkinson, shown teaching the use of the spectroscope in gem identification.

Born in Liverpool in 1937, Hodgkinson began his career as a jeweler after obtaining a gemology diploma from the Gemmological Association of Great Britain (Gem-A). He soon discovered his passion for sharing gemology with others and developed his own coursework, leading gem identification courses in London. The success of the courses led to worldwide lecture and workshop tours, including South Africa, Australia, Asia, Canada, and the United States.

An active member of various gemological associations, Hodgkinson was awarded honorary lifetime memberships to many of them. In 2000, he received the first Antonio C. Bonanno Award for Excellence in Gemology from the Accredited Gemologists Association. He was also the recipient of the Canadian Gemmological Association's inaugural Diamond Award.

Hodgkinson published three books throughout his 50-year career, most recently *Gem Testing Techniques*, which extensively covers 40 years of his research on gem identification using widely available and affordable gem testing equipment.

Hodgkinson will be remembered for his passion for sharing gemology with a broad audience, particularly younger generations. He is survived by his wife, Charlotte, and two daughters. We extend our sincere condolences to his family, friends, and colleagues.

Glenn Lehrer (1953–2024). Renowned gemstone cutter and carver Glenn Lehrer passed away in November at the age of 71 following a battle with cancer. After nearly 50 years transforming stones into incredible works of art, Lehrer will be remembered for his innovative designs and unique carvings, masterfully blending science and artistry in each piece.

Glenn Lehrer next to the rutilated quartz carving "Bahia," created with Lawrence Stoller.

Lehrer discovered his fascination with gemstones after traveling the world extensively in the early 1970s and returning to his native California, when he felt a deep connection to a quartz crystal gifted from his brother. As a self-taught lapidarist and goldsmith, he returned to college to study crystallography, mineralogy, and geology, and earned a graduate gemologist diploma from GIA in 1979.

Inspired by nature, Lehrer was devoted to creating and introducing new designs to the industry, using his own lapidary techniques. Perhaps his best-known design is the patented TorusRing, a gemstone faceted with a hole in the middle to hold another faceted gemstone inside. His groundbreaking creations earned him numerous AGTA Spectrum and Cutting Edge Awards and were featured on the cover of *Lapidary Journal* a record 18 times.

During his career, Lehrer collaborated with other notable artists and designers, including Paula Crevoshay and Lawrence Stoller. Lehrer and Stoller worked for seven years to create the 193 kg (426 lb.) rutilated quartz sculpture "Bahia" (shown in the photo). Widely considered the largest cut crystal in the world, the sculpture has permanently hung in the lobby of GIA's Carlsbad, California, campus since 2003, after being exhibited at the Carnegie Museum in Pittsburgh and the Natural History Museum of Los Angeles.

In later years, Lehrer enjoyed sharing his designs on the television networks Gemporia and QVC. He also penned an autobiography, *In Quest of the Indescribable: The Artistry and Life of a Gem Carver*.

Lehrer is survived by his wife, Sharon, his two brothers, and several nieces and nephews. We extend our heartfelt condolences to Lehrer's family, friends, and colleagues.